Seismic Behavior of Tall Rocking Mass Timber Walls

Sarah Wichman

A dissertation
submitted in partial fulfillment of the
requirements for the degree of

Doctor of Philosophy

University of Washington

2023

Reading Committee:
Jeffrey W. Berman, Chair
Richard Wiebe
Travis Thonstad
Dawn E. Lehman

Program Authorized to Offer Degree:
Civil and Environmental Engineering

University of Washington

Abstract

Seismic Behavior of Tall Rocking Mass Timber Walls

Sarah Wichman

Chair of the Supervisory Committee:
Professor Jeffrey W. Berman
Civil and Environmental Engineering

Mass timber buildings are gaining popularity in the United States and around the world as they offer benefits such as fast construction, unique architectural features, and the use of a sustainable building material. Post-tensioned mass timber rocking wall lateral force-resisting systems have made fully mass timber buildings feasible for high seismic areas. The inherent re-centering behavior of these systems provides an opportunity to design for enhanced seismic objectives, creating a resilient system that exceeds code-minimum performance. Despite these advantages, post-tensioned mass timber rocking wall lateral systems are still relatively new and are thus not currently recognized by United States design codes. While using mass timber post-tensioned rocking wall systems for buildings in the 2-5 story range is gaining popularity in research and in building projects around the world, little research has been completed for these systems in the 6-20 story range.

To demonstrate the resilient capabilities and validate the use of code alternative design procedures for these systems, an integrated experimental and numerical research program was conducted as part of the large, multi-institutional NHERI TallWood Project. The research presented here is a portion of the larger project. First a post-tensioned rocking wall lateral system was designed for a two-story mass timber building that was tested dynamically at full-scale and results were used to validate the proposed numerical modeling methodology. Next, a performance-based design process, including methods for preliminary design and

detailed evaluation with nonlinear response history analysis, was used to design the lateral system for a full-scale 10-story mass timber building. More stringent criteria for interstory drift requirements as well as deformation and force-controlled elements were enforced to target essentially elastic performance under Risk-Targeted Maximum Considered Earthquake (MCE_R) demands. To evaluate the design procedure and numerical modeling methodologies, the building was tested under repeated three-dimensional earthquake records that range from those representing a 43-year return period hazard to those representing MCE_R. This is the tallest building ever tested on a shake table. The outcomes and lessons learned from these tests were used to define a parametric study to investigate wall moment amplification from higher mode effects and make design procedure recommendations for future adoption of this system into building codes. The results of the presented work will help structural engineering practitioners effectively design rocking mass timber wall systems for tall mass timber buildings, provide important experimental and numerical simulation data for eventual inclusion of the system in building codes, and advance the state-of-the-art in earthquake engineering research for mass timber structures.

TABLE OF CONTENTS

LIST OF FIGURES

LIST OF TABLES

ACKNOWLEDGMENTS

I would like to first acknowledge and thank my advisor, Professor Jeffrey Berman. He has been a truly supportive advisor and has always expressed great confidence in my abilities (and oftentimes encourages me to do the same). His guidance and support over the past seven years has been critical to the completion of this work and he has helped me become the researcher that I am today. I would also like to thank Richard Wiebe, Dawn Lehman, and Travis Thonstad for serving on my committee and Tomás Méndez Echenagucia for serving as my graduate student representative. Their guidance was invaluable in helping me navigate through my PhD with numerous experimental delays and the COVID-19 pandemic.

The ground breaking work of completing the world's tallest shake table test would not have been possible without the NHERI TallWood Project Team and collaborators. I extend my gratitude to the large team of professors from around the United States that I have had the pleasure of collaborating with, including John van de Lindt, Andre Barbosa, Shiling Pei, Daniel Dolan, Tara Hutchenson, Arijit Sinha, and Keri Ryan. One of the best parts of working on this project was getting the opportunity to solve challenging problems with numerous industry partners. I would especially like to thank Reid Zimmerman from KPFF and Steve Pryor from Simpson Strong-Tie. The designs presented within this document would not have been possible without their mentorship. I would also like to thank the site staff at the NHERI@UCSD lab and our contractors, Swinerton and Timberlab, for working with me and the team to make the experiments possible. I must also acknowledge and thank the other NHERI TallWood students for their hard work over the many years, throughout design, construction, and testing of the 10-story specimen. A special thanks to Aleesha Busch for being a collaborator, coworker, ally, and friend since day one of two-story construction.

Monetary support from the National Science Foundation (Awards CMMI: 1636164, 1634204, 1635363, 1635227, 1635156, and 1634628) is much appreciated. The use of the shake table facility is supported by the National Science Foundation's Natural Hazards Engineering Research Infrastructure Program. This project was also supported by the US Forest Service through Wood Innovation grants, USDA's Forest Products Lab, and the U.S. Endowment for Forestry and Communities. A full list of the material donors and financial supports can be found at http://nheritallwood.mines.edu/collaboration.html.

I would not have been able to complete my PhD without the help and support from my fellow students at UW. I am so grateful to Dakota Mascarenas whose friendship is one of the best things to come from my time at UW and to Uzo Uwaoma who has been an amazing and reliable in-person office partner in the post-covid era. A special thanks to Andy Sen and Nasser Marafi for showing me how to be an active research student in the department. Finally, thank you to all my fellow office mates and friends of More 236, past and present, particularly: Addie Lederman, Tatsu Sweet, Nicolette Lewis, Kamal Ahmed, Andrew Makdisi, Tom Lin, and Andrew Yang. I am lucky to have learned from such an incredible group of researchers.

On a personal note, I must thank my friends and family for the vital role they played throughout my degree. I will start by apologizing as they all know more about mass timber and the NHERI TallWood group than they would ever care to. Thank you for listening, bringing me joy, and helping me escape from work when I needed the break. Thank you to my twin sister, Laura, for being my biggest fan. Thank you to my older sister, Katie, a fellow PhD, for always understanding how I'm feeling. Thank you to my father for bringing me laughter and compassion whenever I needed it most. Thank you to my mother, my ultimate role model, for showing me how to be strong. Finally, and most importantly, thank you to Chris for believing in me and showing me unbelievable patience. I owe a large portion of this degree to him as it would not have been possible without his love and constant support.

DEDICATION

to Chris

Chapter 1

INTRODUCTION

1.1 Motivation and Background

Urban areas face many competing challenges such as accommodating increasing urban populations, minimizing urban sprawl, and supporting global sustainability to fight climate change. To address these concerns, there is a growing need for 6 to 20 story buildings for residential and commercial use. Steel and concrete are most often the answer for buildings in this height range, however, supplementing or replacing these materials with timber can help create a more sustainable built environment. The embodied energy and CO_2 emissions associated with timber construction are far less than those of steel and concrete construction, as found in many studies. For example, a 40-story reinforced concrete building in Chicago was compared to an equivalent 40-story timber redesign and found the overall carbon footprint of the timber design was 60% to 70% lower than the reinforced concrete building [SOM, 2013].

Traditional light-frame wood construction is not economically or structurally viable at this height range because of its lack of strength and stiffness. However, with developments of engineered wood products such as cross-laminated timber (CLT) and laminated veneer lumber (LVL), tall timber construction is becoming a feasible option. Most mass timber buildings in the United States (US) and other parts of North America are currently constructed with a concrete or steel Lateral Force-Resisting System (LFRS) with a mass timber gravity system or diaphragms. One such example is Ascent MKE (Figure 1.1), currently the world's tallest mass timber building. It is a 284-foot-tall structure located in Milwaukee, Wisconsin. The structure has 19 stories of mass timber residential levels where glulam beams and columns support one-way spanning CLT floors with a gypcrete topping slab on top of a 6-story concrete podium structure for parking and retail. The lateral system consists of

two reinforced concrete cores [Thornton Tomasetti, nd]. Another example is Carbon12, a 85-foot tall condominium and commercial mixed use building in Portland, Oregon with a glulam gravity system. For the lateral force resisting system, it has a buckling restrained braced frame system, including a steel beams and columns core [Kaiser+Path, nd].

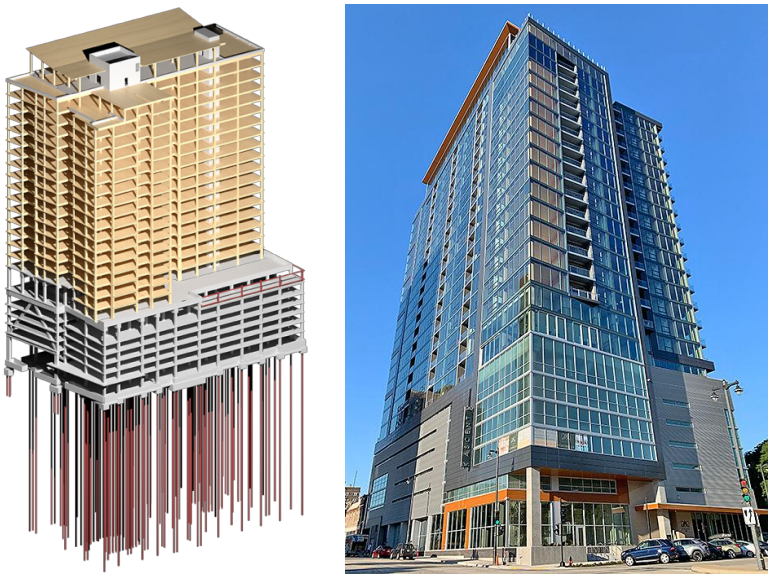

(a) (b)

Figure 1.1: Ascent MKE building (a) schematic and (b) photo [Thornton Tomasetti, nd]

Past research has investigated using mass timber shear walls as the lateral system in areas of high seismicity. Using CLT panels in a conventional shear wall system with mechanical connections has been investigated and shown to be very stiff under small lateral loads but limited in deformation and energy dissipation capacity by the metal connectors [Popovski et al., 2010]. To combat the issues of low deformation capacity and low energy dissipation capabilities, recent research has examined using mass timber walls with unbonded Post-Tension (PT) connections and energy dissipation elements such as U-Shaped Flexural Plates (UFPs). This results in an efficient structural system that can undergo large inelastic displacements while assuring recentering capabilities because of the PT bars and allows for sufficient energy dissipation with the UFPs. Additionally, this system provides the opportunity to improve

upon the usual collapse prevention performance in large earthquakes by developing design methods that enable resilient performance while maintaining an efficient design. The concept of post-tensioned rocking walls for resisting seismic loads was originally developed for precast concrete structures under the Precast Seismic Structural Systems (PRESSS) research program [Priestley, 1991]. Extensive research was conducted on precast concrete rocking wall systems in the 1990s and was codified via ACI ITG 5.1-07 and 5.2-09 [ACI, 2009].

An equivalent timber system was first developed in New Zealand using laminated veneer lumber (LVL). In New Zealand, this concept has grown in popularity and several buildings have been constructed using post-tensioned mass timber walls. For example, The Nelson & Melborough Institute of Technology in Nelson, New Zealand is a three-story timber building with mass timber post-tensioned paired wall lateral force resisting system [Devereux et al., 2011]. Additionally, the Trimble Navigation Building, a two-story building in Christchurch, New Zealand with a post-tensioned timber frames and paired walls [Brown et al., 2012]. Note, all these buildings are shorter and do not fall within the "tall" building range (defined here for mass timber systems to be 6-20 stories).

Although gaining popularity in the United States, post-tensioned rocking mass timber walls are not yet recognized by building codes, making it challenging to implement without advanced design methods such as performance-based design and nonlinear response history analysis that are not commonly used in design offices. The first and only building in the United States with post-tensioned timber walls to date, is the two-story Peavy Building at Oregon State University in Corvallis, Oregon [Sarti et al., 2017]. Additionally, the Framework building was permitted for construction in Portland, Oregon (Figure 1.2). This twelve-story building was designed with a glulam gravity frame and rocking post-tensed CLT shear walls for the lateral system and is the tallest designed and permitted mass timber building in the United States that utilizes a mass timber lateral system [Zimmerman and McDonnell, 2018]. Note, while there is no codified design procedure for this type of lateral system, Busch et al. [2022] has recently proposed a prescriptive design procedure.

Timber construction is becoming a feasible option for high seismic regions and offers

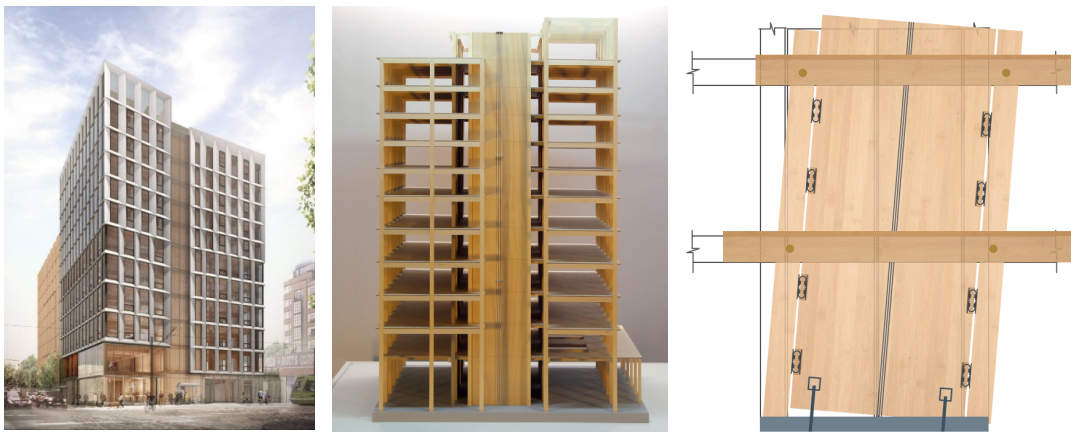

(a) (b) (c)

Figure 1.2: Framework building permitted in Portland, Oregon (a) architectural rendering, (b) photo of scaled physical model, and (c) schematic view of base of one rocking CLT wall for Framework [Zimmerman and McDonnell, 2017]

benefits such as faster construction and the use of a sustainable building materials. However, there is a lack of knowledge with respect to the seismic design and behavior of resilient wood lateral systems and their connections for these buildings. While research has been done in the United States and elsewhere on post-tensioned rocking mass timber systems and buildings have been constructed implementing this system, most of the work has focused on shorter buildings in the 2-6 story range.

1.2 NHERI TallWood Project

The research presented in this document was completed in collaboration with the NHERI TallWood Project, with funding from the National Science Foundation (NSF). The use of the NHERI facility is supported by NSF's National Hazards Engineering Research Institute (NHERI) program. The primary collaborators for this project include University of Washington, Colorado School of Mines, Colorado State University, Washington State University, Lehigh University, and University of Nevada Reno. Other major collaborators are (includ-

ing, but not limited to): KPFF Consulting Engineers (Portland, Oregon), Oregon State University, Simpson Strong-Tie, and University of California San Diego.

The overall vision for the NHERI TallWood Project is to develop a seismic design methodology for tall wood buildings with mass timber lateral systems that incorporates high-performance structural and nonstructural systems and can quantitatively account for building resilience. Key features of the collaboration are: (1) investigative testing at the system level and the holistic building system, (2) structural modeling of tall mass timber buildings considering the contributions of nonstructural systems to the strength and stiffness of the structural system, and (3) development of a resilience-based seismic design methodology that accounts for the building's time to function affect by damage to structural and nonstructural components within the building. This dissertation addresses the work completed for this project, relating to the design, numerical modeling, and testing of lateral force resisting systems for tall wood buildings.

1.3 Research Objectives

The research presented in this document addresses key knowledge gaps on the design and performance of post-tensioned mass timber rocking wall lateral systems that are needed to validate the use of code alternative design procedures for these systems and future adoption into building codes. The specific research objectives are to:

1. Formulate equations for approximating the lateral load response of mass timber rocking walls for paired wall systems and boundary column systems.
2. Demonstrate the resilient capabilities of post-tensioned mass timber rocking wall systems through shake table testing of two large-scale experimental programs.
3. Design and test lateral connections for these systems including embedded epoxy rod connections.
4. Investigate the adequacy of using performance-based design procedures applied to tall

mass timber rocking wall systems through the design, construction, and tri-axial dynamic testing of a full-scale 10-story mass timber building at a range of hazard levels.

5. Develop a nonlinear modeling methodology to simulate behavior of post-tensioned mass timber rocking walls at multiple hazard levels and validate methodology through large-scale shake table tests.

6. Provide recommendations for future code-based design procedures.

1.4 Document Overview

This document describes the comprehensive experimental and computational research program validating the resilient performance capabilities of using post-tensioned mass timber rocking walls in tall mass timber buildings. The remaining chapters are organized as follows:

- *Chapter 2: Literature Review* provides an overview of the research that has led to the rising popularity of mass timber post-tensioned rocking wall lateral systems and an overview of the existing research on mass timber rocking wall lateral systems.

- *Chapter 3: Fundamental Mechanics of Rocking Mass Timber Wall Structures* covers the fundamental mechanics of mass timber rocking wall lateral force resisting systems and behavior information about key individual components in the system. Formulations for approximating the lateral load response of these systems are presented, with emphasis on paired wall systems and single walls with boundary column systems.

- *Chapter 4: Testing of the Two-Story NHERI TallWood Building* explains the design procedure and experimental performance of the post-tensioned rocking mass timber walls used as the LFRS in the two-story NHERI TallWood shake table test. Experimental results are summarized, and a comparison of the predicted performance is presented.

- *Chapter 5: Numerical Modeling of the NHERI TallWood Two-Story Building and Investigation of Foundation Flexibility* presents a nonlinear numerical modeling methodology for post-tensioned mass timber rocking walls. Using OpenSees [Mazzoni et al., 2009], the modeling methodology is validated through comparison with experimental results of the two-story NHERI TallWood building. For numerical and experimental result comparison, the unexpected flexibility in the foundation was included in the model. With the validated model, the effect of the unexpected foundation flexibility on the rocking walls during testing is investigated by adjusting the numerical model to have a rigid foundation boundary condition.

- *Chapter 6: Design and Analysis of the Ten-Story NHERI TallWood Building* presents the characterized hazard used for the design of the full-scale NHERI TallWood ten-story mass timber building and for development of the shake table testing plan. The performance-based design methodology used to design the seismically resilient lateral system (including all lateral connections) that was tested under repeated large hazard ground motions with minimal damage is also presented. A description of the nonlinear numerical OpenSees model used to determine seismic demands for the design of the lateral system as well as other structural and nonstructural components in the building is presented along with performance predictions at multiple hazard levels.

- *Chapter 7: NHERI TallWood Ten-Story Building Testing, Performance, and Comparison of Experimental and Analytical Results* presents the testing plan used for shake table testing of the NHERI TallWood ten-story building. A preliminary assessment of the post-tensioned rocking wall lateral system performance is presented, and the experimental results are compared to the analytical predictions from the OpenSees model.

- *Chapter 8: Effect of Building Period and Wall Aspect Ratio on the Seismic Performance and Moment Amplification of Tall Post-Tensioned Mass Timber Rocking Walls*

presents a parametric study on the performance of tall post-tensioned rocking wall lateral systems. The study focus on quantifying the amplification of wall moment demands from higher mode effects, with respect to the building period and the wall aspect ratio.

- *Chapter 9: Summary, Conclusions, and Future Work* provides a summary of the research program, major conclusions from the experimental and numerical research, and recommendations for future work.

In addition to the chapters outlined above, Appendix A provides detailed calculations for the design of the lateral system and all lateral connections for the NHERI TallWood building. Appendix B includes detailed structural drawings for the NHERI TallWood 10-story building from Busch [2023]. Appendix C provides a detailed table of the full testing plan for the 10-story NHERI TallWood building.

Chapter 2
LITERATURE REVIEW

2.1 Overview

Using post-tensioned mass timber rocking walls as the main lateral force resisting system in buildings located in areas of high seismicity is a relatively new idea in structural engineering, but it builds upon previous research in mass timber and concrete rocking systems. This chapter will review previous studies which the research presented in this document builds upon. The use of mass timber as a building material will first be reviewed, followed by a discussion of traditional mass timber shear wall systems with mechanical connections. Then, significant experimental and numerical work completed on post-tensioned rocking mass timber shear walls will be presented. Finally, a brief discussion on higher mode force amplification effects in rocking systems will be presented.

2.2 Mass Timber as a Building Material

Wood is an orthotropic material with independent mechanical properties in the three orthogonal directions. It is much stronger in the longitudinal, parallel to grain direction than either orthogonal direction perpendicular to grain. Additionally, wood is a natural material subject to constantly changing conditions when growing, such as moisture, soil conditions, and growing space. As a result, the properties of sawn lumber can vary more than most structural materials, making the exact response harder to predict.

Mass timber (sometimes called engineered wood) is a relatively new building material that can be used to supplement or replace more traditional building materials such as steel or concrete. These products are manufactured by fixing either solid sawn lumber laminations or structural composite lumber (SCL) laminations together. SCL is a family of engineered

wood products made by layering wood veneers, strands, or flakes to blocks of materials know as billets. Plywood and orientated strand boards (OSB) are examples of well-known SCL products. Structural adhesives, nails, or dowels are commonly used to join the laminations. By laminating either swan lumber or SCL products to form mass timber, a stronger and more versatile product than traditional sawn lumber is created. Additionally, alternating grain directions between the laminations provides increased dimensional stability. Mass timber can take the form of a panel product that can be used for load-bearing walls and floors or can take the form of beams and columns that can be used in a load-bearing gravity system. Later on in this section, a mass timber product made of sawn lumber (cross-laminated timber in Section 2.2.3) and a product made of SCL (mass plywood panels in Section 2.2.4) will be discussed in detail.

The dimensional limits for mass timber products are defined by the manufacturing capabilities of the supplier as well as transportation restrictions. These products are often cut to size by the mass timber manufacturer. Additionally, many manufactures are now equipped with CNC machines so manufacturers or third party CNC companies are capable of making more intricate cutouts and fastener holes can be precisely pre-drilled into the members. This allows for some of the more challenging prefabrication cutting, drilling, and connection installation to occur off the construction site. The prefabrication capabilities that come with mass timber construction can result in more efficient, simpler, and faster on-site construction.

In addition to faster construction times, mass timber products are often lighter than their comparable steel or concrete counterparts. They also offer a unique architectural design feature that is desirable for building owners as well as building occupants [WoodWorks, 2022]. Another benefit of mass timber is the inherent sustainable nature of the product which will be discussed in more detail in Section 2.2.1.

Note, only cross-laminated timber (CLT) and mass plywood panels (MPP) will be discussed in detail in this section because they were the focus of the research presented in this document. However, many other mass timber products exist, but wont be discussed in detail as they are not commonly used for mass timber shear wall lateral systems. Products such

as glue laminated timber (glulam) and laminated veneer lumber (LVL) are more commonly seen for beam and column members. Other panel products such as glue laminated timber (GLT), nail laminated timber (NLT), and dowel laminated timber (DLT) are not commonly used for shear walls as they do not have the ability to resist in-plane shear because they lack the cross laminations of CLT and MPP (see Section 2.2.3). Typically, plywood or oriented strand board sheathing attached to one face of these panels is needed for in-plane shear capacity when used in diaphragms [WoodWorks, 2022].

2.2.1 Sustainable Nature of Mass Timber Products

The sustainable nature of mass timber is one of the primary factors driving the demand for mass timber buildings. To create a mores sustainable built environment, the choice of primary structural material matters, and wood is a natural and renewable resource that is said to be carbon negative. Timber stores carbon and has the least embodied energy of all major building materials so it requires less energy to harvest, transport, manufacture, maintain, dispose of, and recycle [WoodWorks, 2022]. According to the EPA's Inventory of US Greenhouse Gas Emissions and Sinks (1990-2013), carbon dioxide emitted from from iron, steel, and cement production are the first and second largest sources of industrial carbon dioxide emissions in the United States. Additionally, concrete and steel production for building use emits more carbon dioxide than lumber by a factor of 8 and 21, respectively [Freres Engineered Wood, 2022].

The sustainability of mass timber construction in North America is dependent on the sustainability of the forest practices from which the wood was obtained. In North America, the forests from which the wood for mass timber is obtained comes from sustainably managed forests that utilize active forest management practices and meet North American certification requirements. These active management practices mitigate wildfires, expand wildlife habitat, and create jobs in rural areas. According to Edie Sonne Hall, a deforestation Forestry expert, current forest certification practices have shown to ensure harvesting methods that support water quality, biodiversity, and habitat sustainability [WoodWorks, 2022]. One concern with

the increase in mass timber buildings is if supply of timber can be maintained long term. However, increased demands for mass timber products can incentivize forest land-owners to keep their lands instead of converting to urban development. Hall also argues that increased timber demands actually lead to more forests WoodWorks [2022].

2.2.2 Case for Tall Timber Buildings

Rapid population growth is increasing demands on the built environment and there is pressure to deliver more sustainable solutions to accommodate increased population density. While the many previously mentioned benefits are driving the mass timber industry, there is also a push for not just mass timber construction but also tall mass timber construction [WoodWorks, 2022]. A result of recent advancements in mass timber technology and research, mass timber provisions have recently been accepted in to the 2021 International Building Code (IBC). The 2021 IBC includes three new construction types that are defined based on story height and requirements regarding fire-resistance ratings. These are based on the previous Heavy Timber construction type (Type IV is now Type IV-HT), but with more fire-resistance restrictions. With the new code provisions, mass timber buildings are permitted up to 18-stories but require strict non-combustible protection of all mass timber elements in the building. There are different requirements for shorter buildings, allowing for more exposed elements [WoodWorks, 2022].

These developments have been driven by past research highlighting the potential for tall mass timber buildings. MGA [2017] created a technical report highlighting the potential for mass timber buildings. Their study showed that with growing populations there is an increasing demand for taller buildings. In the past, steel and concrete have been used and there has been no reason to challenge the use of those materials. However, with climate change a switch needs to be made to make buildings more sustainable. It was stated that concrete production represents roughly 5% of the worlds carbon dioxide emissions, more than five times the carbon footprint of the airline industry as a whole. The report argues that when harvested responsibly, wood is one of the best tools for engineers and architects to

reduce greenhouse gas emissions in the construction of buildings. In this study, MGA [2017] show that 10 to 30 story buildings can be achieved using the new mass timber techniques. This was shown through presenting conceptual design solutions that with time and additional design and engineering can become a reality. The study shows how mass timber structures can meet relevant structural design criteria and fire and life safety needs and it can do so in a cost competitive marketplace.

In addition, MGA [2017] introduces a new design concept called Finding the Forest Through the Trees (FFTT) to assist in shifting the way we approach building construction. The system has been engineered to address the seismic codes for markets in Vancouver, BC. The system consists predominately of wood with a solid wood central elevator core and wood floor slabs. Steel beams provide the ductility and concrete is used for the below grade areas.

MGA [2017] also conducted a cost analysis comparison on a 12-story and 20-story mass timber building. For this study concrete construction was used as the benchmark building and fire protection techniques were taken into account in the analysis. Costs were estimated based on the presented preliminary design drawings and results concluded that with development and evolution of the FFTT buildings, there could be a significant reduction in construction costs for this type of system. Finally, MGA [2017] found that it is possible to design tall timber buildings with the FFTT system that are equivalent to concrete structures and this can be achieved through facilitating additional research with structural analysis studies, structural testing, fire assessment, etc.

2.2.3 Cross-Laminated Timber

CLT is a mass timber panel product, originally developed in Austria in the mid-1990's. After being widely used in Europe, it has gained popularity in the United States and is currently considered one of the most well known and widely used mass timber products in the United States [FPInnovations, 2013]. As shown in Figure 2.1a, it consists of multiple layers (called plys) of kiln-dried dimensional lumber. The dimensional lumber in each layer is orientated such that the grains are orthogonal to the adjacent layers. CLT typically has

an odd number of layers, (three, five, seven, and nine-ply are the most common), resulting in parallel orientation of the two outer-most layers. The layers parallel with the outer-most layers are referred to as the longitudinal layers and the other layers are the transverse layers.

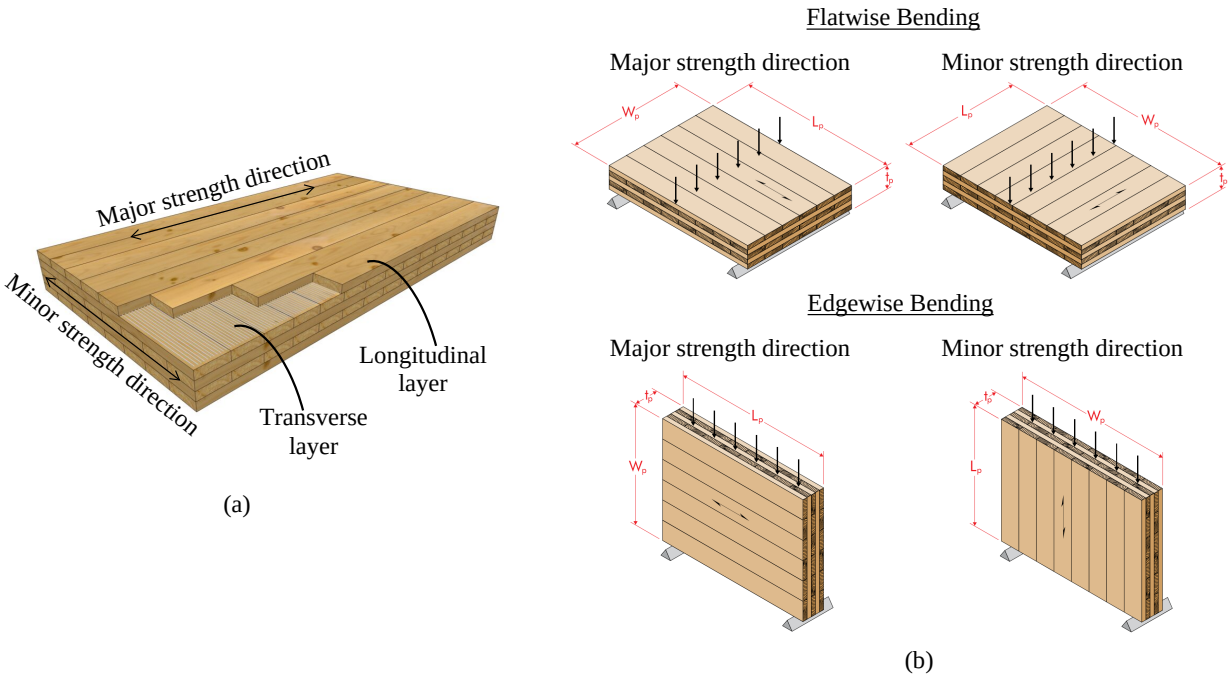

Figure 2.1: CLT (a) panel configuration (figure adopted from Mass Timber Map [2023]) and (b) bending orientations (figure adopted from APA [2019b])

The lumber is kiln dried prior to assembly to prevent dimensional variations and surface cracking. Between each layer, a layer of structural adhesive is used to adhere the layers together. The total assembly process can take 15 to 60 minutes and starts by selecting lumber and grouping them into layers for planing. The layers are then set up and pressed with a hydraulic press. After pressing, the panel product is cut and the surface is machined and marked for packaging [FPInnovations, 2013].

Because CLT layers are orientated perpendicular to each other, CLT panels exhibit relatively high strength and stiffness in both in-plane directions, resulting in two-way action

capabilities, similar to a concrete slab. However, because lumber is significantly stronger in the parallel-to-grain direction, the direction of the longitudinal layers is slightly stronger and thus called the major strength direction, while the other direction is referred to as the minor strength direction (see Figure 2.1b). The resulting product typically has orthogonal properties that are more similar to each other than with sawn lumber, but the general response is still similar to that of sawn lumber since one direction is typicall stronger than the other [He et al., 2018]. Additionally, in accordance with APA standards, longitudinal boards must have a minimum grade of 1200f-1.2E MSR or visual grade No. 2, while transverse boards have a lower minimum grade limit of visual grade No. 3, further emphasising the major and minor strength direction names APA [2019b]. This two-way action differs from other mass timber panel products such as laminated veneer lumber (LVL) or glue laminated timber (glulam/GLT) or even more so with nail laminated timber (NLT) or dowel laminated timber (DLT).

In 2012 a CLT product standard was developed and published by the American National Standards Institute and the Engineered Wood Association, ANSI/APA CLT standard Committee, called APA PRG 320 [APA, 2019b]. In 2013, FPInnovations, a nonprofit Canadian organization that conducts scientific research for the forest industry, released a CLT handbook that summaries the design and construction procedure for CLT markets in the US and Canada [FPInnovations, 2013]. In 2015, CLT was Incorporated into the NDS, allowing CLT to be recognized as a code complaint construction material [AWC, 2018].

2.2.4 Mass Plywood Panels

MPP, sometimes called Mass Ply, is a newer mass timber panel product originally created by Freres Lumber [Freres Engineered Wood, 2022]. In MPP thin wood veneers are layered, glued, and pressed together to form 1 inch layers called lamellas as shown in Figure 2.2. A variety of combinations and orientations of the veneers can be made, creating panels with different strengths in different directions, similar to CLT. This product has been certified under ASTM D5456 (for LVL products) and PRG 320 (for CLT products) and can thus be

used as a substitute for CLT.

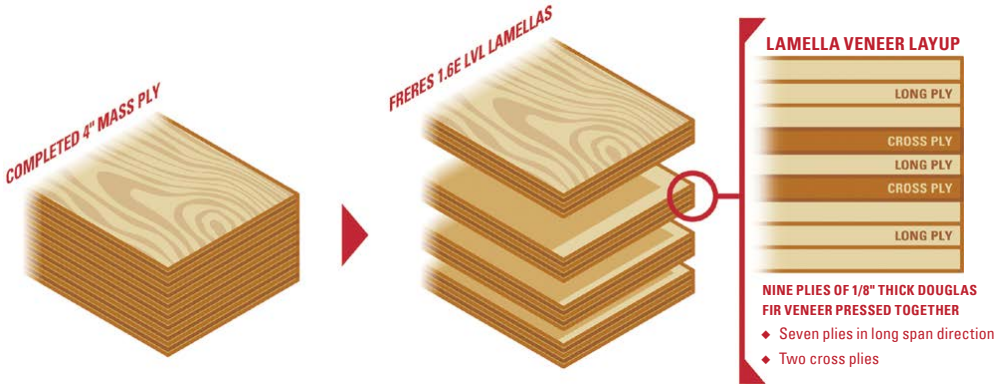

Figure 2.2: Example of MPP panel configuration: shows the Freres F16 Mass Ply Layup [Freres Engineered Wood, 2022]

The strength and stiffness of MPP is larger and typically performs better by volume, relative to other mass timber products. Additionally, because MPP is made of thin veneers, any defects in the wood are distributed throughout the product, resulting in increased dimensional stability with lower moisture content. The thin veneers of MPP also allows for smaller increments of member thickness, thus, saving in overall cost of material, in comparison to other mass timber products [Freres Engineered Wood, 2022].

MPP is considered to be more environmentally efficient in comparison to CLT and other sawn lumber mass timber products. One of the main reasons this is true is because MPP manufacturing results in significantly less wood waste than CLT [Freres Engineered Wood, 2022]. Cutting a piece of rectangular dimensional lumber from a log (needed for CLT) results in a large amount of waste, whereas almost all the wood in a log can be used when creating thin veneers. Additionally, sawn-lumber based products require larger diameter logs than comparable SCL products, making the manufacturing process for MPP more flexible. Less energy is also required to dry smaller logs [Freres Engineered Wood, 2022].

2.3 Fixed Base Mass Timber Shear Walls

Using mass timber for the main lateral force-resisting system of a building in a seismic region is a relatively new concept in comparison to other structural systems. This section will summarize major research completed on traditional mass timber shear walls with a fixed base connection.

2.3.1 Dujic et al. [2006]

One of the first experimental tests studying the lateral resistance of CLT panels was conducted at the University of Ljubljana in Ljubljana, Slovenia by Dujic and Zarnic [2006]. In this study, different anchoring systems were tested under monotonic and cyclic horizontal load in combination with constant vertical load to study the influence of the anchoring systems on the shear stiffness and strength of the CLT wall panels as well as the overall performance. Figure 2.3 shows the three different boundary conditions tested in this study. They were as follows: Case A) a shear cantilever mechanism where the base is fully connected and the top is free to rotate and translate; Case B) a condition where the base is also fully connected and the top is free to translate without rotation; and Case C) a condition where the base is fully connected and the top is restrained only against rotation. Results showed that boundary conditions had a significant impact on the lateral resistance of the panels. Results also showed that the load bearing capacity of the wall was governed by the anchors connecting the panels to the building foundation.

Dujic and Zarnic [2006] also constructed two full-scale models and tested them on the shake table at the IZIIS Laboratory in Skopje, Macedonia to validate the cyclic test results discussed above and to make a correlation between the results. Two single-story box CLT wall assemblies were tested. Specimen 1 consisted of two one-unit wall elements and specimen 2 consisted of two wall elements of half width screwed together. The panels were anchored to the RC foundation through a series of ribbed angle irons. A series of dynamic tests were performed on both specimens to investigate wall behavior under dynamic conditions.

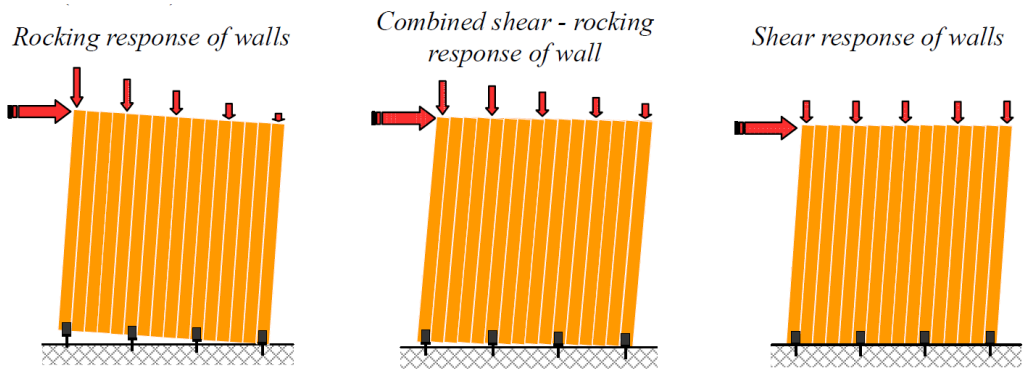

Figure 2.3: Boundary condition configurations tested in Dujic and Zarnic [2006]

Maximum accelerations reached 0.6g for specimen 1 and 0.5g for specimen 2. Results showed that the anchorage connections were the main source of nonlinearity in the system and energy dissipation. In addition, both systems behaved as expected and saw no visible damage. In the end, test results showed that the system exhibited very ductile behavior and there was good correlation to the cyclic testing presented above.

2.3.2 SOFIE Project

The SOFIE project was carried out by the IVALSA Institute of the Italian National Research Council with the support of Trento Province of Italy. The overall project consisted of connection tests [Gavric et al., 2012], CLT panel shear wall tests [Lauriola and Sandhaas, 2006], and several full-scale shake table building tests [Ceccotti et al., 2013].

Gavric et al. [2012] performed tests on different base connections with the overall goal of providing a better understanding of the performance of these connections during seismic events. In-plane monotonic and cyclic shear tests were performed on different configurations of screwed connections between CLT panels. Configurations included, parallel wall to wall, perpendicular wall to wall, floor to floor, and wall to floor details. Properties such as strength, stiffness, energy dissipation, and ductility were all evaluated. In addition, overstrength factors were determined as they had not been studied for CLT walls before. Defined as the

ratio between the 95^{th} percentile of the connection strength distribution and the analytical prediction of the design connection strength, overstrength values ranging from 1.2 to 1.9 with an average value of 1.74 were determined. Results of these tests also provided insight on spacing, edge distances, and panel thickness that are required to prevent brittle failure. It was also determined that the screw head penetration was more critical than the withdrawal of the screw from the panel.

Within the SOFIE project, Lauriola and Sandhaas [2006] performed quasi-static in-plane cyclic tests on CLT walls and pseudo-dynamic tests on a full-scale building. The quasi-static tests looked at the influence of the uplift and shear anchoring systems, the opening layout within a panel, the magnitude of vertical loads, and the inter-story connection. Test results showed that stiffer hold-down connections lead to higher lateral load carrying capacity, lower ultimate displacement, and a less ductile behavior. Overall, it was determined that connection joints strongly influence system behavior and forces concentrate at small regions in the timber, leading to the failure shown in Figure 2.4. Lauriola and Sandhaas [2006] also conducted pseudo-dynamic tests carried out on a single story specimen. Three different opening layout configurations were tested and two earthquake motions were applied at two different peak ground accelerations. Results showed that the walls were stiff and the connections provided ductility. Figure 2.5 shows the resulting pinched hysteric behavior from the three opening configurations under the same earthquake motion.

Also apart of the SOFIE project, Ceccotti et al. [2013] conducted 3-story and 7-story shake table tests. Both buildings were designed according to the European seismic standard, Eurocode 8. The full-scale 1D tests on the 3-story test specimen made of CLT was performed at the NIED shake table in Tsukuba, Japan. The specimen was designed according to the simplified lateral force procedure in Eurocode 8 with a peak ground acceleration of 0.35g, representative of the most hazardous seismic region in Italy. Eurocode 8 uses a behavior factor, q, in the design procedure which is equivalent to the response modification factor, R, used the US code, ASCE 7-10. Ceccotti et al. [2013] defied q as $PGA_{near-collapse}$ / PGA_{design}, where $PGA_{near-collapse}$ is the peak ground acceleration recorded at the defined near-collapse

(a) (b)

Figure 2.4: Localized failure in quasi-static cyclic tests [Lauriola and Sandhaas, 2006]

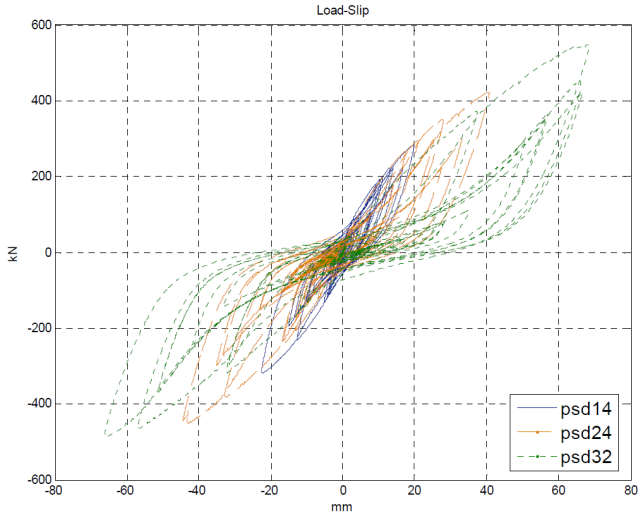

Figure 2.5: Response of the three configurations from the Kobe earthquake with a 0.5g PGA [Lauriola and Sandhaas, 2006]

state, and PGA_{design} is the design peak ground acceleration which was equal to 0.35g in this test. For the design of the 3-story test specimen, $q = 1.0$ was used, meaning it was designed to be purely elastic and ignored overstrength and energy dissipation. Three different floor plan configuration were tested in which the last was not symmetric. The specimen was then exposed to 3 different ground motion events with varying peak ground accelerations. For the third floor plan configuration, a near-collapse peak ground acceleration, $PGA_{near-collapse}$, of 1.20g was observed. This resulted in $q = 3.4$ which was rounded to $q = 3$, showing relatively good energy dissipation and ductility. In the end the building did not collapse and did not sustain significant residual drifts.

Ceccotti et al. [2013] then used $q = 3$ to design the 7-story test specimen (Figure 2.6). The wall to floor joint connections were designed based on the design shear forces per story and consisted of hold-downs, angle brackets, and self-drilling screws. During this test, only one configuration was tested and fewer earthquakes were applied. For each ground motion, the larger earthquake component was applied along the longer, y-direction, and the smaller component was applied along the shorter, x-direction, of the building. The specimen in the 7-story tests in Ceccotti et al. [2013] remained upright and only easy-to-repair damages, such as tightening loose hold-downs and replacing bent and sheared screws, were necessary. The errors in measured maximum story shears and design values from Eurocode 8 ranged between 20% and 25%. These are considered acceptable levels which validate the force-based approach from Eurocode 8 for the design of these CLT specimens. Outcomes from both tests by Ceccotti et al. [2013] showed that the buildings demonstrated recentering capabilities with high stiffness and sufficient ductility to prevent brittle failure.

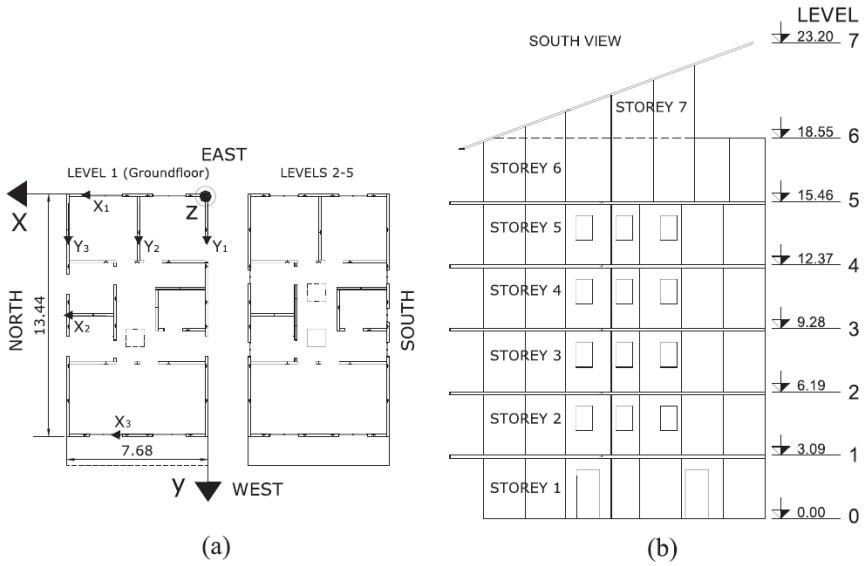

Figure 2.6: (a) Plan and (b) Elevation view of the 7-story test specimen tested in Ceccotti et al. [2013]

2.3.3 Popovski et al. [2010]

Research on the seismic behavior or CLT systems in North American was initiated by FPInnovations to address the moderate seismicity in British Colombia, Canada. Popovski et al. [2010] tested a total of 32 shear walls under monotonic and cyclic loading. All panels were 3-ply European spruce CLT panels. A total of 12 different configurations, both one and two stories, were tested. One story specimens had aspect ratios of either 1:1 or 1:1.5. Two story specimens had aspect ratios of 2.1:1 and were made of either a single panel or two 1:1 single story panels. Four different types of brackets, as shown in Figure 2.7, were used for connecting the CLT walls to the foundation. Two of the brackets (Brackets A and B) were commercial Simpson Strong-Tie brackets that are commonly used in Europe and the other two brackets (Brackets C and D) were custom brackets that accommodated timber rivets. Some panel configurations also included the use of hold-downs with nails at the ends of the wall.

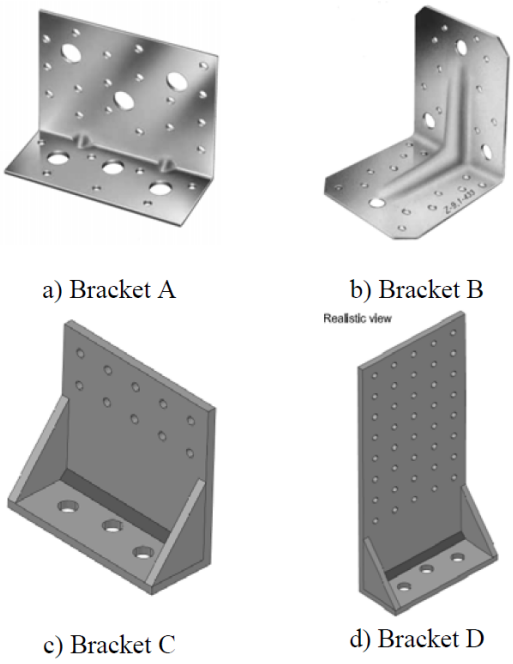

Figure 2.7: Four different brackets tested for the CLT walls Popovski et al. [2010]

Walls were loaded vertically with either a 10 $\frac{kN}{m}$ load to represent the wall being at the bottom of a two story structure, or a 20 $\frac{kN}{m}$ load to represent the wall being at the bottom of a four story structure, and were loaded horizontally using a 110 kN hydraulic actuator. Results from the tests showed that the panels behaved almost rigidly with very small shear deformations measured, while majority of the deformations occurred at the joints connecting the wall to the foundation. As seen in Figure 2.8, connections with spiral nails exhibited bearing failures combined with withdrawal, while ring nails mainly saw withdrawal failures with small chucks of wood breaking away. Connections with timber rivets experienced fastener pull-out combined with with wood shear plug failure as seen in Figure 2.9 (a). With increased spacing, the desired failure mode of rivet yielding was observed, as seen in Figure 2.9 (b).

Results from Popovski et al. [2010] showed that CLT wall panels have adequate seismic performance for low ductility demand applications in regions of moderate seismicity and

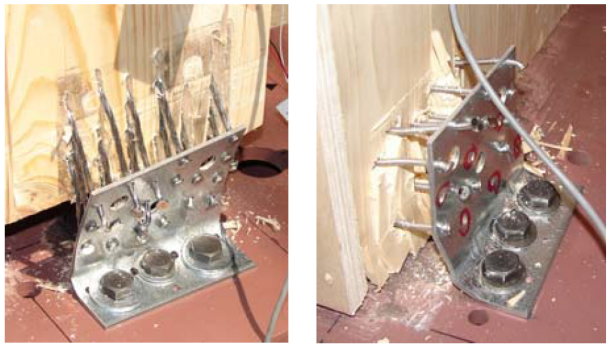

Figure 2.8: Failure modes of the bracket connection for (a) spiral nails and (b) ring nails Popovski et al. [2010]

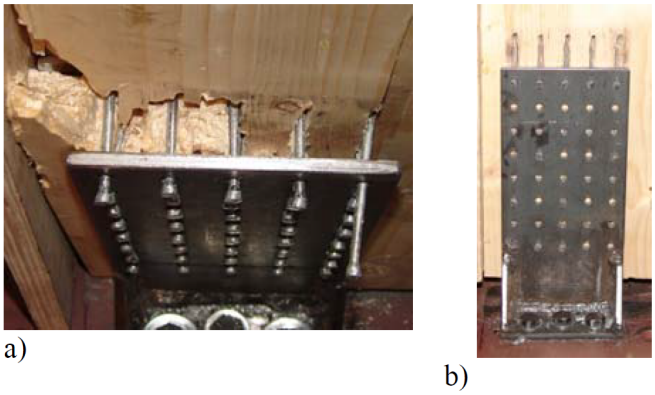

Figure 2.9: Timber rivet failure in brackets (a) showing undesired failure, and (b) showing the desired rivet yielding Popovski et al. [2010]

that the bracket connections are the main source of ductility in the system. The wall panels that used either screws or nails had similar strength capacity, but the screw connections lost strength faster. However, the walls with timber rivets showed a higher capacity than both the nails and the screws and these specimens also saw higher stiffness. Finally, the specimens with hold-downs on the ends showed the highest stiffness and ductility capacity.

2.3.4 FEMA P695 Study of Collapse Capacity

CLT seismic force-resisting systems are not currently recognized by US design codes, thus, they must be designed using code alternative design methods. This can be costly and can result in a less competitive system because it is less accessible. Thus, in collaboration with USDA Forces Service, van de Lindt et al. [2022] conducted a study to investigate the seismic behavior of CLT shear wall systems and to determine seismic performance factors. This study focused on determining the response modification factor, R, and the deflection amplification factor, C_d, using the FEMA P695 procedure. This study consisted of connector tests, quasistatic cyclic tests on isolated shear walls, and numerical analyses. Connector tests were conducted using generic connectors to facilitate building code recognition. These tests revealed that thinner connectors are needed to achieve a desirable ductile behavior. Quasistatic cyclic tests were completed on several CLT shear walls. The following conclusions were drawn from the tests:

- CLT behaved rigidly with energy dissipation concentrated at the base connections
- Boundary constraints and gravity loading were found to have beneficial effect on wall performance (i.e., higher strength and larger deformation capacity)
- Specific gravity effected wall behavior, but CLT thickness was not as influential
- High aspect ratio panels had lower stiffness and larger deformation capacity
- Multipanel configurations with high aspect ratio panels and vertically connected joints had larger deformation capacities

Using test results, a design procedure was developed. A series of archetype buildings were then designed, modeled, and numerically evaluated using nonlinear static and dynamic analyses. Results showed that a value of $R = 3$ can be used for CLT shear walls with a 2:1 aspect ratio or mixed 2:1 with 4:1. A value of $R = 4$ can be used for high aspect ratio walls (i.e., 4:1). For the $R = 3$ case, the average overstrength factors ranged from 2.29 to 3.53. For the $R = 4$ case, the average overstrength ranged from 2.02 to 4.03. A value of $\Omega_o = 3$ was recommended from this study for both cases. Additionally, consistent with the FEMA P695 recommendations, the study recommends using $C_d = R$ for design.

2.4 PRESSS Program

The concept behind post-tensioned mass timber rocking walls was inspired by work completed with post-tensioned concrete rocking systems. This section will recap the first program to introduce post-tensioned rocking systems called: Precast Seismic Structural Systems (PRESSS). Note that extensive research has been completed on these concrete rocking systems, including post-tensioned concrete rocking walls. This rocking system has also been applied to steel systems, but will not be discussed in detail in this document.

The PRESSS Program, coordinated by Priestley [1991] was a combined research program between the United States and Japan on the seismic design and performance of precast concrete structural systems. The goal of the project was to develop an effective seismic structural system for precast buildings, called the hybrid system, and to make design recommendations for incorporation into building codes. The hybrid system is summarized in Figure 2.10a. The unbonded tendons provide recentering capabilities for the system as seen in the nonlinear elastic hysteresis in Figure 2.10b. However, a system with unbonded tendons alone dissipates little to no energy so mild steel energy dissipating devices are added to provide the energy dissipation needs as shown by the damping hysteresis in Figure 2.10b. The resulting hysteretic behavior for the hybrid system with recentering capabilities as well as energy dissipation abilities can be seen in the third hysteresis in Figure 2.10b. This concept can be applied to beam-column connections and shear walls.

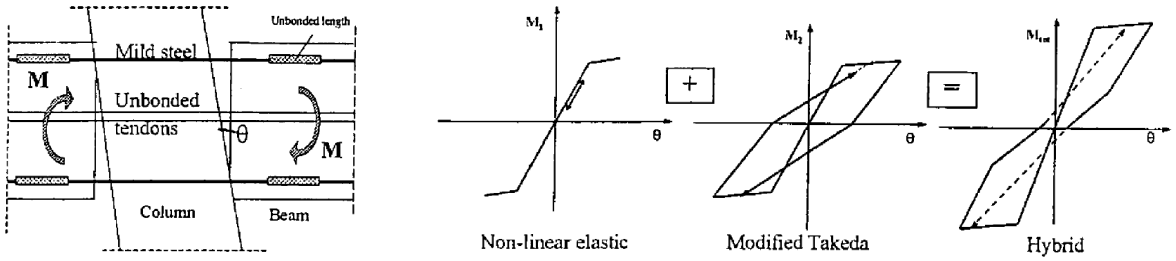

(a) Rocking motion of connection (b) Hysteretic behavior

Figure 2.10: Beam-column hybrid joint from the PRESSS program [Pampanin et al., 2001b]

Kurama et al. [1999] characterized the behavior of the hybrid system and developed a performance-based seismic design approach in which the walls are required to resist design level ground motions with little damage and resist larger earthquakes with more damage but without failure. The behavior of the system was characterized into four states shown in Figure 2.11: 1) decompression state, defined by the initiation of a gap opening along the horizontal joint between the wall and the foundation; 2) softening state, defined by the beginning of significant reduction in lateral stiffness due to the gap opening; 3) yielding state, defined by the point at which the post-tensioning steel reaches it's yield limit; and 4) failure state, identified by axial-flexural failure of the wall which occurs as a result of concrete crushing.

Kurama et al. [1999] then uses the four behavior states to create design objectives and design criteria for the proposed seismic design approach. Figure 2.12a shows the three design objectives. The three design objectives are: 1) immediate occupancy performance under a low level earthquake where limited damage occurs in the structural and nonstructural elements; 2) life safety performance under a design-basis earthquake where significant damage is made but some margin against total or partial collapse remains; and 3) collapse prevention under a survival level ground motion where the building is on the verge of collapse. Figure 2.12b shows the design criteria for the proposed seismic design approach where force and

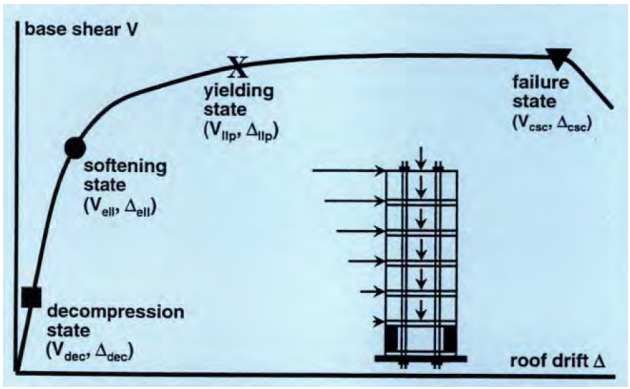

Figure 2.11: Base shear versus roof drift relationship for an unbounded post-tensioned wall with the four behavior states identified [Kurama et al., 1999]

displacement capacities are computed for the wall that exceed estimated demands.

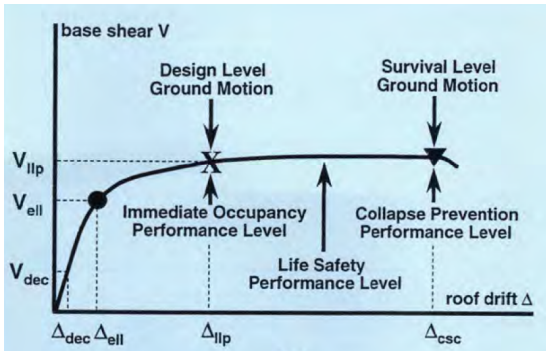

(a) Design objectives

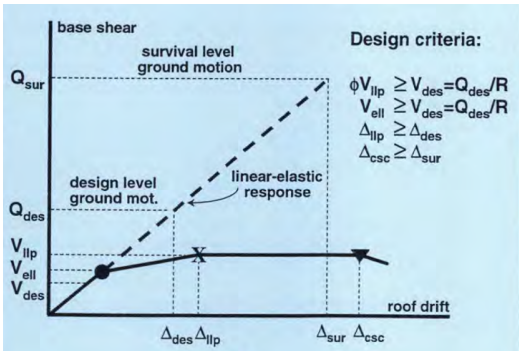

(b) Design criteria

Figure 2.12: Proposed seismic design approach [Kurama et al., 1999]

To validate the seismic design procedure, Kurama et al. [1999] designed six 6-story prototype walls using the design procedure. The prototypes were subjected to more than 200 nonlinear dynamic time history analyses using 15 design level and 15 survival level ground motions. Results showed the desired flag shaped hysteretic behavior with self-centering capabilities and high amounts of energy dissipation. It was concluded that the unbonded PT

hybrid system for precast walls can provide a more desired behavior than typical monolithic concrete shear walls in seismic regions.

Pampanin et al. [2001b] expanded on the work done by Kurama et al. [1999] and further developed the design procedure for the hybrid rocking walls. Pampanin et al. [2001b] developed a section analysis method that can be used with precast members through an analogy with an equivalent cast-in-place solution called the "cross-sectional analysis procedure". The result of the cross section procedure provides a moment-rotation response for the ductile connections. The steps of the procedure are as follows: 1) fix the rotation θ; 2) guess the initial neutral axis depth c for the beam; 3) evaluate the strain in the unbonded PT tendons; 4) estimate the strain in the mild steel and concrete; and 5) section equilibrium to determine a the new neutral axis depth c. As part of step 4, a second procedure called the "monolithic beam analogy" was defined to solve the problem of strain compatibility where the neutral axis position, c and the strain in the concrete, ϵ_c are both unknown. Pampanin et al. [2001b] defines the procedure by relating the local parameters of the rocking wall to the local parameters of an equivalent monolithic wall by equating the global behavior of each wall as seen in Figure 2.13.

Pampanin et al. [2001b] validated the proposed procedure with experimental data from beam-to-column hybrid assembly tests from Stanton et al. [1997]. The connections were $\frac{1}{3}$ scales with PT steel at the center of the section. During tests, the PT steel did not yield or fracture leading to failure. Failure was typically from fracture of the mild steel energy dissipation devices. Results showed satisfactory agreement between the analytical and experimental results, verifying the suggested methodology.

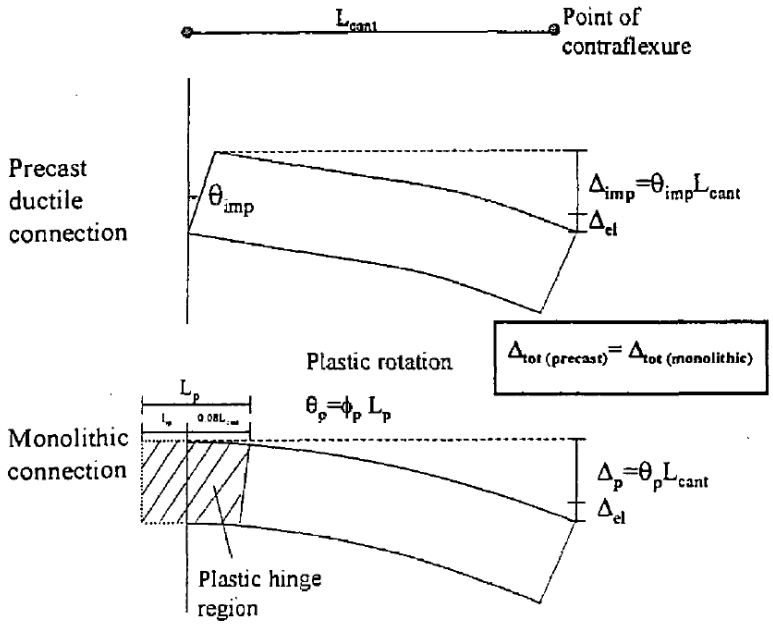

Figure 2.13: Monolithic beam analogy from [Pampanin et al., 2001b]

2.5 Mass Timber Base Rocking Systems

In recent research, the hybrid base rocking system from PRESSS has been applied to timber structures to create a sustainable building system. This section highlights some of the significant research projects focusing on timber structures with base rocking systems.

2.5.1 Palermo et al. [2006]

Post-tensioned mass timber rocking walls were first developed and tested a the University of Canterbury in Christchurch, New Zealand [Palermo et al., 2006]. Developed based on the PRESSS research program, these were some of the first tests and studies completed on the performance of timber lateral systems under seismic loading. In these tests, laminated veneer lumber (LVL) was used. Palermo et al. [2006] performed experimental cyclic quasi-static and pseudo-dynamic tests on connections in two systems. One system with only unbonded PT

bars and one system with hybrid connections that included both unbonded PT bars and a type of energy dissipator. First, quasi-static cyclic tests were performed on three wall-to-foundation hybrid specimens. Figure 2.14 shows the general test setup for the specimens. The first two specimens (HY1 and HY2) had internal dissipators while, the third specimen (HY3) had external dissipators. The PT bar force verses drift response for HY1 can be seen in Figure 2.15 (a) and the top lateral applied load verse drift response for HY1 can be seen in Figure 2.15 (b). During the tests, no visible wall damage occurred on specimens HY1 and HY2 at their peak drifts of 3.5% and no visible wall damage occurred on specimen HY3 at it's maximum drift of 4.4% drift. In addition, no PT bar yielding was observed during any of the three tests. Tests HY1 and HY2 were ended at smaller drifts due to buckling failures of the energy dissipation devices at 3.5% drift.

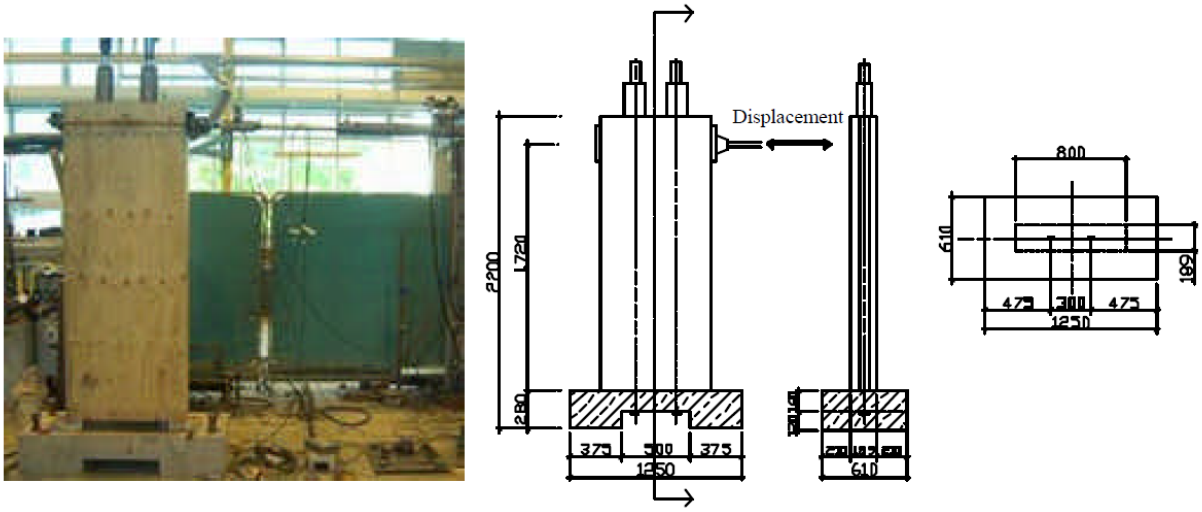

Figure 2.14: Test setup and geometry details for quasi-static cyclic tests on wall-to-foundation connections [Palermo et al., 2006]

Palermo et al. [2006] also conducted pseudo-dynamic cyclic testing on pure unbonded (without energy dissipators) post-tensioned walls. The effect of three different levels of initial post-tensioning (0.2, 0.3, and 0.4 f_{py}) was tested and the PT bar force verse drift response

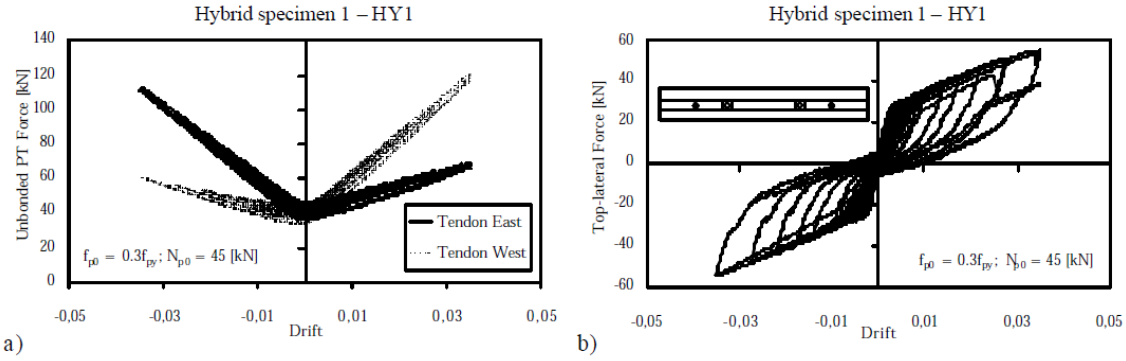

Figure 2.15: (a) Un-bonded PT force verses drift and (b) lateral force vs. drift for hybrid specimen 1 - HY1 [Palermo et al., 2006]

is shown in Figure 2.16. Tests showed that increasing initial PT forces increased the drift at which yielding occurs. More specifically, ranging from an initial PT force of $0.4f_{py}$ to $0.2f_{py}$ correlates to a reduction of 30% in terms of maximum drift demand. Overall, the research conducted by Palermo et al. [2006] showed that mass timber rocking wall systems result in enhanced seismic performance with little to no structural damage and a flag shaped hysteretic behavior that shows self-centering and energy dissipating capabilities. Note, internal and external dissipators resulted in similar performance, but external dissipators may be preferred as they are easier to replace.

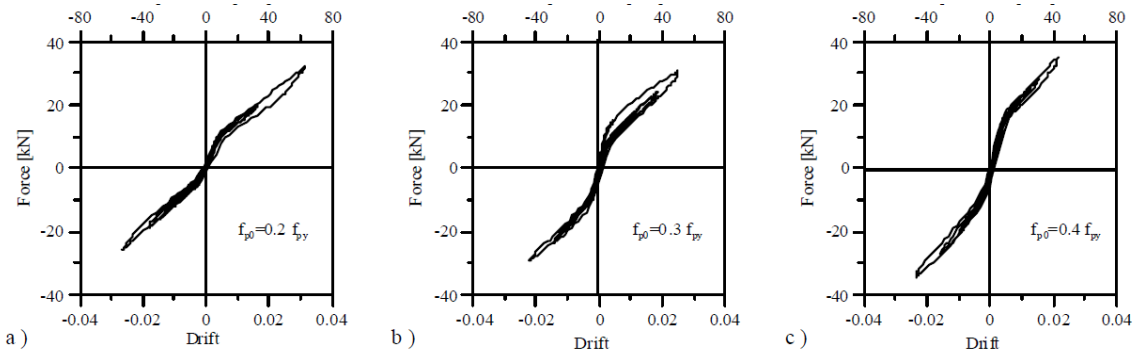

Figure 2.16: Unbonded PT specimens (a) $f_{po} = 0.2f_{py}$, (b) $f_{po} = 0.3f_{py}$, and (c) $f_{po} = 0.4f_{py}$ [Palermo et al., 2006]

2.5.2 Post-Tensioned Timber Rocking Systems with UFPs

UFPs are often used in rocking timber wall systems because they are simple, relatively easy to construct, and easy to model. They were initially proposed by Kelly et al. [1972] and gained popularity with successful implementation in the PRESSS project. With the gain in popularity, Baird et al. [2014] performed parametric studies on UFPs to determine important design characteristics such as the initial and post-yield stiffness, the dissipative capacity, and the maximum possible force developed by the UFPs. A series of displacement controlled test were performed by testing two UFPs in parallel to achieve symmetric loading, as shown in Figure 2.17a. Figure 2.17b shows the force verse displacement behavior for a single UFP in the tests. Baird et al. [2014] also created numerical models for the tests to calibrate UFP properties to the test results and made recommendations for the yield force and initial stiffness.

Iqbal et al. [2015] performed quasi-static cyclic and pseudo-dynamic tests on paired post-tensioned timber LVL walls with UFPs (sometimes referred to as coupled walls). The paired LVL walls were designed as part of a structural system for a multi-story prototype timber building. In panel tests, the UFPs connected to welded brackets that connected to the panels using self-drilling screws. Figure 2.18 shows the test setup. Six specimens were tested. All

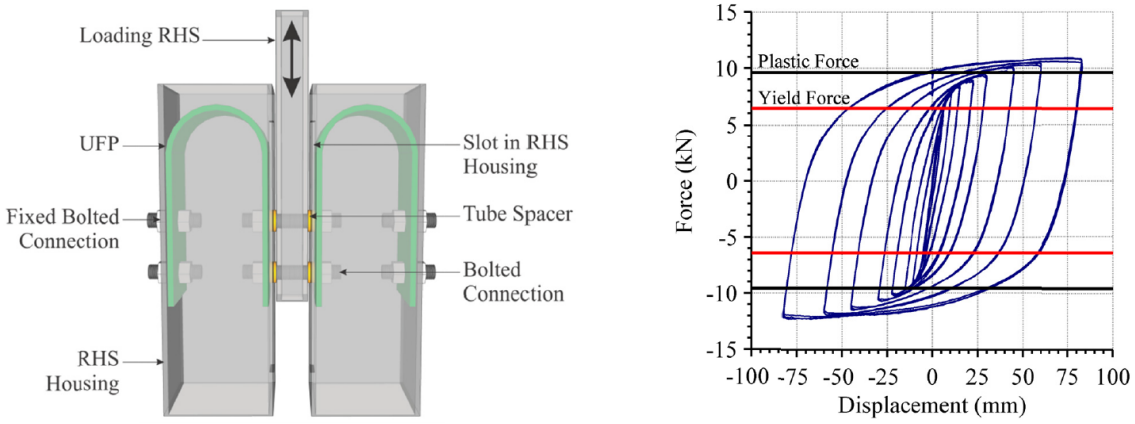

(a) UFP test setup

(b) Experimental hysteresis loop

Figure 2.17: UFP tests performed by [Baird et al., 2014]

specimens had the same panel sizes and PT bar properties with the same initial PT force. The first specimen (PT1) had no UFPs and the other five specimens (HU1 - HU5) had varying UFP sizes. Figure 2.19 shows the force-displacement curve for the paired wall system with a 5 mm thick UFP and the response from the PT1 specimen. It is clear that the typical nonlinear, elastic hysteresis loop was observed for the PT only specimen and the flag shape hysteresis loops with full recentering and energy dissipation was observed for the hybrid solutions. The pseudo-dynamic tests showed similar results and virtually no damage was observed in the structural members for both tests. Results showed that UFPs provide stable energy dissipation characteristics and in combination with the post-tensioning, a desirable flag-shaped hysteresis can be achieved.

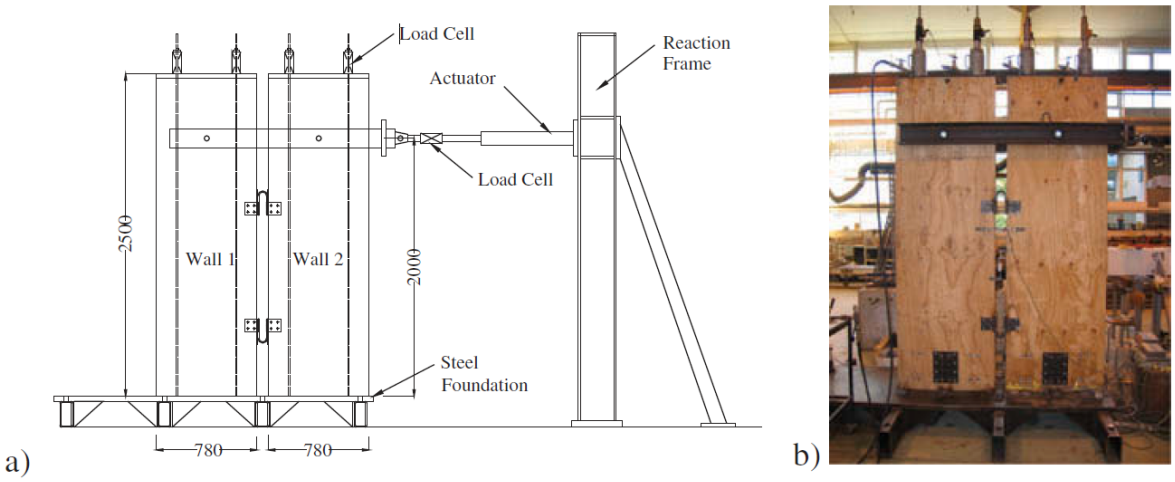

Figure 2.18: (a) Schematic details and (b) view of the paired wall system test set-up [Iqbal et al., 2015]

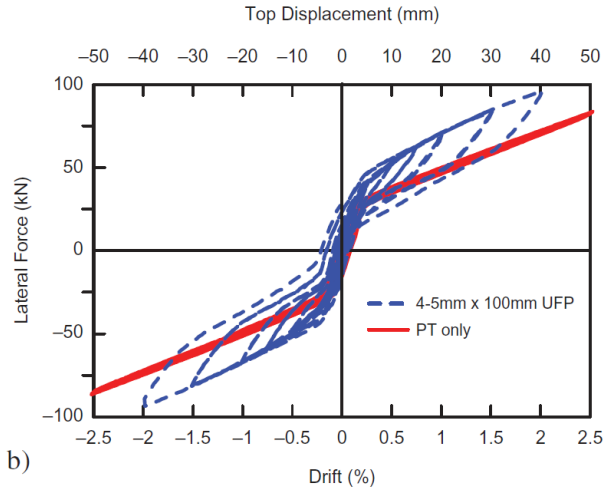

Figure 2.19: Force-displacement plot of specimen HU1 with comparison to specimen PT1 [Iqbal et al., 2015]

2.5.3 Ganey et al. [2017] and Akbas et al. [2017]

Ganey et al. [2017] and Akbas et al. [2017] conducted quasi-static experiments on post-tensioned CLT rocking walls with UFPs. The specimens were designed to achieve a set of structural limit states presented by Akbas et al. [2017] to help understand the lateral load response of the rocking CLT walls based on the level of damage to the CLT panels, PT bars, and UFPs. The limit states are shown in Figure 2.20 on an idealized base shear verses drift curve. The limit states are: 1) decompression at the base of the wall (DEC); 2) UFP yielding (EDP); 3) the effective linear limit that corresponds to the initiation of a visible gap at the base of the wall (ELL); 4) splitting of the CLT panel at the base (SCLT); 5) crushing of the CLT panel at the base (CCLT); and 6) yielding of the PT bars (LLP).

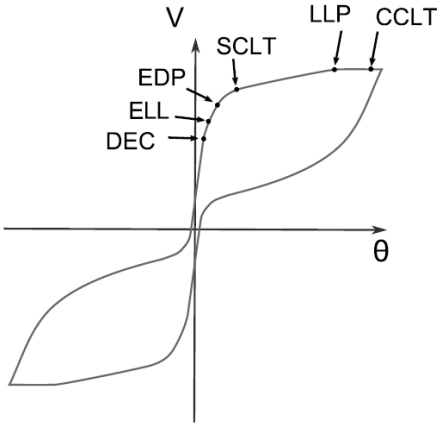

Figure 2.20: Idealized rocking CLT wall response and limit states [Ganey et al., 2017]

The quasi-static testing completed by Ganey et al. [2017] and Akbas et al. [2017] consisted of six different CLT specimens with the same wall thickness, length, and loading height. PT properties were varied to determine their effects on overall system response. The first 5 tests were single panel walls and the 6^{th} test was a paired CLT wall system with UFPs. Figure 2.21 shows the general test setup.

The resulting hysteretic response showed significant pinching at large drifts due to PT

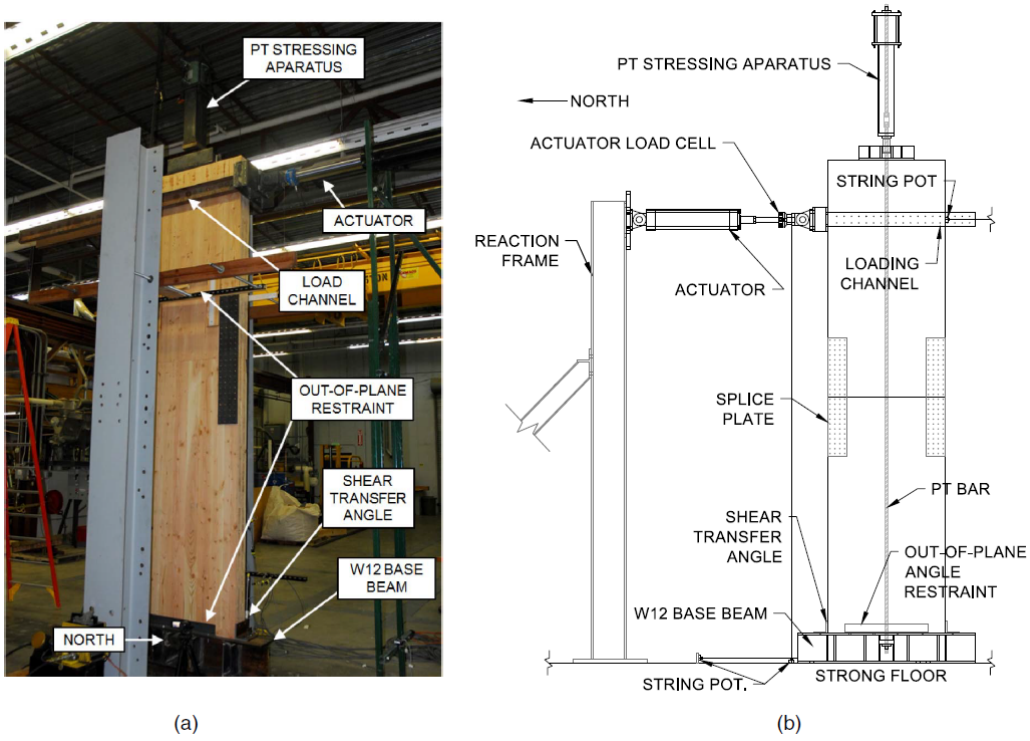

Figure 2.21: General test set-up (a) photo and (b) schematic [Ganey et al., 2017]

bar yielding and CLT crushing as seen in Figure 2.22 (from test 6, a paired CLT wall system). Results showed that larger initial prestress forces resulted in a larger decompression moment and lower drifts at which CLT damage occurred. In addition, larger PT bar area, resulted in larger post-decompression stiffness. Concluding that in design, the initial PT bar stress should be large enough to provided the needed capacity at ELL, but small enough to prevent excessive CLT damage and small enough to push PT yielding off until higher drifts are reached. Overall, results from the tests conducted by Ganey et al. [2017] showed that rocking CLT walls have a ductile response, recentering capabilities, and good strength and energy dissipation capabilities.

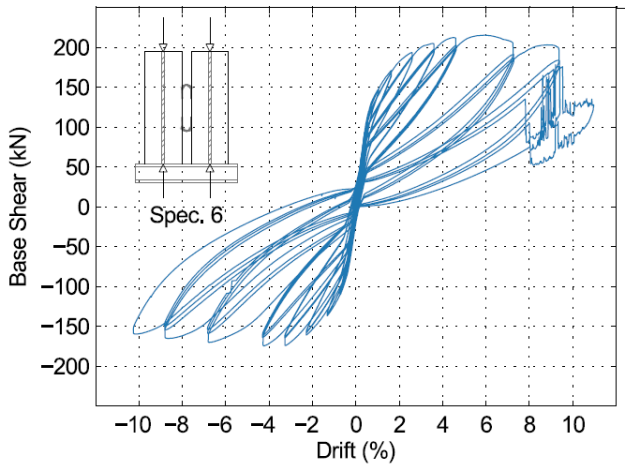

Figure 2.22: Base shear force verse drift response for test specimen 6 [Ganey et al., 2017]

2.5.4 Rocking Mass Timber Shear Walls Utilized in a Core Wall System

Brown et al. [2021] conducted unidirectional and bidirectional cyclic tests on a post-tensioned C-shaped CLT core wall system. The test utilized self-tapping screw connections at the in-plane and orthogonal joints of the core wall system. The testing program looked at the effects of initial PT force, screwed connection details, the use of UFPs, and the effects of loading protocols. The study also looked at composite action among in-plane and orthogonal walls to increase lateral strength and stiffness. The study showed that the core wall system was stable up to a drift of 2.3% (the stroke limit of the actuators) and that the screw connections provided necessary displacement and energy dissipation capacity to the system. It was also determined that composite action between the wall directions decreased with increasing drift. Results from this test showed that the post-tensioned walls provided adequate strength and stiffness with system recentering capabilities. Additionally, only minor damage was observed to the specimen and it occurred at the compression corners of the CLT wall panels and at screwed connections up the height of the walls. Figure 2.23 shows some of the observed damage during testing.

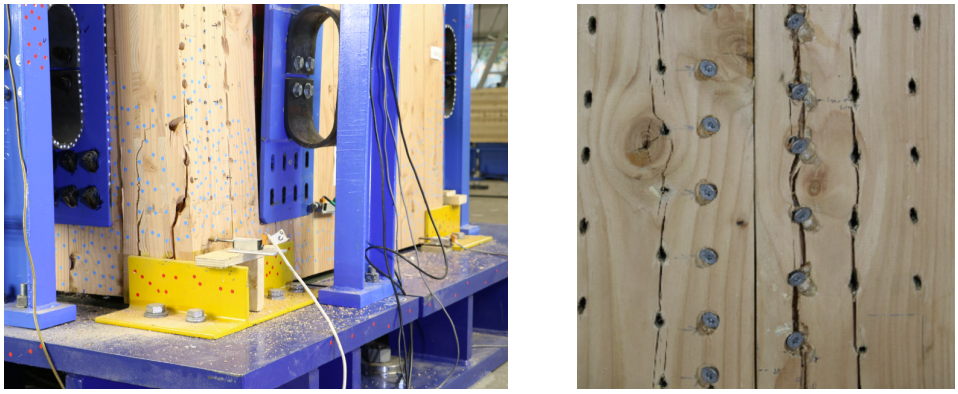

(a) (b)

Figure 2.23: Observed damage (a) CLT wall base crushing during testing and (b) in-plane screw joint [Brown et al., 2021]

2.5.5 Buildings with Mass Timber Shear Walls in the United States

While post-tensioned mass timber rocking wall systems are gaining popularity in research and around the world, they are not currently accepted by US design codes. Thus, to use this system in a building in the US, it must be designed using code alternative design procedures. This typically consists of performance-based design, often coupled with nonlinear dynamic numerical modeling. Work is being done to adopt these systems into US design codes (discussed in Busch et al. [2022] and discussed in this document) to make these systems more competitive with other structural systems. A few buildings with mass timber shear walls have been designed and built (or permitted) in the United States. This section will discuss some of these projects.

The tallest and arguably most notable building project in the United States with a post-tensioned mass timber shear wall is the 12-story Framework building which was permitted for construction in 2017 in Portland, Oregon (Figure 1.2). The design of the lateral system utilized performance-based seismic design methodologies and nonlinear response history analysis conducted in PERFORM 3D. Additionally, project specific experiments were con-

ducted to better understand mass timber material properties and mass timber connections. Code-equivalent design performance was achieved by defining performance objectives at the Design Basis Earthquake (DBE), MCE_R, and under strength-level wind [Zimmerman and McDonnell, 2017]. While the project was ultimately canceled due to funding issues, it was the first mass timber high-rise building in the United States to receive construction approval, advancing the understanding of these systems. As it will be discussed in this document, the lateral system design procedure used for the Framework building (presented in Engineers [2017]) was used as the basis for developing the design procedure for the NHERI TallWood 10-Story test specimen.

Peavy Hall at Oregon State University is a three-story building made entirely of timber. The building was completed in 2018 and was the first building in the United States with a post-tensioned mass timber lateral system. The CLT lateral system was designed using the seismic response history procedure outlined in ASCE/SEI 7-10. A nonlinear numerical model was developed for design based on methodologies presented in Sarti [2015] and Iqbal et al. [2015]. In the design, higher mode effects resulted in amplified shear and moment forces in the wall which had a significant influence on the wall design. Numerical results showed that the post-tensioned rocking wall system was capable of full system re-centering and provided adequate system damping [Sarti et al., 2017].

2.5.6 Mechanics of Post-Tensioned Mass Timber Rocking Wall Systems

The mechanics and lateral load response of these post-tensioned mass timber rocking shear wall systems have been characterized and presented by many researchers (Pampanin et al. [2001b], Newcombe et al. [2008], Sarti [2015], Ganey [2015], and others). This procedure for characterizing the response is often referred to as the cross-sectional analysis procedure and utilizes the monolithic beam analogy to estimate the stain at the base of the wall panels. This procedure was utilized extensively and expanded upon for design purposes in research presented in this document. The procedure is presented in detail in the Chapter 3 of this document.

2.6 Base Rocking Modeling Methodologies

Various modeling procedures have been proposed over the years, ranging from detailed but computationally expensive distributed multispring models, to more simplified but computationally efficient rotational spring models. Although less common, other methods such as fiber based (Akbas et al. [2017]) or shell element based finite element models and simplified analytical single DOF models have also been proposed. This section will review some of the nonlinear numerical modeling work completed on post-tensioned mass timber rocking wall systems.

2.6.1 Distributed Multispring Modeling

A common method for modeling post-tensioned rocking walls and connections is through a series of springs in parallel that distributes the nonlinear compressive timber behavior over the rocking interface. The parallel springs are commonly called a multispring element. This type of element was first developed by [Spieth et al., 2004] for precast concrete rocking systems and has been implemented for many studies (including Palermo et al. [2005]). Since then, it has been used for various rocking systems, including post-tensioned mass timber shear walls. The multispring element simulates the gap opening at the base and the neutral axis variation. With this method, the behavior of the PT bars and the energy dissipators can be physically modeled with springs or truss elements.

Figure 2.24 shows the distributed multispring model created by Sarti [2015] in OpenSees. The walls were modeled with elastic beam-column elements and the base of the wall element was connected to the multispring element. The multispring element consisted of multiple longitudinal zero-length springs in parallel. Each spring was assigned a compression only hysteretic material model to allow for gap opening. The total stiffness of the multispring element, k_{spring}, was calibrated from analytical procedures. Sarti [2015] used an initial approximation of $3E_{conn}A_t/L_{eff}$ where E_{conn} is the connection modulus defined as 70% of the timber modulus of elasticity, A is the area of the wall, and L_{eff} is the effective cantilever

length for the wall system. The post-tensioning was modeled using truss elements and the dissipative reinforcement was modeled using either zero-length spring elements or trusses. When compared with experimental data from quasi-static tests on LVL rocking walls, the distributed multispring model presented by Sarti [2015] was found to accurately capture the force-displacement response, PT force, and neutral axis depth.

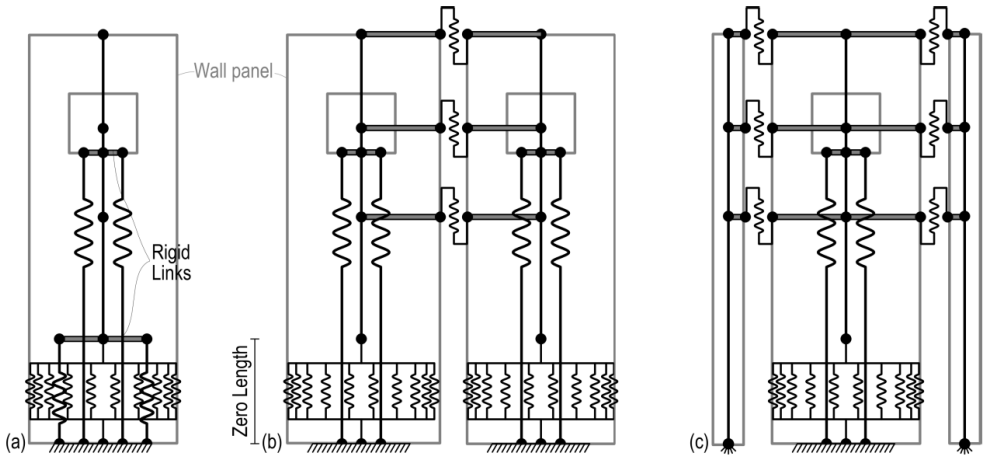

Figure 2.24: Multispring models developed by Sarti [2015] for (a) single wall, (b) paired wall, and (c) column-wall-column system

Ganey [2015] also developed a multispring model in OpenSees for rocking CLT walls that is similar to Sarti [2015]. The overall stiffness of the multispring element was calibrated based on test results of statically loaded, post-tensioned, rocking CLT walls. The overall stiffness was then distributed to the individual springs using the Labatto integration scheme, and an elastic-perfectly plastic material model was used. Overall, this method also accurately captured the behavior from quasi-static experimental results. Figure 2.25 shows a comparison of numerical and experimental results from this study for a paired post-tensioned rocking wall system that was tested under quasi-static loading.

Kovacs [2016] also developed a numerical model for rocking structures, similar to Sarti [2015] and Ganey [2015], but used the Winkler Spring Analogy (WSP), based on work by

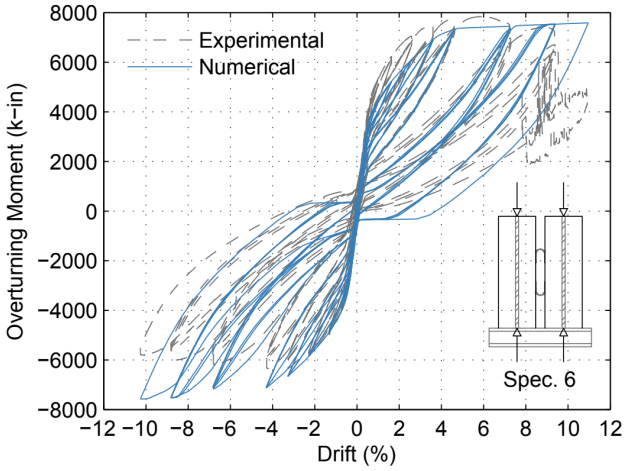

Figure 2.25: Multispring numerical model results comparison with experimental results from Ganey [2015]

Newcombe et al. [2008], to derive the stiffness of the multispring element. Based on WSP, the stiffness of the multispring element is based on an effective length, L_{eff}, which is determined by looking at the stress fields at the wall base when pushed laterally. Newcombe [2015] developed an empirical relationship based on experimental testing considering a variety of different material properties and system parameters. It was determined that L_{eff} is highly dependent on the neutral axis depth, c. However, because c is not directly observed in the analyses and would have to be recalculated at each step, it is difficult to implement. Thus, Kovacs [2016] uses the empirical equation defined by Newcombe [2015], but uses a constant c, determined at the peak expected roof drift. The results from this model compared well with experimental test data from Sarti [2015].

2.6.2 Rotational Spring Modeling

While detailed distributed multispring models capture local behavior, they can be computationally expensive and challenging to develop. Thus, more simplified numerical models with rotational springs at the base of the walls can be valuable when looking only for full

building response such as story drifts and accelerations. In most rotational spring models, the nonlinearity is modeled using two rotational springs in parallel at the base of the wall panels. This modeling methodology was originally developed by Palermo et al. [2005] and Pampanin et al. [2001a] for concrete structures. This section will briefly discuss rotational spring models, but will not be discussed in detail as it was not utilized for the research presented in this document.

Sarti [2015] created a rotational spring model for LVL rocking walls in OpenSees. Shown in Figure 2.26, the model consists of elastic frame elements with material and geometric properties of the LVL wall panels and two parallel zero-length rotational springs at the base of the wall elements that fully concentrate the nonlinear system behavior. As shown, the first spring models the post-tensioning moment using a multi-linear elastic hysteretic material model while the second spring models the dissipative contribution through a bi-linear moment-rotation relationship. The model is calibrated by matching the analytical moment-rotation results to the experimental results. When compared with results from experimental tests on rocking LVL walls, the model slightly underestimates the force-displacement loop, but overall provided very good agreement. It was also determined from this study that the rotational spring model was not able to account for isotropic stain hardening effects, and thus underestimated the hysteretic damping of the system Sarti [2015].

2.6.3 Comparison of Distributed Multispring and Rotational Spring Modeling Methodologies

Rotational spring models are computationally efficient and can accurately predict system response and provide a general understanding of system performance, including story drifts and accelerations. Multispring models are more computationally demanding and more challenging to develop but they also provide a good prediction for system performance. The main difference between the modeling methodologies is that the multispring models can capture the system behavior in more detail. Specifically, PT bar force, energy dissipator forces, and uplift and stresses in the base connection are captured with this model. The rotational spring models are only able to provide overall response parameters such as force-displacement and

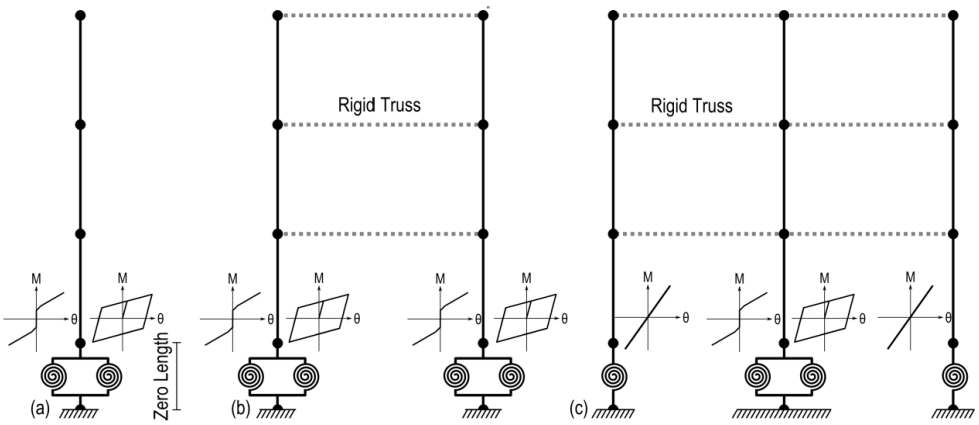

Figure 2.26: Rotational spring models developed by Sarti [2015] for (a) single wall, (b) paired wall, and (c) column-wall-column system

moment-rotation [Sarti, 2015].

Iqbal et al. [2015] compared predictions from a rotational spring model and a multispring model with results from quasi-static cyclic tests on post-tensioned LVL wall panels (discussed in Section 2.5.2). As shown in Figure 2.27, both models were able to predict the response of the experimental tests well. The multispring element model had slightly better performance prediction, especially at the initiation of gap opening. Sarti [2015] also compared model predictions from a rotational spring model to a multispring model. This study also found that both modeling methodologies were effective in the prediction of experimental results, however, the rotational spring model was not capable of accounting for isotropic strain hardening effects, resulting in an underestimation of system damping (although this effect is very minor).

In summary, both methods are accurate in predicting system performance. The largest disadvantage of using the multispring element for modeling is that it is computationally taxing. The largest disadvantage of using the rotational spring model is that it can only provide overall response results and not detailed parameters. Because the understanding of the detailed parameters such as PT bar force, UFP force, and compression at the base

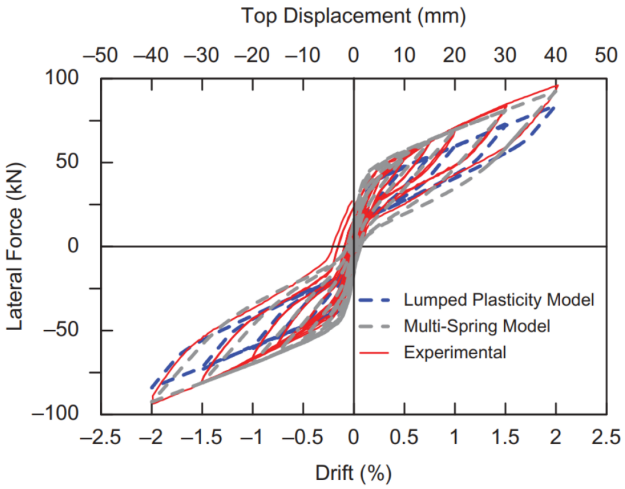

Figure 2.27: Comparison of a rotational spring model and a multispring model to experimental results from Iqbal et al. [2015]

of the wall were important for the designs presented in this document, the multispring model was utilized here. Additionally, Newcombe [2011] recommends using the multispring model for wall modeling (as opposed to beam-column connections) because coupling between neighboring walls and boundary columns (from the presence of energy dissipators) and the influence of the floor system from wall uplift may result in significant axial load variations which can only be accounted for in the multispring models.

2.6.4 Other Modeling Methods

Huang [2023] and Pei et al. [2021] proposed a simplified single rotational spring model intended for conducting fast, dynamic simulations for mass timber post-tensioned rocking wall systems. The wall elements are modeled with beam elements with lumped mass in the horizontal direction at each story and all nonlinear behavior is included with a rotational spring at the base of the wall. Essentially creating a model that is like single degree-of-freedom oscillator. The rotational spring parameters are calculated by considering the dimensions of the CLT wall panel, the PT rods, and the energy dissipating devices. The modeling

technique was validated using test results from the NHERI TallWood shake table test that tested a full-scale two-story mass timber building with post-tensioned CLT rocking walls, described in detail in Chapter 4. The model considered three degrees of freedom: horizontal displacement at the floor and roof levels and rotation at the base of the walls. Model results showed reasonable agreement with the shake table test results considering the simplicity of the model. The authors recommended that higher than measured modulus values from static loading tests should be used to consider load rate effects. Although detailed information about the response is not provided from this model, it could be valuable in preliminary design and assessment [Pei et al., 2021].

Wilson [2018] developed a modeling methodology that consisted of two phases. First, a higher-order finite element model is developed in SAP2000, then, using the results from the higher-order model, a simplified reduced-order model is developed. The higher-order model uses shell elements to model the wall panel and inelastic axial links to model the PT bars. A simple pushover curve is then run to determine the base moment-rotation relationship which is then used to create the reduced-order model. With this methodology, the reduced-order model can be used to run a large number of computationally efficient analyses. Similar to the rotational spring models, this reduced-order model only provides global information about the system, but detailed parameters such as PT bar force and damage to the base of the wall panels can be determined by relating back to the higher-order model. A similar modeling methodology was also used by Alegria [2022] to complete a large parametric study on post-tensioned mass timber rocking wall systems to study the effects of geometric parameters, system damping, and boundary parameters on system response.

2.7 Higher Mode Effects in Base Rocking Systems

Base rocking systems in steel, concrete, and timber have all shown that by limiting the base moment and allowing rocking, structural damage to the rest of the structure can be avoided. However, past research has also shown that structural forces up the height of the structure can increase significantly due to higher mode effects. The increased moment demands up

the height of the structure become particularly problematic.

Wiebe and Christopoulos [2009] suggested that higher mode effects could be reduced by introducing additional rocking segments up the height of the structure. In this study, 24 wall systems of varying height and rocking joint configurations were studied numerically by running suites of ground motions at DBE and MCE hazards. It was found that the bending moment envelope was greatly reduced by adding multiple rocking joints up the height of the structure. It was also found that the introducing multiple rocking joints did not result in dramatic increases in peak displacements meaning that second rocking joints could result in more economical designs since they structure at the location of maximum moment would not have to be designed for the amplified moment.

In a study specific to controlled rocking steel braced frames (CRSBF), Wiebe and Christopoulos [2015] proposed a design method for estimating the peak forces from higher mode effects. These systems are similar to post-tensioned rocking wall systems in which the system is designed to avoid damage to the main structural elements and the primary nonlinear behavior is confined to the rocking joint at the base. Current code based lateral force distributions do not accurately capture the nonlinear dynamic shapes of the shear and moment envelopes which are controlled by higher mode effects. Thus, Wiebe and Christopoulos [2015] proposes a method for calculating shear and moment envelopes that are more representative of the envelopes seen in nonlinear models. The method is based on the overturning moment overstrenth and the fundamental periods and thus does not require a structural model to be developed. The method was developed based on theoretical modal properties of a cantilevered shear beam with uniformly distributed mass and stiffness. In this paper, the method for estimating the forces from higher mode effects was validated through nonlinear modeling of designed buildings. Multiple buildings were subjected to suites of ground motions at MCE and the suite mean response was compared to the proposed method. The left moment diagram in figure 2.28 shows the nonlinear numerical results, in comparison to the proposed design moment envelope equation which is labeled as the “capacity design estimate”. The study found that the capacity design method generally capture the 84th-percentile overturn-

ing moments. Wiebe and Christopoulos [2015] also investigated alternative designs that used multiple rocking joints to mitigate the higher mode effects. The right moment diagram in Figure 2.28 shows the reduction of moment demand that results from adding an additional rocking joint and the comparison to the predicted capacity design estimate.

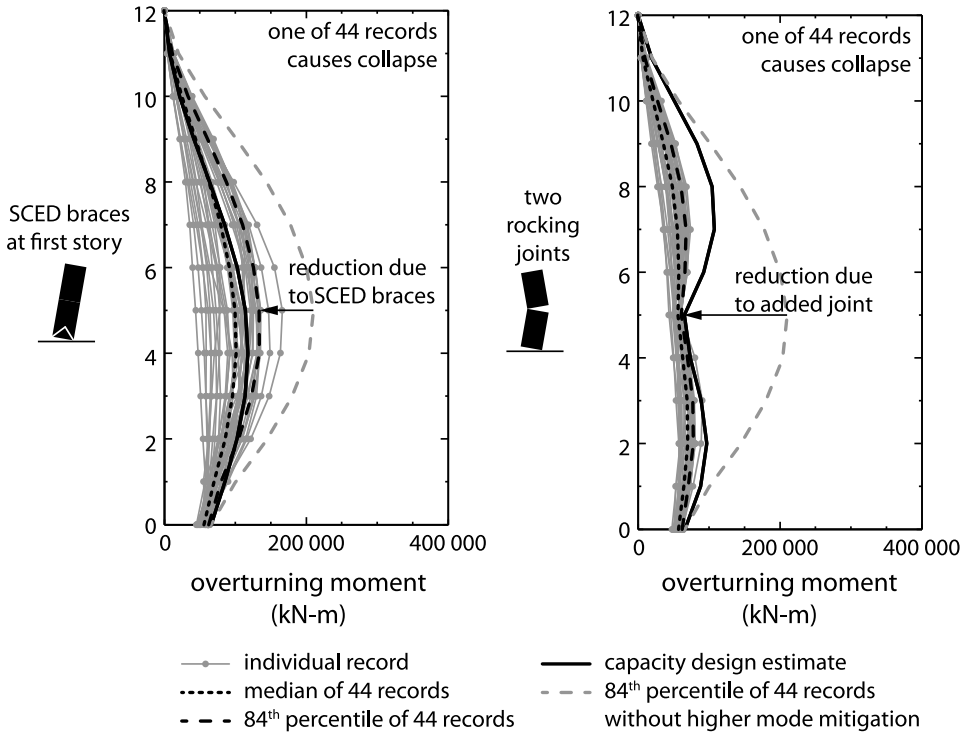

Figure 2.28: Overturning moment results from nonlinear modeling in comparison to the porpoised capacity design estimate for a continuous wall and a wall with a second rocking joint [Wiebe and Christopoulos, 2015]

The method for estimating higher mode effects in Wiebe and Christopoulos [2015] was utilized in Kovacs and Wiebe [2019] which studied the collapse assessment of post-tensioned rocking CLT wall wall systems. In Kovacs and Wiebe [2019], three prototype walls were designed using a force-based design procedure that included the higher mode approximation. Nonlinear time-history analyses and fragility analyses were conducted. The results showed

that using the proposed design method, the probability of collapse for these systems can be limited to less than 10% during an MCE_R earthquake. Additionally, it was found that the design method for estimating the higher mode forces capture the median nonlinear time history analysis results within 15% for all designs.

Pilon et al. [2019] studied how introducing a second rocking joint can also mitigate higher mode effects in CLT and LVL rocking wall systems and the benefits associated with doing so. Pilon et al. [2019] states that for tall mass timber shear walls, multiple wall segments are needed. Creating rigid connections between the panels is costly and can slow down construction. These rigid joints also result in dynamic amplification of forces in the upper stories. This study proposes connection details that would allow for multiple rocking segments at the construction joint. Nonlinear OpenSees analyses were conducted on multiple designs and found that introducing a second rocking joint can reduce moment demands in the walls by nearly 45%.

A recent study by Alegria [2022] investigated the effects of wall aspect ratio in post-tensioned CLT rocking walls on overall performance and moment amplification. In this study, both 6 and 12-story buildings were studied. Four aspect ratios were studied for the 6-story building and three ratios were studied for the 12-story building. For all the buildings, the total wall length was the same (30 feet). To change the aspect ratio, the wall was broken up into multiple segments, coupled together with UFPs, rustling in different building periods for each design. The resulting designs are shown in Figure 2.29. As shown in Figure 2.29, Alegria [2022] found that walls with a larger aspect ratio had larger drifts, likely due to the lower flexural stiffness of these elements. Alegria [2022] also found that the amount of moment amplification from higher mode effects also decreased as aspect ratio (and flexural stiffness) decreased.

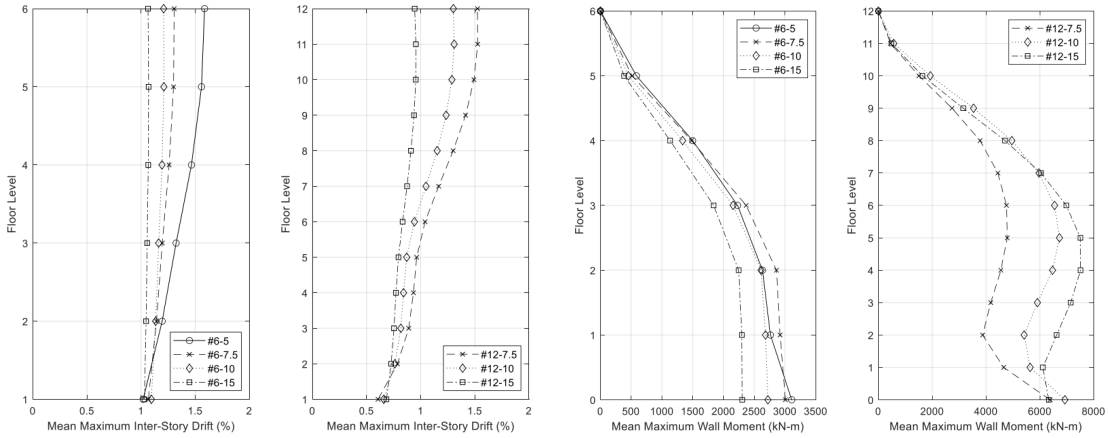

# ID	# Stories	Wall Height, ft (m)	Segment Length, ft (m)	Aspect Ratio (H:L)	# Segments
6-5	6	72 (21.95)	5 (1.52)	14.4 : 1	6
6-7.5			7.5 (2.29)	9.6 : 1	4
6-10			10 (3.05)	7.2 : 1	3
6-15			15 (4.57)	4.8 : 1	2
12-7.5	12	144 (43.89)	7.5 (2.29)	19.2 : 1	4
12-10			10 (3.05)	14.4 : 1	3
12-15			15 (4.57)	9.6 : 1	2

Figure 2.29: Results from Alegria [2022] showing the effects of aspect ratio on the performance and moment amplification in post-tensioned rocking CLT walls

2.8 Conclusions and Research Needs

The research presented in this section has presented the following conclusions:

- Mass timber is a strong and sustainable building material that has grown in popularity in recent years. While it is commonly used in gravity systems and diaphragm systems in buildings, its use in lateral systems is still low as it has not been accepted by US design codes. It shows potential to be a resilient material for lateral systems and is growing in popularity.

- Mass timber shear walls with traditional mechanical connections are good for low-level seismic regions where the system can remain elastic. The only ductility from these

systems come from the mechanical connections which is not sufficient for areas that can experience high accelerations.

- Through quasi-static and pseudo-dynamic tests, post-tensioned base rocking connections in concrete and timber systems with energy dissipators show ductile behavior, good energy dissipation, and recentering capabilities for high seismic areas.

- A method for developing the lateral load response of post-tensioned mass timber rocking walls has been developed and validated through quasi-static and pseudo-dynamic tests.

- A variety of numerical modeling methodologies for response prediction of post-tensioned mass timber rocking walls have been proposed and validated through quasi-static and pseudo-dynamic tests. The most popular methods (rotational spring models and distributed multispring models) have trade offs between efficient computational times and detailed assessment of the system.

- A multispring numerical modeling methodology can most accurately capture the response of the full system and include all interactions between the gravity system and diaphragm systems.

- In tall rocking wall systems, higher mode effects result in dynamic amplification of forces in the upper stories. Notably, the wall moment demands at upper floors far exceed the base moment demands.

The research presented in this section shows promising success for the future implementation of post-tensioned mass timber rocking shear walls for buildings in high seismic areas. However, limited research has been done relating specifically to tall post-tensioned mass timber shear walls, validating the performance of these systems under dynamic loading, and little work has been completed on developing and validating three-dimensional nonlinear numerical

models. The research in this document aims to address these research gaps through full-scale dynamic shake table testing, numerical three-dimensional nonlinear numerical model development and validation, and validation of code-alternative design procedures for these systems, specifically relating to tall buildings.

Chapter 3

FUNDAMENTAL MECHANICS OF ROCKING MASS TIMBER WALL STRUCTURES

3.1 Overview

This chapter first presents an overview of the component level behavior and system behavior of post-tensioned rocking mass timber walls. Then, fundamental mechanics are used to describe the lateral load response of the mass timber rocking walls. This includes a discussion of the cross-sectional analysis procedure which is commonly used to estimate of the lateral load capacity, moment-rotation, and force-displacement behavior of the mass timber rocking wall systems. Throughout this chapter both paired rocking wall systems (such as those used in the NHERI TallWood two-story shake table test discussed in Chapter 4) and rocking walls with bounding columns (such as those used in the NHERI TallWood ten-story shake table tests introduced in Chapter 6) are considered.

3.2 Overview of Mass Timber Rocking Wall Lateral Systems and Component Behavior

In this section, the component level behavior and analysis considerations needed to estimate the moment-rotation behavior of post-tensioned mass timber rocking walls with UFP energy dissipation devices are discussed. Two possible configurations for rocking wall systems are shown in Figure 3.1: (1) two mass timber wall panels connected with UFPs, which will be referred to as "paired walls" and (2) a single mass timber wall panel connected to bounding columns on both sides with UFPs. Note, the paired wall system shown here is sometimes referred to as a "coupled wall" system. The term paired wall has been used in this document because the UFPs do not actually couple the walls together the same way as traditionally

defined in structural engineering. Although other configurations are possible, the two shown in Figure 3.1 are emphasised as they are representative of the wall configurations utilized in the two-story and ten-story NHERI TallWood shake table tests. Note, both configurations in Figure 3.1 depict designs with continuous wall panels extending up the height of the entire structure, which is consistent with the configurations used in both the two-story and ten-story shake table tests.

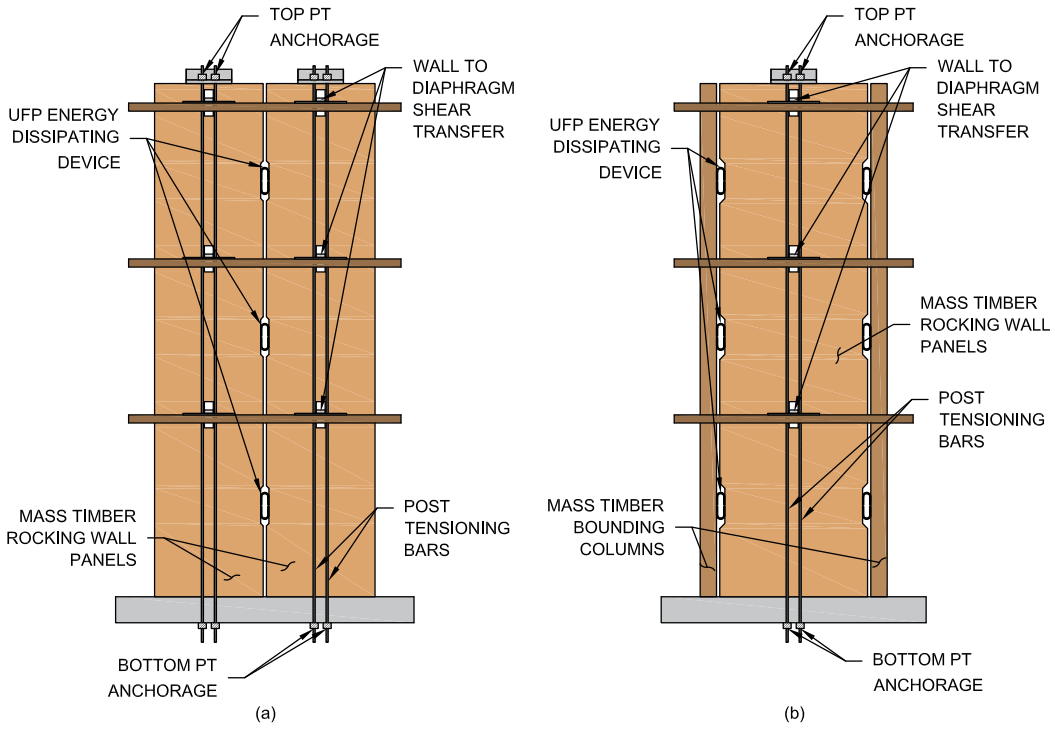

Figure 3.1: Wall systems (a) paired rocking walls and (b) rocking wall with bounding columns

In both configurations shown in Figure 3.1, the system consists of a single post-tensioned (PT) connection, meaning there is just one PT connection at the base with the PT bars anchored to the foundation. At the top, the PT bars anchor to a steel connection attached to the wall itself, so when the wall rocks and a gap opens at the base of the wall, the PT

bars elongate. In the paired wall configuration, Figure 3.1a, the wall panels are connected using UFPs for energy dissipation. In Figure 3.1b, the there is only one wall panel and the UFPs attach to bounding columns on either side of the panel for energy dissipation. In both configurations, the seismic mass from the rest of the structure is transferred to the seismic force resisting walls trough a diaphragm shear transfer connection. This connection transfers horizontal loads while accommodating vertical displacements and rotations of the wall panels.

3.2.1 Mass Timber Wall Panel Behavior

The specific behavior and properties of different mass timber products can vary between type of product, the wood used for the components, and the manufacturer. Additionally, limited testing has been completed on most mass timber products, particularly post-yield behavior testing, so properties beyond those considered in grading certification have some uncertainty. To date, there are no universally accepted compressive constitutive relationships for mass timber. In many studies, elastic-perfectly plastic material properties have been assumed to represent CLT behavior when the strains are limited [Ganey, 2015]. Figure 3.2 shows one example of an assumed compressive stress-strain response for CLT that includes material deterioration. This behavior is based on compression test results completed on DR Johnson CLT at Oregon State University [Barbosa et al., 2018]. As shown in the figure, the compressive behavior can be approximated as elastic, with an elastic modulus of E_w, until the yield stress, $f_{y,clt}$ is reached. After yielding, the behavior can be approximated with a zero strain-hardening plateau until CLT splitting begins at the splitting strain, $\epsilon_{s,clt}$. After splitting, the strength deteriorates until crushing occurs at approximately 25% of the yield stress at the crushing strain, $\epsilon_{cr,clt}$. The compressive behavior illustrated in Figure 3.2 is used for the material response of the CLT walls in the analysis and design of the NHERI two-story and ten-story shake table tests.

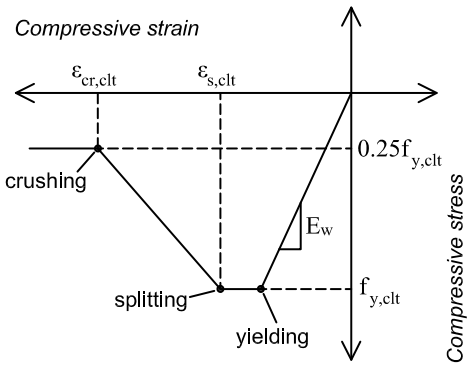

Figure 3.2: Idealized compressive stress-strain relationship for CLT panels based on test data from Barbosa et al. [2018]

3.2.2 UFP Energy Dissipating Devices

Initially proposed by Kelly et al. [1972], UFPs are made by bending a mild steel plate to form a 'U' shape. The UFPs can either be mounted between timber wall panels or between the wall panel and bounding wall columns to provide the primary source of energy dissipation for the system. UFPs are typically anchored to the structural elements using steel saddle (Figure 3.3) or embedded plate connections. The UFPs are field welded or bolted to the connection, allowing for easy replacement after large earthquakes that result in significant UFP yielding. Figure 3.3b shows a schematic of a UFP with the typical dimensions where t_u is the thickness of the plate, b_u is the width of the UFP, and D_u is the average diameter of the UFP.

UFPs dissipate energy when one end moves vertically relative to the other, changing the radius of curvature from straight to curved along the vertical edges, causing the plate to yield [Baird et al., 2014]. The plastic moment, $M_{p,ufp}$, is determined through basic mechanics, assuming the entire cross section yields. Equation 3.1 defines $M_{p,ufp}$ as the product of the yield stress, $f_{y,ufp}$, and the plastic section modulus of the rectangular cross section, Z. As derived by Kelly et al. [1972], the theoretical maximum force, $V_{p,ufp}$, is estimated by equating

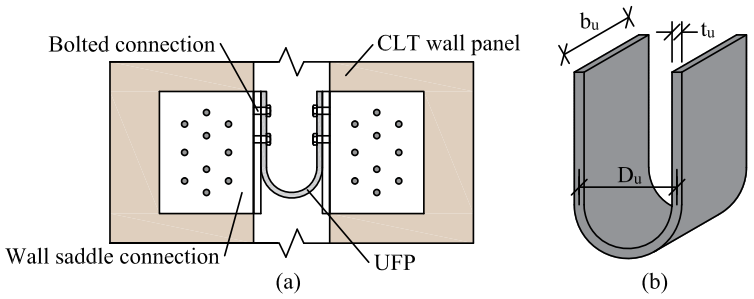

Figure 3.3: UFP (a) saddle mounting connection detail and (b) typical dimensions

the shear couple, from the two ends of the UFP, to the sum of the plastic moments, $M_{p,ufp}$, as shown in Equation 3.2. Note, the yield moment, $M_{y,ufp}$, and the yield force, $V_{y,ufp}$, can also be approximated using a similar procedure with the elastic section modulus, S, instead of the plastic section modulus, Z. This results in a yield force that is 2/3 of the plastic force ($V_{p,ufp}$).

$$M_{p,ufp} = f_y Z = \frac{1}{4} f_y b_u t_u^2 \tag{3.1}$$

$$V_{p,ufp} = \frac{2M_p}{D_u} = \frac{f_y b_u t_u^2}{2D_u} \tag{3.2}$$

When designing UFPs, the maximum strain in the UFP should be considered. Baird et al. [2014] defines the maximum strain as the UFP thickness to Diameter ratio, as given by Equation 3.3. Ideally, the maximum stain should be limited in design to increase the number of cycles until fracture.

$$\epsilon_{max} = \frac{t_u}{D_u} \tag{3.3}$$

The initial vertical stiffness of the UFPs, k_o, is approximated by calculating the yield displacement through energy methods, as shown in Equation 3.4 from [Baird et al., 2014]. E is the elastic modulus of the UFP material, typically a mild steel.

$$k_o = \frac{V_{y,ufp}}{\Delta_y} = \frac{16Eb_u}{27\pi}\left(\frac{t_u}{D_u}\right)^3 \tag{3.4}$$

The energy dissipated by all UFPs in a full wall assembly can be quantified using the energy dissipation ratio, β. For the assembly, β is calculated as the ratio of the area of the flag-shape damping hysteresis (Figure 3.4b) to the area of the full elastic-plastic hysteresis illustrated in terms of base-moment versus rotation in Figure 3.4a, as given by Equation 3.5 [Seo and Sause, 2005]. For the rocking systems presented, the moment contribution from the UFPs, M_{ufps}, is typically taken as the as the force in all the UFPs multiplied by the rocking moment arm (typically the length of the wall). The yield force of the full assembly is defined as M_y.

$$\beta = \frac{M_{UFP}}{2M_y} \tag{3.5}$$

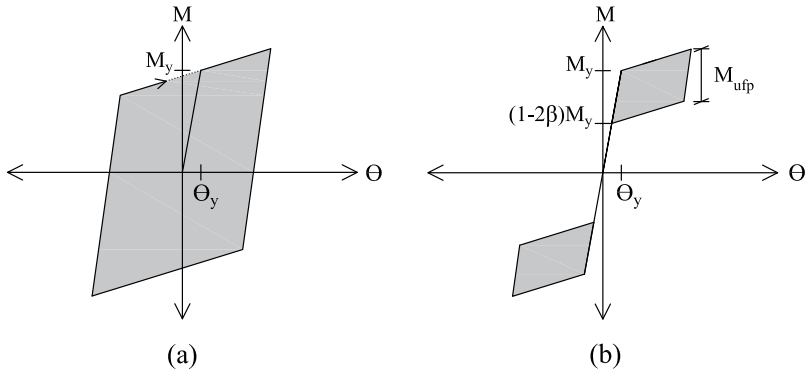

Figure 3.4: (a) the full elastic-plastic hysteresis and (b) the flag-shaped damping hysteresis used to represent the energy dissipation ratio [Seo and Sause, 2005]

3.2.3 Post-tensioned connections

In the rocking mass timber wall systems considered here, the walls are anchored to the foundation using unbonded steel PT bars instead of traditional mechanical brackets that are

used in typical timber shear walls. The bars are fixed to the foundation at the base of the wall and run along the total height of the wall. Multiple bars can be placed symmetrically about the center line of the wall length or just one bar can be placed in the center of the wall thickness. Additionally, the bars may run through a pre-cut cavity in the wall or can run externally on both sides of the walls so the system remains symmetric and balanced. Bars are typically placed close to the center line of the wall to minimize PT strains from wall uplift. With the systems discussed here, the bars attach to the top of the wall through a saddle-like connection and the walls are typically balloon framed. The PT bars are initially stressed to provide recentering capabilities for the system by initially putting the wall in compression add developing a precompression between the wall panels and the foundation. Apart from the PT bars, the wall is not otherwise attached directly to the foundation; however, some form of shear transfer is needed at the base to prevent sliding.

Under small lateral loads the walls behave elastically. As the the lateral load increases, a gap, θ_{gap}, opens at the base of the wall. During uplift, the PT bars stretch, increasing their tension force and the resisting moment. Figure 3.5 shows an example free body diaphragm for a paired post-tensioned rocking wall system and a rocking wall with boundary columns at a points beyond decompression. Upon unloading, the wall panels rock back downward. As θ_{gap} decreases, the bars shorten and their initial PT force results in wall recentering. As long as the PT bars remain elastic, the initial PT force will fully recenter the walls.

As mentioned, under small lateral loads and before rocking, the wall system is elastic. During this phase, the lateral load is resisted fully by the elastic deformations of the wall panels, similar to that of a fixed-base shear wall. System stiffness changes once the decompression moment, M_{dec}, is reached and a gap opens at the wall base. Prior to decompression, the overturning moment is resisted by the initial PT force, $T_{o,pt}$, and gravity loads, W. Assuming a linear distribution of the mass timber compression stress along the wall base, as shown in Figure 3.6a, the decompression moment is approximated by Equation 3.6.

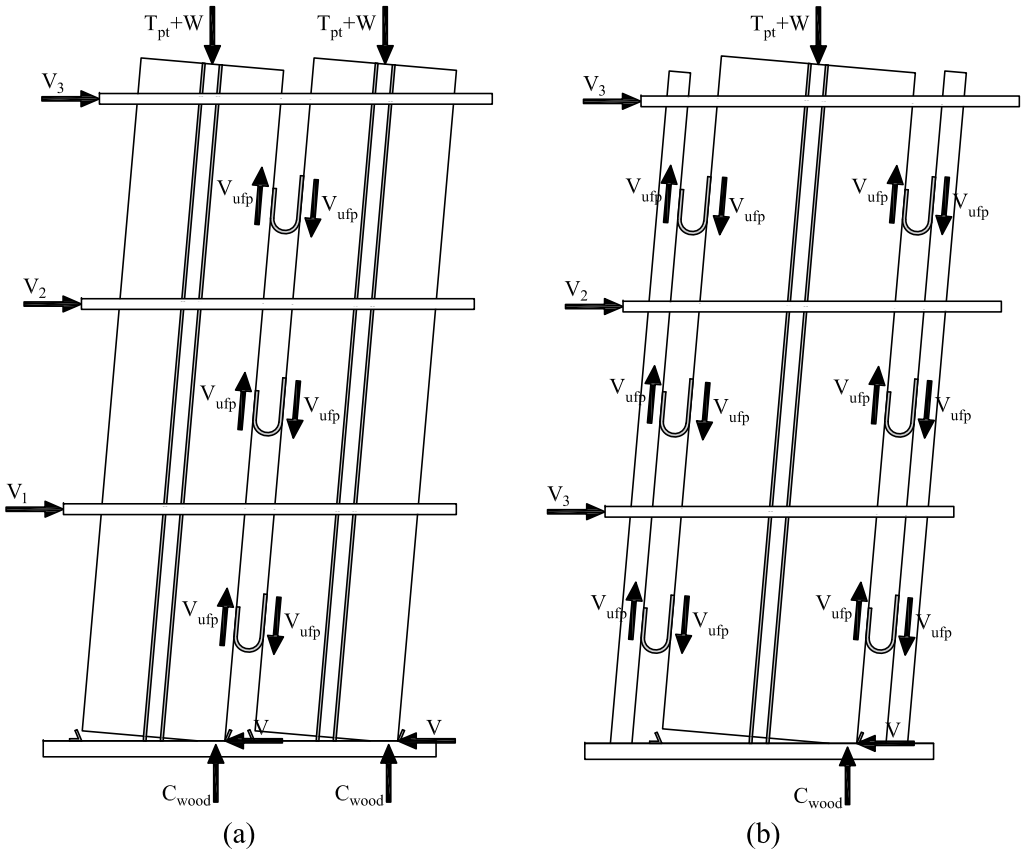

Figure 3.5: Rocking wall system behavior for (a) a paired post-tensioned rocking wall system and (b) a rocking wall with boundary columns

$$M_{dec} = (T_{o,pt} + W)d \tag{3.6}$$

In Equation 3.6, d is the distance between the the resisting timber force, C_{wood}, and the resultant of the initial PT force and the gravity load ($T_{o,pt} + W$). The resultant of the timber compression stress acts at the centroid of its assumed triangular distribution. If the resultant of the initial PT force and the gravity load acts through the wall's centroid at $L_w/2$, where L_w is the length of the wall, then the moment arm, d, is $L_w/6$ at the decompression moment.

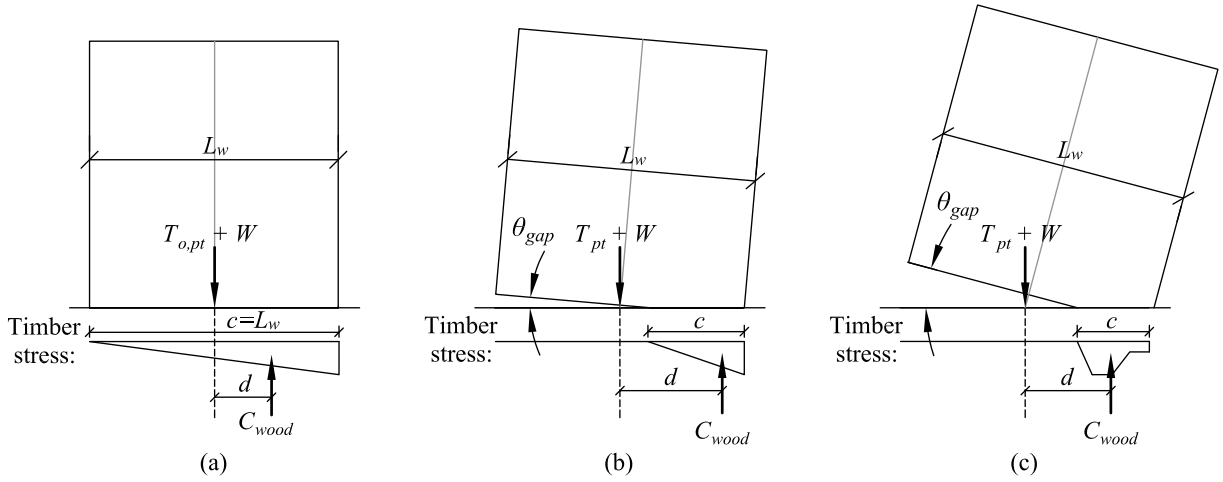

Figure 3.6: Timber stress distribution at the base of the wall (a) at decompression, (b) when the compression stress is less than $L_w/2$ and still linear, and (c) when the wood at the base of the wall has yielded

Post decompression, the wall uplifts and θ_{gap} opens between the base of the wall and the foundation. However, the lateral-load response is essentially linear-elastic until the portion of the wall base in compression and in contact with the foundation, c, is at least less than $L_w/2$, elongating the PT bars. Figure 3.6b shows the stress distribution at the base of the wall when the contact length is less than $L_w/2$. Akbas et al. [2017] defines an effective linear limit (ELL) which corresponds to a visible gap and reduced contact length such that the lateral stiffness of the wall is reduced enough to exhibit significant nonlinear behavior. This point is assumed to occur when the contact length, c, is approximately $3L_w/8$, which was derived from test data from Ganey [2015]. At this point, PT elongation is assumed to be negligible. Thus, similar to Equation 3.6, the moment at the ELL, M_{ell}, is calculated assuming initial PT force, $T_{o,pt}$, and a linear stress distribution along the contact length, resulting in a moment arm, d, also equal to $3L_w/8$.

As the wall panels rock and the mass timber deforms at the base, the portion of the wall base in compression (also called the neutral axis depth or compression zone, c) changes

constantly. The compression stress distribution of the mass timber in the compression zone will remain linear (Figure 3.6b) until the peak strain in the timber exceeds yield. After yield the stress distribution will follow the assumed behavior of the timber (Figure 3.6c shows and example of a commonly used stress behavior for mass timber walls). The cross-sectional analysis procedure, described in Section 3.3.1, is commonly used to solve for the constantly changing neutral axis depth.

The contribution of the UFPs to the moment resistance has not yet been discussed. As the walls rock, the UFPs also deform, further increasing the resisting moment, however the contribution from the UFPs is typically small when compared to the moment generated by the PT bars tension force and wall compression force. Typically the UFPs are assumed to remain elastic and don't contribute significantly to moment resistance until after the decompression moment, but before the ELL. Note, in taller walls, UFPs near the top may yield due to only elastic deformation. Once the UFPs deform significantly, they produce a shear force, V_{ufp}, along the vertical edge of the wall (Figure 3.5). Calculating the contribution of the UFPs to the total moment capacity of the wall will be discussed in more detail in Section 3.3.1.

3.2.4 Cyclic behavior

The mass timber rocking wall concept and system response is similar to a hybrid system, summarized in Figure 3.7. The PT bars, in combination with a gap opening at the base of the wall, provide a nonlinear elastic response with zero residual rotation after unloading (3.7a). However, with only PT bars, the system lacks damping. The hysteretic behavior of the steel yielding energy dissipators provides the needed energy dissipation (3.7b). Adding the response of the unbonded PT bars and the energy dissipating devices, results in the flag shaped hysteresis for the total system show in Figure 3.7c.

The combination of the unbonded PT bars and the energy dissipators produces a system that can undergo large inelastic deformations while assuring recentering and minimized damage. Figure 3.8 shows a more detailed flag shaped hysteresis for mass timber rocking

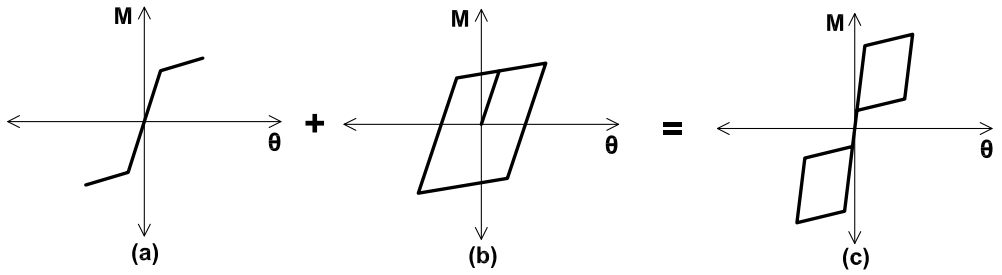

Figure 3.7: (a) Self-centering hysteresis from PT bars and (b) energy dissipating hysteresis combined to get the (c) idealized flag-shape hysteresis loop [Stanton et al., 1997]

systems with a series of structural limit states defined by previous researchers in Akbas et al. [2017] and Ganey et al. [2017]. Under small lateral forces, prior to decompression, the wall remains linear and elastic with a stiffness equal to the elastic shear and flexural stiffness of the mass timber panels. After decompression, the stiffness decreases only slightly. Notable nonlinearity occurs after significant uplift; this point is defined as the ELL [Akbas et al., 2017]. The UFPs typically yield in the region between decompression and ELL or just after the ELL, depending on their strength and stiffness. With increasing lateral displacement, significant uplift and nonlinear behavior begins. The system is designed such that the base of the timber panels will yield, split, and crush (as shown in Figure 3.2) prior to PT yielding.

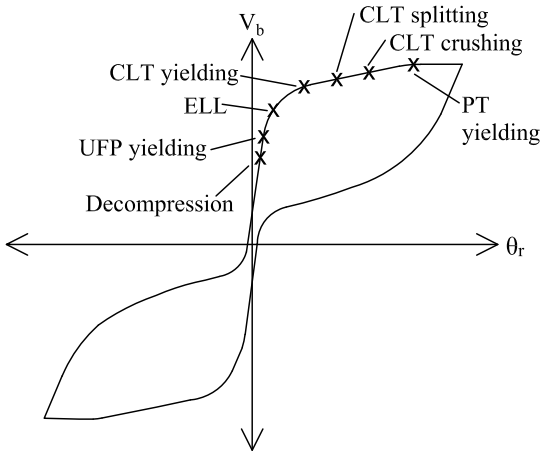

Figure 3.8: Hysteretic behavior of rocking mass timber wall systems

3.2.5 Wall to Floor Diaphragm Shear Transfer

Different diaphragm options have been studied for structures with rocking mass timber walls. Concrete slabs offer more rigid diaphragm behavior, a flexible diaphragm can achieved using plain mass timber, or a combination of a mass timber diaphragm with a composite concrete topping results in a semi-rigid diaphragm. While the response of the wall to floor diaphragm shear transfer will be discussed, the response of the diaphragm is beyond the scope of work presented here and will only be discussed briefly.

To minimize damage to the gravity system, diaphragms, and the walls, a connection between the wall and diaphragm that transfers horizontal shear force while accommodating vertical displacements is necessary. Moroder et al. [2017] tested several wall to diaphragm connection design concepts with varying degrees of rotational and transnational deformation decoupling. Four of the connections studied are shown in Figure 3.9. In situations where a more flexible diaphragm is present, it was shown that more economical connections such as the one shown in Figure 3.9a or Figure 3.9b are sufficient. With a more rigid diaphragm, a more complicated connections such as the one shown in Figure 3.9c are recommended. When rotations need to remain small, end columns can be used to transfer the shear forces

indirectly as shown in Figure 3.9d.

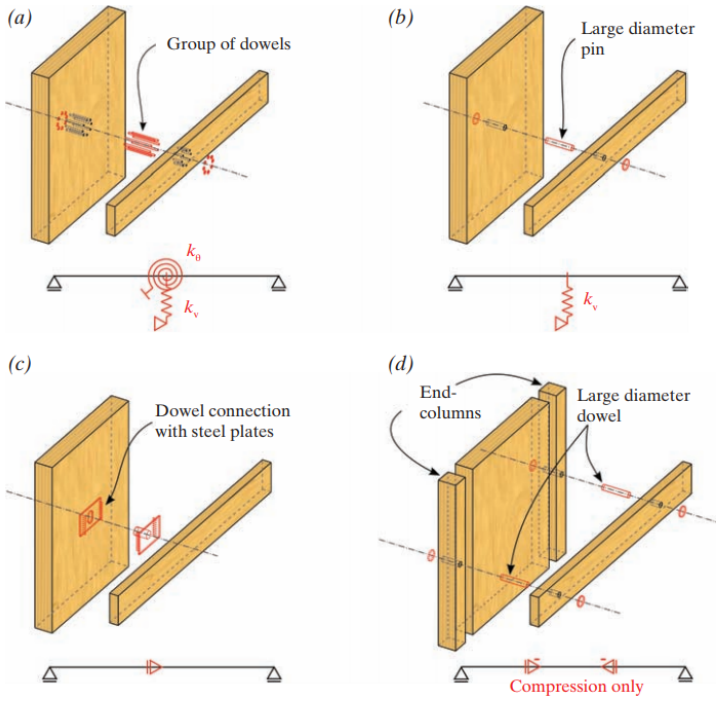

Figure 3.9: Different wall to diaphragm shear transfer connections: (a) vertical and rotational restraint; (b) vertical restraint; (c) horizontal restraint; and (d) use of end columns for no restrains in the walls [Moroder et al., 2017]

The majority of the work presented in this document assumes rigid diaphragm response. As a result, more complicated connections such as the one shown in Figure 3.9c were assumed for modeling purposes and were used for both the two-story and ten-story shake table tests. These connections utilized vertically slotted holes in the rocking walls, with cantilevered dowel-like connections that anchored to the diaphragm and extended through the vertically slotted holes. These connections allowed transfer of horizontal forces without transferring vertical forces or rotational moments.

3.3 Formulations for Approximating the Lateral Load Response of Timber Rocking Walls

This section presents formulations for approximating the lateral load response of rocking mass timber walls. First, a cross-sectional analysis procedure is presented which can be used to solve the moment-rotation response of the system. With this procedure, a gap rotation is imposed at the base of the wall. An iterative procedure is used to solve for the PT forces, the energy dissipator forces, and the compression force in the timber at the base of the wall to satisfy equilibrium and determine the assembly base moment capacity. After presenting the procedure for determining the moment-rotation response, the procedure for determining the force-drift response from the moment-rotation procedure is presented. The concepts presented in this section are used as the basis of the design procedures used in both the two-story and ten-story NHERI TallWood shake table specimens, with some test specific modifications.

This section presents the procedure for a single rocking wall panel with boundary columns on either side, connected with UFPs (Figure 3.1b). An explanation for adapting the procedure to paired walls with UFPs (Figure 3.1a) is presented after, in Section 3.3.3.

3.3.1 Cross-Sectional Analysis Design Procedure

An iterative procedure called the cross-sectional analysis procedure, has been developed to assist in solving for the neutral axis location at the base of rocking wall panels (ie. the length of the compression neutral axis) for any given drift after the decompression. This procedure allows for determining the moment-rotation behavior of the system. This procedure was originally developed by Pampanin et al. [2001b] for precast concrete frames and was then adapted and modified by Newcombe et al. [2008] for LVL walls and Ganey [2015] for CLT walls. The procedure here is recommended for mass timber rocking wall panels. Figure 3.10 summarizes the procedure.

As discussed previously, prior to decompression, the wall behaves as a cantilevered section.

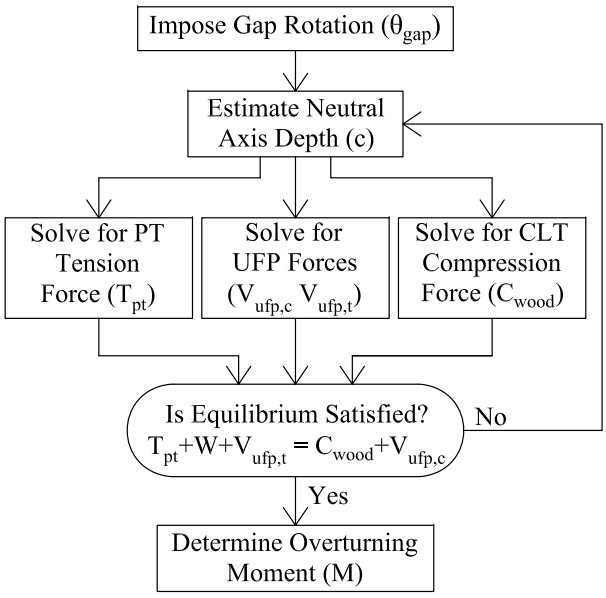

Figure 3.10: Summary of the cross-sectional analysis procedure for determining the moment-rotation response of rocking timber walls

After decompression, a gap opens at the base of the wall and the following procedure can be used to determine the moment-rotation behavior. Note, significant nonlinear behavior does not occur until after the ELL, but this procedure can still be used prior to ELL. Figure 3.11 shows a distribution of the forces at the base of a wall panel that has UFPs on both ends of the wall (similar to the system shown in Figure 3.1b). This figure can be referenced in the following section for nomenclature and derivation of equations.

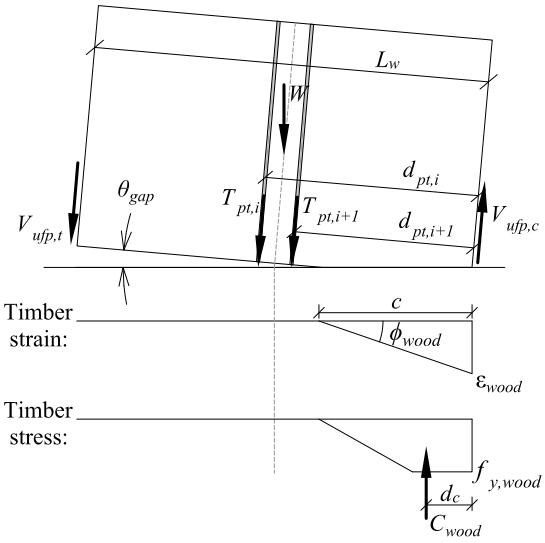

Figure 3.11: Forces distributed at the base of post-tensioned rocking timber walls UFPs connecting the wall to boundary columns

Impose Gap Rotation

The first step of the cross-sectional analysis procedure is to impose a gap rotation, θ_{gap} at the wall base. θ_{gap} is the rotation angle at the base of the wall that occurs after the wall has decompressed, as shown in Figure 3.11. The imposed gap rotation is used to calculate the total story drift, θ_{total}, by adding the rotation representative of elastic wall deformations, as shown in Equation 3.7. Contributions from elastic deformations will be discussed in more detail in Section 3.3.2.

$$\theta_{total} = \theta_{gap} + \frac{\Delta_e}{h_w} \tag{3.7}$$

Estimate Neutral Axis Depth

The next step of the cross-sectional analysis procedure is to estimate the length of the compression zone (also called the neutral axis depth), c, at the wall base. This distance is

iterated on until equilibrium is satisfied in the last step of the procedure (Section 3.3.1).

Solve for PT Tension Force

When θ_{gap} opens at the base of the wall panel, the i-th PT bar will stretch by $\Delta_{pt,i}$. Assuming small angles, the change in length of the PT bars, $\Delta_{pt,i}$ is calculated by multiplying θ_{gap} by the difference between the distance from the corner of the wall and the location of the PT bars, $d_{pt,i}$, and the neutral axis depth c (Equation 3.8). The subsequent increase in PT bar force, $\Delta T_{pt,i}$, is then equal to the change in PT bar length, $\Delta_{pt,i}$, multiplied by the axial stiffness of a PT bar, $k_{pt,i}$ (Equation 3.9). The axial stiffness of the PT bar, $k_{pt,i}$, is equal to the product of the tensile area of each PT bar, $A_{pt,i}$, and the elastic modulus of the PT bar material, E_{pt}, divided by the PT bar length l_{pt} (Equation 3.10). Finally, the total force in each bar is the sum of the initial PT force, $T_{pt,o}$, and the change in PT bar force, $\Delta T_{pt,i}$ (Equation 3.11).

$$\Delta_{pt,i} = \theta_{gap}(d_{pt,i} - c) \tag{3.8}$$

$$\Delta T_{pt,i} = \Delta_{pt,i} k_{pt,i} \tag{3.9}$$

$$k_{pt,i} = \frac{A_{pt,i} E_{pt}}{l_{pt}} \tag{3.10}$$

$$T_{pt,i} = T_{pt,o} + \Delta T_{pt,i} \tag{3.11}$$

Solve for UFP Forces

Unless the UFPs have fully yielded, the force from the UFP on the side of the wall that is in compression, $F_{ufp,c}$, will be smaller than the UFP force on the other side of the wall panel, $F_{ufp,t}$. The compression UFP deformation, $\Delta_{ufp,c}$, can be calculated as the product of θ_{gap} and c (Equation 3.12), while the tension UFP, $\Delta_{ufp,t}$, can be calculated as the product of θ_{gap} and the difference between L_w and c (Equation 3.13). Note, in both cases, the depth of the bounding columns is neglected.

$$\Delta_{ufp,c} = \theta_{gap} c \tag{3.12}$$

$$\Delta_{ufp,t} = \theta_{gap}(L_w - c) \tag{3.13}$$

$$\tag{3.14}$$

Although more complicated material behaviors may be assumed, here a simple elastic-plastic material model is assumed for the UFPs. This is reasonable because the UFPs do not gain much additional strength after yield. Thus, as shown in Equation 3.15, the force in the UFP on the compression side of the wall can be taken as the maximum of the the yield force of the UFP ($F_{y,ufp}$, calculated according to Equation 3.2) and the product of the UFP stiffness (k_{ufp}, calculated according to Equation 3.4) and the deformation of the UFPs, $\Delta_{ufp,c}$. Similarly, the force in the UFPs on the tension side can be calculated using Equation 3.16. For both sides, the number of UFPs on each wall face, n_{ufp}, must also be accounted for. Note, constant UFP deformation, and thus force, up the height of the walls is assumed. Although the UFPs towards the top of the wall will deform more from elastic deformation of the wall panels, this is still a reasonable assumption because yield displacements and post-yield stiffness are small.

$$V_{ufp,c} = max \begin{cases} F_{y,ufp} n_{ufp} \\ k_{ufp} \Delta_{ufp,c} n_{ufp} \end{cases} \tag{3.15}$$

$$V_{ufp,t} = max \begin{cases} F_{y,ufp} n_{ufp} \\ k_{ufp} \Delta_{ufp,t} n_{ufp} \end{cases} \tag{3.16}$$

Solve for the Compression Force in the Wood

To determine the total compression force in the wood, C_{wood}, the maximum strain experienced at the rocking corners of the wall panels is first determined using the monolithic beam

analogy. This was originally developed by Pampanin et al. [2001b] for precast concrete beams and later adopted by Ganey [2015] for CLT rocking walls. The goal of this analogy is to determine a relationship between the maximum compression strain at the outermost fiber of the wall, ϵ_{wood} and the neutral axis depth, c. The analogy relates the unbonded rocking behavior to the behavior of a typical monolithic wall with a plastic hinge (Figure 3.12). Both wall models have the same geometry and material properties so the analogy can relate the local unknown parameters of the walls to the equal global displacement behavior of the walls. Note, other similar methods for determining the compression force have been proposed (such as the revised Monolithic Beam Analogy introduced by Palermo et al. [2004]), but the monolithic beam analogy will be used here.

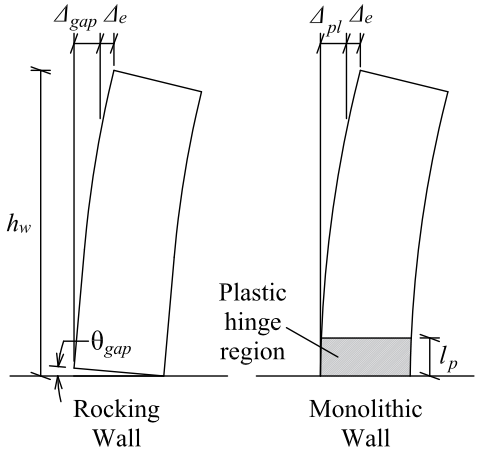

Figure 3.12: Monolithic beam analogy

For the monolithic beam analogy approach, equal displacements are applied to the tops of both walls, as shown in Figure 3.12 and Equation 3.17. For both walls, a portion of the total displacement is from elastic deformations, Δ_e. Because the geometry and material properties of the walls are identical, the elastic deformations are assumed to be equal. For the rocking wall system, the remainder of the wall deformation is from rigid body rotation due to θ_{gap}. This deformation is called Δ_{gap}. For the monolithic wall, the reminder of the

deformation is a result of plastic deformation, called Δ_{pl}. Because the total deformations are equal (Equation 3.18), and the elastic deformations are also equal, the rigid body rotation of the rocking wall, Δ_{gap}, must equal the plastic deformation in the monolithic wall, Δ_{pl} (Equation 3.19).

$$\Delta_{total(rocking)} = \Delta_{total(monolithic)} \tag{3.17}$$

$$\Delta_{gap} + \Delta_e = \Delta_{pl} + \Delta_e \tag{3.18}$$

$$\Delta_{gap} = \Delta_{pl} \tag{3.19}$$

The rigid body deformation of the rocking wall, Δ_{gap} is determined by multiplying the gap rotation at the base by the height of the wall as shown in Equation 3.20.

$$\Delta_{gap} = \theta_{gap} h_w \tag{3.20}$$

The plastic deformation of the monolithic wall is defined using a plastic hinge analysis. Thus, the plastic displacement is defined as the plastic rotation, θ_{pl}, multiplied by the distance between the top of the wall and the midpoint of the plastic hinge length as shown in Equation 3.21. The plastic rotation, θ_{pl}, is defined as the plastic curvature, ϕ_{pl}, multiplied by the plastic hinge length as shown in Equation 3.22. ϕ_{pl} can then be defined as the difference between the total curvature, ϕ_{total}, and the elastic curvature, ϕ_e, as shown in Equation 3.23. Additionally, the total curvature is determined by dividing the unknown strain in the wood, ϵ_{wood}, by the neutral axis depth, c, as shown in Equation 3.24. Finally, elastic curvature is determined through basic mechanics by dividing the yield moment, M_y, by the modulus of elasticity, E_w and the moment of inertia of the wall, I_w, as shown in Equation 3.25. Equation 3.26 combines the previous five equations to present an equation for the plastic deformation of the monolithic wall in terms of ϵ_{wood} and c.

$$\Delta_{pl} = \theta_{pl}\left(h_w - \frac{l_p}{2}\right) \tag{3.21}$$

$$\theta_{pl} = \phi_{pl} l_p \tag{3.22}$$

$$\phi_{pl} = \phi_{total} - \phi_e \tag{3.23}$$

$$\phi_{total} = \frac{\epsilon_{wood}}{c} \tag{3.24}$$

$$\phi_e = \frac{M_y}{E_w I_w} \tag{3.25}$$

$$\Delta_{pl} = \left(\frac{\epsilon_{wood}}{c} - \phi_e\right) l_p \left(h_w - \frac{l_p}{2}\right) \tag{3.26}$$

The next step of the monolithic wall analogy procedure combines the previous equations (Equations 3.19, 3.20, and 3.26) to get the final equation for ϵ_{wood} in terms of the neutral axis depth as shown in Equations 3.27 - 3.29. Note, other research on mass timber rocking walls use different equations for ϵ_{wood}. For example, the strains from elastic deformations are not always included or the plastic hinge length is considered negligible, resulting in ϵ_{wood} being equal to $\theta_{gap}c/l_p$. However, research presented in this document has shown that elastic deformations are not negligible and Equation 3.29 is used.

$$\theta_{gap} h_w = \left(\frac{\epsilon_{wood}}{c} - \phi_e\right) l_p \left(h_w - \frac{l_p}{2}\right) \tag{3.27}$$

$$\frac{\epsilon_{wood}}{c} - \phi_e = \frac{\theta_{gap} h_w}{l_p\left(h_w - \frac{l_p}{2}\right)} \tag{3.28}$$

$$\epsilon_{wood} = \left(\frac{\theta_{gap} h_w}{l_p(h_w - \frac{l_p}{2})} + \phi_e\right) c \tag{3.29}$$

With ϵ_{wood} at the outermost fiber of the timber wall panel, a linearly decreasing strain over the neutral axis depth is assumed until the strain equals zero at the decompression point, as shown in Figure 3.11. The stress distribution, $f_c(x)$, can be determined based on the max strain and the assumed compression behavior of the wood. To compute the final compression force at the base of the wall, C_{wood}, the stress curve can be integrated along the

length of the neutral axis depth, c, and multiplied by the thickness of the wall, b_w, as shown in Equation 3.30. C_{wood} will act at the centroid of the stress distribution, at a distance of d_c, from the compression corner of the wall panel, as shown in Figure 3.11. Note, d_c must be calculated based on the assumed stress distribution at the current rotation.

$$C_{wood} = \int_0^c f_c(x) b_w dx \tag{3.30}$$

If the wood remains elastic, the stress distribution is triangular and the total compression force in the wood is calculated as shown in Equation 3.31, and is located at a distance, d_c, from the corner of the wall of $c/3$.

$$C_{wood} = \frac{1}{2} \epsilon_{wood} E_w b_w c \tag{3.31}$$

Satisfy Equilibrium

The final step of the cross-sectional analysis procedure is to check equilibrium and iterate on the neutral axis depth, c from Section 3.3.1 until equilibrium is satisfied. Again, Figure 3.11 shows a free body diagram of the wall panel. Vertical force equilibrium must be satisfied as shown in Equation 3.32, where n_{pt} is the number of PT bar locations across the width of the wall panel. For each gap rotation, θ_{gap}, the corresponding neutral axis depth, c, is not correct until the vertical equilibrium equation is satisfied.

$$W + \sum_{i=1}^{n_{pt}} T_{pt,i} + V_{ufp,t} = C_{wood} + V_{ufp,c} \tag{3.32}$$

Determine Overturning Moment

Using the results of the cross-sectional analysis procedure, the resulting overturning moment for each imposed gap rotation, θ_{gap} can be calculated through moment equilibrium about the resultant compression force in the wood. The resulting moment of the wall assembly at

the base, $M_{assembly}$, is calculated as seen in Equation 3.33. Alternatively, the moment could be taken about any other point along the base of the wall and would result in the same value. The assembly moment can be broken down into two components: (1) the moment contribution from the UFPs, M_{ufp} and (2) the moment contribution from the PT bars and the compression force in the wood, M_{wall}. This is shown in Equation 3.34 where M_{ufp} and M_{wall} are defined using Equations 3.35 and 3.36, respectively. The moment contribution from the PT bars and compression in the compression force in the wall, M_{wall}, is equivalent to the moment in the wall panel (i.e., the moment that must be capacity designed for).

$$M_{assembly} = (V_{ufp,c} + V_{ufp,t}) \frac{L_w}{2} + \sum_{i=1}^{n_{pt}} T_{pt,i} \left(d_{pt,i} - \frac{L_w}{2} \right) + C_{wood} \left(\frac{L_w}{2} - d_c \right) \tag{3.33}$$

$$M_{assembly} = M_{ufp} + M_{wall} \tag{3.34}$$

$$M_{ufp} = (V_{ufp,c} + V_{ufp,t}) \frac{L_w}{2} \tag{3.35}$$

$$M_{wall} = \sum_{i=1}^{n_{pt}} T_{pt,i} \left(d_{pt,i} - \frac{L_w}{2} \right) + C_{wood} \left(\frac{L_w}{2} - d_c \right) \tag{3.36}$$

3.3.2 Force-Drift Response

Using the base assembly moment, $M_{assembly}$, results (calculated with the moment-rotation cross-sectional analysis procedure) and considering the distribution of earthquake forces up the height of the wall, the total base shear force and deflection at the roof can be approximated.

Base Shear

The distribution of earthquake forces up the height of the wall is either known or can be approximated assuming a design procedure such as the Equivalent Lateral Force (ELF) procedure in ASCE/SEI 7-16 [ASCE, 2016]. This distribution can be quantified by calculating and effective height, h_{eff}. As shown in Figure 3.13, h_{eff} is the effective height a single equivalent lateral shear force would act so the base shear and overturning moment are equivalent

to the system with multiple story shear force. It can be calculated using Equation 3.37. Note, h_{eff} can be calculated without knowing the total base shear or the specific values of the applied forces at each floor, but rather with just knowing the proportion of the total base shear at each floor.

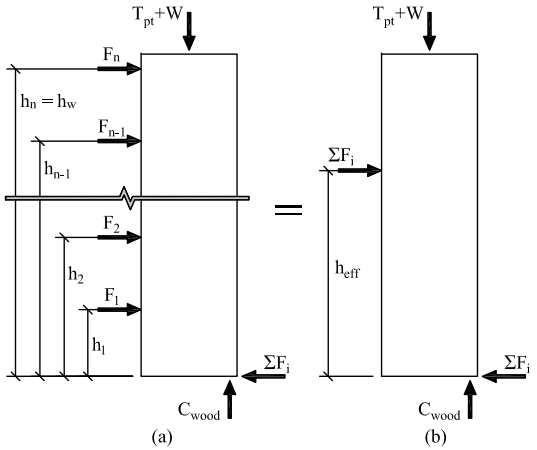

Figure 3.13: Equivalent systems for calculating the effective load height, h_{eff}

$$h_{eff} = \frac{\sum_{i=1}^{n} F_i h_i}{\sum_{i=1}^{n} F_i} \tag{3.37}$$

The assembly moment at the base of the wall can be calculated by summing the product of the applied force at each story, F_i, and the height of each story, h_i, as shown in Equation 3.39. The total base shear can be calculated by summing the applied earthquake force, F_i, for all stories, n, as shown in Equation 3.38.

$$V_b = \sum_{i=1}^{n} F_i \tag{3.38}$$

$$M_{assembly} = \sum_{i=1}^{n} F_i h_i \tag{3.39}$$

The base shear can be calculated as a function of only base assembly moment and h_{eff}, as shown in Equation 3.40.

$$V_b = \frac{M_{assembly}}{h_{eff}} \tag{3.40}$$

Alternatively, if the force distribution is unknown, a triangular distribution of forces can also be assumed as this is a common approximation for seismic applications. Given a triangular distribution, h_{eff} can be calculated as shown in Equation 3.41 where h_w is the height of the wall.The corresponding base shear can be calculated according to Equation 3.40.

$$h_{eff} = h_w \frac{\sum_{i=1}^{n} i^2}{n \sum_{i=1}^{n} i} \tag{3.41}$$

Roof Drift

The total roof displacement, Δ_{total}, can be calculated by summing the displacement due to the gap rotation at the base of the wall, Δ_{gap}, the displacement due to bending deformations, Δ_b, and the displacement due to shear deformations, Δ_s. The deformations due to gap opening at the base of the wall, Δ_{gap}, is a result of rigid body rotation when the wall rocks while the flexural and shear deformations are due to elastic deformations in the wall panels. Note, in rocking wall systems with bounding columns on either side of the wall panel, the boundary columns will contribute to the overall wall system stiffness, however, the contribution is very small (especially for tall buildings) and often neglected. Sarti [2015] recommends only including the contribution from boundary columns for buildings with three or less stories.

The deformation at the roof from rigid body rotation is calculated as the product of the gap rotation at the base of the wall, θ_{gap}, and the the total height of the wall, h_w, as shown in Equation 3.42.

$$\Delta_{gap} = \theta_{gap} h_w \tag{3.42}$$

The deformation at the roof due to flexure, Δ_b, can be calculated assuming the wall is a fixed-base cantilevered wall with applied forces, F_i, at each story. The total deformation from bending can be calculated as a superposition of the force on all n floors, as shown in Equation 3.43, where E_w is the elastic modulus of the timber wall material, and I_w is the moment of inertial of the wall cross section, bending about the strong axis. Note, each story force, F_i, can be solved knowing the vertical distribution of the earthquake forces and the base shear, V_b, calculated in Section 3.3.2.

$$\Delta_b = \sum_{i=1}^{n} \frac{F_i h_i^2}{6 E_w I_w} (3h_w - h_i) \tag{3.43}$$

The deformation at the roof due to shear, Δ_s, can also be calculated assuming the wall is a fixed-base cantilevered beam with applied forces at each story. Similar to flexural deformations, the total deformation from shear forces can be calculated as a superposition of the forces on all n floors, as shown in Equation 3.44, where G_w is the shear modulus of the of the timber wall material. The numerator of Equation 3.44 can be simplified to $M_{assembly}$, resulting in Equation 3.45.

$$\Delta_s = \sum_{i=1}^{n} \frac{F_i h_i}{G_w A_w} \tag{3.44}$$

$$\Delta_s = \frac{M_{assembly}}{G_w A_w} \tag{3.45}$$

Adding the flexural and shear deformations together, the total elastic deformations. Δ_e, can be calculated as shown in Equation 3.46. The total elastic contribution to the drift at the roof can be calculated by dividing the elastic roof displacement, Δ_e, by the total height of the wall, h_w, as shown in Equation 3.47.

$$\Delta_e = \Delta_b + \Delta_s = \sum_{i=1}^{n} \frac{F_i h_i^2}{6E_w I_w}(3h_w - h_i) + \frac{M_{assembly}}{G_w A_w} \tag{3.46}$$

$$\theta_e = \frac{\Delta_e}{h_w} \tag{3.47}$$

Finally, the total deformation at the top of the wall can be calculated by adding the elastic deformations (calculated using Equation 3.46) to the deformations from gap rotation at the base (calculated using Equation 3.42), as shown in Equation 3.48. The total roof drift can then be calculated using Equation 3.7.

$$\Delta_{total} = \Delta_{gap} + \Delta_e \tag{3.48}$$

3.3.3 Application to Paired Wall Systems

The cross-sectional analysis procedure for determining the moment-rotation response and the procedure for determining the force-drift response presented above for a single wall with boundary columns, can also be applied to a paired rocking wall system with some modifications. Figure 3.14 shows the forces distributed at the wall bases for the paired wall system. The forces specific to the left and right panels have 'L' and 'R' superscripts, respectively.

To solve the paired wall system, it is assumed that the roof displacement at the top of each wall panel are equal. It is also assumed that the gap rotations at the base of the walls, θ_{gap}^L and θ_{gap}^R for the left and right panels, respectively, are equal. Thus, the deformation due to rigid body rotation, Δ_{gap}, will also be equal for both walls and so will the elastic deformation, Δ_e. However, the assembly moment at the base of each wall panel will be different because the force contribution from the UFP is different on each wall. As shown in Figure 3.14, the UFP force on the left panel ($V_{ufp,c}^L$) is acting upward (adding to the compression) and the UFP force on the right panel ($V_{ufp,t}^R$) is acting downward (adding to

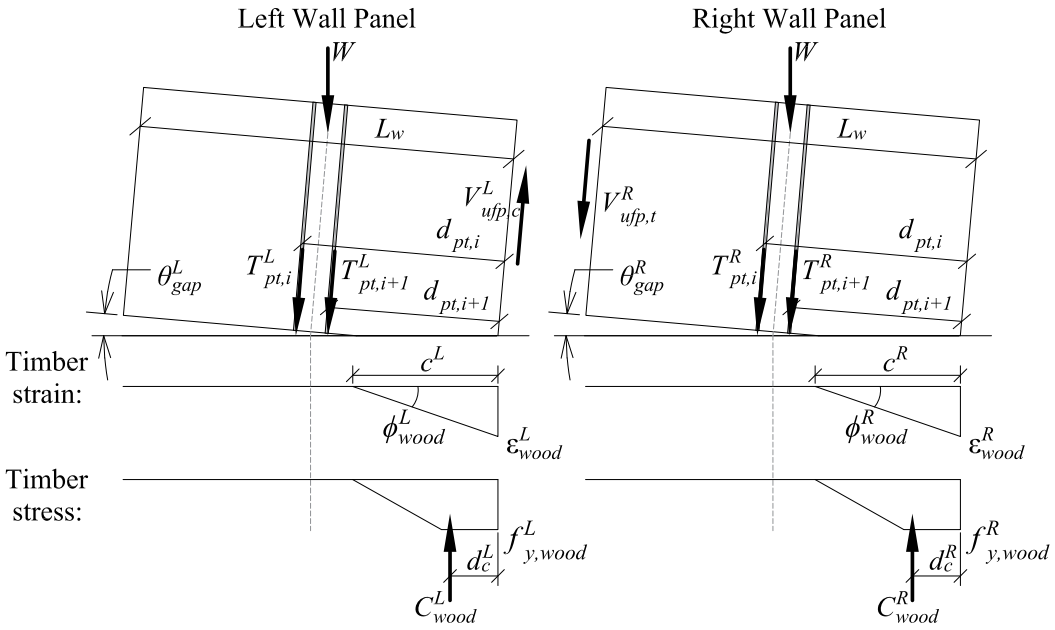

Figure 3.14: Forces distributed at the bases of paired rocking timber walls with UFPs

the tension). Therefore, the wood compression force in the left panel, C^L_{wood}, will be smaller than the wood compression force in the right panel, C^R_{wood}.

To perform, the cross-sectional analysis procedure for paired rocking walls, it is recommend that the wall panels are separated and separate equations are written for each wall panel. The same procedure presented in Section 3.3.1 can be used with the the following modifications to each step:

1. *Impose Gap Rotation:* Impose an equal gap rotation to the base of each wall panel with the assumption that both panels experience the same deformation from rigid body rotation and from elastic deformation (Equation 3.49).

$$\theta^L_{gap} = \theta^R_{gap} \tag{3.49}$$

2. *Estimate Neutral Axis Depth:* Select an initial estimation for the neutral axis depth

on the left (c^L) and right (c^R) wall panels. Initially, these can be equal, but with the presence of UFPs, they will be after iterating to satisfy equilibrium.

3. *Solve for PT Tension Force:* The PT forces in the left wall panel ($T^L_{pt,i}$) and the right wall panel ($T^R_{pt,i}$) can be solved for using the same methods described in Section 3.3.1.

4. *Solve for UFP Forces:* Because the UFPs are located between the walls, the deformation from rotation of both walls must be calculated independently and then added together to calculate the total force in the UFP. Referring to Figure 3.14, when the wall rocks to the right, the UFP deformation from rotation of the left panel ($\Delta^L_{ufp,c}$) can be calculated using Equation 3.15 and the deformation from the rotation of the right panel ($\Delta^R_{ufp,t}$) can be calculated using Equation 3.16. The total deformation of the UFPs for paired walls can then be calculated as the sum of both deformations, as shown in Equation 3.50. The force in the UFP on the left wall panel, $V^L_{ufp,c}$, and the right wall panel, $V^R_{ufp,t}$, can then be calculated using the total sum and thus will both be equal, as shown in Equation 3.51

$$\Delta_{ufp,total} = \left|\Delta^L_{ufp,c} + \Delta^R_{ufp,t}\right| \tag{3.50}$$

$$V^L_{ufp,c} = V^R_{ufp,t} = max\left(F_{y,ufp}, k_{ufp}\Delta_{ufp,total}\right) \tag{3.51}$$

5. *Solve for the Compression in the Wood:* The compression force of the wood of the left wall panel, C^L_{wood} and of the right wall panel, C^R_{wood}, can be calculated using the same methods as outlined in Section 3.3.1. The compression force locations, d^L_c and d^R_c for the left and right wall respectively, can also be calculated.

6. *Satisfy Equilibrium:* Vertical Equilibrium must be satisfied for both the left and right wall panels. The neutral axis depth (c^L and c^R for the left and right panels, respectively) should be iterated on until the equilibrium is satisfied. Equations 3.52 and 3.53 show the vertical equilibrium equations for the left and right panels, respectively.

$$W + \sum_{i=1}^{n_{pt}} T_{pt,i}^{L} = C_{wood}^{L} + V_{ufp,c}^{L} \tag{3.52}$$

$$W + \sum_{i=1}^{n_{pt}} T_{pt,i}^{R} + V_{ufp,t}^{R} = C_{wood}^{R} \tag{3.53}$$

7. *Determine Overturning Moment:* The resulting overturning moment for the left and right wall panel assembly, $M_{assembly}^{L}$ and $M_{assembly}^{R}$ can be calculated as shown in Equation 3.54 and Equation 3.55, respectively. The total base moment, $M_{assembly,total}$, of the paired wall system is calculated by summing the moments from each wall panel as shown in Equation 3.56. The moment contribution from the UFPs in the full paired wall system is calculated as shown in Equation 3.57.

$$M_{assembly}^{L} = \left(V_{ufp,c}^{L}\right) \frac{L_w}{2} + \sum_{i=1}^{n_{pt}} T_{pt,i}^{L} \left(d_{pt,i} - \frac{L_w}{2}\right) + C_{wood}^{L} \left(\frac{L_w}{2} - d_c^{L}\right) \tag{3.54}$$

$$M_{assembly}^{R} = \left(V_{ufp,c}^{R}\right) \frac{L_w}{2} + \sum_{i=1}^{n_{pt}} T_{pt,i}^{R} \left(d_{pt,i} - \frac{L_w}{2}\right) + C_{wood}^{R} \left(\frac{L_w}{2} - d_c^{R}\right) \tag{3.55}$$

$$M_{assembly,total} = M_{assembly}^{L} + M_{assembly}^{R} \tag{3.56}$$

$$M_{ufp,total} = V_{ufp,c}^{L} L_w = V_{ufp,c}^{R} L_w \tag{3.57}$$

To calculated the force-drift response of the paired wall system, the same procedure may be used as presented for the single wall wight boundary columns. The base shear can be approximated using Equation 3.40 with the total moment of the system, $M_{assembly,total}$. Similarly, the roof drifts may be assessed as outlined in Section 3.3.2, but accounting for the stiffness of both wall panels.

3.4 Summary

This chapter presented the component level behavior and system behavior of post-tensioned rocking mass timber walls. The behavior of both paired rocking rocking walls and rocking

wall panels with boundary columns were both discussed. In these systems, the PT connections allow for uplift of the system, resulting in a nonlinear response. The PT connections also allow for recentering after large earthquakes. System damping comes from the UFPs. Additionally, this chapter presented the cross-sectional analysis procedure which is a common method for determining the moment-rotation response of rocking wall systems. A method for determining the force-drift response was also presented. In the cross-sectional analysis procedure, the monolithic beam analogy was used to calculate the peak wood strain at the base of the mass timber panels. In Chapters 4 and 6, these methods were used for as the basis for designing the lateral systems for the two-story and ten-story NHERI TallWood test specimens, respectively.

Chapter 4

TESTING OF THE TWO-STORY NHERI TALLWOOD BUILDING

This chapter has been largely adopted, with variations, from a previously published journal paper written by the author. It is published in the Earthquake Engineering and Structural Dynamics Journal: Wichman et al. [2022].

4.1 Overview

To better understand the performance and behavior of using rocking mass timber walls as the seismic force-resisting lateral system in tall timber buildings, a full-scale two-story mass timber building with CLT rocking walls was tested at the NHERI@UCSD shake table at the University of California San Diego [Van Den Einde et al., 2021]. A key objective of this two-story test was to generate data on the behavior of important components for calibrating numerical models for future simulation of the ten-story test specimen. In this chapter, the design and test setup will be discussed with emphasis on the rocking walls. Note, this chapter is an abbreviated version of Wichman [2018]. In this section, emphasis is put on just the rocking walls, because the remainder of the specimen was designed by project collaborators. Additional information on the design of the diaphragms and gravity system can be found in Barbosa et al. [2021] and Pei et al. [2019], respectively.

4.2 Design considerations

At the beginning of the NHERI TallWood project, researchers collaborated with architects and practicing structural engineers to evaluate the potential market for tall wood buildings. Results from this discussion showed a demand for mixed-use buildings with residential and

commercial spaces and open floor plans that could be reconfigured with nonstructural walls. Because of this discussion, the desire for an open floor plan drove the overall geometry for the two-story specimen, as well as the size limitations of the shake table, and the desired aspect ratio of the diaphragm. The aspect ratio of the diaphragm and CLT walls were selected to be representative of a taller building.

Taking into account the design constraints, there were four key components of the test building the research team wanted to investigate. These components included: (1) a glulam gravity framing design tolerant of large lateral drifts without significant damage, (2) CLT diaphragms with and without a composite concrete deck, (3) resilient post-tensioned rocking CLT wall lateral system, and (4) a low-damage shear transfer mechanism connecting the rocking walls to the diaphragms.

4.2.1 Shake Table Facility Details

The full-scale two-story specimen was tested at the National Hazard Education Research Institute at University of California San Diego (NHERI@UCSD) Large High-Performance Outdoor Shake Table (LHPOST). This laboratory hosts the largest outdoor shake table in the world, making it ideal for conducting this one of a kind test for the mass timber building industry. At the time of this testing, the shake table was uniaxial. The table measures 24.9 feet in the north-south direction and 40 feet in the east-west direction. The table shakes in the east-west direction. The bare table can reach a peak acceleration of 4.2g and with a 900 kip rigid centered payload the table can reach a peak acceleration of 1.28g. The table has a total stroke length of +/- 30 inches in the east-west direction and a vertical payload capacity of 4,400 kips [Van Den Einde et al., 2021].

4.3 Test setup

Figure 4.1 shows a photo and schematic of the test specimen. The gravity system consisted of glulam beams and columns, the floor and roof level diaphragms were made of CLT (the roof diaphragm had a concrete deck topping on top of the CLT panels) and the seismic force

resisting system included two paired rocking walls. The overall structural design configuration was such that the lateral elements and the gravity systems were separated, as commonly adopted for concrete and steel high-rise buildings.

Figure 4.1 shows the four steel gravity frame extender beams anchored to the shake table, cantilevering off the table, perpendicular to the direction of shaking to extend the table width. These beams supported the gravity system, allowing the structure to be larger in the direction perpendicular to shaking. The CLT rocking walls were also placed on top steel foundation beams to make the entire structure start at the same elevation. All steel foundation beams were securely anchored to the shake table using PT rods.

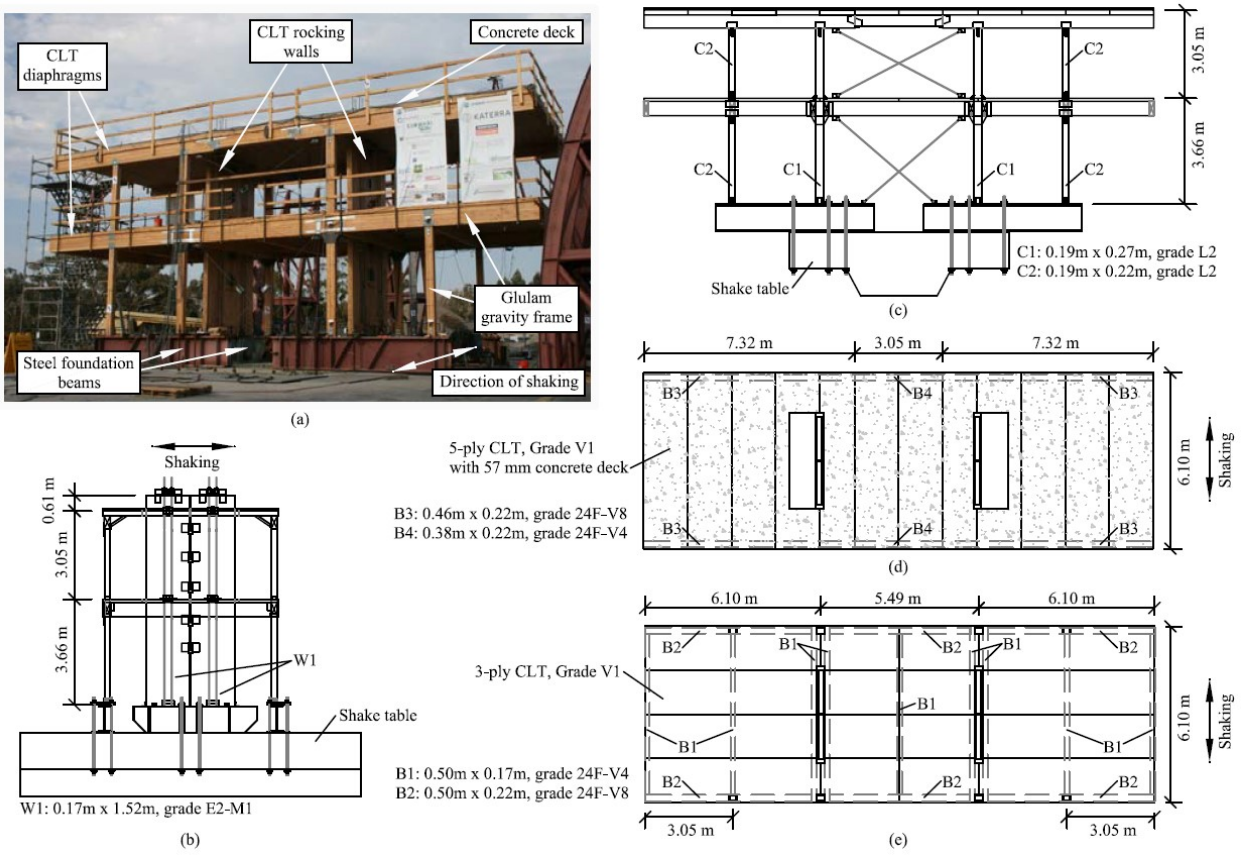

Figure 4.1: Two-story test building: (a) photo, (b) CLT rocking wall elevation view, (c) Building elevation view, (d) roof plan view, and (e) floor plan view.

The gravity system and diaphragms were designed assuming typical office loading with a dead load of 64 psf and 79 psf on the floor and roof, respectively. These loads were determined by summing the estimated as-designed self-weight of the structural elements (assuming concrete on both levels) with a 10 psf partition load and a 14 psf miscellaneous load for finishing items on each level. Because the CLT rocking walls were designed to be independent of the gravity frame and engage only under lateral loads, the weight of the walls was not included in the dead load for design of the gravity system or the diaphragms.

Because nonstructural elements were not included on the test structure and concrete was only added to on the roof level, additional mass was added in the form of large steel trench plates to achieve the intended design seismic mass. Twenty-two and 48 plates, each weighing about 1.3 kips, were added and secured to the roof and floor diaphragms, respectively. Although the intent was for the final weight of the structure to be equivalent to the design dead load (74 kips on the floor level and 92 kips on the roof level), the actual dead load of the floor level exceeded the design load by 14 kips and the actual dead load on the roof level was 2 kips less than then the intended design load. Thus, the total seismic weight, not including the weight of the CLT walls themselves, was 88 kips and 90 kips for the floor and roof, respectively.

4.4 Gravity framing and diaphragm

The gravity frame was designed in accordance with the US 2015 National Design Specification (NDS) for Wood Construction [AWC, 2018] and consisted of glulam beams and columns. All structural timber for the gravity frame was provided by DR Johnson Wood Innovations. The columns were grade L2 and the beams were either 24F-V4 or 24F-V8 grade.

As seen in Figure 4.1, eight glulam columns supported the gravity load. The four columns closest to the center of the building (columns C1 in Figure 4.1c) were continuous through the diaphragm, demonstrating balloon framing. The outside columns (columns C2 in Figure 4.1c) were separated by the floor diaphragm, demonstrating platform framing. The connections between the beams and columns and at column bases and tops utilized vertically

slotted details to allow free rotation and minimize damage to columns, beams, and joints under large lateral drifts. Most connections utilized commercially available connectors with some modifications to accommodate joint rotation during earthquakes. The connection details were completed by KPFF Consulting Engineers, an industry partner for the NHERI TallWood Project, based on connections designed and tested for the permitted Framework building project in Portland, Oregon [Zimmerman and McDonnell, 2018]. Note that considerations for joint fire protection was not incorporated into these details. More details on the gravity connections can be found in Pei et al. [2019] and Wichman [2018].

Also shown in Figure 4.1, the first-floor diaphragm was 3-ply CLT and was more flexible than the roof diaphragm, which was 5-ply CLT with a 2-1/4 inch concrete composite deck. The CLT used for the diaphragm panels was certified as Grade V1 based on APA standard PRG320 [APA, 2019b], also provided by DR Johnson. Both diaphragms had two slots for the CLT post-tensioned rocking wall lateral system. The spans between the beams supporting the diaphragm were designed to satisfy deflection and vibration requirements in the CLT floors for the design office occupancy. The floor and roof diaphragms were designed to be damage-free under the planned seismic excitations and the differing stiffness of each level was an intentional study parameter [Barbosa et al., 2021]. Figures 4.1d and 4.1e show the plan views for the roof and floor diaphragms and show the orientations of the beams and CLT diaphragm panels tested on each level.

4.5 Post-tensioned rocking CLT walls

The seismic force resisting system was designed to meet the seismic demands computed per ASCE/SEI 7-10 [ASCE, 2010] for a class B soil site in San Francisco, California. The same design dead load used for the gravity system and diaphragms was also used as the design seismic weight for the walls. A seismic force reduction factor (R) of six, an importance factor of 1.0, and an approximate period per ASCE/SEI 7-10 were used to compute equivalent lateral force demands used in the design. The design spectral response acceleration parameter at short periods, S_{DS}, and at a period of 1 second, S_{D1}, were 1.06g and 0.34g, respectively,

and the approximate fundamental period, T_a, was 0.20 seconds.

The designs of the two walls were identical. As shown in Figure 4.1b, each wall consisted of two CLT rocking wall panels coupled together with five UFP energy dissipating devices and were post-tensioned with four bars on each wall. The 24-foot tall post-tensioned rocking walls were balloon framed such that they extended 2 feet above the roof elevation to allow for easy PT bar installation. The four wall panels were 5 feet wide, 5-ply grade E2-M1 CLT, and also manufactured by DR Johnson. The walls connected to the diaphragm with a slotted shear key connection allowing for decoupled rotational and vertical movement between the diaphragm and rocking walls.

4.5.1 Rocking wall target performance objectives

The paired rocking wall system was designed to meet four performance objectives, each corresponding to a different seismic demand. At each performance objective, different limit states were targeted for major components in the CLT rocking walls, including: (1) CLT wall panel yielding and crushing at the rocking base, (2) yielding and fracture of the PT bars, and (3) yielding and fracture of the UFPs. These performance objectives are modified versions of the performance objectives presented in Ganey [2015]. The target performance objectives used for the design of the walls in the two-story test specimen, summarized in Figure 4.2, are as follows:

- **Performance objective 1: Wind loading** Targets no wall decompression under design wind load.

- **Performance objective 2: Immediate occupancy** Targets no required repair of the system after a service level earthquake (SLE), defined as a 50%-in-30-year hazard level earthquake (43-year return period). Minor UFP yielding is allowed, however, PT bars and the CLT walls should remain elastic. In addition, SLE level earthquakes at this performance objective should be reach peak drifts of around 1%.

- **Performance objective 3: Limited Repair** Allows for major yielding of the UFPs (with potential replacement) and full system recentring after a design based earthquake (DBE), defined as a 10%-in-50-year hazard level earthquake (475-year return period). After DBE level earthquakes, the UFPs can be heavily damaged and thus replaced, but PT bars should not yield and the rocking CLT panels should only see minor crushing, ensuring rcentering behavior with residual drifts less than 0.2%. In addition, according code-based drift limits, the story drifts should be limited to 2%.

- **Performance objective 4: Collapse prevention** Targets limited overall damage to the system for collapse prevention after a maximum considered earthquake (MCE_R) from ASCE/SEI 7-10. PT bars should only experience minor yielding and CLT wall panels can crush, but damage should still be limited to prevent any major loss of strength or stiffness. The story drift limit for this performance objective is set at 4% based on when the PT bar strains will become large. Beyond an MCE_R level earthquake, the building is expected to see excessive damage and large story drifts.

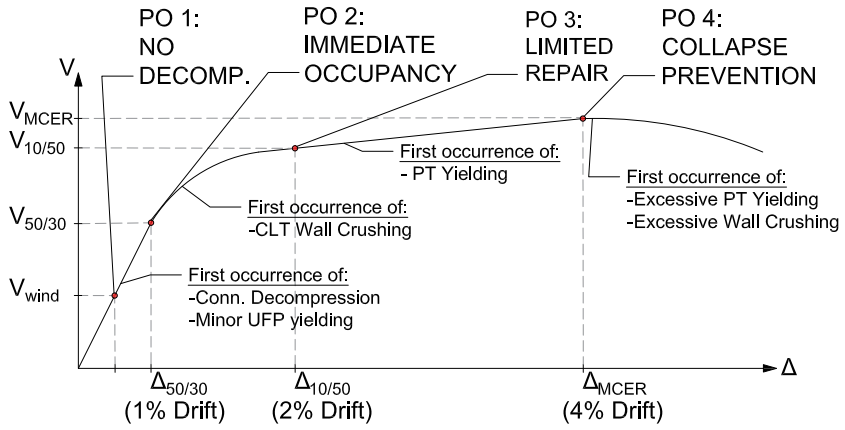

Figure 4.2: Target performance objectives used for the design of the rocking walls in the two-story shake table test. Adopted from Ganey [2015]

4.5.2 Post-tensioned rocking CLT walls design

The following design procedure was adopted for the post-tensioned CLT rocking wall to achieve the performance objectives:

1. *Calculate elastic seismic demands:* ASCE/SEI 7-10 seismic demands were computed using the equivalent lateral force procedure using the approximate fundamental period, T_a, from ASCE/SEI 7-10 and an assumed seismic force reduction factor, R, of 6.

2. *Determine system properties and dimensions:* Initial design parameters and dimensions of the rocking walls and post-tensioning bars were selected. These were adjusted throughout the design procedure to meet performance objectives (Step 7).

3. *Select UFP dimensions and desired dissipation ratio:* The UFP energy dissipators were designed to provide a minimum energy dissipation ratio, β, of 0.3 per the recommendations of Christopoulos et al. [2002]. β, was approximated as shown in Equation 4.1. The moment contribution from the UFPs, M_{ufp}, was approximated as the total plastic force of all 5 UFPs, $V_{p,ufp}$, multiplied by the length of a wall panel, L_w (i.e., Equation 3.57). The yield moment for the system, M_y, was taken as the ELL moment, M_{ell}, calculated ignoring UFP contributions.

$$\beta = \frac{M_{ufp}}{2M_y} = \frac{n_{ufp}(V_{p,ufp}L_w)}{2[n_p(T_{o,pt} + W)d]} \tag{4.1}$$

4. *Calculate elastic moment capacity:* The elastic moment capacity (taken as the moment capacity of the paired wall system at ELL, M_{ell}) was used as the design limit state. As shown in Equation 4.2, M_{ell} was calculated assuming a compression contact length, c, equal to $\frac{3L_w}{8}$ with a linear stress distribution in the CLT, initial PT bar forces, and fully plastic UFPs. In Equation 4.2, n_p is the number of panels per wall system, and n_{ufp} is the number of UFPs. In the calculation of M_{ell}, both wall panels were assumed to have equal moment capacity.

$$M_{ell} = n_p \left[(T_{pt,o} + W) \left(\frac{3L_w}{8} \right) \right] + n_{ufp}(V_{p,ufp} L_w) \tag{4.2}$$

5. *Check that capacity exceeds demand:* The moment capacity of the paired walls at the ELL, M_{ell}, was checked to ensure it exceeded seismic demand. The system properties and dimensions (Step 2) were adjusted and the design procedure was iterated through until this criteria was satisfied.

6. *Determine the moment-rotation response:* Using the cross-sectional analysis procedure and the monolithic beam analogy, discussed in Section 3.3.1, the full moment-rotation behavior of the system was approximated.

7. *Check performance objectives:* Using the approximated moment-rotation response determined from Step 6, all performance objectives from Section 4.5.1 were checked. The system properties and dimensions (Step 2) were adjusted and the design procedure was iterated through until the limit states were satisfied.

CLT wall panels

The four 5-ply CLT wall panels were balloon framed such that they extended 2 feet above the roof elevation for easy PT bar installation. The final dimensions of each panel were:

- Panel thickness: $b_w = 12.375\ in$
- Panel width: $L_w = 5\ ft$
- Panel height: $h_w = 24\ ft$

For design and modeling, the material properties of the CLT were based on compression tests results of 5-ply, E2-M1, DR Johnson CLT, completed at Oregon State University [Barbosa et al., 2018]. The results from this test were used to characterize the equivalent compression stress-strain relationship of the panels, shown in Figure 3.2. Note, exact test

results showed a slight increase in stiffness after yield. The behavior shown is the assumed simplified model. In compression, the behavior can be approximated as elastic, with an elastic modulus of E_w, until the yield stress, $f_{y,clt}$ is reached. After yielding, the behavior can be approximated with a zero strain-hardening plateau until CLT splitting begins at the splitting strain, $\epsilon_{s,clt}$. After splitting, the strength deteriorates until crushing occurs at approximately 25% of the yield stress at the crushing strain, $\epsilon_{cr,clt}$. The material properties used for the constitutive model for the design of the CLT wall panels were:

- Modulus of elasticity: $E_w = 1238\ ksi$
- Shear modulus: $G_w = 80\ ksi$
- Yield stress: $f_{y,clt} = 3.627\ ksi$
- Splitting strain: $\epsilon_{s,clt} = 0.0056\ in/in$
- Crushing strain: $\epsilon_{cr,clt} = 0.0375\ in/in$

Wall to diaphragm connection

The rocking wall lateral system connected to the diaphragm using the vertically slotted shear key connection detail shown in Figure 4.3a, and was designed by engineers at KPFF. The concept for this connection was originally from the permitted Framework building in Portland, Oregon [Zimmerman and McDonnell, 2018]. The connection allows for the diaphragm to remain level by allowing uplift of the wall panels relative to the diaphragm.

As seen in Figure 4.3a, the rounded cantilevered steel shear key (width, w_{key} and thickness, t_{key}) was inserted into a vertically slotted hole in the walls to create a slotted pin connection allowing vertical and rotational movement to decouple the diaphragm from the rocking walls. To reduce vertical resistance at the interface, the shear key was wrapped in a thin Teflon sheet. One end of the shear key was bolted to a steel wing plate to transfer load from the shear key to the diaphragm. The steel wing plate connected to the CLT diaphragm with 45-degree timber screws (on the roof, a portion of the diaphragm did not have

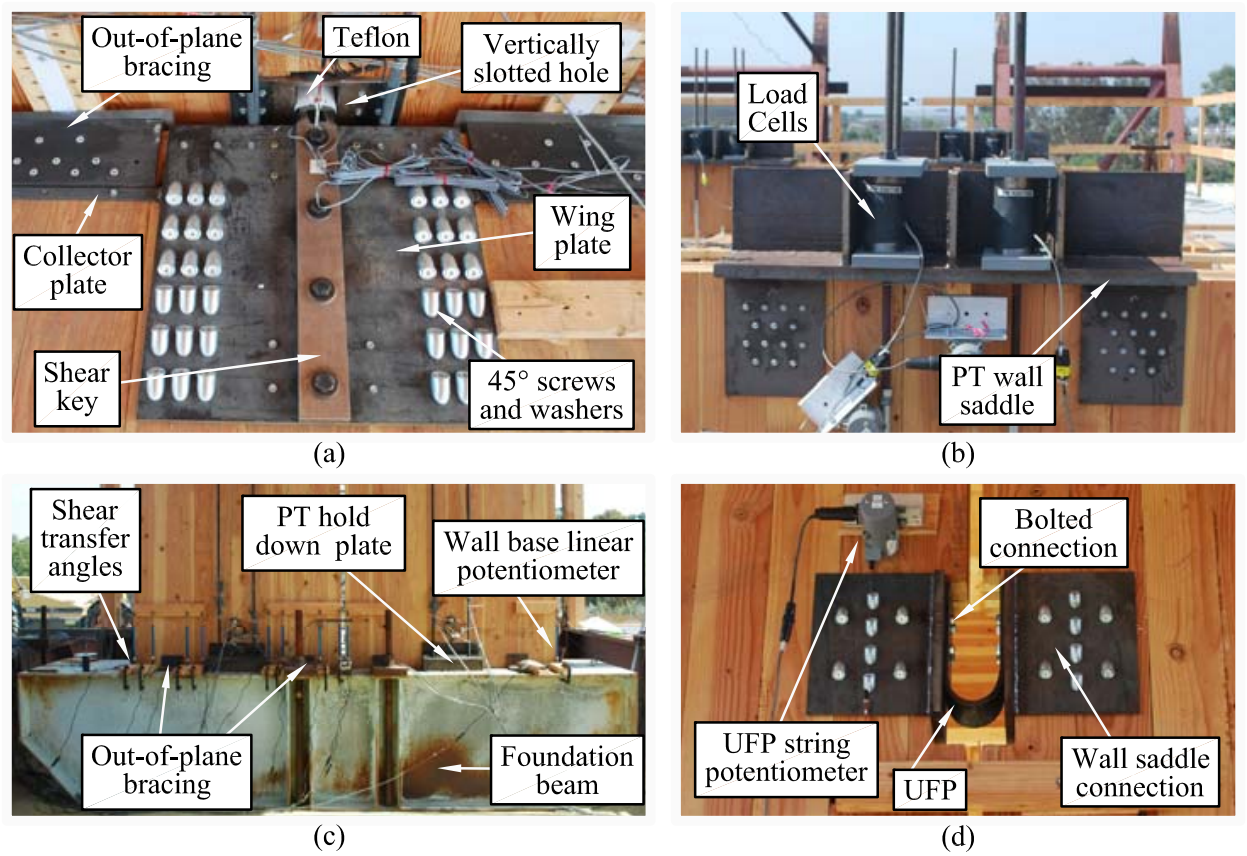

Figure 4.3: CLT rocking wall connection details: (a) wall-to-diaphragm shear transfer connection and out-of-plane bracing; (b) top of wall PT wall saddle connection; (c) base of wall shear transfer, bracing, and PT hold down connection; and (d) UFP energy dissipator connection

a concrete topping, allowing space for this connection). To transfer forces through the diaphragm, steel collector plates were welded to the wing plate and ran along the entire width of the diaphragm (parallel with the walls). The other end of the shear key, sticking through the wall, was left un-attached, creating a cantilevered design with a cantilevered length of L_{key}, measured from the centorid of the wall to the end of the wing plate. The cantilevered design of this connection was intended to represent the worst-case loading scenario for the

connection where the walls are placed on the exterior of the building. The connection was designed based on the estimated rocking wall capacity of 4% drift with an additional safety factor of 1.5. Table 4.1 summarizes the dimensions and properties for the shear keys on the floor and roof levels.

Table 4.1: Dimensions and properties of diaphragm-to-wall shear key transfer connection

Level	w_{key} (in)	t_{key} (in)	L_{key} (in)	E_{key} (ksi)
Roof	2 5/8	1 3/4	16 3/8	29,000
Floor	2 7/8	7/8	16 3/8	29,000

At the intersection of the diaphragms with the rocking shear walls (adjacent to the shear-transfer connection) a series of angles provided out-of-plane bracing as shown in Figure 4.3a. The face of the angle sitting against the wall was lined with a thin stainless-steel plate, while the portion of the wall in contact with these angles were coated with a Teflon sheet to simulate a frictionless surface.

Post-tensioning bars

Each wall panel was post-tensioned with four bars that spanned the entire height of the wall. The bars were Simpson Strong-Tie ATS high-strength, fully-threaded, $\frac{3}{4}$-inch diameter rods (with a net tensile area, $A_{net,pt}$, of 0.334 in^2 and an elastic modulus, E_{pt}, of 29,000 ksi). The manufacturer listed yield stress and ultimate stress were 92 ksi and 120 ksi respectively. As shown in Figure 4.3b, a fabricated steel PT saddle sat atop each CLT wall panel to anchor the PT bars to the top of the wall. While recording the applied force using load cells, each bar was manually tightened to an initial force, $T_{o,pt}$, of 12 kips, about 40% of yield force. At the base of the wall, steel PT hold down plate were welded to the foundation beam to anchor the PT bars to the foundation, as seen in Figure 4.3c.

Foundation beam set up

As mentioned previously, the CLT rocking walls sat steel on foundation beams. Figure 4.3c shows the setup of the rocking wall foundation beam. Under lateral loads, shear forces transferred to the foundation beam through two shear transfer angles, welded to the foundation beam both ends of the wall. Additionally, a series of out-of-plane restraint angles were welded to the foundation beam against the faces of the walls to prevent out-of-plane movement at the base of the walls.

UFP energy dissipation devices

Figure 4.3d shows the typical detail for the UFP energy dissipating devices and connections used to couple the two CLT panels. The edge of each CLT panel had five pre-cut slots for the five UFP devices, spaced approximately evenly up the height of the wall. Steel saddles attached each UFP to the panel. The saddles anchored to the panels with 45-degree self-tapping timber screws and washers. Bolts attached the UFPs to the saddle after the walls were initially post-tensioned to prevent initial prestressing of the UFPs. The diameter of the UFPs, D_u, was 3 5/8 inches, the width, b_u, was 4 1/2 inches, and the thickness, t_u, was 3/8 inch. Grade 60 A572 steel was used for the UFPs with a yield stress, $f_{y,ufp}$, of 50 ksi, and an elastic modulus, E_{ufp}, of 29,000 ksi.

4.5.3 Predicted Performance

The behavior of the CLT rocking walls was predicted using the procedure outlined in Section 4.5.2. The specimen was designed to have a response that met the performance objectives outlined in Section 4.5.1. Table 4.2 shows the general predicted moment-drift response of the specimen with the major events identified and Figure 4.4 shows the corresponding plot.

Table 4.2: Summary of predicted design moment-drift response

Roof Drift	$M_{assembly}$ (k-in)	V_b (k)	Event
0.1%	3365	14.7	M_{demand}
0.2%	3731	16.3	M_{ell}
1.0%	5805	25.3	-
1.3%	6326	27.6	Onset of CLT crushing
2.0%	7490	32.7	-
2.1%	7573	33.1	Onset of PT yielding
3.0%	7999	34.9	-
4.0%	8052	35.2	-
5.0%	8053	35.2	-

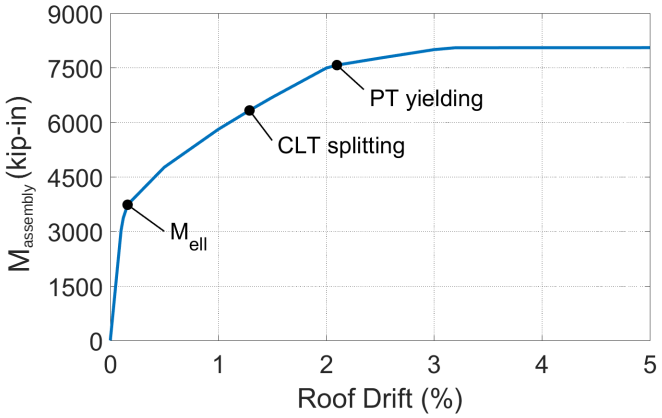

Figure 4.4: Predicted design performance of rocking CLT wall system based on design calculations

4.6 Testing program

The performance at different hazard levels was investigated by subjecting the test specimen to fourteen total earthquake ground motions. The ground motions were chosen to represent the three hazard levels (SLE, DBE, and MCE_R) used to establish the performance objectives. Before and after each ground motion, a two-minute white noise excitation with a 0.03g peak ground acceleration (PGA) was run to obtain the current natural period (where a change in

period could indicate building damage that occurred during the preceding test). The initial white noise test results showed an approximate first mode elastic period of about 0.9 seconds.

The fourteen ground motions came from scaling four different ground motion records from the NGA West PEER ground motion database [Ancheta et al., 2014]. Table 4.3 summarizes the ground motion record information. Note that the normalized FEMA P-695 [NIST, 2010] versions of the Imperial Valley, Loma Prieta, and Superstition Hills records were used. Each of the four ground motion records were scaled to each hazard level, such that the average of the spectra did not fall below the uniform hazard spectra or response spectra between the period range of 0.4 seconds and 2 seconds (based on the approximate first mode fundamental period as determined by results form the initial white noise test Wichman [2018]).

Table 4.3: Summary of PEER-NGA record information for in testing

Event Name	Station Name	RSN	Component
Imperial Valley	Delta	169	1
Loma Prieta	Capitola	752	2
Superstition Hills	Poe Road	725	2
Northridge	Canoga Park	959	2

Table 4.4 shows the testing sequence. The target scale factor is the scale factor that was applied to the ground motion file, while the effective scale factor is the average ratio of the output response spectra to the unscaled input response spectra between the periods of 0.4 seconds and 2 seconds. The difference in these two scale factors is a result of inherent shake table error. The effective peak ground acceleration (PGA) and the effective spectral acceleration at a period of 0.9 seconds are taken from the output ground motion files. Note, tests 6 and 8 used the Northridge motion scaled to be slightly larger than DBE hazard and was repeated back-to-back to demonstrate the ability of the building to withstand multiple strong motions without the need for repair between motions. Also note that the PT bars did not yield during any MCE_R level motions, so the Northridge MCE_R level motion was scaled

by a factor of 1.2 for test 14 to study the response of the building with yielded PT bars.

Table 4.4: Ground motion testing sequence

Test	Event Name	Hazard Level	Target SF	Effective SF	Effective PGA (g)	Effective S_a @ 0.9 sec (g)
1	Loma Prieta	SLE	0.42	0.36	0.16	0.15
2	Loma Prieta	SLE	0.44	0.38	0.18	0.16
3	Northridge	SLE	0.28	0.25	0.19	0.18
4	Superstition Hills	SLE	0.40	0.37	0.13	0.12
5	Northridge	DBE	1.0	0.99	0.53	0.69
6	Northridge [a]	DBE+	1.06	1.13	0.52	0.74
7	Imperial Valley	SLE	0.50	0.42	0.13	0.21
8	Northridge [a]	DBE+	1.06	1.13	0.53	0.74
9	Loma Prieta	DBE	1.21	1.16	0.52	0.49
10	Superstition Hills	DBE	1.42	1.41	0.44	0.42
11	Loma Prieta	MCE_R	1.37	1.32	0.62	0.57
12	Northridge	MCE_R	1.32	1.31	0.73	0.91
13	Superstition Hills	MCE_R	1.98	2.06	0.63	0.63
14	Northridge	MCE_Rx1.20	1.60	1.57	0.85	1.11

[a]Motion was run back to back without a break.

Figure 4.5a and 4.5b show the target uniform hazard curve for the SLE and DBE hazard levels respectively and Figure 4.5c shows the MCE_R response spectra. Each figure includes the target response spectra and response spectra of the effective ground motions completed during testing. Additionally, the average response spectra for the completed tests at that hazard level is plotted. Note, in Figure 4.5b tests 6 and 8 are identical so they lay overlap on the figure. They are not included in the calculation of the average DBE hazard level because they are slightly above the DBE hazard level. Similarly, test 14 was not included in the calculation of the average spectrum for motions scale to the MCE_R hazard level because it was scaled to be 1.2 times the MCE_R spectrum at the building's period. Also included is a vertical line at 0.9 seconds, the approximate first mode elastic period of the building. As shown, the average spectral acceleration of each ground motion set at the building's approximate period exceeds the target hazard level spectral accelerations. This is partially

because the ground motions executed by the shake table were slightly larger than the input motions and because the smallest ground motion in the scaled set was not run.

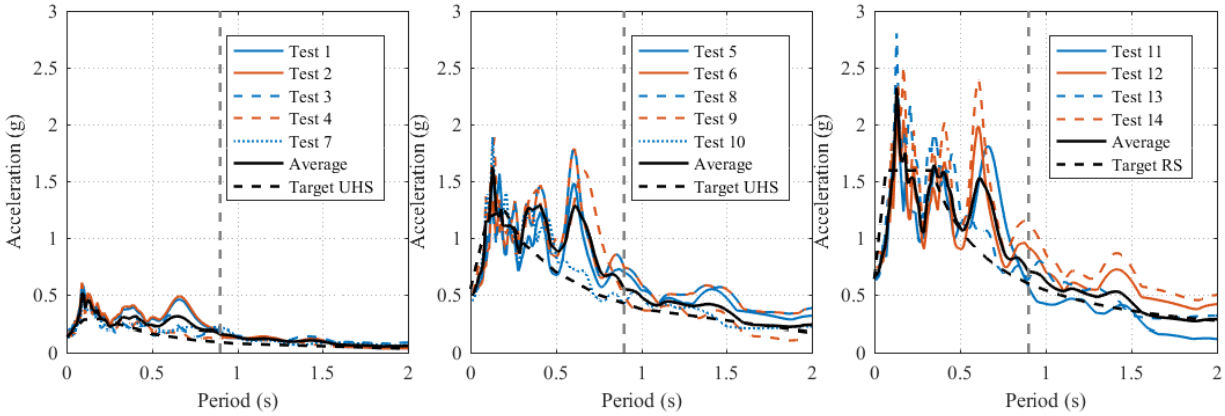

Figure 4.5: Effective spectral acceleration spectra of (a) SLE, (b) DBE, and (c) MCE_R ground motions

4.7 Experimental observations

In general, minimal damage to the structure was observed after the fourteen ground motions and the walls actually performed better than expected. PT bar yielding was not observed until the $MCE_R \times 1.2$ level ground motion was run. Additionally, no major structural damage or crushing occurred anywhere on the walls, and more specifically, the rocking corners at the base of the wall remained damage free throughout testing. Figure 4.6a shows some minor laminate spreading observed. Figure 4.6b shows some minor splitting of the wood at one corner of a wall panel, likely initiated by damage during transportation or installation of the wall panels, prior to testing. After testing, the walls were removed and a square was put up against the corner of the panel. Figure 4.6c shows the little permanent deformations that occurred. The permanent deformations measured at the wall corners ranged from 0.09 inches to 0.13 inches.

The better than expected performance could be largely attributed to the unexpected

Figure 4.6: Photos of CLT rocking wall base corners with minimal (a) laminate spreading (b) crushing and (c) minimal damage at corners after the walls were removed from structure

flexibility of the foundation beams supporting the rocking walls. Figure 4.7a shows an image of one wall panel corner; a notable gap is present between the wall corner and the foundation beam. After removing the walls at the end of testing, it was determined that this gap was a result of both foundation beam deformation and CLT deformation, with the former contributing more substantially. Figure 4.7b shows an exaggerated plan view schematic of the yielded foundation beam and Figure 4.7c shows the corresponding section view of the foundation beam. The permanent vertical deformation at the corners of the panels, $d_{f,p}$, ranged from 0.27 inches to 0.48 inches, and the length over which this deformation occurred, $l_{f,p}$, ranged from 8 inches to 14 inches. Welding the thick PT anchorage plates to the foundation beam at the centerline of each wall panel effectively stiffened the foundation beam in these locations. As a result, this portion of the foundation beam saw no permanent deformations and elastic deformations were not observed in video footage. It is assumed that these portions of the foundation beam remained essentially rigid while the corners were flexible as shown in Figure 4.7b.

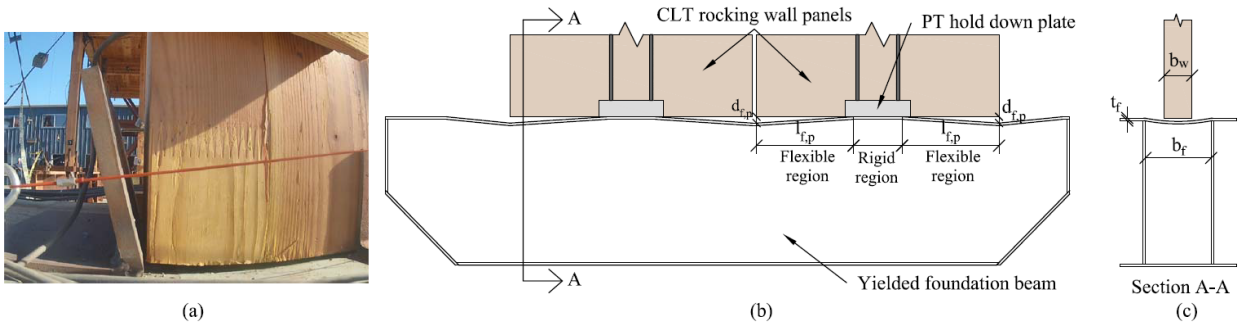

Figure 4.7: Wall base and foundation beam, (a) photo of gap at base of the wall panel and the foundation beam at the end of testing, (b) yielded foundation beam schematic plan view, and (c) cross section view.

Although the structure was essentially undamaged after the fourteen ground motions, no further tests were completed because the gravity frame was only designed for drifts up to 5% and the structural integrity of the gravity frame was necessary for future testing.

4.8 Experimental results and performance

Raw data from the data acquisition system (DAQ) was corrected and filtered prior to data analysis. The data was first down sampled from the collected frequency of 240 Hz to 120 Hz. Additionally, initial offsets were removed from all instrumentation, apart from the load cells. Finally, the accelerometer data was filtered using a band-pass butterworth filter with a lower cutoff frequency of 0.2 Hz and a higher cutoff frequency of 25 Hz to remove random noise. Other instrumentation was not filtered because it did not pick up as much nose. Some sensors malfunctioned, resulting in some lost data.

The overall response of the structure was symmetric. Both paired wall systems performed almost identically and displacements across the diaphragm indicated little torsion, as intended in the design. Thus, in the following section, symmetric response was assumed, torsional effects were neglected during analysis, and the presented results were typically an average between the two walls. Note that the results are only discussed briefly here and a

more thorough collection of plots and data analysis can be found in Wichman [2018].

4.8.1 Global building response

The data from seven accelerometers installed on each diaphragm level was averaged and integrated twice to determine displacement histories of each floor. The maximum 1st story and roof drift, calculated from the integrated acceleration data, is shown in Table 4.5. Figure 4.8 shows a plot of the ground motion spectral acceleration at the building's approximate elastic period of 0.9 seconds (representative of the relative ground motion intensity) verses the roof drift. Only roof drift is summarized in the plot because first-mode response dominated the behavior such that story drifts were similar, as indicated by the ratio of roof drift to first floor drift shown in Table 4.5. Results show a clear positive trend between the increasing spectral acceleration and increasing roof drift ratios, as expected.

Table 4.5: Peak drifts

Test	**Hazard**	S_a **at 0.9 sec (g)**	**Peak Drifts**			**Peak Floor Forces**		
			1st Story drift	**Roof drift**	$\frac{RoofDrift}{1^{st}StoryDrift}$	$\frac{V_{floor}}{V_{base}}$	$\frac{V_{roof}}{V_{base}}$	V_{base} **(kip)**
1	SLE	0.15	0.7%	0.7%	0.97	0.51	0.49	19.9
2	SLE	0.16	0.8%	0.8%	0.97	0.53	0.47	20.4
3	SLE	0.18	0.5%	0.5%	0.95	0.54	0.46	16.7
4	SLE	0.12	0.4%	0.3%	0.95	0.61	0.39	13.0
5	DBE	0.69	2.5%	2.5%	1.00	0.32	0.68	40.4
6	DBE+	0.74	2.5%	2.5%	0.99	0.21	0.79	42.2
7	SLE	0.21	0.9%	0.8%	1.00	0.57	0.43	17.4
8	DBE+	0.74	2.4%	2.5%	1.02	0.57	0.43	35.0
9	DBE	0.49	1.7%	1.7%	1.02	0.45	0.55	26.9
10	DBE	0.42	2.0%	2.1%	1.02	0.47	0.53	33.1
11	MCE_R	0.57	1.9%	2.0%	1.04	0.46	0.54	29.2
12	MCE_R	0.91	3.0%	3.2%	1.07	0.20	0.80	39.2
13	MCE_R	0.63	3.1%	3.3%	1.04	0.44	0.56	41.2
14	$MCE_R \times 1.2$	1.11	4.6%	4.7%	1.02	0.35	0.65	46.4

Because many motions exceeded the target spectral acceleration of the intended hazard level at the building's period of 0.9 seconds, performance objectives were assessed by looking

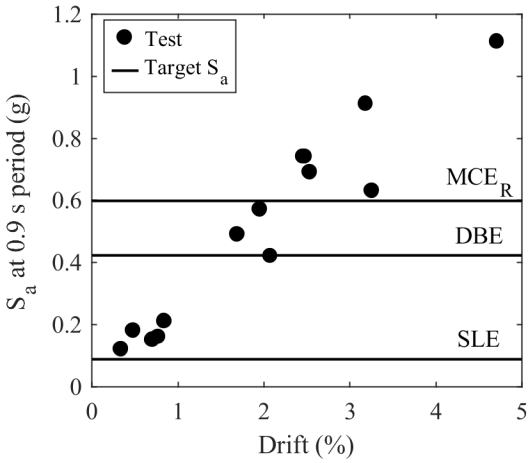

Figure 4.8: Peak roof drifts from experimental results

at the general trends instead of performance at each individual ground motion at it's intended hazard. For example, ground motions 6 and 8 were scaled to be DBE level earthquakes; however, with a spectral acceleration of 0.74g at the building's 0.9 second period, they are more representative of an MCE_R ground motion which has a target spectral acceleration of 0.60g at 0.9 seconds. Thus, also included in Figure 4.8 are horizontal lines indicating the three hazard level target spectral accelerations at the building's approximate period of 0.90 seconds (0.09g for SLE, 0.42g for DBE, and 0.60g for MCE_R).

The design target drift ratios for SLE, DBE, and MCE_R ground motions were 1%, 2%, and 4%, respectively. Referring to Figure 4.8, all motions with spectral accelerations near the SLE hazard line on the plot are below 1% drift. Additionally, motions with spectral accelerations near the DBE line are below the 2% target drift ratio and the motions with spectral accelerations near the MCE_R line are all well below the 4% target drift limit for MCE_R motions. Thus, it can be concluded that the specimen met performance objectives in terms of target drift ratio.

The performance of the specimen was also investigated by calculating the approximate base shear and floor forces. These inertial floor forces were calculated using Newton's second

law and assuming a rigid diaphragm. For each of the floors, the averaged accelerometer readings were multiplied by the approximate mass associated with that floor, and the base shear was calculated by summing the inertial forces of both floors. Figure 4.9 shows the calculated base shear plotted against roof drift for three of the tests, one from each ground motion hazard. The values in these plots are representative of the shear forces in one wall (half of the total structure). Note, the exact base shear and floor forces of the system are unknown because of the assumptions made in calculating these forces from the acceleration records, such as the approximate mass per floor and assuming a rigid diaphragm.

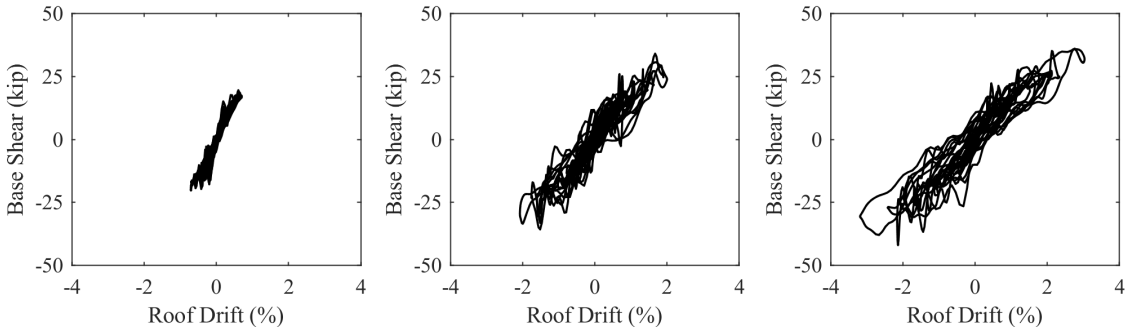

Figure 4.9: Hysteretic response of a single paired wall from experimental results for (a) Test 1, SLE Loma Prieta, (b) Test 10, DBE Superstition Hills, and (c) Test 12, MCE_R Northridge

Looking at the plots in Figure 4.9, the different responses of the specimen at the different hazard levels is evident. The response in the SLE test in Figure 4.9a is relatively linear with some slight nonlinear response due to minor yielding of the UFPs and some rocking of the wall panels. The response in the DBE test in Figure 4.9b is nonlinear and some damping is apparent in the hysteretic response. The response in the MCE_R test in Figure 4.9c shows significant damping and nonlinear behavior, as expected.

The peak base shear per wall for each of the fourteen tests is summarized in Table 4.5. Also included in the table are the approximate values of the floor and roof shears normalized

to the total base shear. The vertical distribution of forces is approximately even between the two stories, as expected because the seismic mass on each floor was very similar. Figure 4.10 shows the calculated peak base shear verse the spectral acceleration of the ground motion at the 0.9 second approximate building period. In general, there is a clear positive trend between base shear and spectral acceleration.

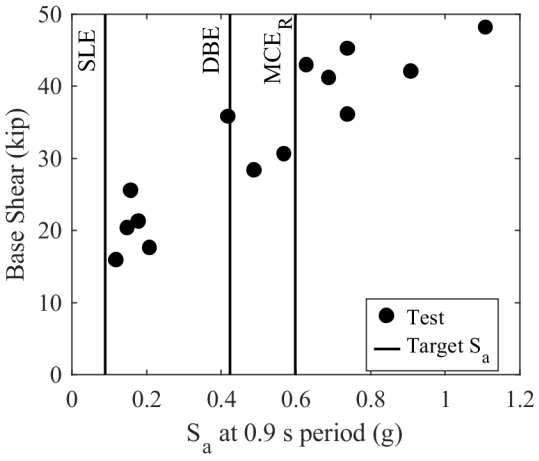

Figure 4.10: Peak Base Shears for a single paired wall system from experimental results

4.8.2 CLT rocking wall response

The force in each PT bar was monitored using load cells. The bars were occasionally re-tensioned between tests to account for prestress losses or gains (a tolerance of ±0.3 kips was used). The overall peak PT force recorded from each test is listed in Table 4.6 as a ratio of peak force to expected yield force. A plot of the peak PT force for each test verses the ground motion's spectral acceleration at the building's approximate first mode period is shown in Figure 4.11. The results from test 5 are not included because load cell data from the DAQ was lost.

Table 4.6: Peak wall values for each ground motion

Test	Hazard	S_a at 0.9 sec (g)	PT Bars $\frac{PeakForce}{ExpectedYield}$	UFPs $\frac{\Delta_{max}}{\Delta_y}$	Peak Wall Base Rotation Uplift (rad)	Compression (rad)
1	SLE	0.15	0.50	1.6	0.25	-0.09
2	SLE	0.16	0.50	1.6	0.26	-0.09
3	SLE	0.18	0.45	1.1	0.15	-0.07
4	SLE	0.12	0.42	0.7	0.08	-0.05
5	DBE	0.69	-	6.8	-	-
6	DBE+	0.74	0.88	6.6	1.08	-0.33
7	SLE	0.21	0.52	1.8	0.32	-0.18
8	DBE+	0.74	0.89	7.0	1.10	-0.34
9	DBE	0.49	0.69	4.7	0.72	-0.27
10	DBE	0.42	0.79	5.3	0.93	-0.29
11	MCE_R	0.57	0.76	5.4	0.85	-0.29
12	MCE_R	0.91	1.02	8.7	1.38	-0.44
13	MCE_R	0.63	1.04	9.2	1.47	-0.44
14	$MCE_R \times 1.2$	1.11	1.12	11.7	2.24	-0.68

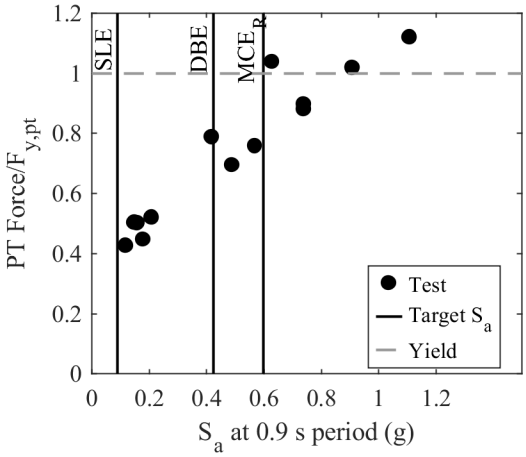

Figure 4.11: Peak PT forces from experimental results

Figure 4.11 shows a general positive trend between the peak PT force ratio and ground motion spectral acceleration. Two of the larger MCE_R level tests (tests 12 and 13) had peak forces larger than the expected yield force, however, they did not actually result in PT

losses, meaning the actual yield stress was slightly larger than the specified yield stress. In the $MCE_R \times 1.2$ hazard level test, the PT bar reached forces 12% above the expected yield force, leading to PT bar yielding and PT losses. However, the PT losses after this test were still minor enough that the walls fully recentered after testing with minimal residual drift. As discussed previously, to meet performance objectives, the PT bars were designed to remain elastic during SLE and DBE earthquakes and were allowed to yield during MCE_R earthquakes. Thus, experimental results met these performance objectives.

String potentiometers measured deformation of the UFP ends relative to each other. Table 4.6 summarizes the ratio of peak UFP displacement to the estimated yield displacement. The expected yield displacement was determined by dividing the initial stiffness calculated using Equation 3.4 by the plastic force calculated using Equation 3.2. These results are also summarized in Figure 4.12 which plots the ratio of peak UFP displacement to the expected yield displacement verses the ground motion spectral acceleration at the building's period for each test.

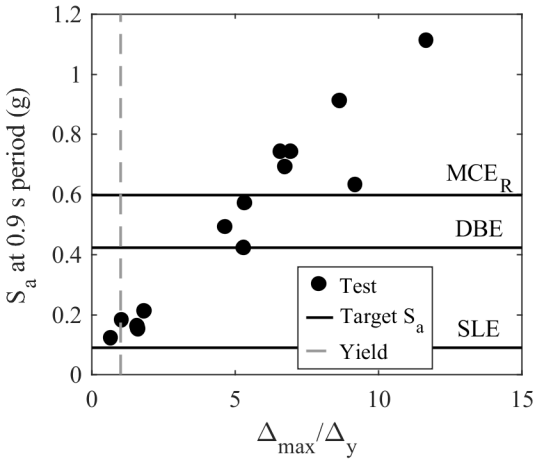

Figure 4.12: Peak UFP yield displacement ratios from experimental results

The design performance objectives allow for initial UFP yielding under SLE earthquakes and the UFPs can undergo large deformations beyond yield during DBE and MCE_R level

earthquakes. The intent is to replace damaged UFPs after DBE and MCE_R level earthquakes but they should not need replacement after SLE level earthquakes. The peak UFP yield displacement ratios summarized in Figure 4.12 show that UFP criteria is met for all ground motion tests as only one earthquake within the SLE region caused UFP yielding. These results also show that the UFPs reach their yield displacements at very small deformations, as expected. Figure 4.12 shows an increase in yield displacement ratio with hazard level, meaning that the walls rocked more with larger hazard level earthquakes. This trend also indicates an increase in energy dissipation for larger hazard earthquakes.

To meet performance objectives, the CLT at the base of the wall has to remain elastic during SLE earthquakes, should only have minor damage during DBE earthquakes, and can have repairable damage under MCE_R level earthquakes. Because no CLT damage was observed during testing, the CLT wall behavior is considered to have met performance objectives. As discussed previously, more damage to the CLT wall panels was predicted, however the foundation beam protected the walls from damage due to it's unexpected flexibility. If a rigid foundation was used during testing, then CLT toe crushing may have been more extensive. This will be explored in Chapter 5.

Linear potentiometers installed at the corners of the wall panels (Figure 4.3c) were used to investigate positive uplift rotations and negative downward rotations at the wall base. The vertically orientated potentiometers were anchored to the portion of the foundation beam flanges outside of the webs (the portion of the foundation beam that did not deform). The downward deformation recorded by these potentiometers were intended to measure compression deformations of CLT. However, because the deformations from foundation beam flange flexibility were substantially larger, the recorded deformations were assumed to be fully attributed to foundation beam deformations. The base rotation was approximated by dividing the recordings by the CLT wall panel length, L_w.

Figure 4.13, shows time history base rotations, calculated from one of the corner linear potentiometers, for three ground motions at three different hazard levels. As shown, the downward base rotations were significant considering that the wall panels remained undam-

aged during testing. Peak uplift rotations and downward base rotation values from each test (from any of the four wall panels) are shown in Table 4.6. Additionally, 4.14 plots the spectral acceleration at the building's period versus the peak uplift rotations and peak downward rotations observed in each test. For both uplift and downward base rotations, the rotations increase with increasing earthquake hazard.

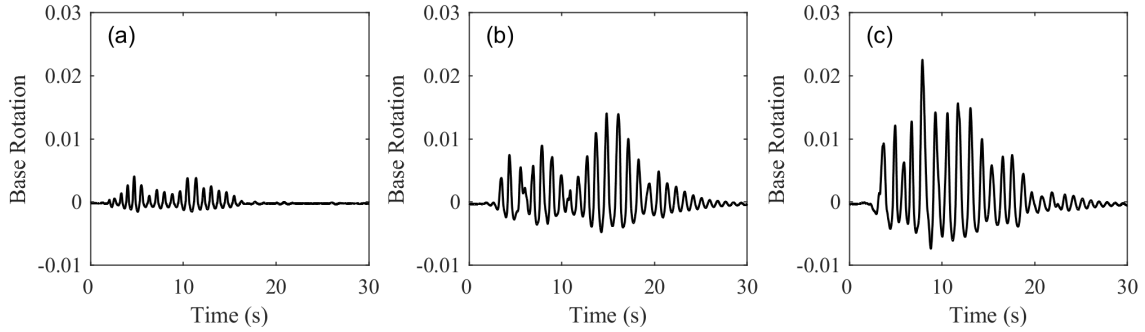

Figure 4.13: CLT wall panel base rotation from experimental results for (a) Test 1, SLE Loma Prieta, (b) Test 10, DBE Superstition Hills, and (c) Test 12, MCE_R Northridge

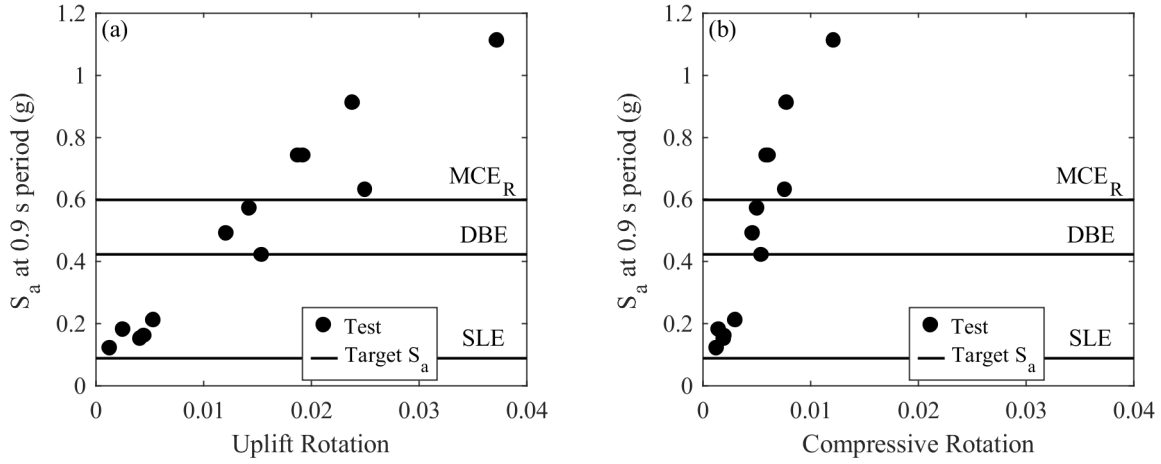

(a) (b)

Figure 4.14: Peak wall base (a) uplift rotations and (b) downward rotations

4.8.3 Comparison of Results to Predicted Behavior

As discussed in Section 4.5.3, the performance of the CLT rocking walls was predicted using the design procedure presented in Section 4.5.2. To compare the predicted design performance to the observed and instrumented response, base shear force per wall was used. Figure 4.15 plots the measured base shear per wall at peak drift verses the peak drift for each test. The predicted design performance from 4.5.3 is also plotted on 4.15. Calculated test results show similar trends to the predicted design performance, but for almost all tests the observed base shear force is lower than the design values. Again, this is most likely due to flexibility in the foundation beam that decreased the stiffness of the structure.

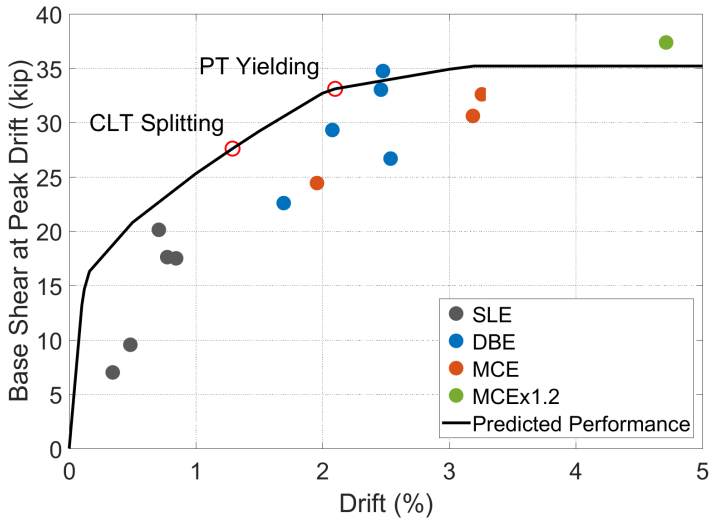

Figure 4.15: Summary of design base shear vs drift compared to observed results

4.9 Summary

Dynamic tests were performed on a full-scale two-story building with paired post-tensioned rocking CLT shear walls as the lateral system to compare the response with the behavior predicted by the performance-based design procedure. The rocking CLT shear walls

utilized unbonded post-tensioned bar connections, UFP energy dissipation devices, and a slotted shear key connection to transfer force between the rocking CLT walls and the CLT diaphragm.

Overall, the test specimen performed well through the fourteen ground motion tests. Target drift limits were met for all three earthquake hazards and all design performance objectives with respect to CLT base crushing, PT bar yielding, and UFP yielding were also met. The specimen performed much better than expected as more damage the the base of the wall and larger PT forces were predicted. The difference in predicted and actual performance is suspected to be a result of the unexpected flexibility in the foundation beams that supported the rocking walls. These beams saw larger downward deformations and permanent yielding below the wall panel corners. An investigation of the impact of the flexible foundation on the overall performance is presented in Chapter 5.

Chapter 5

NUMERICAL MODELING OF THE NHERI TALLWOOD TWO-STORY BUILDING AND INVESTIGATION OF FOUNDATION FLEXIBILITY

This chapter has been largely adopted, with variations, from a previously published journal paper written by the author. It is published in the Earthquake Engineering and Structural Dynamics Journal: Wichman et al. [2022].

5.1 Overview

In this chapter, a numerical modeling technique for post-tensioned rocking walls suitable for seismic performance assessment is presented and validated using results from the full-scale two-story NHERI TallWood shake table test. The numerical models were developed using OpenSees [Mazzoni et al., 2009] and built upon modeling techniques presented in Ganey [2015], where distributed springs are used to simulate the rocking interface. While the techniques presented in Ganey [2015] have been previously validated using cyclic loading test results, this study aims to also validate them for nonlinear dynamic time history analyses using dynamic shake table results.

The two-story specimen was tested at the University of California, San Diego outdoor shake table as part of the NHERI TallWood project (more details on the design and performance of the specimen are discussed in detail in Chapter 4). The building consisted of a glulam gravity frame and a lateral system made of two post-tensioned rocking CLT wall panels connected with UFP energy dissipating devices (i.e., two paired rocking walls). During testing, the paired CLT rocking walls provided strength, energy dissipation, and recentering capabilities necessary for the building to achieve the design performance objectives. Overall

the system performed better than expected. Notably, the CLT rocking walls experienced no damage even though CLT yielding and crushing were expected at the corners of the wall base during MCE_R scaled ground motions. The unexpected flexibility of the foundation beams supporting the rocking walls altered the behavior of the specimen from the as-designed case with rigid foundation boundary conditions, protecting the base of the CLT walls from crushing.

Although the foundation flexibility observed is unique to this test and a more rigid foundation would be expected in actual buildings, further investigation is important to determine it's impact on the system performance. Additionally, it is important to determine if design performance objectives would have still been satisfied had it been tested on a rigid foundation. The comprehensive model presented here provides valuable information about individual wall components including the PT bars, UFPs, and damage to the CLT at the base of the wall. With this level of detail, the model can be used to look further at the impact of the flexible foundation beam on the behavior of the individual wall components.

In this chapter, a numerical model that includes the flexibility of the foundation beam is presented first, followed by a discussion on how well the model replicated results from the shake table experiments, validating the numerical modeling technique. After, a modified numerical model is presented that assumes a rigid foundation boundary condition. This second model is intended to predict the as-designed response of the specimen had it been tested with a more rigid foundation, since that is more likely to represent a realistic building. Finally, the response of the numerical model under rigid foundation boundary conditions is compared to the original design performance objectives for the test specimen and used to further determine the impact of the flexible foundation.

5.2 Numerical Model of Shake Table Experiment

The presented model is two-dimensional and represents only one of the paired walls in the test specimen, with half the gravity system and half the mass included. Figure 5.1 shows a schematic of the numerical model intended to represent the test specimen including the flex-

ible foundation beam. Figure 5.2 shows conceptual behaviors of various component models used within the overall model.

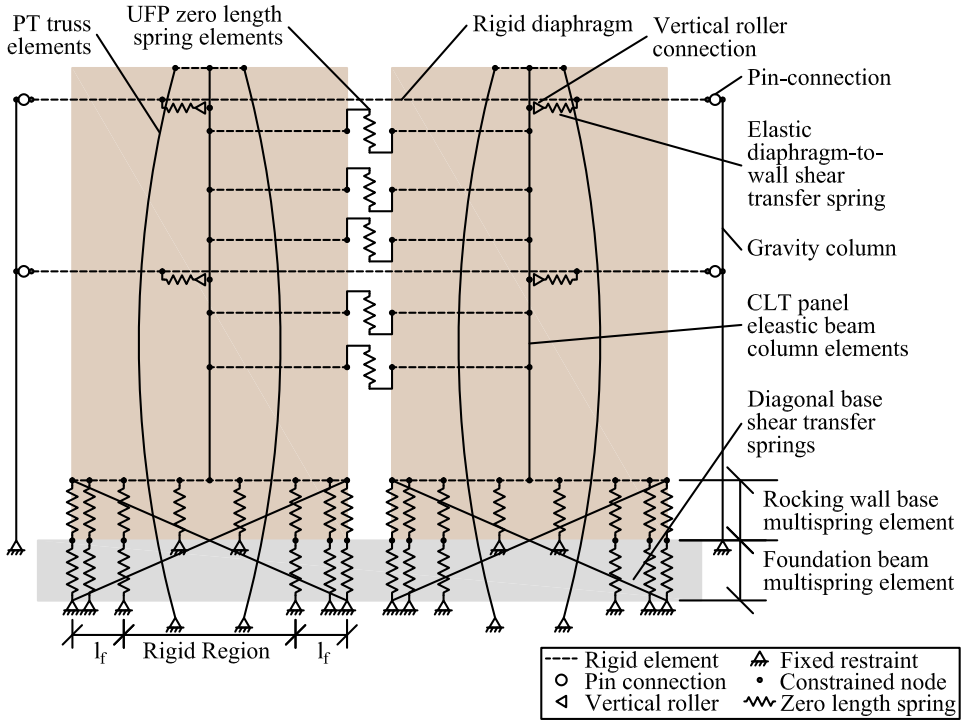

Figure 5.1: Numerical model schematic

The PT bars were modeling using corotational truss elements that spanned from a fixed node at the base to the end of a cantilevered rigid element at the top of the wall, representing the PT offset from the centerline of the wall. A bi-linear hysteretic material model with damage (ElasticPPGap material in OpenSees) limited the element behavior to tension only and allowed for damage accumulation after yielding (shown in Figure 5.2a). An initial strain wrapper (InitStrainMaterial in OpenSees) applied an initial strain to simulate prestressing in the elements. When the initial PT strain is applied in the model, elastic shortening of the CLT wall reduces the apparent load in the PT bars. To correct for the wall shortening, a higher initial PT force ($T^*_{o,pt}$) is applied in the model to ensure the target PT force ($T_{o,pt}$) is achieved. The larger applied PT force is calculated as:

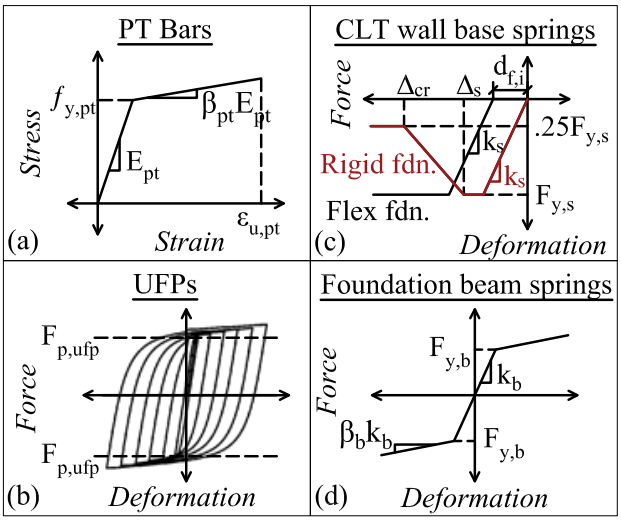

Figure 5.2: Material models used in numerical model

$$T^*_{o,pt} = T_{o,pt}\left(\frac{k_w}{k_w - k_{pt}}\right) \tag{5.1}$$

where k_w is the elastic stiffness of the wall calculated as $A_w E_w / h_w$ and k_{pt} is the elastic stiffness of the PT bars calculated as $A_{pt}E_{pt}/h_w$. Table 5.1 summarizes the various properties for the PT bars.

Table 5.1: PT bar dimensions and material properties

A_{pt} (in^2)	E_{pt} (ksi)	$T_{o,pt}$ (kip)	$f_{y,pt}$ (ksi)	β_{pt}
0.334	29,000	12	92	0.01

As shown in Figure 5.1 and Figure 5.2b, each UFP was modeled using a zero-length spring with a uniaxial Giuffrè-Menegotto-Pinto steel material model with isotropic strain hardening (Steel02 in OpenSees). Yield force and stiffness values were calculated using Equations 3.2 and 3.4, respectively, and properties of the UFPs from the test (summarized again in Table

5.2 for clarity). Because the UFPs primarily impose shear forces on the walls, the UFP springs were only allowed to deform vertically. The UFPs were located at the midpoint between the two wall panels. Rigid elements connected each end of the UFP spring to each of the wall element at the same vertical position.

Table 5.2: UFP dimensions and material properties

b_u (in)	t_u (in)	D_u (in)	E_{ufp} (ksi)	$f_{y,ufp}$ (ksi)
4.5	0.375	3.625	29,000	60

A series of elastic beam-column frame elements (ElasticTimoshenkoBeam element in OpenSees) that included axial, flexure, and shear deformations modeled the elastic portion of the CLT rocking walls. The CLT properties of the walls used in the test were used for these elements (the values are repeated in Table 5.3 for clarity).

Table 5.3: CLT panel dimensions and assumed material properties for design and modeling

b_w (in)	L_w (in)	h_w (in)	E_w (ksi)	G_w (ksi)	$f_{y,clt}$ (ksi)	$\epsilon_{s,clt}$ (in/in)	$\epsilon_{cr,clt}$ (in/in)
6.875	60	288	1238	80	3.63	0.0058	0.0375

The inelastic compressive deformation of the CLT and the rocking behavior at the base of the panels were modeled using a multispring contact element, initially developed by Spieth et al. [2004] for prestressed concrete structures with rocking beam-column connections. The wall base multispring element consisted of 40 parallel zero-length springs distributed along the length of the wall using a Labatto Integration method. The top of each spring was connected to the base of the last wall beam-column element with a horizontal rigid element. The bottom of the wall base multispring element springs within a distance of l_f from the corners of each wall panel were connected to an additional zero-length spring modeling the foundation beam flexibility (discussed in more detail below). The base of the remaining springs near the centers of each wall panel were fixed, modeling the portion of the foundation

that was assumed to be rigid, as shown in Figure 5.1. Additionally, two stiff shear transfer springs were attached diagonally from the outer wall base multispring element springs to the outer foundation beam multispring element springs to transfer shear without significantly inhibiting rocking action.

Each zero-length spring at the wall base was assigned the compression-only hysteretic material model shown in Figure 5.2c. The compression-only portion of the material model simulated the rocking behavior while the hysteretic properties simulated the CLT compression behavior. To transform the CLT stress-strain compression behavior shown in Figure 3.2 to a force-deformation behavior needed for zero-length springs (Figure 5.2c), a plastic hinge length, l_p, was chosen. In this model, a plastic hinge length of $2b_w$ (where b_w is the thickness of the wall) was assumed in accordance with recommendations in Akbas et al. [2017]. An overall initial contact stiffness, K_s, was determined for the entire wall base (all multispring elements representing the CLT) using the following equation:

$$K_s = \frac{A_W E_w}{l_p} \tag{5.2}$$

where A_w is the cross sectional area of the wall panel, equal to the product of b_w and L_w. Wall dimensions and material properties can be referenced in Table 5.3. Referring to Figure 5.2c, each individual spring stiffness, k_s, was a weighted portion of the overall contact stiffness, K_s, based on the spring distribution. The product of the CLT panel yield stress and the Labbatto weighted area of each spring determined the yield strength of each spring, $F_{y,s}$. Similarly, the product of the respective strains, ϵ_s and ϵ_{cr}, and the plastic hinge length, l_p, determined the splitting deformation, Δ_s, and the crushing deformation, Δ_{cr}.

The addition of the multispring elements representing the rocking and CLT compressive deformation at the base of the wall increases the axial flexibility of the wall. Although the increased axial flexibility will not likely affect the performance dramatically, a simple truss element, spanning the length of the CLT beam-column wall elements, can be added to essentially increase the area of the wall and compensate for the reduced stiffness. By

increasing the area with a truss element, the flexural stiffness of the wall in not affected. The truss element has an elastic material model, with elastic modulus E_w and an area, A_w^* calculated as:

$$A_w^* = \frac{l_p}{h_w - l_p} \tag{5.3}$$

The foundation beam was assumed to be undamaged at the beginning of the first two ground motions. After that, initial permanent deformation of the foundation beam was assumed at the beginning of each ground motion from accumulated foundation beam damage. The size of the gap decreased linearly along the flexible portions of the foundation beam (see Figure 5.1) with the corner springs having an initial gap length of $d_{f,i}$ and the springs located at a distance of l_f from the corners having no initial gap. A flexible foundation length (l_f) of 24 inches was used for all tests. Because the gap between the wall panel and the foundation beam increased throughout the testing sequence, $d_{f,i}$ also increased in the model throughout the analyses of the testing sequence. The gap values ($d_{f,i}$) used for each test are shown in Table 5.4 and are based on observations made during the testing.

Table 5.4: Initial gap included in the model

Test Numbers	$d_{f,i}$ (in)
1-2	0.00
3-5	0.05
6-11	0.10
12-14	0.20

As shown in Figure 5.2c, for the flexible foundation model, a compression only elastic-perfectly plastic material with a gap (ElasticPPGap in OpenSees) was used to achieve the initial stiffness of the CLT and account for the initial compression gap from permanent damage to the base beam. Although this material model cannot capture the deterioration, the CLT remained largely elastic during testing and during the simulations, so it did not

affect the behavior. Note, as discussed in section 5.4.1 CLT deterioration was included in the rigid foundation material model shown in Figure 5.2c since initial gaps were not present and more damage to the CLT was expected.

The multi-linear material model (Steel01 in OpenSees) shown in Figure 5.2d was used to model foundation beam flexibility. The initial stiffness of the foundation beam springs was approximated by assuming the top flange of the double webbed beam shown in Figure 4.7c acted as a fixed-fixed beam between the two webs and the base of the wall imposed a uniformly distributed load (along a length equal to the panel thickness, b_w) at the center of the beam. The thickness of the top flange, t_f, was 5/8 inches and the webs were spaced at a distance, b_f, of 17 inches. The elastic stiffness of the beam was calculated for the flange dimensions and loading and the yield force was approximated using plastic analysis. The stiffness, k_b, and yield force, $F_{y,b}$, of each spring was calculated as a weighted portion of the total stiffness and yield force using the same Labatto Integration distribution as the rocking wall base multispring element springs. A yield stress of 60 ksi was assumed for the steel beam.

Because only a single paired wall system was included in the numerical model (as shown in Figure 5.1), only half the gravity system was included. The gravity columns were modeled with two continuous elastic beam-column elements; one on each side of the wall. The columns had cross sectional areas representative of the continuous and platform columns and moment of inertia's corresponding to only the continuous, balloon framed columns. Equivalent gravity loads and seismic masses were applied to each gravity column at each floor level. Rigid elements connected the gravity columns to the wall panels at each floor level simulating a rigid diaphragm. The rigid diaphragm model assumption can predict the fundamental mode behavior and peak story drifts well, but the flexibility in the diaphragm should be included to predict the higher frequency motion and floor accelerations.

The connection between the diaphragm and walls was modeled with a zero-length spring. To model the elastic flexibility of the wall-to-diaphragm connection, the material properties assigned to the horizontal degree of freedom of the zero-length spring was that of a cantilever

beam with the dimensions of the shear key listed in Table 5.5. The spring had zero stiffness in the vertical and rotational degrees of freedom to allow for uplift and rocking.

Table 5.5: Dimensions and properties of diaphragm-to-wall shear key transfer connection

Level	w_{key} (in)	t_{key} (in)	L_{key} (in)	E_{key} (ksi)
Roof	2 5/8	1 3/4	16 3/8	29,000
Floor	2 7/8	7/8	16 3/8	29,000

5.3 Comparison of Experimental and Analytical Results

In this section, a comparison of the experimental results with the numerical results is presented. The numerical model, as described above, includes the flexible foundation which is representative of the boundary conditions in the test. Note, however, that the plots in this section include experimental results as well as results from both the flexible foundation model (labeled "Num Flex" in the figures and representative of the test specimen) and the rigid foundation model (labeled as "Num Rigid" in the figures). The intention of presenting the results of the rigid foundation model is not to validate them against the experimental results, but to predict how the specimen would have responded with the as designed rigid foundation boundary condition. The rigid foundation model results will be discussed in detail in Section 5.4 but are presented on the same plots at the flexible foundation model for comparison and conciseness.

5.3.1 Global building response

Lateral displacement results from the experiments were determined by averaging the recordings from the seven accelerometers located on each diaphragm level and integrating twice to obtain displacements. As discussed in Chapter 4, first-mode response dominated, such that the interstory drifts were very similar between the two stories. The numerical model showed similar results, thus, only the roof drifts are presented and discussed here. Figure

5.3 compares the time history roof drift response from the experimental results with the flexible foundation numerical model for three of the tests, each at a different intensity level. As shown, the numerical model accurately replicates the period and overall behavior, but under predicts the peak drift values. The maximum absolute roof drift for the experimental and numerical results for all 14 tests are summarized in Figure 5.4 which plots the spectral acceleration of each ground motion at the approximate initial period of the building (0.9 seconds) versus the peak roof drift value. The figure shows a clear positive trend between the increasing spectral acceleration and increasing drift ratios. It also shows that the flexible foundation numerical model slightly underestimates the peak drifts.

Assuming a rigid diaphragm, experimental base shear results were approximated by calculating the inertial force at each floor by multiplying the average of the accelerometer readings on each story by the estimated mass on each story. Figure 5.5 shows the base shear versus roof drift hysteretic response for the experimental and numerical results for the same three tests shown in Figure 5.3. Relatively good agreement of the overall structure stiffness is shown, but the base shear values are slightly underestimated with the flexible foundation numerical model. Again, Figure 5.6 summarizes the peak base shear values obtained from each test plotted against the spectral acceleration from the recorded table motion at the building's measured first natural period. Here, the experimental values are consistently larger than the numerical results. Note that results for a single paired wall system are shown in Figure 5.5 and Figure 5.6.

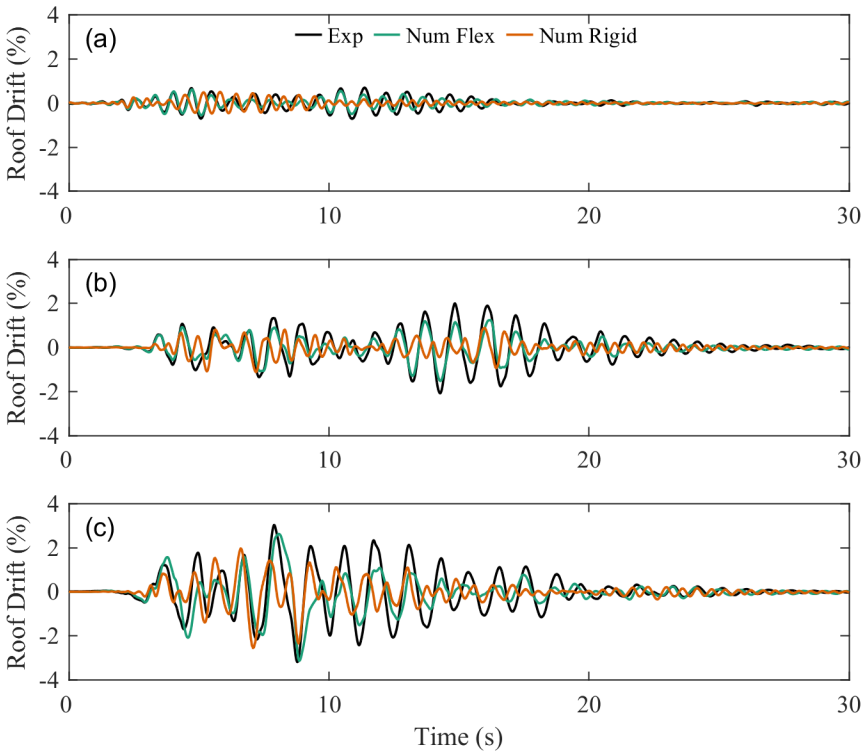

Figure 5.3: Comparison of the roof drift time history response from experimental results, the flexible foundation numerical model, and the rigid foundation numerical model for (a) Test 1: SLE Loma Prieta, (b) Test 10: DBE Superstition Hills, and (c) Test 12: MCE_R Northridge.

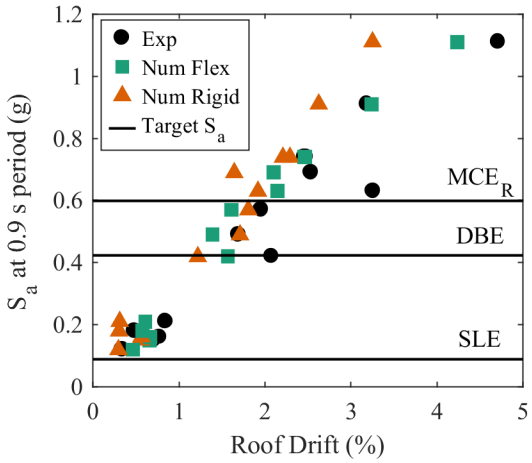

Figure 5.4: Comparison of peak roof drift values from the experimental results, the flexible foundation numerical model, and the rigid foundation numerical model.

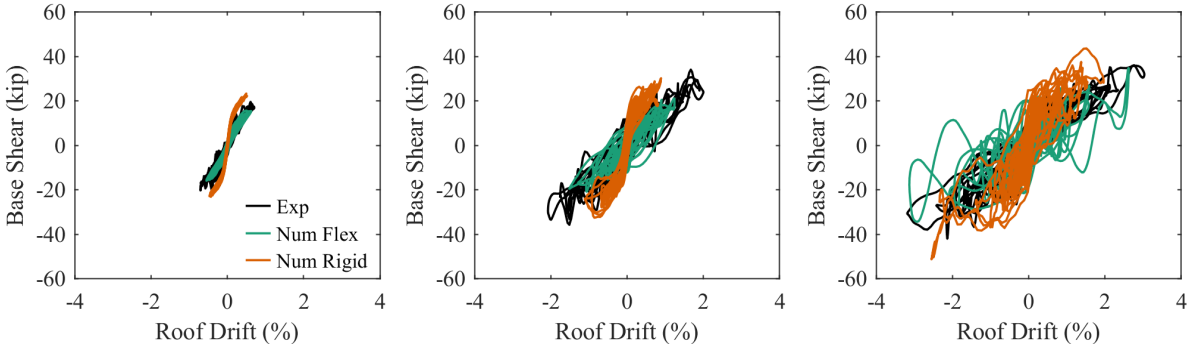

Figure 5.5: Comparison of the hysteretic response from experimental results, the flexible foundation numerical model, and the rigid foundation numerical model for (a) Test 1: SLE Loma Prieta, (b) Test 10: DBE Superstition Hills, and (c) Test 12: MCE_R Northridge.

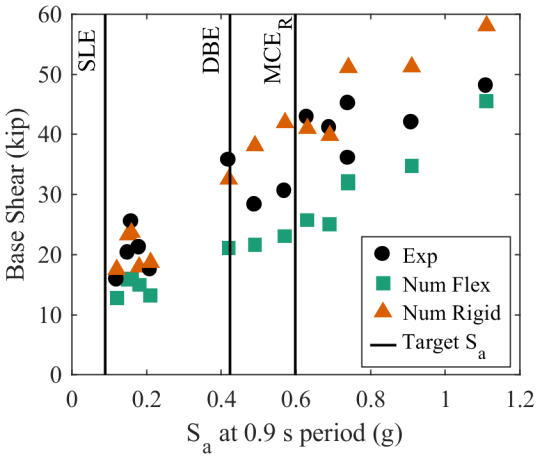

Figure 5.6: Comparison of peak base shear values for a single wall from the experimental results, the flexible foundation numerical model, and the rigid foundation numerical model.

5.3.2 CLT rocking wall response

The PT bar forces were measured using load cells. Wichman [2018] showed that the response of the two paired wall systems were almost identical due to the symmetry of the building, thus, to compare the experimental results to the numerical results, the experimental response history of the PT bars were averaged between the two walls. Figure 5.7 shows the PT bar force normalized by the bar yield force (taken as the manufactures specified yield stress, $f_{y,pt}$, times the tensile area, A_{pt}) versus roof drift for an SLE, DBE, and MCE_R level ground motion. For each test, the figure shows each of the four PT bar locations along the face of the paired wall system (denoted by the graphic on each plot). Figure 5.7 shows that the general behavior of the PT bars is well predicted by the numerical model, but also underestimates peak PT force values. Figure 5.8 summarizes the peak PT force for each test versus the ground motions spectral acceleration at the building's period. Again, it is clear that the peak PT force is consistently underestimated. However, underestimation of the peak PT force values is expected because the roof drift values are also underestimated, meaning the walls uplift of the walls is smaller in the flexible foundation model. As a result, the PT bars do not elongate as much in the model as in the test. The flexibility of the foundation beam also resulted in the compression toe of the walls sinking downwards, decreasing bar elongation. This is clear with the flattened portion of the PT force versus drift response at low drifts in Figure 5.7.

String potentiometers measured deformation of the UFP ends relative to each other, as shown in Figure 4.3d. A ratio of UFP displacement to yield displacement was used to quantify a measure of UFP ductility demand. Figure 5.9 shows the spectral acceleration at the building's period versus peak UFP yield displacement ratio for all tests. As shown in the figure, the UFPs yielded in almost every test, resulting in increased energy dissipation with increasing ground motion intensity. Because the numerical model with foundation flexibility under predicts roof drift, it also under predicts the UFP yield displacement ratio.

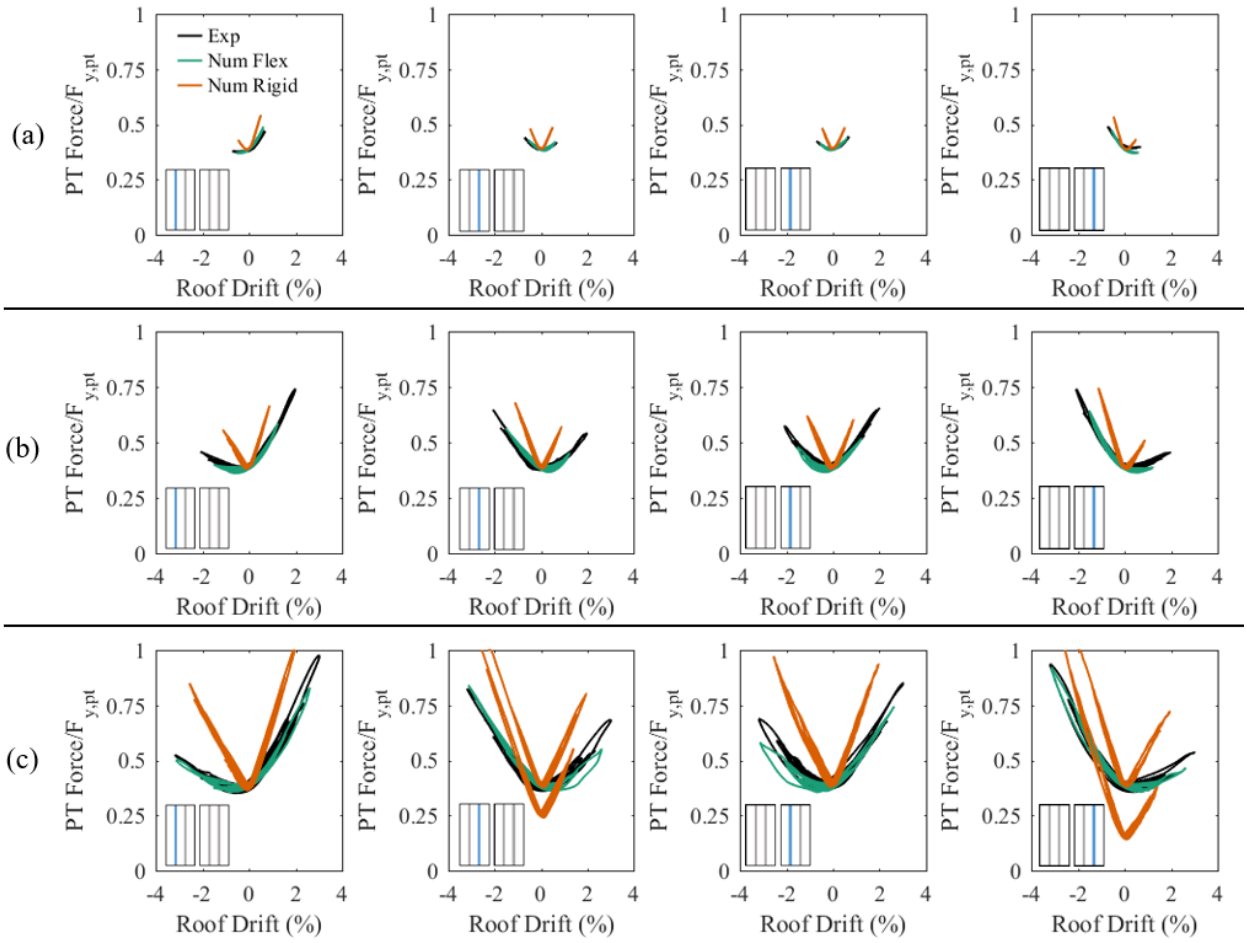

Figure 5.7: Comparison of PT force yield ratio versus roof drift response from experimental results, the flexible foundation numerical model, and the rigid foundation numerical model for (a) Test 1: SLE Loma Prieta, (b) Test 10: DBE Superstition Hills, and (c) Test 12: MCE_R Northridge.

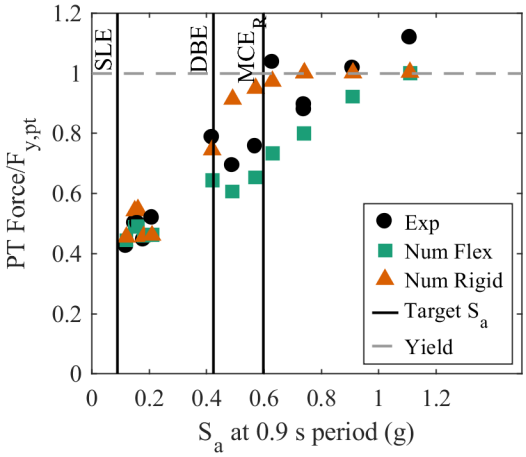

Figure 5.8: Comparison of peak PT force yield ratios from the experimental results, the flexible foundation numerical model, and the rigid foundation numerical model.

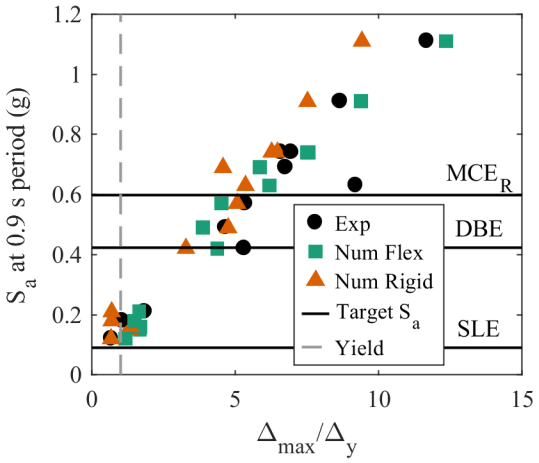

Figure 5.9: Comparison of peak UFP yield displacement ratios from the experimental results, the flexible foundation numerical model, and the rigid foundation numerical model.

Results from linear potentiometers installed at the base of the rocking wall panels (shown in Figure 4.3c) were used to investigate positive vertical uplift rotations and negative compression rotations at the base of the wall (see Figure 5.10). The vertically orientated potentiometers were mounted above the wall base and anchored to the portion of the foundation beam flanges outside of the webs (the portion of the foundation beam that did not deform). The downward deformation recorded by these potentiometers were intended to measure compression deformations of CLT. However, because the deformations from foundation beam flange flexibility were substantially larger the compressive deformations of the CLT panels, the recorded deformations were assumed to be fully attributed to foundation beam deformations.

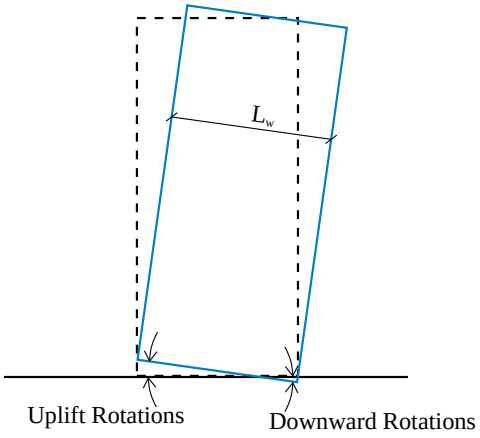

Figure 5.10: Schematic showing the uplift and downward rotations of the rocking wall panels

Using recordings from potentiometers located at the corners of the wall panels, the base rotation was approximated by dividing the recordings by the CLT wall panel length (L_w). Figure 5.11 plots a time history response calculated from one of the wall corner potentiometers. Similarly, the peak uplift rotations and the peak rotations due to the downward deflection of the foundation surface (downward rotation) from numerical results shown in Figure 5.12 are calculated by dividing the displacement recorded by the top node of the out-

ermost spring in the wall base multispring element by the length of the CLT wall panel (L_w). Because the springs at the base of the numerical model are all zero-length, this recorded deformation includes the uplift and deformations of the CLT wall panel and foundation beam.

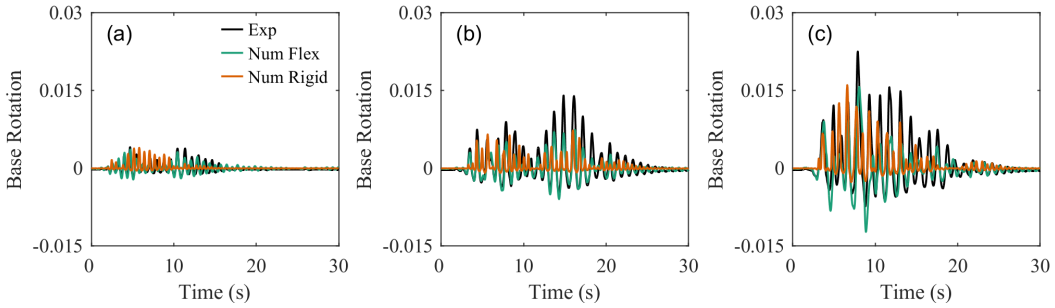

Figure 5.11: Comparison of CLT wall panel base rotation from experimental results, the flexible foundation numerical model, and the rigid foundation numerical model for (a) Test 1: SLE Loma Prieta, (b) Test 10: DBE Superstition Hills, and (c) Test 12: MCE_R Northridge.

Because the numerical model underestimates peak roof drift values, it is logical that the rotations in Figure 5.11 are also underestimated, however, there is good agreement in the general shape of the response. While uplift rotations are underestimated by the model, the negative or downward deformations are slightly overestimated, indicating that the material model used for the foundation beam flange behavior in the numerical model may have been somewhat too flexible. Figure 5.12 summarizes the peak uplift rotations and peak downward rotations observed in each test. Again, this figure shows that the numerical model with foundation flexibility underestimates uplift rotations and overestimates downward rotations. The overestimation of the downward rotations could partially explain the underestimation of the uplift rotations (and similarly the drifts and PT forces) since the wall is settling into the foundation beam more instead of lifting and rocking up. However, apart from peak values, the overestimation of the downward rotations appears to be smaller than the overestimation

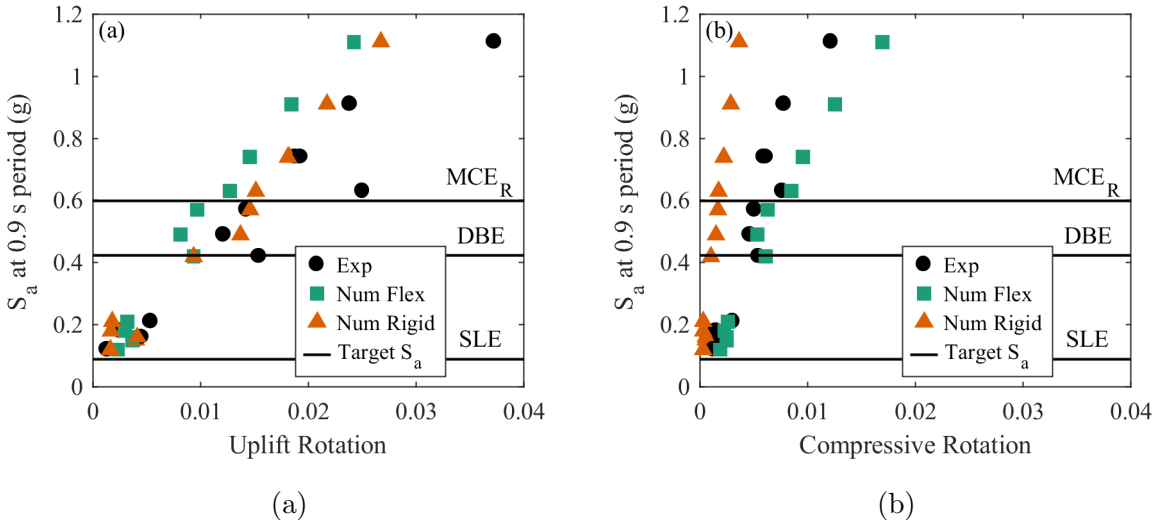

(a) (b)

Figure 5.12: Comparison of peak wall base (a) uplift rotations and (b) downward rotations from the experimental results, the flexible foundation numerical model, and the rigid foundation numerical model.

of the uplift rotations, thus only partially explaining the differences.

Due to the unforeseen flexibility in the foundation beam, instrumentation during testing was not able to accurately measure axial deformations in the CLT at the base of the wall. However, there was not visual damage to the base of the walls after demolition of the structure; the bases of the walls were square at the end of the testing. Similarly, in the numerical model with foundation flexibility, the recorded deformations of the wall base multispring element springs remained below the yield deformation (Δ_y), calculated by dividing the yield force of each spring ($F_{y,s}$) by the stiffness of each spring (k_s) for all fourteen tests.

Overall, the presented numerical model including foundation flexibility does a good job of predicting the response of the tested structure and thus similar modeling techniques can be used to predict the response of structures with comparable rocking wall systems with confidence.

5.4 Investigation of the Impact of Foundation Flexibility

Because the flexibility of the foundation beam was unexpected, it is also important to investigate what the response of the structure would have been if it had been tested on a rigid foundation, as designed. It is important to quantify impact of the foundation flexibility on the overall behavior and to explore if the design would still meet performance objectives with the intended foundation rigid behavior. To do so, the numerical model discussed above was modified and the numerical results were compared to the experimental results. As mentioned previously, the results for the rigid foundation model discussed in this section were included on the plots in Section 5.3 for conciseness. Those previously presented plots will be referenced in this section.

5.4.1 Modified Rigid Foundation Model

To model the test structure with a rigid foundation and predict how results would have differed if the foundation had preformed rigidly, the model described in Section 5.2 and shown in Figure 5.1 was modified. First, the foundation beam multispring elements were removed completely and the bottom nodes of the rocking wall base multispring elements were all assigned full fixity. Additionally, the material model used in the rocking wall base multispring element springs (shown in Figure 5.2c) was modified. Because the foundation is now modeled as rigid, the CLT at the base of the wall is expected to experience more damage. Thus, the material model was modified to include deterioration and the initial gap (that was previously modeling the accumulated permanent deformation of the foundation beam) was removed. In the flexible foundation model, the base of the CLT wall was modeled as elastic-perfectly plastic and because the wall saw no damage, the behavior was not affected. Apart from removing the foundation beam multispring element and modifying the material model for the rocking wall base multispring element springs, the model remained the same.

5.4.2 Comparison of the Rigid Foundation Numerical Model with Experimental Results

The previously presented Figure 5.3, includes results from the rigid foundation numerical model. Comparing experimental results and results from the flexible foundation model (that was intended to replicate test results) with the rigid foundation model, it is clear that the change in foundation boundary condition has a significant effect on the overall response. The initial period shortened with the rigid foundation as a result of the increased system stiffness. For reference, from the numerical models, the initial first mode periods of the flexible foundation and rigid foundation model were 1.22 seconds and 0.74 seconds, respectively. The initial first most period decreased by almost 40% when the rigid foundation model was used instead of the flexible foundation model. The increased stiffness also results in smaller overall peak roof drifts, as seen in Figure 5.4.

The impact of the stiffer rigid foundation model on the overall behavior is also clearly shown in the hysteretic response in Figure 5.5. The idealized flag shape response of rocking systems is more apparent in the response for the rigid foundation model. With a rigid foundation, considerable hysteretic damping does not occur until after the ELL when the wall begins to uplift and the UFPs experience large deformations. However, with the flexible foundation beam, it appears that nonlinearity in the foundation occurs prior to the ELL, resulting in increased damping. This is clear when looking at Figure 5.5a, an example of an SLE test. For the rigid foundation model, there is minimal damping and the peak response has just exceeded the ELL, resulting in a clear bilinear response. In comparison, with the flexible foundation model, while the response is more linear than the comparable DBE and MCE_R response (Figure 5.5b and Figure 5.5c, respectively) there is an increase in damping from the foundation beam deformation. Additionally, the increased system stiffness in the rigid foundation model results in increased peak base shear values as shown in Figure 5.6.

Because the rigid foundation model has smaller drifts, a decrease in peak PT forces may be expected, however, the rigid foundation model has larger peak PT bar forces than the experiment or flexible foundation beam model as shown in Figure 5.8. This is because the

point of uplift shifts towards the compression toe of the wall panels, increasing the PT bar elongation for a given roof drift, when compared to the flexible foundation model. In the flexible foundation model, as the walls rocked, the base of the wall sunk into the beam, flattening the response such that PT bar forces remained constant at a relatively large range of low drift values, as shown in Figure 5.7. Alternatively, Figure 5.7 shows that the rigid foundation model results in higher stiffness and there is a clear increase in PT force with increased drifts, even at low drifts.

With the rigid foundation model, the UFPs still yield during smaller hazard level earthquakes, as shown in Figure 5.9. However, because the drifts were smaller for the rigid foundation model, the peak UFP deformations were also smaller. This resulted in slightly less damping as a result of UFP behavior in the rigid foundation model.

The base rotation response histories shown in Figure 5.11 and the peak uplift rotations summarized in Figure 5.12a indicate that the rigid foundation model has slightly higher uplift rotations than the flexible foundation model. A decrease in drifts would typically result in decreased uplift rotations. However, because the point of uplift of the wall shifted towards compression toe of the wall panels in the rigid foundation model (instead of sinking into the foundation beam), uplift rotations actually increased. The summarized downward rotations (due to the downward deflection of the foundation surface and/or compression of the CLT) in Figure 5.12b show a major decrease in downward base rotations in the rigid foundation model. While the downward rotations were almost entirely a result of foundation beam deformations in the flexible foundation model, the compression rotations in the rigid foundation model are solely the result of deformations in the CLT.

The CLT deformations observed in the rigid foundation model resulted in predicted permanent damage to the CLT base. Because no CLT damage was observed in the experiments or in the numerical model with the flexible foundation, Figure 5.13 only summarizes CLT damage results for the rigid foundation model. Figure 5.13 plots the spectral acceleration at the building's approximate period versus the percentage of the panel length that experienced each type of damage. For each damage state, the length of the panel base over which spring

deformations exceed the respective deformation limit (Δ_y for yielding, Δ_s for splitting, and Δ_{cr} for crushing), was recorded. Of the four wall panel corners, Figure 5.13 summarizes the maximum length as a percentage of the total wall panel length (L_w). While the larger tests experienced some CLT yielding and splitting, CLT crushing was not observed in any of the ground motions with the rigid foundation model.

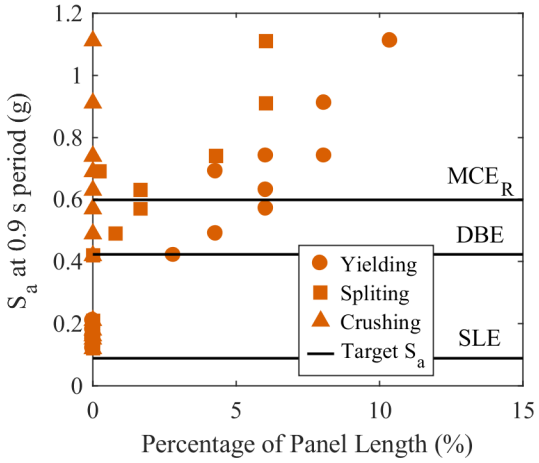

Figure 5.13: Spectral acceleration at the building's period for all tests with the rigid foundation model versus the percentage of the panel length exceeding the CLT damage state of yielding, splitting, and crushing.

5.4.3 Performance of the Rigid Foundation Numerical Model

As discussed in Section 4.8, the CLT test specimen met all design performance objectives during testing. However, it is clear that the flexible foundation beam supporting the rocking walls altered the performance of the specimen. Because the specimen was designed to rock on a rigid foundation surface and realistic buildings would have stiffer foundation surfaces, it is important to assess whether performance objectives would have still been meet had it been tested with a more realistic base condition. The building was designed to meet three performance objectives: (1) immediate occupancy after SLE earthquakes, (2) limited repair

after DBE earthquakes, and (3) collapse prevention after MCE_R earthquakes. To meet each of these three performance objectives, target drifts and damage criteria had to be meet for the UFPs, the PT bars, and the CLT at the base of the rocking wall.

To meet the drift criteria of the performance objectives, story drifts in SLE, DBE, and MCE_R level earthquake should remain under 1%, 2%, and 4%, respectively. Note, for this test specimen, since first mode response controlled, roof drifts were almost identical to story drifts [Wichman, 2018]. As discussed in Section 4.8 with the test results, performance objectives were assessed by looking at the general trends in relation to the hazard level target spectral accelerations at the building's approximate period of 0.9 seconds, as opposed to the intended hazard level of each ground motion. Thus, the rigid foundation model results in Figure 5.4, show that for ground motions with spectral accelerations close to each target hazard level, the predicted roof drifts all satisfy the design criteria. Interestingly, the largest ground motion that had a spectral acceleration 85% larger than the target MCE_R ground motion only had a peak roof drift of 3.2% using the rigid foundation model.

The design performance objectives allow for initial UFP yielding under SLE earthquakes and the UFPs can undergo large deformations beyond yield during DBE and MCE_R level earthquakes. The intent is to replace the damaged UFPs after DBE and MCE_R level earthquakes but replacement not be necessary after SLE level earthquakes. The peak UFP yield displacement ratios summarized in Figure 5.9 show that the UFP criteria is meet for all ground motions for the rigid foundation numerical model. Only one earthquake within the SLE hazard caused UFP yielding.

The PT bars were designed to remain elastic during SLE and DBE earthquakes and were allowed to yield during MCE_R earthquakes. The rigid foundation numerical model results in Figure 5.8 show that PT bar yield criteria was also meet for all performance objectives. It is interesting to note that while both the rigid foundation numerical model results and the experimental results meet PT bar performance objectives, the rigid foundation results are closer to the limits of these performance objectives, but also are much closer to the intended design performance.

Finally, to meet performance objectives, the CLT at the base of the wall has to remain elastic during SLE earthquakes, should only have some damage during DBE earthquakes, and can have repairable damage under MCE_R level earthquakes. For the rigid foundation numerical model, Figure 5.13 shows that ground motions at the SLE hazard level resulted in no CLT yielding, ground motions at the DBE hazard level resulted in some yielding and a small amount of splitting, and the ground motions in the MCE_R region saw significant yielding and minor splitting. However, no CLT crushing was observed in any of the ground motions in the simulations with the rigid foundation model. These are all considered to be meet performance objectives. Again, it is important to note that while performance objectives are met for both the flexible foundation and rigid foundation case, the flexible foundation model predicted zero damage and the rigid foundation model predicted significantly more CLT damage.

5.5 Conclusions

This chapter presented a numerical model for the CLT rocking walls in the NHERI TallWood two-story test specimen. Base rocking was modeled through distributed springs at the base of the wall and the contribution of foundation surface flexibility was included in the model through additional springs below the base rocking springs. Overall, the model showed good agreement with the test results and offered a good prediction of the overall behavior and period. The numerical model slightly underestimated drifts, resulting in lower PT bar forces, lower UFP deformations, and lower base uplift rotations. Additionally, the numerical model slightly overestimated downward base rotations due to downward deflection of the foundation surface, indicating that the assumed foundation model was somewhat too flexible. Similar to test results, the numerical model also resulted in no damage to the base of the CLT rocking walls.

Because the test structure was not designed to have a flexible foundation surface and because a typical building would not be designed with a flexible foundation surface, an additional numerical model was created with a rigid foundation. A comparison of the rigid

foundation numerical model and the flexible foundation numerical showed that altering the boundary condition had a significant effect on the overall behavior of the specimen. As expected, the rigid foundation greatly increased system stiffness, decreased the first mode period, and decreased drifts. Although drifts decreased, the increased stiffness due to the movement of the uplift point closer to the compression toe of the wall panels resulted in larger PT bar forces relative to those observed in the test and predicted using the flexible foundation model. Most importantly, the downward rotations at the base of the wall panels decreased significantly without the foundation beam flexibility, resulting in much higher CLT strains at the base of the wall. Under the rigid foundation boundary condition, the CLT experienced permanent yielding and damage. As a result, it is concluded that even though the flexible foundation beam produced larger peak drifts relative to the rigid foundation beam model, in general, that deformation protected the base of the wall from damage and resulted in better overall performance in terms of CLT damage.

Apart from reduced roof drifts, the numerical model with the rigid foundation did predict somewhat poorer seismic performance as it predicted considerable CLT damage in the DBE and MCE_R ground motions; however, it still predicted the system would meet all design performance objectives and the predicted performance was closer to the design intent. Because of the accurate prediction of overall building performance between test results and the flexible foundation model results, the modeling approaches presented here can be used as a good prediction for mass timber rocking wall systems.

Chapter 6

DESIGN AND ANALYSIS OF THE TEN-STORY NHERI TALLWOOD BUILDING

6.1 Overview

The experimental and numerical research relating to the two-story NHERI TallWood shake table specimen shows promising results for the future of mass timber lateral systems. However, research gaps relating to the application of these ideas to tall buildings existed. With this in mind, the NHERI TallWood Project team tested a full-scale 10-story mass timber building with a mass timber lateral system. The prior work on the two-story test specimen, such as the modeling work and validation of the design procedure, provided valuable insight for work on the 10-story specimen and the development of design recommendations for future design of tall timber buildings.

The work presented in this chapter focuses on the design, modeling, and analysis of the mass timber lateral system in the 10-story specimen. The other components of the test such as the gravity system, diaphragms, and nonstructural elements have been the focus of other collaborators. From a lateral force-resisting system prospective, the overall objective of this test was to (1) study the feasibility of designing and constructing a tall, resilient, fully mass timber building with a post-tensioned rocking wall lateral system for a high seismic region and (2) study the seismic performance of the structure and validate the design and modeling methodologies for use in future buildings and to aid in the codification of this lateral system.

Resiliency was a primary emphasis for this project. For the lateral system, this meant designing the post-tensioned rocking wall system for seismic objectives that exceed code requirements, creating a building that could undergo a large number of high seismic ground motions while sustaining minor damage. As will be discussed, at the MCE_R hazard level,

more stringent criteria was used for interstory drift requirements as well as deformation and force-controlled actions. The criteria at MCE_R was developed to ensure essentially elastic performance apart from the deformation criteria which allowed rocking wall uplift, minor yielding of the wood at the base of the wall, and yielding of the replaceable energy dissipating elements. Because of the essentially elastic performance at MCE_R from the force-controlled components, minimal design criteria were used for the lower hazard levels.

The design of the lateral system was completed by first doing a preliminary design assessment using methods similar to those of a prescriptive procedure that would be used in practice. However, because post-tensioned mass timber rocking walls are not currently recognized by US building codes, a performance-based design methodology was utilized. For this, nonlinear response history analyses (NLRHA) were completed in OpenSees at MCE_R hazard and a series of deformation and force-controlled actions were checked to finalize and validate the design.

The 10-story test specimen was construction by Swinerton and Timberlab. Construction began in June of 2022 and structural construction was completed in January of 2023. After construction instrumentation to measure building response was installed and the specimen was prepped for testing which occurred over four weeks in May of 2023. The test building was subjected to numerous simulated earthquakes on the shake table that far exceeded the number and severity of earthquakes expected for any real building. The testing plan consisted primarily of one- and two-horizontal-component acceleration inputs and some also some test that included vertical accelerations. The input accelerations ranged from those representing a 42-year return period hazard to those representing an MCE_R hazard.

6.2 Summary of Test Specimen and timber materials

The full-scale 10-story NHERI TallWood test specimen is a fully mass timber building with resilient post-tensioned mass timber rocking walls as the lateral force-resisting system. The specimen is representative of a partial footprint of a building. Figures 6.1a and 6.1b show a photo and design schematic of the test specimen, respectively.

(a) (b)

Figure 6.1: 10-Story test specimen (a) photo (b) schematic (courtesy of Aleesha Busch)

As shown in the 10-story elevation view in Figure 6.2b, the first story is 13-feet and all other stories are 11-feet, resulting in a roof elevation of 112 feet. The walls are balloon framed and extend 2.5 feet above the roof. Figure 6.2a shows a typical floor plan with the locations of the lateral system, beams, and columns called out. While the exact details of each floor diaphragm varied floor to floor, the geometry and general structural layout was the same on all floors. The lateral force-resisting system is symmetric and consists of post-tensioned rocking mass timber shear walls with two lines of resistance in each direction. The walls are composed of CLT in the east-west direction and MPP in the north-south direction. Two different mass timber products were chosen for the walls to study the performance of both

materials. Each wall is post-tensioned with external threaded rods that run the full height and are positioned near the center of each panel. At each story, UFPs connect each side of the wall panels to laminated veneer lumber (LVL) boundary columns which support part of the gravity loads. The reminder of the gravity framing system consists of LVL gravity columns and beams. At the base of the walls, a shear transfer mechanism exists to transfer shear forces from the walls into the foundation. A system of steel and concrete elements were bolted to the shake table and serve as the foundation for the structure. A variety of mass timber panel products make up the different floor diaphragm systems.

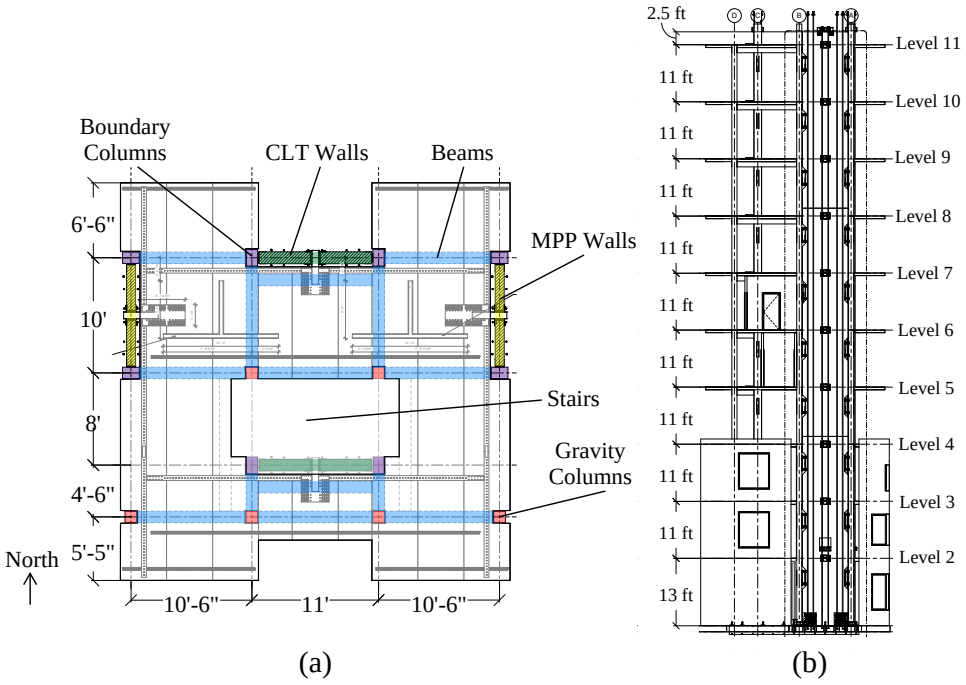

Figure 6.2: 10-Story test specimen (a) typical floor plan showing beam, column, and wall layout (b) elevation view

As shown in Figure 6.2a, each diaphragm is approximately 32 feet in the east-west direction and 34.5 feet in the north-south direction. The floor plan was laid out with both exterior and interior shear walls to study challenges and feasibility associated with the design

and construction of both configurations. The floor plan was also designed to include four small cantilevered diaphragms on the north and south face of the building to study their performance.

While they will not be discussed in detail, the building specimen also included non-structural components which were designed and studied by project collaborators at The University of Nevada, Reno, and University of California San Diego. The nonstructural elements included: (1) a 2-story fire-rated curtain wall subassembly, (2) cold-formed steel framed interior partition walls with drift-compatible track connections, (3) cold-formed steel framed exterior walls with drift-compatible connections, and (4) a resilient stair system with drift-compatible connections located at the center of the floor plan.

6.2.1 Gravity Framing

All beams and columns used in the test specimen were grade 1.8E 2650 LVL, donated by Boise Cascade. They were designed in accordance with AWC [2018] and account for a two hour fire rating. A live load of 65 psf was assumed at all floors (office live loading plus partition loading). The live load was used only for design calculations and was not included during testing. The dead load assumed at all floors was 64.4 psf, approximated based on the estimated building weight calculated at the time when the columns were designed. Detailed design calculations for the gravity members can be found in Busch [2023]. All gravity connections were designed and manufactured by engineers at Simpson Strong-Tie. Details relating to these connections can be found in Busch [2023] The final mass approximation of the 10-story building specimen will be discussed in Section 6.2.4. Table 6.1 summarizes the details for the LVL beams and columns, including the important design values [APA, 2019a], and the member sizes. All gravity columns were orientated for strong axis bending in the east-west direction and all boundary columns are orientated so their strong axis of bending is perpendicular to the strong axis bending of their corresponding wall.

Table 6.1: LVL beam and column design properties and member sizes

LVL Beam and Column Properties		
Grade: 1.8E 2650		
Manufacture: Boise Cascade		
Design Values		
Flexural Stress, F_b	2650	psi
Compressive Stress, F_c	3000	psi
True MOE, E	1800000	psi
Apparent MOE, $E_{apparent}$	1700000	psi
Member Sizes		
Gravity Columns	12.25in x 11.875in	
Boundary Columns	17.5in x 11.875in	
Beams	12.25in x 11.875in	

6.2.2 Diaphragms

Because the effects from the diaphragm were not considered in the design of the lateral system or in the nonlinear numerical model for the building, this section will only include a brief overview of the diaphragms. More information regarding details of the different systems can be found in Huang [2023] and a discussion on their response can be found in Wright [2023]. The material used for the floor diaphragms varies floor to floor to test the performance of different mass timber products and were donated and design by different industry and academic collaborators. The diaphragms on Levels 2 and 3 are made of CLT, donated by Mass Timber Services LTD. The diaphragms on Levels 4 and 5 are made of glue laminated timber (GLT), also donated by Mass Timber Services LTD. The diaphragm on Level 6 is made of nail laminated timber (NLT) and the diaphragm on Level 7 is made of dowel laminated timber (DLT), both donated by StructureCraft. The diaphragms on Levels 7-11 are all made of veneer laminated timber (VLT), donated by Boise Cascade. The GLT diaphragms included orientated strand board sheathing and the NLT and DLT diaphragms included plywood sheathing. These diaphragms required sheathing as they are one-way systems, while the CLT and VLT floors are two-way systems.

6.2.3 Rocking Wall Lateral System

The four post-tensioned mass timber rocking walls defined the lateral force resisting system for the 10-story test specimen and dominated the overall response of the specimen. This section will summarize the key components of the lateral system and list important dimensions and properties of the walls, the CLT and MPP products, and the lateral connections. These are the key values needed for modeling and characterizing the response of the lateral system. The full and detailed design procedure for these walls and all lateral connections can be found in Section 6.6.

CLT Rocking Walls

The CLT used for the two rocking walls was donated by Smartlam. They were 9-ply custom made CLT panels made to resist the earthquake demands in the wall. In the major strength direction of the CLT, the wood was MSR rated lumber, grade 2400f-2.0E. In the minor strength direction, the wood was Southern pine, No. 1, visual grade lumber. The properties used in design calculations were taken from AWC [2018] and are summarised in Table 6.2. Table 6.2 also includes the total dimensions of the CLT walls including the thickness, length, and height.

Table 6.2 also includes the additional CLT material properties needed for numerical modeling and lateral design. Because the modulus of elasticity (MOE) of CLT differs for the two different types of ply layers and the directions of the plys alternate, an effective MOE for the full CLT section ($E_{eff,clt}$) was calculated based on Equation 6.1 which assumes that the MOE of the lumber in the perpendicular to grain direction is 1/30 of the MOE in the parallel to grain direction based on recommendations FPInnovations [2013]. An effective shear modulus for the CLT, $G_{eff,clt}$, of 80 ksi was assumed based on test results shown in Zimmerman and McDonnell [2017].

$$E_{eff,clt} = \frac{5plys \times E_{major,clt} + 4plys \times {}^{E_{minor,clt}}/_{30}}{9plys} \tag{6.1}$$

Table 6.2: CLT wall panel dimensions, design values, and modeling properties

CLT Wall Properties			
Major Strength Direction: MSR rated lumber 2400f-2.0E Minor Strength Direction: Southern Pine, No 1, Visual grade (12" wide) Manufacture: Smartlam			
Wall Dimensions			
Panel Thickness, $b_{w,clt}$	12.375		in
Panel Length, $L_{w,clt}$	117.125		in
Tapered Panel Length, $L_{wt,clt}$	113.125		in
Total Wall height, $h_{w,clt}$	1374		in
Design Values			
	Major Direction	Minor Direction	
Flexural Stress, $F_{b,clt}$	2400	1000	psi
MOE, E_{clt}	2000000	1600000	psi
Tensile Stress, $F_{t,clt}$	1925	650	psi
Compressive Stress, $F_{c,clt}$	1975	1400	psi
Modeling Properties			
Effective MOE, $E_{eff,clt}$	1134.8		ksi
Shear Modulus, $G_{eff,clt}$	80		ksi
Yield Stress, $f_{y,clt}$	2.64		ksi
Splitting Strain, $\epsilon_{s,clt}$	0.0079		in/in
Crushing Strain, $\epsilon_{cr,clt}$	0.0398		in/in

Properties used to define the compressive behavior of the CLT at the base of the wall are also included in Table 6.2. Similar to the assumed behavior used for the 2-story test (summarized in Section 4.5.2), the multilinear behavior shown in Figure 6.3a was assumed for the compressive behavior of the CLT wall panels in the 10-story test.

This behavior and the properties were approximated based on compression test results of 5-ply E1M5 grade CLT specimens [Sinha et al., 2023]. These tests were initially completed for the Framework project [Zimmerman and McDonnell, 2018] and were used as the reference for the 10-story CLT walls because the CLT tested was similar to the CLT used in the 10-story building. Through additional communication with the paper authors, the results presented in Sinha et al. [2023] were modified slightly to get the values used for the 10-story tests. The results were extended to larger strains to capture deterioration and interpreted

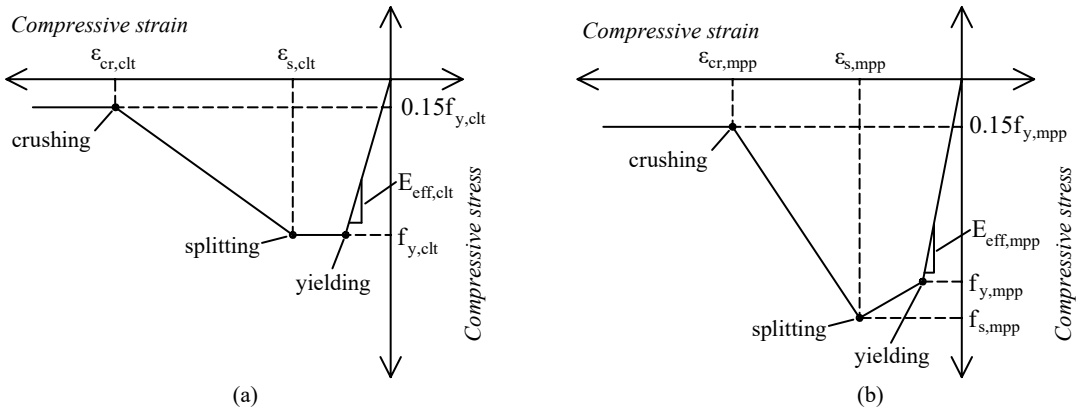

Figure 6.3: Stress-strain relationship used for design of the 10-story building for the (a) CLT wall panels and (b) MPP wall panels

with modifications to get values that fit the desired stress-strain curve. The additional communication with the paper authors resulted in the development of the plastic stress-strain relationship tested shown in Figure 6.4 where $\epsilon_{s,clt}^{plastic}$ and $\epsilon_{cr,clt}^{plastic}$ are the plastic compressive strains at splitting and crushing, respectively, and $f_{y,clt}^{5ply}$ is the yield strain, all for the 5-ply CLT tested. The values taken from Sinha et al. [2023] are: $\epsilon_{s,clt}^{plastic} = 0.0056$ in/in, $\epsilon_{cr,clt}^{plastic} = 0.0375$ in/in, and $f_{y,clt}^{5ply} = 2.85$ ksi.

These values were adopted to the 10-story CLT wall panels by first adjusting the yield stress of the 5-ply CLT to an equivalent 9-ply CLT panel. This adjustment needs to be made because in CLT the plys running in the major strength direction contribute significantly more strength to the panel and the ratio of major plys to total plys is different between 5-ply and 9-ply CLT. This was done by first multiplying the gross yield strength of the 5 ply panel, $f_{y,clt}^{5ply}$ by a ratio of 5/3 to get the projected compressive strength of the plys in the major strength direction and then multiplying that value by a ratio of 5/9 to get the project gross compressive yield strain of the 9-ply CLT used in the 10-story test specimen, $f_{y,clt}$, shown in Table 6.2. The total strain at splitting, $\epsilon_{s,clt}$, and crushing, $\epsilon_{cr,clt}$, used for the 10-story test specimen were calculated by adding the 9-ply yield strain to the plastic

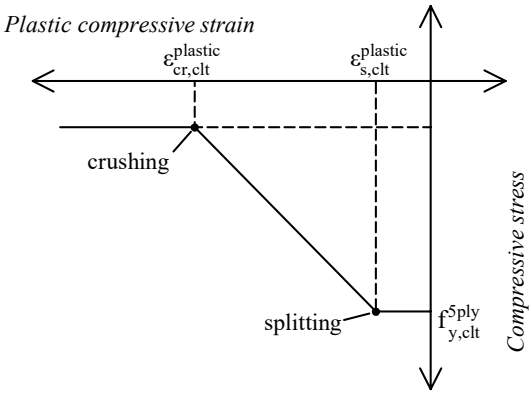

Figure 6.4: CLT plastic compression behavior relationship from Sinha et al. [2023] referenced for the 10-story test specimen

crushing strain results from the tests $\epsilon_{s,clt}^{plastic}$ and $\epsilon_{cr,clt}^{plastic}$. The yield strain was calculated by simply multiplying $f_{y,clt}$ by $E_{eff,clt}$. Doing this results in the behavior shown in Figure 6.3a.

MPP Rocking Walls

The MPP used for the two MPP rocking walls was donated by Freres Lumber. They were 9" thick Grade F16 panels defined by APA [2021]. Table 6.3 summarizes the key design values for the panels, taken from APA [2021]. The plank or flatwise orientation refers to loading perpendicular to the glueline. The joist or edgewise orientation refers to loading parallel to the glueline. As noted by the footnote, some design values must be modified in accordance with APA [2021], based on different implementations. Table 6.3 also includes the total dimensions of the MPP walls.

Table 6.3 also includes the additional MPP material properties used for numerical modeling. Limited testing has been completed to characterize the compressive behavior of MPP. Soti et al. [2021] tested MPP panels in compression and characterized the behavior until the elastic limit. Through additional personal communication with the paper authors, the post yield and softening behavior used for the 10-story design was defined. The resulting stress-strain relationship show in Figure 6.3b was used.

Table 6.3: MPP wall panel dimensions, design values, and modeling properties

MPP Wall Properties			
Grade: F16			
Manufacturer: Freres Lumber			
Wall Dimensions			
Panel Thickness, $b_{w,mpp}$	9.1875		in
Panel Length, $L_{w,mpp}$	105.125		in
Tapered Panel Length, $L_{wt,mpp}$	101.125		in
Total Wall height, $h_{w,mpp}$	1374		in
Design Values			
	Joist	Plank	
Flexural stress, $F_{b,mpp}{}^{a}$	1900	1250	psi
MOE, E_{mpp}	1600000	1400000	psi
Edgewise shear stress, $F_{v,e,90}{}^{a}$	255	90	psi
Compressive stress $\perp$, $F_{c\perp,mpp}$	750	500	psi
Tensile Stress, $F_{t,mpp}{}^{a}$	1300		psi
Compressive stress $\parallel$, $F_{c\parallel,mpp}$	2400		psi
Major $EI_{eff,0}$	1.385E+09		lb-in^2/ft
Major $GA_{eff,0}$	3420000		lb/ft
Modeling Properties			
Effective MOE, $E_{eff,mpp}$	2004		ksi
Shear Modulus, $G_{eff,mpp}$	125		ksi
Yield Stress, $f_{y,mpp}$	4.8096		ksi
Splitting Stress, $f_{s,mpp}$	6.015		ksi
Splitting Strain, $\epsilon_{s,mpp}$	0.0061		in/in
Crushing Strain, $\epsilon_{cr,mpp}$	0.02764		in/in

[a]Design values need adjustment based on implementation per APA [2021].

Design Considerations for Lateral Resistance During Construction

As will be discussed in more detail in the splice design discussion in Section 6.6.3, each rocking wall is made of three panels that are horizontally spliced together to create the monolithic rocking wall in the final design. The rocking walls are in three sections due to manufacturing, transportation, and construction limitations. For construction, the gravity system and diaphragms for a few floors were erected, followed by the installation of a rocking

wall segment and the lateral connections. This procedure was repeated for the three wall panel segments until the full building was constructed. In the final design, each monolithic rocking wall is post-tensioned from the top of the wall which compresses the walls and creates the primary lateral resistance for the building. To provide lateral resistance during construction, prior to the erection of the upper stories of the walls and final post-tensioning, a temporary construction PT connection, located at mid-height of the second story was used. A cutout at the second story provided an anchorage location for the temporary PT connection. Bars spanning from this temporary connection to the base of the walls were post-tensioned and provided lateral resistance for the structure during construction. It was designed to resist overturning moments from the design wind loads in the area. This was done by approximating the moment-rotation behavior of the full wall system with the temporary construction PT, using the cross-sectional analysis procedure (similar to the preliminary design analysis used for seismic design, outlined in Section 6.6.2). Because this situation is unique to this project and other solutions would most likely be used in a real building, the full design procedure will not be presented in detail in this document.

Figure 6.5a shows a phase of the construction sequence when the first segments of the wall panels were installed and lateral resistance was provided through the temporary construction PT connection. On the floors where the gravity system and diaphragms were installed prior to the lateral system, a temporary bracing system, designed by the contractor, were installed (also shown in Figure 6.5a). Figures 6.5b and 6.5c show photos of the temporary construction PT connections for the CLT and MPP walls, respectively. The connection consists primarily of a wind saddle that acts in bearing. However, for the CLT walls, additional drag straps were included as the compression strength of the CLT was less than that of the MPP and all load could not be carried through bearing. Also shown in Figures 6.5b and 6.5c are the custom PT jacking hardware pieces used to post-tension all the bars. After post-tensioning, this jacking hardware was released and did not serve any additional purpose. Once the 10-story walls were fully constructed, additional bars were added, connecting the tops of the bars at the temporary construction connection to the primary anchorage saddle system at

the top of the walls (discussed in the next section). The wall was then post-tensioned from the top and the temporary construction connection was released such that it provided no anchorage after construction. The design calculations completed for these temporary PT components will also not be presented in detail in this document as they are unique to this project and most likely wouldn't need to be referenced.

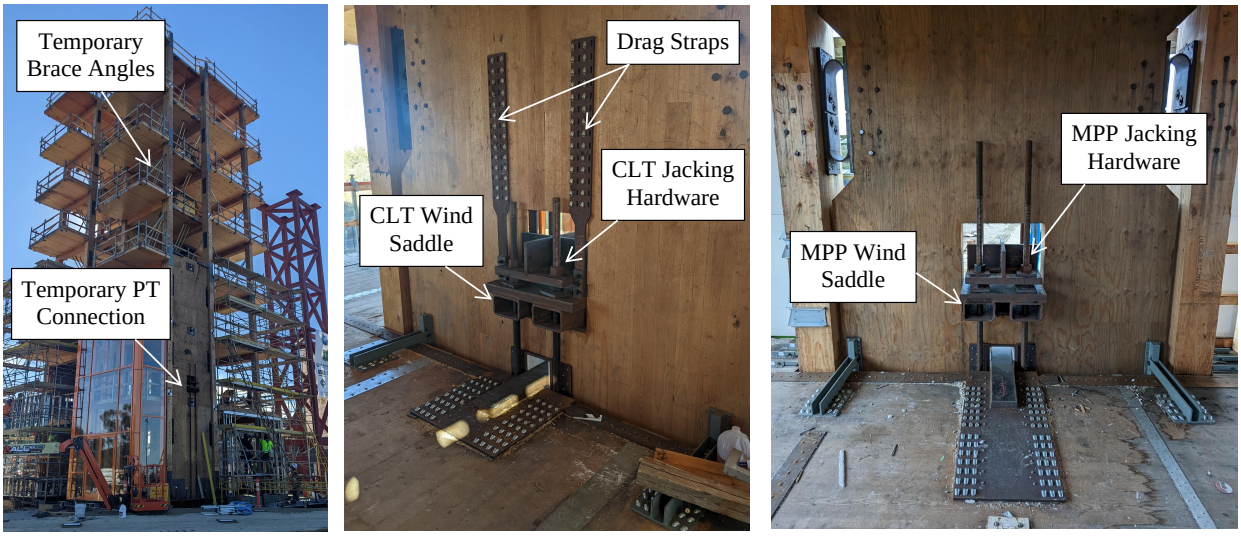

Figure 6.5: Lateral resistance during construction photos (a) temporary post-tensioning of the first wall segment and temporary brace angles and temporary construction PT connections for the (b) CLT walls and (c) MPP walls

Post-tensioning bars

The PT rods were ATS high-strength, fully-threaded rods supplied by Simpson Strong-Tie. Because the bar length during construction was so much shorter, larger diameter bars had to be used over this length. For the first one and a half stories of the building, 2 inch diameter rods were used. For the remainder of the building height, 1-1/4 inch diameter rods were used. The manufacturer listed yield stress, $F_{y,pt}$, and ultimate stress, $F_{u,pt}$, are 105 ksi and

125 ksi, respectively. High-strength coupling nuts, compatible with the PT rods, connected the larger lower rods to the smaller upper rods. Similar coupling nuts were used to connect 12 foot long rod segments to make the full PT rods.

Figure 6.6 shows the primary anchorage saddle system located at the tops of the walls. These were similar for both the CLT and MPP walls and acted in bearing at the tops of the walls. Similar to the temporary construction PT connection, the bars were post-tensioned using the fabricated jacking hardware piece also shown in Figure 6.6. This piece remained during testing to re-tension the bars, if necessary, without the use of a crane. At the base of the walls, the PT bars were anchored into the foundation beam. Each bar was post-tensioned to 50 kips, equivalent to 21% of the yield force for the lower bars and 55% of the yield force for the upper bars. Table 6.4 summarizes the properties for the PT bars. Section 6.6.3 describes these components from a design standpoint.

Figure 6.6: Top of wall PT wall saddle connection details

Table 6.4: Dimensions and properties of the PT bars in the 10-story test specimen

PT Bar Properties			
MOE, E_{pt}	29000		ksi
Yield Stress, $F_{y,pt}$	105		ksi
Ultimate Stress, $F_{u,pt}$	125		ksi
Initial PT force, $T_{o,pt}$	50		kip
	Lower	Upper	
Bar length,$L_{pt,L}$, $L_{pt,U}$	18	96.5	ft
Net Tensile Area, $A_{net,pt,L}$, $A_{net,pt,U}$	2.5	0.969	in^2

UFP Energy Dissipating Devices

The UFPs act as the primary energy dissipating devices in the 10-story building. At every story, a UFP assembly existed on either side of each rocking wall, spanning the gap between the rocking wall edges and the boundary columns. Figure 6.7 shows a typical detail for the UFPs and their connections. Notches in the walls were cut to fit the UFPs so that the gap between the walls and the columns could be small. The UFPs were anchored to the timber using an embedded pi plate connection with steel dowels that acted in bearing. This connection was designed by project collaborators, Sumitomo Forestry at Tsukuba Research Institute, who conducted a payload project in which the demands on these connections are significantly larger that then forces produced by the UFPs. The UFPs connect to the embedded knife plate connections using bolts. Section 6.6.3 describes these bolted connections in more detail and presents design calculations.

The 10-story building had two different UFP designs. The bottom three stories had larger UFPs with two UFPs per location (Figure 6.7a) and the upper seven stories had smaller UFPs with only one UFP per location (Figure 6.7b). While the primary purpose of the UFPs is to provide damping, they also contribute to some of the total wall moment resistance. As mentioned in Section 6.2.3, the lower wall panel that spanned the first three stories was post-tensioned at the beginning of construction and provided all lateral resistance during construction. Thus, the denser UFP layout and larger UFPs were used on the lower

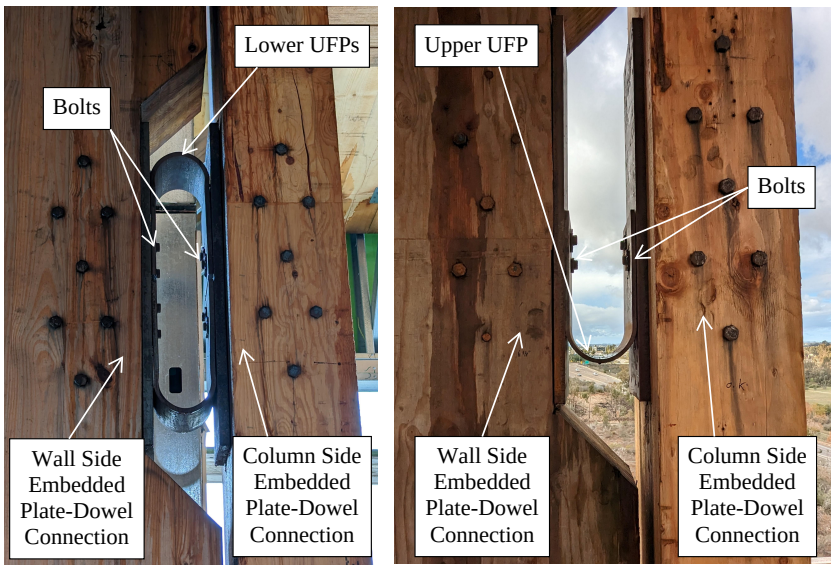

Figure 6.7: UFP energy dissipator connection details for (a) the lower UFPs and (b) the upper UFPs

stories was done to aid in resisting the overturning moment demands during construction.

All UFPs were made of A572 Grade 50 Steel. Table 6.5 summarizes the dimensions and properties of the UFPs in the 10-story test specimen. Note, the table lists the center-to-center diameters that the UFPs were designed and manufactured for ($D_{u,L}$ and $D_{u,U}$ for the lower and upper UFPs, respectively). However, due to larger than expected construction tolerances, the gap in which each UFP was installed varied throughout the building. Each UFP was either compressed or expanded so that it would fit in each location. For the lower UFPs, the as-built bend diameters ranged from about 5.75 inches to 6.375 inches with an average of 6 inches. For the upper UFPs, the as-built bend diameters ranged from about 5.75 inches to 7.1875 inches with an average of 6.3125 inches. In general, the lower UFPs were closer to their design values and smaller than designed. On average, the upper UFPs also had a smaller bend diameter than designed, but closer to the design value than the lower UFPs. The upper UFPs also had a larger range in variability in the as-built diameter sizes.

Table 6.5: Dimensions and properties of the UFPs in the 10-story test specimen

UFP Properties			
MOE, E_{ufp}	29000		ksi
Yield Stress, $f_{y,ufp}$	50		ksi
Ultimate Stress, $f_{u,ufp}$	65		ksi
	Lower	Upper	
UFP width, $b_{u,L}$, $b_{u,U}$	8	8	in
UFP thickness, $t_{u,L}$, $t_{u,U}$	0.5	0.375	in
UFP diameter, $D_{u,L}$[a], $D_{u,U}$[a]	6.25	6.375	in

[a]As-built bend diameters vary from design values, see text.

Wall to Diaphragm Shear Connection

The rocking wall lateral system connected to the diaphragms using a vertically slotted shear key connection that was anchored to the diaphragm using a wing plate system. All floors used the same slotted shear key design presented here, however, the wing plate design presented in this document and shown in Figures 6.8a and 6.8b for the CLT and MPP walls respectively, was only used on floors 2-3 (with the CLT diaphragms) and 8-11 (with the VLT diaphragms). These are the two-way diaphragm systems that do not require sheathing. The remaining floors: 4-5, 6, and 7 with GLT, NLT, and DLT diaphragms are all one-way diaphragm systems that require sheathing. Thus, an alternative wing plate system, designed by engineers at MKA and StructureCraft, was used on these floors. These are shown in Figure 6.8c and will not be presented in detail in this document. The alternate wing plate system was designed to engage the sheathing and spread the loads out further.

The concept for these connections comes from the permitted Framework building in Portland, Oregon [Zimmerman and McDonnell, 2018], designed by KPFF Consulting Engineers. A nearly identical design was also used in the NHERI TallWood 2-story test and performed successfully. See Section 4.5.2 for a conceptual discussion on how the connection transfers forces. One change for this connection between the 2 and 10-story tests was that the shear

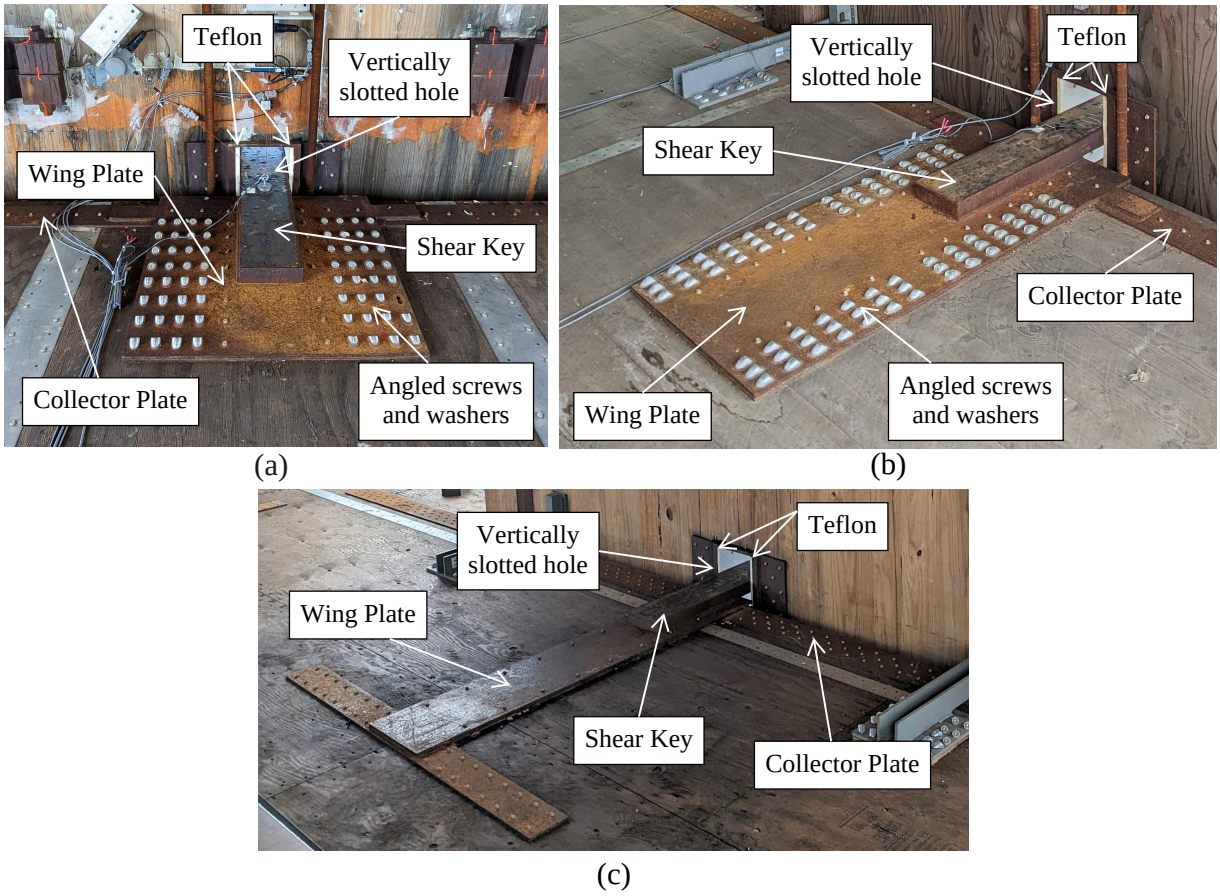

Figure 6.8: Wall-to-diaphragm shear transfer connections for (a) the CLT walls on non-sheathed floors, (b) the MPP walls on non-sheathed floors, and (c) the walls on sheathed floors

key plate was welded to the wing plate instead of bolted to ease construction and make the connection stiffer. Additionally, the Teflon to create a friction-less surface in the slotted hole was pre-installed on the embedded steel plates in the vertically slotted hole, also easing construction and making a more resilient surface. As shown in Figures 6.8a and 6.8b, the wing plates for the CLT and MPP were slightly different. The MPP wing plate were more narrow to spread out the moment arm to accommodate the diaphragm splice on the VLT floors that runs across the middle of the splice plate.

Table 6.6 summarizes the dimensions and properties of the diaphragm-to-wall shear key transfer connection. Note, while the wing plate is different on some floors, the properties in this table relate to the shear key itself which are the same on all floors. Some floors had larger design demands than others so different shear key sizes could have been used on the different floors, creating a more optimized design, however, the same design was used on all floors to ease construction. The height of the slotted hole was calculated to very conservatively account for the peak wall uplift at the wall center and also account for wall shortening during wall post-tensioning.

Table 6.6: Dimensions and properties of the diaphragm-to-wall shear key transfer connections in the 10-story test specimen

Shear Key Properties		
MOE, E_{key}	29000	ksi
thickness, t_{key}	2	in
width, w_{key}	7	in
length, L_{key}	9.5	in

Wall out-of-plane Brace Connections

At the intersection of the diaphragms and the rocking shear walls, out-of-plane wall braces were installed to prevent wall compression buckling. A unique design that could accommodate both the wall rotations and uplifts at the diaphragms and could work for both the interior and exterior wall configurations was designed and manufactured by engineers at Simpson Strong-Tie. The resulting connection is shown in Figure 6.9.

On one face of each wall, two out-of-plane wall brace connections are installed at a distance $d_{oop,clt}$ and $d_{oop,mpp}$ for the CLT and MPP walls, respectively (Figure 6.9a). Each out-of-plane brace connection consists of two legs that are anchored to the diaphragm with a small wing plate and then cantilever over the collector straps, connecting to a fabricated steel vertically slotted pin connection mounted to the walls. The legs are connected to

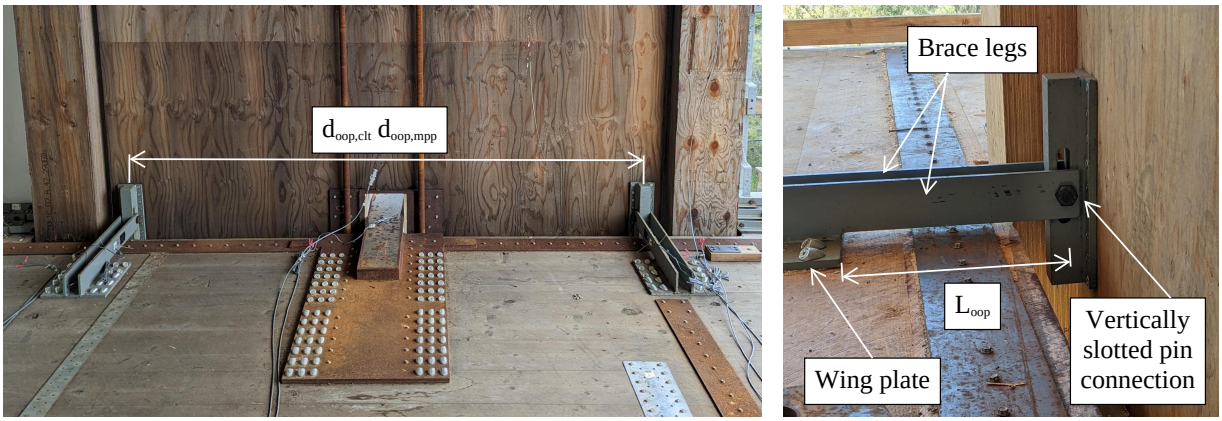

Figure 6.9: Wall out-of-plane bracing connection photos (a) full view of braces and walls and (b) close up of vertically slotted pin connection on wall

the vertically slotted hole using a bolt that was hand-tightened such that it was free to move vertically in the slot during wall uplift (Figure 6.9b). The steel fabricated vertically slotted pin connection mounted on the wall face allows the connection to prevent buckling in both directions even though it is only mounted on one face, making it compatible for both interior and exterior walls. The vertically slotted hole allows for vertical rocking wall movement without locking within the connection. Table 6.7 summarizes the key dimensions and properties of the out-of-plane braces. The distance over which the legs span, L_{oop}, measured from the face of the wing plate to the center of the bolt hole is also included in the table (Figure 6.9b).

Table 6.7: Dimensions and properties of the wall out-of-plane brace connections in the 10-story test specimen

Wall Out-of-Plane Brace Properties			
MOE, E_{oop}	29000		ksi
leg thickness, t_{oop}	0.38		in
leg height, h_{oop}	3		in
leg length, L_{oop}	13.6875		in
	CLT Walls	MPP Walls	
Brace distance, $d_{oop,clt}$, $d_{oop,mpp}$	98.625	97.625	in

6.2.4 Approximation of the 10-Story Building Mass

The total weight of the 10-story building specimen was approximated for design and modeling purposes. The summation of the approximate weight of the mass timber members, nonstructural walls, the stair system, and the major steel connections were used to calculate the approximate total weight of the building. For the timber members, density recommendations with typical moisture content from each supplier were used. For the sheathed diaphragms, the weight of the sheathing was included. The weights of the diaphragms, beams, and columns were all multiplied by a factor of 1.06 to account for additional hardware weight and the weight of the gravity connections. The additional 1.06 factor was not applied to the walls because instead the small cutouts in the walls for the UFPs, shear keys, etc. were also not accounted for to be conservative for the additional hardware and other components not included in the total weight calculation. Approximate weights of the nonstructural walls and the stair system were provided by project collaborators. The weight of the steel connections was approximated using material take off lists from the steel fabricator shop drawings. This weight accounted for all lateral connections. Table 6.8 summaries the approximate breakdown of seismic weight on each floor used for design and modeling. Figure 6.10 represents the contributions of seismic weight on each floor in a plot. As seen in the table and figure, the timber products make up majority of the seismic weight. Additionally, the weight of the

steel connections is not negligible. Note, the weight presented here is approximate and could vary significantly due to increased water content in the wood as there were large amounts of rain in San Diego during construction. Controller data from the shake table should be investigated to validate the total building weight.

Table 6.8: Summary of mass contributions per floor for the 10-story building specimen

Floor	Diaphragm	Beams	Columns	CLT Walls	MPP Walls	NS Walls	Stairs	Steel	Total
-	kip	kip	kip	kip	kip	kip	kip	kip	kip
2	16.9	4.4	7.6	8.7	6.0	14.8	6.7	11.2	76.3
3	16.9	4.4	7.0	8.0	5.5	11.3	8.0	6.0	67.0
4	14.4	4.4	7.0	8.0	5.5	13.1	8.0	15.6	75.8
5	14.4	4.4	7.0	8.0	5.5	2.3	7.9	6.0	55.4
6	14.1	4.4	7.0	8.0	5.5	2.0	7.8	6.0	54.8
7	14.0	4.4	7.0	8.0	5.5	0.0	7.8	6.0	52.6
8	17.2	5.2	7.0	8.0	5.5	0.0	7.8	15.6	66.2
9	17.2	5.2	7.0	8.0	5.5	0.0	6.3	6.0	55.2
10	17.2	5.2	7.0	8.0	5.5	0.0	6.0	6.0	54.9
11	17.2	5.2	6.0	5.8	4.0	0.0	3.6	10.9	52.7
Total	159.6	47.1	69.5	78.3	53.9	43.4	69.9	89.3	611.0

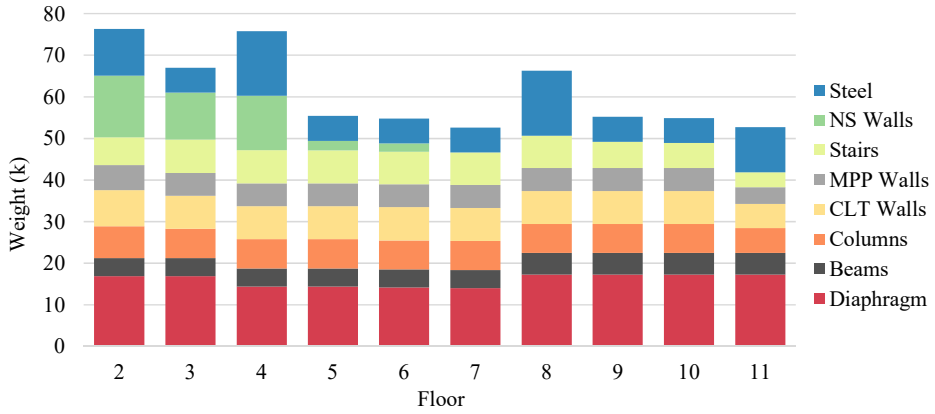

Figure 6.10: Summary of the mass contributions per floor for the 10-story building specimen

Calculating and quantifying distribution of seismic weight on each floor was also important to determine the center of mass (X_{mi} and Y_{mi}) and rotational mass moment of inertia (I_{oi}) on each floor for nonlinear numerical modeling. All components listed in Table 6.8 were accounted for in these calculations. The tributary mass of the walls at each floor were calculated and lumped with the mass of the rocking wall steel connections also tributary to that floor (including the UFP embedded pi plate connections in the walls at each story, the assemblies for the temporary PT connection at Level two, the assemblies for the primary PT connection on the roof, and the splice plate connections at floors 4 and 8). For each floor this lumped wall mass was treated as point masses at the center of each wall. The nonstructural walls were also treated as point masses acting at the center of each individual wall section for these calculations. The mass of the stairs at each floor was evenly distributed over the stair opening and treated as a thin plate for these calculations. The mass of the remaining components including the diaphragms, beams, columns, and any fabricated steel connections not attached to the walls (including the shear keys at each floor, the wing plates at each floor, the diaphragm collectors at each floor, the UFPs at each story, and UFP embedded pi plate connections in the columns at each story) were assumed to be uniformly distributed over the diaphragm. An effective density was calculated using the mass and the approximate area of each floor (900 ft^2). The diaphragm was treated as thin plate sections by splitting the diaphragm into rectangular shapes and using superposition to account for the true distribution of the floor area. The results for these calculations are shown in Table 6.9 under the "Total Properties per Floor". Note, the distances are all measured from the center of the most north-west column in the floor plan where the positive x direction is east and the positive y direction is north. Also included in Table 6.9 is the center of rotation, calculated based on wall stiffness and remains the same at all floors and the eccentricity on each floor. As shown, the eccentricity is minimal for all floors but is slightly larger in the y direction.

Table 6.9: Summary of mass distribution per floor for the 10-story building specimen

Total Properties per Floor													
		Floor, i	2	3	4	5	6	7	8	9	10	11	Total
Center of Rotation	X_{ri}	in	192.9	192.9	192.9	192.9	192.9	192.9	192.9	192.9	192.9	192.9	-
	Y_{ri}	in	-108.1	-108.1	-108.1	-108.1	-108.1	-108.1	-108.1	-108.1	-108.1	-108.1	-
Center of Mass	X_{mi}	in	189.9	194.3	195.8	191.7	191.7	192.3	192.4	192.3	192.3	192.3	-
	Y_{mi}	in	-114.4	-124.5	-127.8	-124.9	-121.6	-123.7	-118.8	-123.2	-122.9	-119.6	-
Rotational MOI	I_{oi}	k in s^2	6237	5270	5006	3453	3398	3309	4248	3616	3613	3624	-
Mass	m_i	k s^2/in	0.1975	0.1735	0.1963	0.1435	0.1419	0.1362	0.1715	0.1429	0.1421	0.1366	1.5820
Eccentricity	x_i	in	-3.04	1.33	2.91	-1.23	-1.25	-0.65	-0.58	-0.67	-0.66	-0.63	-
		%	0.75	0.33	0.72	0.30	0.31	0.16	0.14	0.16	0.16	0.16	-
	y_i	in	-6.29	-16.40	-19.78	-16.81	-13.58	-15.67	-10.77	-15.12	-14.88	-11.58	-
		%	1.52	3.96	4.78	4.06	3.28	3.78	2.60	3.65	3.59	2.80	-
Modeling Parameters per Floor													
		Floor	2	3	4	5	6	7	8	9	10	11	Total
Center of Mass	X_{mi}	in	188.6	194.7	197.3	191.2	191.2	192.0	192.0	192.0	192.0	192.0	-
	Y_{mi}	in	-125.5	-135.9	-148.5	-139.9	-135.6	-139.4	-138.6	-137.6	-137.4	-135.5	-
Rotational MOI	I_{oi}	k in s^2	6237	5270	5006	3453	3398	3309	4248	3616	3613	3624	-
Mass w/o walls	m_i	k s^2/in	0.1395	0.1321	0.1302	0.1021	0.1005	0.0949	0.1054	0.1015	0.1008	0.0921	1.0991
Mass of 1 CLT wall	$m_{i,clt}$	k s^2/in	0.0167	0.0120	0.0187	0.0120	0.0120	0.0120	0.0187	0.0120	0.0120	0.0124	0.1386
Mass of 1 MPP wall	$m_{i,mpp}$	k s^2/in	0.0123	0.0087	0.0143	0.0087	0.0087	0.0087	0.0143	0.0087	0.0087	0.0098	0.1029

Table 6.9 also includes a "Modeling Parameters per Floor" section. These are the adjusted parameters used for modeling. As will be discussed in Section 6.5.4, the mass of the walls were modeled on the wall elements and the remainder of the mass was applied at the center of mass. Thus, the center of mass and rotational MOI in this section were calculated again using the same assumptions listed previously, but without accounting for the mass of the walls or the mass of the steel wall connections. In the model, the mass without the walls, m_i, and the rotational MOI, I_{oi}, were applied to the center of mass on the diaphragm (X_{mi} and Y_{mi}). The per floor mass of the CLT wall, $m_{i,clt}$, and the MPP wall, $m_{i,mpp}$, were then applied on the wall elements at each floor.

6.3 Site Location and Seismic Demands

The building specimen was designed for a location in the Capitol Hill neighborhood of Seattle, Washington (Coordinates: 47.6156, -122.3197) with site class C soil. Because the specimen was designed to represent a mixed-use building, it was classified as a risk Category II building. This location was chosen because, at the time of this test, the Pacific Northwest is a hot spot for mass timber construction and the Capital Hill neighborhood is a growing area where mid-rise mixed-use buildings are in demand. The site seismic parameters were obtained from the Applied Technology Council (ATC) Hazards by Location tool [ATC, 2016] with reference to ASCE/SEI 7-16 and are summarized below:

- Importance factor: $I_e = 1.0$
- Seismic design category: $SDC = D$
- Mapped spectral acceleration parameters: $S_S = 1.378\ g$, $S_1 = 0.48\ g$
- Site coefficients: $F_a = 1.2$, $F_v = 1.5$
- MCE_R spectral acceleration parameters: $S_{MS} = 1.654\ g$, $S_{M1} = 0.72\ g$

As mentioned and discussed more in Section 6.6, the building was designed using performance-based seismic design methodologies and nonlinear response history analysis. Thus in accor-

dance with ASCE/SEI 7-16, the design was finalized at MCE_R, but additional earthquake hazard levels were also selected to assess performance. The earthquake hazard levels identified for this project were as follows:

- 43-year return period (50% in 30 years)
- 225-year return period (20% in 50 years)
- 475-year return period (10% in 50 years)
- 975-year return period (5% in 50 years)
- 2475-year return period (2% in 50 years)
- 4975-year return period (1% in 50 years)
- Site specific Risk-Targeted Maximum Considered Earthquake (MCE_R)

As seen in the list above, all hazard levels except MCE_R, which will be discussed in more detail in the following paragraphs, are defined using return periods (RP). For these six return periods, the target hazard curves were defined using Uniform Hazard Spectra (UHS) curves, developed for the 10-story site location. By definition, these curves are developed by performing probabilistic seismic hazard analysis (PSHA) calculations at multiple periods. The UHS curves were obtained referencing the 2014 US earthquake source model [USGS, 2017a] and generated for a site with a time-averaged shear-wave velocity to 30 meters depth (V_{S30}) equal to 500 m/s (using USGS, 2017b). The plotted hazard curves are shown in Figure 6.11 and the tabulated values are shown in Table 6.10. Note, for the hazard levels represented by return period, geometric mean spectra are shown.

The last earthquake hazard level is the probabilistic site specific Risk-Targeted Maximum Considered Earthquake (MCE_R), defined in accordance with ASCE/SEI 7-16 Section 21.2.1.1. The target curve for MCE_R is defined as the spectral response accelerations in the direction of maximum horizontal response for the 2475-year unified hazard spectra (representative of a 2% in 50 year ground motion exceedance probability) adjusted for risk of

collapse using the ASCE/SEI 7-16 risk coefficients (C_R). Thus, to get the site specific MCE_R curves show in Figure 6.11 and tabulated in Table 6.10, the 2475-year return period UHS

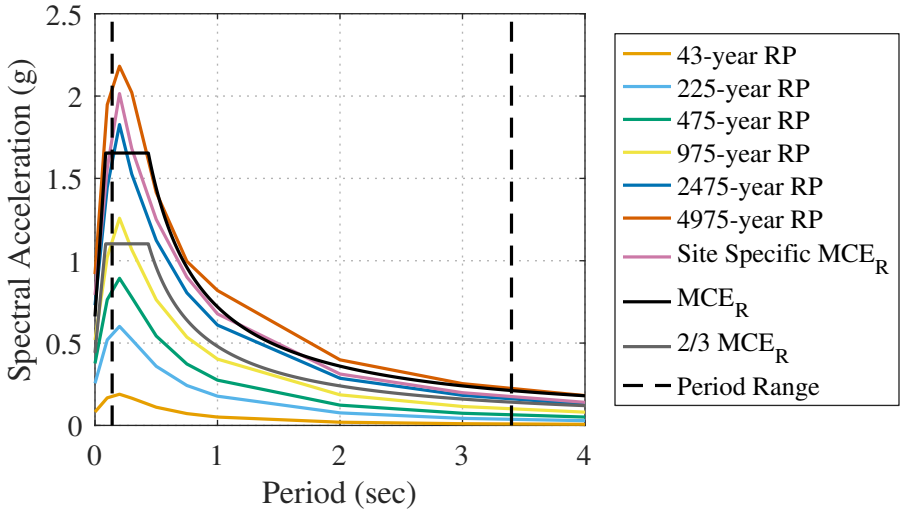

Figure 6.11: Earthquake Hazard Level Curves used for the 10-story test specimen

Table 6.10: Tabulated Uniform Hazard Spectra curves for the different earthquake hazard levels used to design and assess the 10-story building performance

Period	Earthquake Hazard Level						
(sec)	43-yr RP	225-yr RP	475-yr RP	975-yr RP	2475-yr RP	4975-yr RP	MCE_R
0	0.082	0.255	0.376	0.518	0.730	0.919	0.792
0.1	0.167	0.520	0.764	1.022	1.446	1.948	1.561
0.2	0.189	0.602	0.893	1.258	1.827	2.181	2.015
0.3	0.165	0.522	0.778	1.067	1.526	2.022	1.681
0.5	0.110	0.359	0.543	0.763	1.124	1.414	1.251
0.75	0.072	0.242	0.373	0.536	0.805	0.997	0.901
1	0.051	0.178	0.275	0.403	0.609	0.819	0.677
2	0.019	0.076	0.123	0.186	0.286	0.398	0.312
3	0.010	0.043	0.074	0.115	0.183	0.254	0.199
4	0.007	0.029	0.051	0.081	0.130	0.181	0.140
5	0.004	0.020	0.036	0.058	0.102	0.141	0.114
7.5	0.003	0.011	0.022	0.037	0.072	0.107	0.082
10	0.003	0.007	0.014	0.027	0.055	0.085	0.064

curve (shown in Table 6.10), which is representative of the geometric mean, was multiplied by the $^{Sa_{RotD100}}/_{Sa_{RotD50}}$ factors recommended by Shahi and Baker [2014] to get a curve representative of maximum direction spectra. The curve was then multiplied by the ASCE/SEI 7-16 C_R factors to adjust for risk. Note, $Sa_{RotD100}$ is the spectral acceleration of the ground motion components in the orientation that corresponds to the 100$^{\text{th}}$ percentile (maximum spectral) response (maximum direction spectra). Sa_{RotD50} is the spectral acceleration of the ground motion components in the orientation that corresponds to the 50$^{\text{th}}$ percentile value spectral response and is a good representation of the geometric mean ($Sa_{GeometricMean}$) spectral response of the two horizontal ground motion components. Because Sa_{RotD50} is an approximation of the geometric mean, the $^{Sa_{RotD100}}/_{Sa_{RotD50}}$ factors do not produce an exact conversion between maximum direction spectra and geometric mean spectra, however, based on Shahi and Baker [2014], it was deemed an appropriate conversion for this project.

As discussed in Section 6.4, for design and shake table testing, ground motion suites were selected and scaled for the hazard levels shown in Figure 6.11. Note, there are two MCE_R curves shown. The first is the site specific MCE_R curve developed from the 2475-year return period curve. This is the curve that was used for design and ground motion selection at the MCE_R hazard level. The second curve is the more commonly seen version of this curve, defined in accordance with Chapter 11 of ASCE/SEI 7-16. They are both versions of the same curve, the site specific MCE_R curve however has more period definition than the traditional MCE_R curve. Throughout this document, when referencing MCE_R, the site specific MCE_R is being referenced unless noted otherwise.

While ASCE/SEI 7-16 also allows the use of conditional mean spectra (CMS) for design, which may be more representative of true hazard, UHS was used for this project because it is more conservative, meaning the hazard may be larger at some periods.

6.4 Ground Motions

Suites of ground motions were selected and scaled for the Seattle, Washington site to represent the earthquake hazard presented previously in 6.3. These ground motions were first used

to complete nonlinear response history analyses to assess the performance of the 10-story building specimen for design. Then, a subset of the design ground motions were used for testing on the shake table. This section will present the ground motion selection and scaling procedures used to obtain these ground motion suites. Then, a summary of all the selected and scaled ground motions will be presented. Section 7.2 will describe the procedure for selecting the subset of ground motions used for shake table testing, including the procedure for scaling the vertical ground motion components. Note ground motion selection and scaling was completed with assistance from Nasser Marafi from Risk Management Solutions, Inc.

6.4.1 Ground Motion Selection and Scaling Procedures for Design Suite Motions

For design, suites of eleven two-component ground motions were selected and scaled to the target hazard curves presented in Section 6.3: The 5%-damped target UHS curves for each hazard curve are presented in Figure 6.11 and Table 6.10. As described in this section, motions were carefully selected to be consistent with the earthquake hazard in Seattle and were scaled to meet current code recommendations.

The seismic hazard in Seattle is unique in that it can be characterized by three different types of earthquakes from different sources. The first type of earthquake that can occur is the crustal earthquake that comes from shallow crustal faults such as the Seattle fault. The second and third types of earthquakes that can occur are the deep intraslab earthquakes and the shallower interface earthquakes that can both result from the Cascadia Subduction Zone, the subduction of the Juan de Fuca plate beneath the North American Plate [Marafi, 2018]. To properly capture this hazard for design and shake table testing of the 10-story specimen, which has a design site location within Seattle, the ground motions were selected from three different ground motion repositories that each contain motions for the three different earthquake sources in Seattle: crustal, intraslab, and interface. The suites of ground motions were selected such that at each of the seven hazard levels, there were ground motions from all three sources. The crustal earthquakes were obtained from the NGA West-2 PEER Ground Motion Database [Ancheta et al., 2014]. The interface earthquakes were obtained from the

Strong-motion Seismograph Networks KiK-net and K-NET database [NIBS, 2018]. The intraslab earthquakes were obtained from the NGA-Subduction Flatfile dataset [Mazzoni et al., 2021].

For the MCE_R hazard, the ground motions were scaled in accordance with ASCE/SEI 7-16, Chapter 16. Utilizing amplitude scaling methods, maximum direction spectra ($Sa_{RotD100}$) were created for each horizontal ground motion pair and scaled. Identical scale factors were applied to both horizontal components. Upper and lower bounds of 5.0 and 0.1, respectively, were placed on the scale factors to ensure that the ground motions would be reasonably representative of the original ground motion magnitude. The ground motions were scaled such that the maximum-direction spectra matched or exceeded the MCE_R target response spectra (which is also representative of the maximum direction spectra) over a period range from 0.14 seconds to 3.4 seconds. This period range is based on ASCE/SEI 7-16 requirements. The upper bound is defined by twice the first-mode period and the lower bound is defined to ensure that the range includes at least the number of elastic modes necessary to achieve 90% mass participation in each principal horizontal direction. A period of 1.7 seconds was assumed for for the first mode and 90% mass participation was achieved by the 8^{th} elastic mode, corresponding to a period of about 0.14 seconds. Note, ground motion selection and scaling occurred prior to developing the final nonlinear numerical model. Thus, as shown in Section 6.5.5, the final approximate first mode period and period to achieve 90% mass participation are slightly different, but still within an appropriate range. Figure 6.12 shows the scaled maximum direction spectra for all eleven MCE_R motions, the suite mean of the scaled ground motions, the target hazard curve at MCE_R, and the period range over which the ground motions were scaled. Note, 5% damped acceleration spectra were used for ground motion selection and scaling.

While the ground motion scaling procedures in Chapter 16 of ASCE/SEI 7-16 are specified for the MCE_R hazard only, the same methods were applied to the other six hazard levels with a one modification: geometric mean spectra ($Sa_{GeometricMean}$) for each horizontal ground motion pair was used in lieu of the maximum direction spectra. This modification is consis-

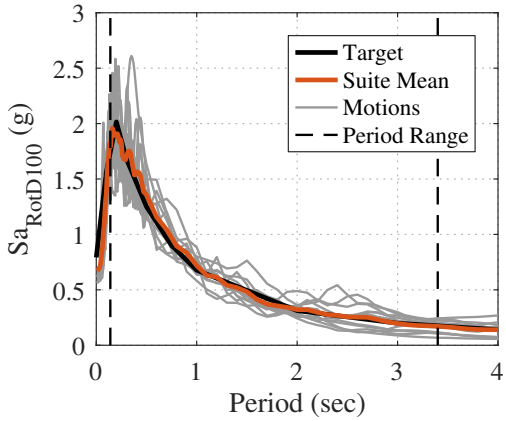

Figure 6.12: Target design spectra and scaled ground motions for MCE_R earthquake hazard

tent with the previously defined target spectra since the MCE_R target UHS is representative of the maximum direction spectra while the other target UHS curves are representative of the geometric mean spectra. Figure 6.13 shows the scaled $Sa_{GeometricMean}$ spectra for all eleven ground motions, the suite mean of the scaled ground motions, the target hazard curve, and the period range over which the ground motions were scaled for the six remaining hazard levels that are defined using return periods.

Section 16.2.4 of ASCE/SEI 7-16 was referenced to check the application of ground motion orientations to the structural model for the nonlinear numerical analyses. This check is performed to minimize issues related to directionality, insuring the larger ground motion component isn't applied in one orthogonal building direction more than the other. Each pair of ground motion components were applied at orthogonal orientations such that the average of the component response spectrum for the records applied in each direction is within $\pm 10\%$ of the component mean response spectra of all records applied for the period range specified previously. Figure 6.14 shows an example of this check for the MCE_R earthquake hazard. This check was satisfied for all hazard levels.

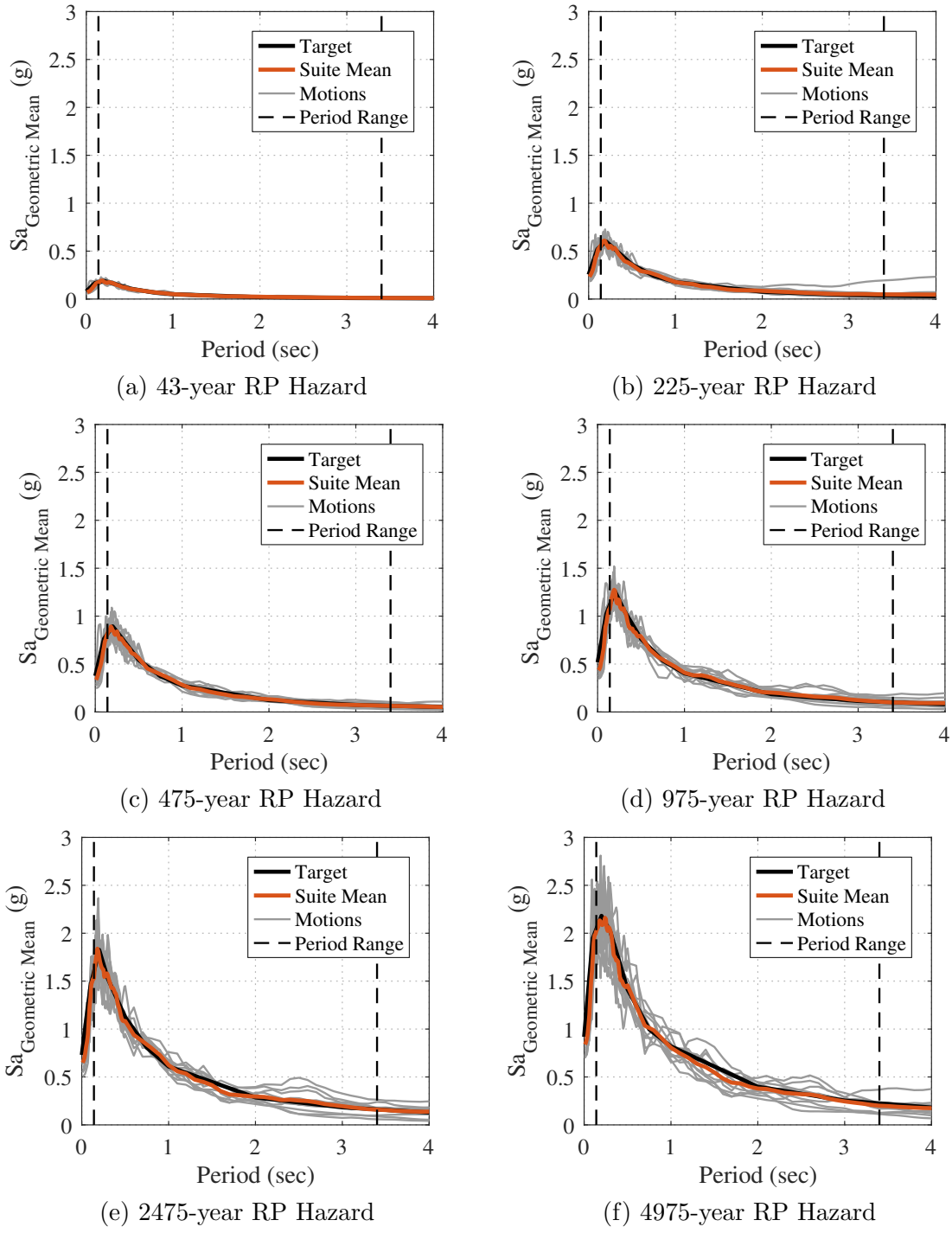

(a) 43-year RP Hazard

(b) 225-year RP Hazard

(c) 475-year RP Hazard

(d) 975-year RP Hazard

(e) 2475-year RP Hazard

(f) 4975-year RP Hazard

Figure 6.13: Target design spectra and scaled ground motions for each design earthquake hazard.

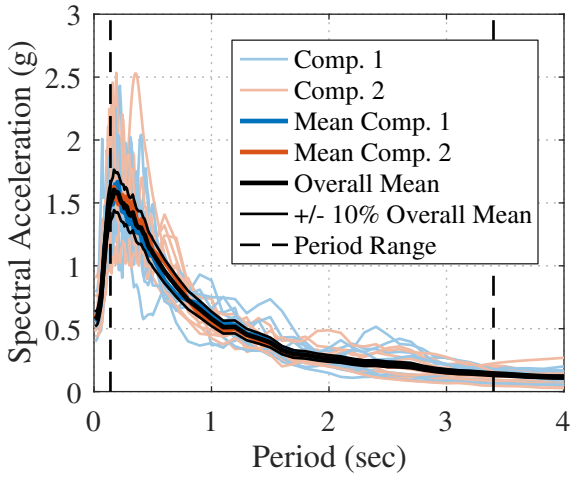

Figure 6.14: Ground motion direction application for the MCE_R earthquake hazard

6.4.2 Summary of Selected and Scaled Ground Motions

The ground motion selection and scaling procedures presented above were used to develop the suites of eleven ground motions at each of the seven hazard levels. Table 6.11 summarizes the ground motion information for the selected and scaled ground motions at the MCE_R hazard level. Table 6.12 summarizes the ground motion information for the six other hazard levels. In both tables, the assigned design suite ground motion number, the earthquake source, earthquake name, earthquake year, and scale factor for the design suite are listed. Additionally, the information needed to look up the original ground motion file from the original sources, including Motion ID and the recording station, are listed. For the crustal and intraslab earthquakes, the motion ID corresponds to the RSN number in the original ground motion repositories. For the interface earthquakes, the motion ID corresponds to an ID generated by KiK-net and K-NET database based on the station, date, and time of the earthquake. Finally, the directionality for which the ground motion was applied in the nonlinear numerical model is presented in the EW Comp. and NS Comp. columns of the table. The inputs listed for these two columns is consistent with the naming scheme present in the ground motion repositories from which they were obtained.

Table 6.11: Ground Motion information for the MCE_R design suite

Suite #	Source	Earthquake	Year	SF	Motion ID	Station	EW Comp.	NS Comp.
1	Crustal	Chi-Chi, Taiwan	1999	1.283	1512	TCU078	-N	-E
2	Crustal	Niigata, Japan	2004	2.236	4213	NIG023	EW	NS
3	Crustal	Niigata, Japan	2004	1.323	4228	NIGH11	EW	NS
4	Crustal	El Mayor-Cucapah	2010	2.903	6005	Holtville Post Office	090	360
5	Crustal	Loma Prieta	1989	3.957	761	Fremont - Emerson Court	180	090
6	Interface	Tohoku	2011	2.67	CHB0101103111446	CHB010	NS	EW
7	Interface	Tohoku	2011	2.298	CHBH041103111446	CHBH04	EW2	NS2
8	Interface	Tohoku	2003	4.693	HKD1270309260450	HKD127	NS	EW
9	Interface	Tokachi	2011	4.462	IWT0221103111446	IWT022	NS	EW
10	Interface	Tohoku	2011	3.074	TKY0071103111446	TKY007	NS	EW
11	Intraslab	Ferndale	2010	4.538	subRSN2000890	89486	090	360

Table 6.12: Ground Motion information for the design suites at all hazard levels except MCE_R

Suite #	Source	Earthquake	Year	SF	Motion ID	Station	EW Comp.	NS Comp.
43-year RP Earthquake Hazard								
1	Crustal	Imperial Valley-06	1979	0.494	167	Compuertas	285	015
2	Crustal	Chi-Chi, Taiwan-06	1999	0.646	3320	CHY111	W	N
3	Crustal	San Simeon, CA	2003	0.154	4031	Templeton - 1-story Hospital	360	090
4	Crustal	Darfield, New Zealand	2010	0.596	6949	PEEC	S79W	N11W
5	Crustal	Northridge-01	1994	1.065	975	Glendora - N Oakbank	170	080
6	Interface	Tohoku - Aftershock	2011	4.17	CHB0121103111526	CHB012	NS	EW
7	Interface	Tokachi	2003	0.816	HKD1310309260450	HKD131	NS	EW
8	Interface	Tohoku	2011	0.905	IBRH171103111446	IBRH17	NS1	EW1
9	Intraslab	Nisqually	2001	0.534	subRSN2000055	PCFR	ENE	ENN
10	Intraslab	Ferndale	2010	0.458	subRSN2000889	89255	090	360
11	Intraslab	Ferndale	2010	0.5	subRSN2000890	89486	090	360
225-year RP Earthquake Hazard								
1	Crustal	Chi-Chi, Taiwan	1999	0.381	1549	TCU129	-E	-N
2	Crustal	Denali, Alaska	2002	3.464	2113	TAPS Pump Station #09	103	-13
3	Crustal	Niigata, Japan	2004	0.79	4213	NIG023	EW	NS
4	Crustal	Darfield, New Zealand	2010	1.911	6949	PEEC	S79W	N11W
5	Crustal	Northridge-01	1994	3.418	975	Glendora - N Oakbank	080	170
6	Interface	Tohoku	2011	0.812	CHBH041103111446	CHBH04	NS2	EW2
7	Interface	Tokachi	2003	2.616	HKD1310309260450	HKD131	EW	NS
8	Interface	Tohoku	2011	2.899	IBRH171103111446	IBRH17	EW1	NS1
9	Intraslab	Nisqually	2001	1.711	subRSN2000055	PCFR	ENE	ENN
10	Intraslab	Ferndale	2010	1.605	subRSN2000890	89486	090	360
11	Intraslab	Ferndale	2010	1.684	subRSN2000905	1746	090	360

continued ...

. . . continued

Suite #	Source	Earthquake	Year	SF	Motion ID	Station	EW Comp.	NS Comp.
475-year RP Earthquake Hazard								
1	Crustal	Chi-Chi, Taiwan	1999	0.57	1549	TCU129	-E	-N
2	Crustal	Chi-Chi, Taiwan-05	1999	4.633	2951	CHY039	E	N
3	Crustal	Chi-Chi, Taiwan-06	1999	4.323	3471	TCU075	E	N
4	Crustal	Niigata, Japan	2004	1.184	4213	NIG023	EW	NS
5	Interface	Tohoku	2011	4.53	AKT0121103111446	AKT012	NS	EW
6	Interface	Tohoku	2011	1.215	CHBH041103111446	CHBH04	EW2	NS2
7	Interface	Tokachi	2003	3.917	HKD1310309260450	HKD131	EW	NS
8	Interface	Tohoku	2011	4.339	IBRH171103111446	IBRH17	EW1	NS1
9	Interface	Tohoku	2011	2.353	IWT0221103111446	IWT022	EW	NS
10	Intraslab	Ferndale	2010	2.404	subRSN2000890	89486	090	360
11	Intraslab	Ferndale	2010	2.524	subRSN2000905	1746	090	360
975-year RP Earthquake Hazard								
1	Crustal	Chi-Chi, Taiwan	1999	0.796	1549	TCU129	-E	-N
2	Crustal	Victoria, Mexico	1980	4.999	268	SAHOP Casa Flores	280	010
3	Crustal	Chi-Chi, Taiwan-05	1999	4.916	2937	CHY015	W	N
4	Crustal	Northridge-01	1994	3.931	964	Compton - Castlegate St	270	000
5	Interface	Tohoku	2011	1.696	CHBH041103111446	CHBH04	EW2	NS2
6	Interface	Tokachi	2003	3.462	HKD1270309260450	HKD127	NS	EW
7	Interface	Tohoku	2011	4.051	IBRH161103111446	IBRH16	EW1	NS1
8	Interface	Tohoku	2011	3.29	IWT0221103111446	IWT022	EW	NS
9	Interface	Tokachi	2003	3.695	NMRH050309260450	NMRH05	NS1	EW1
10	Interface	Tohoku	2011	2.275	TKY0071103111446	TKY007	NS	EW
11	Intraslab	Ferndale	2010	3.356	subRSN2000890	89486	090	360

continued . . .

. . . continued

Suite #	Source	Earthquake	Year	SF	Motion ID	Station	EW Comp.	NS Comp.
2475-year RP Earthquake Hazard								
1	Crustal	Kobe, Japan	1995	4.008	1115	Sakai	090	000
2	Crustal	Chi-Chi, Taiwan	1999	2.013	1521	TCU089	-N	-E
3	Crustal	Chi-Chi, Taiwan	1999	1.157	1549	TCU129	-N	-E
4	Crustal	Niigata, Japan	2004	2.401	4213	NIG023	NS	EW
5	Crustal	Darfield, New Zealand	2010	4.29	6961	RKAC	S76E	N14E
6	Interface	Tohoku	2011	2.862	CHB0101103111446	CHB010	NS	EW
7	Interface	Tohoku	2011	2.466	CHBH041103111446	CHBH04	NS2	EW2
8	Interface	Tohoku	2011	3.463	GNM0101103111446	GNM010	NS	EW
9	Interface	Tohoku	2011	4.79	IWT0221103111446	IWT022	NS	EW
10	Interface	Tohoku	2011	3.31	TKY0071103111446	TKY007	NS	EW
11	Intraslab	Ferndale	2010	4.879	subRSN2000890	89486	090	360
4975-year RP Earthquake Hazard								
1	Crustal	Chi-Chi, Taiwan	1999	2.568	1521	TCU089	-N	-E
2	Crustal	Chi-Chi, Taiwan	1999	1.472	1549	TCU129	-N	-E
3	Crustal	Imperial Valley-06	1979	1.878	184	El Centro Differential Array	360	270
4	Crustal	Niigata, Japan	2004	3.06	4213	NIG023	EW	NS
5	Crustal	El Mayor-Cucapah	2010	4.025	5838	El Centro-Meloland Geotechnic	270	360
6	Interface	Tohoku	2011	3.649	CHB0101103111446	CHB010	EW	NS
7	Interface	Tohoku	2011	3.136	CHBH041103111446	CHBH04	EW2	NS2
8	Interface	Tohoku	2011	3.715	FKSH161103111446	FKSH16	NS2	EW2
9	Interface	Tohoku	2011	2.667	IWT0111103111446	IWT011	EW	NS
10	Interface	Tohoku	2011	4.216	TKY0071103111446	TKY007	NS	EW
11	Intraslab	Olympia	1949	3.475	subRSN2000001	OLY0	086	356

6.5 Nonlinear Numerical Model of the 10-Story Test Specimen

This section presents the three-dimensional nonlinear numerical model of the NHERI 10-story test specimen used for design of the lateral system. The model was developed in OpenSees [Mazzoni et al., 2009] and includes a detailed representation of the post-tensioned rocking wall lateral system and the lateral connections. It assumes a rigid diaphragm and includes the boundary and gravity columns. The building was designed such that the response is controlled by the post-tensioned rocking walls and contributions from the stairs and nonstructural elements are minimal. Thus, they were not included in this model. While this model focused primarily on the lateral system and its design, force and deformation demands results were also used to inform and aid in the design of other key building components including the diaphragms, stairs, and nonstructural walls. This model uses 2% Rayleigh damping on the 1st and 9th mode (i.e., capturing the first three modes x, y, and torsional modes, see Section 6.5.5) and uses the elements' current stiffness matrix. The modeling methodologies presented in this section built upon two-dimensional techniques presented in Ganey [2015] and Wichman et al. [2022] (Chapter 5) which validated the techniques using cyclic and dynamic loading tests, respectively. This model was not developed to study the response of vertical input motions.

6.5.1 Rocking Wall Lateral System Modeling

A schematic of the post-tensioned rocking wall OpenSees model is shown in Figure 6.15. With these lateral systems, the walls remain elastic up the height of the wall and all inelastic behavior of the wall system occurs at the base through uplift and compressive deformations. The elastic portion of the rocking wall is modeled using a series of force beam column elements with a rectangular fiber cross section. The fiber cross section is equivalent to the size of the wall panels (b_w by L_w) and consisted of 348 fibers (a 58 by 6 patch) for the CLT walls and 208 fibers (a 52 by 4 patch) for the MPP walls. An elastic material model, with stiffness equal to the effective MOE, E_{eff}, was assigned to the wall fiber section to model

flexural stiffness. The section aggregator command in OpenSees was used to account for shear deformations, which are significant for these walls. An elastic material model with slope equal to $G_{eff} \times k_s \times A_w$ was used for shear flexibility, where G_{eff} is the effective shear modulus, k_s is the shear shape factor equal to 5/6 for a rectangular cross section, and A_w is the cross sectional area of the wall. This material was then aggregated to the elastic fiber section in both in-plane shear directions. Reference Tables 6.2 and 6.3 for the model input parameters used for the CLT and MPP walls, respectively.

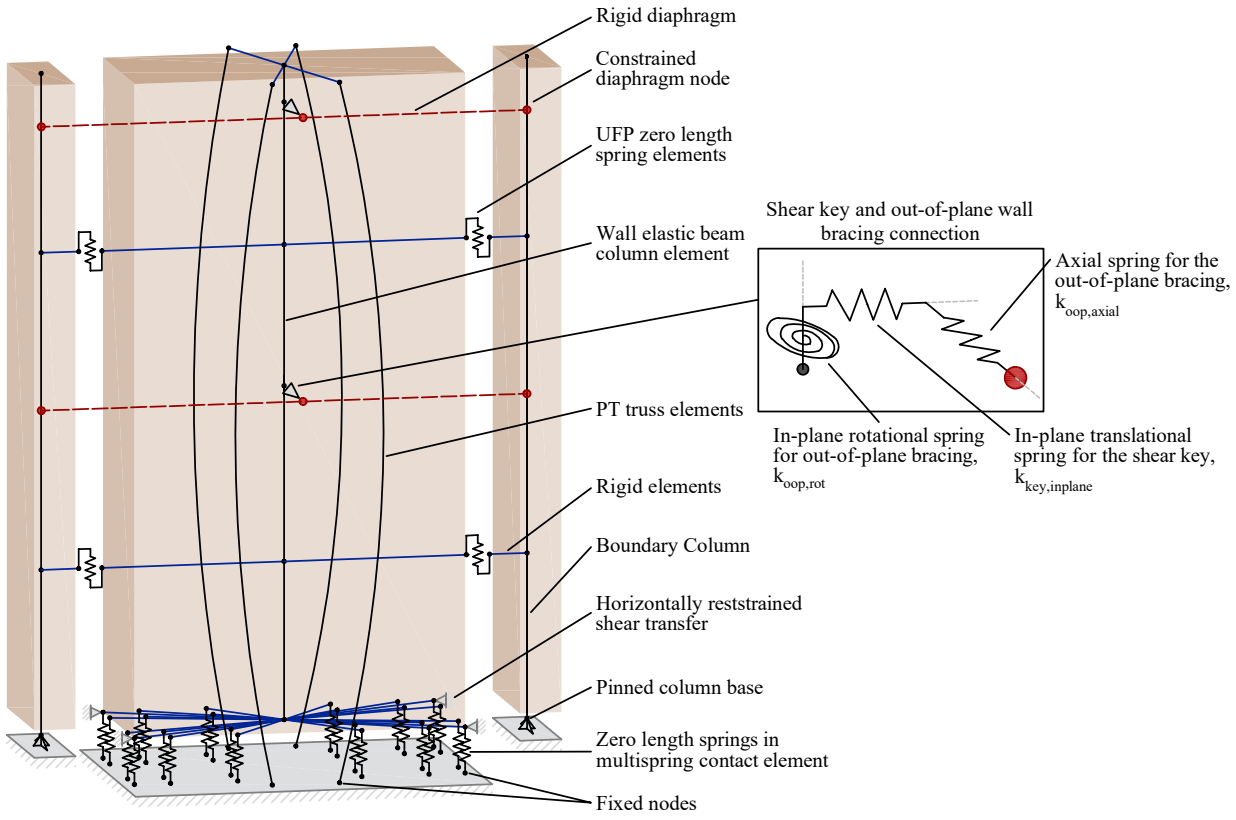

Figure 6.15: Post-tensioned rocking wall numerical model schematic for the 10-story building specimen

The inelastic compressive deformation of the wall base and the rocking behavior was modeling using a multispring contact element, initially developed by Spieth et al. [2004] for

prestressed concrete structures and utilized in two-dimensions by Ganey [2015], Wichman et al. [2022] (Section 5.2), and others. For the 10-story model, this multispring element methodology was extrapolated to develop a three-dimensional multispring element that can capture rocking in both the in-plane direction and out-of-plane direction. In the 3D multispring contact element, vertically orientated zero-length springs are distributed along the base using a Labatto Integration method in both directions, such that there is a higher concentration of springs at the rocking corners. The distribution used here consisted of 30 springs along the length of each wall base and 7 rows of springs through the thickness of each panel. Figure 6.15 includes a simplified illustration of this multispring element. The top of each spring connected to the base of the bottom wall element using a horizontal elastic beam column element with a high MOE to represent a rigid connection. The bottom of each spring was fixed. To transfer shear at the wall base, the tops of the zero length springs in the four corners of the multispring element were restrained in both horizontal directions.

Presented previously, Figure 6.3 shows the target compressive stress-strain behavior this model aims to capture for the bases of the CLT and MPP walls. An assumed plastic hinge length, l_p, is used to transform the desired stress-strain behavior to the compression only force-deformation behavior needed for the zero length springs in the multispring element. In this model, a plastic hinge length of $2b_w$ was assumed in accordance with recommendations in Akbas et al. [2017] and validated in Wichman et al. [2022] (Chapter 5). Similar to the two-story OpenSees model presented in Chapter 5, the plastic hinge length was utilized by calculating an overall contact stiffness of the multispring element, K_s, using Equation 6.2. This stiffness was then proportionally scaled based on the Labatto Integration method to determine the stiffness of each zero-length spring, k_s. For each spring, the product of the wall yield stress, $f_{y,clt}$ or $f_{y,mpp}$, and the Labatto weighted area determines each yield strength, $F_{y,clt}$ and $F_{y,mpp}$ (similarly, $f_{s,mpp}$ is used to calculate $F_{s,mpp}$ for the wood splitting point in the MPP behavior). Using the same logic, the product of the respective strains, ϵ_s and ϵ_{cr}, and the plastic hinge length, l_p, determine the splitting deformation, Δ_s, and the crushing deformation, Δ_{cr}, for all the springs in the element. Tables 6.2 and 6.3 can be

referenced for the model input parameters used for the CLT and MPP walls, respectively. Figure 6.16a and 6.16b show the resulting force-deformation constitutive model assigned to the zero-length springs in the multispring element of the CLT and MPP walls, respectively.

$$K_s = \frac{b_w L_w E_{eff}}{l_p} \tag{6.2}$$

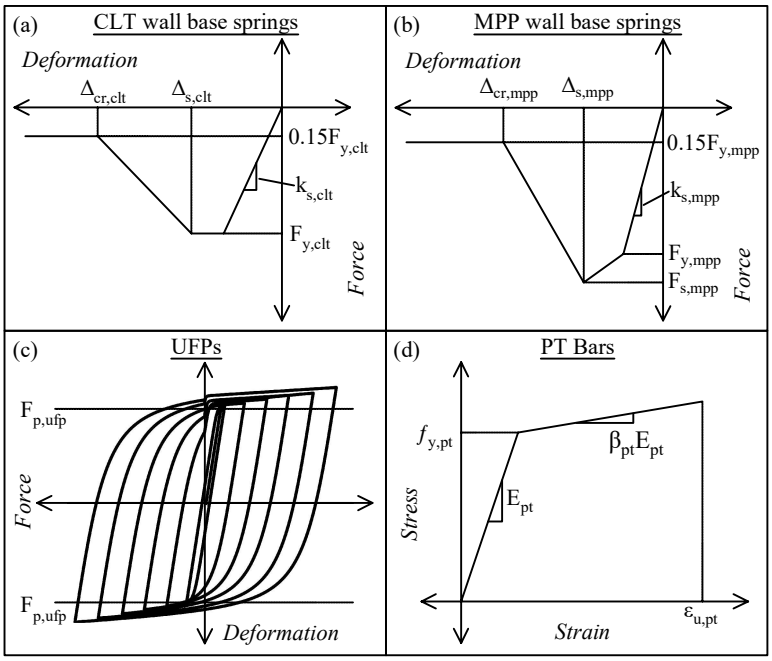

Figure 6.16: Material models used in the post-tensioned rocking wall numerical model for the 10-story building specimen

To combat the increased axial flexibility of the wall that results from the addition of the multispring element, a truss element, spanning from the top of the wall panel to the top of the multispring element, is added to increase the area of the wall. The truss element has an elastic material model, with an elastic modulus equal to the wall, E_{eff}, and an area, A_w*, calculated as show in Equation 6.3. Again, reference Tables 6.2 and 6.3 for the model input parameters used for the CLT and MPP walls, respectively.

$$A_w* = b_w L_w \frac{l_p}{h_w - l_p} \tag{6.3}$$

The PT bars are modeled using corotational truss elements that connect a fixed node at the wall base elevation to the end of a cantilevered rigid element at the top of the wall representing the PT offset from the centerline of the wall. A tension-only bilinear hysteretic material model that allows for damage accumulation after yielding was used for the PT elements (show in Figure 6.16d). The initial post-tensioning of the PT elements was simulated by applying an initial strain wrapper in OpenSees. For simplicity in the model, the 1 1/4" diameter bars (the upper bars) were assumed for the entire height of the walls. Because the length of the larger lower bars is short in comparison to the whole building, this approximation will not have a significant effect on the overall performance of the model. A higher initial PT force, $T^*_{o,pt}$, is applied to the bars to correct for the initial elastic wall shortening from the initial PT force and ensure the target PT force ($T_{o,pt}$) is achieved. This larger force is calculated in accordance with Equation 6.4 where k_w is the elastic stiffness of the wall calculated using Equation 6.5 and k_{pt} is the elastic stiffness of the PT bars calculated using Equation 6.6. Reference Table 6.4 for the PT properties used (use the upper bar size) and Tables 6.2 and 6.3 for the properties of the CLT and MPP walls, respectively.

$$T^*_{o,pt} = T_{o,pt}\left(\frac{k_{pt}}{k_w} + 1\right) \tag{6.4}$$

$$k_w = \frac{b_w L_w E_{eff}}{H_w} \tag{6.5}$$

$$k_{pt} = \frac{A_{net,pt} E_{pt}}{h_w} \tag{6.6}$$

The boundary and gravity columns were modeled using continuous elastic beam column elements with pinned bases. The geometric and material properties shown in Table 6.1 were referenced for model input properties. The true MOE, E, shown in Table 6.1 was used and an effective shear modulus, G_{eff}, of 35 ksi was assumed for the column model. Note, because

contributions from the gravity connections were designed to be small, they were not included in this model.

Each UFP is modeled as a zero-length spring element located at the midpoint between the wall edge and the respective boundary columns. Note, the UFP wall cutouts are not accounted for in the location offset, but are not expected affect the results. Based on recommendations by Ganey [2015] and Wichman [2018], a Giuffre-Menegotto-Pinto steel material model with isotropic strain hardening is used for the vertical direction of the zero-length spring to model the UFP behavior (Figure 6.16c). A yield force and stiffness are calculated in accordance with Equations 3.2 and 3.4, respectively. Properties from Table 6.5 were used for modeling. Note, for the lower UFPs, the input stiffness and yield forces values were multiplied by two because there were two UFPs at each location. The assigned stiffness in all remaining degrees of freedom is near-zero to represent no contribution. In the model, the UFP locations were assumed to be at mid-height of every story.

6.5.2 Diaphragm-to-Wall Shear Key Connection and Out-of-Plane Wall Bracing Modeling

The connection between the diaphragms and walls (shear key) and the out-of-plane braces were modeled by adding a second node at each wall and floor intersection and connecting the two nodes with a zero length spring. Different elastic stiffness values were applied to the different directions of the zero length springs to model the flexibility from the shear key and the out-of-plane braces. The free end of the spring was incorporated into the diaphragm model as discussed in the next section. A schematic showing the stiffness in each direction of this spring is included in Figure 6.15.

The flexibility of the cantilevered shear key (Figure 6.8) was modeled by assigning an elastic material model to the horizontal in-plane wall translational direction of the zero length spring. The stiffness for this degree of freedom, $k_{key,inplne}$, accounted for both flexural stiffness, $k^f_{key,inplane}$, and shear stiffness, $k^s_{key,inplane}$, and was calculated using Equation 6.9. Properties and dimensions for these equations are found in Table 6.6. The shear modulus of the shear key, G_{key}, was calculated using poisons ratio for steel. While shear contributions

were included in the cantilevered flexibility of the shear key, it is not expected to effect the stiffness significantly. The zero length spring had zero stiffness in the vertical degree of freedom to allow for uplift of the rocking walls.

$$k^{f}_{key,inplane} = \frac{3E_{key}(w^{3}_{key}t_{key}/12)}{L^{3}_{key}} \tag{6.7}$$

$$k^{s}_{key,inplane} = \frac{G_{key}w_{key}t_{key}}{L_{key}} \tag{6.8}$$

$$k_{key,inplane} = \frac{k^{f}_{key,inplane}k^{s}_{key,inplane}}{k^{f}_{key,inplane} + k^{s}_{key,inplane}} \tag{6.9}$$

To model the axial flexibility from the cantilevered out-of-plane brace legs (Figure 6.9), an elastic material model was assigned to the zero length spring in the horizontal degree of freedom that is perpendicular to the face of the walls. The stiffness for this degree of freedom, $k_{oop,axial}$, was calculated using Equation 6.10 and referencing values in Table 6.7. In the equation, the 4 legs per wall is divided by 2 because the legs are pin-connected to the walls.

$$k_{oop,axial} = \frac{t_{oop}h_{oop}E_{oop}}{L_{oop}} \times \frac{4\,legs}{2} \tag{6.10}$$

The rotational stiffness from the two wall out-of-plane braces at each wall on each floor level (Figure 6.9) is modeled by assigning an elastic material model to the out-of-plane wall rotational degree of freedom in the zero length spring. The stiffness of this spring was calculated using Equation 6.11 and referencing Table 6.7 for the input values. In this equation the number of legs is divided by 2 because the full moment arm length, d_{oop}, was used. The other two rotational degrees of freedom for this zero length spring were assigned negligible stiffness to allow uplift and rocking of the post-tensioned walls.

$$k_{oop,rot} = \frac{t_{oop}h_{oop}E_{oop}}{L_{oop}} \times \frac{4\,legs}{2} \times d_{oop} \tag{6.11}$$

6.5.3 Diaphragm Modeling

Diaphragms were modeled using a rigid diaphragm constraint. Because the spans in the diaphragms are relatively short in this building, their flexibly is assumed to be small, justifying this assumption. The rigid diaphragm model was implemented by first adding a node at the calculated approximate center of mass (COM) location (X_{mi},Y_{mi}), shown in Table 6.9 under the "modeling parameters per floor" section. The rigid diaphragm command in OpenSees was then utilized by assigning the new COM node as the retained node. The constrained nodes were the four free end nodes of the diaphragm-to-wall shear transfer spring on each floor and the fourteen column nodes on each floor (See the red nodes in Figure 6.17). The vertical direction was defined as the direction perpendicular to the rigid plane.

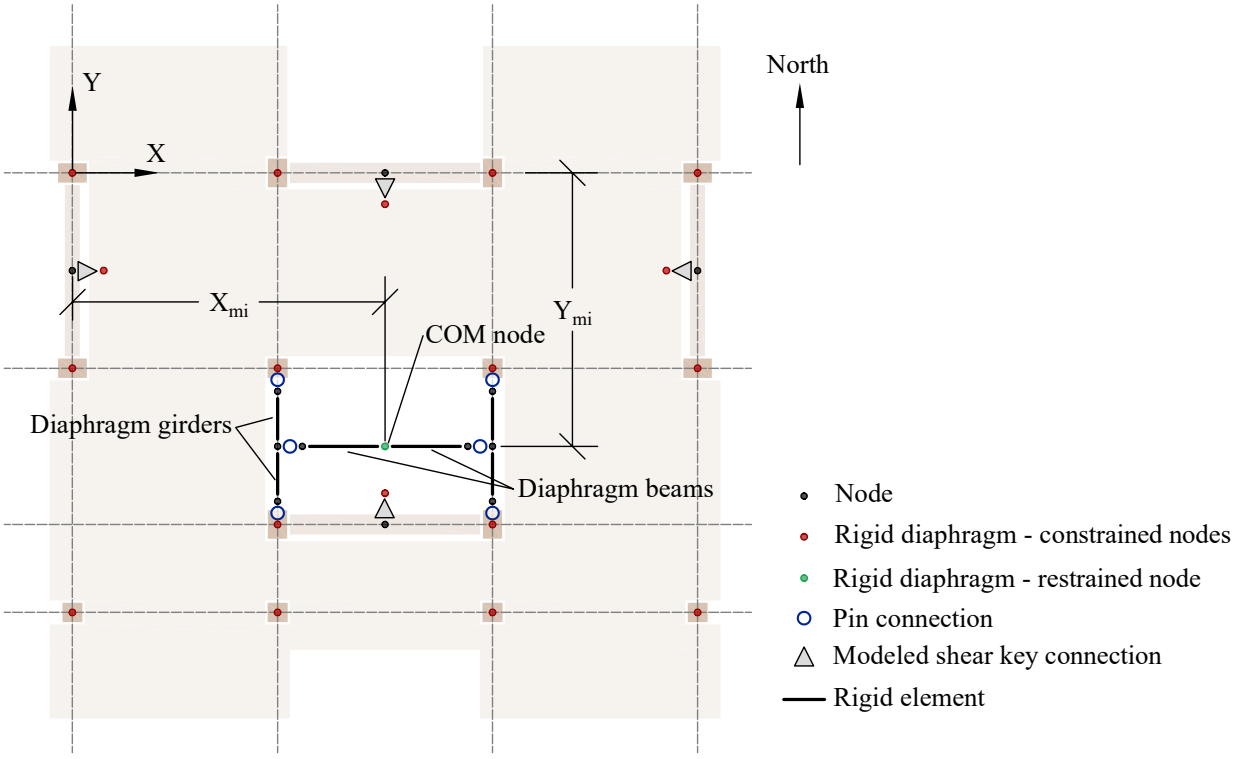

Figure 6.17: Schematic of the diaphragm model used in the 10-story OpenSees model on each floor

As shown in Figure 6.17, an assembly of beams and girders were modeled to support the new COM node. With the rigid diaphragm assumption, the real beams in the building would not contribute to the response of the structure. These added beams and girders are not representative of the real beams in the model, but were only added to the model to support the new COM node and allow appropriate transfer of vertical gravity loads to the diaphragm and distribute into the columns. The diaphragm beam and girder assembly was constructed in the stair opening because the COM modeling node falls within this bay for all floors. Diaphragm girder elements spanned in the north-south direction and a diaphragm beam element spanned across the girders. Fully pinned rotational springs were added at intersections. The beam and girder elements were modeled with elastic beam column elements with a high MOE to model a rigid member. Figure 6.18 shows a schematic of the full 10-story building OpenSees model. Note, Wright [2023] developed a numerical model for each of the diaphragm types and studied the vertical response of the systems during shake table testing.

6.5.4 Application of Seismic Mass and Gravity Loads

The seismic mass of the wall panels and the mass of any significant lateral connections on the walls (as described in Section 6.2.4) was distributed up the height of the wall panels. The mass per floor for the CLT, $m_{i,clt}$, and MPP, $m_{i,mpp}$ walls can be found in Table 6.9. These mass values were evenly distributed and assigned to nodes spaced at quarter-points of each story. The mass was assigned to the two horizontal degrees of freedom. The remainder of the mass on each story, m_i, and the approximate rotational MOI, I_{oi}, from the "modeling parameters per floor" section of Table 6.9 were applied to the COM node on each diaphragm. The mass, Mmi, was applied to the two horizontal degrees of freedom and the rotational MOI, I_{oi}, was applied to the rotational degree of freedom about the vertical axis. For the gravity loading analysis, vertical loads equivalent to the seismic masses were applied to the structure. For the walls, equivalent load wall applied, but lumped at floor levels instead of at quarter points. The remaining gravity load was applied to the COM node.

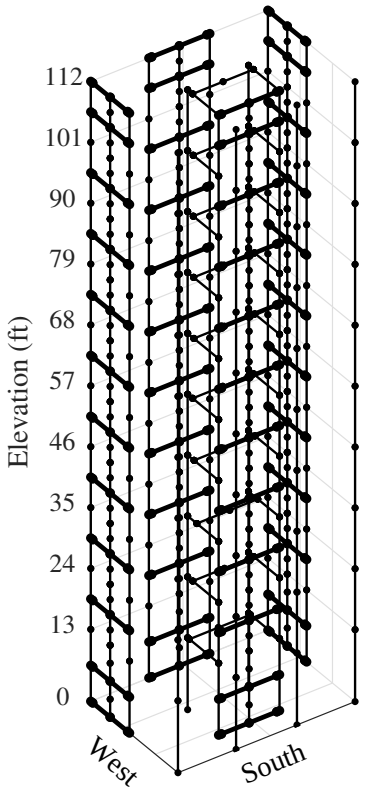

Figure 6.18: Schematic of the full OpenSees model of the 10-story test specimen

6.5.5 Linear Model and Eigenvalue Analysis

A linear model of the 10-story building was also developed in OpenSees. Because base rocking is not part of the linear analysis, a fixed base was used. Additionally, the PT bars were neglected in the linear model because their contributions to initial stiffness (pre-uplift) is small compared to that of the mass timber panel. While it is sometimes recommended to also neglect the UFPs in the linear model [Busch et al., 2022], it was determined that their contribution to the initial stiffness is not negligible and thus, elastic UFP springs were kept in the linear model.

An eigenvalue analysis was performed on the linear model to characterize the modal properties of the 10-story building specimen. The resulting periods for the first 9 modes

of the building are summarized in Table 6.13 and schematics of the corresponding mode shapes are shown in Figure 6.19. These first 9 building modes capture the first three x-direction (east-west) modes, the first three y-direction (north-south) modes, and the first three torsional (θ_z) modes. Note, while the results from the eigenvalue analysis of the linear OpenSees model is presented here, performing an eigenvalue analysis on the nonlinear OpenSees model yields nearly identical results.

Table 6.13: Building periods from an eigenvalue analysis of the linear 10-story test building OpenSees model

Mode	Period (sec)		
	T_x	T_y	$T_{\theta z}$
1	1.68	1.74	1.22
2	0.34	0.35	0.25
3	0.15	0.15	0.11

Table 6.14 summarizes the modal participation masses. In this table the modes are listed in order of descending periods. As shown from the mode shape plots and the modal participation masses, each mode is dominated by one primary degree of freedom, as expected. However, the x-direction dominated modes have some torsional component as well. The first three modes in each direction are discussed as these capture 90% modal mass participation for the horizontal degrees of freedom, a common benchmark used in ASCE/SEI 7-16.

Table 6.14: Mass participation values from an eigenvalue analysis of the OpenSees model for the 10-story test building

Mode	Period (sec)	Modal Participation Masses (%)			Cumulative Modal Participation Masses (%)		
	T	M_x	M_y	M_z	M_x	M_y	M_z
Y_1	1.74	0.0	63.4	0.0	0.0	63.4	0.0
X_1	1.68	63.2	0.0	0.4	63.2	63.4	0.4
θ_{z1}	1.22	0.5	0.0	41.3	63.7	63.4	41.6
Y_2	0.35	0.0	22.5	0.0	63.7	85.9	41.6
X_2	0.34	22.2	0.0	0.2	85.9	85.9	41.8
θ_{z2}	0.25	0.3	0.0	16.5	86.2	85.9	58.3
X_3	0.15	7.0	0.4	0.1	93.2	86.4	58.4
Y_3	0.15	0.4	7.2	0.0	93.6	93.5	58.4
θ_{z3}	0.11	0.1	0.0	8.2	93.7	93.5	66.6

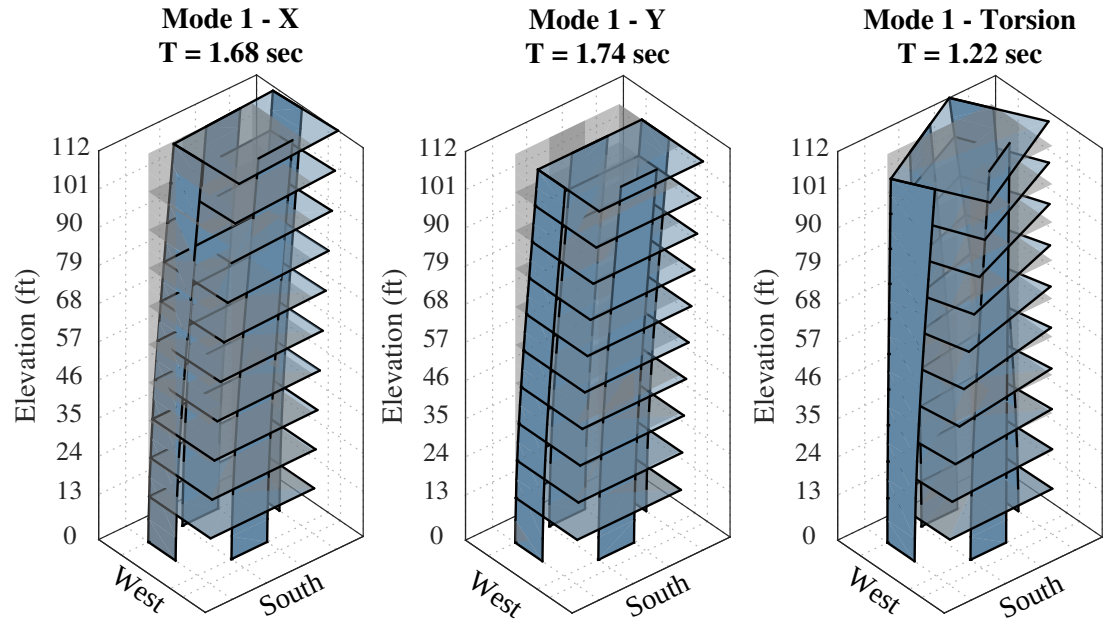

(a) Mode 1

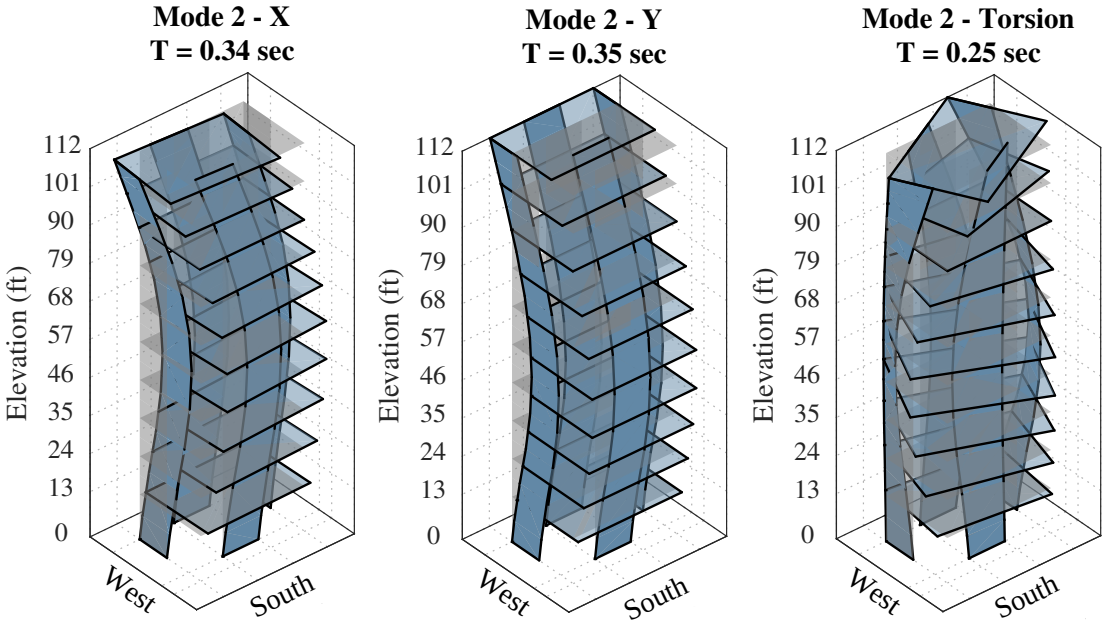

(b) Mode 2

Figure 6.19: Mode shapes from and eigenvalue analysis on the 10-story test specimen OpenSees model

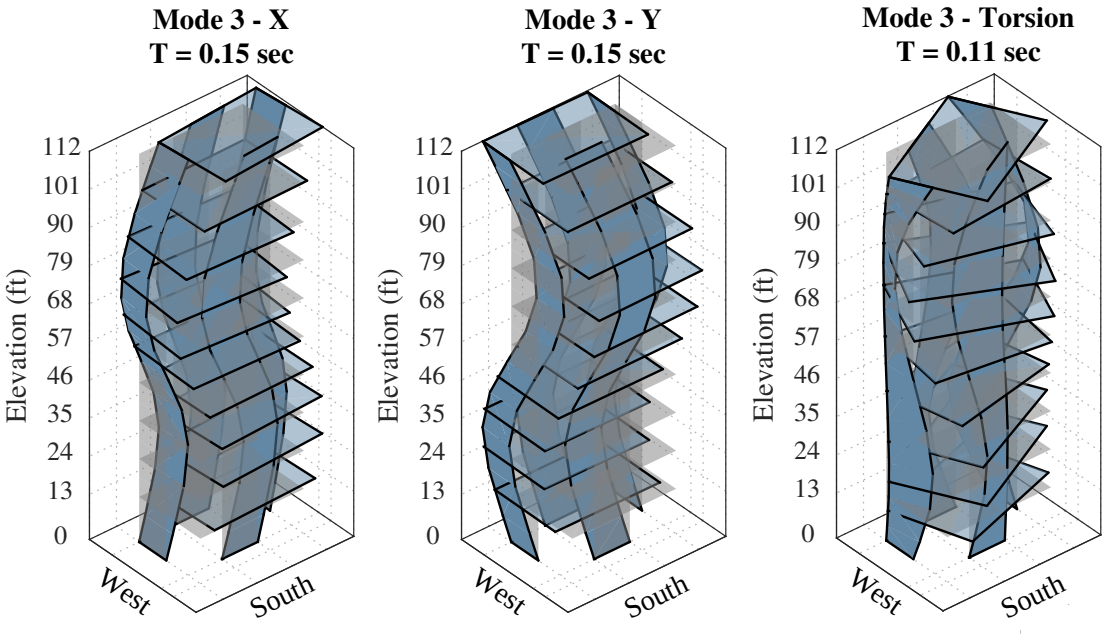

(c) Mode 3

Figure 6.19: Mode shapes from and eigenvalue analysis on the 10-story test specimen OpenSees model

6.6 Lateral Design of the 10-Story Building Specimen

This section will present the performance-based design methodology and nonlinear response history analyses completed for the design of the resilient post-tensioned rocking wall lateral force resisting system used in the NHERI TallWood 10-story mass timber building. The intent of this design process was to be reflective of the procedure that would be done in practice for a lateral system not recognized by the codes, but does target performance that exceeds code requirements. Many of the design philosophies presented here were inspired by the design of the Framework building [Engineers, 2017]. Note, the design of this lateral system under wind loads is not presented in this document.

While mass timber lateral force-resisting systems are gaining popularity in research, they are not fully recognized in the US building code and design standards. Thus, performance-based seismic design methodologies were used for the 10-story lateral system. In other words, lateral force-resisting systems included in Table 12.2-1 of ASCE/SEI 7-16 can be designed for earthquake loads using prescriptive provisions in ASCE/SEI 7-16, however, systems not included in the table are still permitted, but must follow performance-based design procedures of ASCE/SEI 7-16 Section 1.3.1.3. The limits used on both local and global acceptance criteria are consistent with current performance-based design guidelines (Chapter 16 ASCE/SEI 7-16 and 2014 LATBSDC). For design, the following codes and references were applied:

- 2018 International Building Code
- Minimum Design Loads and Associated Criteria for Buildings and Other Structures ASCE/SEI 7-16, American Society of Civil Engineers, Structural Engineering Institute.
- National Design Specification for Wood Construction, 2018 Edition, American Wood Council.
- Seismic Performance Assessment of Buildings, Volume 1 - Methodology, FEMA P-58-1, Federal Emergency Management Agency.

- Special Design Provisions for Wind and Seismic, 2015 Edition, American Wood Council.
- Specification for Structural Steel Buildings, ANSI/ AISC 360-16, American Institute of Steel Construction.

The overall design of the post-tensioned rocking wall lateral system for the NHERI Tall-Wood building can be summarized into three phases as shown in Figure 6.20. The first phase of the design procedure was to perform a modal response spectrum analysis (MRSA) in accordance with ASCE/SEI 7-16 on a linear OpenSees model to check preliminary drift limits and establish preliminary rotation design demands for a Design Basis Earthquake and an MCE_R earthquake. For the second phase of the design procedure, the rotation demands were used to perform a cross-sectional analysis procedure (outlined in Section 3.3.1) and determine a preliminary design. The preliminary design was iterated on until a series of limit state checks (based on modified recommendations in Busch et al. [2022]) were satisfied.

The third and final phase of the design procedure was to finalize the design using the MCE_R seismic design criteria summarized in Table 6.15. Nonlinear response history analysis (NLRHA) was performed in OpenSees on a suite of eleven two-component ground motions selected and scaled to the 5% damped MCE_R spectrum. These results were assessed at suite mean demand and suite maximum demand. Suite mean demand is defined as the geometric mean over all earthquakes of the maximum demand for each earthquake. Geometric mean was used to account for dispersion of the peak values. Suite maximum demand is defined as the maximum over all earthquakes of the maximum demand for each earthquake. Using the suite mean and suite maximum results, stringent criteria for ISD limits, force-controlled actions, and deformation-controlled actions were enforced to validate and finalize the design. Details for the 2.25% ISD limit check will be discussed Section 6.6.3 and force and deformation criteria checks will be discussed in Sections 6.6.3 and 6.6.3, respectively. Note, checks for residual drifts will not be checked directly, however, code requirements are assumed to be met if PT bars do not yield, allowing the structure to fully re-center.

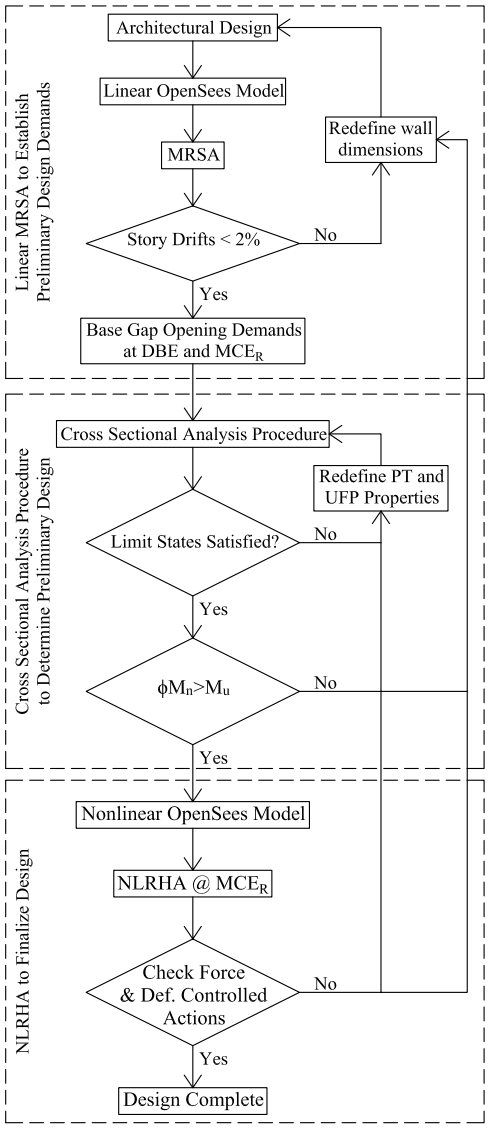

Figure 6.20: Summarized design procedure used for the 10-story test specimen

The stringent criteria used at MCE_R results in essentially elastic performance apart from the deformation criteria which allows rocking wall uplift, minor yielding of the wood at the base of the wall, and yielding of the replaceable energy dissipating elements. Because of the essentially elastic performance at MCE_R from the force-controlled components, minimal criteria performance criteria are enforced at the lower hazard levels.

Table 6.15: MCE_R seismic hazard criteria

Criteria	**Value**
Analysis Procedure	Nonlinear Response History
Software	OpenSees
Risk Category	II
Seismic Design Category	D
P-Δ Effects	Considered
Earthquake Hazard	Eleven two-component ground motions scaled to the 5% damped MCE_R spectrum. Note, no vertical ground motions will be applied for design.
Inherent Damping	2%
Accidental Torsion	Not Considered
Analysis Load Combination	$D + E_h$
Peak ISD Limit	2.25% for suite mean
Force-Controlled Actions	See Table 6.32
Deformation-Controlled Actions	See Table 6.33

6.6.1 MRSA and Preliminary Design Demands

The first phase of the lateral design procedure (Figure 6.20) used for the 10-story specimen was to complete a modal response spectrum analysis (MRSA) using a linear OpenSees model for preliminary drift checks and develop preliminary design demands. This phase of the design procedure was inspired by recommendations in Busch et al. [2022].

Architectural Design

The floor plan of the 10-story specimen and the schematic architectural design of the walls was initially selected based on architectural constraints such as shake table size, desired building floor plan, and desired building period. In this phase of planning, collaborators

from architectural and structural design firms were included for additional input based on what they commonly see in floor plans of real building designs.

Initial wall widths and locations were selected based on desired columns spacing for the building so that all columns and walls would sit directly on the shake table, as opposed to sitting on a portion of the foundation cantilevered off the shake table. Additionally, to study the conductibility of using both interior and exterior lateral walls in the building, the South rocking wall was placed inside the floor plan and the remaining walls were all exterior walls. Cantilevered portions of the diaphragm were incorporated at all four corners to study the design challenges and response associated with with different mass timber diaphragms configurations. Referring to the final floor plan shown in Figure 6.2a, only minor floor plan changes such as small wall length adjustments and the shapes of the cantilevered portions of the diaphragms were changed from the architectural phase to the final floor plan.

Linear OpenSees Model

The three-dimensional linear OpenSees model presented in Section 6.5.5 was used for this portion of the design procedure. As discussed in the following two sections, this model was used to calculate preliminary deformation demands to be used in the cross-sectional analysis procedure. Thus, a response modification coefficient (R) was needed. Because this has not been established for mass timber rocking walls, a value of 6 was used based on recommendations in Busch et al. [2022]. The value of 6 was recommended because ACI ITG 5.1 and 5.2 permit the use of the same R as the equivalent concrete system (listed as "Building Frame Systems - Special Reinforced Concrete Shear Walls" in ASCE/SEI 7-16) for post-tensioned precast rocking walls and the behavior of concrete and mass timber post-tensioned systems is similar [Zimmerman and McDonnell, 2017].

Modal Response Spectrum Analysis (MRSA) and Drift Check

A MRSA was conducted on the linear OpenSees model to complete a preliminary drift analysis. For the MRSA the design parameters of interest (story drift values in this case) were

computed using properties of each mode and the design basis earthquake (DBE) response spectra demands for the design site, divided by the quantity R/I_e (in accordance with Section 12.9.1.2 of ASCE/SEI 7-16). Per ASCE/SEI 7-16, the story drifts for the various modes were multiplied by the quantity C_d/I_e and combined using the square root of the sum of the squares method. The deflection amplification factor, C_d, was set equal to R per recommendations in Busch et al. [2022]. The story drifts were checked to ensure they were less than the allowable story drifts of 2% based on ASCE/SEI 7-16 Table 12.12-1. The wall dimensions and locations were then refined and the MRSA was repeated until this drift check was satisfied. Figure 6.21a shows the distribution of story drifts under the DBE event. As shown, the maximum drift response does not exceed the 2% limit state check in either building direction. Figure 6.21b shows the floor displacements used for this check (δ_x).

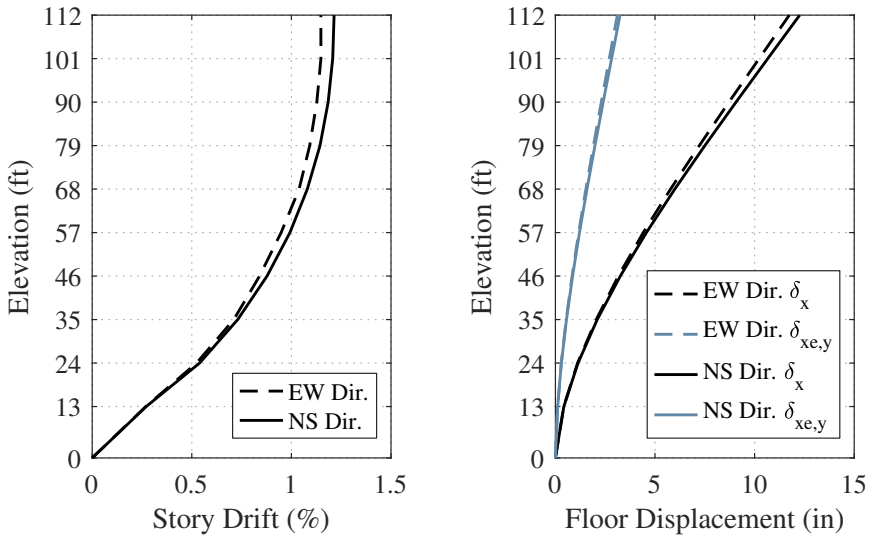

(a) Story drifts

(b) Story displacements

Figure 6.21: Results from the linear OpenSees analyses for preliminary design purposes showing (a) story drifts and (b) floor displacements

Gap Opening Demands at DBE and MCE_R

The rocking wall rotation demands at DBE and MCE_R were approximated using the procedure outlined by Busch et al. [2022]. These values are calculated by subtracting the elastic deformation at the top of the wall that corresponds to yielding at the base of the wall ($\delta_{xe,y}$) from the total deflection at the top of the wall and dividing by the total height of the wall (h_w) as show in Equations 6.12 and 6.13. At DBE, the total deflection at the top of the wall is defined as the deflection at the top of the wall from the linear MRSA, δ_x, (same value from the linear drift analysis check in the previous section) multiplied by the inelastic displacement amplification factor (C_1) taken in accordance with ASCE 41-17 (equal to 1.0). At MCE_R, the total deflection at the top of the wall is assumed to be 1.5 times DBE. The elastic deflection at the top of the wall, $\delta_{xe,y}$, was calculated using strength-level design earthquake forces that correspond to the base shear calculated using the equivalent lateral force procedure (ELF) defined in ASCE/SEI 7-16.

$$\theta_{DBE} = \frac{C_1\delta_x - \delta_{xe,y}}{h_w} \tag{6.12}$$

$$\theta_{MCE_R} = \frac{1.5C_1\delta_x - \delta_{xe,y}}{h_w} \tag{6.13}$$

Figure 6.21a shows the floor displacement results from the linear analyses used to calculate θ_{DBE} and θ_{MCE_R}. The resulting rotation demands used for the preliminary design of the post-tensioned rocking wall lateral system for the 10-story building specimen are shown in Table 6.16. Wall shear and wall moment values from the MRSA using strength-level design earthquake forces that correspond to the base shear calculated using the ELF procedure were also obtained and are shown in Figure 6.22. These figures will be used for discussion later on in this document. The peak wall shear and wall moment are summarized in Table 6.17 (tabulated for a single wall).

Table 6.16: Rotation demands used for preliminary design of the 10-story specimen

	CLT Direction	MPP Direction	
θ_{DBE}	0.0064	0.0067	rad
θ_{MCE_R}	0.0108	0.0113	rad

Table 6.17: Maximum story shear and moment from the MRSA of the 10-story lateral system

	CLT Direction	MPP Direction	
M_u	12827	12381	kip-in
V_u	27.04	25.7	kip

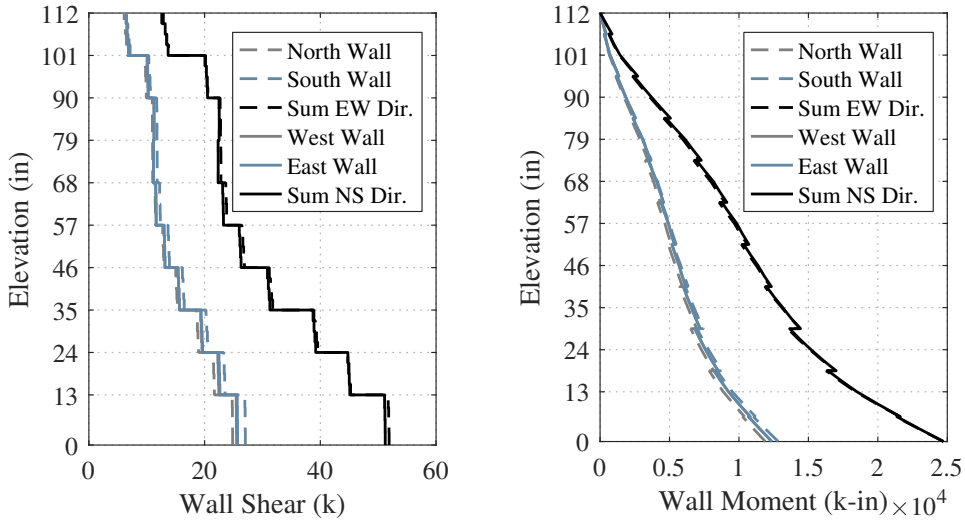

(a) Wall shear

(b) Wall moment

Figure 6.22: Wall (a) shear and (b) moment results from the MRSA on the OpenSees model of the 10-story test specimen

6.6.2 Preliminary Design and Capacity Analysis

As shown in Figure 6.20, the second phase of the design procedure used to design the lateral system for the 10-story test building was to determine the preliminary design using an iterative procedure involving the cross-sectional analysis procedure with component level

and overall moment capacity checks. In this phase the rotation demands from phase 1 were input into the cross-sectional analysis procedure to determine component forces and overall moment capacity. Different input parameters for the UFPs and the PT bars were iterated on until component level checks and the global moment capacity check were satisfied. For this phase, recommendations for component level checks were taken from Busch et al. [2022] with some modifications.

Cross-Sectional Analysis Design Procedure

A modified version of the cross-sectional analysis procedure presented in Section 3.3.1 was then performed using the DBE and MCE_R base rotations from above. For clarity, the cross-sectional analysis procedure is summarized again below and the key modifications made to the previously presented procedure are identified. Figure 6.23 shows a free-body diagram with the forces on the 10-story rocking wall system. The results from this procedure at DBE and MCE_R are shown in Table 6.18.

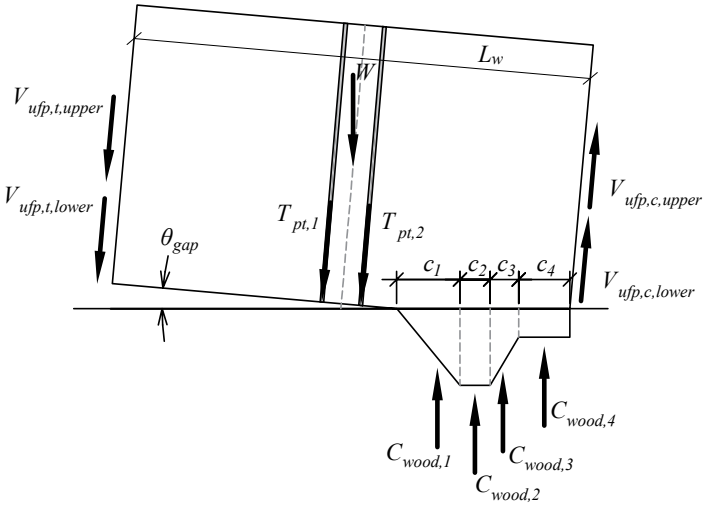

Figure 6.23: Force diagram at wall base used for preliminary 10-story lateral system design

Table 6.18: Preliminary moment capacity calculation values for the design of the lateral system of the 10-story test specimen

Design Level		CLT		MPP		Units
		DBE	MCE_R	DBE	MCE_R	
Inputs	θ	0.0064	0.0108	0.0067	0.0113	rad
	W	0	0	0	0	kip
PT Bars	$T_{pt,1}$	115	126	115	126	kip
	$T_{pt,2}$	110	119	110	119	kip
UFPs	$V_{ufp,t,lower}$	48.00	68.64	48.00	68.64	kip
	$V_{ufp,t,upper}$	30.88	44.16	30.88	44.16	kip
	$V_{ufp,c,lower}$	11.52	68.64	8.75	68.64	kip
	$V_{ufp,c,upper}$	5.34	44.16	4.06	44.16	kip
Wood	ϵ_{wood}	0.0039	0.0050	0.0039	0.0049	in/in
	c	13.39	10.24	9.71	7.21	in
	c_1	9.17	5.43	6.58	3.90	in
	$C_{wood,1}$	149.3	88.5	145.4	86.2	kip
	c_2	4.23	4.81	3.13	3.30	in
	$C_{wood,2}$	137.7	156.8	145.4	158.1	kip
	c_3	0	0	0	0	in
	$C_{wood,3}$	0	0	0	0	kip
	c_4	0	0	0	0	in
	$C_{wood,4}$	0	0	0	0	kip
Moment Capacity	M_{ufp}	5416	5885	4636	4926	kip-in
	M_{wall}	14886	15476	13738	14439	kip-in
	$M_{assembly}$	20302	21361	18374	19365	kip-in
	ϕM_n	18272	-	16537	-	kip-in

- Impose Gap Rotation

  The imposed gap rotation, θ_{gap}, was set equal to θ_{DBE} and θ_{MCE_R} for the two rotation checks performed.

- Estimate Neutral Axis Depth

- Solve for PT Tension Force

  The PT bar forces were solved for using Equations 3.8 through 3.11 as presented previously. The effects of the two different PT bars sizes were accounted for in the stiffness calculation by assuming two springs in series. Note, with these calculations, each PT bar force, $T_{pt,i}$, is representative of two PT bars, one from either face of the wall. For the 10-story test building, the horizontal spacing of the PT bars was 14.25 inches.

- Solve for the UFP Forces

  The UFP forces on the compression and tension face of the walls were calculated using Equations 3.12 and 3.13 as presented previously. Because there were two types of UFPs up the height of the specimen, two force values were calculated on each face: $V_{ufp,c,lower}$ and $V_{ufp,c,upper}$ for the compression face UFPs and $V_{ufp,t,lower}$ and $V_{ufp,t,upper}$ for the tension face UFPs.

- Solve for the Compression Force in the Wood

  The peak compressive strain in the wood, ϵ_{wood}, was calculated using Equation 3.29, where the elastic yield moment, M_y, was set equal to the moment at ELL, M_{ell}. M_{ell} was calculated as specified by Equation 3.6 with a distance, d, equal to $^{3L_W}/_8$. The stress-strain behavior shown in Figure 6.3 was then used to calculate the total compression force in the wood. As shown in Figure 6.23, this was done by assuming four compression regions each with a corresponding compression length, c_i, and equivalent compression force $C_{wood,i}$. If the peak strain in the wood ϵ_{wood} did not exceed a limit on the stress-curve, then those remaining were zero. For example, as shown in Table 6.18, at DBE for the CLT wall, the peak strain in the wood is 0.0035 in/in. Because this does not exceed the splitting strain, $\epsilon_{s,clt}$, of 0.0049 in/in, c_3, c_4, $C_{wood,3}$, and $C_{wood,4}$, were equal to zero and c_1, c_2, $C_{wood,1}$, and $C_{wood,2}$, were calculated accordingly.

- Satisfy Equilibrium

- Determine Overturning Moment

  The resulting moment capacity of the rocking wall assembly, $M_{assembly}$, was calculated using Equation 3.33. With this equation, the multiple types of UFPs were accounted for as well as all four compression regions of the wood. The final results are included in Table 6.18. The moment contribution from the UFPs, M_{ufp}, and the moment contribution from the PT bars and wood compression, M_{wall}, are also shown in the table (calculated per Equations 3.34, 3.35, and 3.36). Recall, M_{wall}, is the moment in the wall panels that must be capacity designed to.

Check Limit States

The results from the cross-sectional analysis procedure completed at DBE and MCE_R rotation demands were then used to check preliminary component level design limit states, prior to using the designed wall in the NLRHA. The checks used at this phase are listed below, if any of the checks are not satisfied, then the PT and UFP properties were redefined and the cross-sectional analysis procedure was repeated. The results from all four limit state checks are summarized in Table 6.19.

Table 6.19: Summary of preliminary design limit state checks for the lateral system of the 10-story test specimen

Limit State Checks		
	CLT	MPP
Restoring Ratio ≥ 1.0	0.89	0.89
Energy Dissipation Ratio, $\beta \geq 0.125$	0.13	0.13
DCR_{wood} at DBE ≤ 1.0	0.53	0.29
$DCR_{pt,yield}$ at $MCE_R \leq 1.0$	0.69	0.69

- Restoring Ratio:

  The restoring ratio was checked to ensure that the restoring force from the initial post-tensioning was large enough to exceed the maximum resistance force from the UFPs. This was calculated as shown in Equation 6.14. Where $F_{pt,i}$ is the total initial force in the PT bars and $V_{u,ufp}$ is the ultimate force in the UFP calculated as the plastic UFP force using the ultimate steel force, f_u. This equation is derived by approximating the ratio of the moment contribution of the initial PT bar force (moment arm length equal to $L_w/2$ if summing moments at the compression corner of the wall) to the the moment contribution of the ultimate force of the UFPs on the tension face (moment arm length equal to L_w if summing moments at the compression corner of the wall). For this calculation the total initial PT force of the walls was equal to 100 kips and the ultimate force from both the lower and upper UFPs were accounted for.

$$\frac{F_{pt,i}}{2V_{u,ufp}} \geq 1.0 \tag{6.14}$$

  Results from this limit state check are shown in Table 6.19. The ratios are slightly less than 1.0, however, this was determined to be acceptable because this restoring ratio check is very conservative. It is conservative because the PT bars will likely have a larger force than their initial PT force when the UFPs are all at their ultimate force. Additionally, there would be inertial energy in the system that would help the system re-center.

- Energy Dissipation Ratio:

  The energy dissipation ratio, calculated using Equation 6.15, was checked to ensure that it exceeded 0.125 (per recommendations in ACI [2009] and Busch et al. [2022]). This equation is derived based on Equation 3.5, where M_{ufp} is the approximate moment contribution from the UFPs (Equation 3.35) and and M_y was taken as the full assembly moment, M_n, from Table 6.18. For this check, both terms (M_{ufp} and M_y)

were calculated under DBE demands. The results from this limit state check are shown in Table 6.19.

$$\frac{(V_{ufp,t} + V_{ufp,c})L_w/2}{2M_n} \geq 0.125 \tag{6.15}$$

- Limited Wood Damage at DBE:

  Using Equation 6.16, the peak strain at the base of the wall panels, ϵ_{wood}, under DBE demands was checked to ensure that it was less than the splitting strain ($\epsilon_{s,CLT}$ for the CLT panels and $\epsilon_{s,MPP}$ for the MPP panels). A resistance factor ϕ of 0.9 was included in this check. The splitting strain was used as opposed to the yield strain because the yield strain for mass timber panels can vary greatly and conservative values were assumed for yield. Additionally, for the material model used here, major damage to the wood does not occur until the crushing point (reference Figure 6.3 for limit states). The results from this limit state check are shown in Table 6.19.

$$\frac{\epsilon_{wood}}{\phi\epsilon_s} \leq 1.0 \tag{6.16}$$

- No PT Yielding at MCE_R:

  The PT bars were checked to ensure that yielding does not occur during MCE_R ground motions. While yielding under MCE_R would be allowed in design of a typical building [Busch et al., 2022], MCE_R was used as the limit for this test since the building will be subjected to many MCE_R ground motions throughout the testing sequence and all the payload projects. This check was completed using Equation 6.17. The maximum in the numerator of the equation is to use the bar with the largest force for this check. A resistance factor ϕ of 0.9 was included in this check. For the 10-story building, the upper PT bars (with the smaller net tensile area) were used as they would yield first. The results from this limit state check are shown in Table 6.19.

$$\frac{max(T_{pt,i})}{\phi A_{pt} f_{y,pt}} \leq 1.0 \tag{6.17}$$

Check Flexural Demand verses Capacity

With the completion of local component checks, the last step of the preliminary design phase was to check the overall moment capacity of the rocking mechanism in accordance with Equation 6.18. The resistance factor ϕ is 0.9, defined by the AWC [2018] for compression parallel to wood grain and M_n, the factored design strength, was taken as the capacity of the wall assembly $M_{assembly}$ at DBE design rotations. See Table 6.18 for the tabulated values. The moment demand for the wall, M_u, was taken from the MRSA procedure with the base shear scaled to be equal to the base shear calculated from ELF. See Table 6.17 for tabulated values of M_u. Table 6.20 shows the final preliminary design ratio for the CLT and MPP direction.

$$M_u \leq \phi M_n \tag{6.18}$$

Table 6.20: Summary of moment capacity checks for the preliminary design of the lateral system for the 10-story test specimen

Moment Capacity Checks		
	CLT	MPP
$M_u/\phi M_n \leq 1.0$	0.70	0.75

6.6.3 NLRHA and Final Design Demands

The third and final phase of the 10-story building specimen lateral system design procedure (Figure 6.20) was to finalize the design using NLRHA and complete key, ISD, force-controlled,

and deformation-controlled limit state checks at MCE_R. Again, this phase was completed to meet requirements of a performance-based design procedure since mass timber post-tensioned rocking wall lateral systems are not currently accepted by code. Results from phase 2 of the design procedure were used to create the nonlinear OpenSees model of the 10-story building. If component level checks were not meet using the result of the NLRHA, then PT and UFP properties were modified and the full design procedure was repeated, starting at phase 1 (as shown in Figure 6.20). This procedure was iterated until all component level checks using NLRHA results were satisfied (unless otherwise noted in this section).

Nonlinear OpenSees Model

For this step of the design procedure, the nonlinear three-dimensional OpenSees model presented in Section 6.5 was used. PT bar and UFP properties from phase 2 of the design procedure were used.

Nonlinear Response History Analysis at MCE_R

The next step of the design procedure was to complete a NLRHA using a suite of eleven two-component ground motions selected and scaled to MCE_R and the nonlinear numerical model developed in OpenSees. Key demand values from the analyses were recorded and saved for the component level design checks discussed in the following sections. As mentioned previously, results were assessed at suite mean demand and suite maximum demand. Suite mean demand is defined as the geometric mean over all earthquakes of the maximum demand for each earthquake. Geometric mean was used to account for dispersion of the peak values. Suite maximum demand is defined as the maximum over all earthquakes of the maximum demand for each earthquake.

Figure 6.24 shows the peak absolute floor accelerations at MCE_R for both the east-west (CLT wall) direction and the north-south (MPP wall direction). In the plot, the light gray lines represent the peak results from each of the 11 MCE_R design suite ground motions. The solid black line shows the geometric mean of the results from the suite of 11 ground

motions at each floor and the max values are highlighted using the thick, black dashed line. The horizontal grid lines are positioned at each floor level. Note, this plot format will be consistent for many of the results summarized in this section. As shown by the figure, the building has some whipping action, resulting in high accelerations at the roof. This is common for taller buildings. Table 6.21 summarizes the suite geometric mean and suite maximum peak floor accelerations for each floor, in each direction.

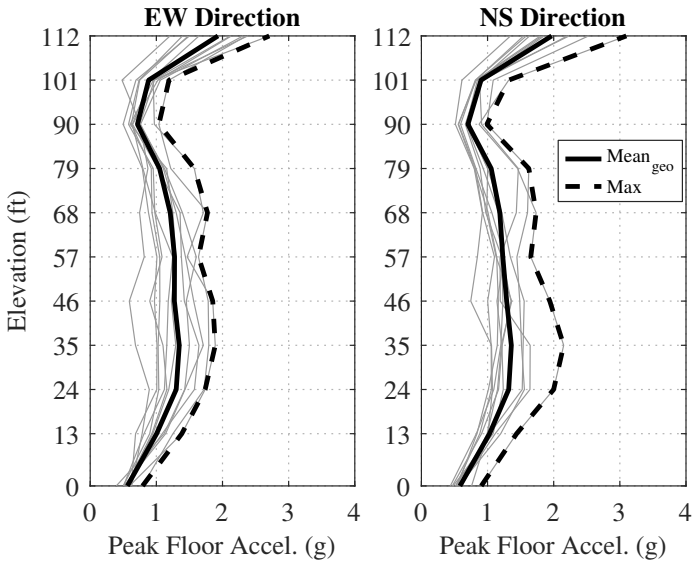

Figure 6.24: Peak absolute floor acceleration from NLRHA at MCE_R hazard level

Table 6.21: Peak absolute floor acceleration from NLRHA at MCE_R hazard level

Peak MCE_R Absolute Floor Accelerations (g)					
Floor	Elevation (ft)	East-West Dir.		North-South Dir.	
		$Mean_{geo}$	Max	$Mean_{geo}$	Max
Ground (pga)	0	0.55	0.79	0.57	0.90
2	13	0.98	1.38	1.02	1.44
3	24	1.27	1.74	1.29	2.00
4	35	1.29	1.89	1.33	2.15
5	46	1.21	1.85	1.25	1.94
6	57	1.25	1.64	1.22	1.65
7	68	1.17	1.77	1.16	1.73
8	79	1.03	1.57	1.02	1.62
9	90	0.70	1.04	0.69	0.99
10	101	0.86	1.19	0.89	1.32
11/Roof	112	1.87	2.71	1.92	3.10
Overall	-	1.87	2.71	1.92	3.10

Figure 6.25 shows the peak inter-story drift (ISD) values at MCE_R for the two directions. The peak values for each story and each direction are tabulated in Table 6.21. As discussed previously (and summarized in Table 6.15), suite mean ISD limits were restricted to 2.25% for the design of this system. This limit is based on 1.5 × 1.5% design-basis earthquake ISD limit. The 1.5 factor is to account for the ratio between MCE_R hazard and the design-basis earthquake hazard. The 1.5% drift is for enhanced resiliency, as compared to the 2% required by ASCE/SEI 7-16 Table 12.12-1. As summarized in Table 6.22, the suite mean ISD ratio for the CLT and MPP building directions are 1.87% and 1.92%, respectively. Both satisfying the resilient design criteria for ISD.

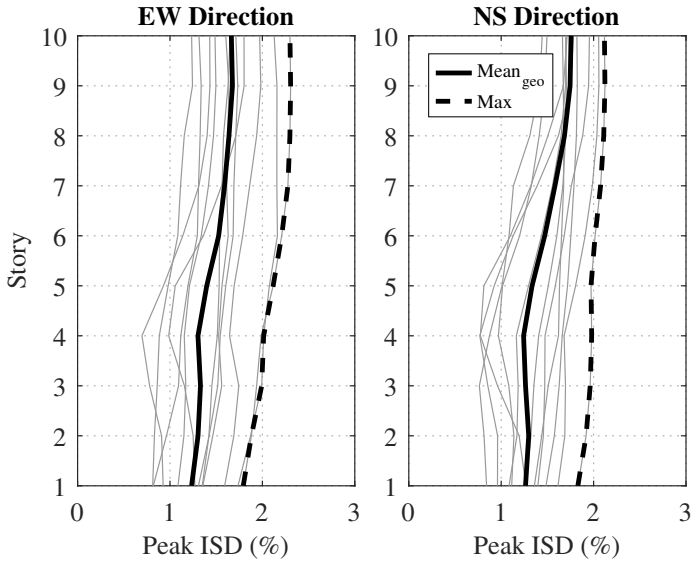

Figure 6.25: Peak ISDs from NLRHA at MCE_R hazard level

Table 6.22: Peak ISDs from NLRHA at MCE_R hazard level

Peak MCE_R ISD (%)				
	East-West Dir.		North-South Dir.	
Story	$Mean_{geo}$	Max	$Mean_{geo}$	Max
1	1.23	1.79	1.26	1.83
2	1.30	1.88	1.30	1.92
3	1.33	1.99	1.26	1.96
4	1.30	2.01	1.24	1.98
5	1.40	2.12	1.33	1.97
6	1.53	2.21	1.47	2.02
7	1.59	2.28	1.58	2.08
8	1.64	2.30	1.68	2.11
9	1.68	2.31	1.75	2.12
10	1.66	2.30	1.76	2.12
Overall	1.68	2.31	1.76	2.12

Figure 6.26 summarizes the peak wall shear values at MCE_R for the for walls and also summarizes the suite geometric mean values and suite maximum values. Note, the title

of each plot for the wall location. The plots on the left are the CLT walls running in the est-west direction while the plots on the right are the MPP walls running in the north-south direction. The similarity of plot shapes for the walls running in the same direction indicate little torsion in the building. These plots can also be compared to the wall shear force plots from the MRSA shown in Figure 6.22a. While the MRSA plots have a shape similar to that of a simple cantilever, results from NLRHA at MCE_R indicate that higher mode effects greatly affect the performance of these walls and should be accounted for in a future prescriptive design procedure. Table 6.23 summarizes the peak values per story. Note, this table is summarized by direction instead of individual walls, however, the reported value is still for a single wall.

Table 6.23: Peak wall shear forces from NLRHA at MCE_R hazard level

Peak MCE_R Story Shears (kip) - per wall				
	East-West Dir.		North-South Dir.	
Story	$Mean_{geo}$	Max	$Mean_{geo}$	Max
Base Shear	125.7	178.5	125.7	165.6
1	125.7	178.5	125.7	165.6
2	98.5	132.2	101.3	137.3
3	75.1	106.1	76.2	99.6
4	61.3	81.6	56.5	71.4
5	54.9	71.4	52.9	75.1
6	58.5	74.6	57.5	81.8
7	61.4	83.9	60.3	91.1
8	68.3	93.0	70.7	100.5
9	70.1	94.2	71.4	108.5
10	50.7	73.9	52.2	81.4
Overall	125.7	178.5	125.7	165.6
Splice	61.4	83.9	60.3	91.1

Table 6.25 also includes overall maximum values at the bottom of the table. These are the values that will be used for capacity checks of the wall system in Section 6.6.3. The table also includes overall splice demands, for the splices located at stories 4 and 7. The

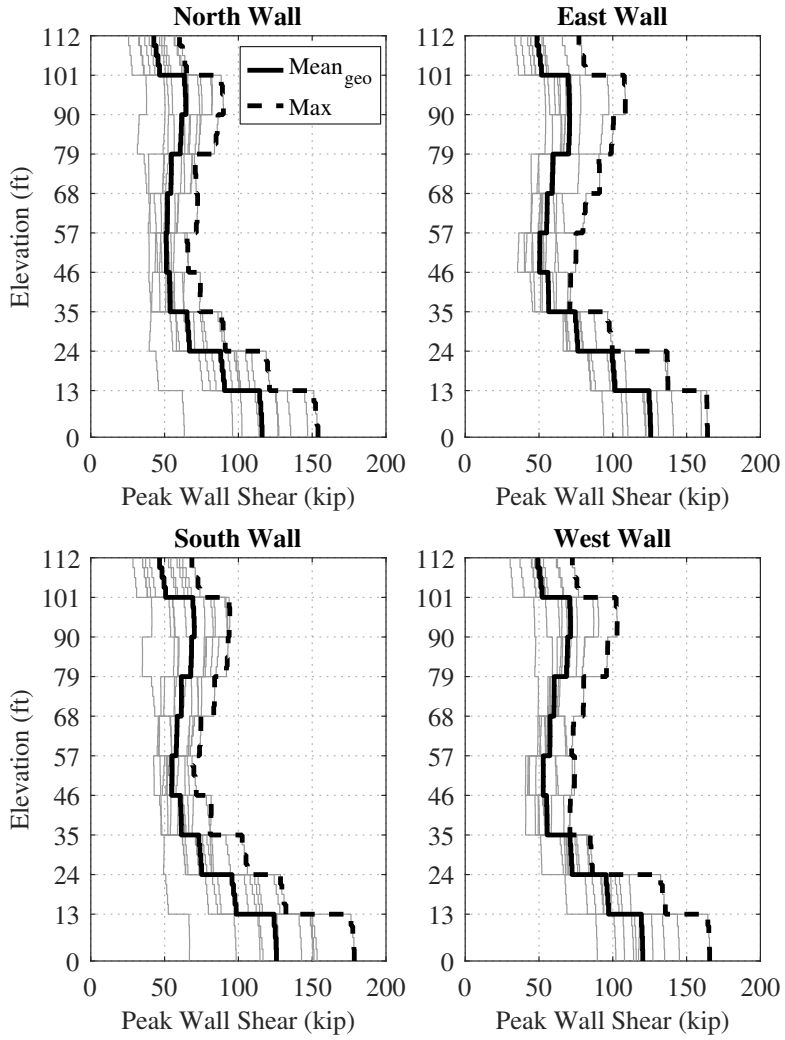

Figure 6.26: Peak wall shear forces from NLRHA at MCE_R hazard level

table splice values were taken as the maximum of the values at stories 4 and 7. These are the values that the splice was designed for, as discussed in Section 6.6.3.

The peak assembly moment values at MCE_R are summarized in Figure 6.27. Recall, the assembly moment accounts for the contribution of the wall panels, the UFPs, and the PT bars. This plot can be compared to the wall moment plots calculated from MRSA shown in Figure 6.22b. The shape of the two diagrams is vastly different. The results from the NLRHA

show a defined "bubble" on the moment diagram, a result of higher mode effects common for taller buildings. However, this dramatic of a "bubble" is not typically seen equivalent concrete or steel buildings until much taller and this may be a result of the relatively long period for the building. This indicates that the effects of higher mode effects are important to consider for the design of tall post-tensioned rocking wall lateral systems. Note, the moment at the base of the walls is limited by the moment capacity of the rocking connection. Table 6.24 includes tabulated values of these results. The table shows results for a single wall, but just shows peak values for each direction. Note, the peak values provided in this plot are larger than the values needed to check the moment capacity of the wall panels (the moment in just the wall panel are shown next in Figure 6.28 and Table 6.25).

Table 6.24: Peak assembly moment values from NLRHA at MCE_R hazard level

Peak MCE_R Story Assembly Moments (kip-in) - per wall				
	East-West Dir.		North-South Dir.	
Story	$Mean_{geo}$	Max	$Mean_{geo}$	Max
Base Moment	24353	25852	21701	22978
1	25465	28721	24211	26599
2	31572	38680	30496	33466
3	34271	44649	34021	44590
4	34271	44726	34759	46360
5	33297	44726	34759	46360
6	31943	44205	33761	44921
7	29088	39908	30461	43588
8	23648	31823	24250	36962
9	15139	21318	15771	24608
10	6218	9152	6546	10373
Overall	34271	44726	34759	46360

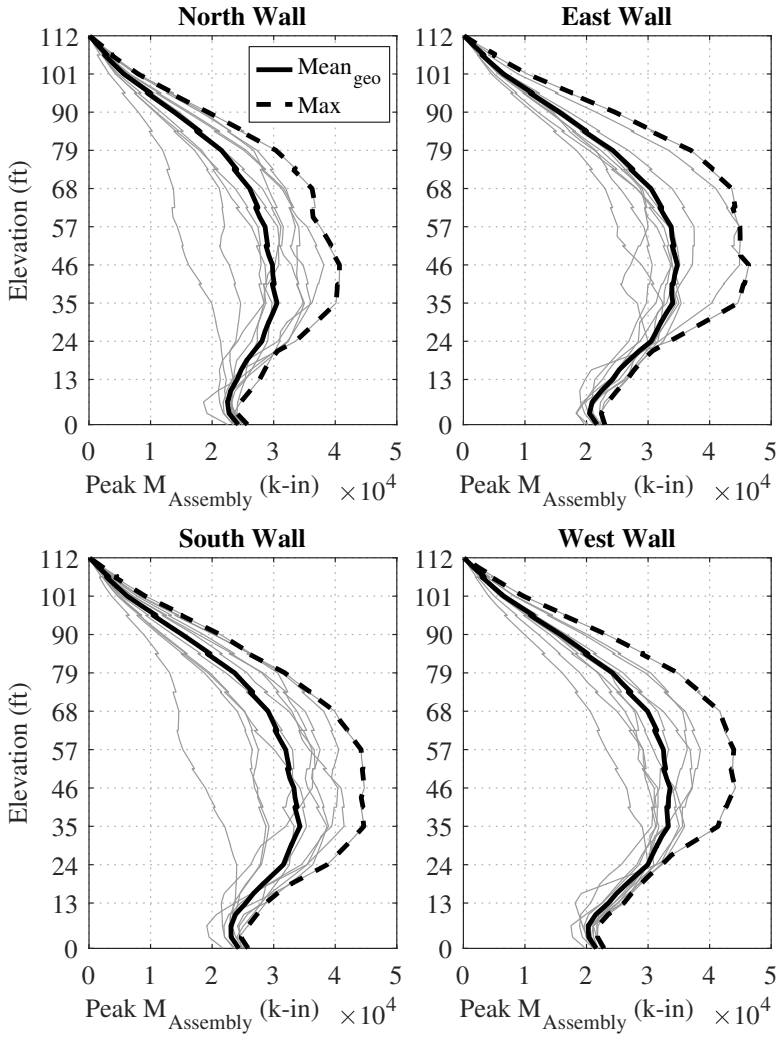

Figure 6.27: Peak wall assembly moment values from NLRHA at MCE_R hazard level

The peak wall moment values at MCE_R are summarized in Figure 6.28. In the plot, the increased moment demands at the middle floors from higher mode effects are also clear. Table 6.25 includes tabulated values of these results. The table shows results for a single wall, but just shows peak values for each direction. Table 6.25 also includes overall maximum values at the bottom of the table. These are the values that will be used for capacity checks of the wall system in Section 6.6.3. The table also includes overall splice demands, for the

splices located at stories 4 and 7. The table splice values were taken as the maximum of the values at stories 4 and 7. These are the values that the splice was designed for, as discussed in Section 6.6.3.

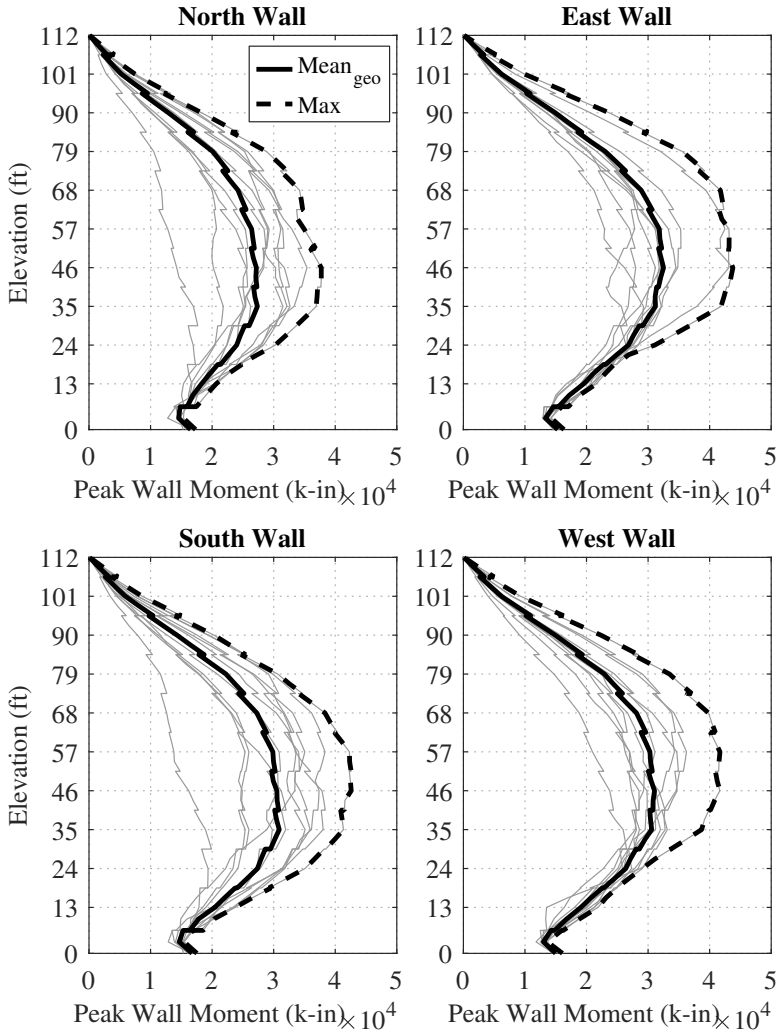

Figure 6.28: Peak wall moment values from NLRHA at $\mathrm{MCE_R}$ hazard level

Table 6.25: Peak wall moment values from NLRHA at MCE_R hazard level

Peak MCE_R Story Wall Moments (kip-in) - per wall				
	East-West Dir.		North-South Dir.	
Story	$Mean_{geo}$	Max	$Mean_{geo}$	Max
Base Moment	16737	17532	15330	16344
1	20424	23757	19547	21859
2	27364	35098	26812	31080
3	30903	41331	31178	41849
4	30903	42594	32511	43776
5	30515	42594	32511	43776
6	29866	42300	31816	43134
7	27253	38328	28886	41740
8	22248	30656	23056	35566
9	14300	20306	14924	23694
10	5905	8644	6199	9915
Overall	30903	42594	32511	43776
Splice	30903	42594	32511	43776

Figure 6.29 shows the peak diaphragm floor forces transferred from the diaphragm into each wall at each floor level at the MCE_R hazard. These plots summarize the forces that the diaphragm-to-wall shear keys transfer. Similar to the peak floor acceleration plots in Figure 6.24, there is a clear whipping action in the building, resulting in high force demands at the roof. Like the wall shear plots in Figure 6.26, the similarity of plot shapes for the walls running in the same direction indicates that torsion is likely negligible. Table 6.26 summarizes the peak values. Note, the table is summarized by direction instead of individual wall such that each value is the maximum geometric mean or the largest maximum value of the walls in the same direction (the reported value is still on a per wall basis).

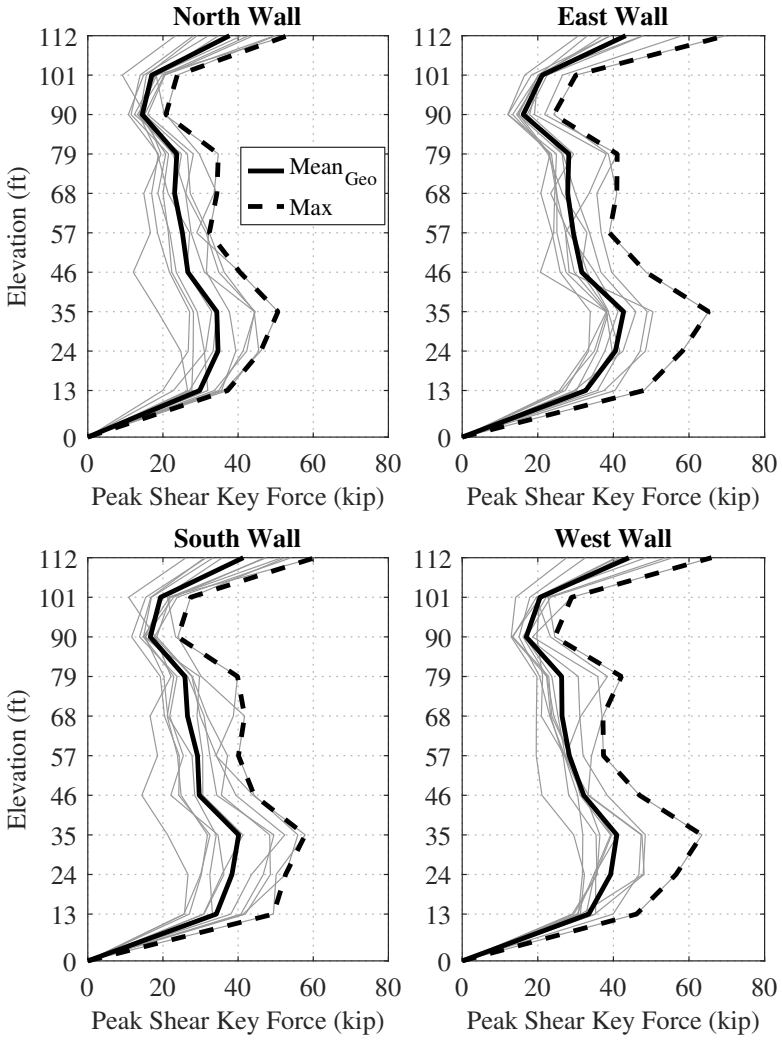

Figure 6.29: Peak diaphragm floor forces from NLRHA at $\mathrm{MCE_R}$ hazard level

Table 6.26: Peak diaphragm floor forces from NLRHA at MCE_R hazard level

Peak MCE_R Diaphragm Floor Forces (kip) - per wall					
Floor	Elevation (ft)	East-West Dir.		North-South Dir.	
		$Mean_{geo}$	Max	$Mean_{geo}$	Max
2	13	34.2	49.4	33.5	48.1
3	24	38.4	52.6	40.5	58.2
4	35	40.2	57.9	42.7	65.2
5	46	29.7	44.3	32.2	48.6
6	57	29.2	40.1	29.4	38.9
7	68	26.5	41.7	27.9	40.9
8	79	25.9	39.9	28.2	42.1
9	90	16.6	24.0	16.9	24.5
10	101	19.4	27.3	21.2	30.1
11/Roof	112	41.4	60.4	44.1	69.7
Overall	-	41.4	60.4	44.1	69.7

Figure 6.30 shows the peak wood strain distributions at the base of each wall panel from the suite of eleven MCE_R ground motions. On these plots, the key strain limit states are called out. As shown, at MCE_R, the base of the wall panels have reached their expected yield strengths, however, only a few ground motions reach the splitting strain. Table 6.27 summarizes the peak strains for each direction and Table 6.28 summarizes suite geometric mean and suite maximum values for the percentage of the wall base that has reached each strain limit state.

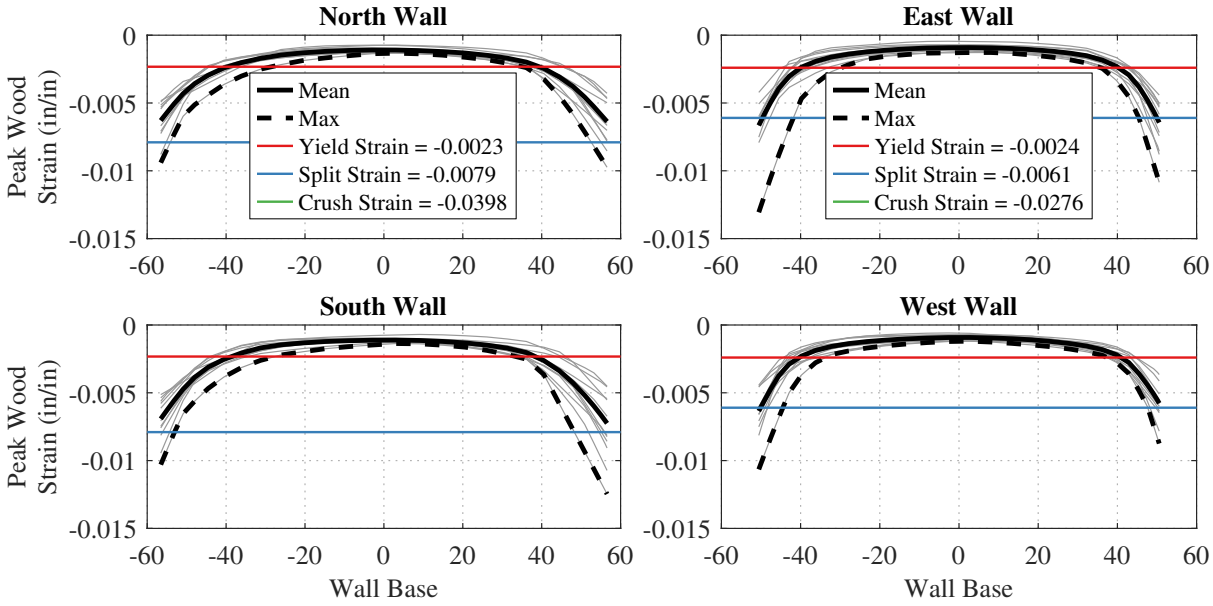

Figure 6.30: Peak wood strain distributions at the base of the wall panels from NLRHA at MCE_R hazard level

Table 6.27: Peak wood strains at wall panel bases from NLRHA at MCE_R hazard level

Peak MCE_R Wood Strain (in/in)				
	East-West Dir.		North-South Dir.	
	$Mean_{geo}$	Max	$Mean_{geo}$	Max
Base	0.0076	0.0125	0.0072	0.0131

Table 6.28: Proportion of damaged wall length from NLRHA at MCE_R hazard level

MCE_R Proportion of Damaged Wall Base (%)				
	East-West Dir.		North-South Dir.	
Strain Reached	$Mean_{geo}$	Max	$Mean_{geo}$	Max
Yield	15.7	22.3	9.1	18.1
Splitting	0.0	5.0	0.0	7.6

Table 6.29 summarizes the suite geometric mean and suite maximum for the PT bars for the walls in the either direction. The reported values were taken from the maximum bar force from a bar on either wall in each direction. The values are reported in terms of ratio of peak force to yield force. As shown, these yield force ratios are well below 1.0 and thus, the bars are not expected to yield. This also means that the building should re-center after an MCE_R level earthquake and residual drift requirements should be satisfied.

Table 6.29: Peak PT bar forces from NLRHA at MCE_R hazard level

Peak MCE_R PT Force/Yield Force (kip/kip)				
	East-West Dir.		North-South Dir.	
	$Mean_{geo}$	Max	$Mean_{geo}$	Max
Overall	0.61	0.68	0.62	0.67

Table 6.30 shows results of the peak joint rotations at the base of the walls at MCE_R hazard level. These results can be compared to the MCE_R joint rotation design values calculated from MRSA and shown in Table 6.16. As shown, the geometric suite mean results from the NLRHA are slightly larger than the ones calculated from MRSA.

Table 6.30: Peak joint rotations at the wall base from NLRHA at MCE_R hazard level

Peak MCE_R Base Rotation (rad)				
	East-West Dir.		North-South Dir.	
	$Mean_{geo}$	Max	$Mean_{geo}$	Max
Base	0.0116	0.0173	0.0123	0.0181

Table 6.31 shows the peak UFP deformations at MCE_R hazard level. In design, these values are used to check the UFP deformation compatibility of the connections.

Table 6.31: Peak UFP deformations from NLRHA at MCE_R hazard level

Peak MCE_R UFP Deformations (in)		
	$Mean_{geo}$	Max
Overall	1.46	1.90

Design Criteria for Force-Controlled Actions

With the ISD limitations satisfied, the design of the wall system was finalized using the results from NLRHA at MCE_R and checking a set of force and deformation-controlled action limit states. The force-controlled actions that were checked are summarized in Table 6.32. As shown, the design criteria for many components were checked at both suite mean and suite maximum demands. This section includes a brief discussion of the force evaluation procedures and a discussion on each performed check. If any of the following checks were not satisfied, then the dimensions of the PT bars and UFPs were modified (and if necessary the wall panel dimensions) and the design procedure was repeated as shown in Figure 6.20. Tabulated suite mean and suite maximum values in Section 6.6.3 were used for these checks.

The force-controlled actions are those which are intended to remain essentially elastic during a seismic event. The force-controlled actions were assessed following Equation 6.19 which was inspired by the force-controlled actions check equation from ASCE/SEI 7-16

Section 16.4.2.1 for nonlinear response history analyses. In this equation, the load factor, γ is taken in accordance with Table 6.32, I_e is the earthquake importance factor, Q_u is the demand parameter taken as either suite mean or suite maximum, $Q_{ns,analysis}$ is the demand parameter from the nonseismic loads included in the analysis, $Q_{ns,design}$ is the demand parameter from

Table 6.32: Criteria for force-controlled actions under MCE_R seismic hazard

Component	**Action**	**Criteria**	
		Suite Mean [a]	**Suite Maximum** [b]
CLT Wall Panels (except at base)	Axial-Flexure	$\gamma = 1.3$ ϕ per material standard	$\gamma = 1.0$ $\phi = 1.0$
	Shear	$\gamma = 1.3$ ϕ per material standard	$\gamma = 1.0$ $\phi = 1.0$
MPP Wall Panels (except at base)	Axial-Flexure	$\gamma = 1.3$ ϕ per material standard	$\gamma = 1.0$ $\phi = 1.0$
	Shear	$\gamma = 1.3$ ϕ per material standard	$\gamma = 1.0$ $\phi = 1.0$
CLT Wall Splices	Axial-Flexure	$\gamma = 1.3$ ϕ per material standard	$\gamma = 1.0$ $\phi = 1.0$
	Shear	$\gamma = 1.3$ ϕ per material standard	$\gamma = 1.0$ $\phi = 1.0$
MPP Wall Splices	Axial-Flexure	$\gamma = 1.3$ ϕ per material standard	$\gamma = 1.0$ $\phi = 1.0$
	Shear	$\gamma = 1.3$ ϕ per material standard	$\gamma = 1.0$ $\phi = 1.0$
Sliding at Base	Shear	$\gamma = 1.3$ ϕ per material standard	$\gamma = 1.0$ $\phi = 1.0$
UFP Connections	All	Capacity-Based Design ϕ per material standard	
Diaphragm-to-Wall Connection	All	$\gamma = 1.3$ ϕ per material standard	$\gamma = 1.0$ $\phi = 1.0$
PT bars	Axial	N/A	$\gamma = 1.0$ $\phi = 1.0$
PT Bar Connections	All	Capacity-Based Design ϕ per material standard	

[a]Suite mean demand is calculated as the mean over all ground motion records of the peak demand for each record

[b]Suite maximum demand is calculated as the maximum over all ground motion records of the peak demand for each record

the nonseismic loads in the design load combinations, ϕ is the strength reduction factor taken in accordance with Table 6.32, and Q_n is the nominal component strength taken in accordance with the applicable material standard.

$$\gamma I_e(Q_u - Q_{ns,analysis}) + Q_{ns,design} \leq \phi Q_n \tag{6.19}$$

Because elastic behavior is targeted with these checks, most force-controlled actions for this building (and buildings that could be designed similarly) also achieve the collapse and repairability performance objectives at the other analyzed hazard levels. This section will describe each of the force-controlled checks completed for the design of the post-tensioned rocking wall lateral system in the 10-story building specimen. Note, the design of the boundary columns (including the splices and base connections), the diaphragms and collectors, and the foundation beams and connections are not included in the scope of work presented here.

Mass Timber Wall Panels - Except at wall Base

The mass timber wall panels, at all locations between splices, were designed to remain elastic in shear and combined axial-flexure (except at the base of the walls). This section will conceptually describe these checks. Full design calculations and final values for the 10-story test can be found in Appendix A, Section A.2 and Section A.3 for the CLT and MPP walls respectively.

To check for shear, a parabolic shear stress distribution was assumed over the wall length with a maximum value occurring at the center of the wall with a value of 1.5 times the average over the wall. Thus, the maximum shear demand was calculated by taking the ratio of 1.5 times the peak wall shear force to the shear area of the wall panels [Zimmerman and McDonnell, 2018]. To check the walls for combined axial-flexure in compression, Section 3.9.2 of the NDS [AWC, 2018] was used with modifications. To check the walls for combined axial-flexure in tension, Section 3.9.1 of the NDS [AWC, 2018] was used with modifications. Detailed calculations for these three checks with all modifications can be found in Sections

A.2 and A.3 for the CLT and MPP walls, respectively.

For the 10-story building CLT walls, the final DCRs for wall capacity shear, combined axial-flexure in compression, and combined axial-flexure in tension were 0.38, 0.77, and 0.73, respectively. These are all acceptable and reasonable DCRs for design. For the 10-story building MPP walls, the final DCRs for wall capacity shear, combined axial-flexure in compression, and combined axial-flexure in tension were 1.34, 1.32, and 1.11, respectively. The greater than 1.0 values for the MPP walls are a result of many limitations inherent to large-scale experimental work. First, the moment demands that control the DCRs are largely a result of higher mode effects found in the nonlinear numerical model which was not complete when key design choices had to be made. For example, ideally, the wall dimensions would have been adjusted to meet these design checks, however, the floor plan was finalized prior to completion of the nonlinear numerical model to ensure adequate time to procure materials and support from donors. The floor plan, and thus the size of the wall panels was also limited to fit the building on the shake table. Additionally, due to cost and scope of work limitations, the length of the wall was limited to avoid the need for vertical wall splices. Higher strength materials could have also been used for the CLT and MPP to get the DCRs below 1.0, however, these selections were limited due to cost and donation options. Note, at the time of this writing limited testing and research has been done on these checks and thus they are likely conservative. In particular, the MPP flexural capacity is not well-established as there are no tests to failure at this scale. Additionally, the bending stability factor (which is highly dependent on the defined effective length, l_u), C_L, in the NDS for flexural strength was established for smaller sections in conventional beam applications under sustained loading.

As discussed in Section 7.2, the issue of insufficient wall flexural capacity was addressed during testing by limiting the simulated MCE_R ground motions. The design DCR checks presented in this section are for the MCE_R ground motion suite. For the selection of ground motions to be used during the shake table testing sequence, the design MCE_R ground motions were assessed on an individual basis and only ground motions that resulted in individual

DCRs that did not exceeded 1.0 were considered for testing.

Mass Timber Wall Splices

In the United States, mass timber panel dimensions are typically restricted to approximately 10 feet by 40 feet due to manufacturing, construction, and transportation constraints. Thus, when mass timber walls are utilized in tall building applications, wall splice design becomes an important consideration. In the initial design phase of the 10-story building, the floor plan of the building was constrained such that the wall lengths were limited to less than 10 feet so only horizontal splices were necessary and the need for vertical splicing was eliminated. In the building, each shear wall had two horizontal splices up the height of the wall such that the three wall segments from lowest to highest were 36'-6", 44'-0", and 34'-0", creating the total wall height of 114'-6". Note, the roof top of diaphragm is at an elevation of 112'-0" and the shear walls are balloon framed such that the wall extend 2'-6" above the top of diaphragm.

The original design of the horizontal spice connection for the 10-story building specimen was inspired by the splice connection developed and tested for the Framework building [Zimmerman and McDonnell, 2018]. The connection utilizes vertically embedded and epoxied rods in the ends of each wall panel, spanning the splice, creating an architecturally desirable connection that is essentially hidden within the timber. This involves pre-drilling vertical holes in the edges of the mass timber panel at the splice interface. Midway through construction it was discovered that the wall panels were unfortunately manufactured incorrectly, such that many of the pre-drilled embedded rod holes did not line up with the mirrored holes in the connecting wall panel. Because new panels could not be procured within time and financial limitations of this test, the connection was modified to accommodate the mis-matched holes by adding 4" thick steel splice plates to the interface. Figure 6.31a shows an photo of the resulting splice connection and Figures 6.31b-d show of the details for the CLT wall splice connection. The splice details for the MPP wall are similar.

Referencing Figure 6.31, the longer rods (referred to as the tension rods) resist the com-

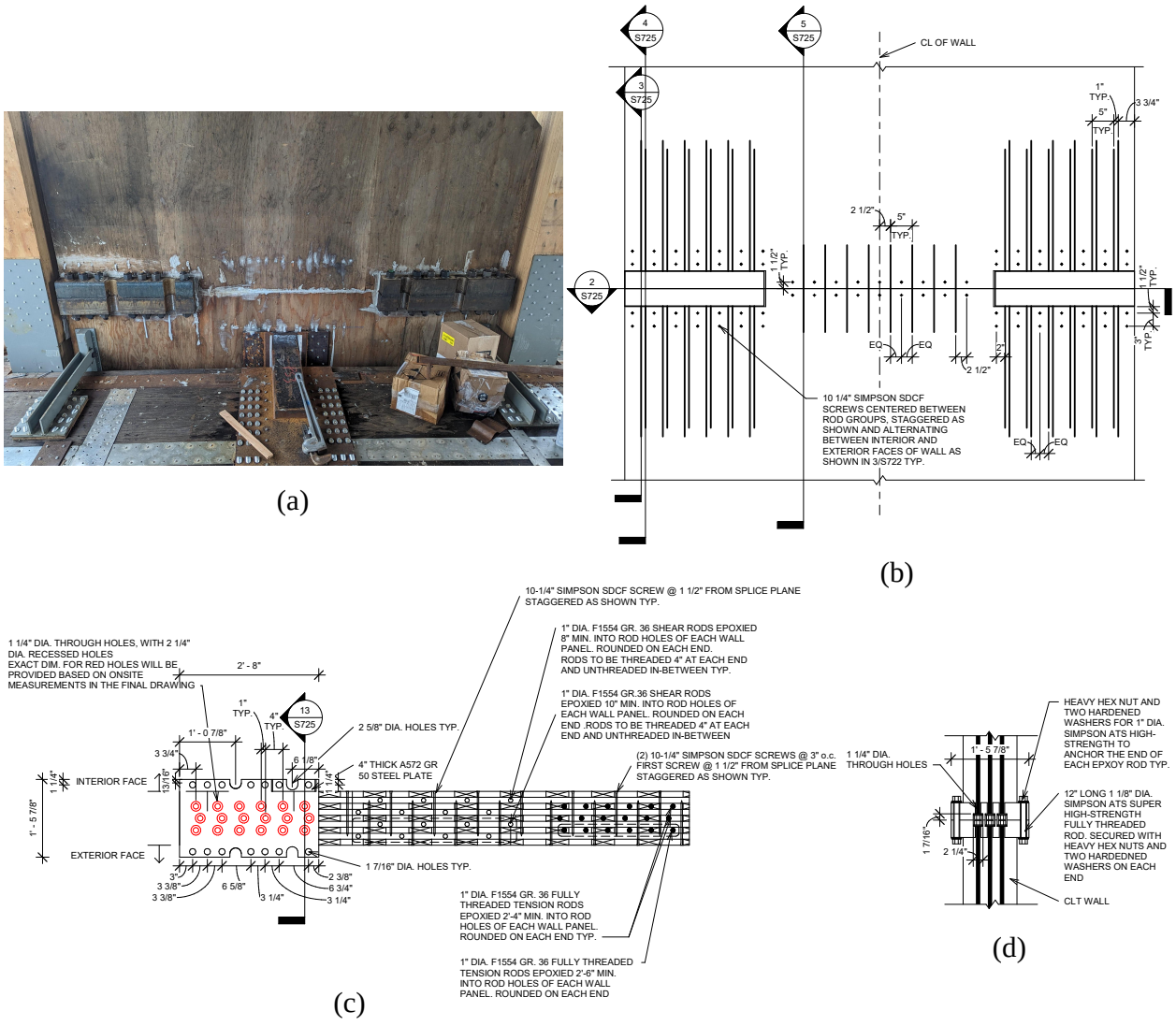

Figure 6.31: Shear wall horizontal splice (a) photo showing constructed connection (b) elevation view details (c) plan view details, and (d) section view details

bined axial compression and flexural demands in the walls. They are concentrated on the outer thirds of the cross section to create the largest moment arm for in-plane wall bending. These rods are have long embedment lengths and are fully-threaded to develop sufficient epoxy bond development. Lower strength (F1554 Grade 36 steel) threaded rods were used to ensure a ductile failure mode with steel yielding controlling over bond failure. Assuming

plane sections remain plane, the stress, strain, and force diagrams shown in Figure 6.32 were developed for the cross section. The flexural capacity of this connection was determined through section analysis by limiting the strain in the outer most tension bar (ϵ_{rod1}) to twice the yield strain of the bars ($2\epsilon_y$) and satisfying axial equilibrium with a demand axial load, P_u, equal to the initial post-tensioning force of the PT bars (200 kips). Because the addition of the splice plates results in non-continuous rods that cannot transfer compression forces over the splice plane, the bars in compression are assumed to have zero compression capacity. In the original design without the splice plate and with continuous bars, the bars in compression could transfer compression stresses over the splice.

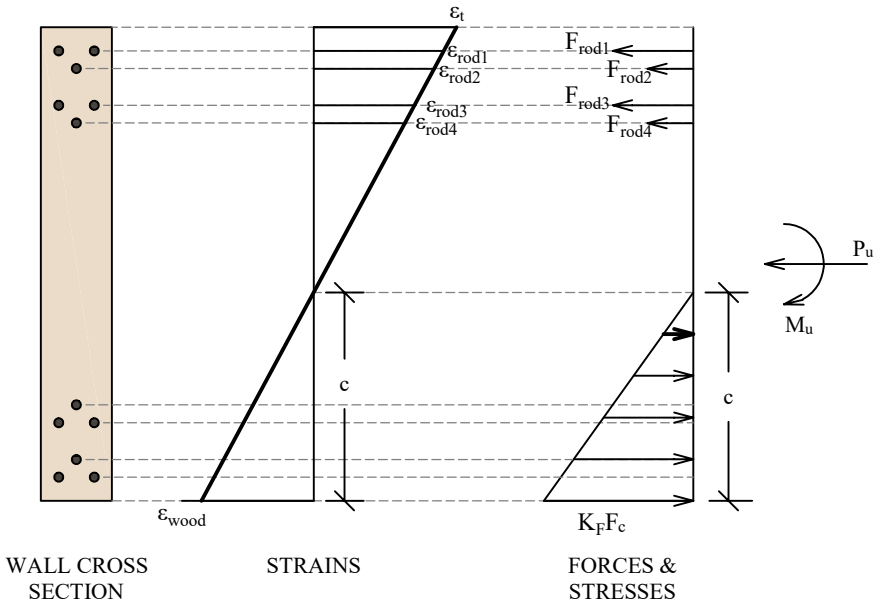

Figure 6.32: Axial-flexural interaction of the shear wall splices

As shown in Figure 6.31, the inner third of the cross section contains similar embedded epoxy rod details to transfer shear forces. These rods were shorter because only shear needs to be transferred so long development lengths are not needed. Additionally, the rods were only threaded 4 inches at either end for epoxy bond. They were un-threaded in the middle for a smooth surface spanning the splice. Lab testing, specific to this test, was completed

for these shear rods to aid in predicting the strength of this connection in shear. The tests were completed at Oregon State University and found that each shear rod could transfer approximately 5.5 kips of shear force for both the CLT and MPP walls. These values were used in design because yield limit equations for the lateral design of dowel type fasteners are not yet well known for dowels in the ends of mass timber panels.

As shown in Figure 6.31, the large steel splice plates were only added for the tension rods. Because the transfer of shear forces through relays primarily on bearing and not on bond between the epoxy, rods, and wood, the tension rod holes were over-drilled to accommodate the errors from pre-drilling of the holes. Additionally, the drilled shear rod holes had minor errors in comparison to the tension holes, most likely because they had shorter embedment lengths. Unique splice plates were custom made for each of the 32 splice plate locations using precise as-built measurements of the hole locations. As shown in Figure 6.31d, at each rod location, a through hole was drilled along with a recessed hole for a washer and nut. Each rod was then epoxied into place using the procedure outlined below. This created a bond between the splice plates, rods, and the wall panels at each corner of the wall panels. Once the splice plates were attached to the ends of all the wall panels, the walls were lifted into the building and the two splice plates at each corner were then bolted together to create a monolithic wall panel.

The splice connection was installed by first coating all the holes (both shear and tension rod holes) with a thin layer of the epoxy to seal any large voids in the wood. Then, the large splice plates were clamped onto the corners of the panels. The splice plates were installed in the vertical orientation for the bottom panels of the splice and installed in the horizontal orientation for the top panels of the splice, as shown in Figures 6.33a and 6.33b respectively. With the plates clamped on, each hole was carefully filled with a calculated amount of epoxy, then rods with attached nuts and washers were lowered into each hole while spinning the rod clockwise to fully coat the rod and reduce air pockets (Figure 6.33b). This epoxy procedure was tested at Simpson Strong-Tie labs prior to construction and cross sections were taken to ensure that the procedure resulted in limited air pockets and full epoxy coverage. The

epoxy was then allowed to cure for a minimum 24 hours. The shear rods were then placed into their respective holes of the lower panel and the upper wall panel was lowered into the building in place (Figure 6.33c). On both ends, the exterior nuts, bolts, and washers were installed in the large steel splice plates, clamping the walls pieces together. Cracks between and around the splice plates were filled with epoxy to create an even contact surface (Figure 6.33d). At the center splice rods, epoxy was injected into the holes using the fill and weep holes shown in the detailed drawings in Appendix B (Figure 6.33e). Finally, the confining screws detailed in Figure 6.31c were installed. Note, the offset arrow pattern and staggering lengths of the tension rods in the CLT and MPP splices and the shear rods in the MPP splice was to allow for use of fill and weep holes for epoxy injection that the contractor was comfortable using. In the end, the fill and weep holes were not drilled for the tension rods because of the splice plate addition.

Detailed design equations for the design of the the CLT and MPP splices are included in Appendix A, Section A.4. For the axial-flexural interaction check, the DCRs for the CLT and MPP splices were 1.07 and 1.13, respectively. For shear capacity check for the CLT and MPP walls, the DCRs were 0.91 and 0.69, respectively. The greater than 1.0 DCR ratios for the axial-flexural interaction checks for both the CLT and MPP walls are a result of many limitations inherent to the large-scale experimental work and previously discussed with the wall capacity checks. As previously mentioned, the issue of insufficient splice flexural capacity was addressed during testing by limiting the simulated MCE_R ground motions. The design of the large steel splice plates was checked by Simpson Strong-Tie, using a finite element model to ensure the plates remain elastic under suite maximum demands.

Note, while there were significant construction issues with this connection, they were a result of errors made by the wall fabricators and is not reflective of the construction feasibility of the design. Similar epoxy rod connections have been design and constructed successfully at a smaller scale in other projects. Notably, similar connections exist in the five-story mass timber Catalyst building in Spokane, Washington [Zimmerman et al., 2020].

Figure 6.33: Shear wall splice installation procedure: (a) horizontal installation of splice plates on upper wall panels, (b) vertical installation of splice plates on lower wall panels and rod epoxying, (c) lowering of upper wall panel, (d) final tension rod and splice plates, and (e) final shear rods

Wall Panels Sliding at Base

At the base of the rocking wall panels, the force due to friction is not large enough to prevent sliding of the panels, thus, a shear shoe (shown in Figure 6.34) was designed to transfer the remaining force from the wall panel into the foundation. At both ends of the wall panel, a shear shoe was welded to the foundation beam and wrapped around the corners to keep the wall in place. The demand for this connection was determined using the wall base shear results (V_b) from the NLRHA at MCE_R minus the approximate force due to friction.

The force due to friction was calculated using the initial post-tensioning force ($F_{pt,i}$) as the normal force and an assumed coefficient of friction (μ) of 0.3. Note, using the initial post-tensioning force as the normal force is conservative since peak base shear is likely to occur when the walls are rocking and the PT bars are stretched producing a larger force. This conservative approach was used to simplify calculations.

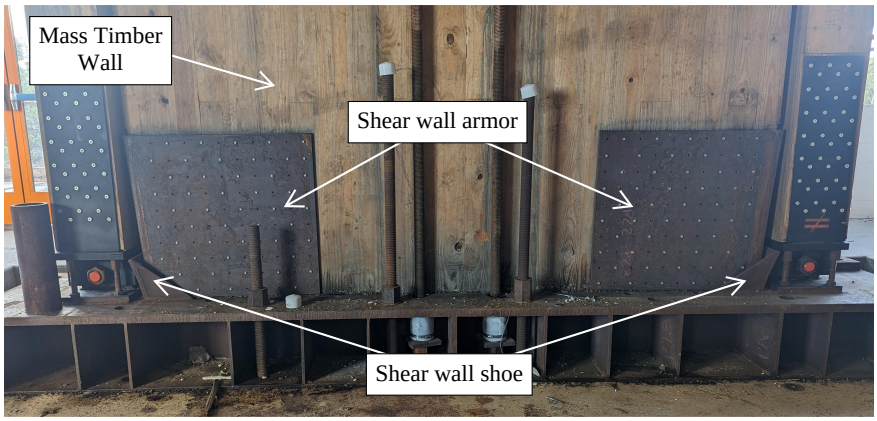

Figure 6.34: Shear shoe and wall armor detail located at the base of the post-tensioned rocking walls

Figure 6.34 also shows the wall armor. Because the base corners of the wall panels are expected to sustain some damage with the large number of earthquakes this specimen will experience, the armor was included to protect and reinforce the corners of the panels. The wall armor wraps around the corner of the wall and is anchored to the wall using Simpson Strong-Tie SDS wood screws. The shear shoe then wraps around the wall armor, but is welded to the foundation beam instead of connected to the wall panel. The shear force in the wall is first transferred to the wall armor through bearing. Then transfer to the shear shoe through bearing along its height. The load is then transferred to the foundation through shear along the weld between the shear shoe and the foundation beam.

Detailed calculations for this design can be found in Appendix A, Section A.5. The DCRs for all checks on the MPP walls were below 1.0. For the CLT walls, there was one DCRs that

exceeded 1.0. The DCR for the bending check of shear wall armor end plate was 1.30. It was determined that this would be okay since the elastic section modulus was used, making the check relatively conservative.

UFP Connections

The UFPs span between the post-tensioned rocking walls and the boundary columns (Figure 6.7). As discussed in Section 6.2.3, an embedded pi plate mount with steel dowels (designed by project collaborators) is attached to the edges of the walls and the columns. The portion of the UFP connection design discussed here is the bolted connection for connecting the UFPs to the face of the embedded UFP mounts. As shown in Figure 6.35, one face of the UFP has two slotted holes and the other face has two non-slotted holes. The face of the UFP mounts have drilled and tapped holes for the bolts. The UFPs were installed by first connecting the side of the UFPs with the round holes to the column face. The side with the slotted holes was then bolted down with the addition of a rectangular weld washer. Because of construction tolerances, slotted holes and weld washers were used for easier installation of the UFPs. After all the bolts were tightened, the weld washers were welded to the UFPs. Note, the intent was for UFP weld washer welding to occur after post-tensioning the rocking walls. With this method, the walls would compress slightly during pre-stressing and the bolts would be able to slide in the slotted holes, resulting in un-stressed UFPs for the beginning of testing. However, due to construction sequence timing, the weld washers were welded prior to post-tensioning of the walls, resulting in minor UFP loading at the beginning of testing.

As noted in Table 6.32, the UFPs connections were capacity designed so the ultimate force in the UFP was used as the demand force. For ease of construction, the weld washer and bolt design was constant up the height of the building. Because the lower UFPs are larger and thus have a larger ultimate force, they were used for the demand calculations.

Detailed calculations for the design of the UFP to UFP mount connections can be found in Appendix A, Section A.6. As shown in Figure 6.35, the weld washers on the upper UFP are rotated 90 degrees from the weld washers on the bottom UFP. At this location, the

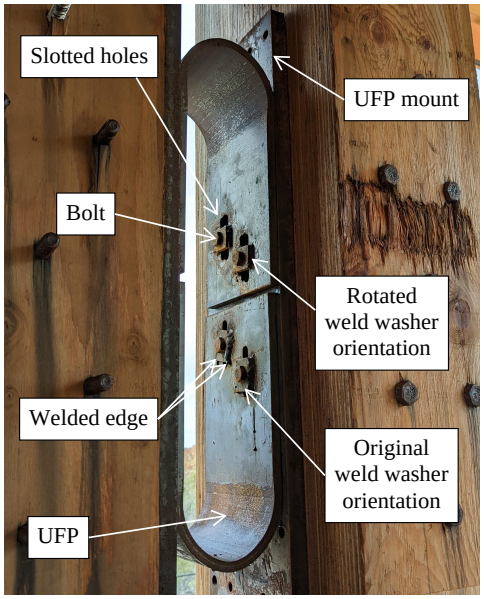

Figure 6.35: Connection details for the UFPs to the UFP mounts

lower UFP has the original as-designed orientation of the weld washers. However, during construction, there were more tolerance errors than expected and the UFPs did not fit into the building as expected. Thus, the slotted holes had to be enlarged and the weld washers at some locations had to be rotated in order to span the enlarged holes. The capacity of the welds and failure of the weld washer was checked for the rotated weld washer orientation as this is the controlling case. The resulting DCRs for all the checks for this connection were below 1.0, satisfying all design criteria.

Diaphragm-to-Wall Connections

As discussed in Section 6.2.3, this document only contains a discussion of the diaphragm to wall connections located on the CLT and VLT diaphragms (two-way systems that are not sheathed). The diaphragm to wall connections located on the other floors were designed by project collaborators. Figure 6.36 shows a schematic of the connection design that will be discussed here, with the distribution of designed forces. The demand used to design this

connection was taken as the peak floor forces, calculated from the NLRHA in the OpenSees model.

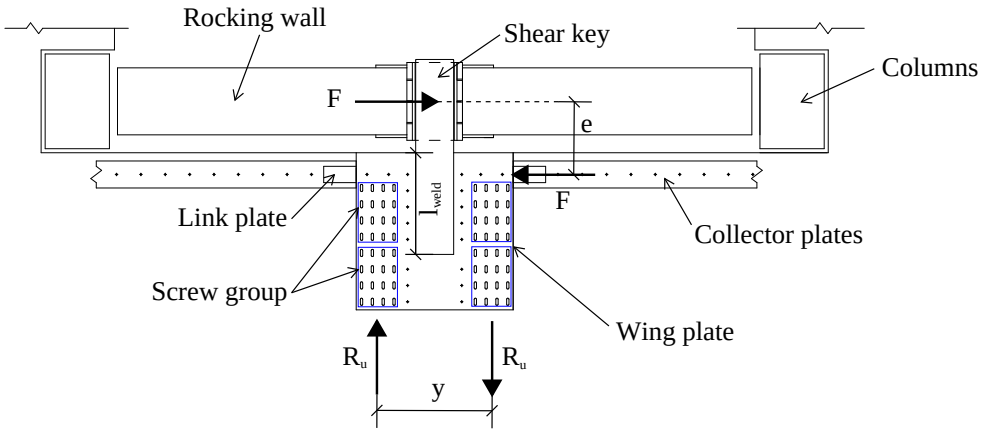

Figure 6.36: Schematic of the diaphragm to wall shear transfer connections showing the transfer of forces

This connection is designed to transfer shear load from the diaphragm to the walls without transferring moment. A shear key is inserted into a vertically slotted hole in the wall to allow for the wall panels to uplift while the floor diaphragms remain level. As shown in Figure 6.36, the collector plates transfer shear force into the shear key assembly and then force is transferred to the shear wall through bearing of the shear key on the inside of the wall panel. Because these forces are spaced at an eccentricity (e), a moment is formed as shown in Figure 6.36. The moment is resisted by introducing a wing plate that is anchored to the diaphragm using four screw groups that have 45-degree angled washers to resist moment. These screws result in forces R_u (spaced at a distance y) shown in Figure 6.36. The two screw groups closest to the wall are angled towards the wall panel, while the other two screw groups are angled away from the wall panel so the wing plate can resist moment in both directions. Installing the screws at 45-degrees results in a stronger and stiffer connection since the screws can resist forces through withdrawal instead of shear. The 45 degree screws used in this connection were supplied by Simpson Strong-Tie and were designed in accordance

the manufacture recommendations. Traditional screws were also installed in the wing plate, along the face of the diaphragm and along the shear key weld. These were installed to prevent uplift from small uplift and bending forces in the wing plates. The portion of the shear key inserted in the wall slot has rounded corners to allow the wall to rock up without getting jammed or stuck.

Detailed calculations for the design of these diaphragm to wall connections can be found in Appendix A, Section A.7. The DCRs for all the connection calculations on the CLT walls were less than 1.0, satisfying design criteria. Two DCRs for the MPP wall direction slightly exceeded 1.0. The DCR for bearing of the shear key on the inside of the wall was 1.05 and the DCR for withdrawal of the screws in the wing plate was 1.03. These DCRs are only slightly above 1.0 so they were deemed acceptable.

PT Bars

The PT bars were designed such that they do not yield under MCE_R loading. As shown in Table 6.32 the design check was performed using just the suite maximum PT force value. In a typical design, the ultimate PT bar force would be used, however, for this project, the yield force was used to ensure a more resilient building that could withstand multiple MCE_R during the testing sequence. Limiting PT bar yielding becomes easier for taller buildings. As the bars get longer, the strains spread out along the length. The capacity of the PT bars was calculated using ANSI/AISC 360-16. The PT bar force results from the nonlinear OpenSees model are shown in Table 6.29. Because the specified γ and ϕ factors are both equal to 1.0, these tabulated values represent the final DCR for the axial capacity of the PT bars. As shown, the DCR is equal to 0.68, meaning the peak PT forces are well below the yield force, satisfying this design check.

PT Bar Connections

The PT bars attached to the top of the walls using the PT saddle connection shown in Figure 6.6. As indicated by Table 6.32, this connection was also capacity designed. Detailed

calculations for the design of the PT saddle are included in Appendix A, Section A.8. For the PT saddle, the ultimate force in the PT bars were used for the demand calculations. This is highly conservative as NLRHA results indicated that the bars are not expected to exceed 70% of their yield strength.

To aid in applying the initial post-tensioning force to the bars, the additional jacking hardware piece shown in Figure 6.6 was also designed. This piece was designed so all four bars could be stressed at the same time. The hydraulic jack was placed between the two pieces while the bars were initially anchored to the top of the jacking hardware piece. Once the initial force in the PT bars was achieved, the bars were anchored to the PT saddle and the jack and the hardware was removed. For the design of the jacking hardware, the initial PT bar force was used to make the connection more economical. This piece was only used during initial post-tensioning of the bars so it should not experience forces larger than that.

Detailed calculations for the PT jacking hardware design are also included in Appendix A, Section A.8. For these connection assemblies, the DCR values were all below 1.0, satisfying design checks, except for one check on the CLT and MPP walls. DCRs for longitudinal bending of the PT saddles exceeded 1.0. However, as explained in the Appendix, this check was considered conservative because beam approximations were used with the hand calculations, as opposed to developing an FEM model.

Design Criteria for Deformation-Controlled Actions

In addition to the force-controlled action limit states checked in Section 6.6.3, a series of deformation-controlled action limit states were also checked to finalize the design. These checks were performed using results from NLRHA at MCE_R seismic hazard. The deformation-controlled actions that were checked are summarized in Table 6.33. Similar to the force criteria, the components were checked at both suite mean and suite maximum demands. This section includes a brief discussion of each deformation check performed. If any of the following checks were not satisfied, then the dimensions of the PT bars and UFPs were modified (and if necessary the wall panel dimensions) and the design procedure was repeated as

shown in Figure 6.20. The limited number of deformation-controlled action checks elude to the resilient performance capabilities of the post-tensioned rocking wall system.

Table 6.33: Criteria for deformation-controlled actions under MCE_R seismic hazard

Component	**Action**	**Criteria**	
		Suite Mean [a]	**Suite Maximum** [b]
CLT Wall Panels (at base)	Axial-Flexure	$\epsilon_{wood} < \epsilon_{s,CLT}$	$\epsilon_{wood} < \epsilon_{cr,CLT}$
MPP Wall Panels (at base)	Axial-Flexure	$\epsilon_{wood} < \epsilon_{s,MPP}$	$\epsilon_{wood} < \epsilon_{cr,MPP}$
UFPs	Axial	$\Delta_u < 0.75\Delta_{limit}$	$\Delta_u < \Delta_{limit}$

[a]Suite mean demand is calculated as the mean over all ground motion records of the peak demand for each record

[b]Suite maximum demand is calculated as the maximum over all ground motion records of the peak demand for each record

Mass Timber Wall Panels - at Base

As shown in Table 6.6.3, the axial-flexure capacity of the wall panels at the base was checked by comparing the suite mean of the peak strain demands from the rocking multi-spring elements in the OpenSees models (ϵ_{wood}, values found in Table 6.27) to the design splitting strains for the CLT ($\epsilon_{s,CLT}$ in Table 6.2) and MPP ($\epsilon_{s,MPP}$ in Table 6.3). This was also checked by comparing the suite maximum of the peak strain demands from the rocking multi-spring elements (also found in Table 6.27) in the OpenSees models to the design crushing strains for the CLT ($\epsilon_{cr,CLT}$ in Table 6.2) and MPP ($\epsilon_{cr,MPP}$ in Table 6.3).

Compression yielding at the base of the walls were permitted under this check to allow these structures to be more economical. If yielding was not permitted, then the wall designs would have to be very large and not feasible for a real building. Additionally, the failure mode for the wood at the base of the walls is gradual and not catastrophic. Once part of the wall yields and even splits, it can redistribute load to adjacent fibers. As discussed in Section 6.6.3, developing a design that prevents PT bar yielding can be achieved easily. Additionally, as discussed in the following check for the axial deformation of UFPs, UFP are designed to

be replaceable. Thus, controlling the failure of the wood at the wall bases is the primary concern for collapse prevention of these systems [Zimmerman and McDonnell, 2018].

Table 6.34 summarizes the resulting DCRs. As shown, the check is well satisfied for the CLT walls. The MPP walls have an overall DCR greater than 1.0. However, this was determined to be acceptable because this came from the suite mean check which is fairly conservative in limiting to splitting strain. The suite maximum check is well below 1.0.

Table 6.34: DCR summary for the wood strain at the base of the wall panels

Wall Base Strain DCR Summary		
	Mean_{geo}	Max
CLT Walls	0.96	0.31
MPP Walls	1.19	0.47

UFPs

The deformation capacity of the UFP connections were checked as shown in Table 6.33. The maximum deformation of the UFPs from the NLRHA at MCE_R (results summarized in Table 6.31) were compared to $0.75\Delta_{limit}$ and Δ_{limit} for the suite mean and suite maximum, respectively. Δ_{limit} is defined as the distance from the nearest bolt to point of tangency for the bend in the UFP (5.25 inches for both the upper and lower UFPs). This is to ensure that the UFPs will not rip out of their connections due to too large of deformations. The resulting DCR values are summarized in Table 6.35. The 0.75 value is taken from ASCE/SEI 7-16 Section 7.6.3 for collapse prevention performance of primary components. Collapse prevention was used as opposed to a higher performance objective because the UFP connections can be design for easy replacement after a large earthquake. However, during 10-story testing, repeated use of the same UFPs did appear to be acceptable.

Table 6.35: DCR summary for the deformation capacities of the UFP connections

Wall Base Strain DCR Summary		
	Mean_{geo}	Max
Overall	0.37	0.36

Final Design Complete

After completing all checks outlined in Tables 6.15, 6.32, and 6.33, all requirements for NLRHA with performance-based design methodologies, were satisfied and the final design of the post-tensioned rocking wall lateral system was complete. This procedure focused on performance at MCE_R hazard and the limit states were developed to achieve essentially elastic and better than code required performance. No direct limit states were checked at the lower hazard levels. The general performance of the structural at the other hazard levels were investigated qualitatively, as discussed in the next section.

6.7 Predicted Performance

Full ground motion design suites were run at all seven hazard levels to predict the performance and assess the resiliency of the structure at various hazard levels. The design suites of eleven two-component ground motions presented in Section 6.4 were used for these predictions. The following section will present plots summarizing the predicted performance at each hazard level. For this study, only peak response values are presented. In each plot, the geometric mean spectral acceleration ($S_{aRotD50}$) for each ground motion at the buildings approximate first mode period is plotted versus the peak response parameter. A period of 1.74 seconds was used for these plots. The suite mean response for each hazard level is also included on the plot. Summaries for the peak global response will be presented first, followed by the response of the timber material at the wall base (arguably, the most critical portion of the design), and then the other key structural components (forces in the shear keys and PT bar forces).

6.7.1 Global Building Response

Figures 6.37, 6.38, and 6.39 summarize the peak floor accelerations, ISDs, and roof drifts, respectively. As shown, these peak values increase with increasing hazard level and corresponding ground motion intensity (represented by $S_{aRotD50}$ at the buildings first elastic period). Although not explicitly defined for this design, the 43-year return period earthquake is commonly used to assess service-level seismic performance criteria. At this hazard level, the OpenSees model predicts very minimal drift, likely resulting in little to no structural or nonstructural damage. Additionally, the 475-year return period earthquake is commonly used to study repairability seismic performance criteria. However, the procedure used for the 10-story building results in structural repairability at the MCE_R hazard level. Suite mean ISDs at the 475-year return period hazard level are approximately 1%.

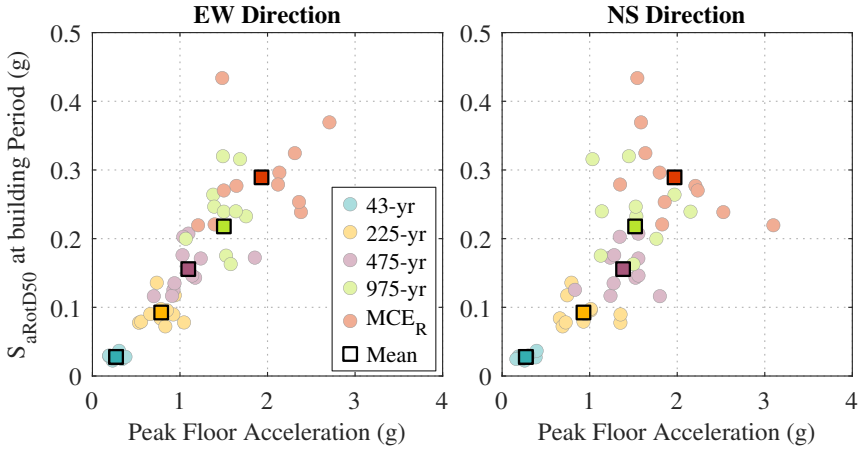

Figure 6.37: Peak absolute floor acceleration predictions from NLRHA at all design hazard levels

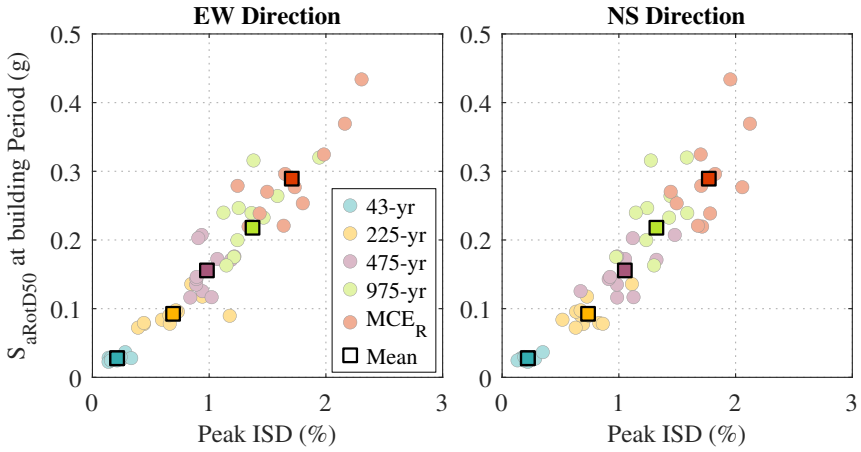

Figure 6.38: Peak ISD predictions from NLRHA at all design hazard levels

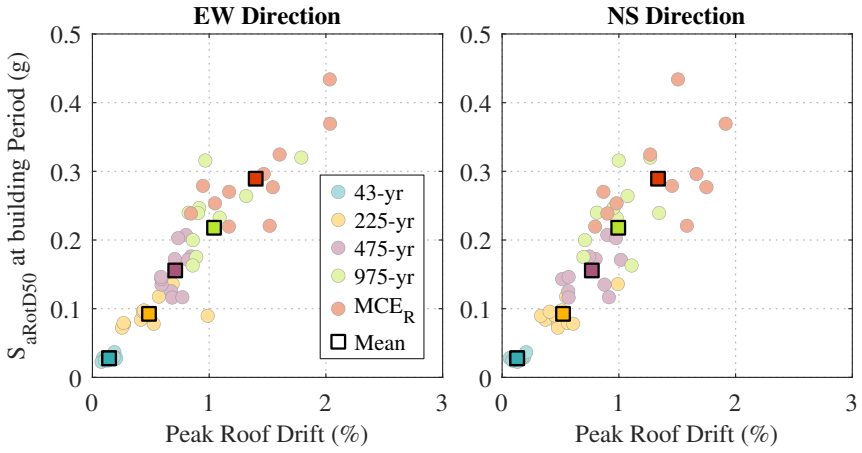

Figure 6.39: Peak roof drift predictions from NLRHA at all design hazard levels

Figures 6.40 and 6.41 show the OpenSees NLRHA predictions for peak uplift rotation at the base of the rocking walls and peak elastic rotation of the full walls, respectively. The peak joint rotations were recorded from rotations of the node at the base of the rocking walls. The elastic rotation was then calculated as the rotation at the roof (i.e., the roof drift ratio) minus the joint rotation at the base of the wall. The joint rotation values are intended to represent the rotation of the walls from uplift and the elastic rotations represent the deformation rotations from elastic cantilever rotation of the walls. As shown, the joint rotations at the base of the wall are essentially zero for the 43-year return period earthquake, indicating no wall uplift and all deformation coming from elastic cantilever action. As the hazard level increases, the amount of rotation from elastic deformations tappers off while the rotations from joint uplift continue to increase.

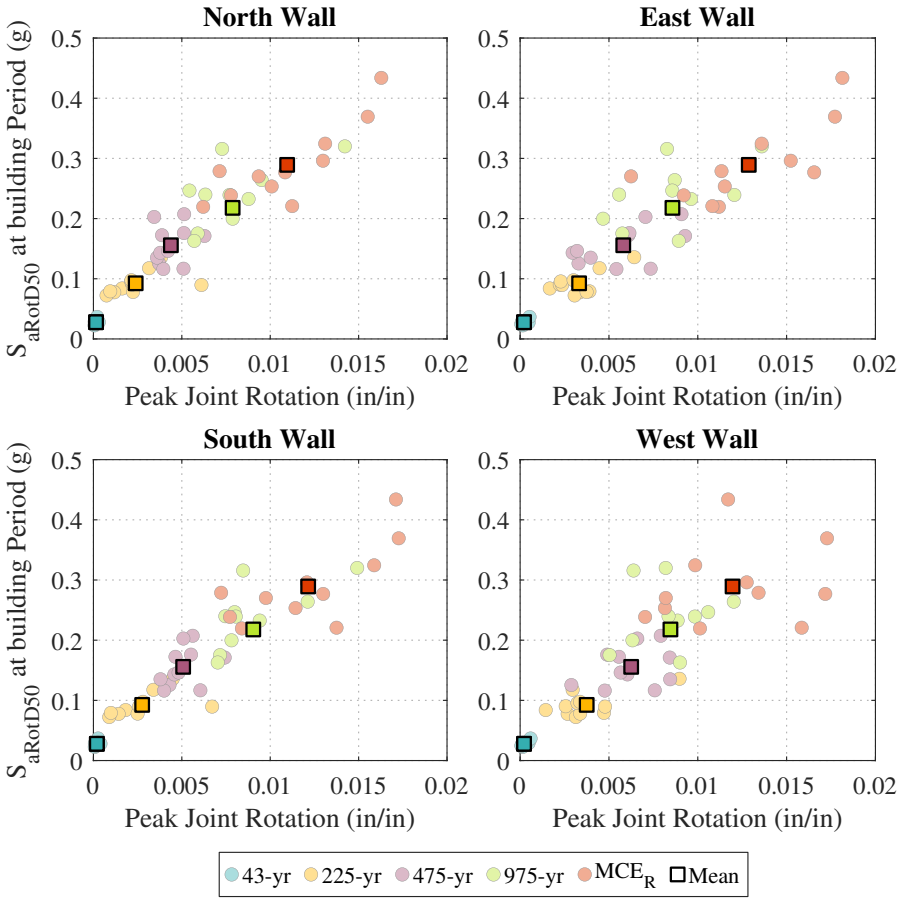

Figure 6.40: Peak uplift rotation at the base of the rocking walls from NLRHA at all design hazard levels

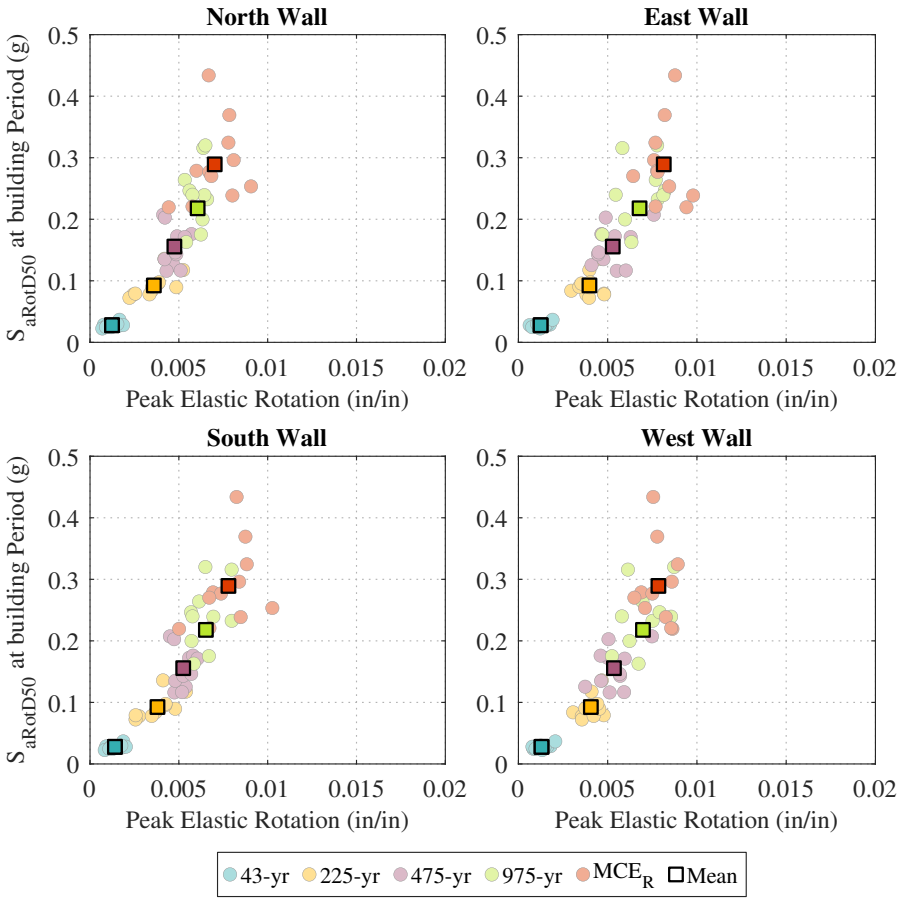

Figure 6.41: Peak elastic rotation in the wall panels from NLRHA at all design hazard levels

6.7.2 Rocking Wall Timber Material Response

Peak wall shear and wall moment values (M_{wall}) are summarized in Figures 6.42 and 6.43, respectively. The similar shapes of the plots for the walls running in the east-west direction (CLT walls on the left side of the plots) and the north-south direction (MPP walls on the right side of the plots) indicate minimal torsion in the building.

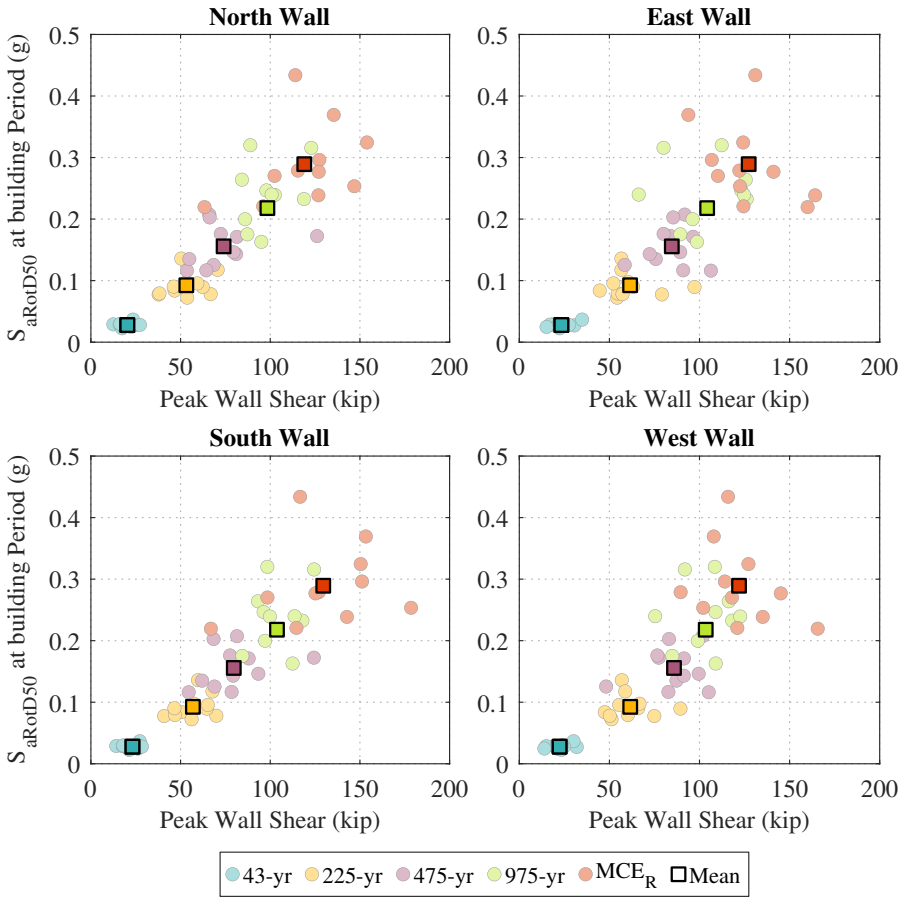

Figure 6.42: Peak wall shear predictions from NLRHA at all design hazard levels

Referring back to Table 6.18, the calculated moment in the wall panels, M_{wall}, at the base of the walls, were 14886 kip-in and 13738 kip-in at DBE demands for the CLT and MPP walls, respectively (note, per Figure 6.11, the uniform hazard response spectrum for the 975-year

return period most closely represents $2/3MCE_R$). At MCE_R, they were 15476 kip-in and 14439 kip-in for the CLT and MPP walls, respectively. For both of these benchmarks, the peak moment values from NLRHA far exceed the approximate wall base moment capacity calculated from the cross-sectional analysis procedure. This indicates that increased moment demands from higher mode effects are significant.

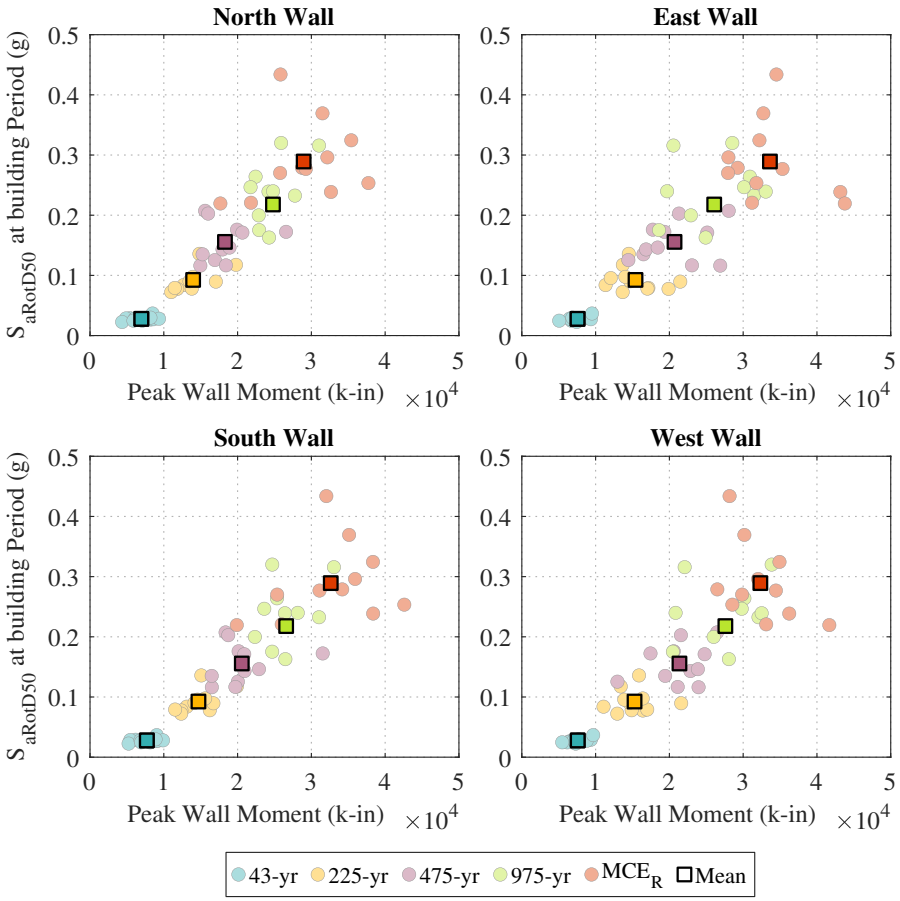

Figure 6.43: Peak wall moment predictions from NLRHA at all design hazard levels

Figure 6.44 summarizes the peak strain at the base of the walls. These are the strains occurring at the outer most corners of the wall panels where stresses are the largest. Recall, Tables 6.2 and 6.3 summarize the strain limits states. Vertical lines on these plots indicate the limits as well. As shown, the wall bases remain essentially elastic in compression through

the 225-year return period hazard level. Splitting does not occur until MCE_R, and crushing (which indicates extreme damage at the base of the wall) does not occur until well beyond MCE_R. As shown, it is challenging to avoid yielding of the base of the walls in compression. However, more subassembly testing still needs to be done to better characterize the behavior of mass timber under large combined axial and bending loads. Additional testing could aid in better understanding of the strain limits and material modeling, especially as needed to model such buildings through collapse in FEMA P-695 type analyses.

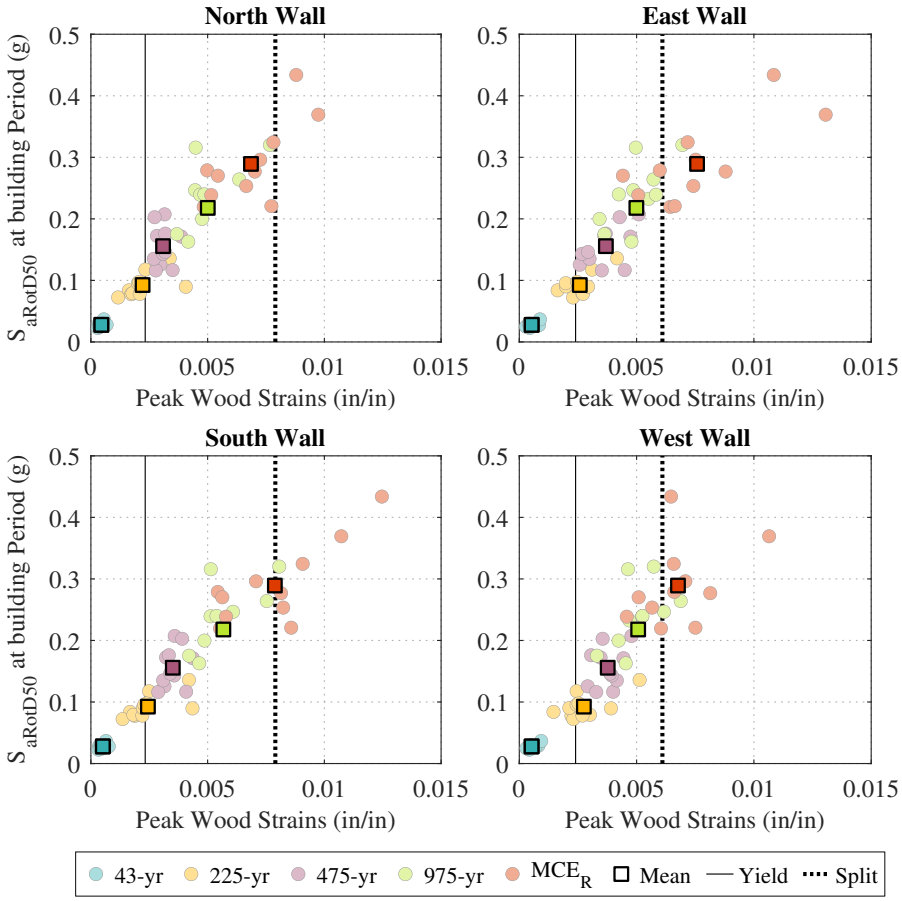

Figure 6.44: Peak wood strains at the base of the rocking walls from NLRHA at all design hazard levels

Figures 6.45 and 6.46 show the peak percentage of wall base that reaches yield and splitting limit states, respectively. These lengths are calculated for one corner of the wall panel. While a decent percentage of the wall panels reach yield at larger hazard levels, an almost irrelevant proportion of the wall base reaches splitting strain at MCE_R. A crushing plot is not show because the wall panels do not exceed the crushing strain.

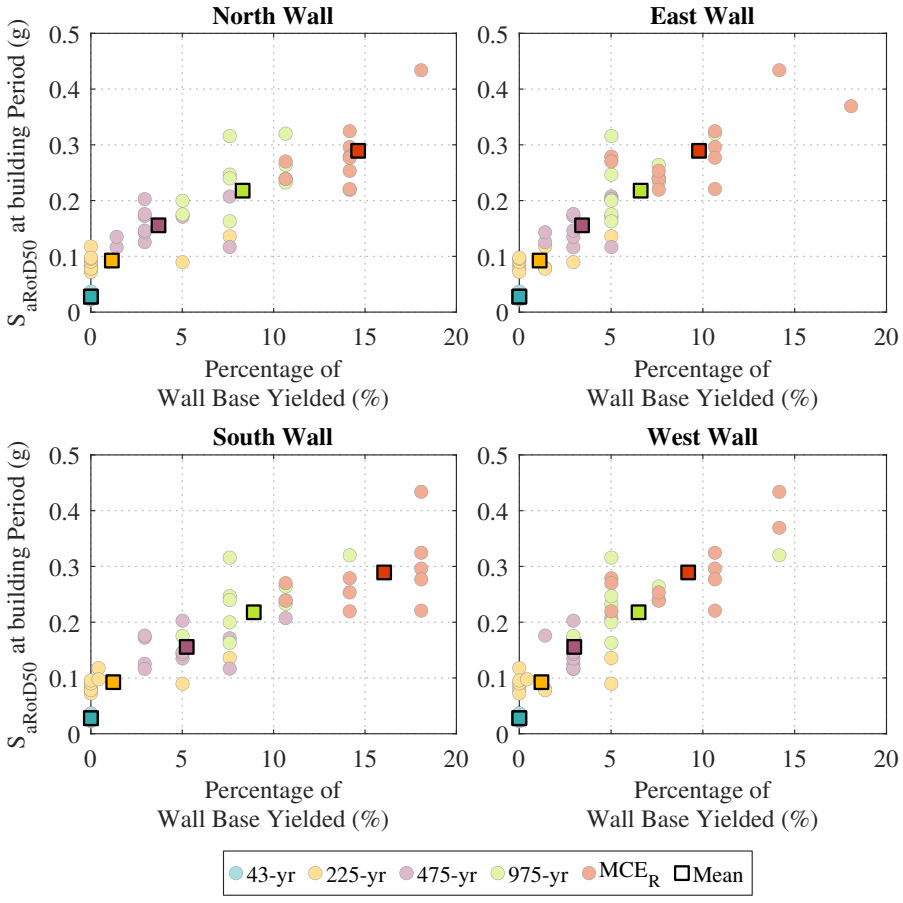

Figure 6.45: Proportion of the base of the rocking wall reaching yield strains from NLRHA at all design hazard levels

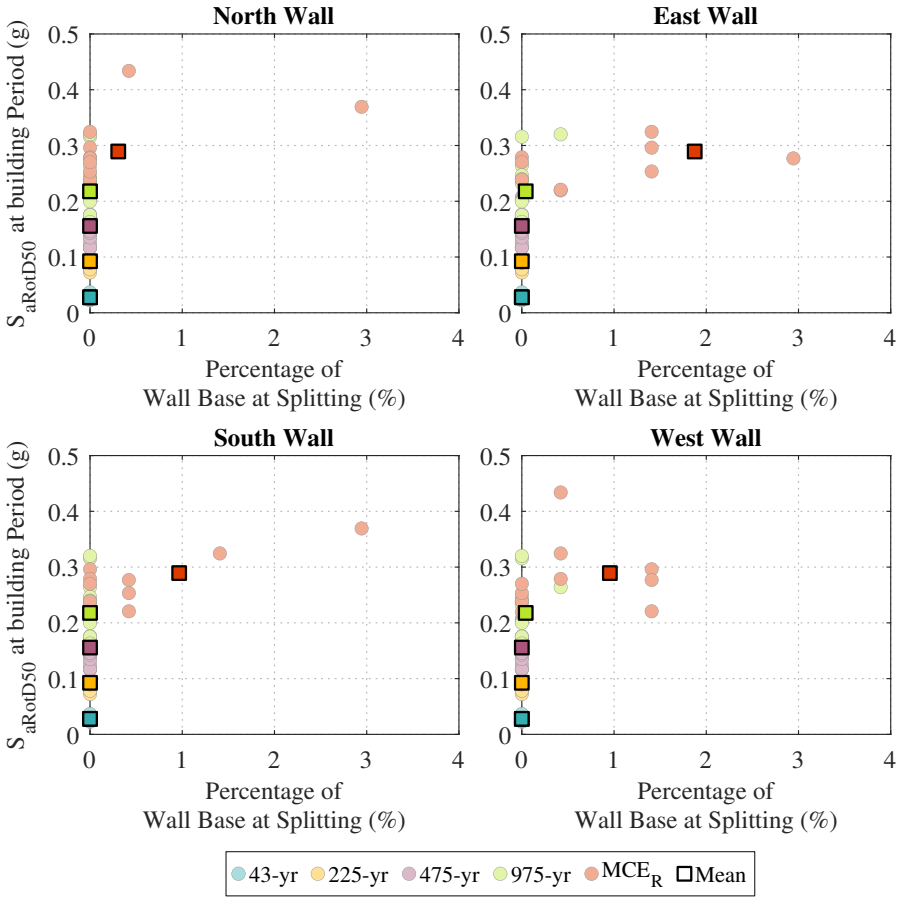

Figure 6.46: Proportion of the base of the rocking wall reaching splitting strains from NLRHA at all design hazard levels

6.7.3 Rocking Wall Structural Component Response

Figure 6.29 summarizes the peak floor diaphragm values at each hazard level. These are the force predictions for the shear key wall-to-diaphragm connections. The similarity of plot shapes for the walls running the same orthogonal directions indicate little torsion in the building.

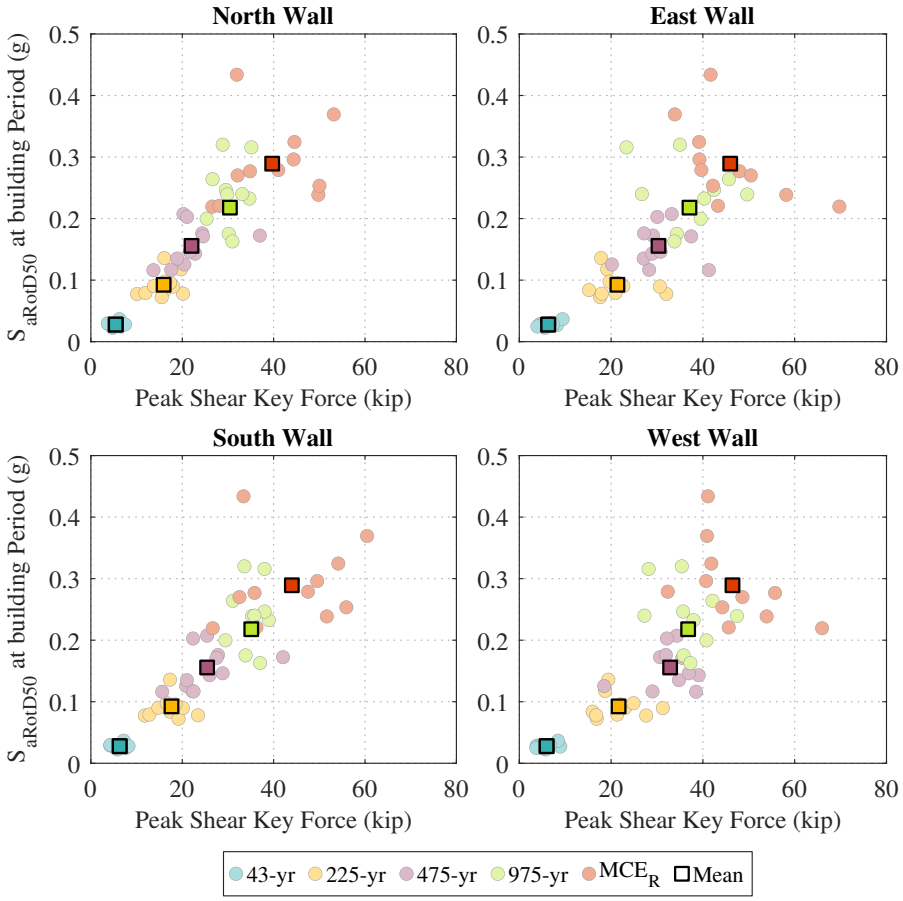

Figure 6.47: Peak floor diaphragm forces from NLRHA at all design hazard levels

Figure 6.48 shows the peak PT force for all hazard levels. As shown, the PT forces are similar to their initial prestressing force for the lower hazard levels because wall uplift is small. The peak PT forces at the larger hazard levels have increased beyond their initial prestressing force, however, they are not near yield. Indicating that the walls will re-center after even large earthquakes and residual drifts will be small.

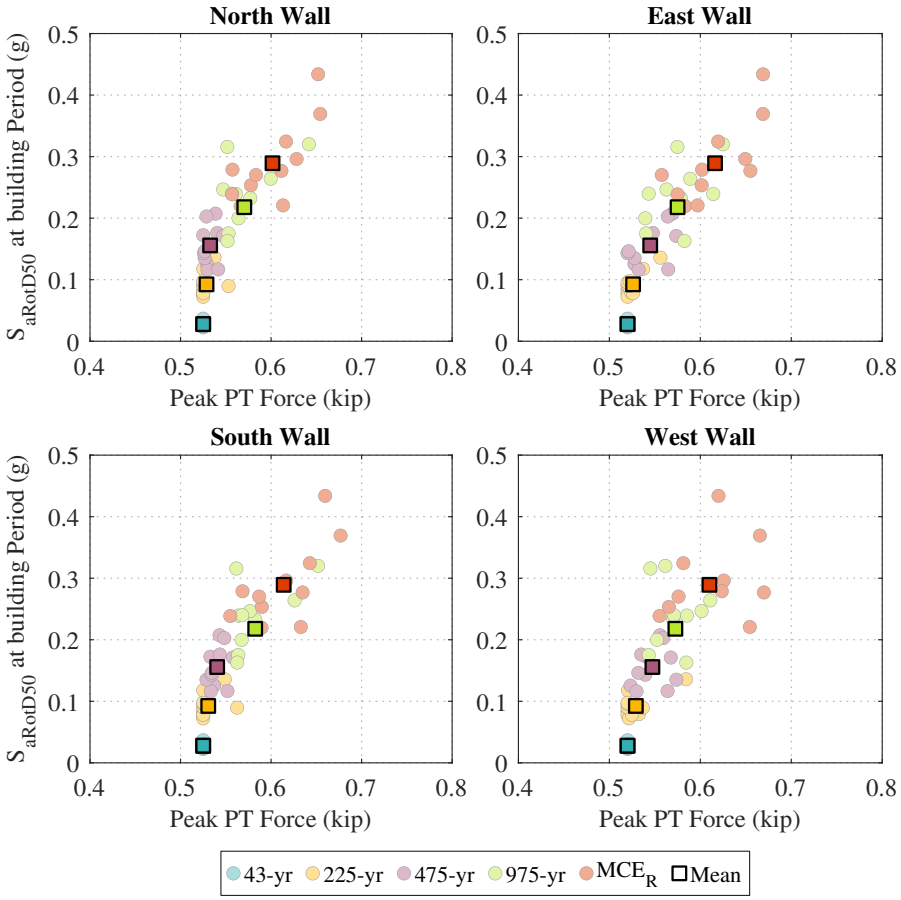

Figure 6.48: Peak PT bar forces from NLRHA at all design hazard levels

Chapter 7

NHERI TALLWOOD TEN-STORY BUILDING TESTING, PERFORMANCE, AND COMPARISON OF EXPERIMENTAL AND ANALYTICAL RESULTS

7.1 Overview

The performance-based design procedure and nonlinear numerical modeling methodology used to design the 10-story NHERI TallWood post-tensioned mass timber rocking wall lateral system was tested and validated at the NHERI@UCSD outdoor shake table facility. An extensive testing program was developed that tested the building using earthquake recordings representative of three earthquake sources (crustal, interface, and intraslab) scaled to five hazard levels ranging from a 43-year return period hazard to MCE_R hazard. The testing plan consisted primarily of one- and two-horizontal-component acceleration inputs and some tests also included vertical accelerations.

In this chapter, the testing plan will be presented, followed by a presentation of the minimal visual damage observed on the lateral system during testing. Next, a discussion of the instrumentation used for data processing in this document will be presented. The filtering and double integration procedures used for the accelerometer recordings will be discussed in detail. After, a short study on building damping will be presented. Lastly, a comparison of predicted building response from the nonlinear numerical model used for design will be compared to the experimental building performance. This discussion includes a discussion on the performance of the lateral system and the validation of the nonlinear numerical modeling methodology used for design.

7.1.1 Shake Table Facility Details

The 10-story specimen was tested at the NHERI@UCSD outdoor shake table, the same facility used for the 2-story shake table test discussed in Chapter 4. Between the 2-story and 10-story tests, testing facility underwent a large upgrade and expansion to improve the table's capabilities of producing more realistic earthquake ground motions. During the 2-story test, the shake table could only move uniaxially in the east-west direction. For the 10-story test, the upgraded shake table (now called LHPOST6) could move in six degrees of freedom (DOF): east-west, north-south, vertically, and rotations about those three axes. While the 10-story testing plan did not utilize the three rotational degrees of freedom, the shake table may have inherently produced some rotations due to the large overturning moment from the shaking of the building. The size of the shake table did not change during the upgrade. With the upgrades the bare table can reach peak accelerations of 5.9g, 4.6g, and 4.7g in the east-west, north-south, and vertical DOFs respectively. With a 1,100 kip rigid centered payload the table can reach peak accelerations of 1.6g, 1.2g, and 2.0g in the east-west, north-south, and vertical DOFs respectively. The table has stroke lengths of +/- 35 inches, 15 inches, and 5 inches in the east-west, north-south, and vertical DOFs respectively. The vertical payload capacity of the upgraded table is 4,500 kips [Van Den Einde et al., 2021].

7.2 Testing program

Due to the magnitude of this project, the test specimen was used for additional pay-load projects after the completion of the testing discussed in this chapter (referred to as phase 1). For each pay-load project, the specimen was modified and tested again. This resulted in more economical testing phases and allowed for more scientific studies to come out of this ground breaking project and one of a kind test-specimen. Because the testing described within was for phase 1, the building could not be tested until collapse and the major structural components of the building, including the lateral system, could not be significantly damaged. Keeping this in mind, the performance of the test specimen was investigated using ground

motions at five of the seven hazard levels discussed in Section 6.3: 43-year return period, 225-year return period, 475-year return period, 975-year return period, and MCE_R. The largest two hazard levels - 2475-year return period and 4975-year return period - were not tested and limited tests were completed at MCE_R to keep damage minimal.

The ground motions selected for testing on the shake table were chosen from the design suites of ground motions summarized in Tables 6.11 and 6.12, with the exception of the 43-year return period motions which are discussed in the following paragraph. Table 7.1 summarizes the ground motions selected and used for testing and Figure 7.1 shows the target response spectra for each ground motion (keeping in mind that there is some error in ground motion execution with the shake table). Tables 6.11 and 6.12 can be referenced for more details regarding the exact records used. Note, Table 7.1 includes the target vertical scale factors which are discussed in detail in Section 7.2.1. As shown, at each hazard level at least one ground motion from each earthquake source type was selected. In general, the ground motions with predicted response near the suite mean response from the OpenSees model at each hazard level were selected. However, as discussed in Section 6.6, the capacities of the rocking walls in combined axial compression and bending and the splice connections in the rocking walls were critical at the MCE_R design criteria. Thus, at MCE_R smaller motions in the suite were selected to ensure predicted wall demands from the OpenSees model did not exceed calculated wall and splice capacity.

Table 7.1 shows the directions for which the table was tuned, where X is the east-west direction, Y is the north-south direction, and Z is the vertical direction. Shake table tuning is an iterative process completed by the shake table facility to determine the acceleration parameters needed to input such that the shake table produces a ground motion near the target acceleration time history, accounting for the for and moment feedback from the response of the building. As shown, at the 475-year return period, 975-year return period, and at MCE_R, the interface motions were only tuned for the X direction. This is because the interface motions have large ground displacements and the shake table has a smaller stroke capacity in the Y direction so the shake table was not able to execute these ground

Table 7.1: Ground motions selected for shake table testing

Hazard Level	Tuned Directions	EQ Source	Event Name	Suite #	Target Scale Factor Horiz.	Vert.
43	XYZ	Crustal	Niigata, Japan	3[a]	0.246	0.246
	XYZ	Interface	Tohoku	6[a]	0.253	0.075
	XYZ	Intraslab	Ferndale	11[a]	0.525	0.525
225	XYZ	Crustal	Niigata, Japan	3	0.790	0.790
	XYZ	Interface	Tohoku	6	0.812	0.240[b]
	XYZ	Intraslab	Ferndale	11	1.684	1.684
475	XYZ	Crustal	Chi-Chi	3	4.323	1.400
	X	Interface	Tohoku	6	1.215	-
	XYZ	Intraslab	Ferndale	11	2.524	2.524
975	XYZ	Crustal	Victoria, Mexico	2	4.999	4.000
	XYZ	Crustal	Northridge-01	4	3.931	3.931
	X	Interface	Tohoku	5	1.696	-
	X	Interface	Tokachi	6	3.462	-
	XYZ	Intraslab	Ferndale2	11	3.356	1.257
MCE_R	XYZ	Crustal	Loma Prieta	5	3.957	1.720[b]
	X	Interface	Tohoku	7	2.298	-
	XYZ	Intraslab	Ferndale2	11	4.538	2.250

[a]Ground motion not taken from design suite, instead scaled down from 225-year hazard.

[b]Vertical scale factor limited by table stroke capacity.

motions in the Y direction at the larger hazard levels. The stroke limitations as well as the oil capacities of the shake table had to be considered in the selection of these ground motions. As mentioned, the 43-year return period motions used for testing were not taken from the 43-year return period design suite. This is because these ground motions were too small for the shake table facility to successfully tune on the shake table. Thus, the suite of 225-year return period motions were scaled down to match the 43-year return period target design spectra.

Testing for phase 1 consisted of both ground motion tests and white noise tests. The ground motion tests were records taken from Table 7.1 and executed in either the X direction only, the Y direction only, the X and Y directions, or the X, Y, and Z directions. The white

noise tests were executed in either the X direction or the Y direction and consisted of small ambient-sized ground motion accelerations, used to obtain the natural elastic period of the building. Generally, a white noise test in the X direction and the Y direction were run at the beginning and end of each day and between some ground motion tests. White noise tests were run between ground motion tests when new ground motion records were run and there was potential for damage to the structure or the nonstructural elements. Appendix C summarizes the full testing plan for phase 1. For the purposes of this document, the official phase 1 tests spanned 12 days and consisted of 59 ground motion tests and 70 white noise tests. However, as discussed in more detail in Appendix C, there were some additional tests where instrumentation data was not properly collected. Including the unofficial tests, a total of 99 ground motion tests and 115 white noise tests were completed over a span of 19 days during phase 1 of testing. In general, the ground motions tests were completed such that they gradually increased in hazard level throughout the testing plan.

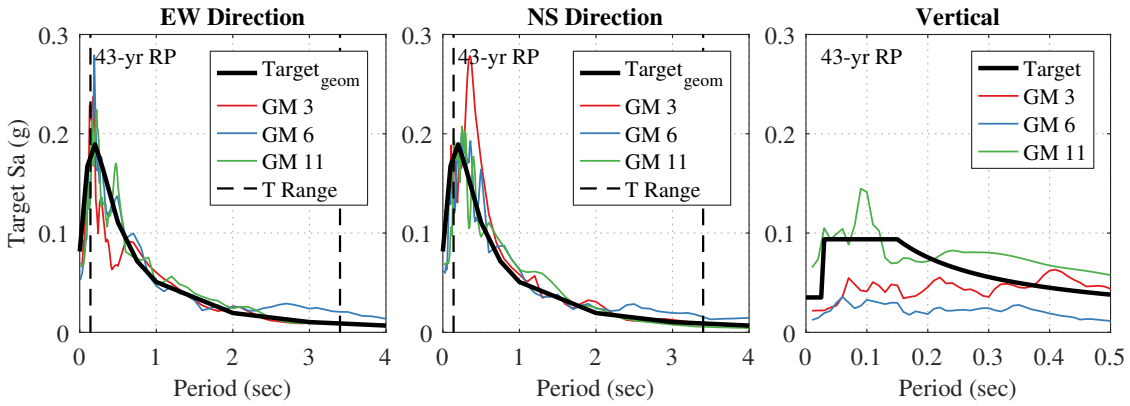

(a) 43-year return period

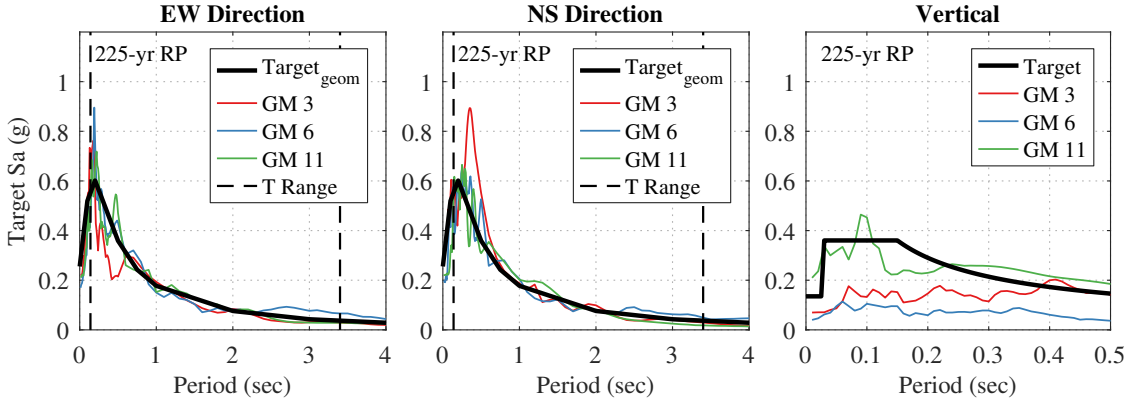

(b) 225-year return period

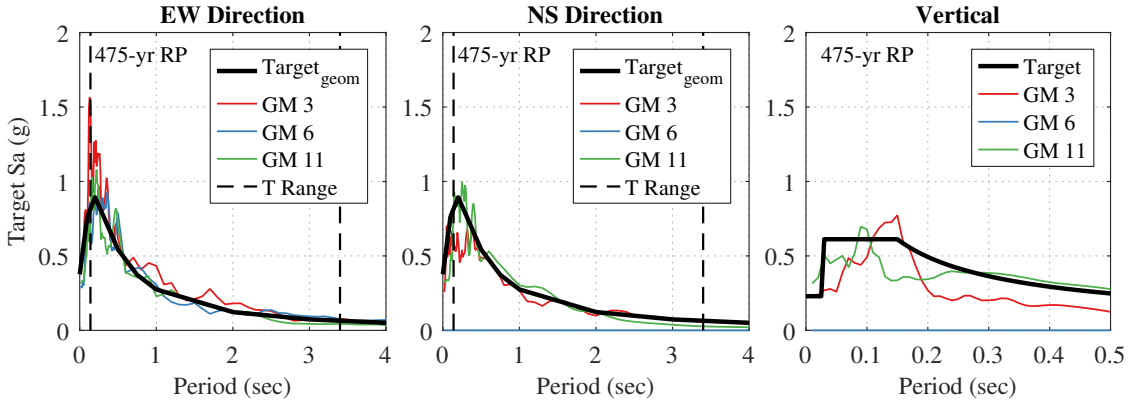

(c) 475-year return period

Figure 7.1: Target response spectra for the ground motions used for shake table testing

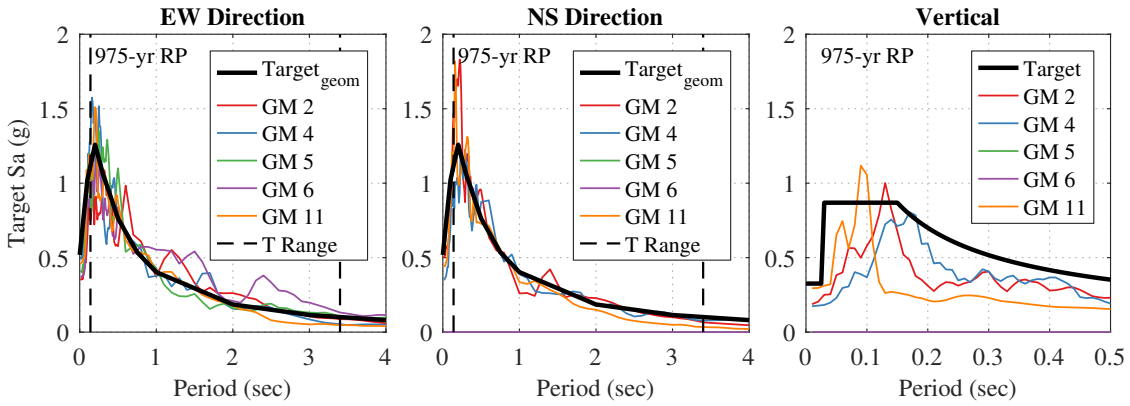

(d) 975-year return period

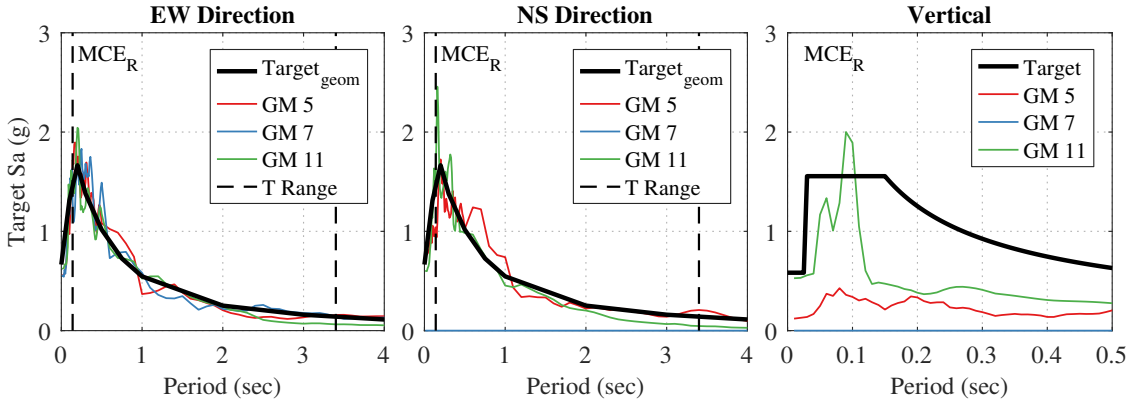

(e) MCE$_R$

Figure 7.1: Target response spectra for the ground motions used for shake table testing

7.2.1 Vertical Ground Motion Scaling

The 10-story NHERI TallWood specimen was tested under vertical ground motion excitations in some cases. While the response of the lateral system to vertical excitations is not within the scope of the work presented here, scaling the vertical ground motions fell within the overall ground motion selection, scaling, and testing plan development and are thus presented here.

The procedure outlined in Section 11.9 of ASCE/SEI 7-16 was used to develop the target vertical response spectra for the MCE_R hazard curve. ASCE/SEI 7-16 does not include a procedure for developing a target vertical response spectra curves for the other hazard levels used in this test and limited literature exists for developing them. Thus, the procedure outlined in Section 11.9 of ASCE/SEI 7-16 was modified and adopted for the remaining hazard levels using engineering judgement. At MCE_R the curve is developed based on, S_{MS} (referred to in this section as the spectral parameter), S_s, and the site class. For the other hazard levels, the spectral acceleration of the target horizontal hazard curve at 0.1 seconds was used in lieu of the MCE_R spectral parameter, S_{MS}. This value can be found in Table 6.10. This spectral parameter was then divided by F_a and this value was used in lieu of S_S which was used for the MCE_R procedure. Values for the resulting target vertical response spectra curves, S_{av} are shown in Table 7.2 and visually in Figure 7.1.

The vertical ground motion components were not initially considered during ground motion selection and scaling since they were not used during the design phase. As a result, the spectral shape of the vertical spectra do not match the shape of the target spectra as well as the horizontal components. Vertical ground motion components were only collected for the suite of ground motions selected for testing and were scaled independently of the horizontal components. Because full vertical ground motion suites were not collected, each vertical ground motion scale factor was scaled on an individual basis to roughly match the target spectra as opposed to looking at suite mean and matching that to the target spectra. When selecting the vertical scale factor for each ground motion, a maximum limit equal to the horizontal scale factor was set. The resulting vertical scale factors for each ground motion are

Table 7.2: Tabulated target vertical response spectra for the different earthquake hazards used for testing of the 10-story building

	Hazard Level				
	43-yr RP	225-yr PR	475-yr RP	975-yr RP	MCE_R
Spectral Parameter (g)	0.167	0.520	0.764	1.022	1.654
Cv	0.700	0.889	1.009	1.063	1.176
T (sec)			S_{av} (g)		
0	0.029	0.115	0.193	0.272	0.486
0.025	0.029	0.115	0.193	0.272	0.486
0.03	0.047	0.185	0.308	0.434	0.778
0.04	0.070	0.277	0.462	0.652	1.167
0.05	0.094	0.369	0.616	0.869	1.556
0.1	0.094	0.369	0.616	0.869	1.556
0.15	0.094	0.369	0.616	0.869	1.556
0.2	0.076	0.298	0.497	0.700	1.254
0.25	0.064	0.252	0.420	0.592	1.061
0.3	0.056	0.220	0.367	0.517	0.925
0.35	0.050	0.196	0.327	0.460	0.824
0.4	0.045	0.177	0.295	0.416	0.745
0.45	0.041	0.162	0.270	0.381	0.682
0.5	0.038	0.150	0.250	0.352	0.631

included in Table 7.1. Additionally, the vertical scale factors of some ground motions were limited by the stroke capacity of the shake table (as noted in Table 7.1). Vertical response of the building with a focus on the floor systems can be found in Wright [2023].

7.3 Visual Experimental Observations

The post-tensioned rocking wall lateral system saw very little damage during phase 1 of testing. As discussed in Chapter 6, which details the design of the post-tensioned rocking wall lateral system and the connections, the lateral system and the lateral connections were designed to remain mostly elastic through MCE_R level ground motions. The only deformation-controlled actions that the structure was designed for at MCE_R demands were:

(1) allowing inelastic behavior at the base of the wall panels and (2) yielding of the UFPs. The remainder of the lateral system, including the PT bars, was designed to remain elastic. The lateral system achieved and surpassed the performance objectives for which it was designed. Note, drift performance will be discussed in Section 7.8. This section will summarize the observed visual damage to the lateral system.

While strains beyond yield were allowed at the base of the post-tensioned rocking walls during design, no visual damage to the base of the wall panels was observed. Full inspections at the base of the walls were challenging due to the presence of the armor plates around the corners of the wall panels, however, gaps between the foundation and the base of the armor plates (see Figure 7.2) were present at the beginning of testing due to construction tolerances and the gaps did not appear to close during the duration of phase 1 testing. Instrumentation data measuring wall uplift and compressive deformation at the base of the wall panels should be processed to confirm that no permanent deformation (that could not be identified visually) in the form of yielding, splitting, or crushing occurred at the base of the wall panels.

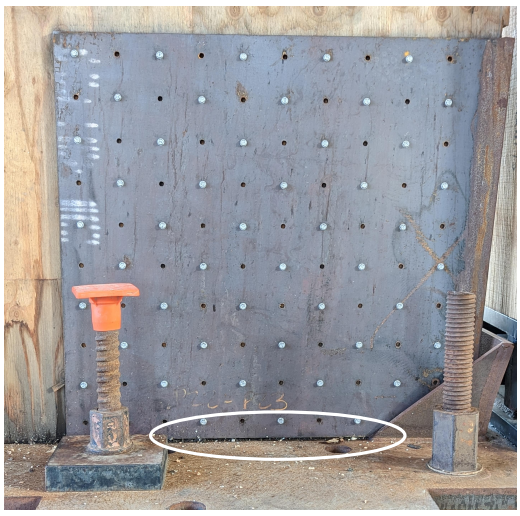

Figure 7.2: Gap between wall armor and foundation beam at the base of the post-tensioned rocking walls

The UFP damping elements were also designed to yield during testing. While instrumentation measuring UFP deformations have not yet been processed, video footage of the UFPs during testing show significant deformations during testing, as designed. While the UFPs most likely yielded early during the testing sequence, no damage was observed on the UFPs at any point during testing and they appeared to work through the many ground motions. Additionally, the bolted connection design also appeared to be undamaged.

As mentioned, observed visual damage to the post-tensioned rocking wall lateral system was minimal. Figure 7.3 shows two minor instances of damage seen during testing. Figure 7.3a shows damage to the Teflon lining inside the shear key cutout in the post-tensioned rocking wall. This is likely due to construction debris at the interface. This type of damage was observed at only two or three out of the forty total shear key locations. Figure 7.3b shows the dowels in the UFP pi plate connections. These connections were used on the wall panels and the boundary columns. As shown by the figure, some of the dowels started to work their way out of the holes during testing. This is likely due to the high number of cycles, that far exceeds what any real building would experience. Once the issue was observed, they were monitored during inspections and were pounded back into place when they started to come out. Note, both these examples of damage are minimal and were not expected to affect the overall performance significantly.

The other form of visual damage observed on the lateral system was sun damage to un-protected mass timber elements. Figure 7.4 shows photos of the CLT, MPP, and LVL material at the beginning of construction, compared to at the beginning of shake table testing. Note, this damage is not a result of earthquake loading, but has been documented for future reference. Figures 7.4d-f are all photos of the mass timber elements at the roof which had high exposure to direct sunlight and rain for many months. In comparison to the pre-construction photos (Figure 7.4a-c), the exposed mass timber shows a lot of cracks and separations of the timber plys. Exterior structural elements showed more of this type of damage than interior components. When mass timber is used in a real building, contractors typically protect the elements using UV resistant or plastic coatings.

(a) (b)

Figure 7.3: Examples of the minimal visual damage observed during phase 1 of testing (a) Teflon damage at the shear key locations and (b) dowels at the UFP connections

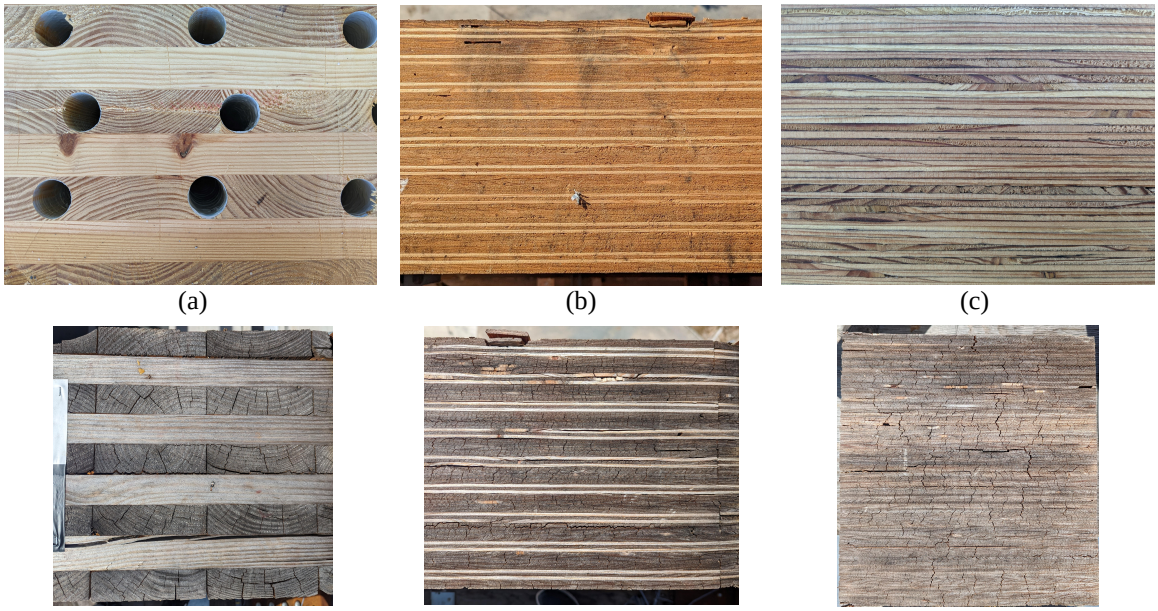

(a) (b) (c)

(d) (e) (f)

Figure 7.4: Mass timber before construction for (a) CLT, (b) MPP, and (c) LVL and weather damaged mass timber at the start of testing for (d) CLT, (e) MPP, and (f) LVL

7.4 Ground motion subset for data processing

As mentioned, this document includes only a short preliminary analysis of the performance, discussion of the experimental results, and comparison to the analytical results. A small subset of the data was processed, including 17 ground motion tests. All 17 of the ground motions were selected from the official phase 1 testing subset when the DAQ was properly collecting data. In this study, one ground motion test of each ground motion listed in Table 7.1 was selected from the full testing plan listed in Table 4.4. The ground motion tests selected for this analysis are shown in Table 7.3. The table includes the test ID that can be tracked back to the testing schedule. Note from the direction column, ground motion tests that excluded the vertical component were selected when possible. This is because the effects of vertical excitations was outside of the scope of this work and the nonlinear OpenSees model also did not include vertical excitations. Full three component ground motion tests were only chosen for analysis when a two component test was not run.

Figure 7.5 shows the spectral accelerations computed using the recorded shake table acceleration histories for the ground motion tests analyzed. These spectral accelerations can be compared to the target spectral acceleration shown in Figure 7.1. Note, the vertical excitations shown in the target spectra were not always used in the ground motion tests selected for analysis. Table 7.3 notes the ratio of achieved to target spectral acceleration (S_a) ratios at the building's approximate period. For the horizontal components a period of 1.74 seconds from the OpenSees model is used. For the vertical component, a period of 0.05 seconds was assumed based on the approximate first mode period of the diaphragms that have frequencies in the range of 10 to 35 Hz [Wright, 2023]. Additionally, Table 7.3 notes the ratio of effective to target scale factors in each direction. These were calculated for each ground motion component by dividing the response spectra of the effective ground motion executed by the shake table by the response spectra of the target ground motion used in design and then finding the average ratio over a specified period range. The period range used for the horizontal components was equal to the range used for horizontal ground

Table 7.3: Ground motions selected for experimental and analytical results comparison

Test ID	Dir.	EQ Source	Event Name	Suite #	Achieved/Target Sa at Period			Achieved/Target Scale Factor		
					X	Y	Z	X	Y	Z
43-09	XY	Crustal	Niigata, Japan	3	1.05	1.13	-	1.03	1.04	-
43-06	XY	Interface	Tohoku	6	1.07	1.04	-	0.96	1.00	-
43-03	XY	Intraslab	Ferndale	11	1.04	1.08	-	1.00	1.06	-
225-10	XY	Crustal	Niigata, Japan	3	1.02	1.06	-	1.08	1.06	-
225-07	XY	Interface	Tohoku	6	1.02	1.04	-	1.08	1.09	-
225-04	XY	Intraslab	Ferndale	11	0.96	1.01	-	1.00	1.10	-
475-01	XY	Crustal	Chi-Chi	3	0.98	0.96	-	1.15	1.04	-
475-08	X	Interface	Tohoku	6	0.88	-	-	1.03	-	-
475-06	XY	Intraslab	Ferndale	11	0.95	1.00	-	1.00	1.12	-
975-11	XYZ	Crustal	Victoria, Mexico	2	0.95	0.94	1.54	1.09	1.07	1.91
975-03	XY	Crustal	Northridge-01	4	0.97	1.00	-	0.98	1.12	-
975-04	X	Interface	Tohoku	5	0.88	-	-	1.05	-	-
975-10	X	Interface	Tokachi	6	0.86	-	-	0.98	-	-
975-07	XY	Intraslab	Ferndale2	11	0.98	0.98	-	1.03	1.10	-
MCER-01	XYZ	Crustal	Loma Prieta	5	0.91	0.96	1.32	0.98	1.03	1.74
MCER-03	X	Interface	Tohoku	7	0.88	-	-	1.08	-	-
MCER-02	XYZ	Intraslab	Ferndale2	11	0.98	0.99	1.35	1.04	1.10	1.37

motion scaling, specified in Section 6.4.1. The period range used for the vertical components was 0.01 seconds to 0.1 seconds. The ratio values for the horizontal components are all near 1.0 indicating that the shake table replicated the target ground motion with relatively good precision in the horizontal direction. In general the scale factor ratios were slightly larger than 1.0 and the ratios of S_a at the building's period were generally slightly less than 1.0, especially at larger hazard levels. In the vertical direction, the the scale factor ratios and the S_a at the building's period ratios were consistently and significantly greater than 1.0 meaning the shake table did not replicate the vertical ground motion components as accurately as the horizontal components.

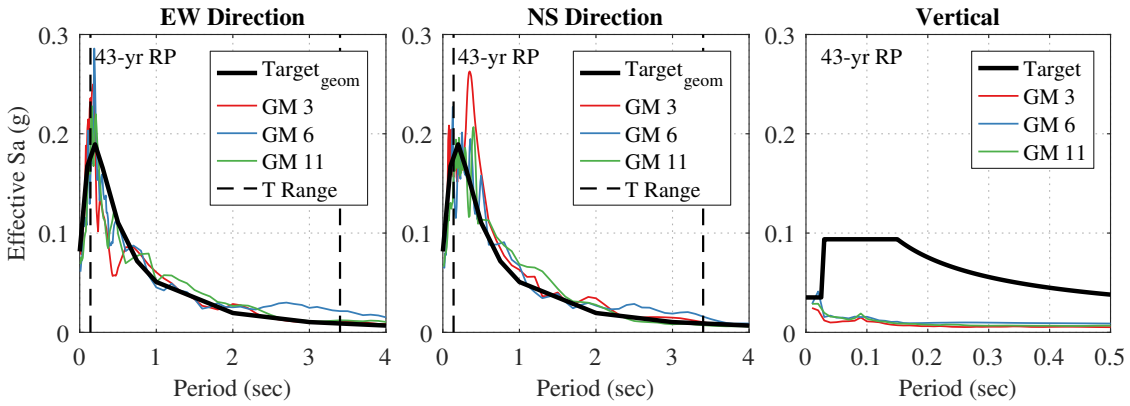

(a) 43-year return period

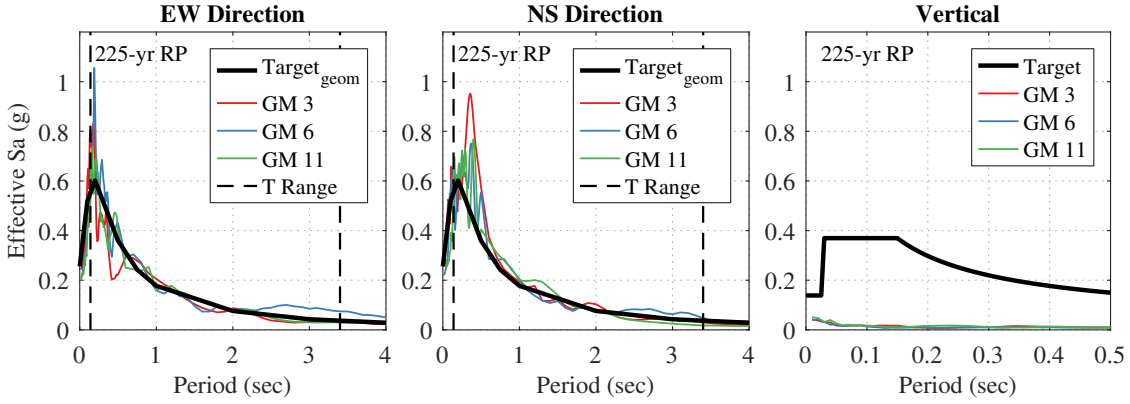

(b) 225-year return period

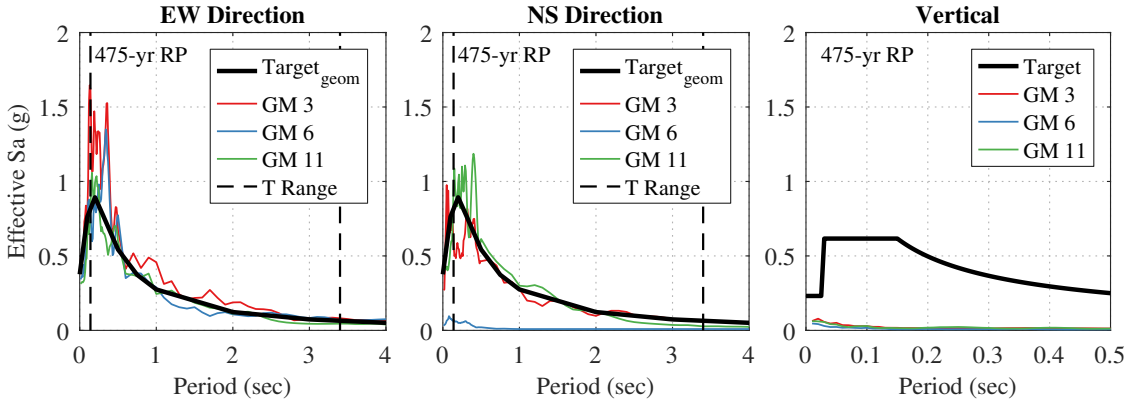

(c) 475-year return period

Figure 7.5: Response spectra for effective executed ground motions

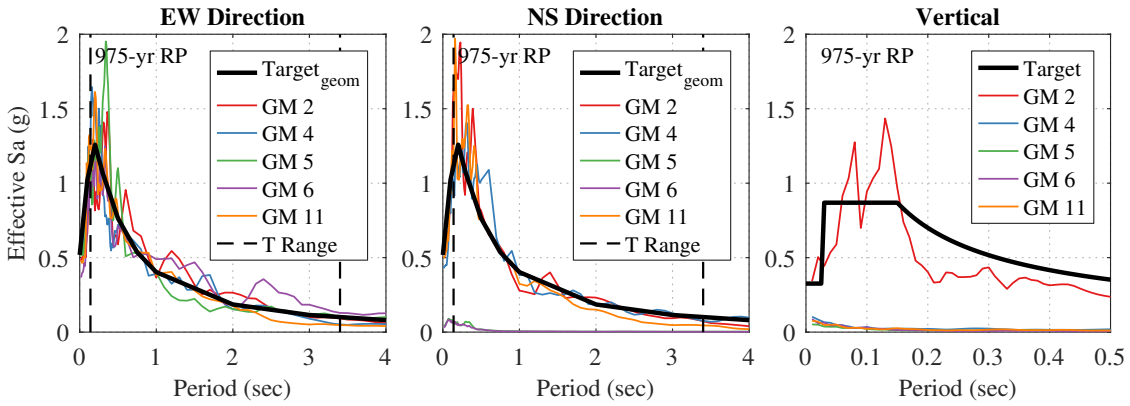

(d) 975-year return period

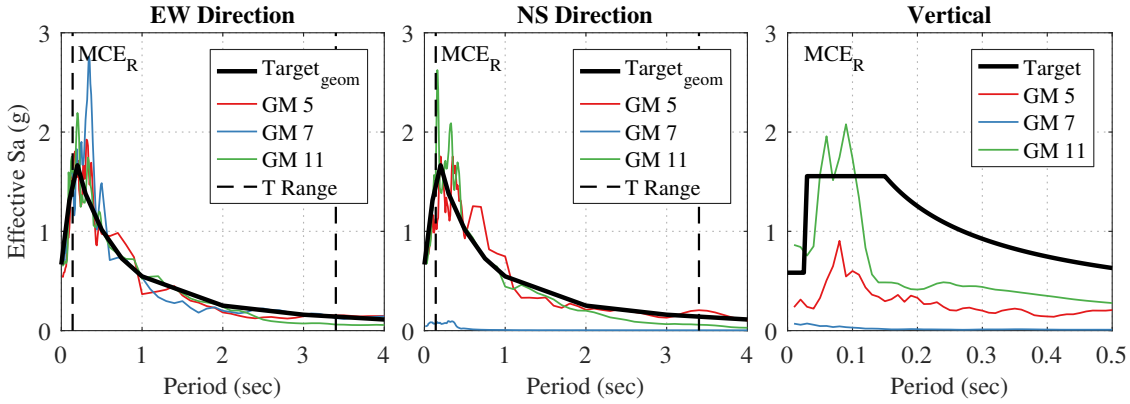

(e) MCE$_R$

Figure 7.5: Response spectra for effective executed ground motions

7.5 Instrumentation

The primary instrumentation plan for the 10-story shake table tests consisted of 733 instruments; a combination of MEMS-based accelerometers, linear displacement transducers, string potentiometer displacement transducers, inclinometers, strain gauges, and load cells. These instruments were connected to the primary data acquisition (DAQ) system at the LHPOST6 facility. The DAQ system consisted of 13 nodes, each with 64 channels, and was newly installed with the recent facility upgrade. This DAQ, along with a series of video cameras, were time synced to the shake table controller. Data was recorded and stored at a frequency of 256 Hz. Busch [2023] can be referenced for detailed documentation of the primary instrumentation plan. Additional instruments for data collection including GPS sensors, highly-sensitive ambient vibration sensors, and a variety of video-image tracking devices were also used during testing by project collaborators.

In this document, the response of the building was characterized using a small subset of the instrumentation. This included horizontal accelerometers located on the floor diaphragms, horizontal string potentiometers on the lower floors that measured global displacements, diagonal string potentiometers that measured interstory displacements, and linear potentiometers at the wall bases that measured uplift. This section contains a brief overview of these instruments. Busch [2023] contains descriptions and drawings of the full instrumentation plan.

7.5.1 Horizontal Floor Accelerometers and Horizontal String Potentiometers

To measure global building accelerations and displacements, horizontal accelerometers were added at various locations on each floor (summarized in Figure 7.6a). On every floor an accelerometer measuring east-west (EW) and north-south (NS) accelerations were placed at the approximate center-of-mass location (determined as discussed in Section 6.2.4), as well as one or two additional locations on each floor (specified as shown in Figure 7.6a). Also shown in Figure 7.6a, horizontal string potentiometers (SP) on lower floors directly measured

global floor displacements. These potentiometers spanned horizontally from the diaphragm edges to stationary safety towers located off the table. These string potentiometers were only located on the lower floors (floors 2-4 on the south edge and floors 2-3 on the east edge) because the safety towers were significantly shorter than the test specimen (see the red safety towers located on the south side of the building in Figure 6.1a).

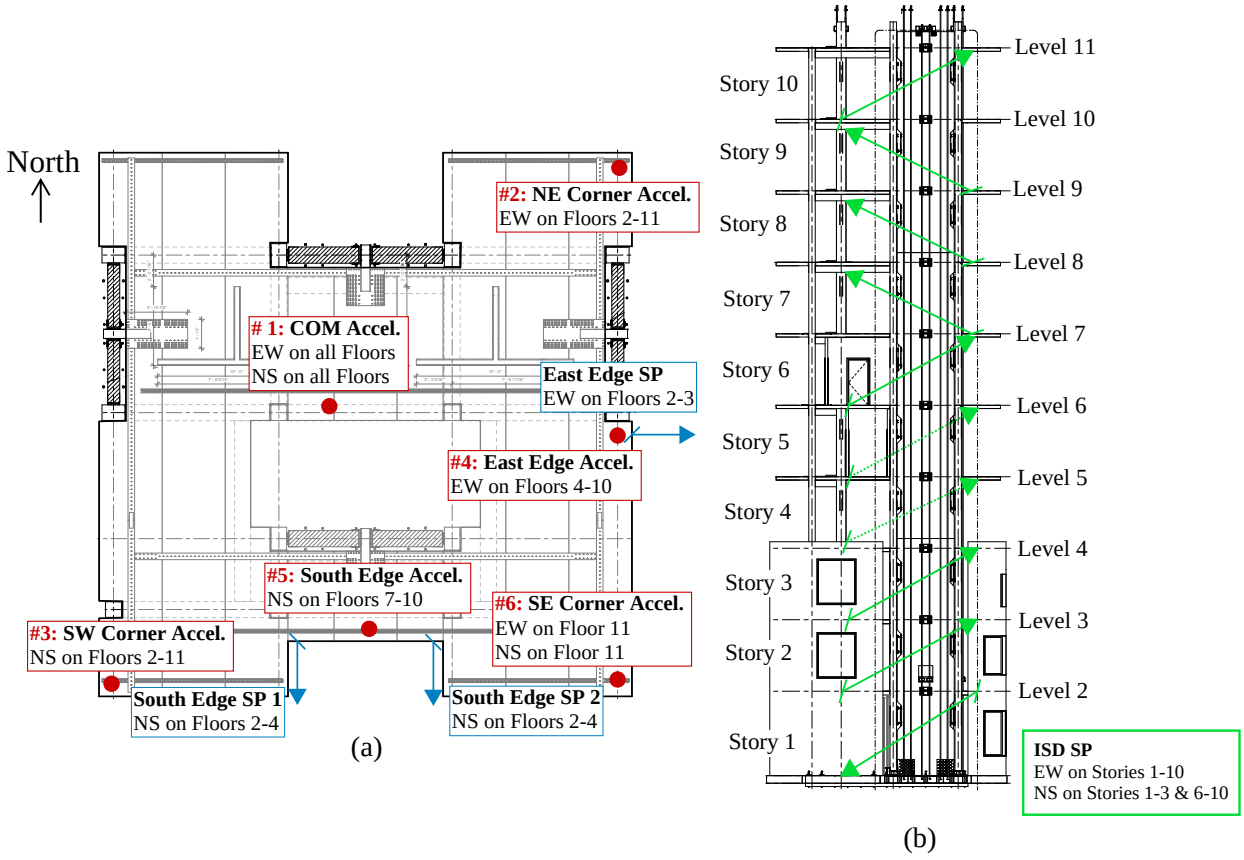

Figure 7.6: Global displacement instrumentation schematics (a) horizontal floor accelerometers (accel.) and horizontal string potentiometers locations and (b) diagonal ISD string potentiometer locations

7.5.2 Diagonal String Potentiometers

Shown by the schematic in Figure 7.6b, diagonal string potentiometers were installed on most floors to measure interstory displacements. These were installed on every story on the north face of the building to measure displacements in the east-west direction. To measure story displacements in the north-south direction, diagonal string potentiometers were installed on the east face. They were installed on all stories except Stories 4 and 5 because of interference with nonstructural walls. Note, the arrows shown in Figure 7.6b are only schematic. Orientations and exact install locations varied from floor to floor. Table 7.4 summarizes the installed locations of the diagonal string potentiometers. x_o, y_o, and z_o are the coordinates of the installed string potentiometer of the origin (i.e., the start of the string). x_t, y_t, and z_t are the coordinates of the installed string potentiometers of the target (i.e., the end of the string). In the table, the locations are measured relative to an origin located at the center of the most north-west column (same origin as shown in Figure 6.2a). The positive x direction is east, the positive y direction is north, and the positive z direction is up. All locations in the table are rounded to the nearest quarter inch and any small out-of-plane offsets between the origin and target were considered negligible for data processing in this document and are thus omitted from the table.

Recordings from the diagonal string potentiometers were used to calculate horizontal interstory displacements. This was done by assuming negligible vertical diaphragm movement (i.e., the vertical z distance was constant). For the east-west string potentiometers, the horizontal story displacement, Δx, was calculated by subtracting the x-component of the initial string potentiometer length, x_i, from the x-component of the string potentiometer length at any point during the ground motion, x_f, as shown in Equation 7.1. x_i was calculated as shown in Equation 7.2. x_f was calculated as shown in Equation 7.3, where z_i is the z-component of the initial string potentiometer length that is assumed to remain constant throughout the motion (calculated using Equation 7.4), l_o is the initial length of the string potentiometer (calculated using Equation 7.5), and Δ is the length change recorded by the

Table 7.4: Diagonal string potentiometer locations

Story	EW Measurement Direction						NS Measurement Direction					
	Origin (in)			Target (in)			Origin (in)			Target (in)		
	x_o	y_o	z_o	x_t	y_t	z_t	x_o	y_o	z_o	x_t	y_t	z_t
1	315.5	-	21	1	-	161.5	-	43.75	20.75	-	-270	149
2	25.75	-	174.75	384	-	293.5	-	-266.75	174.5	-	0.25	281
3	358.5	-	306.5	0	-	425.25	-	-2.75	306.25	-	-269.75	413.25
4	18.75	-	438.25	384	-	557.75	-	-	-	-	-	-
5	357.25	-	570.25	-0.25	-	690	-	-	-	-	-	-
6	27	-	702.5	387	-	822	-	-267.75	702.5	-	-0.25	809.75
7	357.25	-	831.75	0	-	953.5	-	-1.25	824.5	-	-270.25	942
8	27.5	-	966.5	386.5	-	1085.5	-	-266.25	966.5	-	-0.5	1073.5
9	359	-	1098.5	-3.75	-	1217.25	-	-3.25	1098.5	-	-270.25	1205.5
10	25.75	-	1230.25	385.75	-	1349.25	-	-266	1230.5	-	0	1337.25

string potentiometer. In the north-south direction, an equivalent procedure was used.

$$\Delta x = x_f - x_i \tag{7.1}$$

$$x_i = x_t - x_o \tag{7.2}$$

$$x_f = \sqrt{(l_o + \Delta)^2 - z_i} \tag{7.3}$$

$$z_i = z_t - z_o \tag{7.4}$$

$$l_o = \sqrt{x_i^2 + z_i^2} \tag{7.5}$$

7.5.3 Wall Uplift Linear Potentiometers

Linear potentiometers were installed vertically at the base of the walls to measure rocking wall uplift and compression at the base of the wall panel. As shown in Figure 7.7a, the lower end of the linear potentiometer was anchored to the foundation beam. The other end of the linear potentiometer was anchored to the face of the wall panel. Figure 7.7b shows a plan view schematic of the building with relative locations and instrument ID #s of all of the

linear potentiometers. In this figure the rocking walls are enlarged for clarity. As shown, each wall panel had a linear potentiometer at each of the four corners. One face of the north and west walls had four additional linear pots along the face to measure the distribution of uplift. On these faces, the linear pots were more concentrated towards the corners as this is where damage was expected. To avoid interference with foundation to shake table PT bars, the exact location of each installed linear potentiometer varied wall-to-wall. The exact location of each linear potentiometer is provided in Table 7.5. As shown in Figure 7.7b, d_i is the distance from the nearest wall edge to the linear potentiometer location. This distance is measured from the edge of the full panel width, not from the edge of the tapered wall section.

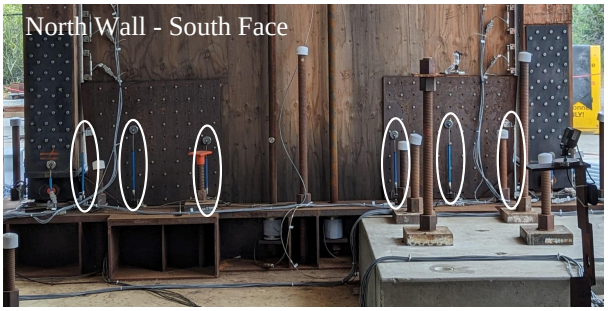

(a)

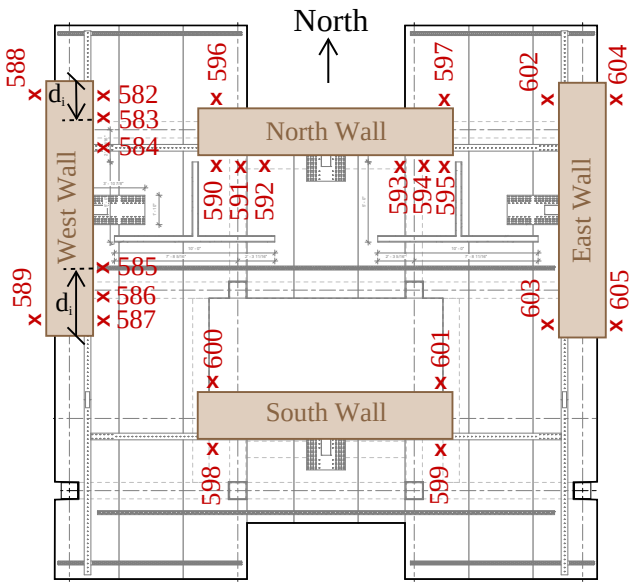

(b)

Figure 7.7: Linear potentiometers measuring wall uplift (a) example photo of instruments and (b) schematic showing locations of all wall uplift linear potentiometers

Table 7.5: Wall base uplift linear potentiometer locations

North Wall		South Wall		East Wall		West Wall	
ID #	d_i (in)	ID #	d_i (in)	ID #	d_i (in)	ID #	d_i (in)
596	2.5	598	2.75	602	2.25	588	2
590	2.25	600	11.25	604	3.75	582	3.25
591	13	-	-	-	-	583	17.25
592	26.875	-	-	-	-	584	30.875
593	26.5	-	-	-	-	585	30.25
594	14.25	-	-	-	-	586	12.75
595	2.375	599	4.25	603	2.25	589	5.75
597	2	601	2.25	605	2.25	587	2.25

7.6 Accelerometer Data Processing

This section will discuss the procedures used for processing the recorded acceleration data. First, the filtering and double integration procedure used to convert the acceleration recordings to displacements will be presented, followed by a validation of the procedure. Then, the selection process for which accelerometer instruments were used for data processing will be discussed.

7.6.1 Accelerometer Data Filtering Procedure and Validation

The recorded accelerometer signals on each floor were filtered and double integrated to get floor displacements. As discussed, string potentiometers measuring global displacements on floors 2, 3, and 4 were used for validation of the filtering and double integration techniques used. The following procedure was implemented in Matlab for filtering and double integrating the accelerometer signals to obtain displacement time history data:

1. Load raw acceleration signal.
2. Zero accelerometer signal by taking the average of the first 100 data points (equivalent to approximately 0.4 seconds) and subtracting that from the signal.

3. Add 1 second of zeros to beginning and end of signal to help with filtering.
4. Apply a Butterworth bandpass filter to the acceleration signal.
5. Integrate the acceleration signal using the cumulative trapezoid rule to get velocity.
6. Apply a Butterworth bandpass filter to the velocity signal.
7. Integration the velocity signal using the cumulative trapezoid rule to get displacement.
8. Apply a Butterworth bandpass filter to the displacement signal.
9. Remove the added 1 second of zeros at the beginning and end of the signal.

In the procedure above, the same Butterworth bandpass filter was used in steps 4, 6, and 8. The filter was created using the Butterworth filter design in Matlab. A filter order of 2n where n was equal to 4 was used. The lower and upper cutoff frequencies were 0.1 and 50 Hz, respectively. Note, this procedure cannot be used to assess residual drifts.

The presented filtering and double integration method for determining displacement time histories from the accelerometer data was validated by comparing calculated results from the accelerometers to un-filtered, raw results recorded by the horizontal string potentiometers that directly measured absolute floor displacements on the lower levels. Figures 7.8, 7.9, and 7.10 show plots validating the procedure for three example tests (test ID indicated in Figure caption). While results for only three tests are provided here, similar trends were observed in the remaining tests. In each figure, plots comparing absolute floor displacement calculations and plots comparing interstory drift (ISD) calculations in both horizontal direction are shown. For this section ISDs are defined as the difference in floor displacements above and below a story, divided by the story height. For the absolute displacement plots, both the double integrated accelerometers and horizontal string potentiometers measured absolute displacements directly. For the ISD plots, drift values on each story were calculated by subtracting recordings of floor below from the recordings from the story above and then dividing by the total height of each story. Due to height limitations of the off-table safety towers, horizontal string potentiometers only measured absolute floor displacements on floors 2 and 3 for the east-west direction and floors 2-4 for the north-south direction. Thus, this

accelerometer filtering and integrating procedure validation could only be done for the lower levels. The location of the accelerometer used on each floor for these figures will be discussed in Section 7.6.2.

Absolute floor displacement results in Figures 7.8a, 7.9a, and 7.10a show that using the presented accelerometer filtering and double integration procedure results in floor displacement data that matches relatively well with the floor displacement data recorded directly from the horizontal string potentiometers. However, ISD results in these Figures 7.8b, 7.9b, and 7.10b show that ISDs calculated using the presented accelerometer filtering and double integration procedure do not match the ISDs calculated from the horizontal string potentiometers as well. When calculating ISD, two floor displacement recordings from the accelerometers are subtracted from each other. In doing so, an unexplainable, and likely erroneous, response appears in the time history data. This response is particularly clear in Figure 7.8b. In this figure, relatively large ISD data is visible at the very beginning of the ground motion when floor displacements are still very small (see the corresponding figure, Figure 7.8a). While these large oscillations are very clear at the beginning of the ground motion, they occur throughout.

The presence of this erroneous building ISD response from the integrated accelerometer data appears to be more dominant at smaller hazard levels (i.e., comparing the 43-year return period hazard motion response in Figure 7.8 with the MCE_R hazard motion response in Figure 7.10). This is likely because whatever is causing the erroneous response is a larger proportion of the total response for the smaller hazards. In other words, the true building response is likely masking the contributions of the erroneous response more at larger hazards compared to smaller hazards. The errors in accelerometer ISD calculations are also very prominent in the 1D tests. One example is test ID 975-10, shown in Figure 7.9. In this test, ISD values, calculated from the accelerometers recording in the direction of the building that was not shaking (north-south direction), were relatively very large. Figure 7.9a shows that the floor displacements on the lower levels are negligible in the north-south direction. However, Figure 7.9b shows that these negligible displacements result in sizable ISD values

which is not likely a real building response. While the author is not exactly sure the source of this erroneous response, it could be a result of multiple sources including: improper orientation installation of the accelerometer (i.e., the instrument was installed slightly rotated), improper wiring of the cables, a small phase shift of the recorded instruments, or an issue with the presented filtering and double integration procedure. Additionally, because the test specimen was so large and because the tests were conducted outdoors over a long period of time, the overall testing environment for the specimen was hard to control. Over the four week testing period, accelerometers could have been bumped and instrumentation wires could have been pulled by people walking around the test specimen. These factors could affect the quality of the recordings.

In summary, because the presented accelerometer filtering and double integration procedure resulted in floor displacements that matched closely with the horizontal string potentiometer results on the lower floors, the procedure and filtering range was assumed to be viable for all horizontal accelerometers in the building and on the upper floors. For some ground motions, ISD time history response calculated from the accelerometer data showed some unusual response with large peaks that were likely erroneous, especially for data from smaller hazard ground motion recordings. These issues occur when the response from one floor is subtracted from the other floor and are likely a result of the integration and filtering techniques used and/or improper installation of the instrument. Thus, while the author is confident in the floor displacement values calculated from the accelerometer data, the author is less confident with the ISD values calculated from the accelerometer data.

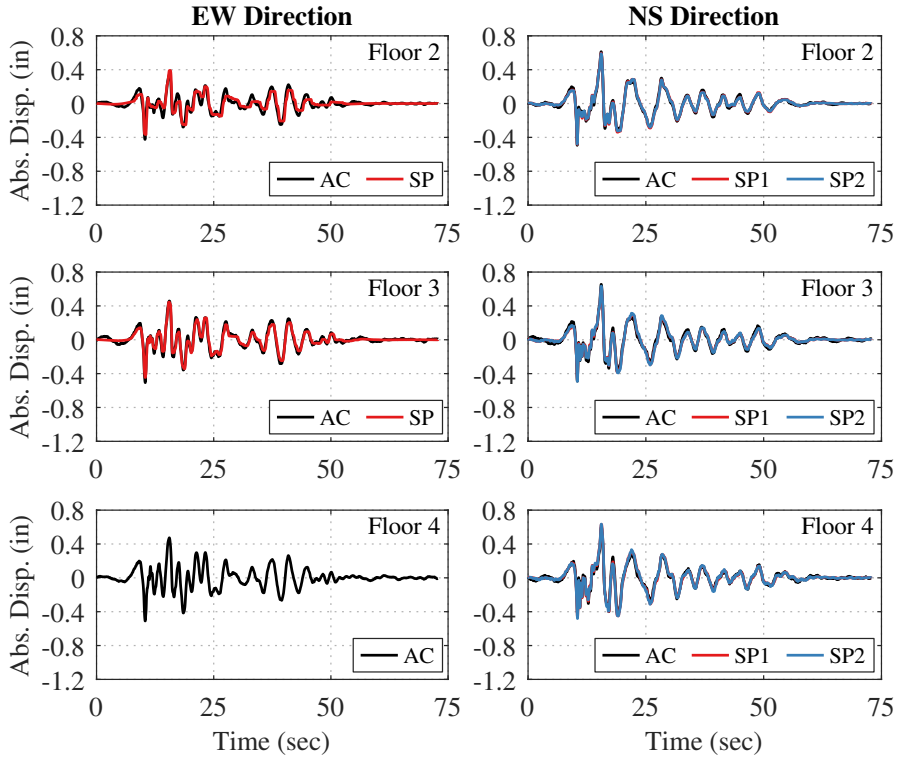

(a) Absolute floor displacement

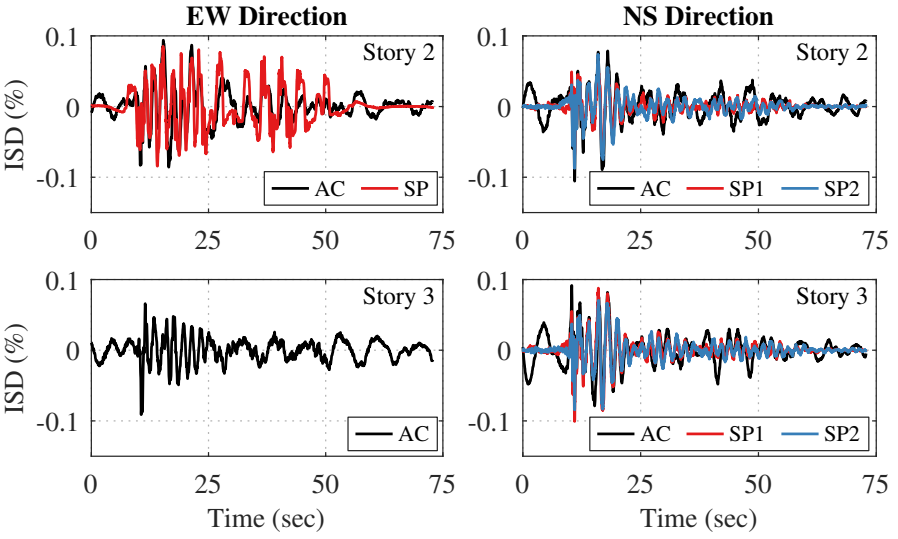

(b) ISD

Figure 7.8: Comparison of floor movement results calculated from accelerometer data and horizontal string potentiometers for test ID 43-09

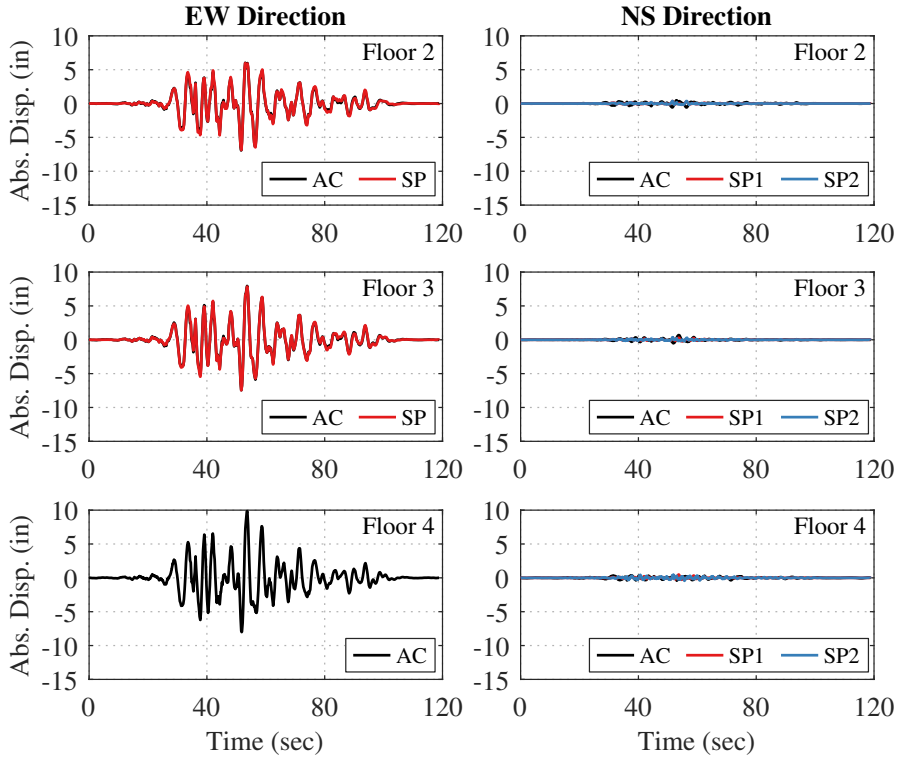

(a) Absolute floor displacement

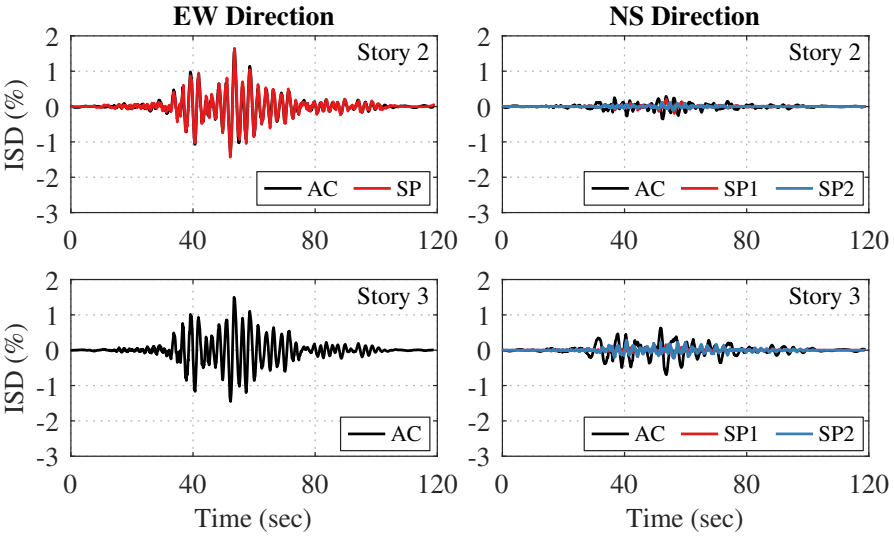

(b) ISD

Figure 7.9: Comparison of floor movement results calculated from accelerometer data and horizontal string potentiometers for test ID 975-10

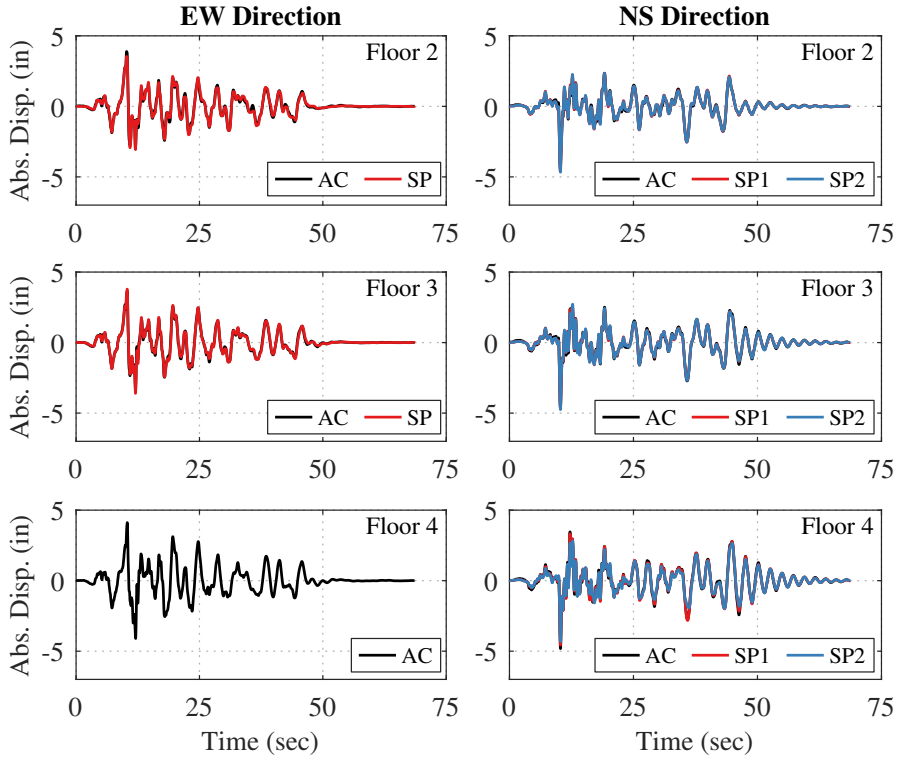

(a) Absolute floor displacement

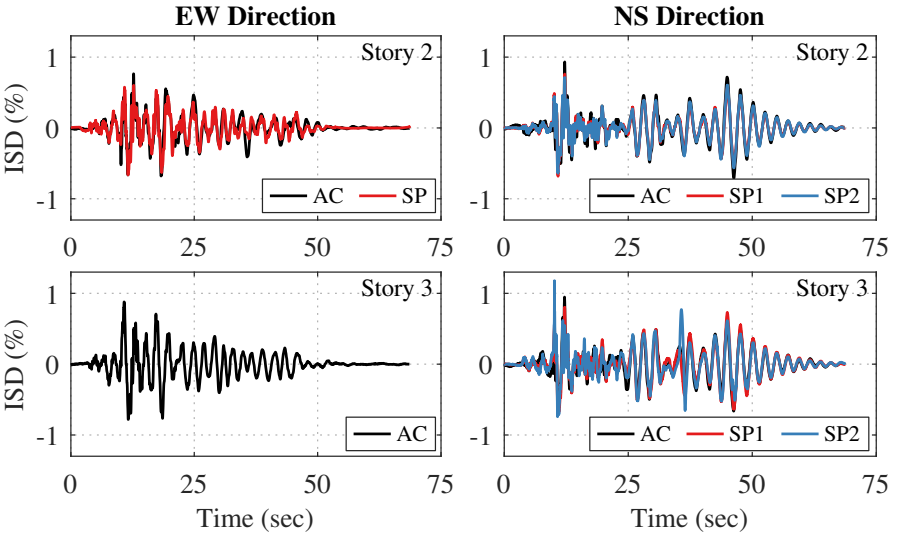

(b) ISD

Figure 7.10: Comparison of floor movement results calculated from accelerometer data and horizontal string potentiometers for test ID MCER-02

7.6.2 Accelerometer Selection for Data Processing

Ideally, the accelerometers located at the approximate center of mass (COM) location would be used for floor displacement and ISD data processing calculations. However, it was determined that some of the COM floor accelerometers did not record the most usable or reliable data. An example of this can be seen in Figure 7.11 which plots displacement data calculated from all accelerometers located on floor 6 from test ID 43-09. In the figure, each accelerometer location is labeled. Location #1 is the approximate center of mass location on each floor. Figure 7.6a can be reference for a schematic showing the locations of the remaining accelerometers. In Figure 7.11, the plot showing the displacement data from the accelerometers recording east-west motion (left plot), it is clear that the COM accelerometer (labeled as #1 in the plot) is showing recorded behavior that is likely erroneous. While there is probably some diaphragm torsion that would result in slightly different recordings from each accelerometer, the large oscillations from accelerometer #1 in the east-west direction plot differ significantly from the two other accelerometer readings and cannot be justified from torsion. Additionally, it was determined that if these instruments (with the relatively large oscillations) were used for ISD calculations, it would result in very large and unreasonable values. Thus, it was determined that this instrument, along with others, should not be used for data processing.

For each floor, plots similar to the ones shown in Figure 7.11 were examined and the accelerometer producing the most reliable data was selected for all data processing in this document. Table 7.6 summarizes the selected accelerometer location for each floor in each horizontal direction. Note, two different east-west accelerometers were used for floor 7 depending on the test ID, as specified by the table footnote. By using recordings from accelerometers located at different locations floor to floor, it is assumed that the torsional response of the building is negligible. This is likely a reasonable assumption as the building was symmetric and differences in accelerometer readings on the same floor are small. This can be seen in Figure 7.12, which shows displacement data calculated from all accelerometers

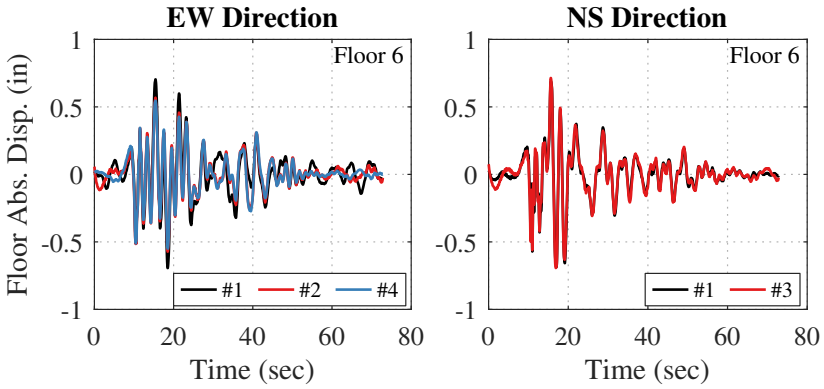

Figure 7.11: Absolute floor displacement recordings calculated from all accelerometers located on floor 6 (from test ID: 43-09)

located on four floors from a large ground motion (test ID MCER-01). As shown, the displacements from multiple accelerometers on the same floor are very similar, indicating small amounts of torsion. This process also assumes a rigid diaphragm. This is also a reasonable assumption because the floor spans in the test specimen were small.

Table 7.6: Accelerometer locations used for data processing of the 10-story data

Dir.	Floor										
	Ground	2	3	4	5	6	7	8	9	10	11
EW	1	1	2	4	1	4	2[a] or 4[b]	1	1	1	1
NS	1	1	3	3	1	3	3	1	1	1	1

[a]Test IDs: 43-06, 225-10, 225-07, 225-04, 475-01, 475-06, 975-11, 975-03, 975-07, MCER-01, MCER-02

[b]Test IDs: 43-09, 43-03, 475-08, 975-04, 975-10, MCER-03

While not using some of the most problematic accelerometer recordings likely improved the overall results, the issues with the accelerometer recordings and the filtering and double integration techniques indicate that these results may still vary slightly from the true performance of the building. This is shown and discussed more in Section 7.8. These inaccurate

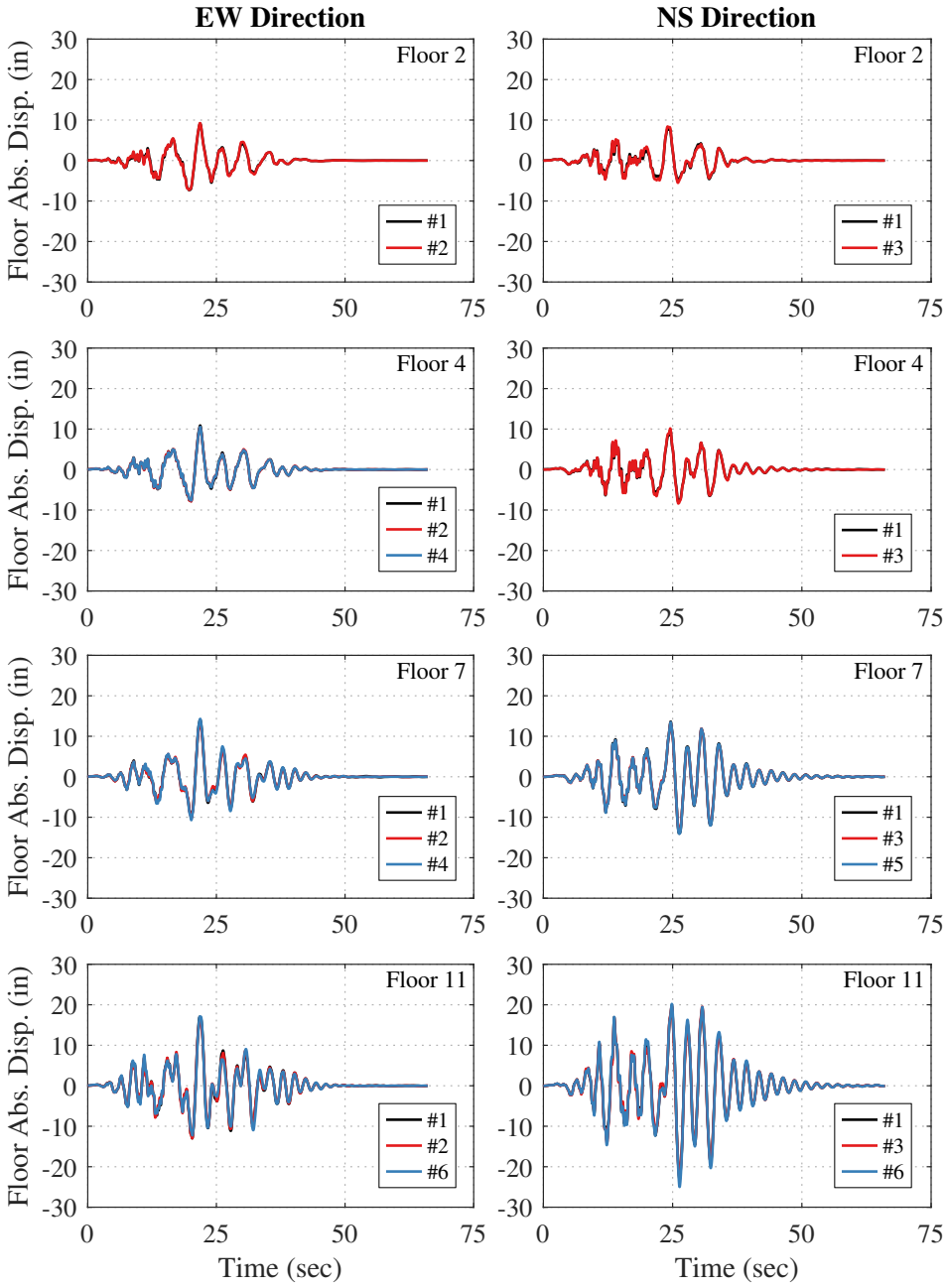

Figure 7.12: Absolute floor displacement recordings calculated for all accelerometers located on each floor (from test ID: MCER-01)

displacements calculated from the recorded accelerometer data is likely a result of the less-controlled testing environment inherent to large-scale testing or indicates the need for more sophisticated filtering and double integration techniques.

7.7 Estimated Damping Coefficient

The damping coefficient for the building was estimated using free vibration data that was recorded at the end of four larger ground motions that had input excitations in both horizontal directions. The four test IDs used for this calculation were: 975-11, 975-03, MCER-01, and MCER-02. For this calculation the east-west and north-south accelerometers located at the roof's approximate center-of-mass location were double integrated to get displacements (using the procedure outlined in 7.6.1). Figure 7.13 shows the roof displacement plots from the experimental data for the four test IDs that were used to estimate the damping coefficient. The dashed vertical line on each plot indicates the end of the input motion and the start of free vibration.

Decay of motion was used to determine the damping coefficient and assuming free vibration of a single degree of freedom, linear spring mass system. For each ground motion and direction, the local maxima and minima were identified during the free vibration range as shown by the marked peaks in Figure 7.13. For each ground motion, the period of oscillation, T_{free}, was determined as shown in Equation 7.6. The time of the first free vibration peak in the free vibration range, t_o, was subtracted from the time of the last prominent peak in the free vibration range, t_n, and divided by the number of cycles, n (i.e., the number of maxima/minima minus 1). The damping coefficient ξ was then determined using Equation 7.7 [Chopra, 2007], where $x(t_o)$ and $x(t_n)$ are the roof displacements at the first and last maxima/minima point in the free vibration range, respectively. Note, with this procedure, the free vibration period and damping coefficient were calculated for the maxima and minima points separately. The calculated free vibration periods and damping coefficients from each test ID and building direction, calculated from both the maxima and minima peaks, are shown in Table 7.7. The results in each building direction were averaged and are also shown

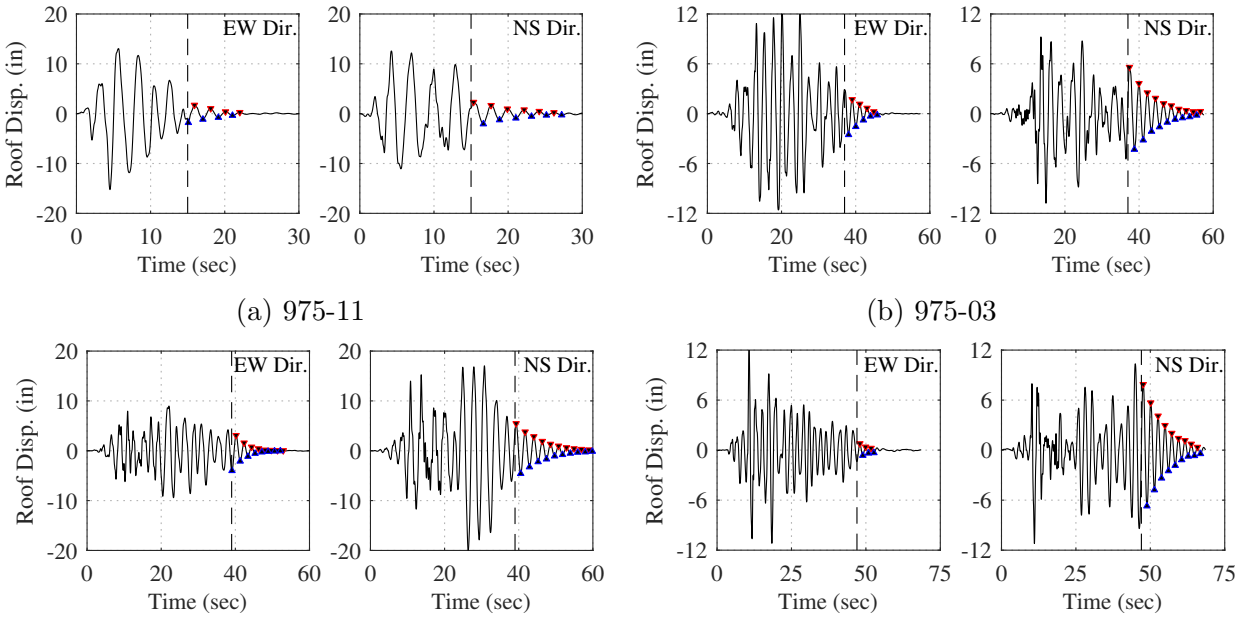

(a) 975-11

(b) 975-03

(c) MCER-01

(d) MCER-02

Figure 7.13: 10-Story test damping calculations

in the Table. The average damping coefficient in the east-west and north-south building directions were 9.2% and 6.0%, respectively.

$$T_{free} = \frac{t_n - t_o}{n} \tag{7.6}$$

$$\xi = \frac{1}{2\pi n} ln \frac{x(t_o)}{x(t_n)} \tag{7.7}$$

Table 7.7: 10-Story test damping calculations

Test ID	Peak Dir.	EW Direction		NS Direction	
		T_{free} (sec)	ξ	T_{free} (sec)	ξ
975-11	max	2.04	9.9%	2.17	7.3%
	min	1.98	8.4%	2.11	6.3%
975-03	max	1.95	10.2%	1.91	4.8%
	min	1.94	10.7%	2.10	6.2%
MCER-01	max	1.82	9.7%	2.18	5.9%
	min	1.86	10.0%	2.15	6.3%
MCER-02	max	1.88	9.5%	2.28	6.2%
	min	1.88	5.4%	2.25	5.4%
Average	-	1.92	**9.2%**	2.14	**6.0%**

7.8 Comparison of Experimental and Analytical Results

In this section, the experimental results and numerical results are compared as a means to validate the presented nonlinear numerical modeling methodology that was used for design of the 10-story NHERI TallWood lateral system. For this section, the nonlinear OpenSees model for the 10-story NHERI TallWood building (presented in Section 6.5), was re-run using the acceleration recordings for the shake table. Additionally, the damping was increased from 2% to 6% because the study presented in Section 7.7 indicates larger damping. The presented damping study shows approximately 9.2% and 6% damping in the east-west and north-south directions, respectively. Implementing different damping coefficients in the two building directions was out of the scope of work, thus, the smaller damping value was assumed. Aside from using the true table output ground motion as the OpenSees input motion and modifying the model damping, no other changes were made from the original model that was used for design. The scope of the comparison presented in this document was limited to the 17 ground motion tests presented in Table 7.3.

Note, for this comparison, only the two horizontal ground motion components recorded

from testing were input into the numerical model (for all 1D tests, both executed horizontal components were input into the model even though one component was small). The presented numerical model was not developed to properly model vertical ground motion effects, so they were not included. Studying the effects of unintentional movement in the three rotational degrees of freedom was outside the scope of this work. For this study, they were neglected, however, even minor table rotations could affect the results. Investigating the effects of observed table rotations is included in the recommendations for future work presented in Section 9.4.

7.8.1 Floor Displacements

Experimental and numerical results were first compared by looking at relative floor displacements. For the experimental results, floor displacements were calculated using two methods. The first method used results from the filtered and double integrated accelerometers on each floor (as described in Section 7.6). For this method, relative displacements were determined by subtracting recorded table acceleration (recorded at location #1 in Figure 7.6a) from the recordings at each floor level. The second method used unfiltered story displacement recordings from the diagonal string potentiometers. See Section 7.5.2 for information about these instruments and a discussion on how they were used to calculate relative story displacements. Total displacements on each floor were calculated by summing the story displacements from all stories below the floor (i.e., for example, the total floor displacement of floor 3 was calculated by summing the story displacements of stories 1 and 2). Note, floor displacements in the north-south direction, could only be calculated up to floor 4 because the diagonal string potentiometers were not present in the north-south direction on Stories 4 and 5.

Figures 7.14, 7.15, and 7.16 show floor displacement time history comparisons of experimental and numerical results for three example tests. In these plots, the OpenSees numerical results (Num.) are plotted as well as the experimental results calculated using the accelerometers (Exp. AC) and the string potentiometers (Exp. SP). For conciseness time history results are only shown for three tests and only four floors are shown for each

ground motion, however, similar trends were present on the other floors and for the other tests. Note, experimental string potentiometer data is missing for the upper floors in the north-south direction due to the missing string potentiometers.

Experimental results in Figures 7.14, 7.15, and 7.16 show that relative floor displacements calculated from the accelerometer data and the string potentiometer data match relatively well for the larger hazard ground motions. While peak floor displacements are very small in Figure 7.14 (showing a 43-year return period motion) the results calculated from the string potentiometers are less than the data calculated from the accelerometers. For the smaller ground motions, it is likely that the accelerometer data is more representative of the true building response because the string potentiometers are measuring displacement over a very long distance, making it more likely that the instrument is not picking up the full movement. In summary, when comparing numerical and experimental floor displacement results, it is recommended to use the accelerometer data for lower hazard motions, while either accelerometers or string potentiometers can be used at larger hazards.

Referring to the experimental and numerical floor displacement result comparisons for the three example ground motions in Figures 7.14, 7.15, and 7.16, results from the nonlinear numerical OpenSees model used to design the 10-story NHERI TallWood building appear to match experimental results relatively well. While the numerical prediction results are off in some parts of the ground motion, it is a fairly good match for a full-scale 10-story building in terms of building period and overall displacement prediction. These results show that the nonlinear model seems to slightly over predict response in the east-west direction and slightly under predict the response in the north-south direction. This discrepancy is likely do to the contributions of the stairs which are not accounted for in the nonlinear model. The stairs were designed to contribute little stiffness to the overall building, however, they may be contributing more than expected. Based on the orientation of the stair system, they are expected to be slightly stiffer in the east-west shaking direction. The larger stair system contribution to the east-west building response likely results in the large observed damping in that direction (which was also shown in the damping study in Section 7.7). Additionally, the

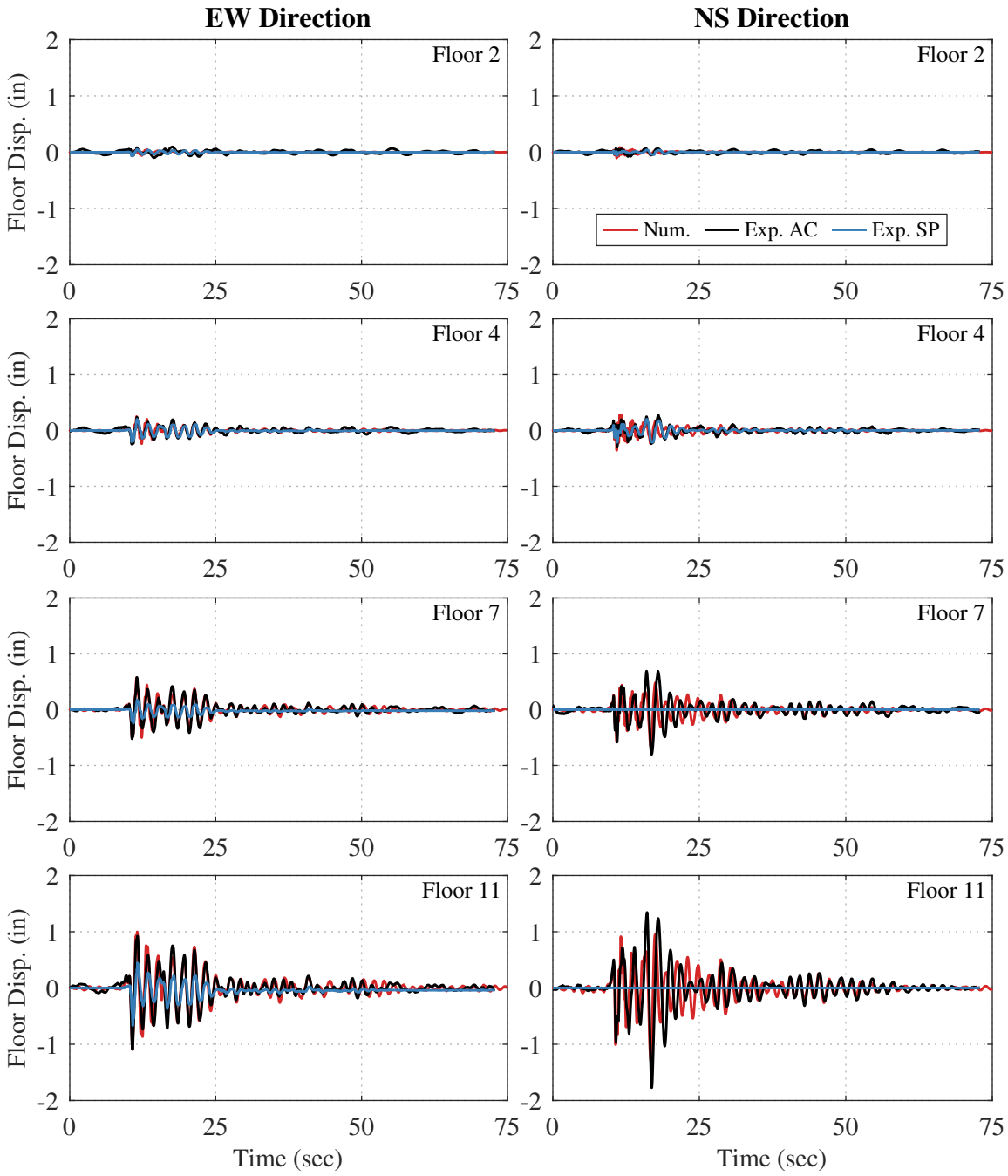

Figure 7.14: Floor displacement time history comparisons of 10-story numerical and experimental results for test ID 43-09

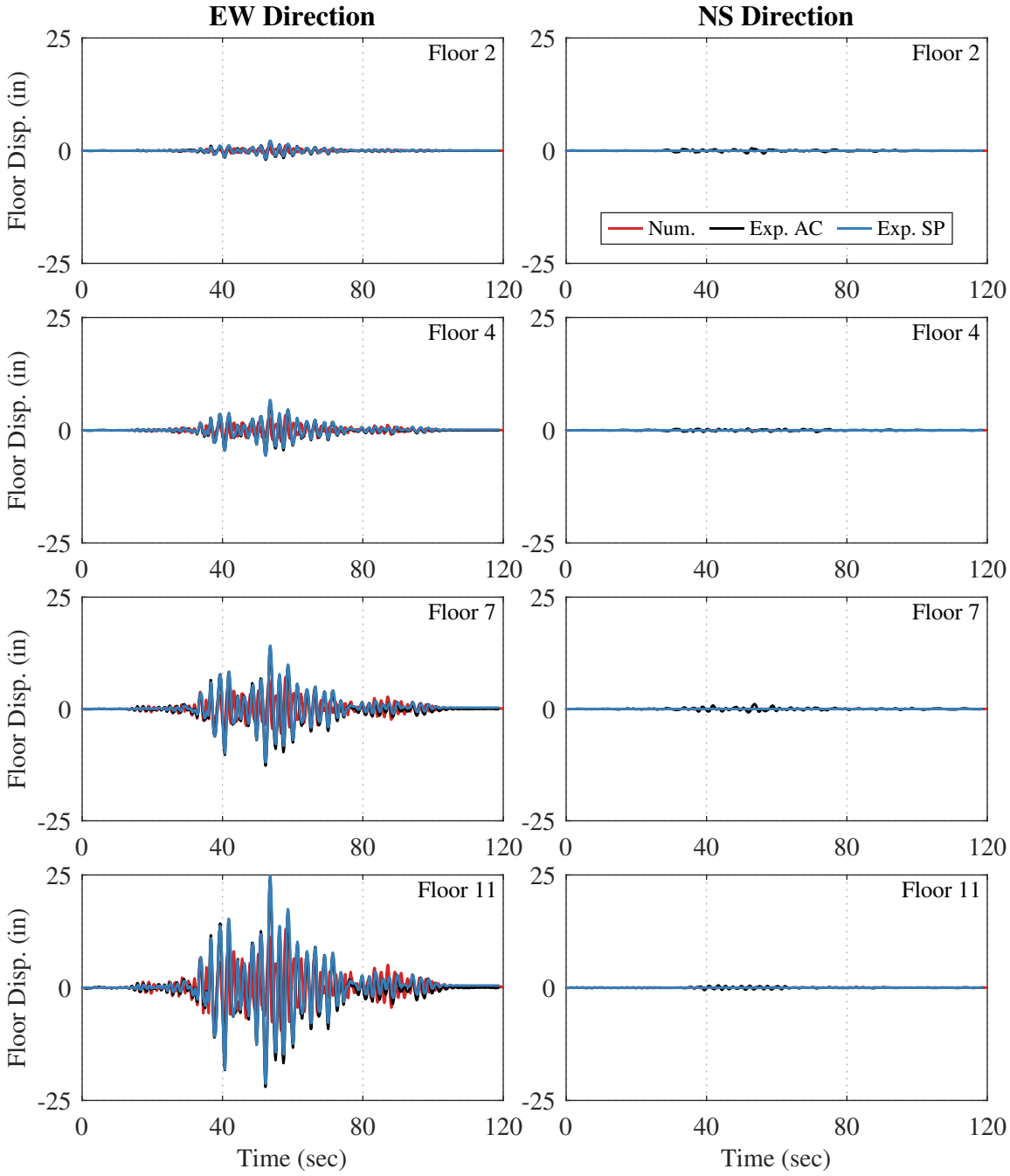

Figure 7.15: Floor displacement time history comparisons of 10-story numerical and experimental results for test ID 975-10

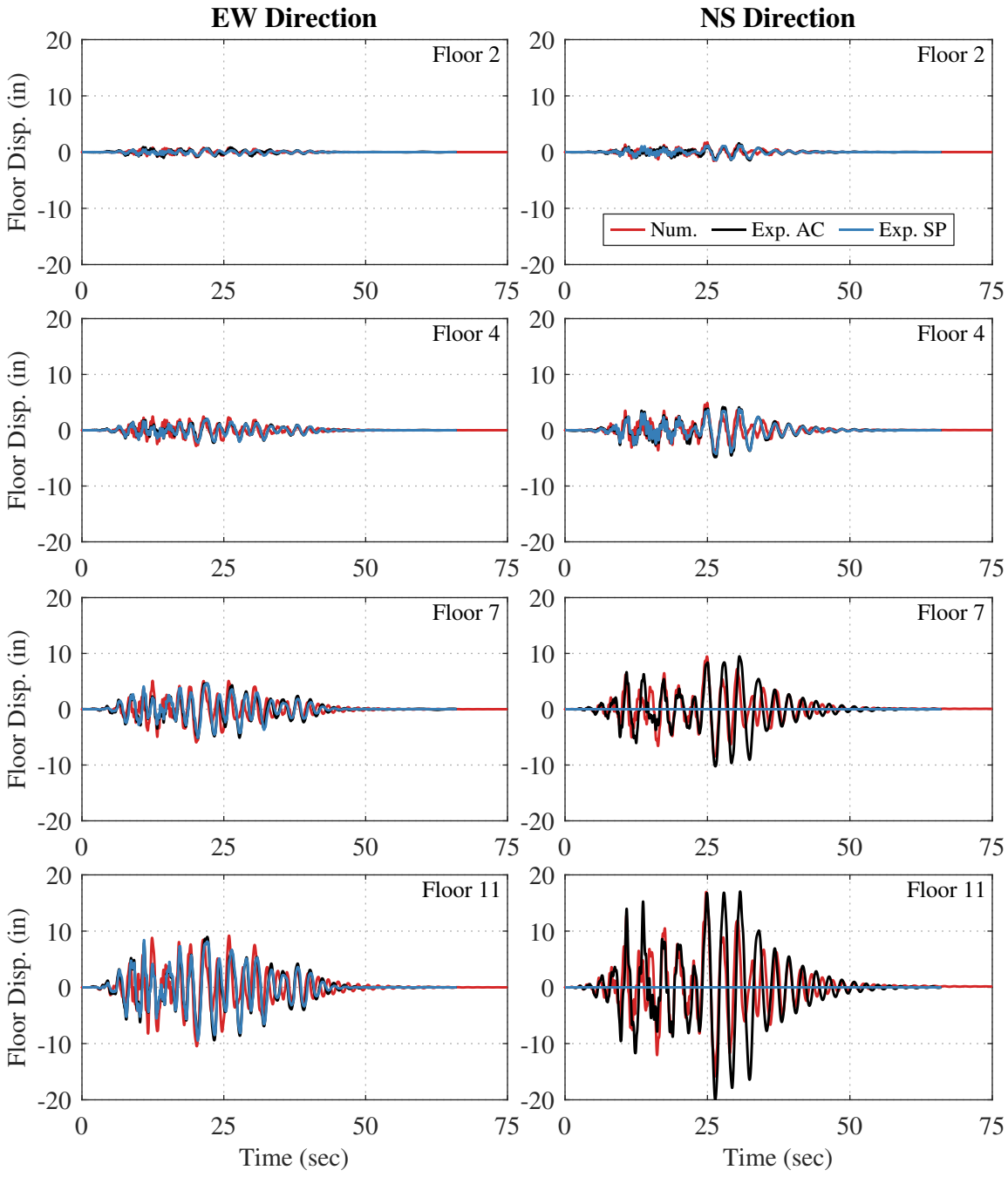

Figure 7.16: Floor displacement time history comparisons of 10-story numerical and experimental results for test ID MCER-01

gravity frames are also orientated in the east-west direction and while their contributions are likely small, they are not included in the model. The gravity system may also contribute to the larger observed damping in that direction. The damping coefficient applied to the model is more representative of the calculated building damping in the north-south direction, which could explain the numerical model's over-prediction of floor displacements in the east-west direction.

Peak floor displacement profile comparisons were also developed and are shown in Figure 7.17. While time history results were only shown for three ground motions, drift profiles are presented for all 17 tests shown in Table 7.3. In this figure, experimental results calculated from the accelerometers and the string potentiometers are both provided. Additionally, peak positive and peak negative response is shown. In the north-south direction, peak values are only show for floors 1 through 4 due to the missing string potentiometers on floors 4 and 5. As discussed with the time history results, the experimental results calculated from the string potentiometers are likely less representative of the true building response at small hazards. Overall, this figure shows that the numerical model does a relatively good job at predicting peak floor displacement response.

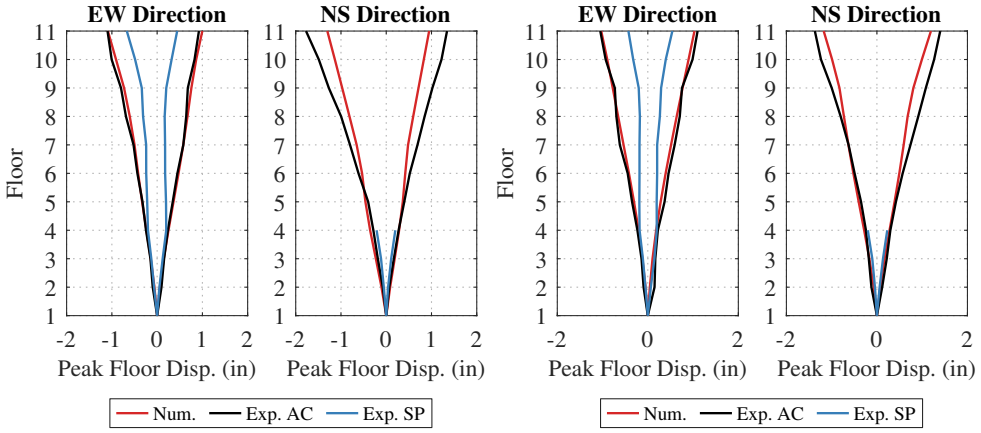

(a) Test ID: 43-09

(b) Test ID: 43-06

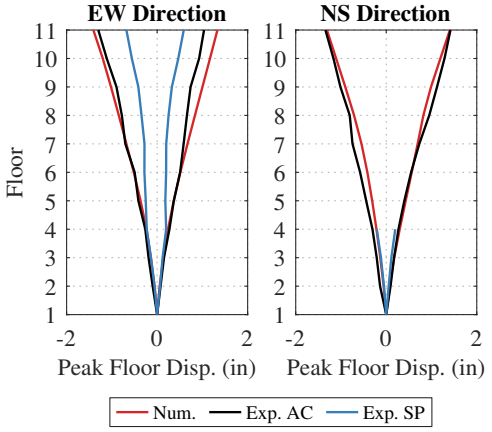

(c) Test ID: 43-03

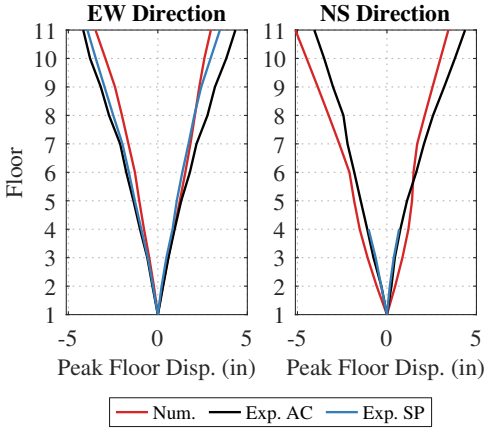

(d) Test ID: 225-10

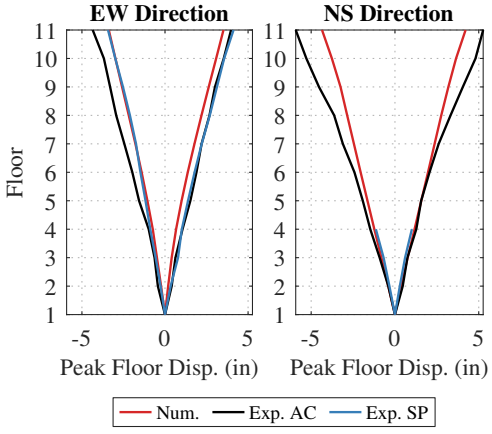

(e) Test ID: 225-07

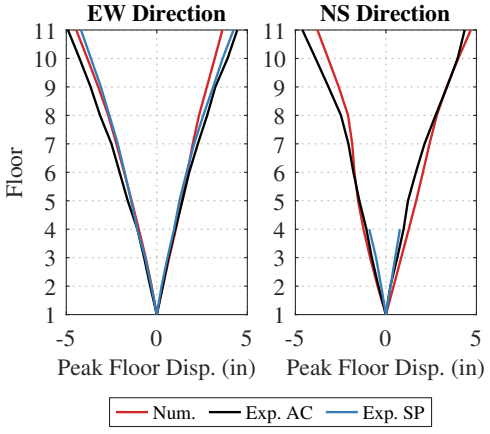

(f) Test ID: 225-04

Figure 7.17: Peak floor displacement comparisons of numerical and experimental results

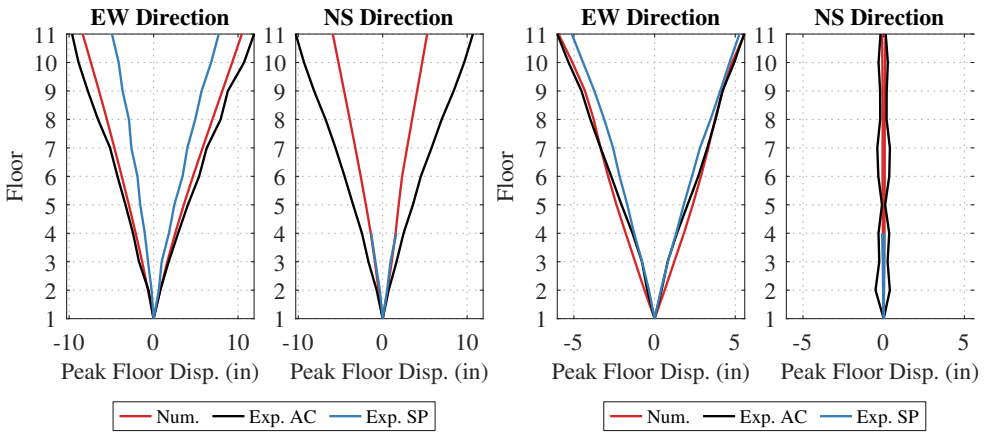

(g) Test ID: 475-01

(h) Test ID: 475-08

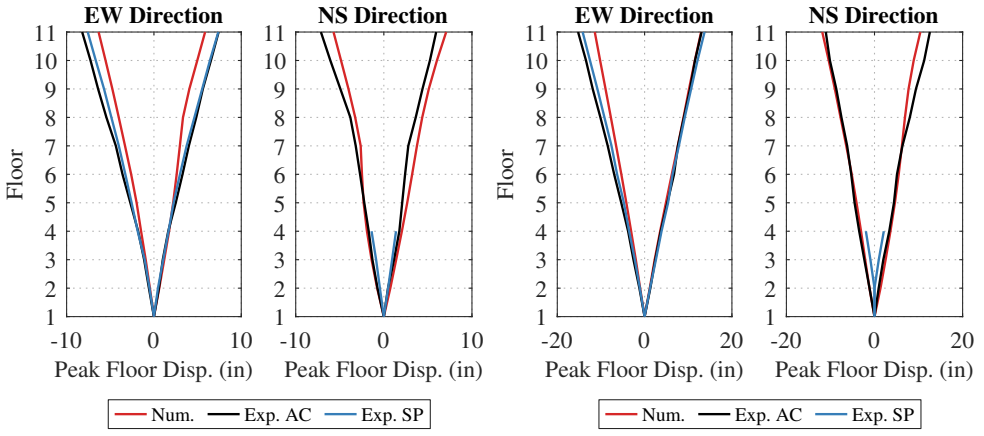

(i) Test ID: 475-06

(j) Test ID: 975-11

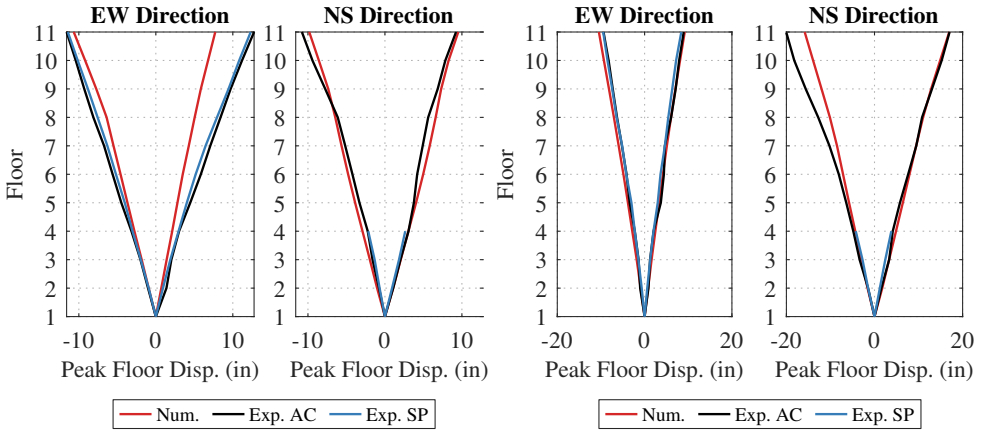

(k) Test ID: 975-03

(l) Test ID: 975-04

Figure 7.17: Peak floor displacement comparisons of numerical and experimental results

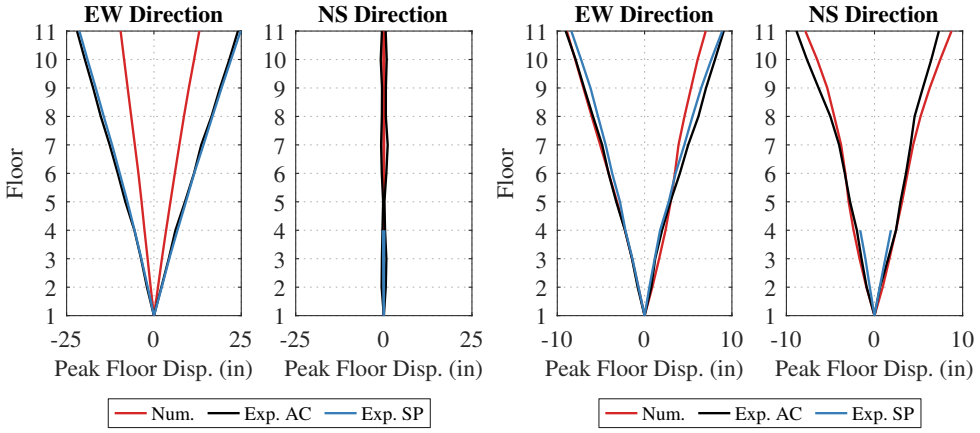

(m) Test ID: 975-10

(n) Test ID: 975-07

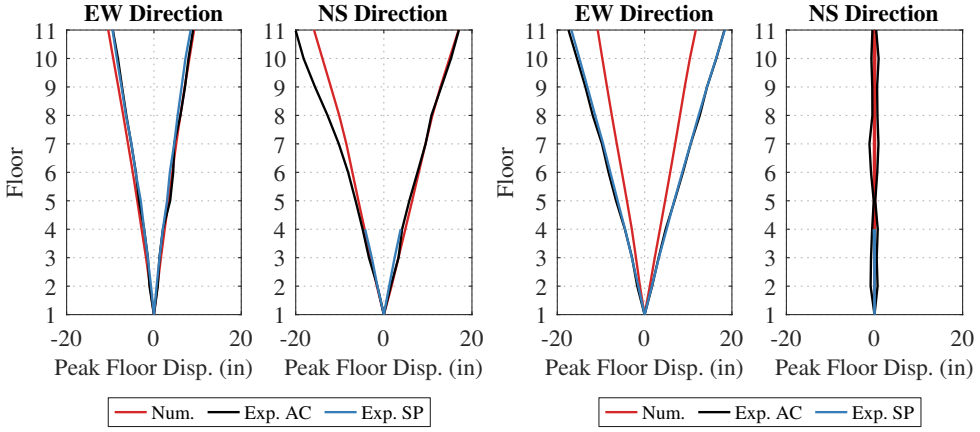

(o) Test ID: MCER-01

(p) Test ID: MCER-03

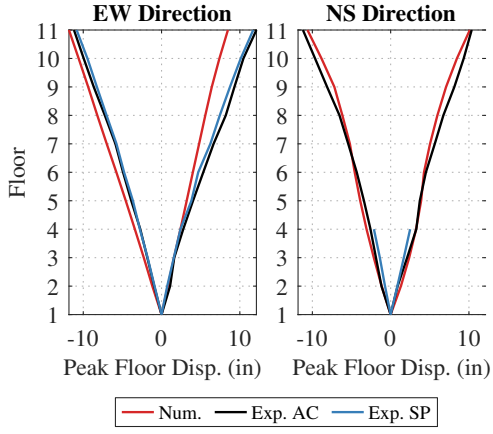

(q) Test ID: MCER-02

Figure 7.17: Peak floor displacement comparisons of numerical and experimental results

The displacement response of the building was summarized by looking at peak roof drift for all 17 ground motions studied in this document. Figure 7.18 plots the spectral acceleration of the ground motion component at the building's approximate first mode period (1.74 seconds, assumed from the eigenvalue analysis in Section 6.5.5) versus the peak roof drift in each direction. The spectral acceleration of the ground motion component was used as a way to represent ground motion intensity. On this plot, both numerical and experimental results are summarized for each ground motion. In addition, the mean response for each hazard level is also shown. For the experimental results, peak values were taken from the accelerometer results because they seem to be more representative of the true building response across all hazards. This figure shows a relatively linear relationship between ground motion intensity and peak roof drift. The mean roof drift values shown in the figure are summarized in Table 7.8. Note, for the 1D motions that only had east-west input excitations, the peak response in the north-south direction was omitted for the mean hazard value shown in both the figure and the table.

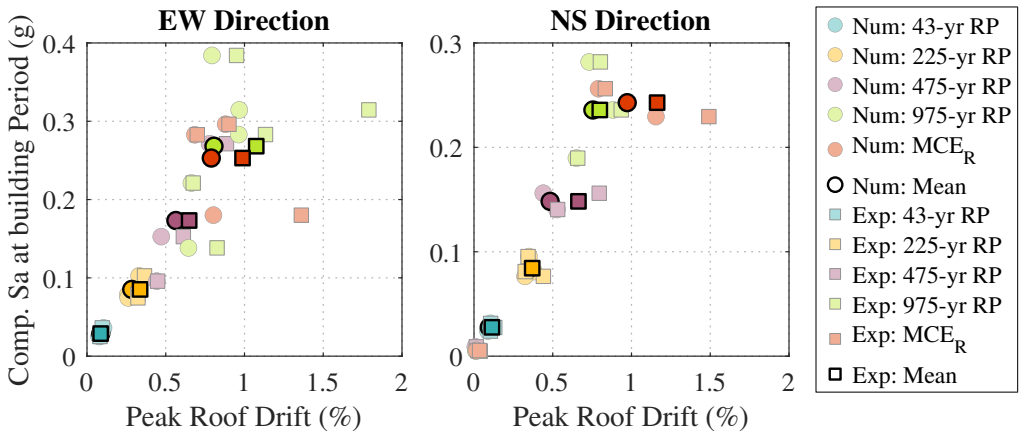

Figure 7.18: Summary of numerical and experimental peak roof drifts

By comparing the mean peak roof drifts from each hazard level in Figure 7.18, it can be determined that the numerical model under-predicted peak roof drift response slightly. This comparison is more clear in Figure 7.19 which shows the peak roof drift from the numerical

results versus the peak roof drift from the experimental accelerometer results. A 1:1 diagonal line is also shown on the figure, representing a prefect correlation between numerical and experimental results. This figure also shows the slight under-prediction of the numerical peak floor displacement results compared to the experimental results. The under-prediction is slightly more prominent in the east-west direction, again likely due to the contribution of the stairs and gravity framing. However, overall the presented nonlinear OpenSees model does a relatively good job at prediction building floor displacement response.

Table 7.8: Experimental and numerical mean peak roof drift results for each hazard level

Mean Peak Roof Displacement (in)						
Hazard	EW Direction			NS Direction		
Level	Num.	Exp.	% Diff.	Num.	Exp.	% Diff.
43-year RP	0.09	0.09	-0.9%	0.10	0.11	17.7%
225-year RP	0.28	0.34	18.7%	0.35	0.37	5.2%
475-year RP	0.56	0.65	15.0%	0.48	0.66	37.3%
975-year RP	0.81	1.07	33.3%	0.75	0.80	5.8%
MCE_R	0.79	0.99	25.1%	0.97	1.16	19.5%

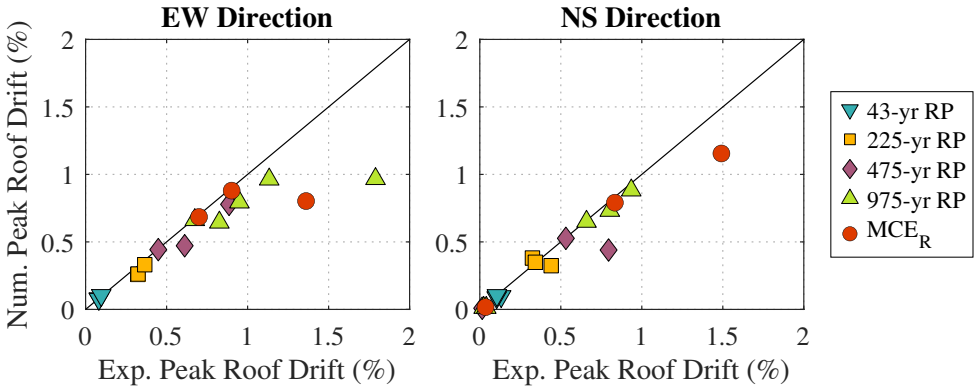

Figure 7.19: Summary comparison of numerical and experimental peak roof drifts

7.8.2 Interstory Drifts

Experimental and numerical results were also compared in terms of interstory drifts (ISD). Similar to the floor displacement comparison, experimental results were computed using two methods. The first method used results from the filtered and double integrated accelerometers on each floor (as described in Section 7.6). For this method, ISDs on each story were calculated by subtracting the displacements of the floor below from the floor above and dividing by the story height. The second method used unfiltered recordings from the diagonal string potentiometers. Section 7.5.2 explains how the displacements at each story were calculated. These story displacements were then divided by the story height to get ISD. Note, because of the missing string potentiometers, north-south direction ISD values could not be calculated on Stories 4 and 5 using this method.

Figures 7.20, 7.21, and 7.22 show ISD time history comparisons of experimental and numerical results for three example tests. Similar to the floor displacement plots, experimental ISD results calculated from both the horizontal floor accelerometers and the diagonal string potentiometers are shown in comparison to the numerical results. For conciseness, time history plots for only three of the 17 tests are presented for this discussion, however, similar trends were found for the remaining tests. Additionally, with these plots, only four of the ten stories are plotted for conciseness.

Looking at the experimental ISD results in Figures 7.20, 7.21, and 7.22, the two methods for calculating ISD do not produce results that are as similar as when used for calculating the floor displacements in Section 7.8.1. The difference in experimental ISD values calculated using the two methods is particularly clear for smaller hazard ground motions (see example results for a 43-year return period ground motion in Figure 7.20). At lower hazard levels, the ISD values calculated from the accelerometers show large oscillations that are likely erroneous because they physically do not make a lot of sense (see discussions in Section 7.6), but also because they do not appear in the results calculated from the string potentiometers. Similar to the floor displacement comparisons, at low hazards the results calculated from the

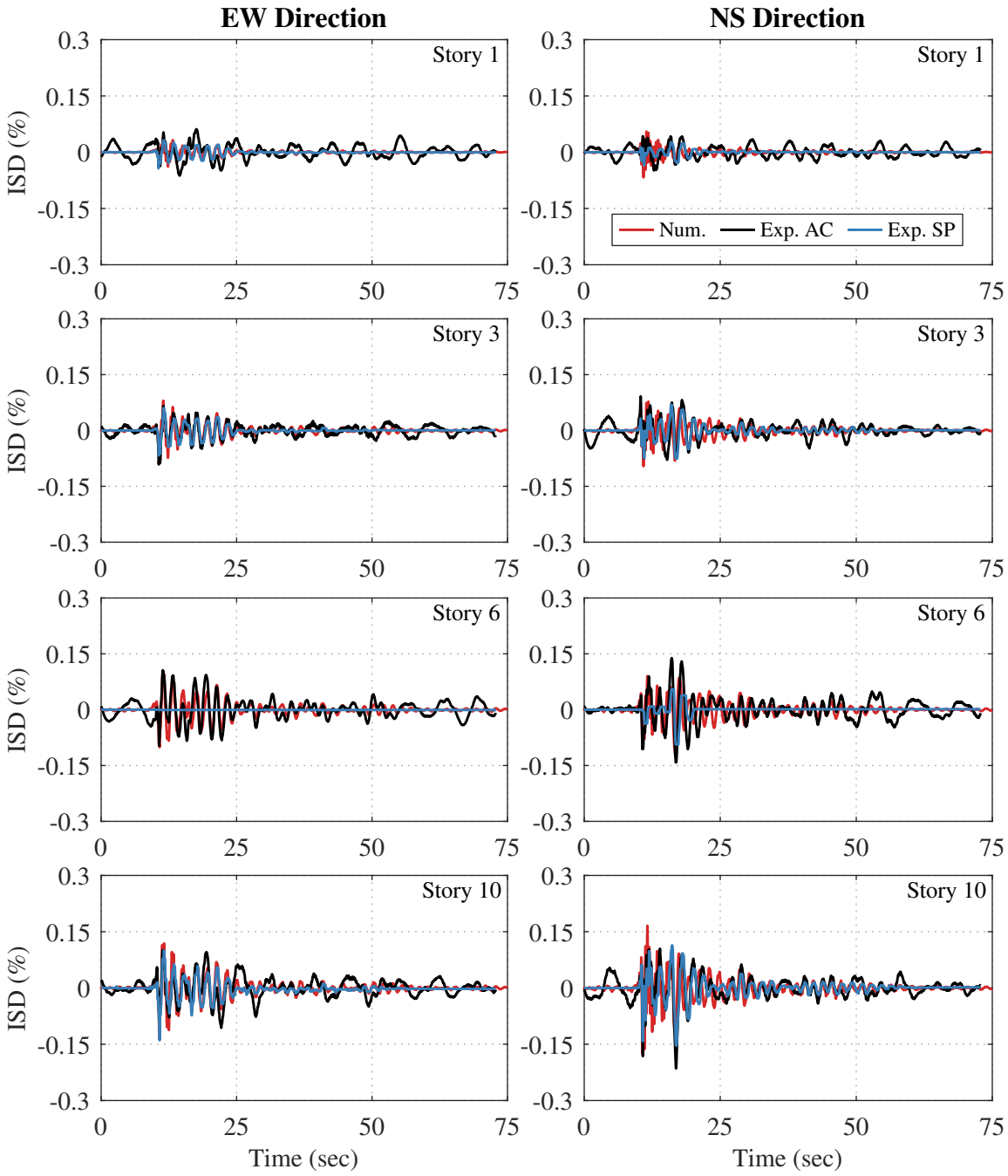

Figure 7.20: ISD time history comparisons of 10-story numerical and experimental results for test ID 43-09

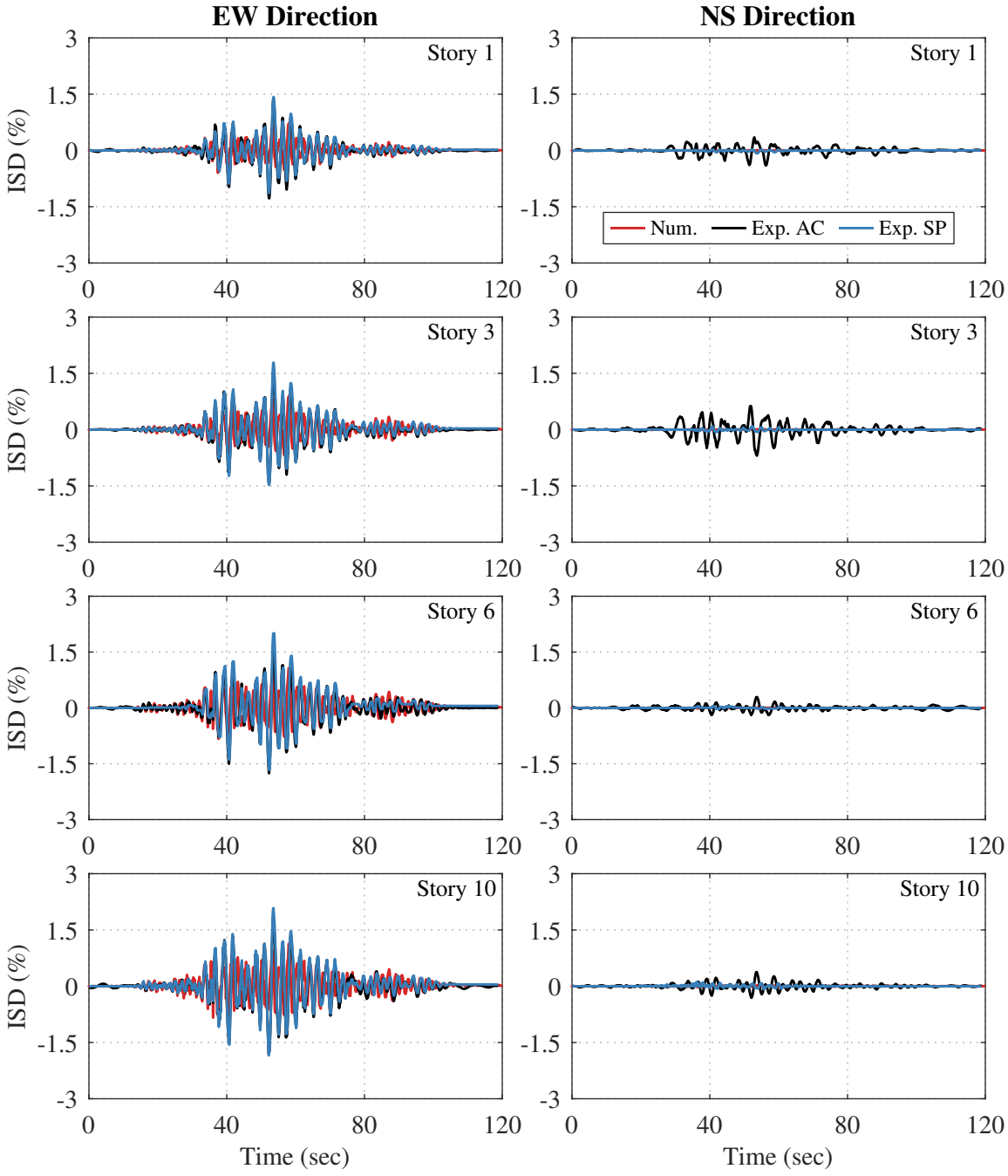

Figure 7.21: ISD time history comparisons of 10-story numerical and experimental results for test ID 975-10

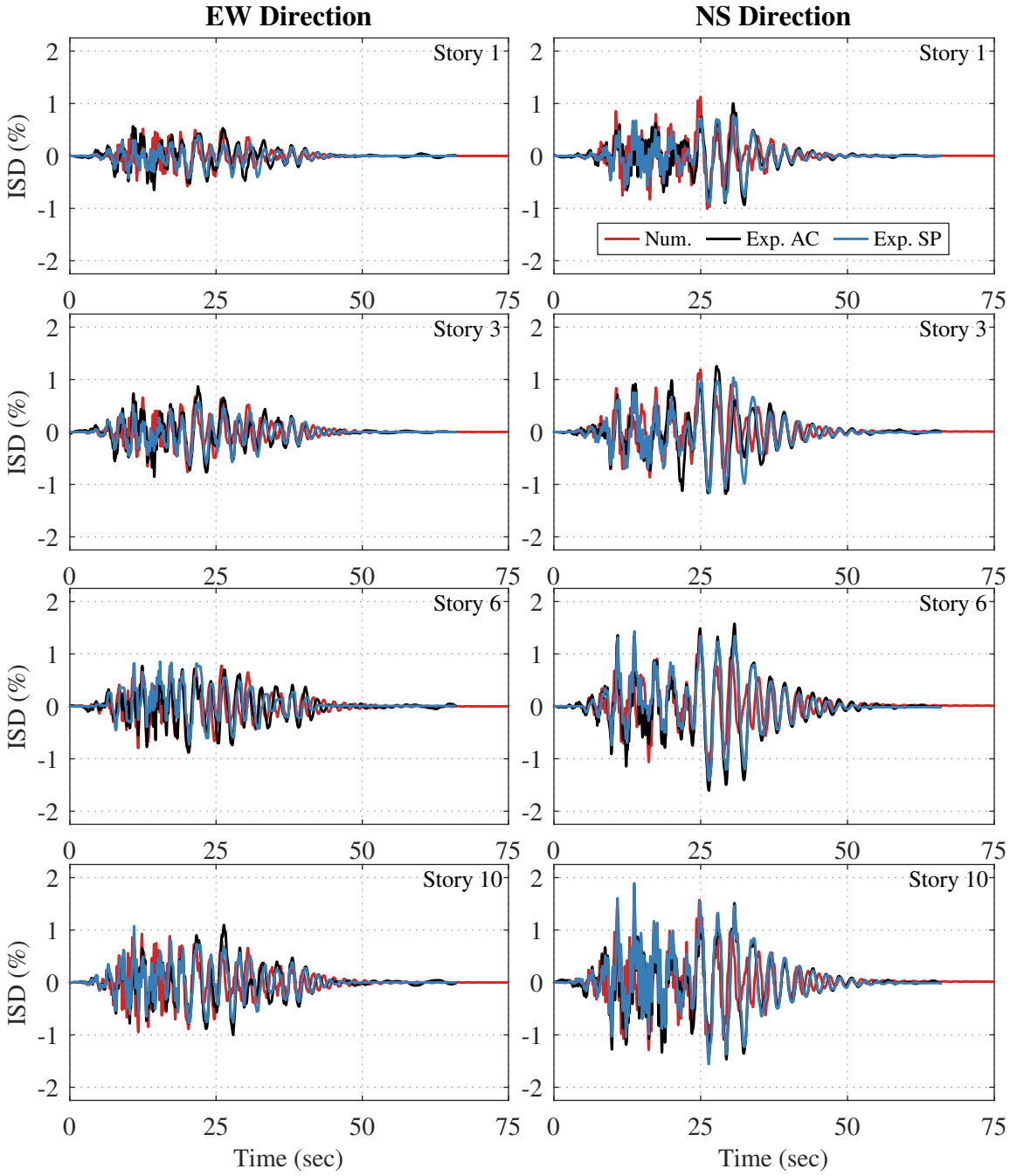

Figure 7.22: ISD time history comparisons of 10-story numerical and experimental results for test ID MCER-01

string potentiometers are smaller than the accelerometer results (however, at smaller hazards all measured displacements are very small). The difference in results calculated using the two methods is also clear with 1D motions for the values calculated in direction that the building was not shaking. For example, see the north-south direction plots in Figure 7.21 which shows a 1D 975-year return period motion where the table only executed an east-west excitation. As discussed in Section 7.6, ISD values calculated from the accelerometers for these motions resulted in relatively large ISD values that are likely erroneous because the corresponding floor displacements (see Figure 7.15) are so small. Referring to Figure 7.21, these large oscillations are also probably erroneous because the string potentiometers are showing near zero ISD values. At larger hazard levels (like the one shown in Figure 7.22), the ISD values calculated from the accelerometer data and the string potentiometer data are more similar.

In summary, there is less confidence in the experimental calculations of the ISD values being representative of the true building performance, in comparison to the floor displacement values. At low hazard levels, ISDs calculated from accelerometer data result in behavior that is not representative of the observed building performance (i.e., no damage) and ISDs calculated from string potentiometer data appears to under-estimate the true drifts. For 1D motions, ISDs calculated from the string potentiometers are more representative of the observed building performance. At larger hazard levels, both methods produce similar time history results.

While experimental ISD results calculated in this document may differ slightly from the actual building behavior, the numerical and experimental results can still be compared in the three example ground motion tests shown in Figures 7.20, 7.21, and 7.22. In general, the numerical model was able to predict ISD behavior relatively well. Similar to the floor displacement discussion, the numerical model seems to slightly over predict response in the east-west direction and slightly under predict response in the north-south direction. This discrepancy is likely because the numerical model does not include the stair system and gravity framing contributions that are more prominent in the east-west shaking direction.

Peak ISD profile comparison were also developed and are shown in Figure 7.23. While time history results were only shown for three ground motions, ISD profiles are provided for all 17 tests outlined in Table 7.3. In this figure, experimental results calculated from both the accelerometers and the string potentiometers are provided. Additionally, peak positive and peak negative response is shown. In the north-south direction, peak values calculated from the string potentiometer data were not computed for Stories 4 and 5 due to the missing string potentiometers. In the plots, a dashed line is added between story 3 and 6 results. This dashed line is intended to represent an extrapolation or prediction of what likely occurred on those floors. In these plots, the numerical results show a much smoother response up the height of the building. Both experimental methods (but particularly the accelerometer calculation method) show the ISD profile up the height of the building to be more jagged. These kinks in the profiles are likely from instrumentation recording errors or insufficient data filtering (as discussed previously). While some of the smaller kinks could be real building response, the larger kinks would mean the walls would have had to undergo extreme curvature changes between stories. Most likely, this did not happen because the rocking walls were continuous and saw no damage during testing. In general, the results calculated from the accelerometer data are predicting larger peak response in comparison to the string potentiometer data. Overall, these results show that the numerical model does a relatively good job at predicting peak ISD values.

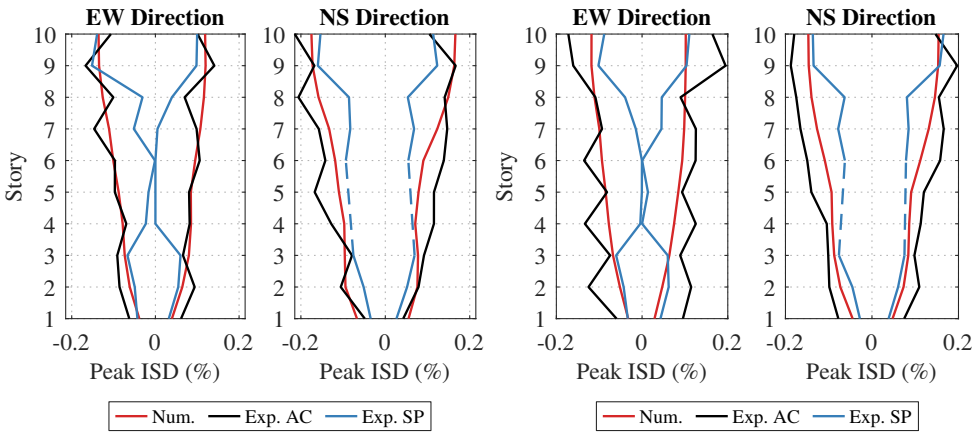

(a) Test ID: 43-09

(b) Test ID: 43-06

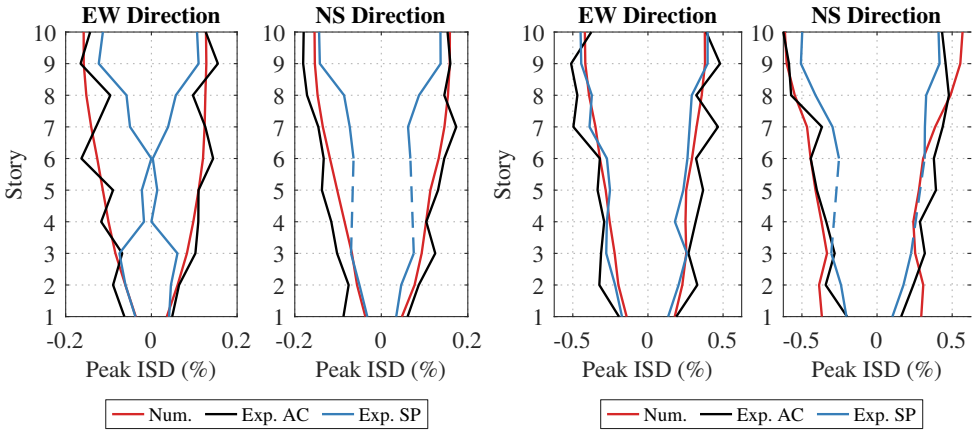

(c) Test ID: 43-03

(d) Test ID: 225-10

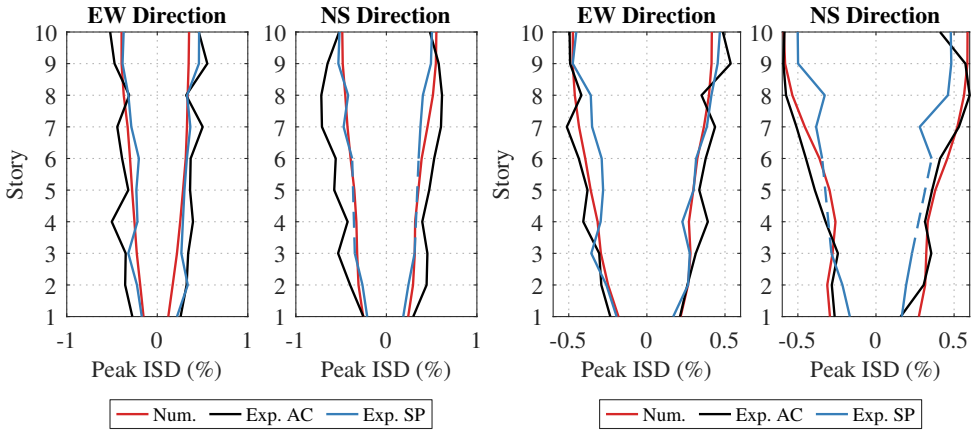

(e) Test ID: 225-07

(f) Test ID: 225-04

Figure 7.23: Peak ISD comparisons of numerical and experimental results

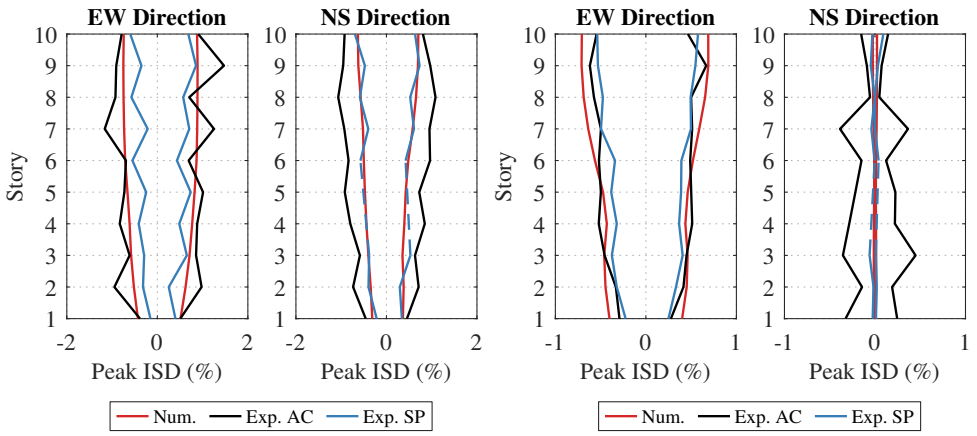

(g) Test ID: 475-01

(h) Test ID: 475-08

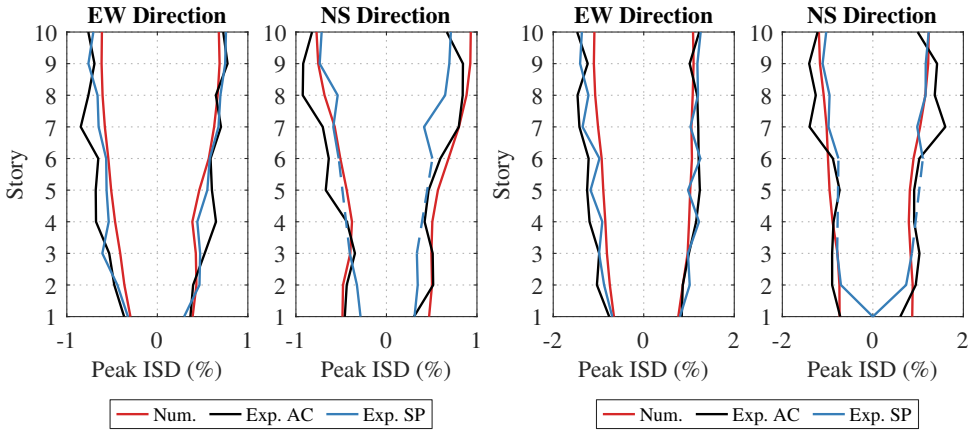

(i) Test ID: 475-06

(j) Test ID: 975-11

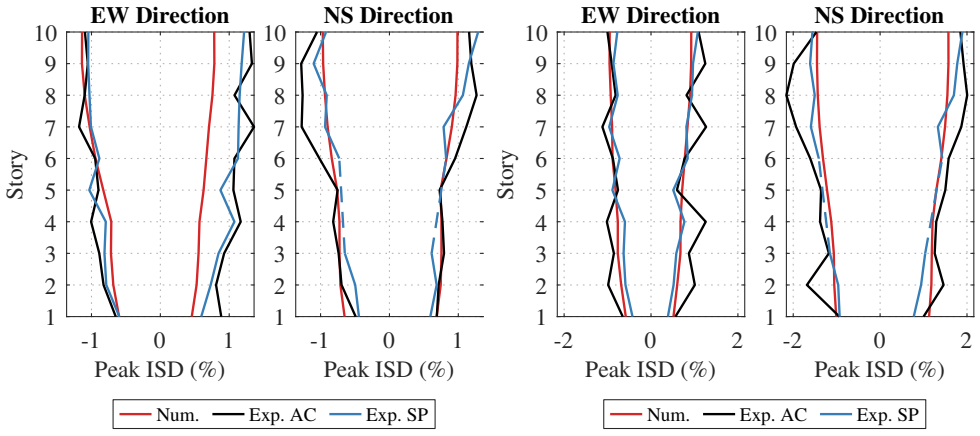

(k) Test ID: 975-03

(l) Test ID: 975-04

Figure 7.23: Peak ISD comparisons of numerical and experimental results

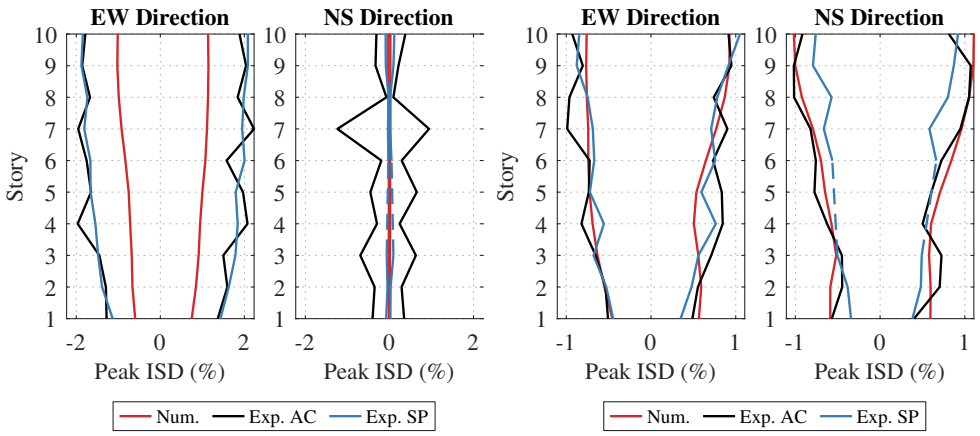

(m) Test ID: 975-10

(n) Test ID: 975-07

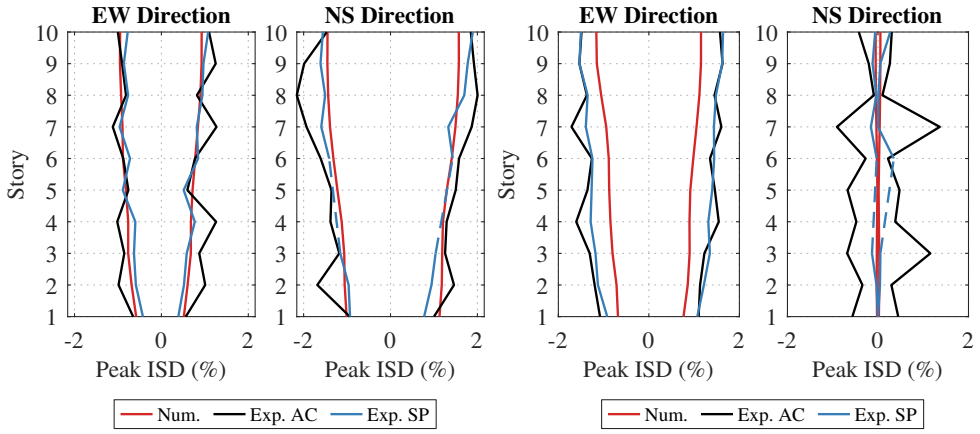

(o) Test ID: MCER-01

(p) Test ID: MCER-03

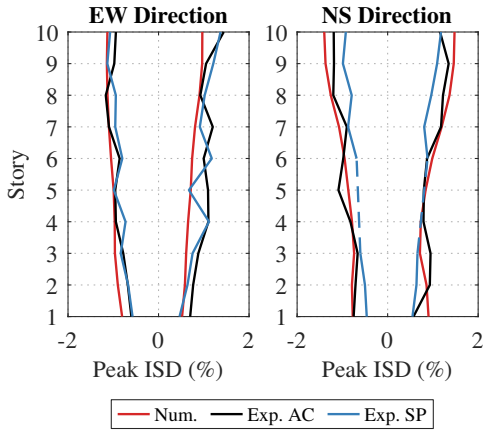

(q) Test ID: MCER-02

Figure 7.23: Peak ISD comparisons of numerical and experimental results

Peak ISD response of the building was summarized by looking at the peak ISD for all 17 ground motions studied in this document. Figures 7.24 and 7.25 plot the spectral acceleration at the building's period versus the absolute peak ISD for each component for both experimental and numerical results. In addition, the mean response for each hazard level is also shown. Similar to Figure 7.18, the vertical axis of this plot is intended to represent earthquake intensity. In Figure 7.24, experimental results were calculated using accelerometer (AC) data. In Figure 7.25, experimental results were calculated using string potentiometer (SP) data. For Figure 7.25, it was assumed that peak ISD values did not occur on Floors 4 or 5 in the north-south direction because the string potentiometers here were missing. These figures shows a relatively linear relationship between ground motion intensity and ISD. The mean values shown in these plots are also summarized in Tables 7.9 and 7.10 for the accelerometer and string potentiometer experimental result calculations, respectively. Note, in both the figures and the tables, for the 1D motions (that only shook in the east-west direction), the peak ISD results in the north-south direction were omitted from the mean calculation. At MCE_R hazard, the experimental mean peak ISD, calculated from the accelerometer data was 1.47% and 1.75% for the east-west and north-south directions, respectively. At MCE_R hazard, the experimental mean peak ISD, calculated from the string potentiometer data was 1.36% and 1.41% for the east-west and north-south directions, respectively. Recall, lateral system design criteria aimed to limit peak ISDs to 2.25%.

Comparing mean peak ISDs for each hazard level in Figures 7.24 and 7.25 and in Tables 7.9 and 7.10, it can be determined that the numerical model generally under-predicted peak ISD response. Note, especially for the results calculated from the accelerometer data, part of this over-prediction could be attributed to errors in experimental ISD calculations as discussed in this chapter. This comparison is more clear when looking at Figures 7.26 and 7.27, which plot numerical peak ISDs versus experimental peak ISDs, calculated from the accelerometer data and string potentiometer data, respectively. A 1:1 diagonal line is also shown in the figures, representing a perfect correlation between numerical and experimental results. These figures show that experimental ISD results calculated from the string

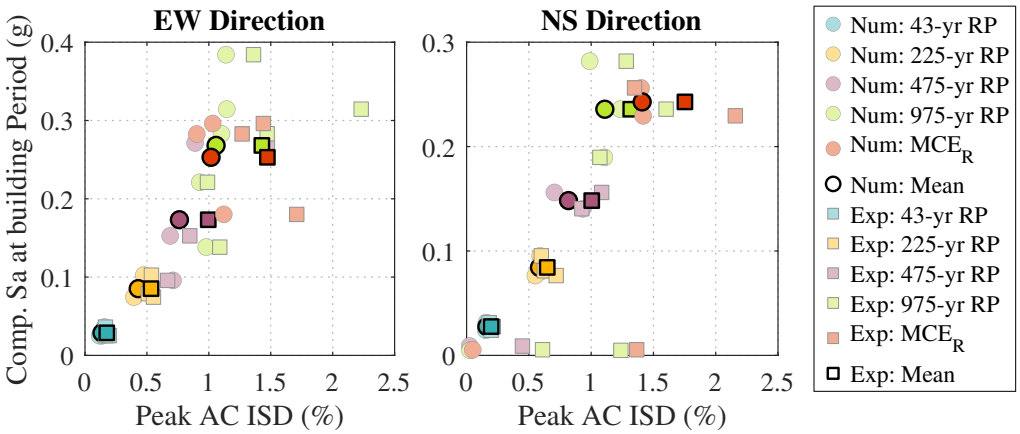

Figure 7.24: Summary of numerical and experimental peak interstory drifts - experimental results calculated using accelerometer data

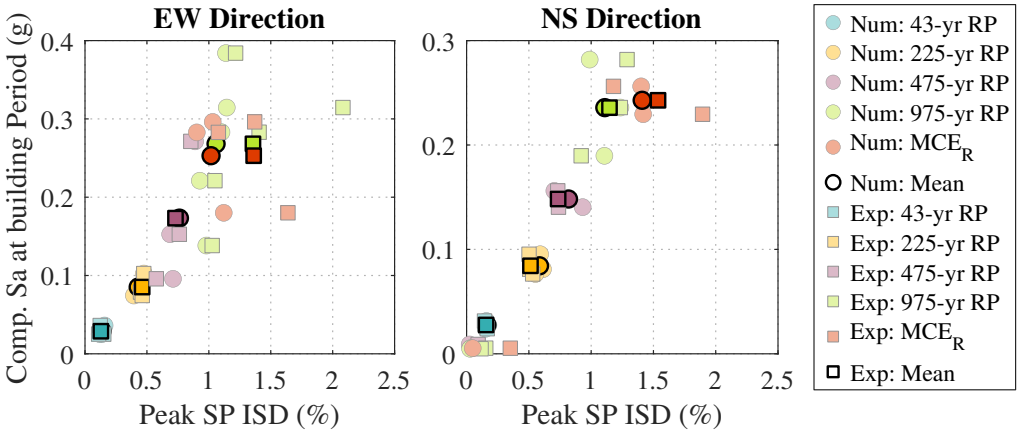

Figure 7.25: Summary of numerical and experimental peak interstory drifts - experimental results calculated using string potentiometer data

potentiometer data matched better with the numerical OpenSees data, in comparison to the experimental results calculated from the accelerometer data. In the east-west direction, the numerical model generally under-predicted peak ISD results, in comparison to both experimental calculation methods. With the experimental results calculated from accelerometer

Table 7.9: Experimental and numerical mean ISD results for each hazard level - experimental results calculated using accelerometer data

Mean Peak ISD (%) - from Accelerometers						
Hazard	EW Direction			NS Direction		
Level	Num.	Exp.	% Diff.	Num.	Exp.	% Diff.
43-year RP	0.14	0.18	27.9%	0.16	0.20	21.4%
225-year RP	0.43	0.53	24.2%	0.59	0.65	10.6%
475-year RP	0.76	1.00	30.5%	0.82	1.00	22.8%
975-year RP	1.06	1.43	34.9%	1.11	1.32	18.7%
MCE_R	1.02	1.47	44.7%	1.41	1.75	24.4%

Table 7.10: Experimental and numerical mean ISD results for each hazard level - experimental results calculated using string potentiometer data

Mean Peak ISD (%) - from String Potentiometers						
Hazard	EW Direction			NS Direction		
Level	Num.	Exp.	% Diff.	Num.	Exp.	% Diff.
43-year RP	0.14	0.13	-6.7%	0.16	0.16	-3.8%
225-year RP	0.43	0.46	7.4%	0.59	0.51	-12.4%
475-year RP	0.76	0.73	-4.2%	0.82	0.73	-10.2%
975-year RP	1.06	1.36	28.2%	1.11	1.15	3.4%
MCE_R	1.02	1.36	33.8%	1.41	1.54	9.0%

data, the numerical OpenSees model also under-predicted peak ISD values in the north-souh direction. However, with the experimental results calculated from string potentiometer data, the numerical OpenSees model did a relatively good job at prediction peak ISD values in the north-south direction. Note, the points with near zero numerical peak ISD values in the north-south direction are the 1D motions where ISDs calculated from the accelerometer data resulted in large erroneous building response.

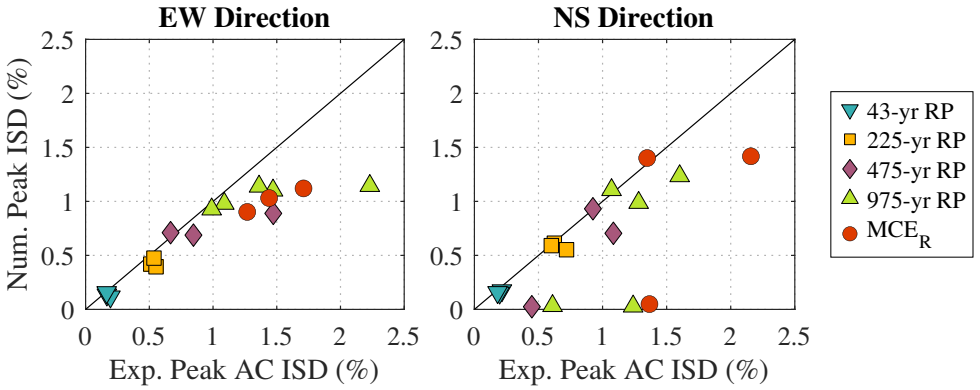

Figure 7.26: Summary comparison of numerical and experimental peak interstory drifts - experimental results calculated using accelerometer data

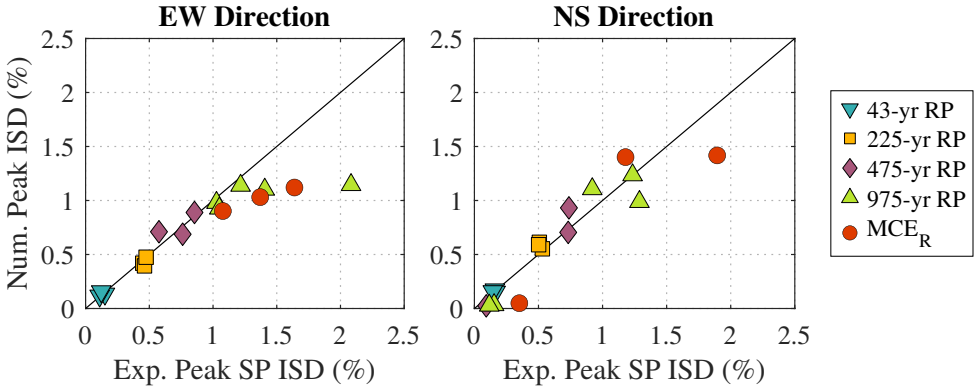

Figure 7.27: Summary comparison of numerical and experimental peak interstory drifts - experimental results calculated using string potentiometer data

7.8.3 Wall Base Uplift and Compression

Lastly, experimental and numerical results were compared by looking at rocking wall uplift and compression at the base of the wall panels. For this comparison, experimental results were taken from unfiltered recordings of the linear potentiometers described in Section 7.5.3. These results were compared to numerical results by identifying the zero length spring in the multispring element that is closest to the location of each linear potentiometer. Figures

7.28, 7.29, and 7.30 show time history uplift comparison plots for three example ground motions. In each figure there are four sub-figures, one showing the uplift comparisons for the linear potentiometers on each of the four walls. In each sub-figure the comparison plots are organized in an orientation representative of the linear potentiometers layout on each wall (refer back to the linear potentiometer layout schematic in Figure 7.7b). For example, Figure 7.28a shows the uplift comparisons for all linear potentiometer locations on the north wall. The two plots in the top row correspond to the two linear potentiometers on the corners of the north face of the north wall (ID #s 596 and 597 left to right). The six plots on the bottom row correspond to the locations of the six linear potentiometers on the south face of the north wall (ID #s 590, 591, 592, 593, 594, and 595, left to right).

Figures 7.28, 7.29, and 7.30 show that the numerical model can capture and predict the general uplift behavior, however, it does not predict peak uplift and compression values very well, particularly for small ground motions. This indicates that the multispring element utilized in the OpenSees model can model uplift well to predict overall building performance, however, the multispring input parameters, such as plastic hinge length and the mass timber material model, likely need to be revised. This is consistent with visual performance assessment of the building. Damage to the base of the wall panels was predicted, however, none was observed during testing.

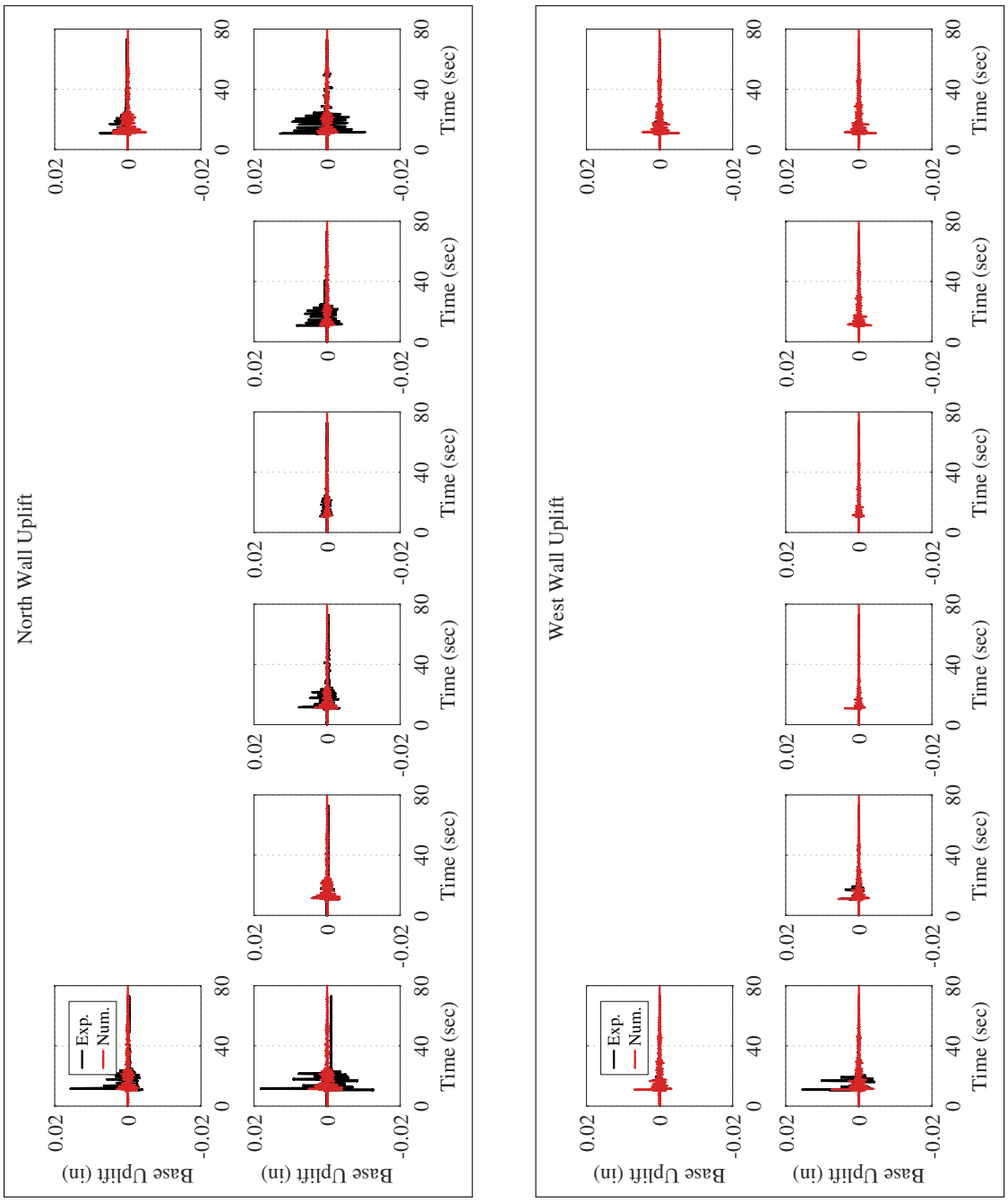

(a) North wall

(b) West wall

Figure 7.28: Comparison of experimental and numerical results for wall base uplift for test ID 43-09

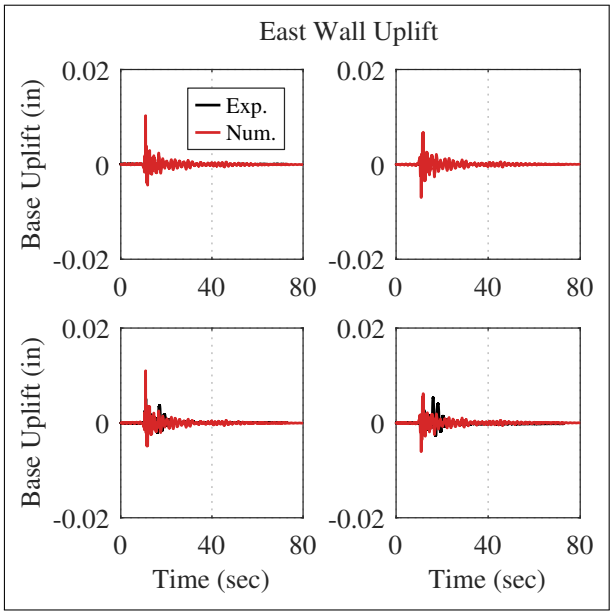

(c) East wall

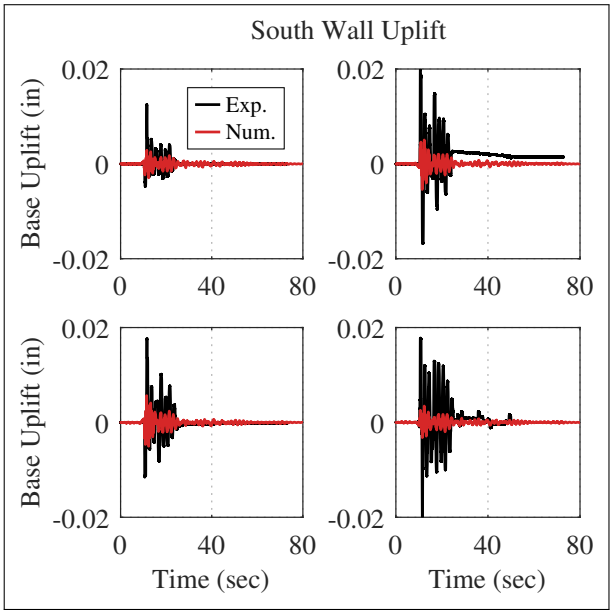

(d) South wall

Figure 7.28: Comparison of experimental and numerical results for wall base uplift for test ID 43-09

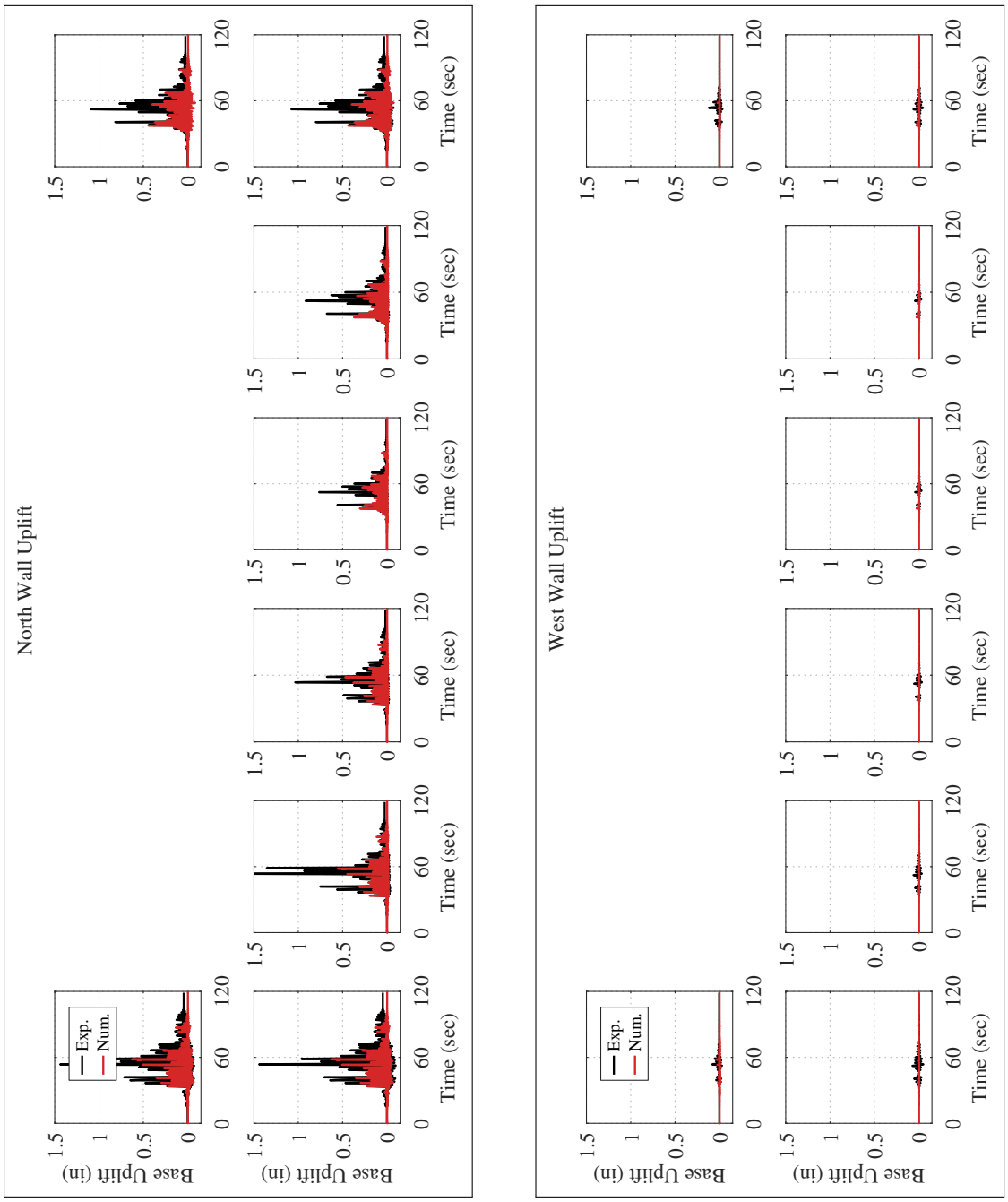

(a) North wall

(b) West wall

Figure 7.29: Comparison of experimental and numerical results for wall base uplift for test ID 975-10

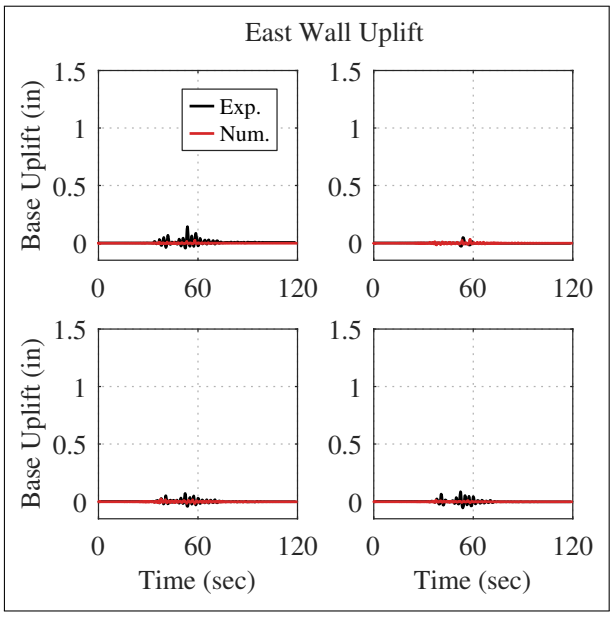

(c) East wall

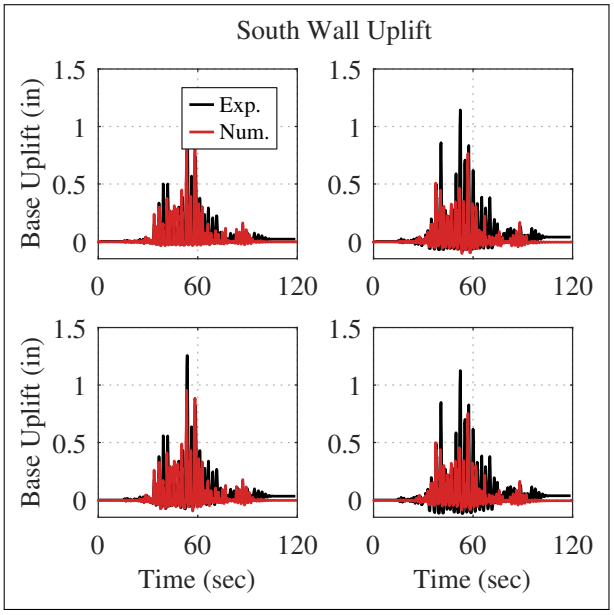

(d) South wall

Figure 7.29: Comparison of experimental and numerical results for wall base uplift for test ID 975-10

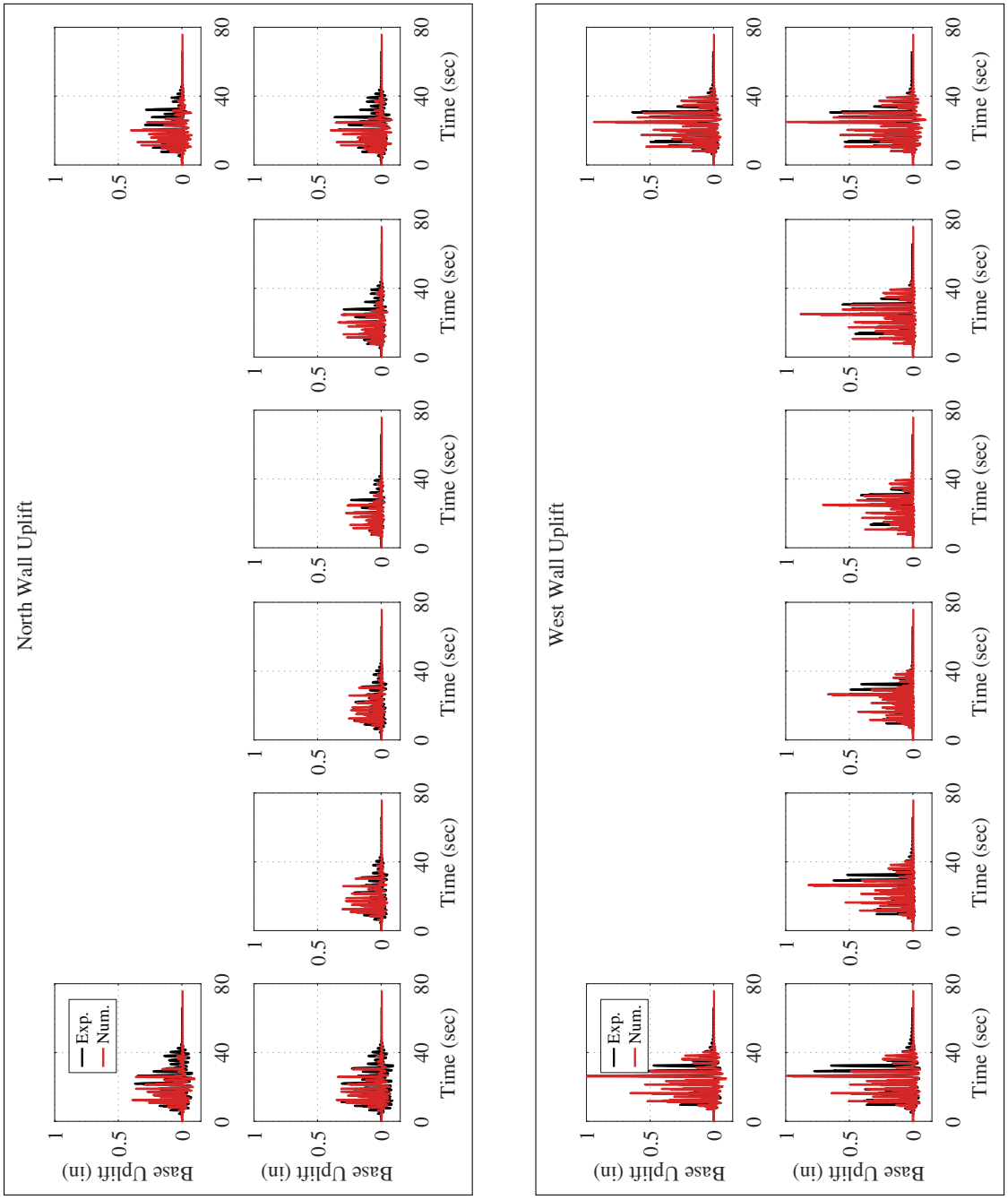

(a) North wall

(b) West wall

Figure 7.30: Comparison of experimental and numerical results for wall base uplift for test ID MCER-01

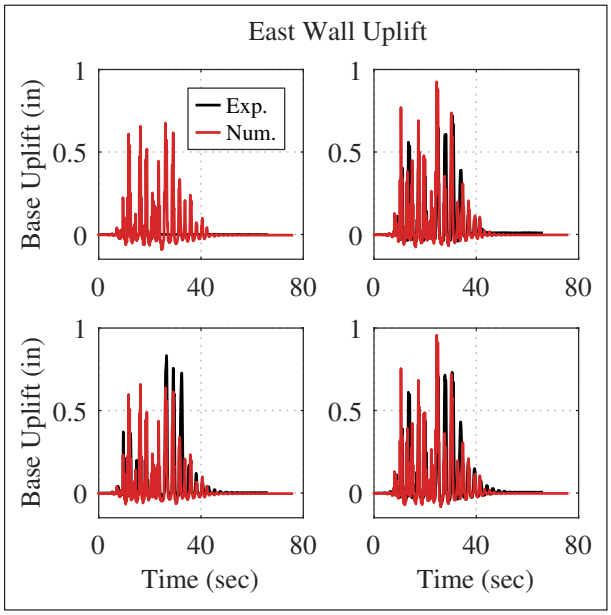

(c) East wall

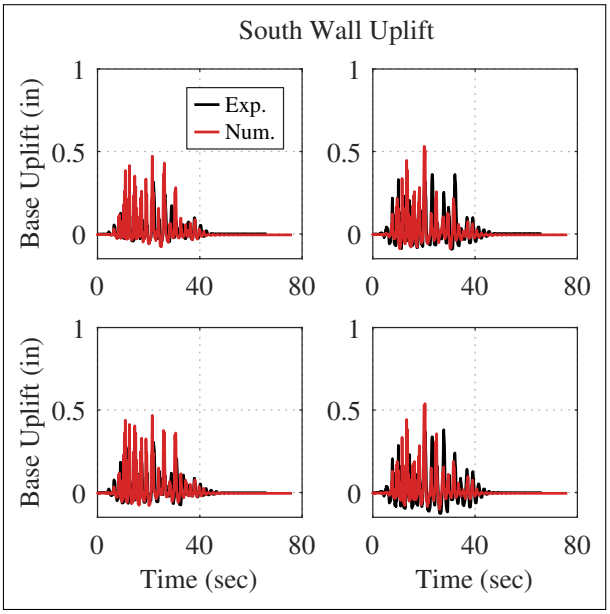

(d) South wall

Figure 7.30: Comparison of experimental and numerical results for wall base uplift for test ID MCER-01

Peak wall base uplift and compression deformation was summarized by looking at peak values for all 17 ground motions studied in this document. Figures 7.31 and 7.31 plot spectral acceleration at the building's period versus peak wall base uplift and peak compressive deformation for each wall, respectively. For the north and south walls, the spectral acceleration at the building's period was taken from the east-west ground motion component. For the east and west walls, the spectral acceleration at the building's period was taken from the north-south ground motion component. In these plots, experimental and numerical results from each individual ground motion are shown, in addition to the mean response value from each hazard level. These plots show a slight nonlinear response. The mean peak uplift and peak compressive deformation values are also summarized in Tables 7.11 and 7.12. Note, these results are showing the peak uplift and peak compressive deformation results at the location of one of the linear potentiometers on each of the walls, not the displacement of the outer most fiber on the corner. While the location of the outer most linear potentiometer was slightly different for each wall panel, they were in the same general area.

Table 7.11: Experimental and numerical mean wall base uplift results for each hazard level

Mean Peak Wall Uplift (in)												
Hazard	North Wall			South Wall			East Wall			West Wall		
Level	Num.	Exp.	% Diff.	Num.	Exp.	% Diff.	Num.	Exp.	% Diff.	Num.	Exp.	% Diff.
Level	Num.	Exp.	% Diff.	Num.	Exp.	% Diff.	Num.	Exp.	% Diff.	Num.	Exp.	% Diff.
43-year RP	0.00	0.02	2696.1%	0.00	0.01	197.3%	0.00	0.01	37.8%	0.00	0.02	1640.2%
225-year RP	0.07	0.13	74.5%	0.19	0.12	-37.9%	0.19	0.11	-39.7%	0.10	0.15	44.5%
475-year RP	0.30	0.31	5.9%	0.33	0.27	-19.3%	0.25	0.32	27.4%	0.33	0.31	-6.4%
975-year RP	0.49	0.89	81.7%	0.66	0.43	-34.7%	0.46	0.47	0.6%	0.54	0.67	24.1%
MCE_R	0.53	0.74	39.2%	0.82	0.64	-22.9%	0.68	0.64	-5.8%	0.58	0.58	-1.0%

Figures 7.33 and 7.34 compare numerical results versus experimental results for peak wall base uplift and peak compressive deformation values, respectively. A 1:1 diagonal line is also shown on the plots, representing a perfect correlation between numerical and experimental results. On the north and south walls there were two ground motions where the numerical model significantly under-predicted uplift, however, on the east and west walls, the numerical

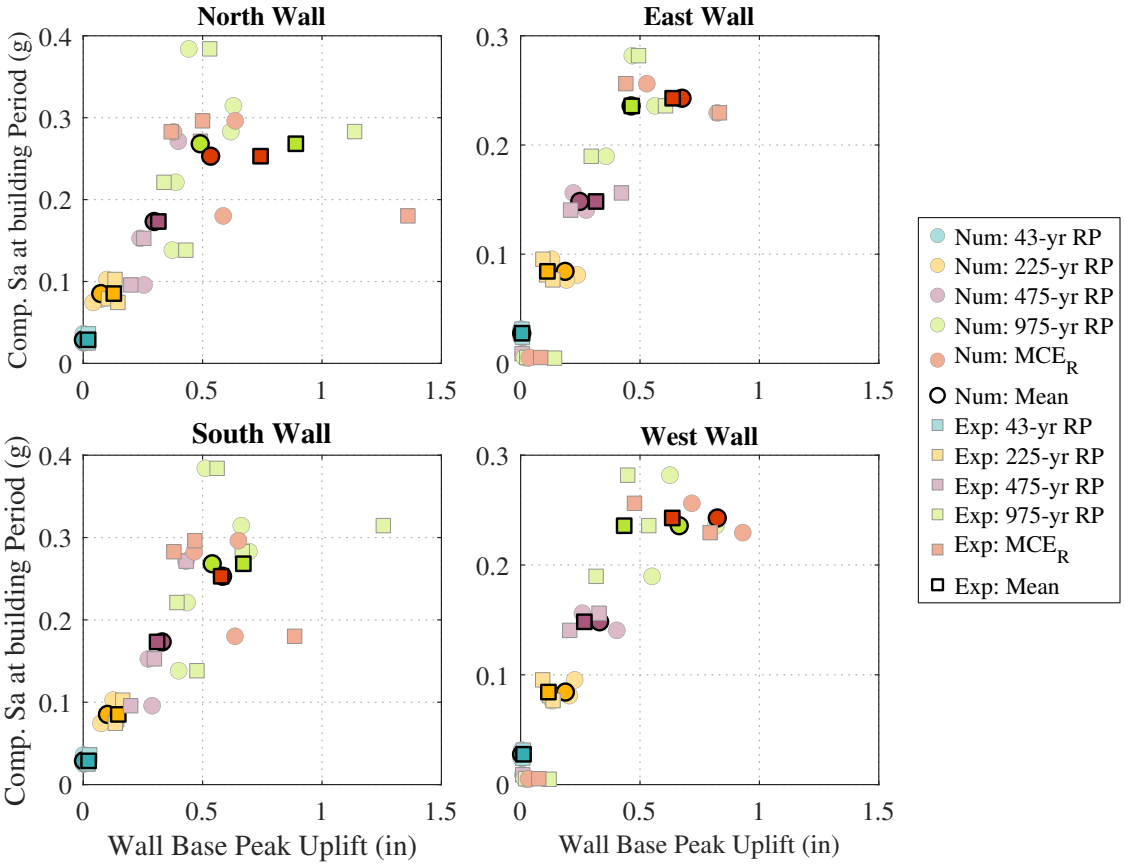

Figure 7.31: Summary of numerical and experimental peak wall base uplifts

Table 7.12: Experimental and numerical mean wall base compressive deformation results for each hazard level

Mean Peak Wall Compressive Deformation (in)												
Hazard	North Wall			South Wall			East Wall			West Wall		
Level	Num.	Exp.	% Diff.	Num.	Exp.	% Diff.	Num.	Exp.	% Diff.	Num.	Exp.	% Diff.
43-year RP	-0.01	-0.01	47.7%	-0.01	0.00	-37.0%	-0.01	0.00	-61.1%	-0.01	-0.02	154.8%
225-year RP	-0.03	-0.06	74.2%	-0.03	-0.02	-33.6%	-0.03	-0.02	-37.3%	-0.04	-0.07	83.7%
475-year RP	-0.06	-0.07	28.5%	-0.05	-0.03	-33.8%	-0.04	-0.03	-32.0%	-0.06	-0.08	45.9%
975-year RP	-0.08	-0.09	16.3%	-0.07	-0.05	-31.4%	-0.06	-0.04	-40.8%	-0.08	-0.12	43.5%
MCE_R	-0.09	-0.11	15.7%	-0.08	-0.06	-31.8%	-0.08	-0.05	-39.2%	-0.09	-0.14	55.5%

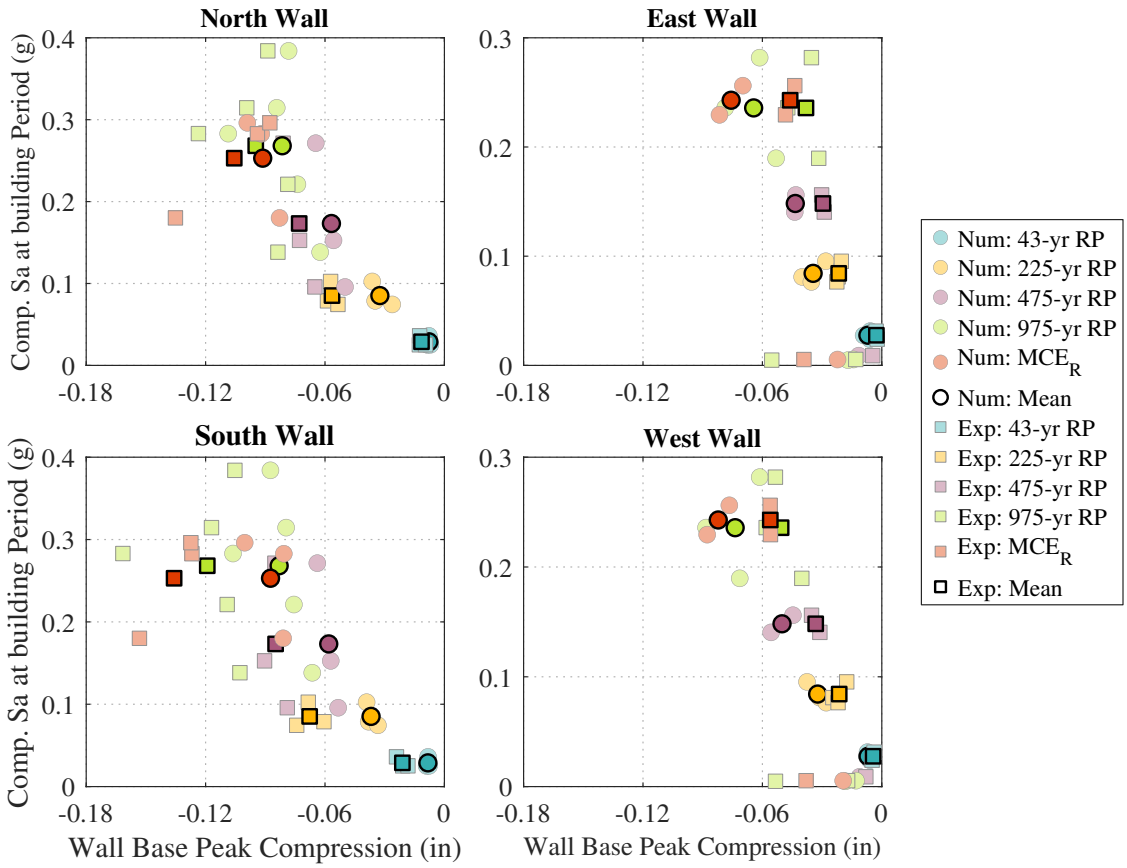

Figure 7.32: Summary of numerical and experimental peak wall base compression deformations

model generally over-predicted uplift slightly. For peak wall base compressive deformation values, the numerical model slightly under-predicted experimental results on the north and south walls. For the east and west walls, the numerical model slightly over-predicted experimental results for peak compressive deformations at the base of the wall panels. Overall, the model prediction is in reasonably good agreement with the experimental results in terms of predicting uplift response.

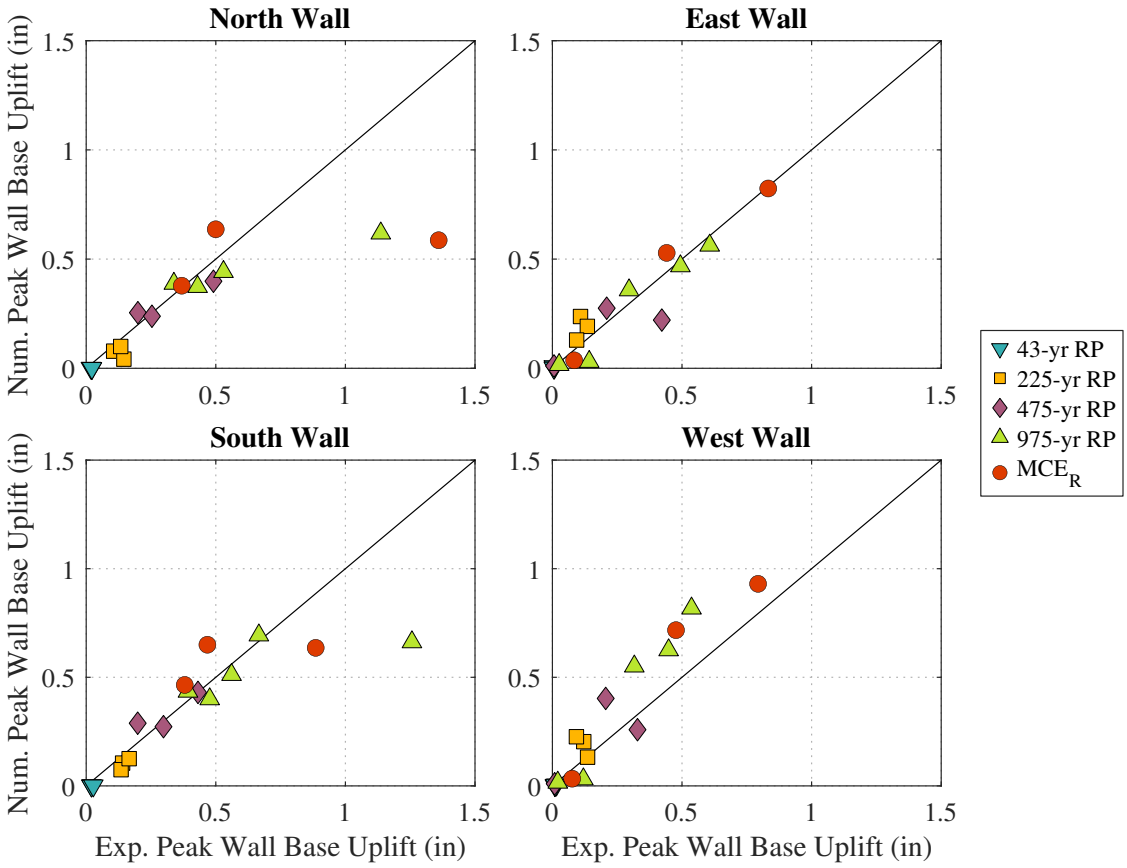

Figure 7.33: Summary comparison of numerical and experimental peak wall base uplifts

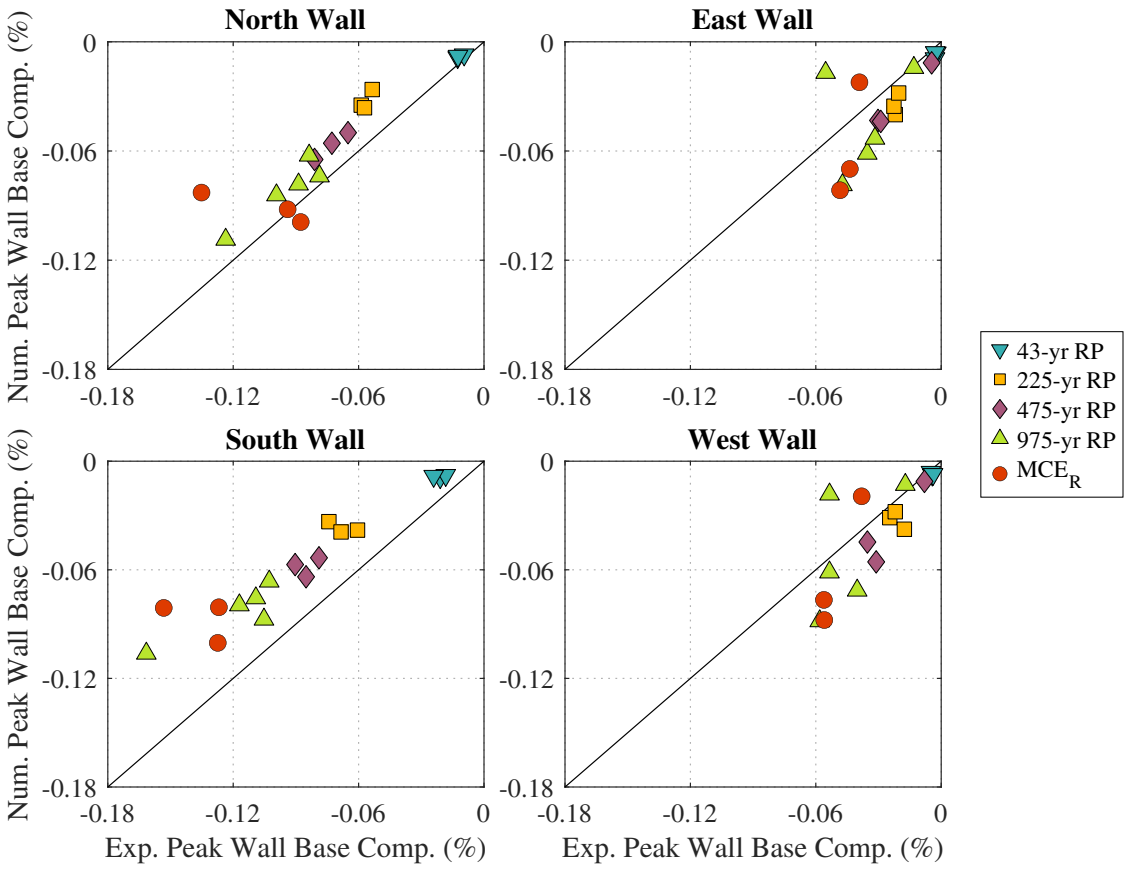

Figure 7.34: Summary comparison of numerical and experimental peak wall compressive deformations

7.9 Summary

In this chapter, the testing plan, performance, and comparison of experimental and analytical results for the post-tensioned mass timber rocking wall system in the NHERI TallWood building are presented. The test specimen was tested during May 2023 at the large outdoor shake table facility at UCSD. The building was tested under uniaxial, biaxial, and triaxial ground motion records scaled to five hazard levels (43-year return period, 225-year return period, 475-year return period, 975-year return period, and MCE_R). The unique seismic hazard of Seattle, Washington was captured by testing interface, intraslab, and crustal ground motions at all hazard levels. The experimental building behavior was determined from a variety of instrumentation recordings.

7.9.1 Performance of 10-Story NHERI TallWood Lateral Force-Resisting System

The four post-tensioned mass timber rocking walls met and exceeded design performance objectives. During the intensive testing plan that included more ground motions than any real building would ever experience, the rocking walls and their connections experienced little to no damage. The design criteria at MCE_R seismic hazard limited peak ISDs to 2.25% for the suite mean. Three MCE_R ground motions were run in the testing plan. The mean peak ISDs, calculated using filtered and double integrated accelerometers on each floor, were 1.47% and 1.75% for the east-west and north-south directions, respectively. The mean peak ISDs, calculated using the diagonal string potentiometer data, were 1.36% and 1.54% for the east-west and north-south directions, respectively. These values are all below the 2.25% ISD limit, indicating the lateral system met design criteria limits for ISD. At MCE_R, design criteria was also enforced for a series of force and deformation-controlled actions. Building components with enforced force-controlled actions are intended to remain elastic during earthquake shaking. All components designed for force-controlled actions (most of the lateral connections and the mass timber wall panels under axial-flexural loads and shear loads) appeared to remain elastic, satisfying this design criteria. Building components with

enforced deformation-controlled actions are expected to undergo nonlinear behavior during earthquake shaking. Two primary deformation checks were used for design and both satisfied design limits during testing. The first was limiting deformation of the UFPs to prevent fracture of the UFP and it's connections. The second was limiting deformation of the wood at the base of the wall panels. In design, yielding was allowed at MCE_R, however, in testing no damage to the base of the walls was observed. In summary, the post-tensioned rocking wall lateral system performed as designed, or perhaps better than designed, validating the presented performance-based design procedure used to design the system.

7.9.2 Comparison of Experimental and Analytical Results

As part of the performance-based design procedure used to design the post-tensioned rocking wall lateral system, a 3D nonlinear numerical model was developed to determine component demands and predict building performance. In this chapter, predictions from the numerical model were compared to experimental building performance. For this comparison, the true ground motions executed by the shake table were input into the OpenSees model and the damping was increased from 2% to 6% based on the damping study presented in Section 7.7. Apart from these two modifications, no other changes were made to the OpenSees model. For this comparison, floor displacements, ISDs, and wall uplift values were examined. Overall, predictions from the numerical OpenSees model matched well with measured building response at all five hazard levels.

Using the filtered and double integrated accelerometer data to determine experimental results, floor displacement values match very well while calculated ISDs did not match as well. When recorded data from two floors are subtracted to calculate ISDs, results are produced that are not representative of the observed building behavior. It is suspected that minor issues with accelerometer installation or issues with the filtering and double integration procedure used is the cause of these issues. The erroneous building behavior that shows up in ISD calculations could explain why the experimental and numerical floor displacement data matches better than the ISD data. Despite these differences, it is concluded that from a

global performance standpoint, the presented numerical modeling methodology does a good job at predicting true building performance. Note, the numerical model does not include strength or stiffness contributions of the gravity framing connections, nonstructural walls, or stairs. Because the model can still predict overall building performance, it is concluded that the rocking walls dominate the overall behavior of the building system.

From a global building response prospective, the numerical model was able to predict building performance well. At the local level, numerical and experimental results were compared by looking at base uplift of the post-tensioned rocking wall lateral system. The model did a good job at predicting overall uplift behavior when looking at time history results. However, the model did not capture peak response as well. This indicates that the true material model for the behavior of the rocking wall in compression and/or the plastic hinge length assumed for modeling purposes may not predict true performance as well. This is also true because the the numerical model predicted damage to the base of the wall panels, but no damage was observed during testing.

Chapter 8

EFFECT OF BUILDING PERIOD AND WALL ASPECT RATIO ON THE SEISMIC PERFORMANCE AND MOMENT AMPLIFICATION OF TALL POST-TENSIONED MASS TIMBER ROCKING WALLS

8.1 Overview

The most critical part of the post-tensioned rocking wall lateral system design for the NHERI TallWood 10-story building was the capacity of the splice connection and the capacity of the rocking wall panel under combined axial loads and bending. These were the demand to capacity checks that were either closest to 1.0 or exceeded 1.0. In design, they were controlled by the moment envelop demands from nonlinear response history analysis (NLRHA) which showed a large amplification of moment demands at mid-height of the rocking wall due to higher mode effects. As discussed in Section 2.7 of the literature review, dynamic amplification of forces in upper stories from higher mode effects is common for base rocking systems due to the flexibility of these systems. Typical code-based lateral force distributions for determining the design base overturning moment, such as equivalent lateral force (ELF) procedure or modal response spectrum analysis (MRSA), do not capture the amplified shape of the force envelopes. A nonlinear model needs to be created, which is not typical for standard code-based design procedures. However, as shown in the 10-story design, this amplification needs to be accounted for. It is important to quantify an amplification relationship between standard design practice and observed response for nonlinear models that could someday be adopted into code.

Understanding the true design moment envelope becomes particularly important for the discussion of tall buildings as past research has shown that moment amplification increases

with increasing period. It is also important as horizontal construction joint splices must be introduced into the design once the height of the wall exceeds manufacturing and transportation size limitations. Design and construction experience from the 10-story NHERI TallWood project showed that meeting design requirements and executing the construction of these joints was challenging, thus, avoiding the location of maximum moment should an important design consideration.

As discussed in Section 2.7 of the literature review, previous researchers have observed and studied these force amplifications from higher mode effects in many types of base rocking systems including precast concrete rocking walls, rocking steel braced frames, and post-tensioned mass timber rocking walls. Wiebe and Christopoulos [2015] proposed and validated a method for calculating the peak moment demand that accounts for higher mode effects without developing a nonlinear model. Introducing additional rocking joints up the height of the structure has been proposed by many (Wiebe and Christopoulos [2009], Wiebe and Christopoulos [2015], Kovacs and Wiebe [2019], Pilon et al. [2019], Alegria [2022], and other) as means to reduce the effects of moment amplification. These studies have shown that introducing additional rocking planes is effective in reducing demands and does not have a large impact on drift performance. While adding additional joints is effective, little research has been done to quantify the magnitude of moment amplification that exists if a continuous wall is used or to study how different parameters affect the moment amplification of continuous walls. Alegria [2022] studied post-tensioned rocking wall lateral systems with different wall aspect ratios and found that narrower panels are more susceptible to higher mode effects, moment amplification, and increased drifts, however, also indicated that this was likely a result of increased flexibility in the more narrow walls.

The study presented in this chapter focuses on continuous walls post-tensioned mass timber rocking walls. Six total archetypes, three 6-story buildings and three 12-story buildings, were designed following force-based prescriptive procedures. For designs of the same height, the overall building period was held constant to study the impact of aspect ratio independently of building period. Nonlinear models for each design were assessed using ground

motion suites at seven hazard levels. The results from this study are used to look at four different relationships that have not been addressed in past research. They are as follows:

1. Study the impact of wall aspect ratio in terms of building performance and its effect on moment amplification, independent of building period
2. Study the effect of building period using building at different weight
3. Study the effect of increasing hazard level on moment amplification
4. Study the location of peak moment up the height of the walls to aid in splice design
5. Perform these comparisons with respect to demands calculated from MRSA, a typical code-based method for determining force demands

8.2 Archetype Descriptions

This study looks at a 6-story building and a 12-story building to investigate the effects of period on building performance and moment amplification from higher mode effects. Three different lateral system designs are presented for each of the two building heights, resulting in six total archetype designs. The three different designs for the two building heights investigate the effects of wall aspect ratio. This was done by changing the number of walls in each direction to maintain a constant first-mode elastic period and overall building stiffness at each weight. The six archetypes are summarized in Table 8.1. The first linear period shown in this table is the period of the first mode, obtained from the eigenvalue analysis on the linear elastic model used to complete the MRSA (discussed in more detail in Section 8.4.1). The number of walls listed in Table 8.1 are the number of walls in one building direction.

The building floor plans used for this study are intended to represent typical mid-rise office buildings (risk category II) in the United States. The archetypes were designed for the same Seattle, Washington location used for the 10-story NHERI TallWood test specimen. Given that both the 10-story specimen and these archetypes are designed for office occupancy, the same site seismic parameters were used (see Section 6.3). For design, a constant dead load of 60 psf and a constant live load of 65 psf (50 psf for office loading and 15 psf for office

Table 8.1: Parametric Study matrix of analyzed building archetypes

	Archetype ID					
	6-AR1	6-AR2	6-AR3	12-AR1	12-AR2	12-AR3
Number of Stories	6	6	6	12	12	12
1^{st} Linear Period	1.51	1.51	1.51	2.84	2.84	2.84
Number of Walls X	4	8	12	4	8	12
Wall Aspect Ratio	4.1	5.4	6.3	6.0	7.7	8.9
Floor Weight	1347 k	1347 k	1347 k	1316 k	1316 k	1316 k
Floor Plan	100 ft x 200 ft					

partition loading per ASCE/SEI 7-16) was assumed on all floors. A total seismic weight of 70 psf was assumed on all floors (1347 kips and 1316 kips per floor accounting for core openings for the 6-story and 12-story archetypes, respectively).

All six building archetypes had the same symmetric 100 feet by 200 feet rectangular floor plan. The story height for the first floor was 20 feet and the remaining stories were all 12 feet. Figure 8.1 shows the baseline floor plan for both the 6- and 12-story archetype designs. These floor plans are for the designs with the smallest wall aspect ratios and fewest number of walls for each building height (labeled as AR1). The floor plans for the archetype designs with the higher aspect ratios and larger number of walls in each direction (labeled as AR2 and AR3), are not shown directly, but are proportionally equivalent. As discussed in the numerical modeling section (Section 8.3) all analyses were conducted in two-dimensions. For each archetype, a single post-tensioned rocking wall in the x-direction was designed and analyzed and torsional effects were neglected. Because the buildings are symmetric, the presented designs could be representative of all the walls in the building.

This study used APA certified IB MAX-CORE glulam columns from SmartLam [APA, 2022]. The columns were designed for the 6-AR1 and 12-AR1 archetypes based on the floor plans shown in Figure 8.1. The 6-AR1 column design was assumed for all three 6-story buildings and the 12-AR1 column design was assumed for all three 12-story buildings. This is a reasonable assumption as the column layout would only have to be modified slightly to

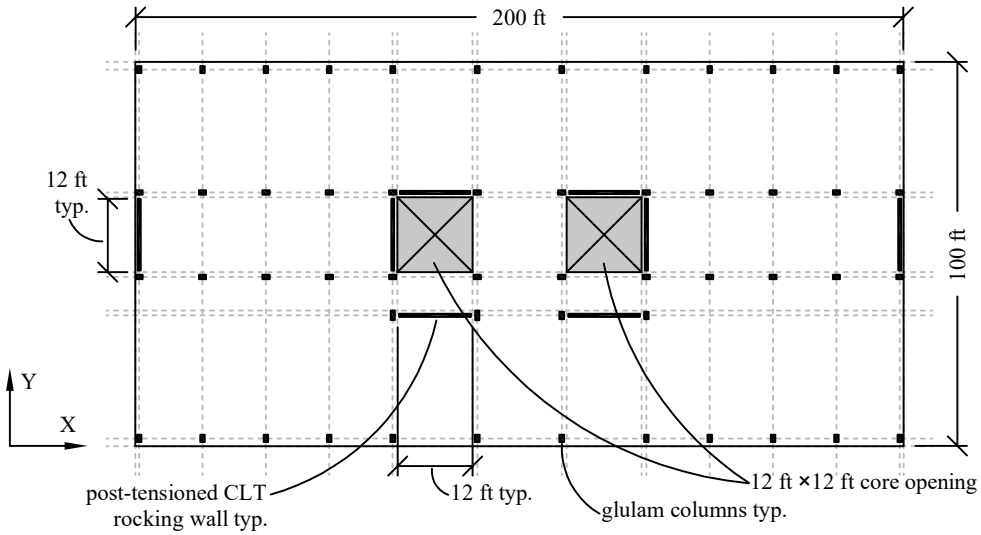

(a) Archetype 6-AR1 floor plan

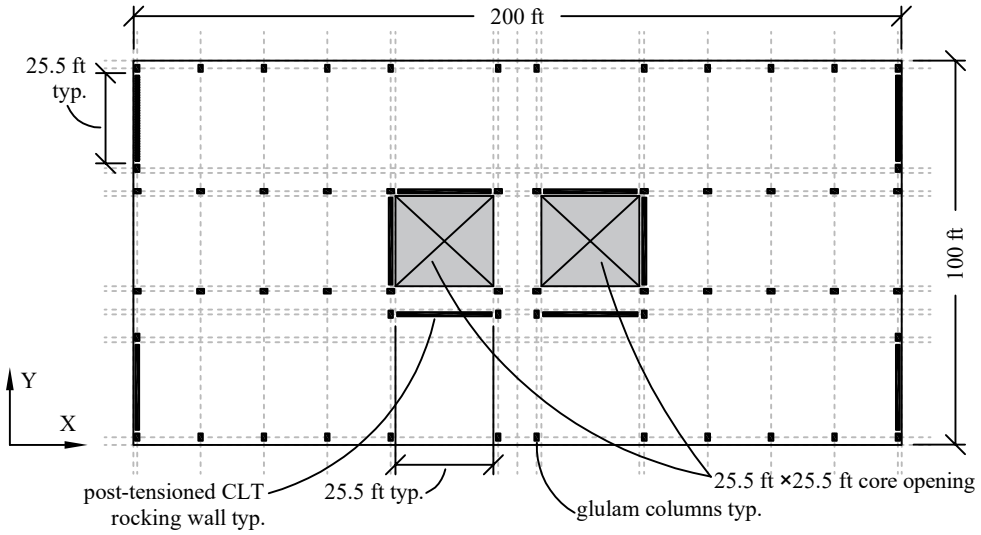

(b) Archetype 12-AR1 floor plan

Figure 8.1: Building floor plans for (a) 6-AR1 and (b) 12-AR1 archetypes

accommodate the increased number of walls in each direction and the different wall lengths since the total lateral building stiffness remains the same for all buildings of the same story height. All column sizes, including the gravity and the boundary columns, were the same for each building height and a constant cross section was assumed for the whole height. The

columns were designed using ASD in accordance with the NDS with a 2-hour fire safety rating. The ASD load case D + L was used for design and accounted for live load reduction. Detailed calculations for the column design will not be included in this document as standard design procedures were used. Table 8.2 summarizes the reference values needed for design, the modeling parameters (which will be used in Section 8.3), and the final column dimensions.

Table 8.2: Glulam column properties used for the archetype designs

IB MAX-CORE Glulam Column Properties				
Grade: N1D14				
Combination Symbol: MAX-CORE Combination No. 50				
Manufacture: SmartLam				
Reference Design Values				units
Comp. parallel to grain	F_c	2300		psi
MOE for x-x axis buckling	$E_{x,min}$	1.00E+06		psi
MOE for y-y axis buckling	$E_{y,min}$	1.00E+06		psi
Modeling Properties				
MOE for x-x bending	$E_{x,true}$	2.00E+06		psi
MOE for y-y bending	$E_{y,true}$	2.00E+06		psi
Glulam Column Dimensions				
		6-Story	12-Story	
Column width	w	14.25	18	in
Column depth	d	16.5	22	in
Number of columns	n_{col}	52	56	

Grade E21M2 CLT from SmartLam was used for the post-tensioned rocking walls in this study [APA, 2023b] [SmartLam, 2023]. As discussed in Section 8.4, the 7-maxx and 9-maxx layup were used for the 6- and 12-story archetype designs, respectively. These layups are slightly different than a traditional CLT panel as the outer two laminations on each face are both longitudinal layers, oriented in the strong axis direction. This results in a slightly stronger material when utilized as shear walls, which was needed to meet design requirements for these tall building designs. Table 8.3 includes the design reference values from the manufacturer that are needed to complete the design. Note, for the in-plane shear stress design value, $F_{v,e,90}$, a value from a different manufacturer, with a comparable CLT

grade and layup design (E1M7 from APA [2023a]), was used. This was done because the values reported by SmartLam in SmartLam [2023] were derived analytically and were very conservative. The values used from APA [2023a] were obtained from certified material tests and are more representative of the real strength.

Table 8.3: CLT wall properties used for the archetype designs

CLT Wall Properties				
Grade: E21M2 Manufacture: SmartLam				
Design values - major strength direction				units
		7-maxx	9-maxx	
Compressive stress	F_c	1875		psi
Tensile stress	F_t	1575		psi
Flexural stress	F_b	2100		psi
MOE	E_0	1.80E+06		psi
Eff. bending stiffness	$EI_{eff,0}$	1.49E+09	2.96E+09	lb in^2/ft
Eff. bending shear stiffness	$GA_{eff,0}$	1.20E+06	1.50E+06	lb/ft
In-plane shear stress[a]	$F_{v,e,90}$	235	235	psi
Modeling parameters				
long/total lamination ratio	-	5/7	6/9	-
Effective MOE	E_{eff}	1.29E+06	1.20E+06	psi
Effective shear modulus	G_{eff}	8.00E+04	8.00E+04	psi
Yield stress	$f_{y,clt}$	3214	3000	psi
Splitting strain	$\epsilon_{s,clt}$	0.0079		in/in
Crushing strain	$\epsilon_{cr,clt}$	0.0398		in/in
Plastic hinge length	l_p	28.80	54.72	in

[a] In-plane shear stress design values taken from different manufacturer specifications

Also included in Table 8.3 are the modeling parameters that are utilized in Section 8.3. The effective MOE values shown, E_{eff}, were calculated by multiplying the MOE of the major strength direction panels, E_0, by the ratio of longitudinal layers to total number of layers (5/7 for the 6-story archetypes with the 7-maxx layup and 6/9 for the 12-story archetypes with the 9-maxx layup). Note, this is a simplified and more conservative version of the previously presented Equation 6.1. As shown, the same effective shear modulus, G_{eff}, as

the one used for the 10-story NHERI TallWood modeling was assumed. The compression strength of the wood parallel to grain, $f_{y,clt}$, was taken as the LRFD strength defined per the NDS and adjusted by the ratio of longitudinal layers to total number of layers (i.e., $K_F \times \lambda \times F_c \times 5/7$ for the 7-maxx CLT in the 6-story archetypes and $K_F \times \lambda \times F_c \times 6/9$ for the 9-maxx CLT in the 12-story archetypes, where K_F is equal to 2.4 and λ is equal to 1.0). Again, the compression behavior of CLT in the parallel to grain direction past yield has not been standardized. Thus, for this study, the same post-yield behavior assumed in the 10-story NHERI TallWood building model was used here (presented graphically in Figure 6.3a). This includes using the same splitting, $\epsilon_{s,clt}$, and crushing, $\epsilon_{cr,clt}$, strains as used for modeling the 10-story test. This is a valid assumption as the two materials are similar and the primary purpose of this study is to investigate the relative performance between the designs and not define final recommendations. The assumed plastic hinge length used for modeling is also included in Table 8.3. Details and assumptions relating to the plastic hinge length are discussed in the numerical modeling section (Section 8.3).

As shown in Figure 8.1, this study assumes a boundary column configuration for post-tensioned rocking walls. In all designs the walls are post-tensioned with a number of ASTM F1554 Grade 105 fully threaded rods (E_{pt} = 29000 ksi, $f_{y,pt}$ = 105 ksi, $f_{u,ufp}$ = 125 ksi) that run the entire height of the walls and are located at mid-width and on each face of the walls. Note, any center-line offsets of the bars that would be necessary for installation are neglected in the models since these models will only consider 2D behavior. For all the designs, rocking wall panels connect to the boundary columns using a number of UFPs. The UFPs are all made of ASTM A572 Grade 42 steel (E_{ufp} = 29000 ksi, $f_{y,ufp}$ = 42 ksi, and $f_{u,ufp}$ = 60 ksi). Table 8.4 summarizes the final designs for the six archetypes. Details discussing the procedure for designing the lateral systems and the limit state checks made will be discussed in detail in Section 8.4.

Table 8.4: Summary of the archetype lateral system designs

		Archetype ID						
		6-AR1	6-AR2	6-AR3	12-AR1	12-AR2	12-AR3	units
Wall Panel Details								
CLT Layup		7-maxx	7-maxx	7-maxx	9-maxx	9-maxx	9-maxx	
Wall thickness	b_w	9.625	9.625	9.625	12.375	12.375	12.375	in
Eff. wall thickness	$b_{w,eff}$	6.875	6.875	6.875	8.25	8.25	8.25	in
Wall length	L_w	234	178.25	153.25	306	237.75	206	in
height of walls	h_w	960	960	960	1824	1824	1824	in
UFP Details								
UFPs per wall side	n_{ufp}	24	12	12	12	12	12	
UFP width	b_u	7	6	7.25	12.5	7.75	5.75	in
UFP thickness	t_u	0.5	0.625	0.5	0.625	0.625	0.625	in
UFP diameter	D_u	4.25	4.25	4.25	4.25	4.25	4.25	in
PT Bar Details								
Number of PT bars	n_{pt}	8	6	6	8	8	6	
Area of one PT bar	A_{pt}	1.9	1.405	1.155	2.5	1.405	1.405	in^2
Total Initial PT force	$T_{o,pt}$	640	420	330	880	520	420	k
Initial PT force ratio	$T_{o,pt}/T_{y,pt}$	0.40	0.47	0.45	0.42	0.44	0.47	

8.3 Numerical Model Development

As discussed below in Section 8.4, a linear numerical model for each archetype was developed in OpenSees to perform the modal response spectrum analysis needed for the prescriptive design of the different lateral systems. Additionally, a nonlinear model was also developed in OpenSees for conducting a NLRHA on the final designs for performance assessment and to study moment amplification from higher mode effects. Both models were developed in two-dimensions and represented just one of the walls in the x-direction. Both models were developed using techniques similar to those used for modeling of the 2-story and 10-story NHERI TallWood test specimens. This section will give an overview of each model and will highlight the differences from the previously presented modeling procedures in this document.

8.3.1 Linear model development

The linear model used for MRSA was a simple single cantilevered wall model. As recommended by Busch et al. [2022] and to maintain consistency with currently industry methods, the wall was modeled with a fixed base and excludes the PT bars, the UFP elements, and the boundary columns. The goal of this model was for it to be representative of what would be used by practicing engineers, likely using a commercial software such as SAP2000 or ETABS. In practice, the full building would be modeled to capture torsional effects in the building. However, because the buildings investigated in this study are symmetric, resulting in low torsional effects, a 2D linear model of a wall and its proportional mass are used for the linear analysis. The walls were modeled using force beam column elements with the wall dimensions b_w and L_w shown in Table 8.4 and used approximately a 2 inch $\times$ 2 inch mesh size. Similar to the NHERI TallWood 10-story model, an elastic material model with slope equal to E_{eff} from Table 8.3 was applied to the element. Shear deformations were accounted for using the section aggregator command in OpenSees and an effective shear modulus of G_{eff} from Table 8.3 (see Section 6.5.1 from the 10-story chapter for more explanation). As shown in the results of this study (Section 8.5), the moment contribution from the UFPs, even in the linear model, is non-negligible, however, they were excluded to be consistent with industry standards. In this model, mass proportionally equivalent to the total number of shear walls was applied at wall nodes located at each floor level. Gravity loads were not applied as this model was only used for MRSA.

8.3.2 Nonlinear model development

Two-dimensional nonlinear numerical models were also developed for each archetype design. One wall was modeled for each of the archetype designs. As discussed below, the gravity columns, mass, and gravity loads applied to each model were proportionally equivalent to the total number of walls in the x-direction of the building. Figure 8.2 shows a schematic of the nonlinear numerical model developed in OpenSees for the 6 different archetype designs.

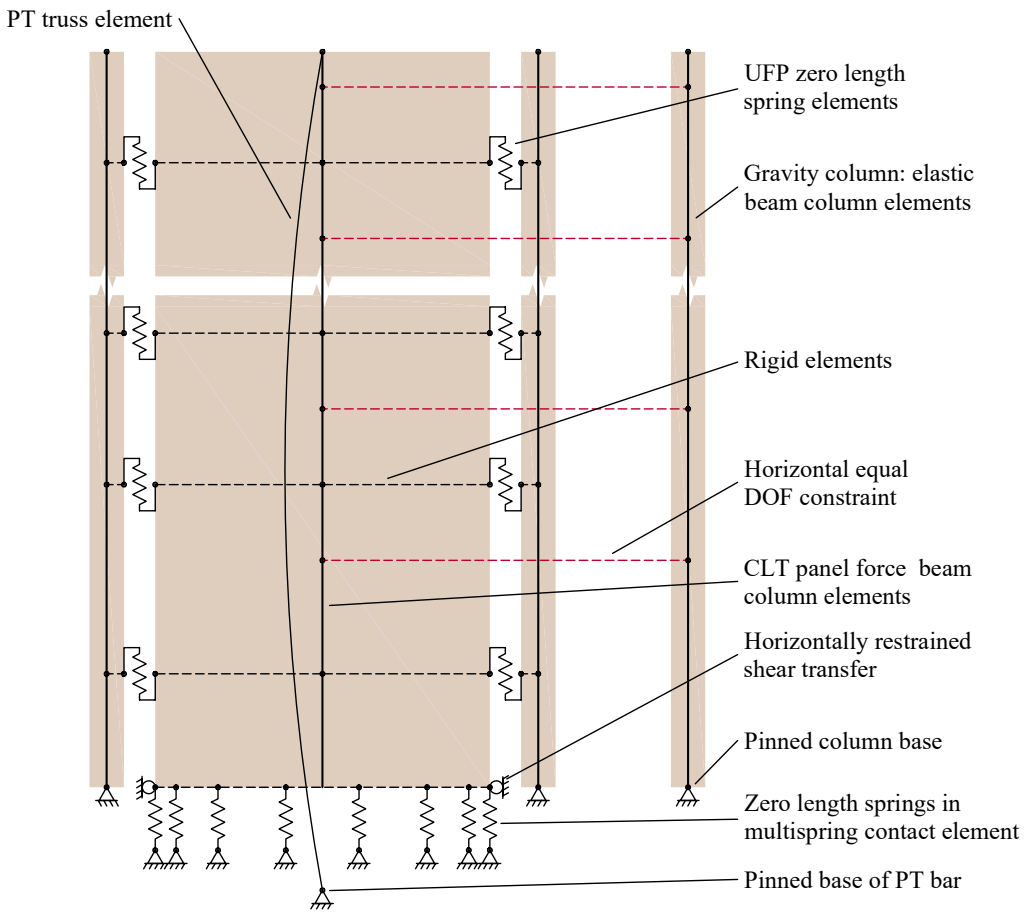

Figure 8.2: Numerical model schematic used for the parametric study

The elastic portion of the rocking wall was modeled as described in the preceding linear model developed section. The inelastic compressive deformation of the wall base and the rocking behavior was modeled using the same multispring contact element used for both the 2-story and 10-story NHERI TallWood models. See Section 6.5.1 from the 10-story design chapter for a detailed explanation of this element and the shear resisting supports at the upper corners of the spring elements. The only modification made to this element is the conversion from 3D to 2D. Because these models were completed in 2D, only a single line of springs, distributed using the Labatto Integration method, was used. Figure 6.16a shows the material model applied to each spring. Reference Table 8.3 for the material properties

used. Also, see Section 6.5.1 for a discussion on how the assumed plastic hinge length, l_p, is used to convert from the stress-strain constitutive model to the force-deformation model needed for the zero length springs. Similar to the 10-story model, an additional elastic truss element with area calculated using Equation 6.3 was added to combat the increased axial flexibility from the multispring element.

As discussed in the modeling sections for the 2-story and 10-story NHERI TallWood building specimens, the concept of the plastic hinge length is adopted from reinforced concrete walls. ACI [2009] defines the plastic hinge length as $0.06 \times h_w$ for unbonded post-tensioned precast shear walls. Currently there is no defined value for what should be used with post-tensioned rocking mass timber walls. Thus, a plastic hinge length of $0.03 \times h_w$ was used for this study, resulting in plastic hinge lengths of 28.80 inches and 54.72 inches for the 6-story and 12-story archetypes respectively (Table 8.3). This was based on the $0.06 \times h_w$ recommendation in ACI [2009], but reduced. This value was reduced as research in post-tensioned rocking mass timber walls have typically used shorter plastic hinge lengths [Akbas et al., 2017]. For example, Busch [2023] used a plastic hinge length of 24 inches and 36 inches for walls that were 80 feet and 152 feet respectively (the same wall heights used in this study).

The PT bars were modeled using corotational truss elements that connect a fixed node at the base to the top of the rocking wall element. The material model used for the 10-story model (shown in Figure 6.16d) was also used for these models. Reference Table 8.4 for the PT bar details for each archetype. Similar to the 10-story model, an increased PT bar force, $T_{o,pt}*$, calculated using Equation 6.4, was applied to the PT elements using the initial strain wrapper in OpenSees to compensate for prestress losses due to wall shortening.

The boundary columns were modeled using continuous elastic beam column elements pinned at the bases. The geometric and material properties used for these columns are shown in Table 8.2. Each UFP was modeled using a zero length spring element located at the midpoint between the wall edge an the respective boundary column edge (note, for all archetypes, the distance from the edge of the wall face to the center of the respective boundary column was equal to 15 inches). Material properties were only assigned to the

vertical degree of freedom, as described in the 10-story modeling discussion (Section 6.5.1). The material model shown in Figure 6.16c was used with stiffness and yield force defined by Equations 3.4 and 3.2, respectively. Reference Table 8.4 for the input parameters for each archetype design.

For each archetype, the gravity system was modeled using a p-delta column, as shown in Figure 8.2. While detailed calculations and drawings were only done for archetypes 6-AR1 and 12-AR1, the size of the p-delta gravity column in each archetype was scaled so it was proportional to the full building based on the number of rocking walls in each design. In these models, the gravity loads were applied at nodes on the p-delta column, located at each floor level. A fraction of the total building floor weight (shown in Table 8.1) was applied in each model, based on the total number of structural walls in each building direction. For example, a load of 1347 kips $\times$ 1/4 was applied to each floor level for archetype 6-AR1. An equivalent horizontal seismic mass was assigned to the wall node each each floor level. The p-delta gravity column was tied to the wall nodes using a horizontal equal degree of freedom constraint in OpenSees at each floor level.

8.4 Rocking Wall Design Procedure

The six archetypes studied were designed using a procedure representative of a prescriptive procedure that would be used by practicing engineers if these rocking wall lateral systems were accepted into US design codes. It is similar to the prescriptive procedure presented in Busch et al. [2022] and the first two phase of the design procedure used for the 10-story NHERI TallWood building design (described in detail in Sections 6.6.1 an 6.6.2). First, a MRSA was completed to check drift limits and determine design rotation demands. Then, the design rotation demands were used with a set of component level limit state checks to design the PT and UFP elements and determine the design moment capacity of the connection. Finally, the capacity of the wall panels in shear and combined axial loading and flexure (net-compression and net-tension) were checked. This section will outline the exact procedure used and identify the modifications made from the 10-story design procedure.

8.4.1 Modal Response Spectrum Analysis

The first phase of the design procedure was to complete a drift analysis check and determine rotation demands at the base of the rocking wall using results from a MRSA using DBE demands. The linear model presented in Section 8.3.1 was used to complete this analysis.

As part of the MRSA, an eigenvalue analysis was conducted on the linear models. The first mode period from these analyses are shown in Table 8.5 which summarizes the results from the MRSA. By design, the elastic first mode periods are identical for all archetypes of the same height. The ISDs for each archetype were checked against a 2% limit state using a MRSA and DBE demands. For this check $R = 6$ and $C_d = 6$ were used. See Section 6.6.1 for a more detailed discussion and background information for this check. Figure 8.3 shows the distribution of story drifts under the DBE demand for all six archetypes. As shown, all archetypes meet the 2% ISD limit state check. The drift distributions for the three 6-story archetypes are very similar to each other and the drift distributions for the three 12-story archetypes are also similar to each other. This is expected as the elastic first mode period across the archetypes of the same height are identical. The 12-story archetypes reach slightly larger ISDs which is also expected since the building period is larger.

Table 8.5: MRSA results per wall for each archetype design

		Archetype ID						
		6-AR1	6-AR2	6-AR3	12-AR1	12-AR2	12-AR3	units
1st Linear Period	$T_{1,linear}$	1.51	1.51	1.51	2.84	2.84	2.84	sec
DBE rotation demand	θ_{DBE}	0.0069	0.007	0.007	0.0075	0.0077	0.0078	rad
MCE_R rotation demand	θ_{MCE_R}	0.0121	0.0122	0.0122	0.0129	0.0131	0.0123	rad
MRSA moment demand	M_u	123186	60096	39734	207952	98455	64173	k in
MRSA shear demand	V_u	216	108	72	261	130	87	k

Using results from the MRSA at DBE demands, the rocking wall rotation demands at the base of the walls at DBE, θ_{DBE}, and MCE_R, θ_{MCE_R}, were calculated as described in Section 6.6.1, using Equations 6.12 and 6.13. The rotation demands calculated for each archetype are summarized in Table 8.5. Because the linear first mode periods are the same

for archetypes of the same building height, the rotation demands are also similar. These are the rotation demands that will be used in the prescriptive design procedure.

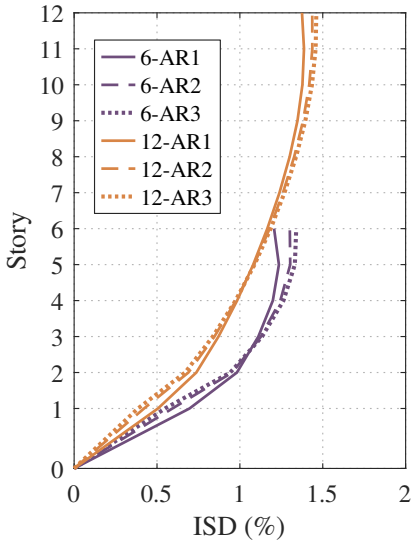

Figure 8.3: ISD results from MRSA of the six archetypes

Figure 8.4 shows the wall shear and moment distributions from the MRSA for each of the six archetypes. For these plots, the wall shears and moments representative of the whole building are shown (i.e., the results from the analysis were multiplied by the total number of walls in the building). Additionally, the heights have been normalized by total wall height to compare the distributions up the wall heights of the two different period buildings. These plots show that only period (i.e., building height for these archetypes) affect the demands calculated from MRSA and wall aspect ratio does not. The peak shear, V_u, and moment, M_u, demands per wall from MRSA at DBE hazard are summarized in Table 8.5. These are the values that will be referenced for capacity checks.

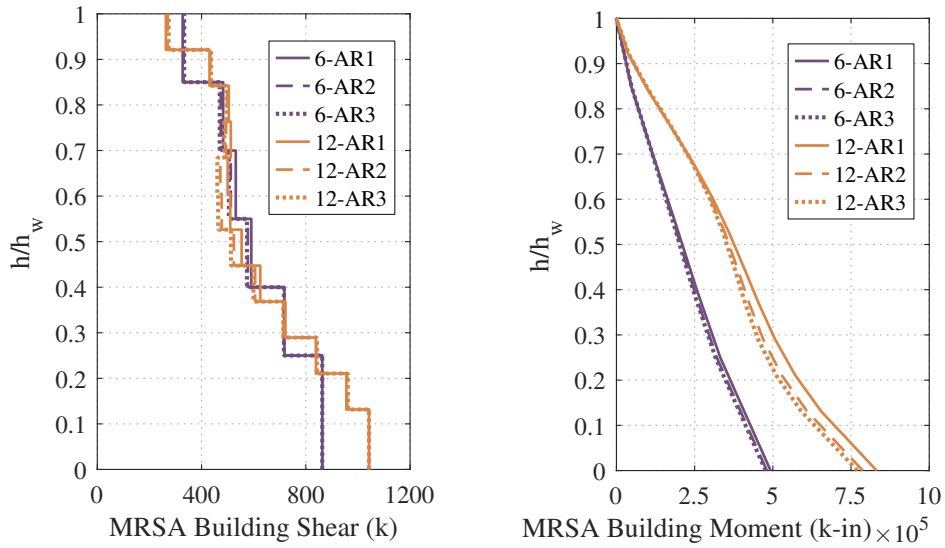

(a) Wall shear

(b) Wall moment

Figure 8.4: Wall (a) shear and (b) moment results from the MRSA on the OpenSees model of the six archetype designs

8.4.2 Cross-Sectional Analysis Design Procedure

The second phase of the design procedure uses a modified version of the previously presented iterative cross-sectional analysis procedure (Section 3.3.1) to estimate the moment capacity of the rocking wall systems at DBE and MCE_R, using the rotation demands from the MRSA. Another example of the cross-sectional analysis procedure can be found in Section 6.6.2 for the 10-story NHERI TallWood building design. One modification to the procedure used for the 10-story building, was that the yield strain for the UFP steel was used to calculate the yield force of the UFPs at MCE_R demands as opposed to the ultimate strain. It was found that using the yield force in these calculations more closely matched the UFP forces in the numerical models since the increase in force past yield is minimal for the deformations in these UFPs. For this step of the design procedure, the UFP and PT bar properties were adjusted until the required checks were met and the desired designs were achieved. Figure 8.5

shows a free-body diagram of the base of the wall panels that was used for this procedure to calculate the total moment capacity of the wall system. Table 8.6 summarizes the key forces and compression distances for the DBE and MCE_R rotations for each of the six archetypes.

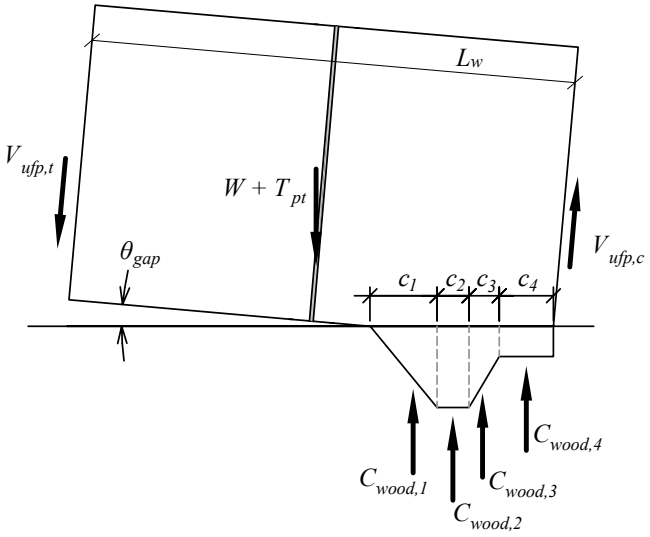

Figure 8.5: Free-body diagram of the rocking walls used for the design of the six archetypes in the parametric study

In Table 8.6 the calculated moment capacity of the lateral system is shown at the bottom. Here, the moment of the full wall assembly, $M_{assembly}$, has been separated into two components: (1) the moment capacity from the UFPs, M_{ufp}, and (2) the moment capacity from the wall panel itself, M_{wall}, calculated as the contribution from the compression forces at the base of the wall and the PT bar forces. When added together, these equal the full assembly moment (see Equation 3.34). Table 8.6 also shows ϕM_n. This is the moment capacity at DBE demands that would typically be used for design, where ϕ is the strength reduction factor equal to 0.9 for compression parallel to grain in accordance with the NDS.

Table 8.6: Moment capacity calculation values for the design of the six archetypes

		Archetype ID												
		6-AR1		6-AR2		6-AR3		12-AR1		12-AR2		12-AR3		
		DBE	MCE_R	DBE	MCE_R	DBE	MCE_R	DBE	MCE_R	DBE	MCE_R	DBE	MCE_R	units
Inputs	θ	0.0069	0.0121	0.007	0.0122	0.007	0.0122	0.0075	0.0129	0.0077	0.0131	0.0078	0.0123	rad
	W	0	0	0	0	0	0	0	0	0	0	0	0	k
PT Bars	T_{pt}	902	1061	539	624	415	479	1149	1336	647	739	504	556	k
UFPs	$V_{ufp,t}$	208	208	139	139	107	107	290	290	180	180	133	133	k
	$V_{ufp,c}$	208	208	139	139	102	107	290	290	180	180	133	133	k
CLT	ϵ_{wood}	0.0102	0.0213	0.0068	0.0122	0.0057	0.0096	0.0068	0.0121	0.0046	0.0074	0.0040	0.0057	in/in
	c	34.41	41.28	22.55	23.40	18.74	18.42	40.08	41.76	26.32	25.14	22.35	20.54	in
	c_1	10.43	5.95	10.29	5.90	10.29	5.90	18.24	10.60	17.77	10.44	17.54	11.12	in
	$C_{wood,1}$	161	92	159	91	159	91	339	197	330	194	326	206	k
	c_2	22.54	12.85	12.27	12.75	8.45	12.75	21.84	22.91	8.55	14.70	4.81	9.41	in
	$C_{wood,2}$	697	398	380	394	262	394	811	850	318	546	179	349	k
	c_3	1.43	22.48	0	4.75	0	-0.23	0	8.25	0	0	0	0	in
	$C_{wood,3}$	43	571	0	139	0	7	0	289	0	0	0	0	k
	c_4	0	0	0	0	0	0	0	0	0	0	0	0	in
	$C_{wood,4}$	0	0	0	0	0	0	0	0	0	0	0	0	k
Moment Capacity	M_{ufp}	48562	48562	24772	24772	16024	16470	88594	88594	42677	42677	27435	27435	k in
	M_{wall}	92177	102289	43183	49132	29236	32932	157539	179653	70822	80368	48043	52909	k in
	$M_{assembly}$	140739	150851	67954	73904	45260	49402	246133	268246	113499	123045	75478	80344	k in
	ϕMn	126665	-	61159	-	40734	-	221520	-	102149	-	67930	-	k in

8.4.3 Check Design Limit States

The next step of the design procedure was to check the same design limit states outlined in Section 6.6.2. The four limit states were: (1) restoring ratio, (2) energy dissipation ratio, (3) limit damage to the base of the wall, and (4) limit PT bar yielding at MCE_R demands.

The only limit state check that was modified from the 10-story design was the check for damage at the base of the wall. For the 10-story design, the strains at the base of the wall were defined to limit splitting of the wood under DBE demands (recall, $\epsilon_{s,clt} = 0.0079\ in/in$ and $\epsilon_{c,mpp} = 0.0061\ in/in$ for the NHERI TallWood 10-story building). This was a fairly strict limit state and was enforced to ensure the integrity of the wall through the repeated ground motions and multiple phases of testing. However, for this parametric study, a less conservative strain of 0.015 in/in was used as the limit for the wood strain at the base of the walls under DBE demands. This value was used as recommend by Busch et al. [2022]. It results in a less stringent check but would still be considered code compliant and more reasonable for a typical building that will not experience the large quantity of ground motions experienced by the NHERI TallWood 10-story specimen.

Table 8.7 summarizes the results of the four limit state checks. The results of these four limit states were used to determine the different designs. Similar restoring ratios, energy dissipation ratios, and PT yielding ratios were targeted when selecting the designs for the six archetypes. The PT bar and UFP properties were modified for each archetype design until these ratios were all similar and satisfied. The damage to the base of the wall limit state check decreases as aspect ratio increases. This is reasonable as one would expect the strains to decrease with more slender walls since the lever arm at the base decreases. Additionally, because the archetypes of the same height had similar rotation demands, the strains were larger for the longer walls.

Table 8.7: Summary of design limit state checks and moment ratios for the six archetypes

	Archetype ID					
	6-AR1	6-AR2	6-AR3	12-AR1	12-AR2	12-AR3
Limit State Checks						
Restoring Ratio ≥ 1.0	1.08	1.06	1.07	1.06	1.01	1.10
Energy Dissipation Ratio, $\beta \geq 0.125$	0.17	0.18	0.18	0.18	0.19	0.18
DCR_{wood} at DBE ≤ 1.0	0.76	0.50	0.42	0.50	0.34	0.29
$\text{DCR}_{pt,yield}$ at $\text{MCE}_\text{R} \leq 1.0$	0.63	0.68	0.63	0.61	0.61	0.63
Assembly Capacity at DBE						
$M_u/\phi M_n$	0.97	0.98	0.98	0.94	0.96	0.94
Moment Ratio						
$M_{assembly,MCE_R}/M_n$	1.072	1.088	1.092	1.090	1.084	1.064
Periods						
$T_{1,linear}$ (sec)	1.51	1.51	1.51	2.84	2.84	2.84
$T_{1,nonlinear}$ (sec)	1.33	1.24	1.23	2.35	2.24	2.19

8.4.4 Check Flexural Demand versus Capacity

After completing the local component limit state checks, the last step of the design procedure is to check the reduced moment capacity of the rocking connection at DBE demands (i.e., $\phi M_n = \phi M_{assembly,DBE}$) with the MRSA moment demand, M_u. Table 8.7 shows the results of this check for all six archetypes. This ratio was another key parameter used to determine the final designs for this parametric study. The PT bar and UFP properties were adjusted to ensure this ratio was close to 1.0 for all designs.

Also shown in Table 8.7 is a moment ratio of the calculated assembly moment capacity at MCE_R demands to DBE demands (i.e., $M_{assembly,MCE_R}/M_{assembly,DBE} = M_{assembly,MCE_R}/M_n$). This ratio will be discussed in more detail in the results section, however, it is important to note that this factor is relatively low. In a linear elastic design, a value of about 1.5 can be expected for this ratio because that is the ratio between the two hazards. However, because this is a force limiting system where the base of the walls rock, the base moment is limited after uplift and additional moment capacity comes only from the small increase in PT bar force.

The first mode period from eigenvalue analyses of the linear model and the nonlinear model are also shown in Table 8.7. As discussed previously, the archetypes were designed such that the linear first period modes would be the same for all archetypes of the same height. The first mode period of the nonlinear model is smaller than from the linear model due to the addition of the UFPs, which makes the system stiffer.

8.4.5 Wall Shear Check

The next step of the design procedure was to check the shear capacity of the CLT wall panels under DBE demands. The procedure outlined in Section A.2.1 was used. Table 8.8 summarizes the key values for this check and the DCRs for each archetype. For the demand calculations, the peak shear value, V_u, from MRSA at DBE demands was used. Manufacture design values were used to calculate the capacity. As shown in the Table, the shear DCRs decrease with increasing aspect ratio because the stress demands also decrease with increasing aspect ratio. Note however, that all the DCRs are well below 1.0. This is common for post-tensioned rocking mass timber shear walls. As discussed in the next section, satisfying moment capacity requirements is more challenging than shear requirements for these systems.

Table 8.8: Summary of the CLT wall shear capacity checks

		Archetype ID						
		6-AR1	6-AR2	6-AR3	12-AR1	12-AR2	12-AR3	units
Shear Demand								
MRSA peak wall shear DBE	V_u	216	108	72	261	130	87	k
shear stress	f_v	0.144	0.094	0.073	0.103	0.066	0.051	ksi
Shear Capacity								
Adj. shear stress	F'_{ve}	0.508	0.508	0.508	0.508	0.508	0.508	ksi
Shear DCR	DCR	0.28	0.19	0.14	0.20	0.13	0.10	

8.4.6 Wall Combined Edgewise Bending and Axial Loading Check

Next, the capacity of the CLT wall panels were checked under combined axial and bending in net compression and net tensioned under DBE demands. The procedures outlined in Section A.2.2 and A.2.3 were used for the net compression and net tension checks, respectively. Table 8.9 summarizes the key values for both checks and the resulting DCRs for each archetype. For the compression demand, the total PT bar force, calculated under DBE demands (from Table 8.6) was used. For the bending demand, the total force in the wall, M_{wall}, was used (also from Table 8.6). Note, this wall moment is equivalent to the total moment capacity of the assembly $M_{assembly}$ minus the moment contribution from the UFPs, M_{ufp}.

One modification made for this check with the archetype designs, compared to the 10-story design checks is the modification of the effective panel length used in the bending capacity calculations. The unbraced length used in the effective panel length calculation was divided by a factor of 2 (i.e., $L_e = 1.84(l_u/2)$). This was done because the C_L factor is highly dependent on this length and varies significantly with modifications. This calculation is thought to be highly conservative for the bending portion of the check and little experimental research has been completed to date to refine this check.

Note, the net compression DCR checks are significantly higher than the net tension DCR checks, meaning compression design controls. This was expected as the same was true for the design of the 10-story NHERI TallWood building. As shown in the Table the DCRs also decrease with increasing aspect ratio (i.e. the DCRs decrease as the walls become more slender). This is because both the compression and bending demands decrease with increasing aspect ratio. Additionally, while the compression capacity stays the same for the different aspect ratios, the bending capacity increases with increasing aspect ratio because the wall length is decreasing. This is also largely a result of contributions from C_L.

Table 8.9: Summary of the CLT wall combined axial load and bending checks

		Archetype ID						
		6-AR1	6-AR2	6-AR3	12-AR1	12-AR2	12-AR3	units
Compression Demand								
DBE Peak PT Force	P_u	902	539	415	1149	647	504	k
Compression stress	f_c	0.560	0.440	0.394	0.455	0.330	0.297	ksi
Bending Demand								
MRSA peak wall moment DBE	M_{wall}	74624	35324	23710	119358	55778	36738	k in
Bending Stress	f_b	1.189	0.970	0.881	0.927	0.718	0.630	ksi
Compression Capacity								
Unbraced panel length	l_u	240	240	240	240	240	240	in
PcE	P_{cE}	3087	2352	2022	7188	5585	4839	k
Column stability factor	C_p	0.44	0.44	0.44	0.61	0.61	0.61	
Critical buckling design value	F_{cE}	1.919	1.919	1.919	2.847	2.847	2.847	ksi
Adj. compression design value	F'_c	1.780	1.780	1.780	2.464	2.464	2.464	ksi
Bending Capacity								
Effective panel length	l_e	220.8	220.8	220.8	220.8	220.8	220.8	in
FbE	F_{bE}	3.121	4.098	4.766	3.542	4.558	5.261	ksi
Bending stability factor	C_L	0.63	0.77	0.84	0.70	0.82	0.87	
Adj. bending design value	F'_b	2.873	3.503	3.794	3.172	3.715	3.944	ksi
Tension Capacity								
Adj. tension design value	F'_t	3.402	3.402	3.402	3.402	3.402	3.402	ksi
Combined Bending and Axial DCRs								
Net Compression	DCR	0.68	0.42	0.34	0.38	0.24	0.19	
Net Tension	DCR	0.18	0.16	0.14	0.14	0.11	0.10	

8.5 Analysis Parameters

The performance of the six archetypes was studied using nonlinear response history analysis (NLRHA). Nonlinear two-dimensional OpenSees models were developed for each archetype as outlined in Section 8.3.2. The archetypes were then analyzed using the ground motion suites developed for the 10-story NHERI TallWood building design which had the same design location as the archetypes in this parametric study. For the 10-story design, suites of eleven two-component ground motions were selected and scaled to seven hazard levels in accordance with procedures outlined in ASCE/SEI 7-16. See Section 6.3 for a discussion on the site location and the hazard levels and see Section 6.4 for a discussion on the ground motion

selection and scaling procedures and the presented ground motion suites. The parametric study models were two-dimensional, requiring single component ground motions, while the 10-story model was three-dimensional, requiring two-component ground motions. Thus, for the parametric study, both components of the eleven ground motions were run as separate analyses, resulting in twenty-two total ground motion analyses at each of the seven hazard levels.

For this study, peak ISDs, peak strains at the base of the wall panels, peak wall shears, and peak wall moments were studied. As an example, this section will show detailed analysis results from the full MCE_R ground motion suite for archetype 12-AR3. Sections 8.6 and 8.7 will use just the overall peak values from each ground motion and the suite geometric mean results for comparison purposes between the archetypes. Figure 8.6 shows the peak ISD values for each story from each of the twenty-two MCE_R ground motions. Additionally, the suite geometric mean of the peak ISD values on each floor is shown. This plot shows that for this archetype, peak ISDs stayed below 2%, apart from four ground motions in the suite. The geometric mean of all the ground motions was around 1.5%

Figure 8.7a and 8.7b show the peak wall shear and peak moment connection results up the height of the building for all twenty-two ground motions at the MCE_R hazard. Again, on both of these plots, the suite geometric mean of the peak values is also shown. The peak assembly moment, $M_{assembly}$, plotted in Figure 8.7b is the moment demand of the entire rocking wall connection (i.e., $M_{assembly} = M_{ufp} + M_{wall}$ as shown in Equation 3.34 for the base of the wall). This includes the contributions from the moment in the wall panel and the moment contributions from the UFPs. At each point up the height of the building, this value was calculated by taking the moment in the wall panel plus the moment contributions from the UFPs. At each point up the height of the building the moment contribution from the UFPs was calculated by taking the force in all UFPs above the specific height on the left side of the wall multiplied by $L_w/2$ plus the force in all the UFPs above the specific height on the right side of the wall multiplied by $L_w/2$. Figure 8.7c shows a comparison of the peak suite mean moment values for the moment in the wall, compared to the moment capacity of

the full connection. As show, the contribution to overturning moment from the UFPs is not negligible. The moment diagrams show a large "bubble" around mid-height of the building from higher mode effects. This also existed in the 10-story design. Quantifying the amount of moment amplification that occurs from higher mode effects is one of the primary focuses for this study and will be discussed in detail in Section 8.7.

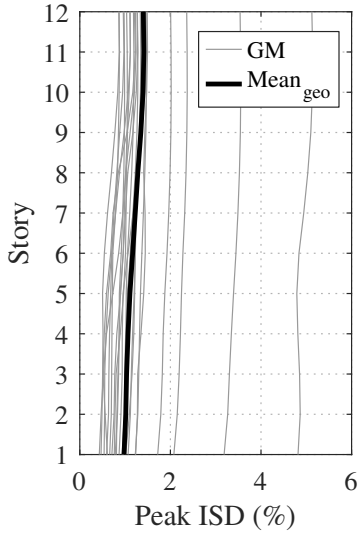

Figure 8.6: Example peak ISD results for archetype 12-AR3 at MCE_R

Figure 8.8 shows the peak strain experienced at all points along the base of the wall panels for all twenty-two ground motions at the MCE_R hazard. Again, the suite geometric mean of the peak values is also shown. The yield strain and splitting strain limits are also identified on this plot to provide a visual measure of the proportion of wall that has reached each limit state. As shown, for this archetype, a few ground motions at MCE_R produced strains that exceeded the splitting strain, however, the geometric mean of the results indicate that only a small portion of the wall panel, at the corners, exceed the yield strain. The crushing strain is not shown on the plot because no ground motions produced strains that exceeded crushing.

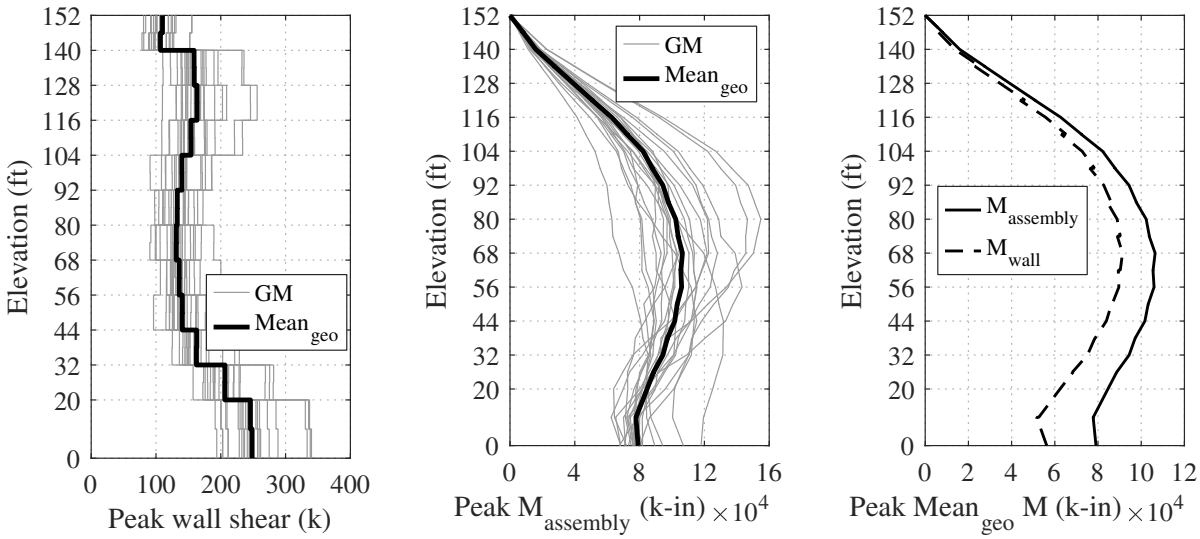

Figure 8.7: Example peak results for archetype 12-AR3 at MCE_R for (a) wall shear, (b) assembly moment, and (c) a comparison of assembly moment verses wall moment

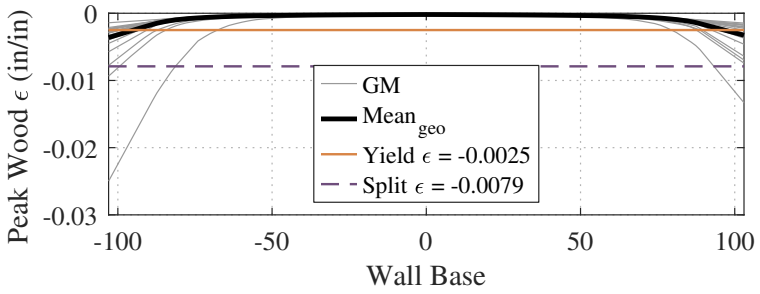

Figure 8.8: Example peak wall strain at the base of the rocking wall results for archetype 12-AR3 at MCE_R

8.6 Performance Assessment

First the overall performance of the six archetypes was compared to see how wall aspect ratio and building period affects ISDs and wall strains at the base of the wall. This was done

by running multiple stripe analyses for each of the six archetypes and developing fragility functions based on the results. For this study, fragility function fitting was completed by fitting a log-normal cumulative density function to observed building response data using optimization on the likelihood function for the data, as presented in Baker [2013]. The suites of twenty-two ground motions at the seven hazard levels were used to complete these multiples stripes analyses (MSA). For these fragility curves, the ground motion intensity measure (IM) was defined as the mean spectral acceleration, S_a, of the ground motion suite at the buildings first mode linear period, $T_{1,linear}$. Recall, $T_{1,linear}$ was calculated from an eigenvalue analysis for the linear OpenSees models used to complete the MRSA. The values of $T_{1,linear}$ are presented in Table 8.7.

8.6.1 Peak Interstory Drifts

The performance of the six archetypes was first assessed by looking at the peak ISDs. Figure 8.9a presents the MSA analysis results for archetype 12-AR3 looking a peak ISDs. At each IM level on the y-axis, the peak ISD from each of the twenty-two ground motions is plotted and the suite mean is highlighted. As shown, the peak ISDs increase with increasing IM level. Figure 8.9b presents the observed fractions of motions exceeding a 1% peak ISD limit as a function of mean spectral acceleration at the buildings first mode linear period, Figure 8.9b also shows the fitted fragility function which was estimated using maximum likelihood optimization, as presented in Baker [2013]. A drift limit of 1% was used to achieve a well fitted fragility function for comparison between the archetypes. Note, collapse assessment is not investigated here. The 1% drift limit was selected to achieve good comparison of response between the archetypes.

The procedure presented in Figure 8.9 was repeated for all six archetypes and the resulting fragility curves are presented in Figure 8.10. The results show that wall aspect ratio does not affect overall drift performance for post-tensioned rocking wall systems with the same building period. For both the 6-story archetypes and the 12-story archetypes, nearly identical drift fragility curves were calculated for each of the three aspect ratios of the same building

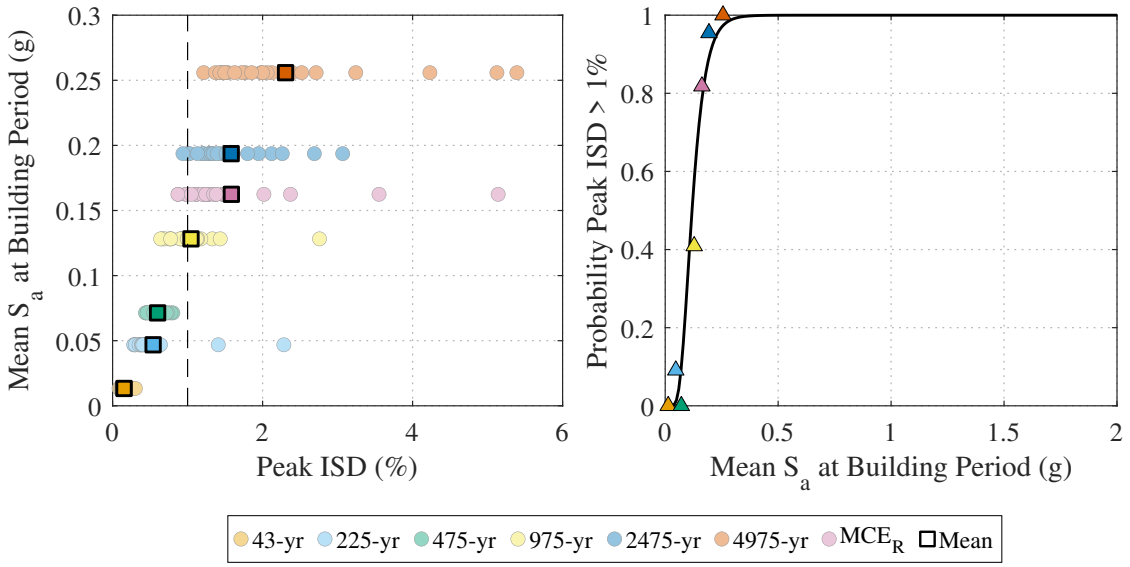

Figure 8.9: (a) MSA analysis results for archetype 12-AR3 looking at peak ISDs and (b) the observed fractions of motions exceeding a 1% peak ISD limit as a function of the mean spectral acceleration at the buildings first mode linear period and the fragility function estimated using maximum likelihood optimization as presented in Baker [2013]

height. As expected, building period does have an effect on overall drift performance. At a given spectral acceleration at the first building period, the 12-story archetypes have a higher probability of exceeding 1% ISDs. Table 8.10 summarizes metrics needed to define the fragility curves for each of the six archetypes. The median of the fragility function, θ, and the standard deviation (sometimes called the dispersion of IM) of $lnIM$, β, are both shown in the table.

Table 8.10: Summary of the fragility curve metrics for ISDs exceeding 1%

	6-Story Archetypes				12-Story Archetypes			
Metric	6-AR1	6-AR2	6-AR3	6-All	12-AR1	12-AR2	12-AR3	12-All
θ	0.277	0.310	0.300	0.294	0.110	0.114	0.119	0.114
β	0.237	0.148	0.177	0.198	0.379	0.397	0.397	0.392

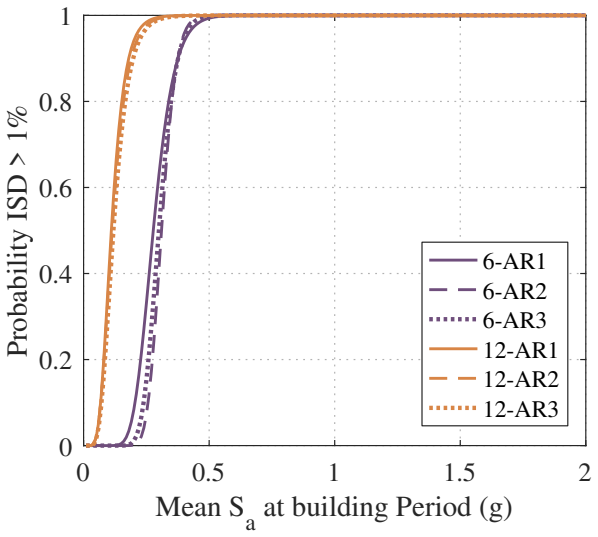

Figure 8.10: Fragility curves comparison of the six archetypes for ISDs exceeding 1%

8.6.2 Damage at the base of the walls

Archetypes performance was also assessed looking at the peak strains at the base of the wall panels and inelastic damage they experienced. Figure 8.11 shows the profile of the suite mean of the peak strains at the base of the walls at MCE_R hazard level for all six archetypes. Note, the length of all the archetypes are different, so the location along the base of the wall was normalized by the total wall length in the figure. The strain profiles for the other hazard levels are not shown, however, the general trends are consistent between them. Figure 8.11 shows that for the 6-story archetypes, the peak strains at the base of the wall panels decrease with increasing aspect ratio. The same trend is true for the 12-story archetypes. The plot also shows that for buildings with a longer period (i.e., the 12-story archetypes compared to the 6-story archetypes), the peak strains are less, indicating a relationship between increasing period and decreasing peak wall strains at the base of the wall panels. Peak wood strains decrease with increasing aspect ratio for buildings with the same period because the peak rotation demands and drifts are all similar. This means that the longer walls (i.e., the smaller aspect ratios) will reach higher strains for the same rotation demand.

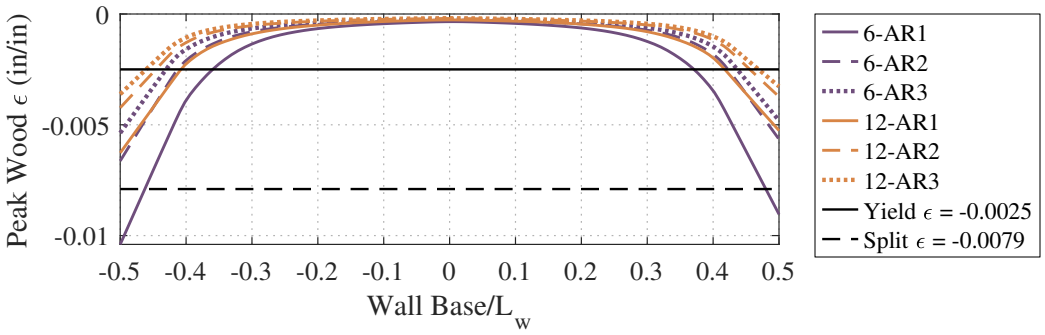

Figure 8.11: Fragility curves comparison of the six archetypes for ISDs exceeding 1%

Fragility data for peak wood strains at the base of the wall panels exceeding yield ($\epsilon_{y,clt}$), splitting ($\epsilon_{s,clt}$), and crushing ($\epsilon_{cr,clt}$) were also calculated. However, the spread of data at each hazard level was limited, resulting in fragility curve plots that are not well defined. Figure 8.11 does a better job at showing the relationships between peak wood strains, wall aspect ratio, and building period. While the plots are not included, Table 8.11 summarizes the fragility curve metrics for each of the six archetypes for completeness. Metrics are shown for peak wood strains at the base of the wall panels exceeding all three limit states.

Table 8.11: Summary of the fragility curve metrics for peak wall strains at the base of the wall panels exceeding drift limits

	6-Story Archetypes			12-Story Archetypes		
Metric	6-AR1	6-AR2	6-AR3	12-AR1	12-AR2	12-AR3
$\boldsymbol{\epsilon_{wood} > \epsilon_{y,clt}}$						
θ	0.109	0.137	0.163	0.072	0.106	0.117
β	0.055	0.275	0.221	0.375	0.382	0.427
$\boldsymbol{\epsilon_{wood} > \epsilon_{s,clt}}$						
θ	0.310	0.409	0.481	0.219	0.394	0.376
β	0.270	0.236	0.278	0.709	0.885	0.588
$\boldsymbol{\epsilon_{wood} > \epsilon_{cr,clt}}$						
θ	0.667	0.556	0.571	0.442	N/A[a]	N/A[a]
β	0.257	0.040	0.040	0.469	N/A[a]	N/A[a]

[a]Insufficient data to compute fragility parameters

8.7 Moment Amplification Study

This section will present the findings from this study relating to the effects wall aspect ratio and building period on moment amplification in the wall panels. At MCE_R, numerical analyses from the NHERI TallWood 10-story building will also be used for comparison.

Figure 8.12 shows suite mean moment envelopes for the six archetypes at all seven hazard levels. In this plot, the height up the wall panels are normalized by the total height of the walls. Figure 8.12a shows the results for the 6-story archetypes and Figure 8.12b shows the results for the 12-story archetypes. In this figure the full assembly moment (i.e. the moment from the wall panels plus the moment contribution from the UFPs) are shown, normalized by the calculated assembly moment at DBE demands, M_n (also called $M_{assembly,DBE}$). The moment profiles from MRSA (shown initially in Figure 8.4b of Section 8.4.1), normalized by M_n are also shown in Figure 8.12. Including the results from MRSA on this plot gives a comparison of what would typically be used to determine the design of the wall in a prescriptive design procedure to what NLRHA shows the wall panel may experience.

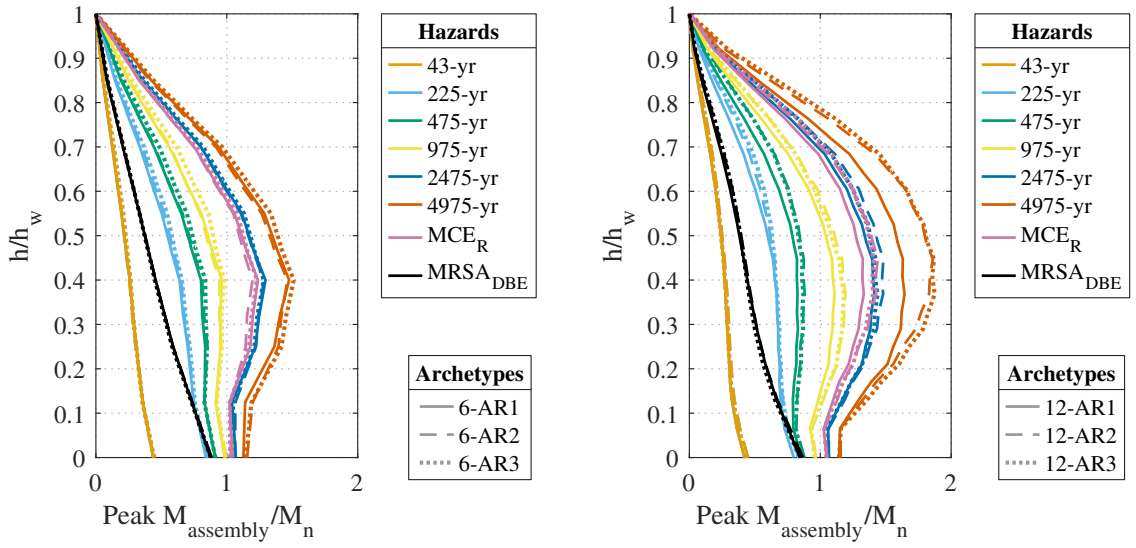

(a) (b)

Figure 8.12: Suite mean envelopes showing peak assembly moments for the rocking wall systems at each hazard level, normalized by M_n for (a) the 6-story archetypes and (b) the 12-story archetypes

Figure 8.12 shows that aspect ratio of the wall panel does not effect the moment demands in the wall panels. From these plots, however, it is clear that higher mode effects result in moment amplification and moment amplification effects increase with increasing hazard level. At lower hazard levels, the effects of moment amplification are minimal, however, at higher hazard levels, there is a "bubble" at mid-height up the wall panel.

Figure 8.13 shows a comparison of the 6-story archetypes to the 12-story archetypes at the MCE_R hazard level to compare the trends of moment amplification with respect to building period. On this plot, the MCE_R numerical analysis results from the NHERI TallWood 10-story building are also included (originally presented in Section 6.6.3). The geometric mean response of the north and south walls (10-NS) are shown as well as the geometric mean response of the east and west walls (10-EW) from the NHERI TallWood

10-story building. On this plot, only MCE_R is shown for clarity, however, the same trends occur at the remaining hazard levels. Archetype results on this figure shows that while the moment amplification is not dependent on wall aspect ratio, it is dependent on building period. Walls with a longer period have larger moment amplification effects. This is similar to what other studies have shown.

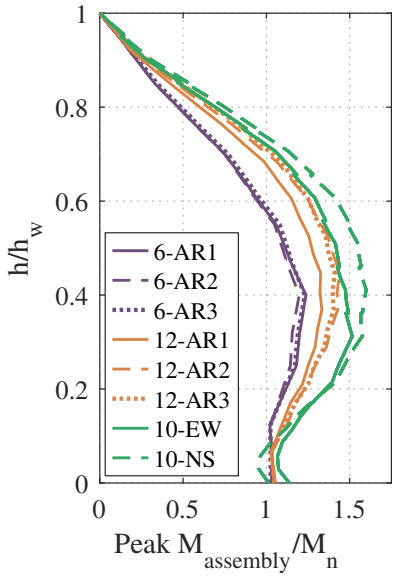

Figure 8.13: Suite mean envelopes showing peak assembly moments for the rocking wall system at MCE_R, normalized by M_n, for all six archetypes

Referring to the 10-story results included in Figure 8.13, the period trend does match as well with the archetype results. Recall, the first mode periods for the 10-story building were 1.68 seconds and 1.74 seconds for the east-west and north-south directions, respectively and the periods for the 6-story and 12-story archetypes were 1.51 seconds and 2.84 seconds, respectively. While the longer period building direction of the 10-story building has larger moment amplification effects (i.e., a larger "bubble") in comparison to the shorter period building direction, both directions have less moment amplification than all 12-story archetypes, even though the period is shorter. This incompatibility in trends with

the archetype buildings could be a result of a couple of factors. First, the 10-story results were from a 3D model, thus, these larger moments could be a result of torsional effects. Additionally, the overall design assembly moment DCR (i.e., $M_u/\phi M_n$ shown in Tables 6.18 and 8.7 for the 10-story building and archetype designs, respectively) for the 10-story building was lower than the archetype designs, meaning the 10-story design is stronger relative to the archetype designs. Different mass timber materials were also used for the archetype designs, the 10-story east-west direction walls (CLT), and the 10-story north-south direction walls (MPP). These factors could all contribute to this trend. However, based on only the archetype designs where most factors were held constant, walls with a longer period have larger moment amplification effects.

The next section aims to quantify the moment amplification that should be used for wall design if full NLRHA is not performed (which is typical for a prescriptive design procedure for wall systems accepted in US design codes). The next section first present the base moment demands at each hazard level, compared to the calculated connection capacity, M_n (Section 8.7.1). Then the amplification of moment up the height of the walls, relative to the base moment (Section 8.7.2), is presented. This will consist of quantifying the amplification of moment as well as studying where along the height of the wall panels the amplification occurs.

8.7.1 Base Moment Demands at Different Hazard Levels

Referring to Figure 8.12, the base moment demands, normalized by M_n, do not change based on aspect ratio. Additionally, referring to Figure 8.13, the base moment demands, normalized by M_n, also do not change based on building period (they change up the height, but not at the base). Note, this is also a result of designing the archetypes to all have $M_u/\phi M_n$ values very similar to each other. This relationship is further emphasised by Figure 8.14 which plots the base moment demands, normalized by M_n, for all archetypes at all hazard levels. These values are also tabulated in Table 8.12. Because the normalized base moment demands do not vary based on aspect ratio, the average values (calculated using the geometric mean) for

the archetypes of the same height were also calculated included in Figure 8.14 and Table 8.12.

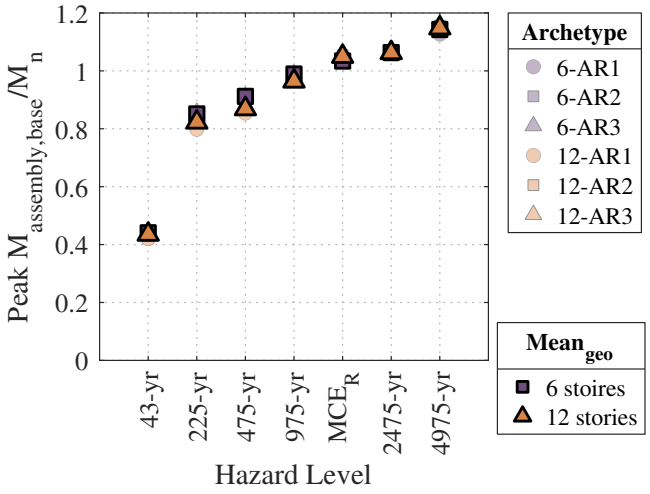

Figure 8.14: Scatter plot showing peak base moment demands, normalized by M_n for all six archetypes at all hazard levels

Table 8.12: Tabulated base assembly moment demands normalized by M_n for all six archetypes at all hazard levels

Hazard	6-Story Archetypes				12-Story Archetypes				Overall
Level	6-AR1	6-AR2	6-AR3	Mean$_{geo}$	12-AR1	12-AR2	12-AR3	Mean$_{geo}$	Mean$_{geo}$
43-yr RP	0.44	0.44	0.44	0.44	0.42	0.45	0.44	0.44	0.44
225-yr RP	0.84	0.86	0.86	0.85	0.80	0.83	0.84	0.82	0.83
475-yr RP	0.91	0.91	0.91	0.91	0.85	0.88	0.87	0.87	0.89
975-yr RP	0.98	1.00	0.99	0.99	0.97	0.97	0.96	0.96	0.97
MCE$_R$	1.05	1.03	1.03	1.03	1.05	1.05	1.05	1.05	1.05
2475-yr RP	1.07	1.06	1.06	1.06	1.07	1.07	1.06	1.06	1.07
4975-yr RP	1.13	1.16	1.16	1.14	1.14	1.16	1.14	1.15	1.14

The tabulated values can be used to reference the increase in base moment demand for different hazard levels. Note, as shown in Figure 8.12, not only does MRSA produce the incorrect shape of moment diagram for this system, but the base MRSA moment is also closer

to the 475-year return period motion than the 975-year return period motion. Referring to Figure 6.11, the uniform hazard response spectrum for the 975-year return period is more representative of the DBE design curve ($2/3MCE_R$ in the figure) than the 475-year return period hazard.

Referring to the tabulated values for the base moment demands at MCE_R (Shown in Table 8.12), the average value for all archetypes is equal to 1.04. Given a fully linear-elastic building, this ratio would be equal to 1.5 because that is the ASCE/SEI 7-16 defined ratio between MCE_R and DBE. However, because this is a force limiting system (as mentioned previously in Section 8.4.3), this value is significantly closer to 1.0 because the moment capacity does not increase significantly post uplift. The normalized base moment demands at MCE_R (i.e., $M_{assembly,MCE_R}/M_n$) calculated during design (shown in Table 8.7) can be compared to the results from NLRHA (shown in Table 8.12). The ratios are very similar, indicating a relatively good calculation prediction. However, the calculated ratio is slightly larger than the one determined from NLRHA, indicating that the calculated predictions for MCE_R are slightly high.

8.7.2 Moment Amplification as a Function of Wall Height

After studying the effects of aspect ratio and building period on base moment demands at different hazards, the amount of moment amplification for each hazard level and archetype was studied. Both the magnitude of amplification and location of peak moment were studied. This was done by normalizing the suite mean assembly moment demand envelopes by the base moment, as shown in Figure 8.15. Figure 8.15a shows peak $M_{assembly}/M_{base}$ up the height of the walls for the 6-story archetypes at all hazard levels. Figure 8.15b shows peak $M_{assembly}/M_{base}$ up the height of the walls for the 12-story archetypes at all hazard levels. These plots show that for walls with the same period and different aspect ratios, the magnitude of moment amplification does not change. While there may be some difference in moment for different archetypes with the same period at higher hazard levels, there is not a clear trend to define a relationship. On both plots, the moment profile, normalized by the

peak base moment, from MRSA is also included. The inclusion of this line shows that MRSA does not accurately capture the higher mode effects that result in moment amplification for these plots.

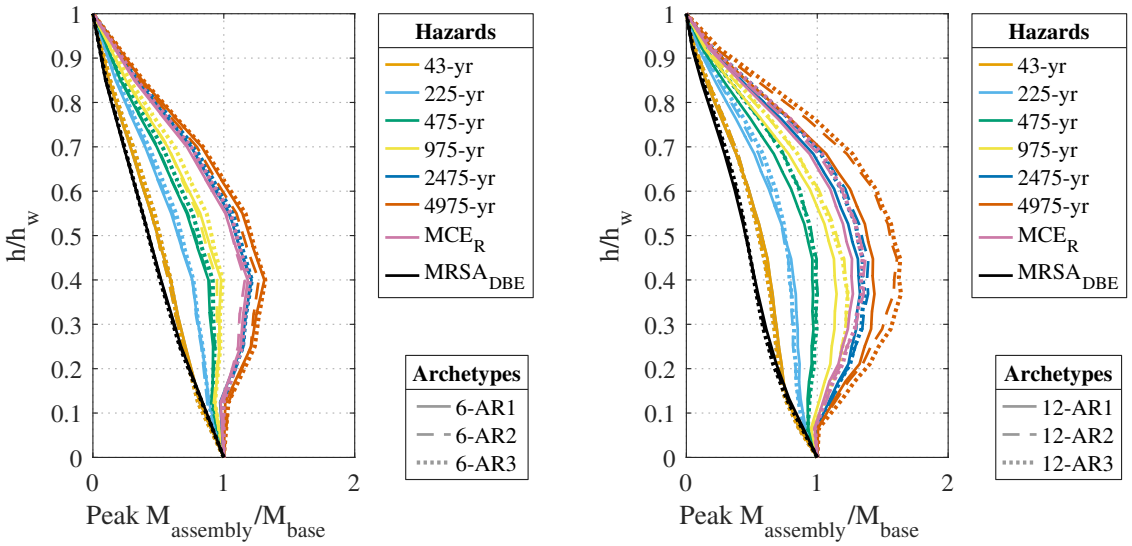

(a) (b)

Figure 8.15: Suite mean envelops showing peak assembly moments for the rocking wall systems at each hazard level, normalized by the base moment for (a) the 6-story archetypes and (b) the 12-story archetypes

While Figure 8.13 shows that the aspect ratio of the post-tensioned rocking wall does not significantly affect the amount of moment amplification compared to the base moment, comparing Figures 8.15a and 8.15b may indicate that the effects of moment amplification are larger for the 12-story archetypes than the 6-story archetypes. This is shown by the slightly larger "bubble" in the moment plots in the 12-story archetypes. This relationship is also seen in Figure 8.16, which only shows the MCE_R hazard. Numerical results from the NHERI TallWood 10-story building are also included. From just the archetype design results on this plot, it is clear that the moment amplification compared to the base is significantly larger for

the 12-story archetypes that have a longer period. While the other hazards are not shown, the same patterns exist. When comparing with results for the 10-story design, this trend is not as consistent. In other words, even though the period of the 10-story building was shorter than the 12-story archetypes, the moment amplification is larger. See the discussion associated with Figure 8.13 for more discussion on these discrepancies.

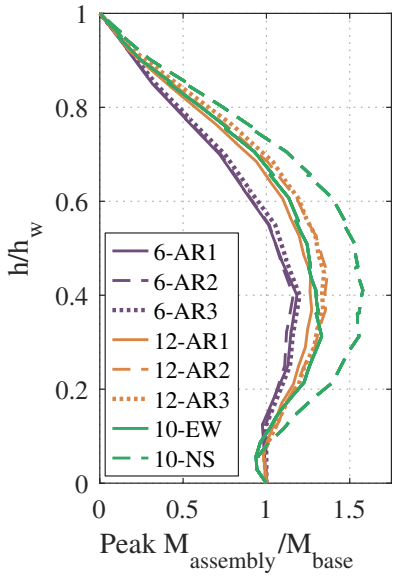

Figure 8.16: Suite mean envelopes showing peak assembly moments for the rocking wall system, normalized by the base moment, at MCE_R for all six archetypes

Figure 8.17 shows a scatter plot of the peak assembly moments up the height of the walls, normalized by the moment at the base for all archetypes at all hazard levels. Because the impact of aspect ratio on peak M_{max}/M_{base} values is small for buildings with the same period, the mean ratio for archetypes of the period is also calculated (using geometric mean) and shown in Figure 8.17. This plot shows that the moment amplification from higher mode effects is larger for the 12-story archetypes. It also shows that the amount of moment amplification increases with increasing hazard. For the lower hazard levels, the peak assembly moment up the height of the walls occurs at the base (i.e., Peak M_{max}/M_{base} is equal to 1.0).

For the 6-story archetypes, this is true for all hazard levels smaller than MCE_R. However, for the 12-story archetypes where the moment amplification is larger, the peak moment up the height of the wall occurs at the base only for hazard levels lower than a 975-year return period. The variation of points from the mean values on this plot show that there may be some relationship between aspect ratio and peak M_{max}/M_{base}, meaning that moment amplification does change with aspect ratio. However, the dispersion of points from the mean is small and the pattern of which aspect ratio produces the largest moment is inconsistent, so a clear relationship can not be deduced from the results and the variations from the mean is considered negligible. Table 8.13 also summarizes these results.

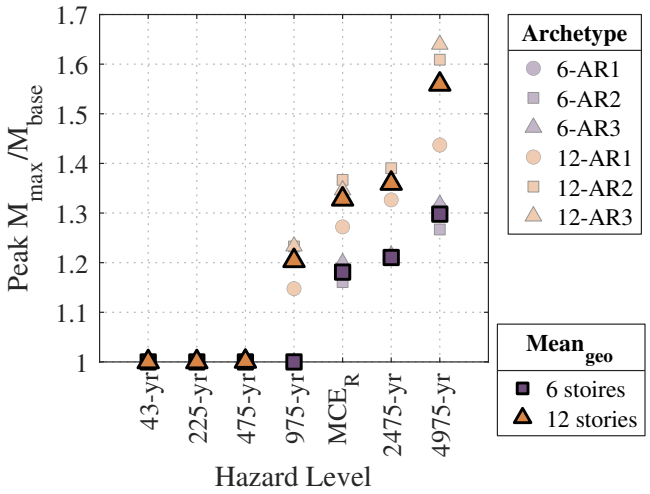

Figure 8.17: Scatter plot showing peak maximum assembly moment values, normalized by the moment at the base of the wall for all six archetypes at all hazard levels

At MCE_R the ratios peak assembly moments up the height of the walls to the moment at the base were investigated further by plotting the ratio $PeakM_{max}/M_{base}$ versus building period, as shown in Figure 8.18. On this plot, results from the 12 archetype buildings and the results from the two building directions of the NHERI TallWood 10-story budding are included. This plot shows that moment amplifications are not negligible at MCE_R hazard levels. The relationship between increasing moment amplification with increasing period is

clear for the archetype designs. See the discussion associated with Figure 8.13 for a discussion on the relationship with the 10-story results.

Table 8.13: Tabulated peak assembly moment values up the height of the walls, normalized by the base moments, for all six archetypes at all hazard levels

Hazard	6-Story Archetypes				12-Story Archetypes			
Level	6-AR1	6-AR2	6-AR3	Mean$_{geo}$	12-AR1	12-AR2	12-AR3	Mean$_{geo}$
43-yr RP	1	1	1	1	1	1	1	1
225-yr RP	1	1	1	1	1	1	1	1
475-yr RP	1	1	1	1	1	1	1	1
975-yr RP	1	1	1	1	1.15	1.23	1.23	1.20
MCE$_R$	1.18	1.16	1.20	1.18	1.27	1.37	1.35	1.33
2475-yr RP	1.21	1.21	1.21	1.21	1.33	1.39	1.36	1.36
4975-yr RP	1.31	1.27	1.32	1.30	1.44	1.61	1.64	1.56

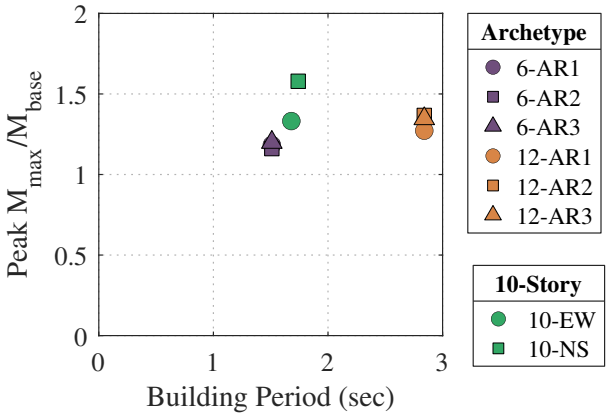

Figure 8.18: Plot showing peak maximum assembly moment values, normalized by the moment at the base of the wall verses building period at MCE$_R$

The last portion of this study was to determine the location where the maximum peak assembly moment, normalized by the base moment occurs up the height of the wall. The heights of the envelope plots that have been presented have been normalized by the total height of the walls to determine if the location of peak assembly moment changes with the

aspect ratio of period of the walls. Figure 8.19 plots the results for all hazard levels and archetypes. Table 8.14 also summarizes these values. The mean values for the archetypes of the same hazard level (calculated using the geometric mean) is also included in the figure and table. For the lower hazard levels, the location of peak assembly moment occurs at the base of the wall (i.e., h/h_w equals 0), as discussed previously. For the larger hazard levels, the peak moment occurs fairly consistently at a value of 0.4 for the 6-story archetypes and between 0.37 and 0.45 for the 12-story archetypes. While these locations are slightly off, this is likely a result of modeling decisions and not a result of the different periods. In the model, the periods were only recorded at nodes located at the floor levels and at the locations of the UFPs. For example, for the 6-story archetype, the location h/h_w of 0.4 correlates to the node at floor 2. The number of nodes up the height of the walls could be increased to get more discretization up the height of the wall, resulting in a more consistent location h/h_w.

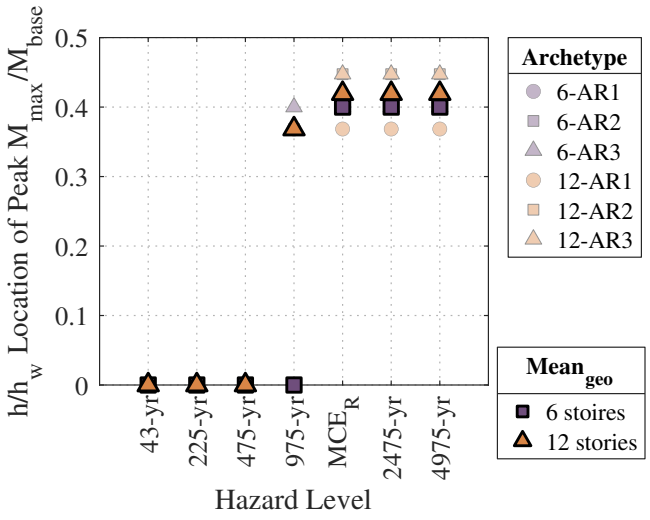

Figure 8.19: Scatter plot showing the h/h_w location up the height of the walls where the peak maximum assembly moment occurs, normalized by the base moment for all six archetypes at all hazard levels

Table 8.14: Tabulated locations of the peak maximum assembly moment, normalized by the base moment, for all six archetypes at all hazard levels, in terms of h/h_w

Hazard	6-Story Archetypes				12-Story Archetypes				Overall
Level	6-AR1	6-AR2	6-AR3	Mean$_{geo}$	12-AR1	12-AR2	12-AR3	Mean$_{geo}$	Mean$_{geo}$
43-yr RP	0	0	0	0	0	0	0	0	0
225-yr RP	0	0	0	0	0	0	0	0	0
475-yr RP	0	0	0	0	0	0.37	0	0	0
975-yr RP	0	0	0	0	0.37	0.37	0.37	0.37	0
MCE$_R$	0.40	0.40	0.40	0.40	0.37	0.37	0.45	0.42	0.41
2475-yr RP	0.40	0.40	0.40	0.40	0.37	0.45	0.37	0.39	0.40
4975-yr RP	0.40	0.40	0.40	0.40	0.37	0.45	0.37	0.39	0.40

8.8 Summary

The most critical limit states evaluated in the design of the lateral system for the NHERI TallWood 10-story building were the flexural capacities of the wall panels and wall splices. Large moment demands from NLRHA controlled these designs. The NLRHA results showed large moment demands at mid-height, a result of higher mode effects. This will likely be a critical design check for a future buildings with post-tensioned mass timber rocking wall lateral systems. While past research has shown that introducing additional rocking joints up the height of the wall panels can greatly reduce the moment demands, little work has been done to quantify the amount of moment amplification and study the impact of building period and wall aspect ratio on overall building performance and moment amplification. This is important research as designing connections for multiple rocking planes will likely be challenging and expensive. This issue was addressed through a parametric study on six different archetype designs of post-tensioned mass timber rocking walls. Three 6-story buildings and three 12-story buildings were designed following the prescriptive design procedure used for the design of the 10-story building. For designs of the same height, the wall aspect ratio was changed while keeping the overall building period constant to study the impact of wall aspect ratio, independent of the building period. MSAs were completed for each of

the designs using the seven hazard levels defined for the design of the 10-story NHERI Tall-Wood building to compare performance of the different designs and to study how moment amplification changes with the different designs and across hazard levels.

Results from this study showed that for buildings of the same height, aspect ratio does not affect overall performance in terms of drifts, however, walls with a larger aspect ratio (i.e., more slender walls) had lower peak wall strains at the base of the wall. In terms of building period, as expected, the buildings with a longer period saw larger drifts and lower strains at the base of the wall panels. Looking at wall moment amplification, the following conclusions were drawn:

1. Wall panel aspect ratio does not affect the amount of moment amplification for walls with the same period.
2. A longer period wall will result in a larger amplified moment.
3. For lower hazards, higher mode effects do not significantly amplify the moment at mid-height and the maximum wall moment occurs at the wall base
4. For larger hazards where moment amplification is present, the location of maximum moment occurs at about 40% of the wall height for all walls.

Based on these results it was determined that at MCE_R hazard, the base moment was amplified by 18% for buildings with a 1.51 second first mode elastic period and the base moment was amplified by 33% for buildings with a 2.84 second first mode elastic period. For future adoption of these systems into US buildings codes, these amplified moments should be accounted for as typical code-based lateral force distributions for determining wall moment demands, such as MRSA or ELF, do not capture the the amplified shape of the force envelopes. A linear interpolation between the two periods and amplification factors is reasonable. It is recommended to avoid putting a wall splice joint at 40% up the wall height to avoid the location of maximum moment.

Chapter 9

SUMMARY, CONCLUSIONS, AND FUTURE WORK

9.1 Overview

The goals of this research were to study the response of post-tensioned mass timber rocking wall lateral force resisting systems, advance numerical modeling methods for predicting their seismic performance, and validate the use of code-alternative design procedures through nonlinear numerical modeling and dynamic shake table tests on large-scale mass timber buildings. The post-tensioned rocking mass timber shear walls studied in this document utilize unbonded post-tensioned bar connections, UFP energy dissipation devices, and slotted pin connections at the wall and diaphragm interfaces. This chapter contains a brief summary of the work completed, the conclusions drawn from the research, and suggestions for future work to be completed.

9.2 Summary

The presented research can be divided into four phases: (1) formulating approximations for lateral load response, (2) design, testing, and modeling of the lateral system in the NHERI TallWood 2-story building, (3) design, testing and modeling of the lateral system for the NHERI TallWood 10-story building, and (4) conducting a parametric study on tall wood buildings. A summary of the work completed for each phase is presented here:

9.2.1 Formulations for Approximating Lateral Load Response

Formulations for approximating the lateral load response of mass timber rocking walls were developed, building upon previous work. A procedure for approximating the moment capacity of the wall system and the forces in all major elements such as the PT bars, the UFPs,

and the compression force in the wall based on the rotation opening at the base of the wall panels was presented. This procedure is called the cross-sectional analysis procedure. The differences between the formulations for paired wall systems and boundary column systems were discussed. These formulations were used as the basis for the design procedure used for the two-story and ten-story NHERI TallWood building specimen designs.

9.2.2 Two-Story NHERI TallWood Shake Table Test

The post-tensioned rocking wall lateral force resisting system for the two-story NHERI TallWood building was designed using a code alternative performance-based design procedure. Using the formulations for approximating lateral load response, the predicted moment-rotation behavior for the system was developed and the design was modified until a set of performance objectives were achieved. The performance objectives used for the two-story design were as follows:

- **PO 1: Wind Loading** No wall decompression under design wind loading.
- **PO 2: Immediate Occupancy** No required repairs to the system after a 50% in 30 year hazard level earthquake. Minor UFP yielding is permitted. PT bars and CLT walls should remain elastic. Drifts limited to 1%.
- **PO 3: Limited Repair** Minimal repairs required after a 10% in 50 year hazard level earthquake. Residual drifts limited to 0.2%. Full UFP yielding is permitted. No PT bar yielding. Minor yielding of the CLT wall panels is permitted. Drifts limited to 2%.
- **PO 4: Collapse Prevention** Damage to the system is limited to prevent building collapse during MCE_R level earthquake. PT bar yielding is permitted. Yielding of the CLT wall panels is permitted. Damage should still be limited to prevent any major loss of strength of stiffness. Drifts limited to 4%.

Performance objectives two and four were defined to match requirements of LATBSDC [2014]. For this design, damage limits for the UFPs, PT bars, and damage to the base of the CLT walls were less stringent than what would typically be targeted, in particular, permitting PT bar yielding under MCE_R motions. This was done because the walls were

only 24 feet tall, and the structure was small, relative to a typical building. The short and stiff walls resulted in large uplift and short PT bars that made PT bar yielding after 4% drift unrealistic. Note, a nonlinear numerical model was not used for the design of this lateral system. Because the test structure was short and the behavior was deemed predictable, a nonlinear model was not completed for design.

The structure was tested uniaxially at the NHERI@UCSD shake table, using a test sequence of fourteen ground motions categorized as follows: (1) five 50% in 30 year motions called SLE, (2) five 10% in 50 year motions called DBE, (3) three MCE_R motions, and (4) one motion that was 1.2 $\times$ MCE_R. Extensive data analysis was completed to assess lateral system performance. The main results from the test are summarized below:

- The fundamental period of the building, determined from white noise tests, was around 0.9 seconds. The relatively long period for a two-story building can likely be attributed to the unexpected flexibility in the foundation.
- Peek roof and floor drifts ranged from 0.5% to 0.9% for the SLE motions, 1.7% to 2.5% for the DBE motions, and 1.9% to 3.3% for the MCE_R motions.
- Residual drifts were less than 0.06% for motions at or below the MCE_R hazard level.
- Measured base shear versus drift response was linear for SLE motions. Nonlinearity and some damping were seen in DBE motions and considerable nonlinearity and damping was shown in MCE_R motions.
- No damage to the base of the CLT walls was observed during any of the tests, likely due to the presence of the flexible foundation.
- UFPs yielded at very low drifts.

Overall, the building specimen performed well, and the observed and instrumented response of the test specimen met performance objectives for PT bar yielding, CLT crushing at the base, and UFP yielding. In terms of building drift response, the 1% drift limit for SLE hazard level tests were met, as well as the 4% drift limit for MCE_R hazard level tests. The

DBE hazard level tests had a drift limit of 2% which was exceeded for four of the five DBE tests, but only had an average drift of 2.24% for all the DBE tests which only exceeds the performance objective slightly. The predicted base shear response calculated from the design procedure was slightly higher than the measured base shear forces. The lower measured values were most likely a result of the flexible foundation decreasing the overall stiffness of the structure and in turn, decreasing the base shear forces. While the building performed better than expected, it is clear that the flexible foundation had a large impact on the performance.

To study the impact of the flexible foundation on the performance of the structure and to validate a modeling methodology for use in the design of the ten-story NHERI TallWood building, two nonlinear numerical models were developed in OpenSees. The first model accounted for foundation flexibility and the second modeled the as-designed rigid foundation case. In these models, nonlinear crushing at the base of the wall and wall uplift was modeled using distributed springs at the base of the wall and contribution of foundation surface flexibility was included through additional springs below the rocking springs. Overall, the flexible foundation model showed good agreement with the test results in terms of global and local behavior and building period.

The response of the rigid foundation model was compared to the flexible foundation model to study the impact of the flexible foundation on building performance. It was determined that altering the boundary condition had significant effects on the overall behavior. As expected, the rigid foundation greatly increased system stiffness, decreased the first mode period, and decreased drifts. Most importantly, the downward rotations at the base of the wall panels decreased significantly without the foundation beam flexibility, resulting in much higher CLT strains at the base of the wall. Under the rigid foundation boundary condition, the CLT experienced permanent yielding and damage. Apart from reduced roof drifts, the numerical model with the rigid foundation did predict somewhat poorer seismic performance as it predicted considerable CLT damage in the DBE and MCE_R ground motions.

9.2.3 Ten-Story NHERI TallWood Shake Table Test

The third phase of the research presented in this document was related to the design, numerical modeling, testing, and performance assessment of the post-tensioned mass timber rocking wall lateral force resisting system in the 10-story NHERI TallWood building. The building was designed for a location in the Capital Hill neighborhood of Seattle, Washington. The unique seismic hazard in Seattle was captured by including shallow crustal earthquakes, deep intraslab subduction earthquakes, and shallower interface subduction earthquakes in the design suites of ground motions selected at seven different hazard levels.

The lateral system for this building was designed using performance-based design methodologies that enforced stringent criteria to produce a design with seismic performance that meets or exceeds code minimum requirements. This was done in three phases. First, a MRSA was performed using a linear OpenSees model to complete preliminary drift checks and develop preliminary rotation design demands at the base of the rocking walls. The second phase of the design was to complete a preliminary design and capacity analysis of the walls using the cross-sectional analysis procedure. The rotation demands from phase 1 were used to determine component forces and overall moment capacity of the assembly. Results from this analysis were used to complete component level and overall moment capacity checks. Phases one and two of this design procedure are intended to represent a prescriptive design procedure that would be used in practice.

However, because post-tensioned mass timber rocking wall lateral systems are not currently recognized by US building codes, a detailed evaluation of the design was completed using NLRHA, as recommended by LATBSDC [2014], and conducted in OpenSees. Suite mean and suite maximum results from the MCE_R ground motion suites were then used to check a series of force and deformation-controlled actions to finalize the design of the lateral system and all lateral connections. By enforcing many force-controlled checks, an essentially elastic response at MCE_R was targeted. The two primary deformation-controlled checks, resulting in minimal inelastic behavior for the system were: (1) yielding of the replaceable

energy dissipating elements and (2) yielding of the wood at the base of the wall panels. Because near elastic performance was targeted for MCE_R level earthquakes, minimal criteria were enforced at lower hazards as it would have been redundant.

The most critical part of the lateral system design for the NHERI TallWood 10-story building was the capacity of the rocking wall panels under combined axial and bending loads and the capacity of the splice connection. These were controlled by the large moment demands in the walls from NLRHA at MCE_R. Higher mode effects resulted in the largest moment demands being at mid-height. The location of peak moment up the height of the walls happened to coincide with the location of the horizontal splice joint in the walls. Loads were transferred over the splice joint using an embedded epoxy rod connection.

NLRHA was done using a three-dimensional nonlinear OpenSees model. Similar to the model developed for the two-story NHERI TallWood building, the nonlinear compressive behavior at the base of the wall panels and uplift were modeled using distributed parallel springs along the base of the wall panels. For this model, additional rows of springs in the out-of-plane direction were added to capture both in-plane and out-of-plane rocking at the base of the walls. This model was also used to predict the performance of the structure at all hazard levels as well as provide design demands to project collaborators to complete the design of other building components such as nonstructural elements and gravity connections.

Structural construction of the NHERI TallWood 10-story test specimen was completed in January 2023 and dynamic testing occurred over a four-week period in May 2023. The test building was subjected to numerous earthquake recordings on the shake table that far exceeded the number and severity of earthquake expected for any real building. The testing plan consisted primarily of one- and two-horizontal-component acceleration inputs. Some tests also included vertical accelerations. The input accelerations ranged from those representing a 43-year return period hazard to those representing an MCE_R hazard. At the time of publication, this was the world's tallest shake table test. Over the duration of testing, no major visual damage was observed to the lateral system. Because damage to the lateral system was minor, the building was able to be tested and assessed at all five hazard levels,

resulting in a unique and intensive testing plan that is only possible for buildings with a resilient lateral system such as the one designed and tested here.

A preliminary performance assessment of the 10-story rocking wall lateral system during shake table testing was completed. This also consisted of a preliminary comparison of the building performance to the predicted performance from the nonlinear OpenSees model used to design the building. A thorough performance assessment was outside the scope of work due to time constraints. The preliminary assessment showed that the 10-story building met desired performance objectives and exceeded code minimum requirements. Interstory drifts at MCE_R hazard were below 1.5% and no damage to critical elements was observed. No damage was observed at the bases of the wall panels, indicating that the mass timber did not yield, thus exceeding the allowable performance which permitted mass timber yielding at the base of the wall panels.

For the last part of this research phase, the predicted OpenSees results were compared to the experimental results. Assessment of the experimental results showed that the actual damping exceed the expected damping of 2%, likely due to the presence of the nonstructural walls and stairs. Because of this, the original OpenSees model was modified, and the damping was increased to 6%. Apart from the damping modification, no additional changes were made to the model used for design. The comparison showed that the OpenSees model agreed with the experimental results relatively well in terms of predicting global measures, such as story drift, for such a large-scale test and that the agreement was consistent over all five tested hazard levels.

9.2.4 Parametric Study

The most critical limit states evaluated in the design of the lateral system for the NHERI TallWood 10-story building were the flexural capacities of the wall panel and wall splices. Large moment demands from NLRHA controlled these designs. The NLRHA results showed large moment demands at mid-height, a result of higher mode effects. This will likely be a critical design check for a future buildings with post-tensioned mass timber rocking wall

lateral systems. While past research has shown that introducing additional rocking joints up the height of the wall panels can greatly reduce the moment demands, little work has been done to quantify the amount of moment amplification and study the impact of building period and wall aspect ratio on overall building performance and moment amplification. This is important research as designing connections for multiple rocking planes will likely be challenging and expensive. For the fourth phase of this research program, this issue was studied through a parametric study on six different archetype designs. Three 6-story buildings and three 12-story buildings were designed following the prescriptive design procedure used for the design of the 10-story building. For designs of the same height, the wall aspect ratio was changed while keeping the overall building period constant to study the impact of wall aspect ratio, independent of the building period. MSAs were completed for each of the designs using the seven hazard levels defined for the design of the 10-story NHERI Tall-Wood building to compare performance of the different designs and to study how moment amplification changes with the different designs and across hazard levels.

Results from this study showed that for buildings with the same period, aspect ratio does not affect overall performance in terms of drifts, however, walls with a larger aspect ratio (i.e., more slender walls) had lower peak wall strains at the base of the wall. In terms of building period, as expected, the buildings with a longer period saw larger drifts and lower strains at the base of the wall panels. Looking at wall moment amplification, the following conclusions were drawn:

- Wall panel aspect ratio does not affect the amount of moment amplification for walls with the same period.
- A longer period wall will result in a larger amplified moment.
- For lower hazards, higher mode effects do not significantly amplify the moment at mid-height and the maximum wall moment occurs at the wall base
- For larger hazards where moment amplification is present, the location of maximum moment occurs at about 40% of the wall height for all walls.

9.3 Conclusions

The research program presented in this dissertation resulted in the following conclusions, advancing the state-of-the-art in earthquake engineering research for mass timber structures:

9.3.1 Rocking Wall Behavior

- Post-tensioned mass timber rocking wall lateral force-resisting systems can be designed to be seismically resilient. Seismic performance objectives exceeding code-minimum requirements can be easily achieved by capitalizing on the inherent behaviors of the rocking wall systems in design. This was demonstrated both numerically as well as experimentally, through two large-scale shake table tests of full-scale fully mass timber buildings with post-tensioned mass timber rocking walls.

- The unintentional flexible foundation in the 2-story building increased the overall flexibility of the system. A numerical model that included foundation flexibility and matched experimental results, was compared to an equivalent rigid foundation model. Results showed that even though the flexible foundation beam produced larger peak drifts relative to the rigid foundation beam model, in general, that deformation protected the base of the wall from damage and resulted in better overall performance in terms of CLT damage. The rigid foundation model still predicted the system would meet all design performance objectives and the predicted performance was closer to the design intent.

- The overall drift performance of post-tensioned mass timber rocking walls is not affected by wall aspect ratio for walls with the same period. Interstory drifts increase for walls with a longer period. Larger wall aspect ratio and larger building periods result in smaller peak strains and less damage at the base of the wall panels.

- Typical code-based lateral force distributions for determining wall moment demands, such as MRSA, do not accurately capture amplified moment demands that result from higher mode effects. Wall aspect ratio does not affect the relative magnitude of the amplified moment if building period is held constant, however, buildings with a longer period experience increased amplified moments. At lower hazard levels, moment amplification is minimal. At larger hazard levels, higher mode effects result in peak moments occurring at about 40% up the height of the wall. This location should be avoided for splice connection locations. Results from the research presented in this document highlight the importance of accounting for moment amplification effects in future design codes for this system.

9.3.2 Lateral Connection Design

- Embedded epoxy rod splice connections are capable of transferring large forces and moments through a mass timber splice. These types of connections are essential for the future of tall mass timber buildings and mass timber lateral systems in real buildings. While there were construction issues related to the embedded epoxy rod connection in the rocking walls of the 10-story NHERI TallWood building, the resulting connection performed well under the intensive shake table testing plan. This connection was the first of its type to be tested under dynamic flexural and shear demands. The tests validate the use of these connections in splices of mass timber wall under large flexural demands and the design procedure used to design them. These connections can be used confidently in both gravity and lateral systems.

9.3.3 Modeling Methodology

- The 2D OpenSees modeling methodology for post-tensioned mass timber rocking walls can fairly accurately predict the response. The multispring element with Labatto Integration distributed zero-length springs does a good job at predicting uplift response at the base of the walls. The additional foundation flexibility spring layer, extrapolated

from the rocking multispring element, also showed to accurately model the response of a flexible foundation present in the NHERI TallWood 2-story shake table test. Because of the accurate prediction of overall building performance between test results and the flexible foundation model results, the modeling approaches presented here can be used as a good prediction for mass timber rocking wall systems.

- The presented 3D nonlinear numerical OpenSees modeling methodology is successful for code-alternative design purposes. The methodology was validated through the design of the lateral system for the 10-story NHERI TallWood building. The demands produced by the model resulted in a resilient design. Comparison between preliminary experimental results and numerical model results showed relatively accurate predictions of the 10-story building response at multiple hazard levels.

9.3.4 Design Procedure

- The performance-based design procedure used for the design of the post-tensioned mass timber rocking walls in the 2-story NHERI TallWood building was successful and the design procedure was able to closely predict the experimental response of the structure.

- The code-alternative design procedure used to design the lateral system in the 10-story NHERI TallWood building was successful in creating a resilient design and was validated through dynamic testing in the world's largest shake table test. This procedure closely followed recommendations from LATBSDC [2014], which had not been previously tested for this lateral system.

- The first two phases of the design procedure used for the 10-story NHERI TallWood building lateral system were representative of a prescriptive design procedure commonly seen in building design codes. While a nonlinear numerical model was developed to validate the final design for the 10-story building, the prescriptive design was successful

in determining the key components of the design. The findings in this research have identified three concepts that should be incorporated into a building code prescriptive design procedure that have not been discussed in detail in previous research. The concepts are as follows:

  - Amplification of moment demands from higher mode effects must be incorporated into a building code design procedure. The conclusions from the parametric study presented in this document can be incorporated, however, more research should be done to develop final recommendations.

  - For the calculation of peak wood strain in the cross-sectional analysis procedure, strains from elastic and inelastic deformations should be accounted for. Some previous work has neglected the strains for elastic deformations, however, they are not negligible and should be considered to ensure a resilient design.

  - When developing a prescriptive design procedure, special attention should be given to estimating the global overturning moment demands in the wall versus those that that are resisted by the whole assembly. For example, overturning moment resisted by the UFPs can be subtracted from the overall assembly overturning moment (as done with the parametric study designs) when calculating the demands for combined axial and flexural checks in the walls. This will create a more economical, but still structurally viable demand.

- Based on the research presented in this document, the performance-based design levels summarized in Figure 9.1 are recommended for the design of post-tensioned mass timber rocking wall systems. In this figure, the minimum recommended performance levels are highlighted along the diagonal. Based on the limit states shown, the minimum recommended performance cases produce system level (i.e., ISD limits) consistent with

code requirements, however, at the component level (i.e., ...), the design is resilient and exceeds code minimum requirements. The cases identified as producing resilient performance are not only resilient at the component level but also produced system level performance that exceeds code minimum requirements. On this table, the design and achieved performance objectives are identified for both the 2-story and 10-story tests. Note, for both test specimens, the design ISD limit and the achieved ISD varied slightly from recommendations. These modifications are called out in the footnotes.

		Earthquake Performance Level			
		Occupant Comfort	**Immediate Occupancy**	**Limited Repair**	**Collapse Prevention**
Component and System Limit States		- No wall uplift - No PT yielding - UFPs elastic - Walls elastic - Lateral connections elastic	- ISD Limit: 1% - Residual drift limit: 0.2% - No PT yielding - Walls elastic - Lateral connections elastic	- ISD Limit: 2% - No PT yielding - Walls elastic (except base) - Yielding at wall base - Lateral connections elastic	- ISD Limit: 3% - PT yielding - Walls elastic (except base) - Crushing at wall base - Lateral connections elastic
Service Level Wind Event					
Earthquake Design Level	**Frequent (43-year)**	10-Story Performance	2-Story Performance		
	Occasional (475-year)		10-Story Performance 2-Story Performance (2.5% ISD[2])		
	Rare (975-year)		10-Story Performance (1.5% ISD[2])		
	Very Rare (MCE_R)		10-Story Performance (2% ISD[2]) 2-Story Performance (3% ISD[2])	10-Story Design (2.25% ISD[1])[3]	2-Story Design (4% ISD[1])

[1] Modified desing ISD limit state

[2] Achieved better ISD performance

[3] Splitting was allowed at the wall base in design

Performance Not Recommended
Minimum Recommended Performance
Resilient Performance

Figure 9.1: Recommended performance-based design levels

9.4 Recommendations for Future Work

The research program presented in this dissertation has highlighted additional work that is needed to fully characterize the seismic performance of post-tensioned mass timber rocking wall systems. In addition to the work presented, the recommended future work can aid in future code adoptions for this system and eliminate knowledge gapes to make the design more efficient. The recommendations for future research are as follows:

- Additional material property tests are needed on all mass timber products to study post-yield behavior. This is particularly important for the compression behavior at the base of the wall panels and determining a correct plastic hinge length for modeling purposes. For both the two-story and ten-story NHERI TallWood tests, damage to the base of the wall panels was expected, but not observed. Indicating that the assumed post-yield behavior or assumed plastic hinge length for this loading type is incorrect. Experimental work should be completed to study the impacts from non-uniform loading, time dependency, wall height, etc.

- Additional experimental research is needed on key mass timber capacity checks. In particular, minimal research has been completed to validate the current capacity checks defined by the NDS for lateral torsional bucking of large panels used for walls. Specifically, the calculation of the bending stability factor, C_L, is likely very conservative. Refining this capacity check could result in more economical and efficient designs. Additionally, the failure mode for many of these checks is widely unknown.

- The studies presented in this dissertation highlighted the significance of moment amplification from higher mode effects on creating a resilient design and showed that wall aspect ratio dose don't change moment amplification effects. However, more research should be completed on quantifying the moment amplification at MCE_R demands for

different periods.

- Detailed data processing and performance assessment of the post-tensioned mass timber rocking wall lateral system in the 10-story NHERI TallWood building was outside of the scope of this work due to time limitations. The list below identifies a list of key aspects of the 10-story results data that should be analyzed:

  - Conduct a more complete assessment of the 10-story lateral system performance with data processing. A few important things to study includes: (1) comparison of mass predictions presented in this document with recordings collected from the shake table controller data, (2) using shear key strain gauge data to determine floor forces and develop envelops for experimental shear and moment demands in the wall panels, (3) examining instrumentation used to measure the plastic hinge length, and (4) studying building period and changes to period throughout testing as a way to assess damage.

  - Incorporate strength and stiffness contributions of nonstructural wall and stair system to the nonlinear numerical model to quantify their impact on the overall building performance.

  - Complete a more thorough comparison of the experimental and numerical results to identify model modifications that could improve future model predictions.

  - Investigate any unintentional shake table rotations during testing and incorporate them into the structural models to determine their potential impact.

REFERENCES

ACI (2009). *Requirements for Design of a Special Unbounded Post-Tensioned Precast Shear Wall. ACI ITG-5.1 and Commentary.* American Concrete Institute, Farmington Hills, MI.

AISC (2016). *Specification for Structural Steel Buildings, ANSI/AISC 360-16.* American Institute of Steel Construction.

Akbas, T., Sause, R., Ricles, J. M., Ganey, R., Berman, J., Loftus, S., Dolan, J. D., Pei, S., van de Lindt, J. W., and Blomgren, H.-E. (2017). "Analytical and experimental lateral-load response of self-centering posttensioned CLT walls." *Journal of Structural Engineering*, 143(6), 04017019.

Alegria, G. A. A. (2022). "Effects of geometric, damping, and boundary parameters on the dynamic response of cross-laminated timber rocking wall systems." Ph.D. thesis, Washington State University, Pullman, Washington.

Ancheta, T. D., Darragh, R. B., Stewart, J. P., Seyhan, E., Silva, W. J., Chiou, B. S.-J., Wooddell, K. E., Graves, R. W., Kottke, A. R., Boore, D. M., Kishida, T., and Donahue, J. L. (2014). "Nga-west2 database." *Earthquake Spectra*, 30(3), 989–1005.

APA (2019a). "Joint evaluation report esr-1040 versa-lam code report." *Report No. ESR-1040*, APA - The Engineered Wood Association.

APA (2019b). *Standard for Performance-Rated Cross-Laminated Timber, ANSI/APA PRG 320-2019.* APA - The Engineered Wood Association.

APA (2021). "Apa product report pr-l325 freres mass ply panels (mpp) and mass ply lams

(mpl) beams and columns." *Report No. PR-L325*, APA - The Engineered Wood Association.

APA (2022). "Apa product report pr-l326 ib max-core glulam beams and columns." *Report No. PR-L326*, APA - The Engineered Wood Association.

APA (2023a). "Apa product report pr-l314 ok laminators crosslam clt." *Report No. PR-L314*, APA - The Engineered Wood Association.

APA (2023b). "Apa product report pr-l319 smartlam cross-laminated timber." *Report No. PR-L319*, APA - The Engineered Wood Association.

Applied Technology Council (ATC) (2016). "Hazards by location, <`https://hazards.atcouncil.org`>. Accessed on February 19, 2019.

ASCE (2010). *Minimum Design Loads for Buildings and Other Structures*. ASCE/SEI 7-10. American Society of Civil Engineering, Reston, VA.

ASCE (2016). *Minimum Design Loads for Buildings and Other Structures*. ASCE/SEI 7-16. American Society of Civil Engineering, Reston, VA.

AWC (2018). *National Design Specification for Wood Construction*. American Wood Council.

Baird, A., Smith, T., Palermo, A., and Pampanin, S. (2014). "Experimental and numerical study of U-shape flexural plate (UFP) dissipators." *2014 NZSEE Conference; 2014*.

Baker, J. (2013). "Efficient analytical fragility function fitting using dynamic structural analysis." *Earthquake Spectra*, 31.

Barbosa, A. R., Rodrigues, L. G., Sinha, A., Higgins, C., Zimmerman, R. B., Breneman, S., Pei, S., van de Lindt, J. W., Berman, J., and McDonnell, E. (2021). "Shake-table experimental testing and performance of topped and untopped cross-laminated timber diaphragms." *Journal of Structural Engineering*, 147(4), 04021011.

Barbosa, A. R., Sinha, A., Higgins, C., and Soti, R. (2018). "Structural testing for the DR Johnson's CLT panels." *Report No. 17-03*, Oregon State University.

Brown, A., Lester, J., Pampanin, S., and Pietra, D. (2012). "Pres-lam in practice - a damage-limiting rebuild project." *SESOC NZ Conference*, New Zealand.

Brown, J. R., Li, M., Palermo, A., Pampanin, S., and Sarti, F. (2021). "Experimental testing of a low-damage post-tensioned c-shaped clt core-wall." *Journal of Structural Engineering*, 147(3), 04020357.

Busch, A. (2023). "Design and construction of tall mass timber buildings with resilient post-tensioned mass timber rocking walls." Ph.D. thesis, Colorado School of Mines, Golden, CO.

Busch, A., Zimmerman, R. B., Pei, S., McDonnell, E., Line, P., and Huang, D. (2022). "Prescriptive seismic design procedure for post-tensioned mass timber rocking walls." *Journal of Structural Engineering*, 148(3), 04021289.

Ceccotti, A., Sandhass, C., Okabe, M., Yasumura, M., Minowa, C., and Kawai, N. (2013). "Sofie project - 3d shaking table test on a seven-storey full-scale cross-laminated timber building." *Earthquake Engineering and Structural Dynamics*, 42, 2003–2021.

Chopra, A. K. (2007). *Earthquake Dynamics of Structures: Theory and Applications to Earthquake Engineering*. Prentice Hall, Upper Saddle River, New Jersey, 3rd edition.

Christopoulos, C., Filiatrault, A., and Folz, B. (2002). "Seismic response of self-centring hysteretic sdof systems." *Earthquake Engineering & Structural Dynamics*, 31(5), 1131–1150.

Devereux, C. P., Holden, T. J., Buchanan, A. H., and Pampanin, S. (2011). "Nmit arts & media building - damage mitigation using post-tensioned timber walls." *Ninth Pacific Conference on Earthquake Engineering*, Auckland, New Zealand.

Dujic, B. and Zarnic, R. (2006). "Study of lateral resistance of massive x-lam wooden wall system subjected to horizontal loads." *International Workshop on Earthquake Engineering on Timber Structures*.

Engineers, K. C. (2017). "Framework: Basis of design - performance-based design." *Report No. Project No. 215135*, KPFF Consulting Engineers.

FPInnovations (2013). *CLT Handbook: Cross-Laminated Timber, U.S. Edition*. FPInnovations, Pointe-Claire, Quebec, Canada.

Freres Engineered Wood (2022). *Mass Ply Design and Construction Guide*. Freres Engineered Wood.

Ganey, R., Berman, J., Akbas, T., Loftus, S., Dolan, J. D., Sause, R., Ricles, J., Pei, S., van de Lindt, J., and Blomgren, H.-E. (2017). "Experimental investigation of self-centering cross-laminated timber walls." *Journal of Structural Engineering*, 143(10), 04017135.

Ganey, R. S. (2015). "Seismic design and testing of rocking CLT walls." M.S. thesis, University of Washington, Seattle, WA.

Gavric, I., Fragiacoma, M., and Ceccotti, A. (2012). "Strength and deformation characteristics of typical x-lam connections." *12th World Conference on Timber Engineering*.

He, M., Sun, X., and Li, Z. (2018). "Bending and compressive properties of corss-laminated timber (clt) panels made from canadian hemlock." *Construction and Building Materials*, 185, 175–183.

Huang, D. (2023). "Optimized seismic design and dynamic response analysis of mass timber rocking wall lateral system." Ph.D. thesis, Colorado School of Mines, Golden, CO.

Iqbal, A., Pampanin, S., Palermo, A., and Buchanan, A. H. (2015). "Performance and design of lvl walls coupled with ufp dissipaters." *Journal of Earthquake Engineering*, 19(3), 383–409.

Kaiser+Path (n.d.). "Carbon12 design and approval: A leap into the unknown, <https://buildingcarbon12.com/design-and-approval/>. Accessed 25 July 2023.

Katerra (2020). "Katerra clt product definition." *Report no.*, Katerra.

Kelly, J. M., Skinner, R. I., and Heine, A. J. (1972). "Mechanics of energy absorption in special devices for use in earthquake resistant structures." *Bulletin of the New Zealand Society for Earthquake Engineering; 1972*.

Kovacs, M. (2016). "Design of controlled rocking heavy timber walls for low-to-moderate seismic hazard regions." M.S. thesis, McMaster University, Hamilton, Ontario.

Kovacs, M. A. and Wiebe, L. (2019). "Controlled rocking clt walls for buildings in regions of moderate seismicity: Design procedure and numerical collapse assessment." *Journal of earthquake engineering : JEE*, 23(5), 750–770.

Kurama, Y., Pessiki, S., Sause, R., and Lu, L. (1999). "Seismic behavior and design of unbonded post-tensioned precast concrete walls." *PCI Journal*, 44(3), 72–89.

LATBSDC (2014). *An Alternative Procedure for Seismic Analysis and Design of Tall Buildings Located in the Los Angeles Region*. Los Angeles Tall Buildings Structural Design Council.

Lauriola, M. and Sandhaas, C. (2006). "Quasi-static and pseudo-dynamic tests on xlam walls and buildings." *International Workshop on Earthquake Engineering on Timber Structures*.

Marafi, N. (2018). "Impacts of an m9 cascadia subduction zone earthquake on structures located in deep sedimentary basins." Ph.D. thesis, University of Washington, Seattle, Washington.

Mass Timber Map (2023). "Mass timber products, <https://masstimbermap.com/mass-timber-products/>. Accessed 19 July 2023.

Mazzoni, S., Kishida, T., Contreras, V., Ahdi, S. K., Kwak, D. Y., Bozorgnia, Y., and Stewart, J. P. (2021). "NGA-Sub Flatfile: R211022." The B. John Garrick Institute for the Risk Sciences. Dataset, <https://doi.org/10.34948/N3Z59T>.

Mazzoni, S., McKenna, F., Scott, M., and Fenves, G. (2009). *Open Systems for Earthquake Engineering Simulation User Command-Language Manual - OpenSees version-2.0.* Pacific Earthquake Engineering Research Center, University of California, Berkeley, Berkely, CA.

MGA (2017). "The case for tall wood buildings." *Report No. 2*, MGA Michael Green Architecture.

Moroder, D., Pampanin, S., Palermo, A., Smith, T., Sarti, F., and Buchanan, A. (2017). "Diaphragm connections in structures with rocking timber walls." *Struct Eng Int*, 27(2), 165–174.

National Research Institute for Earth Science and Disaster Resilience (NIED) (2018). "Strong-motion seismograph networks (k-net, kik-net), <https://www.kyoshin.bosai.go.jp/kyoshin/docs/overview_kyoshin_index_en.html>.

Newcombe, M. P. (2011). "Seismic design of post-tensioned timber frame and wall buildings." Ph.D. thesis, University of Canterbury, Christchurch, New Zealand.

Newcombe, M. P. (2015). "The connection response of rocking timber walls." *New Zealand Timber Design*, 23(1), 21–28.

Newcombe, M. P., Pampanin, S., Buchanan, A., and Palermo, A. (2008). "Section analysis and cyclic behavior of post-tensioned jointed ductile connections for multi-story timber buildings." *Journal of Earthquake Engineering*, 12(sup1), 83–110.

NIST (2010). *Evaluation of the FEMA P-695 Methodology for Quantification of Building Seismic Performance Factors, NIST GCR 10-917-8.* National Institute of Standards and Technology, Gaithersburg, MD, USA.

Palermo, A., Pampanin, S., and Buchanan, A. (2006). "Experimental investigation on lvl seismic resistant wall and frame subassemblies." *First European Conference on Earthquake Engineering and Seismology*, Geneva, Switzerland.

Palermo, A., Pampanin, S., and Calvi, G. M. (2004). "The use of controlled rocking in the seismic design of bridges." *13th World Conference on Earthquake Engineering*, number 4006, Vancouver, B.C., Canada.

Palermo, A., Pampanin, S., and Carr, A. (2005). "Efficiency of simplified alternative modeling approaches to predict the seismic response of precast concrete hybrid systems." *www.eat.bme.hu/fibSymp2005/*.

Pampanin, S., PRIESTLEY, M., and Sritharan, S. (2001a). "Analytical modeling of the seismic behavior of precast concrete frames designed with ductile connections." *Journal of Earthquake Engineering - J EARTHQU ENG*, 5, 329–367.

Pampanin, S., Priestley, M. J. N., and Sritharan, S. (2001b). "Analytical modeling of the seismic behavior of precast concrete frames designed with ductile connections." *Journal of Earthquake Engineering*, 5(3), 329–367.

Pei, S., Huang, D., Berman, J. W., and Wichman, S. K. (2021). "Simplified dynamic model for post-tensioned cross-laminated timber rocking walls." *Earthquake Engineering & Structural Dynamics*, 50(3), 845–862.

Pei, S., van de Lindt, J. W., Barbosa, A. R., Berman, J. W., McDonnell, E., Dolan, J. D., Blomgren, H.-E., Zimmerman, R. B., Huang, D., and Wichman, S. (2019). "Experimental seismic response of a resilient 2-story mass-timber building with post-tensioned rocking walls." *Journal of Structural Engineering*, 145(11), 04019120.

Pilon, D. S., Palermo, A., Sarti, F., and Salenikovich, A. (2019). "Benefits of multiple rocking segments for clt and lvl pres-lam wall systems." *Soil Dynamics and Earthquake Engineering*, 117, 234–244.

Popovski, M., Schneider, J., and Schweinsteiger, M. (2010). "Lateral load resistance of cross-laminated wood panels." *11th World Conference on Timber Engineering*, Trentino, Italy.

Priestley, N. (1991). "Overviw of presss research program." *PCI Journal*, 36(4), 50–57.

Sarti, F. (2015). "Seismic design of low-damage post-tensioned timber wall systems." Ph.D. thesis, University of Canterbury, Christchurch, New Zealand.

Sarti, F., Smith, T., Danzig, I., and Karsh, E. (2017). "Pres-lam in the us: the seismic design of the peavy building at oregon state university." *New Zealand Timber Design Journal*, 25(2), 11–18.

Seo, C. Y. and Sause, R. (2005). "Ductility demands on self-centering systems under earthquake loading." *ACI Structural Journal*, 102(2), 275–285.

Shahi, S. K. and Baker, J. W. (2014). "Nga-west2 models for ground motion directionality." *Earthquake Spectra*, 30(3), 1285–1300.

Sinha, A., Barbosa, A. R., Ho, T. X., Zimmerman, R., and McDonnell, E. (2023). "Compression behavior of cross-laminated timber panels with different reinforcement mechanisms. (in preparation).

SmartLam (2023). "Clt specifier guide." *Report no.*, SmartLam North America.

SOM (2013). "Timber tower research project: Final report." *Skidmore, Owings and Merrill Final Report*.

Soti, R., Ho, T. X., and Sinha, A. (2021). "Structural performance characterization of mass plywood panels." *Journal of Materials in Civil Engineering*, 33(10), 04021275.

Spieth, H. A., Carr, A. J., Pampanin, S., Murahidy, A. G., and Mander, J. (2004). "Modeling of precast prestressed concrete frame structures with rocking beam-column connections." *Report No. 2004-01*, University of Canterbury. Christchurch, New Zealand.

Stanton, J., Stone, W., and Cheok, G. S. (1997). "A hybrid reinforced precast frame for seismic regions." *PCI Journal*, 42(2), 20–32.

Thornton Tomasetti (n.d.). "Project: Ascent, <https://www.thorntontomasetti.com/project/ascent>. Accessed 25 July 2023.

United States Geological Survey (USGS) (2017a). "Nshm: Conterminous u.s. 2014." *GitHub repository*, <https://github.com/usgs/nshm-cous-2014>.

United States Geological Survey (USGS) (2017b). "National seismic hazard mapping project (nshmp) code." *GitHub repository*, <https://github.com/usgs/nshmp-haz>.

van de Lindt, J., Amini, M. O., Rammer, D., Line, P., Pei, S., and Popovski, M. (2022). "Determination of seismic performance factors for cross-laminated timber shear walls based on FEMA p695 methodology." *Report no.*, <https://doi.org/10.2737%2Ffpl-gtr-281> (jun).

Van Den Einde, L., Conte, J. P., Restrepo, J. I., Bustamante, R., Halvorson, M., Hutchinson, T. C., Lai, C.-T., Lotfizadeh, K., Luco, J. E., Morrison, M. L., Mosqueda, G., Nemeth, M., Ozcelik, O., Restrepo, S., Rodriguez, A., Shing, P. B., Thoen, B., and Tsampras, G. (2021). "Nheri@uc san diego 6-dof large high-performance outdoor shake table facility." *Frontiers in Built Environment*, 6, 181.

Wichman, S. (2018). "Large-scale dynamic testing of rocking cross laminated timber walls." M.S. thesis, University of Washington, Seattle, WA.

Wichman, S., Berman, J. W., and Pei, S. (2022). "Experimental investigation and numerical modeling of rocking cross laminated timber walls on a flexible foundation." *Earthquake Engineering & Structural Dynamics*, 51(7), 1697–1717.

Wiebe, L. and Christopoulos, C. (2009). "Mitigation of higher mode effects in base-rocking systems by using multiple rocking sections." *J Earthq Eng*, 13(sup1), 83–108.

Wiebe, L. and Christopoulos, C. (2015). "Performance-based seismic design of controlled rocking steel braced frames. ii: Design of capacity-protected elements." *Journal of Structural Engineering*, 141(9), 04014227.

Wilson, A. W. (2018). "Numerical modeling and seismic performance of post-tensioned cross-laminated timber rocking wall systems." M.S. thesis, Washington State University, Pullman, Washington.

WoodWorks (2022). *Mass Timber Design Manual vol. 2*. Think Wood.

Wright, D. (2023). "Vertical vibration of mass timber floors subjected to seismic and footfall loading." M.S. thesis, University of Washington, Seattle, WA.

Zimmerman, R. and McDonnell, E. (2017). "Framework - a tall re-centering mass timber building in the united states." *New Zealand Society for Earthquake Engineering Conference*, Vol. 9, Wellington, New Zealand.

Zimmerman, R. and McDonnell, E. (2018). "Framework - innovation in re-centering mass timber wall buildings." *Proceedings of the 11th National Conference in Earthquake Engineering*, Los Angeles, CA, Earthquake Engineering Research Institute.

Zimmerman, R. B., Blomgren, H.-E., McCutcheon, J., and Sinha, A. (2020). "Catalyst - a mass timber core wall building with high ductility hold-downs in a seismic region." *2020 World Conference on Timber Engineering*, Santiago, Chili.

Appendix A

10-STORY TEST SPECIMEN: ROCKING WALL DESIGN CRITERIA CHECKS

A.1 Overview

This appendix includes detailed design calculations for the the 10-story test specimen. Each section summarizes a different design check. Conceptual explanations for each check can be found in the main text in Section 6.6.3 of the 10-story design chapter.

A.2 CLT Rocking Wall Capacity Design

This section includes the capacity calculations for the CLT shear walls in the 10-story test specimen. The walls were checked for shear, combined edgewise bending and axial loading in net compression, and combined edgewise bending and axial loading in net tension. See Section 6.6.3 for a conceptual discussion of these checks. In most cases, the 2018 NDS [AWC, 2018] was referenced for material properties of the walls. For this check the design equations and design methodology are outlined first, followed by spreadsheets summarizing the final values and final demand to capacity ratios (DCRs).

To calculate the demands used for these checks, suite mean and suite maximum results were taken from NLRHA results. Peak wall moment, wall shear, PT bar force values were used for these calculations. The results from the NLRHA used for the wall designs are summarized in Table 6.23, 6.25, and 6.29 for the shear, moment, and PT bar values, respectively.

A.2.1 CLT Shear Capacity Check

The shear stress capacity of the CLT wall was checked at the location of the UFPs, where the length of the CLT wall is smallest. Capacity checks were completed using suite mean

and suite maximum wall shear values from the nonlinear numerical model.

Demand:

The demand shear stress in the CLT wall was calculated in accordance with Equation A.1 where A_v is the shear area, defined by Equation A.2 and V_u is the factored shear demand force, defined as shown in Equation A.3. For the shear stress capacity, the total area is to be used in accordance with manufacturer standards. The 1.5 factor in Equation A.3 accounts for the maximums shear stress at the center of the wall [Zimmerman and McDonnell, 2018].

$$\boxed{f_v = \frac{1.5V_u}{A_v}} \tag{A.1}$$

$$A_v = L_{red} b_w \tag{A.2}$$

$$V_u = \gamma V \tag{A.3}$$

Capacity:

The shear stress capacity was calculated in accordance with Equation A.4. Note, at the time of this writing there is no standardization for edgewise shear stress strength properties and thus, it is not always reported. Because the CLT wall panel grades were created specifically for this test (i.e. a standard manufacture grade was not used), edgewise shear strength values were not available. Design values for edgewise shear in the CLT was taken from Katerra CLT Product Definition for 9-ply CLT [Katerra, 2020] as it is somewhat similar to the CLT used for the 10-story test. The lumber used to create the CLT for the 10-story test is higher quality and thus this will be a conservative check.

$$\boxed{F'_{ve} = \phi K_F F_{ve}} \tag{A.4}$$

DCR:

The demand to capacity ratio for in-plane shear stress of the CLT wall was calculated according to Equation A.5.

$$\boxed{\frac{f_v}{F'_{ve}} \leq 1.0} \tag{A.5}$$

A.2.2 CLT Combined Edgewise Bending & Axial Loading - Net Compression

At all points along the height of the wall, except at the base rocking interface, the stress from combined edgewise bending and axial loading that produced net compression at any point in the cross section of the CLT was checked. This check was completed using the wall cross sectional area at the location where the UFPs were present since this was the smallest area. Capacity checks were completed using suite mean and suite maximum wall moment demands and PT force demands from the nonlinear numerical model. The following checks for CLT combined edgewise bending and axial loading in net compression are based on Section 3.9.2 of the NDS [AWC, 2018] with area modifications to represent just the effective area of the CLT (the vertical laminates that are orientated parallel to loading). Chapter 3, Section 2.2.2 of the CLT handbook [FPInnovations, 2013] are referenced for the CLT modifications.

Demand:

The demand axial compression stress value was calculated in accordance with Equation A.6 where the effective compression area, A_{eff} is calculated using Equation A.7, and the factored ultimate load, P_u is calculated using Equation A.8. The demand bending stress value was calculated in accordance with Equation A.9 where the effective section modulus, S_{eff} was calculated using Equation A.10, and the factored ultimate wall moment was calculated using Equation A.11.

The suite mean and suite maximum axial force values were calculated using the maximum total wall PT force for each ground motion from the numerical model. The suite mean and suite maximum wall moment values were calculated using the maximum wall moments

along the whole height of the wall for each ground motion from the numerical model. Note, this may be slightly conservative since these two instances may not occur at exactly the same time, however, they are likely to occur around the same time.

Compression:

$$\boxed{f_c = \frac{P_u}{A_{eff}}} \tag{A.6}$$

$$A_{eff} = L_{red} b_w \frac{N_{vert}}{N_{total}} \tag{A.7}$$

$$P_u = \gamma P \tag{A.8}$$

Bending:

$$\boxed{f_b = \frac{M_u}{S_{eff}}} \tag{A.9}$$

$$S_{eff} = b_w \frac{N_{vert}}{N_{total}} \frac{L_{red}^2}{6} \tag{A.10}$$

$$M_u = \gamma M \tag{A.11}$$

Capacity:

The axial stress capacity of the CLT wall in compression was calculated in accordance with Equations A.12 and A.13. Required variables are defined using Equations A.14 through A.20. Bending stress capacity of the CLT wall was calculated in accordance with Equation A.21, where Equations A.22 through A.24 define all needed variables. Again, this calculation procedure is based on Section 3.9.2 of the NDS with modifications.

Compression:

$$\boxed{F'_c = \phi \times F_c \times C_p \times K_F} \tag{A.12}$$

$$\boxed{F_{cE} = \frac{P_{cE}}{A_{eff}}} \tag{A.13}$$

$$C_p = \frac{1 + {}^{P_{cE}}/_{P^*_{c,eff}}}{2c} - \sqrt{\left[\frac{1 + \left({}^{P_{cE}}/_{P^*_{c,eff}}\right)}{2c}\right]^2 - \frac{{}^{P_{cE}}/_{P^*_{c,eff}}}{c}} \tag{A.14}$$

$$c = 0.9 \tag{A.15}$$

$$P^*_{c,eff} = (F_c \times K_F \times \phi) A_{eff} \tag{A.16}$$

$$P_{cE} = \frac{\pi^2 EI'_{app-min}}{l_u^2} \tag{A.17}$$

$$EI'_{app-min} = EI_{app-min} \times K_F \times \phi \tag{A.18}$$

$$EI_{app-min} = 0.5184 EI_{app} \tag{A.19}$$

$$EI_{app} = \frac{EI_{eff}}{1 + \frac{K_s EI_{eff}}{GA_{eff} l_u^2}} \tag{A.20}$$

Bending:

$$\boxed{F'_b = \phi \times F_b \times C_L \times K_F} \tag{A.21}$$

$$C_L = \frac{1 + {}^{F_{bE}}/_{F^*_b}}{1.9} - \sqrt{\left[\frac{1 + {}^{F_{bE}}/_{F^*_b}}{1.9}\right]^2 - \frac{{}^{F_{bE}}/_{F^*_b}}{0.95}} \tag{A.22}$$

$$F^*_b = \phi \times F_b \times K_F \tag{A.23}$$

$$F_{bE} = \frac{2.4 EI'_{app-min}}{S l_e} \tag{A.24}$$

DCR:

The demand to capacity ratio for combined edgewise bending and axial loading in net compression of the CLT wall was calculated according to Equation A.25 which is based on Section NSD 3.9.2 with modifications for CLT.

$$\boxed{\left[\frac{f_c}{F'_c}\right]^2 + \frac{f_b}{F'_b\left[1 - \left(\frac{f_c}{F_{cE}}\right)\right]} \leq 1.0} \tag{A.25}$$

(A.26)

A.2.3 CLT Combined Edgewise Bending & Axial Loading - Net Tension

At all points along the height of the wall, except at the base rocking interface, the stress from combined edgewise bending and axial loading that produced net tension at any point in the cross section of the CLT was checked. The check was completed using the wall cross sectional area at the location where the UFPs were present since this was the smallest area. Capacity checks were completed using suite mean and suite maximum wall moments and PT forces from the nonlinear numerical model. Tension forces occurred from bending but were reduced by PT compression forces, resulting in net tension forces. The following checks for CLT combined edgewise bending and axial loading in net tension are based on Section 3.9.1 of the NDS [AWC, 2018] with area modifications to represent just the effective area of the CLT.

Demand:

The demand axial compression stress value was calculated in accordance with Equation A.27 where the effective compression area, A_{eff} is calculated using Equation A.28, and the factored ultimate load, P_u is calculated using Equation A.29. The demand bending stress value was calculated in accordance with Equation A.30 where the effective section modulus, S_{eff} was calculated using Equation A.31, and the factored ultimate wall moment was calculated using Equation A.32.

For both suite mean and suite maximum, initial PT forces were used for axial force values. The suite mean and suite maximum wall moment values were calculated using the maximum wall moments along the whole height of the wall for each ground motion from the numerical model. Note, this load combination is conservative because the PT bars will likely be stressed beyond their initial PT forces when the wall rocks and reaches maximum bending moment. This would increase the compression force from the PT bars, thus decreasing the net tensile force in the wood. While completing the check as shown results in a very conservative check, this check was not critical for the design so it was done to ease calculations. However, because

it is highly conservative, the axial demand factor, γ, for suite mean was taken as 1.0 instead of 1.3 since the minimum possible value is already being used.

Compression:

$$\boxed{f_c = \frac{P_u}{A_{eff}}} \tag{A.27}$$

$$A_{eff} = L_{red} b_w \frac{N_{vert}}{N_{total}} \tag{A.28}$$

$$P_u = \gamma P \tag{A.29}$$

Bending:

$$\boxed{f_b = \frac{M_u}{S_{eff}}} \tag{A.30}$$

$$S_{eff} = b_w \frac{N_{vert}}{N_{total}} \frac{L_{red}^2}{6} \tag{A.31}$$

$$M_u = \gamma M \tag{A.32}$$

Capacity:

The axial stress capacity of the CLT wall in tension was calculated in accordance with Equation A.33.

Tension:

$$F_t' = \phi \times K_F \times F_t \tag{A.33}$$

DCR:

The demand to capacity ratio for combined edgewise bending and axial loading in net tension of the CLT wall was calculated in according to Equation A.34 which is based on Equation 3.9-1 in the NDS with modifications for CLT [AWC, 2018]. Note, in Equation A.34, f_c can be taken as a negative value since it is in compression and f_b is in tension.

$$\boxed{\frac{f_b + f_c}{F'_t} \leq 1.0} \tag{A.34}$$

A.2.4 CLT Wall Capacity Check Calculations

The following section summarizes all the values and calculations used to check the capacity of the CLT walls panels at all locations other than the splices and the wall bases.

CLT Shear Wall Timber Capacity Design

CLT Species:
Longitudinal Layers: MSR rated lumber 2400-2.0E
Transverse Layers: Southren Pine, No. 1 Visual grade (12" wide)

CLT Material Properties:

MOE (long. Layers):	E_1 =	2.00E+06	psi	NDS sup. Table 4C for MSR 2400f-2.0E
MOE (trans. Layers):	E_2 =	1.60E+06	psi	NDS sup. Table 4B for No. 1 Visual Grade
Comp. design value (parallel):	F_c =	1975	psi	NDS sup. Table 4C for MSR 2400f-2.0E
Bending design value (parallel):	F_b =	2400	psi	NDS sup. Table 4C for MSR 2400f-2.0E
Tension design value:	F_t =	1925	psi	NDS sup. Table 4C for MSR 2400f-2.0E
Edgewise shear stress:	$F_{v,e,90}$ =	235	psi	Katerra Prodcut Definition

Geometric Properties:

CLT wall thickness:	b_w =	12.375	in	
Laminate thickness:	t =	1.375	in	
No. of total laminates:	N_{total} =	9		
No.of vertical laminates:	N_{vert} =	5		
CLT wall length total:	L_{tot} =	117.125	in	
CLT wall length reduced	L_{red} =	102.625	in	Wall length at the UFP cutouts
Unbraced panel length:	l_u =	132	in	Story height
Effective panel length:	l_e =	242.88	in	Assume equal end moments, NDS Table 3.3.3

Calculated Geometric Properties:

Effective area:	A_{eff} =	705.5	in^2	Area of vertical laminations
Effective section modulus:	S_{eff} =	12068	in^2	Section modulus of vertical laminations

EI_{eff} Calculation - per CLT handbook:

Layer	E	z	$Ebh^3/12$	EAz^2	sum
-	psi	in	lb in^2	lb in^2	lb in^2
1	2.00E+06	5.5	4.45E+07	8.54E+09	8.58E+09
2	5.33E+04	4.125	1.19E+06	1.28E+08	1.29E+08
3	2.00E+06	2.75	4.45E+07	2.13E+09	2.18E+09
4	5.33E+04	1.375	1.19E+06	1.42E+07	1.54E+07
5	2.00E+06	0	4.45E+07	0.00E+00	4.45E+07
6	5.33E+04	1.375	1.19E+06	1.42E+07	1.54E+07
7	2.00E+06	2.75	4.45E+07	2.13E+09	2.18E+09
8	5.33E+04	4.125	1.19E+06	1.28E+08	1.29E+08
9	2.00E+06	5.5	4.45E+07	8.54E+09	8.58E+09

EI_{eff} =	2.19E+10	lb in^2
EI_{eff} =	2.56E+09	lb in^2/ft

CLT in Shear:

Shear Calculations:

Effective shear area:	A_v =	1270	in^2	Per Katerra standards, use total b_w
Format conversion Factor:	K_F =	2.88		NDS Table 10.3.1
Resistance Factor:	φ =	0.75		NDS Table 10.3.1
Adj. shear stress (w/o φ):	**F_{ve}' =**	**677**	**psi**	

CLT Shear Capacity Check:

		Suite Mean	Suite Max	
Shear Demands	γ =	1.3	1	
	V_u =	163	179	kip
	f_v =	193	211	psi
Shear Capacity	φ =	0.75	1	
	F_{ve}' =	508	677	psi
DCR		0.38	0.31	

CLT Combined Axial-Flexure in Compression :

Compression Capacity Calculations:

Loading condition Factor:	K_s =	11.5		NDS Tbl. 10.4.1.1 uniform dist. pinned
Effective bending stiffness (per ft):	EI_{eff} (per ft) =	2.56E+09	lb in^2/ft	CLT Handbook Ch. 3 Eq. 24
Effective bending stiffness:	EI_{eff} =	2.19E+10	lb in^2	Adj. for the reduced wall length
Effective shear stiffness (per ft):	GA_{eff} (per ft) =	1.80E+06	lb/ft	Katerra Prodcut Definition
Effective shear stiffness:	GA_{eff} =	1.54E+07	lb	Adj. for the reduced wall length
Apperent bending stiffness:	EI_{app} =	1.13E+10	lb in^2	CLT Handbook Chapter 3 Eq. 5
Min. app. bending stiffness:	$EI_{app-min}$ =	5.85E+09	lb in^2	CLT Handbook Chapter 3 Eq. 8
Format conversion factor $EI_{app-min}$:	K_F =	1.76		NDS Section 10.3, Table 10.3.1
Resistance Factor:	φ =	0.85		NDS Section 10.3, Table 10.3.1
Adj. Min. app. bending stiffness:	$EI_{app-min}'$ =	8.75E+09	lb in^2	NDS Section 10.3
P_{cE} :	P_{cE} =	4956	kip	CLT Handbook Ch. 3 Sec. 2.2.2
Format conversion factor F_c:	K_F =	2.4		NDS Section 10.3, Table 10.3.1
Resistance Factor:	φ =	0.9		NDS Section 10.3, Table 10.3.1
Adj. Comp. ‖ to grain (w/o C_p):	$P_{c,eff}$* =	3010	kip	NDS Section 10.3 - Modified
For CLT:	c =	0.9		NDS Equation 3.7-1
Column stability factor:	C_p =	0.89		NDS Equation 3.7-1 - Modified
Adj. comp. design value (w/o φ):	**F_c' =**	**4237**	**psi**	NDS Section 10.3
Critical buckling design value:	**F_{cE} =**	**7025**	**psi**	P_{cE} divied by the effective area

Bending Capacity Calculations:

Resistance Factor:	φ =	0.85		NDS Section 10.3, Table 10.3.1
Format conversion factor F_b:	K_F =	2.54		NDS Section 10.3, Table 10.3.1
Adj. Bending (w/o C_L):	F_b* =	5182	psi	NDS Section 10.3
F_{bE}:	F_{bE} =	7165	psi	NDS Equation 3.3-6 - Modified
Bending stability factor:	C_L =	0.91		NDS Equation 3.3-6
Adj. Edgewise bending design value (w/o φ):	**F_b' =**	**5558**	**psi**	NDS Section 10.3

CLT Combined axial-flexure in compression check:

		Suite Mean	Suite Max	
Bending Demands	γ =	1.3	1	
	M_u =	40174	42594	kip-in
	f_b =	3329	3530	psi
Axial Demands	γ =	1.3	1	
	P_u =	324	275	kip
	f_c =	460	390	psi
Bending Capacity	φ =	0.85	1	
	F_b' =	4724	5558	psi
Axial Capacity	φ =	0.9	1	
	F_c' =	3813	4237	psi
	F_{cE} =	7025	7025	psi
DCR		0.77	0.68	

CLT Combined axial-flexure in tension :

Shear Capacity Calculations:

Format conversion factor F_t :	K_F =	2.7	NDS Section 10.3, Table 10.3.1
Resistance Factor:	φ =	0.8	NDS Section 10.3, Table 10.3.1
Adj. tension design value (w/o φ):	**F_t' =**	**5197.5 psi**	NDS Section 10.3

CLT Combined axial-flexure in tension check:

		Suite Mean	Suite Max	
Bending Demands	γ =	1.3	1	
	M_u =	40174	42594	kip-in
	f_b =	3329	3530	psi
Axial Demands	γ =	1	1	
	P_u =	-200	-200	kip
	f_c =	-283	-283	psi
Tensile Capacity	φ =	0.8	1	
	F_t' =	4158	5197.5	psi
DCR		0.73	0.62	

A.3 MPP Rocking Wall Capacity Design

This section includes the design calculations for the MPP shear walls in the 10-story test specimen. The walls were checked for shear, combined edgewise bending and axial loading in net compression, and combined edgewise bending and axial loading in net tension. See Section 6.6.3 for a conceptual discussion of these checks. The current APA product report from Freres Lumber was reference for material properties [APA, 2021] of the MPP walls. For this check the design equations and design methodology is outlined first, followed by spreadsheets summarizing the final values and final demand to capacity ratios (DCRs).

To calculate the demands used for these checks, suite mean and suite maximum results were taken from NLRHA results. Peak wall moment, wall shear, PT bar force values were used for these calculations. The results from the NLRHA used for the wall designs are summarized in Table 6.23, 6.25, and 6.29 for the shear, moment, and PT bar values, respectively.

A.3.1 MPP Shear Capacity Check

The shear stress capacity of the MPP wall was checked at the location of the UFPs were the length of the MPP wall is smallest. Capacity checks were completed using suite mean and suite maximum wall shear values from the nonlinear numerical model.

Demand:

The demand shear stress for the MPP wall was calculated in accordance with Equation A.35 where A_v is the shear area, defined by Equation A.36 and V_u is the factored shear demand force, defined as shown in Equation A.37. For the shear stress capacity, the blank area is to be used per something. The 1.5 factor in Equation A.37 accounts for the maximums shear stress at the center of the wall [Zimmerman and McDonnell, 2018].

$$\boxed{f_v = \frac{1.5V_u}{A_v}} \tag{A.35}$$

$$A_v = Lb_w \tag{A.36}$$

$$V_u = \gamma V \tag{A.37}$$

Capacity:

The shear stress capacity was calculated in accordance with Equation A.38.

$$\boxed{F'_{ve} = \phi K_F F_{ve}} \tag{A.38}$$

DCR:

The demand to capacity ratio for in-plane shear stress of the MPP wall was calculated according to Equation A.5.

$$\boxed{\frac{f_v}{F'_{ve}} \leq 1.0} \tag{A.39}$$

A.3.2 MPP Combined Edgewise Bending & Axial Loading - Net Compression

At all points along the height of the wall, except at the base rocking interface, the stress from combined edgewise bending and axial loading that produced net compression at any point in the cross section of the MPP was checked. This check was completed for two different wall cross sectional areas and the case with the smallest DCR was taken as the controlling condition. The considered cross sectional areas were the areas at the location where the UFPs were present and the location where the UFPs were not present. For MPP, the smaller cross sectional area (i.e. the locations where the UFPs are present) do not necessarily control as the bending design value (F_b) is dependent on the depth of the wood when loaded edgewise (i.e. the length of the wall for the given cross sectional area), in accordance with APA Product Report PR-L325, Table 2, footnote d. Capacity checks were completed using

suite mean and suite maximum wall moments and PT forces from the nonlinear numerical model. The following checks for MPP combined edgewise bending and axial loading in net compression are based on Section 3.9.2 of the NDS [AWC, 2018] with some modifications.

Demand:

The demand axial compression stress value was calculated in accordance with Equation A.40 where the area, A, is calculated using Equation A.41 or Equation A.42 for the section check without the UFPs and the section check with the UFPs, respectively. The factored ultimate load, P_u, is calculated in accordance with Equation A.43. The demand bending stress value was calculated in accordance with Equation A.44 where the section modulus, S, was calculated using Equation A.45 or A.46 for the section check without the UFPs and the section check with the UFPs, respectively. The factored ultimate wall moment, M_u, was calculated in accordance with Equation A.47.

The suite mean and suite maximum axial force values were calculated using the maximum total wall PT force for each ground motion from the numerical model. The suite mean and suite maximum wall moment values were calculated using the maximum wall moments along the whole height of the wall for each ground motion from the numerical model. Note, this may be slightly conservative since these two instances may not occur at exactly the same time, however, they are likely to occur around the same time.

Compression:

$$\boxed{f_c = \frac{P_u}{A}} \tag{A.40}$$

$$A = L_{tot} b_w \tag{A.41}$$

$$A = L_{red} b_w \tag{A.42}$$

$$P_u = \gamma P \tag{A.43}$$

Bending:

$$\boxed{f_b = \frac{M_u}{S_{eff}}} \tag{A.44}$$

$$S = \frac{b_w L_{tot}^2}{6} \tag{A.45}$$

$$S = \frac{b_w L_{eff}^2}{6} \tag{A.46}$$

$$M_u = \gamma M \tag{A.47}$$

Capacity:

The axial stress capacity of the MPP wall in compression was calculated in accordance with Equations A.49 and A.50. Required variables are defined using Equations A.51 through A.56. Bending stress capacity of the MPP wall was calculated in accordance with Equation A.57, where Equations A.58 through A.61 define all needed variables. Again, this calculation procedure is based on Section 3.9.1 of the NDS with modifications

As mentioned previously, in accordance with APA Product Report PR-L325, the bending stress design value, F_b, is dependent on the depth of the wood when loaded edgewise. This, this check was performed at two locations using the corresponding two different design values. The first location is where the UFPs are present and the second location is where the UFPs are not present. Per APA Product Report PR-L325, Table 2, footnote d, the bending design value, F_b, should be adjusted by the factor show in Equation A.48, where L_{wall} is the length of the wall at that section.

$$\left({}^{12}/_{L_{wall}}\right)^{1/6} \tag{A.48}$$

Compression:

$$\boxed{F'_c = \phi \times F_c \times C_p \times K_F} \tag{A.49}$$

$$\boxed{F_{cE} = \frac{0.822 E'_{min}}{\left(l_u/b_w\right)^2}} \tag{A.50}$$

$$C_p = \frac{1 + F_{cE}/F_c^*}{2c} - \sqrt{\left[\frac{1 + \left(F_{cE}/F_c^*\right)}{2c}\right]^2 - \frac{F_{cE}/F_c^*}{c}} \tag{A.51}$$

$$c = 0.9 \tag{A.52}$$

$$F_c^* = (F_c \times K_F \times \phi) A_{eff} \tag{A.53}$$

$$E'_{min} = E_{min} \times K_F \times \phi \tag{A.54}$$

$$E_{min} = E\left[1 - 1.645 COV_E\right]^{(1.03)/1.66} \tag{A.55}$$

$$COV_E = 0.1 \tag{A.56}$$

Bending:

$$\boxed{F'_b = \phi \times F_b \times C_L \times K_F} \tag{A.57}$$

$$C_L = \frac{1 + F_{bE}/F_b^*}{1.9} - \sqrt{\left[\frac{1 + F_{bE}/F_b^*}{1.9}\right]^2 - \frac{F_{bE}/F_b^*}{0.95}} \tag{A.58}$$

$$F_b^* = \phi \times F_b \times K_F \tag{A.59}$$

$$F_{bE} = \frac{1.2 E'_{min}}{R_B^2} \tag{A.60}$$

$$R_B = \sqrt{\frac{l_e L_w}{b_w^2}} \tag{A.61}$$

DCR:

The demand to capacity ratio for combined edgewise bending and axial loading in net compression of the MPP wall was calculated according to Equation A.62 which is based on Section NSD 3.9.2 [AWC, 2018] with modifications for MPP.

$$\boxed{\left[\frac{f_c}{F'_c}\right]^2 + \frac{f_b}{F'_b\left[1-\left(\frac{f_c}{F_{cE}}\right)\right]} \leq 1.0} \tag{A.62}$$

(A.63)

A.3.3 MPP Combined Edgewise Bending & Axial Loading - Net Tension

At all points along the height of the wall, except at the base rocking interface, the stress from combined edgewise bending and axial loading that produced net tension at any point in the cross section of the MPP was checked. This check was completed for two different wall cross sectional areas and the case with the smallest DCR was taken as the controlling condition. The considered cross sectional areas were the areas at the location where the UFPs were present and the location where the UFPs were not present. For MPP, the smaller cross sectional area (i.e. the locations where the UFPs are present) do not necessarily control as the bending design value (F_b) and the tension design value (F_t) are both dependent on cross sectional properties. The bending design value is dependent on the depth of the wood when loaded edgewise (i.e. the length of the wall for the given cross sectional area), in accordance with APA Product Report PR-L325, Table 2, footnote d. The tension design value is dependent on the length of the wood in tension (i.e. the height of the wall with the given cross sectional area), in accordance with APA Product Report PR-L325, Table 2, footnote f. Capacity checks were completed using suite mean and suite maximum wall moments and PT forces from the nonlinear numerical model. Tension forces occurred from bending but were reduced by PT compression forces, resulting in net tension forces. The following checks for MPP combined edgewise bending and axial loading in net tension are based on Section 3.9.1 of the NDS [AWC, 2018] with area modifications for MPP.

Demand:

The demand axial compression stress value was calculated in accordance with Equation A.64 where the effective compression area, A is calculated using Equation A.65 or Equation

A.66 for the section check without the UFPs and the section check with the UFPs, respectively. The factored ultimate load, P_u is calculated in accordance with Equation A.67. The demand bending stress value was calculated in accordance with Equation A.68 where the effective section modulus, S was calculated using Equation A.69 or Equation A.70 for the section check without the UFPs and the section check with the UFPs, respectively. The factored ultimate wall moment was calculated in accordance with Equation A.71.

For both suite mean and suite maximum, initial PT forces were used for axial force values. The suite mean and suite maximum wall moment values were calculated using the maximum wall moments along the whole height of the wall for each ground motion from the numerical model. Note, this load combination is conservative because the PT bars will likely be stressed beyond their initial PT forces when the wall rocks and reaches maximum bending moment. This would increase the compression force from the PT bars, thus decreasing the net tensile force in the wood. While completing the check as shown results in a very conservative check, this check was not critical for the design so it was done to ease calculations. However, because it is highly conservative, the axial demand factor, γ, for suite mean was taken as 1.0 instead of 1.3 since the minimum possible value is already being used.

Compression:

$$\boxed{f_c = \frac{P_u}{A}} \tag{A.64}$$

$$A = L_{tot} b_w \tag{A.65}$$

$$A = L_{red} b_w \tag{A.66}$$

$$P_u = \gamma P \tag{A.67}$$

Bending:

$$\boxed{f_b = \frac{M_u}{S}} \tag{A.68}$$

$$S = \frac{b_w L_{tot}^2}{6} \tag{A.69}$$

$$S = \frac{b_w L_{eff}^2}{6} \tag{A.70}$$

$$M_u = \gamma M \tag{A.71}$$

Capacity:

The axial stress capacity of the MPP wall in tension was calculated in accordance with Equation A.73.

As mentioned previously, in accordance with APA Product Report PR-L325, the tensile stress design value, F_t, is dependent on the length of the wood in tension. This, this check was performed at two locations using the corresponding two different design values. The first location is where the UFPs are present and the second location is where the UFPs are not present. Per APA Product Report PR-L325, Table 2, footnote f, the bending tension value, F_t, should be adjusted by the factor show in Equation A.72, where H_{wall} is the height of the wall at that section.

$$^4/_{H_{wall}}{}^{1/7} \tag{A.72}$$

Tension:

$$F_t' = \phi \times K_F \times F_t \tag{A.73}$$

DCR:

The demand to capacity ratio for combined edgewise bending and axial loading in net tension of the MPP wall was calculated in according to Equation A.74 which is based on Equation 3.9-1 in the NDS [AWC, 2018]. Note, in Equation A.74, f_c can be taken as a negative value since it is in compression and f_b is in tension.

$$\boxed{\frac{f_b + f_c}{F'_t} \leq 1.0} \tag{A.74}$$

A.3.4 MPP Wall Capacity Check Calculations

The following section summarizes all the values and calculations used to check the capacity of the MPP walls panels at all locations other than the splices and the wall bases.

MPP Shear Wall Timber Capacity Design

MPP Species:

Assumed grade F16
9 inch thick MPP (Layup ID F16-9)

MPP Material Properties:

MOE (Joist):	E =	1.60E+06	psi	PR-L325, Table 2
MOE (Plank):	E =	1.40E+06	psi	PR-L325, Table 2
Eff. bending stiffness (per ft):	$EI_{eff,0}$ =	1.39E+09	lb in^2/ft	PR-L325, Table 1, major dir.
Eff. shear stiffness (per ft):	$GA_{eff,0}$ =	3.42E+06	lb/ft	PR-L325, Table 1, major dir.
Comp. design value (parallel):	F_c =	2400	psi	PR-L325, Table 2
Bending design value (raw):	F_b raw =	1900	psi	PR-L325, Table 2
Tension design value (raw):	F_t raw =	1300	psi	PR-L325, Table 2
Edgewise shear stress (raw):	$F_{v,e,90}$ (raw) =	255	psi	PR-L325, Table 2
Edgewise shear stress:	$F_{v,e,90}$ =	102	psi	PR-L325, Table 2 Footnote h

Geometric Properties:

MPP wall thickness:	b_w =	9.1875	in	
MPP wall length total:	L_{tot} =	105.125	in	
MPP wall length reduced:	L_{red} =	90.625	in	Wall length at the UFP cutouts
Unbraced panel length:	l_u =	132	in	Story height
Effective panel length:	l_e =	243	in	Equal end moments, NDS Table 3.3.3
Tension height - Full length:	H_{full} =	7	ft	Height for F_t adj. factor calc. - full length
Tension height - UFP cutout:	H_{ufp} =	4	ft	Height for F_t adj. factor calc. - ufp cutout

MPP in Shear:

Shear Calculations:

Shear area (total area):	A_v =	833	in^2	
Format conversion Factor:	K_F =	2.88		NDS Section 8.3 Table 8.3.1
Resistance Factor:	φ =	0.75		NDS Section 8.3 Table 8.3.1
Adj. shear stress (w/o φ):	**F_{ve}' =**	**294**	**psi**	

MPP Shear Capacity Check:

		Suite Mean	Suite Max	
Shear Demands	γ =	1.3	1	
	V_u =	163	166	kip
	f_v =	294	298	psi
Shear Capacity	φ =	0.75	1	
	F_{ve}' =	220	294	psi
DCR		1.34	1.02	

MPP Combined axial-flexure in compression:

Calculated Geometric Properties:		UFP Cutout	Full length		
Area:	A=	832.6	965.8	in^2	Area of Section
Section Modulus:	S =	12576	16922	in^3	Section modulus of section
Compression Capacity Calculations:					
Loading condition Factor:	K_s =	11.5	11.5		NDS Tbl. 10.4.1.1 uniform dist. pinned
Coefficient of variation in MOE:	COV_E =	0.1	0.1		NDS Section F.2, Table F1
Minimum MOE (Plank):	E_{min} =	7.26E+05	7.26E+05	psi	NDS Equation D-4
Format converstion factor for E_{min}:	K_F =	1.76	1.76		NDS Section 10.3 Table 10.3.1
Resistance Factor E_{min}:	φ =	0.85	0.85		NDS Section 10.3 Table 10.3.1
Adjusted Minimum MOE:	E'_{min} =	1.09E+06	1.09E+06	psi	NDS Section 8.3
F_{cE}:	**F_{cE} =**	**4324**	**4324**	**psi**	NDS Equation 3.7-1
Format converstion factor for F_c:	K_F =	2.4	2.4		NDS Section 8.3 Table 8.3.1
Resistance Factor F_c:	φ =	0.9	0.9		NDS Section 8.3 Table 8.3.1
Adj. comp. design value (w/o C_p):	F_c* =	5184	5184	psi	NDS Section 8.3
For mass timber panels:	c =	0.9	0.9		NDS Equation 3.7-1
Column stability factor:	C_p =	0.69	0.69		NDS Equation 3.7-1
Adj. comp. design value (w/o φ):	**F_c' =**	**3946**	**3946**	**psi**	NDS Section 8.3
Bending Capacity Calculations:					
F_b adjustment factor:	$F_{b\ factor}$ =	0.71	0.70		PR-L325, Table 2, Footnote (d)
Bending design value (adjusted):	F_b =	1356	1323	psi	PR-L325, Table 2, Footnote (d)
Slenderness ratio for bending:	R_B =	16.15	17.39		NDS Equation 3.3-5
F_{bE}:	**F_{bE} =**	**4997**	**4307**	**psi**	NDS Equation 3.3-6
Format converstion factor for F_b:	K_F =	2.54	2.54		NDS Section 8.3 Table 8.3.1
Resistance Factor F_b:	φ =	0.85	0.85		NDS Section 8.3 Table 8.3.1
Adj. bending design value (w/o C_L):	F_b* =	2929	2857	psi	NDS Section 8.3
Bending stability factor:	C_L =	0.94	0.93		NDS Equation 3.3-6
Adj. Edgewise bending design value (w/o φ):	**F_b' =**	**3245**	**3113**	**psi**	NDS Section 8.3

MPP Combined axial-flexure in compression check - UFP Cutout:

		Suite Mean	Suite Max	
Bending Demands	γ =	1.3	1	
	M_u =	42265	43776	kip-in
	f_b =	3361	3481	psi
Axial Demands	γ =	1	1	
	P_u =	250	273	kip
	f_c =	301	327	psi
Bending Capacity	φ =	0.85	1	
	F_b' =	2759	3245	psi
Axial Capacity	φ =	0.9	1	
	F_c' =	3551	3946	psi
	F_{cE} =	4324	4324	psi
DCR 1		1.32	1.17	

MPP Combined axial-flexure in compression check - Full Length:

		Suite Mean	Suite Max	
Bending Demands	γ =	1.3	1	
	M_u =	42265	43776	kip-in
	f_b =	2498	2587	psi
Axial Demands	γ =	1	1	
	P_u =	250	273	kip
	f_c =	259	282	psi
Bending Capacity	φ =	0.85	1	
	F_b' =	2646	3113	psi
Axial Capacity	φ =	0.9	1	
	F_c' =	3551	3946	psi
	F_{cE} =	4324	4324	psi
DCR 1		1.01	0.89	

MPP Combined axial-flexure in tension :

Shear Capacity Calculations:		UFP Cutout	Full length		
F_t adjustment factor:	F_t factor =	1.00	0.92		PR-L325, Table 2, Footnote (f)
Tension design value (adj.):	F_t =	1300	1200	psi	PR-L325, Table 2, Footnote (f)
Format conversion factor F_t :	K_F =	2.7	2.7		NDS Section 8.3 Table 8.3.1
Resistance Factor:	φ =	0.8	0.8		NDS Section 8.3 Table 8.3.1
Adj. tension design value (w/o φ):	**F_t' =**	**3510**	**3240**	**psi**	NDS Section 10.3

MPP Combined axial-flexure in tension check - UFP Cutout:

		Suite Mean	Suite Max	
Bending Demands	γ =	1.3	1	
	M_u =	42265	43776	kip-in
	f_b =	3361	3481	psi
Axial Demands	γ =	1	1	
	P_u =	-200	-200	kip
	f_c =	-240	-240	psi
Tensile Capacity	φ =	0.8	1	
	F_t' =	2808	3510	psi
DCR		1.11	0.92	

MPP Combined axial-flexure in tension check - Full Length:

		Suite Mean	Suite Max	
Bending Demands	γ =	1.3	1	
	M_u =	42265	43776	kip-in
	f_b =	2498	2587	psi
Axial Demands	γ =	1	1	
	P_u =	-200	-200	kip
	f_c =	-207	-207	psi
Tensile Capacity	φ =	0.8	1	
	F_t' =	2592	3240	psi
DCR		0.88	0.73	

A.4 Rocking Wall Splice Design

This section includes the design calculations for the CLT and MPP shear wall splices for the 10-story test specimen. The wall splices were checked for axial-flexural interaction and for shear capacity. See Section 6.6.3 for a conceptional discussion of this splice connection design, construction process, and figures. For the CLT walls, the 2018 NDS [AWC, 2018] was referenced for material properties. For the MPP walls, the current APA product report from Freres Lumber was reference for material properties [APA, 2021]. For this check the design equations and design methodology is outlined first, followed by spreadsheets summarizing the final values and final demand to capacity ratios (DCRs).

To calculate the demands used for these checks, suite mean and suite maximum results were taken from NLRHA results. Peak wall moment and wall shear values at stories 4 and 7 were used for these calculations. The same CLT splice design was used at all CLT splice locations and the same MPP splice design was used at all MPP splice locations, so the overall maximum value at all four locations was used for each wall panel splice design. The results from the NLRHA used for the splice design are summarized in Table 6.23 and 6.25 for the shear and moment values, respectively.

A.4.1 Axial-Flexural Interaction Design

To complete the axial-flexural interaction check, the minimum tension rod spacing was first calculated such that the tensile capacity of the mass timber section was greater than or equal to the tensile capacity of the tension rods. The minimum spacing (s_{min}) for a tension rod group was calculated as the ratio of the yield force of the tension rods to the tensile capacity of the timber section, as shown in Equation A.76. A tension rod group was defined as a group of three tension rods as shown in Figure A.1. For the CLT walls, it was assumed that the tensile stress in the wood acts only on the total area of the vertical laminations. For the MPP walls, the entire cross section area was used (Equation A.75). With this check, the spacing of the groups of tension rods, s, was designed to be greater than or equal to s_{min}.

$$b_{w,eff} = \begin{cases} 5/9 b_w & \text{for CLT Wall} \\ b_w & \text{for MPP Wall} \end{cases} \tag{A.75}$$

$$\boxed{s_{min} = \frac{R_y F_y A_{net} n_{rods}}{\phi K_F F_t b_{w,eff}}} \tag{A.76}$$

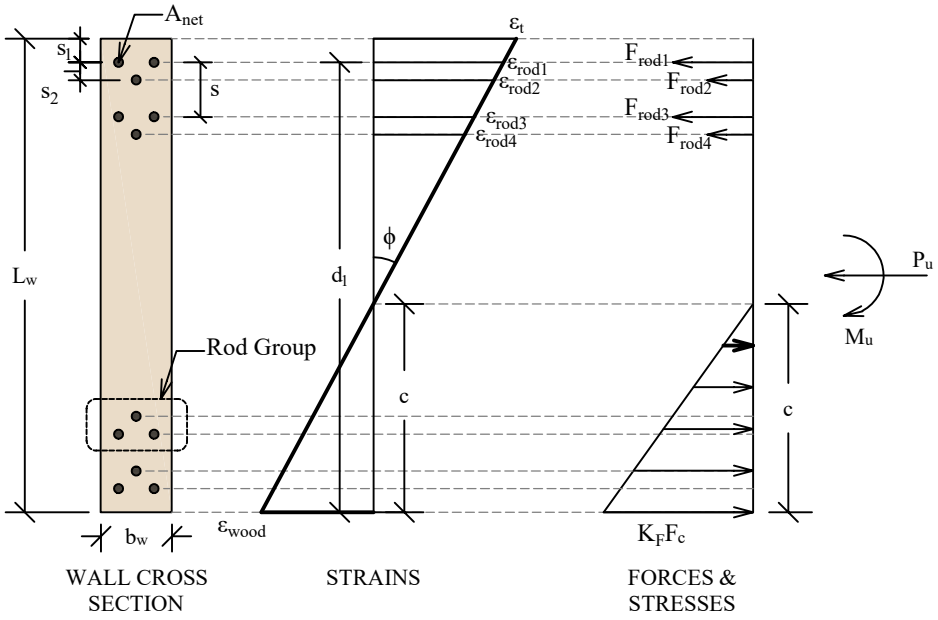

Figure A.1: Axial-flexural interaction of the shear wall splices

Demand:

The demand moment for the wall splice was taken from the nonlinear numerical model results. The moment in each wall at the locations of both of the splices were considered and a single design was used for all the splices in each type of wall panel. The overall demand was calculated in accordance with Equation A.77.

$$\boxed{M_u = \gamma M} \tag{A.77}$$

Capacity:

The capacity of the wall splice in combined flexural and axial compression was calculated assuming plane sections remain plane over the cross section. The stress, strain, and force diagrams shown in Figure A.1 were then constructed. In the cross section, the ultimate applied axial load (P_U) was set equal to the initial post-tensioning force for the entire wall (Equation A.78) and the outer most rod in tension was limited to twice the yield strain of the bars (Equation A.79).

$$P_u = initialPTforce \tag{A.78}$$

$$\epsilon_{rod1} = 2\epsilon_y \tag{A.79}$$

Then, a compression length, c, was estimated and the maximum tensile strain, ϵ_t, and maximum compressive strain, ϵ_{wood}, in the wood was calculated (Equation A.80 through A.82).

$$\phi = \frac{\epsilon_{rod1}}{L - s_1 - c} \tag{A.80}$$

$$\epsilon_t = \phi(L_w - c) \tag{A.81}$$

$$\epsilon_{wood} = \phi(0 - c) \tag{A.82}$$

The peak compressive strain, ϵ_{wood}, was then compared to the calculated yield strain, ϵ_y (Equation A.83). If ϵ_{wood} exceeded ϵ_y, then an elastic perfectly plastic compression distribution was assumed for the compression zone, otherwise a linear elastic relationship was used. The wood in the CLT and MPP splices of the 10-story specimen both remained elastic in compression, so that is what is depicted within these calculations. With the linear elastic force distribution, the compression force in the wood was then calculated in accordance with Equation A.84. Note, for CLT, the stress in the wood acts only on the total area of the vertical laminations.

$$\epsilon_y = \frac{K_F F_c}{E_{wood}} \tag{A.83}$$

$$F_{wood} = 0.5 E_w \epsilon_{wood} c b_{w,eff} \tag{A.84}$$

The strains, stress, and forces in the bars in the tension region were also calculated based on the estimated compression length, c (Equations A.85 through A.88). The stress in each bars was calculated using a simple elastic perfectly plastic constitutive model (Equation A.86). For the 10-story building splices the bars had all reached or exceeded their yield strain during this check. As mentioned in Section 6.6.3, the capacity of the rods in compression were assumed to be zero due to the discontinuity in the rods from the addition of the splice plate.

$$\epsilon_{rodi} = \phi(d_i - c) \tag{A.85}$$

$$\sigma_{rodi} = \begin{cases} \epsilon_{rodi} E & \text{if } \epsilon_{rodi} < \epsilon_y \\ \epsilon_y & \text{if } \epsilon_{rodi} \geq \epsilon_y \end{cases} \tag{A.86}$$

$$F_{rodi} = \epsilon_{rod1} A_{net} n_{rods} \tag{A.87}$$

$$F_{rods} = \sum F_{rodi} \tag{A.88}$$

The compression length, c, was iterated on until vertical equilibrium (Equation A.89) was satisfied. The total axial-flexural capacity of the wall was calculated by summing moments about the center of the wall (Equations A.90 through A.92).

$$P_n = P_u + F_{wood} + F_{rod} \tag{A.89}$$

$$M_{wood} = F_{wood}(-L_w/2 + c_1/3) \tag{A.90}$$

$$M_{rods} = \sum F_{rodi}(d_i - L_w/2) \tag{A.91}$$

$$M_n = M_{wood} + M_{rods} \tag{A.92}$$

DCR:

The demand to capacity ratio of the splice under combined axial-flexural interaction was calculated in accordance with Equation A.93.

$$\boxed{DCR = \frac{M_u}{\phi M_n}} \tag{A.93}$$

This assumption is likely conservative because the largest moment demand at the splice connection likely occurs when the wall is not perfectly vertical, resulting in some stretch in the PT bars and thus a larger axial compression force, which increases the connection's flexural capacity.

A.4.2 Shear Design

Material test data was used to check the shear capacity of the splices.

Demand:

The demand shear for the wall splice was taken from the nonlinear numerical model results. The shear in each wall at the locations of both the splices were considered. The overall demand was calculated in accordance with Equation A.94.

$$\boxed{V_u = \gamma V} \tag{A.94}$$

Capacity:

The shear capacity of the wall splice was calculated using test data. The lateral capacity of each rod, taken from test data, was multiplied by the total number of rods, as shown in Equation A.95.

$$\boxed{\phi V_n = \phi Z_{\perp,ref} n_{rods}} \tag{A.95}$$

DCR:

The demand to capacity ratio of the splice in shear was calculated in accordance with Equation A.96.

$$\boxed{DCR = \frac{V_u}{\phi V_n}} \tag{A.96}$$

A.4.3 Axial-Flexural Interaction Design Calculations

The following section summarizes all the values and calculations used to check the capacity of the walls splices. The calculations for the CLT wall splice are provided first, followed by the MPP wall splice.

CLT Shear Wall Splice

CLT Wall Properties:

Longitudinal Layers: MSR Rated lumber 2400-2.0E

Wall width:	b_w =	12.375	in	
Effective wall width:	$b_{w,eff}$ =	6.875	in	
Wall length:	L_w =	117.125	in	
Modulus of Elasticity:	E_{wood} =	2000	ksi	NDS sup. Table 4C for MSR 2400f-2.0E
Format conversion factor F_c':	K_F =	2.4		NDS Table 10.3.1
Compression design value:	F_c =	1975	psi	NDS sup. Table 4C for MSR 2400f-2.0E
Adj. compression design value:	$K_F F_c$ =	4740	psi	
Format conversion factor F_t':	K_F =	2.7		NDS Table 10.3.1
Tension design value:	F_t =	1925	psi	NDS sup. Table 4C for MSR 2400f-2.0E
Adj. tension design value:	$K_F F_t$ =	5197.5	psi	
CLT yield strain:	ε_y =	0.0024	in/in	

Tension Epoxy Rod Properties:

F1554 Gr. 36 Fully Threaded

Yield Stress Ratio:	R_y =	1.1	
Yield stress:	F_y =	36	ksi
Tensile stress:	F_u =	58	ksi
Modulus of Elasticity:	E =	29000	ksi
Ultimate strain:	ε_u =	0.05	in/in
Yield strain:	ε_y =	0.00124	in/in
Rod net area:	A_{net} =	0.606	in^2
Edge distance:	s_1 =	3.75	in
Offset spacing:	s_2 =	1	in
Spacing:	s =	5	in

Axial-Flexural Interaction Design:

Calcualte Min Tension Rod Spacing:

Rods per group:	n_{rods} =	3	
Resistance factor for F_t =	φ =	0.8	
minimum tension rod spacing:	s_{min} =	2.52	in

Calculate Flexural Capacity:

Applied axial load:	P_u =	200	kip
Tensile strain in last rod:	$\varepsilon_{rod,1}$ =	0.00248	in/in
Compression length:	c =	47.7	in
Curvature:	φ =	3.78E-05	1/in
Peak wood tensile strain:	ε_t =	0.00262	in/in
Peak wood compression strain:	ε_{wood} =	-0.00181	in/in
Linear compression length:	c_1 =	47.7	in
Yielded compression length:	c_2 =	0.0	in
Eq. wood compression force 1:	$F_{wood,compr1}$ =	-593	kip
Eq. wood compression force 2:	$F_{wood,compr2}$ =	0	kip
Strain in rods:	$\varepsilon_{rod,i}$ =	See Table	
Stress in rods:	$\sigma_{rod,i}$ =	See Table	
Force in rods:	$F_{rod,i}$ =	See Table	
Total force in rods:	F_{rod} =	392.7	kip
Resultant axial force:	P_n =	0	kip
Wood moment capacity 1:	$M_{wood,compr1}$ =	25278	kip-in
Wood moment capacity 2:	$M_{wood,compr2}$ =	0	kip-in
Rod moment capacity:	M_{rods} =	16485	kip-in
Total moment capacity:	M_n =	41762	kip-in

Tension Rod strains, stresses, and forces table

	i	d_i	n_{rods}	$\varepsilon_{rod,i}$	$\sigma_{rod,i}$	$F_{rod,i}$	$M_{rod,i}$
	-	in	-	in/in	ksi	k	k in
Rods in Compression	1	3.75	2	0	0	0	0
	2	4.75	1	0	0	0	0
	3	8.75	2	0	0	0	0
	4	9.75	1	0	0	0	0
	5	13.75	2	0	0	0	0
	6	14.75	1	0	0	0	0
	7	18.75	2	0	0	0	0
	8	19.75	1	0	0	0	0
	9	23.75	2	0	0	0	0
	10	24.75	1	0	0	0	0
	11	28.75	2	0	0	0	0
	12	29.75	1	0	0	0	0
Rods in Tension	13	87.375	1	0.0015	36.0	21.8	629
	14	88.375	2	0.0015	36.0	43.6	1301
	15	92.375	1	0.0017	36.0	21.8	738
	16	93.375	2	0.0017	36.0	43.6	1519
	17	97.375	1	0.0019	36.0	21.8	847
	18	98.375	2	0.0019	36.0	43.6	1737
	19	102.375	1	0.0021	36.0	21.8	956
	20	103.375	2	0.0021	36.0	43.6	1955
	21	107.375	1	0.0023	36.0	21.8	1065
	22	108.375	2	0.0023	36.0	43.6	2173
	23	112.375	1	0.0024	36.0	21.8	1174
	24	113.375	2	0.0025	36.0	43.6	2392
					Total	392.7	16485

Axial-Flexural Interaction CLT Wall Splice Check:

		Suite Mean	Suite Max	
Flexure demands	γ =	1.3	1	
	M_u =	40174	42594	kip-in
Flexure capacity	φ =	0.9	1	
	φM_n =	37586	41762	kip-in
DCR	$M_u/\varphi M_n$ =	1.07	1.02	

Shear Design:

Shear Epoxy Rod Properties:

F1554 Gr. 36 Partially Threaded

Yield stress:	F_y =	36	ksi
Tensile stress:	F_u =	58	ksi
Modulus of Elasticity:	E =	29000	ksi
Net area:	A_{net} =	0.606	in^2
Rod diameter:	D =	1	in
Total number of shear rods:	n_{rods} =	16	
Lateral capacity per rod:	$Z_{\perp,ref}$ =	5500	lb

Shear Capacity CLT Wall Splice Check:

		Suite Mean	Suite Max	
Shear Demands	γ =	1.3	1	
	V_u =	80	84	kip
Shear Capacity	φ =	1	1	
	φV_n =	88	88	kip
DCR	$V_u/\varphi V_n$ =	0.91	0.95	

MPP Shear Wall Splice

MPP Wall Properties:

Wall width:	b_w =	9.1875	in	
Effective wall width:	$b_{w,eff}$ =	9.1875	in	
Wall length:	L_w =	105.125	in	
Modulus of Elasticity:	E_{wood} =	1600	ksi	PR-L325, Table 2
Format conversion factor F_c':	K_F =	2.4		NDS Table 8.3.1
Compression design value:	F_c =	2400	psi	PR-L325, Table 2
Adj. compression design value:	$K_F F_c$ =	5760	psi	
Format conversion factor F_t':	K_F =	2.7		NDS Table 8.3.1
Tension design value:	F_t =	1300	psi	PR-L325, Table 2
Adj. tension design value:	$K_F F_t$ =	3510	psi	
CLT yield strain:	ε_y =	0.0036	in/in	

Tension Epoxy Rod Properties:

F1554 Gr. 36 Fully Threaded

Yield Stress Ratio:	R_y =	1.1	
Yield stress:	F_y =	36	ksi
Tensile stress:	F_u =	58	ksi
Modulus of Elasticity:	E =	29000	ksi
Ultimate strain:	ε_u =	0.05	in/in
Yield strain:	ε_y =	0.00124	in/in
Rod net area:	A_{net} =	0.606	in^2
Edge distance:	s_1 =	3.25	in
Offset spacing:	s_2 =	1	in
Spacing:	s =	4	in

Axial-Flexural Interaction Design:

Calcualte Min Tension Rod Spacing:

Rods per group:	n_{rods} =	3	
Resistance factor for F_t =	φ =	0.8	
minimum tension rod spacing:	s_{min} =	2.79	in

Calculate Flexural Capacity:

Applied axial load:	P_u =	200	kip
Tensile strain in last rod:	$\varepsilon_{rod,1}$ =	0.00248	in/in
Compression length:	c =	45.2	in
Curvature:	φ =	4.38E-05	1/in
Peak wood tensile strain:	ε_t =	0.00263	in/in
Peak wood compression strain:	ε_{wood} =	-0.00198	in/in
Linear compression length:	c_1 =	45.2	in
Yielded compression length:	c_2 =	0	in
Eq. wood compression force 1:	$F_{wood,compr1}$ =	-658	kip
Eq. wood compression force 2:	$F_{wood,compr2}$ =	0	kip
Strain in rods:	$\varepsilon_{rod,i}$ =	See Table	
Stress in rods:	$\sigma_{rod,i}$ =	See Table	
Force in rods:	$F_{rod,i}$ =	See Table	
Total force in rods:	F_{rod} =	458.1	kip
Resultant axial force:	P_n =	0.0	kip
Wood moment capacity 1:	$M_{wood,compr1}$ =	24676	kip-in
Wood moment capacity 2:	$M_{wood,compr2}$ =	0	kip-in
Rod moment capacity:	M_{rods} =	16941	kip-in
Total moment capacity:	M_n =	41617	kip-in

Tension Rod strains, stresses, and forces table

	i	d_i	n_{rods}	$\varepsilon_{rod,i}$	$\sigma_{rod,i}$	$F_{rod,i}$	$M_{rod,i}$
	-	in	-	in/in	ksi	k	k in
Rods in Compression	1	3.25	2	0	0	0	0
	2	4.25	1	0	0	0	0
	3	7.25	2	0	0	0	0
	4	8.25	1	0	0	0	0
	5	11.25	2	0	0	0	0
	6	12.25	1	0	0	0	0
	7	15.25	2	0	0	0	0
	8	16.25	1	0	0	0	0
	9	19.25	2	0	0	0	0
	10	20.25	1	0	0	0	0
	11	23.25	2	0	0	0	0
	12	24.25	1	0	0	0	0
	13	27.25	2	0	0	0	0
	14	28.25	1	0	0	0	0
Rods in Tension	15	76.875	1	0.0014	36.0	21.8	530
	16	77.875	2	0.0014	36.0	43.6	1104
	17	80.875	1	0.0016	36.0	21.8	618
	18	81.875	2	0.0016	36.0	43.6	1279
	19	84.875	1	0.0017	36.0	21.8	705
	20	85.875	2	0.0018	36.0	43.6	1453
	21	88.875	1	0.0019	36.0	21.8	792
	22	89.875	2	0.0020	36.0	43.6	1628
	23	92.875	1	0.0021	36.0	21.8	879
	24	93.875	2	0.0021	36.0	43.6	1803
	25	96.875	1	0.0023	36.0	21.8	967
	26	97.875	2	0.0023	36.0	43.6	1977
	27	100.875	1	0.0024	36.0	21.8	1054
	28	101.875	2	0.0025	36.0	43.6	2152
					Total	458.1	16941

Axial-Flexural Interaction MPP Wall Splice Check:

		Suite Mean	Suite Max	
Flexure demands	γ =	1.3	1	
	M_u =	42265	43776	kip-in
Flexure capacity	φ =	0.9	1	
	φM_n =	37455	41617	kip-in
DCR	$M_u/\varphi M_n$ =	1.13	1.05	

Shear Design:

Shear Epoxy Rod Properties:

F1554 Gr. 36 Partially Threaded

Yield stress:	F_y =	36	ksi
Tensile stress:	F_u =	58	ksi
Modulus of Elasticity:	E =	29000	ksi
Net area:	A_{net} =	0.606	in^2
Rod diameter:	D =	1	in
Total number of shear rods:	n_{rods} =	24	
Lateral capacity per rod:	$Z_{\perp,ref}$ =	5500	lb

Shear Capacity MPP Wall Splice Check:

		Suite Mean	Suite Max	
Shear Demands	γ =	1.3	1	
	V_u =	78	91	kip
Shear Capacity	φ =	1	1	
	$φV_n$ =	132	132	kip
DCR	$V_u/φV_n$ =	0.59	0.69	

A.5 Sliding at Base Connection Design

This section includes the design calculations for the CLT and MPP wall to foundation shear transfer connections located at the base of the walls for the 10-story test specimen. See Section 6.6.3 for a conceptional discussion of this assembly and figures. In this section, each capacity check is presented, followed by a figure showing the resulting DCRs and the equations used. These calculations were completed in accordance with AISC [2016]. Refer to Figure A.2 for a schematic of the connection with dimension labels.

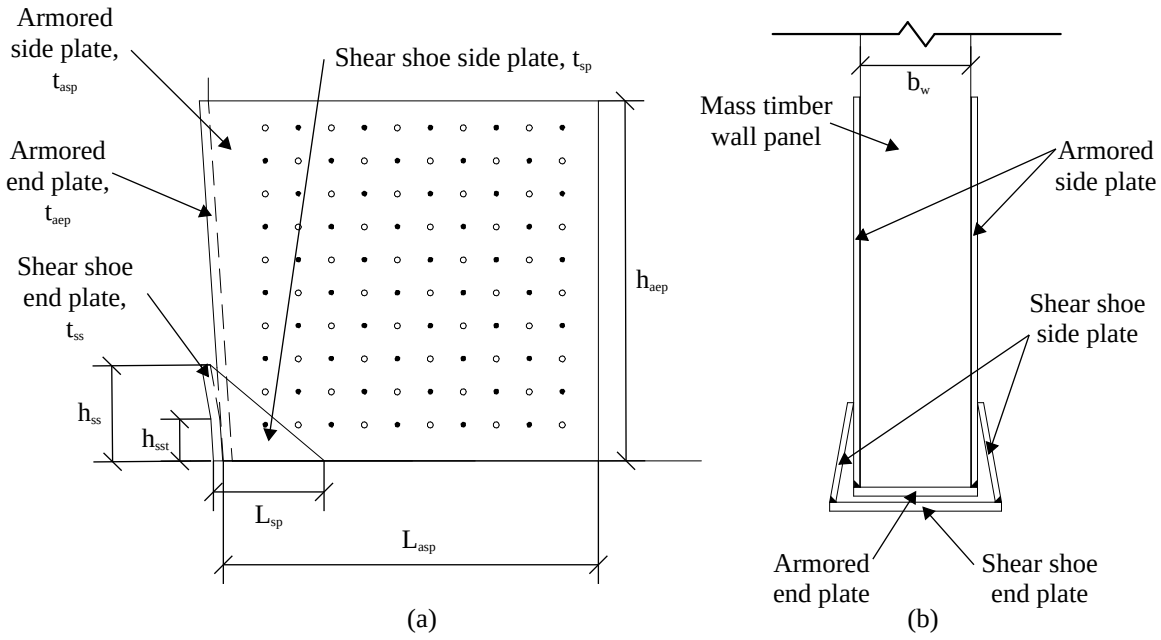

Figure A.2: Schematic of the wall base shear transfer connection

A.5.1 Demands

The demands for this calculation were based on peak base shear results from NLRHA at MCE_R (summarized in Table 6.23). The procedure for calculating the demand for this connection is shown below. The base shear values per wall are shown first, followed by the

shear demand per wall on the base connections. As mentioned in the main text, the demand on the connection was calculated by taking the base shear in the wall panels, minus the force from friction.

CLT Wall Calculations

Peak MCER base shear demands - per wall

from NLRHA

	Suite Mean	Suite Max	
V_b =	126	179	kip

Base shear connection demands - per wall

	Suite Mean	Suite Max	
V =	65.7	118.5	kip

MPP Wall Calculations

	Suite Mean	Suite Max	
V_b =	126	166	kip

	Suite Mean	Suite Max	
V =	65.7	105.6	kip

Demand:

$$V = V_b - \mu(n_{bars}F_i)$$

A.5.2 Input Parameters

The following page shows the input parameters used to perform all capacity checks for this assembly and can be referenced for the following sections.

Wall Base Shear Transfer Calculations

Wall Geometry and Properties:		**CLT**	**MPP**	
Bearing Format Conversion Factor:	K_F =	2.4	2.4	
Compression design value (trans.):	$F_{c,trans}$ or F_{cL} =	1400	750	psi
Adj. compression design value (trans.):	$F_{c,trans}$* =	3360	1800	psi
CLT lam thickness:	t_{lam} =	1.375	-	in
number of horizontal lams wall:	n_{horz} =	4	-	lams
Thickness of walls:	b_w =	12.375	9.1875	in
Coeffcient of friction:	μ =	0.3	0.3	
PT Bars:				
Number of bars:	n_{bars} =	4	4	bars
Initial PT force:	F_i =	50	50	kip
Armored end plate:				
Yiled stress:	F_y =	50	50	ksi
Height of armored end plate:	h_{aep} =	30	30	in
Thickness of armored end plate:	t_{aep} =	0.75	0.75	in
Shear shoe end plate:				
Yiled stress:	F_y =	50	50	ksi
Height of shear shoe (total):	h_{ss} =	8	8	in
Height of transfer point:	h_{sst} =	3.5	3.5	in
Thickness of shear shoe end plate:	t_{ss} =	0.75	0.75	in
Armored side plate:				
Yiled stress:	F_y =	50	50	ksi
Thinkness of armored side plate:	t_{asp} =	0.5	0.5	in
Length of armored size plate:	l_{asp} =	31.25	31.25	in
Number of screws (per side):	n_{screws} =	50	50	
x direction eccentricity:	e_x =	15.25	15.25	in
y direciton eccentricity:	e_y =	15	15	in
Shear shoe side plate:				
Yiled stress:	F_y =	50	50	ksi
thickness of shear shoe side plate:	t_{sp} =	0.5	0.5	in
Length of shear shoe side plate:	L_{sp} =	8.5	8.5	in
Shear shoe weld:				
Fillet weld length:	l_{weld} =	8.5	8.5	in
Fillet weld size:	D =	0.5	0.5	in
Electrode strength:	F_{EXX} =	70	70	ksi
Moment of inertia of weld group:	I =	51	51	in^3
eccentricity of weld group:	e =	2.66667	2.66667	in
Radial distance from CG:	c =	4.25	4.25	in
Simpson Strong-Tie SDS Screws:				
Mechanical connections formation conversion factor:	K_F =	3.32	3.32	
Diameter of Screws:	d_{screw} =	0.25	0.25	in
Shear strength of screws:	V_{screw} =	420	420	lb
Length of collector screws:	L_{screw} =	3.5	3.5	in

A.5.3 Timber Bearing on the armored end plate

The first phase of the load path is to transfer load from the wood into the armored end plate through bearing. For this check the bearing area was defined as the product of the wall thickness and the total height of the shear shoe. The height of the shear shoe was use as opposed to the height of the full armor plate because most of the load transfer will occur where the armor plate is in contact with the shear shoe. The calculations for this check are shown below.

CLT Wall Calculations

Check timber bearing on armored end plate

		Suite Mean	Suite Max	
Bearing Demands	γ =	1.3	1	
	P_u =	85	119	kips
Bearing Capacity	φ =	0.9	1	
	φP_n =	133	148	kips
DCR:	$P_u/\varphi P_n$ =	0.64	0.80	

Demand:

$$P_u = \gamma V$$

Capacity:

$$\Phi P_n = \Phi F^*_{c,trans} A_{||}$$

$$= \Phi K_F F_{c,trans} \left(\frac{1.375in}{lam}\right)(4lam)h_{ss}$$

DCR:

$$DCR = \frac{P_u}{\Phi P_n}$$

MPP Wall Calculations

		Suite Mean	Suite Max	
Bearing Demands	γ =	1.3	1	
	P_u =	85	106	kips
Bearing Capacity	φ =	0.9	1	
	φP_n =	119	132	kips
DCR:	$P_u/\varphi P_n$ =	0.72	0.80	

Demand:

$$P_u = \gamma V$$

Capacity:

$$\Phi P_n = \Phi F^*_{c\perp} A_{||} = \Phi K_F F_{c\perp} b_w h_{ss}$$

DCR:

$$DCR = \frac{P_u}{\Phi P_n}$$

A.5.4 Shear and Moment in armored end plate

Next, the capacity of the armored end plate was check in shear and bending, using the procedure shown below. For this check, a width (into and out of the page) of 1 inch was used. The armored end plate was modeled as a simply supported beam with the timber bearing acting as a uniformly distributed load, as shown by the image at the top of the figure. The ends of the armored end plate are assumed to be supported by the armored

side plates. As shown, for this check, the DCR value for the CLT wall armored end plate in bending is greater than 1.0. This was determined to be okay as the check uses the elastic section modulus as opposed to the plastic section modulus, so it is conservative.

CLT Wall Calculations **MPP Wall Calculations**

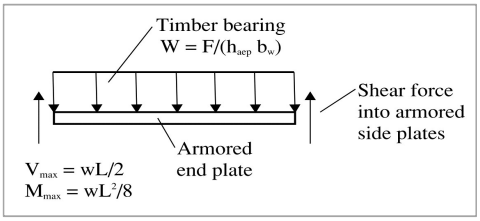

Check shear in armored end plate:

		Suite Mean	Suite Max				Suite Mean	Suite Max	
Shear	γ =	1.3	1		Shear	γ =	1.3	1	
Demands:	V_u =	1.42	1.98	kips	Demands:	V_u =	1.42	1.76	kips
Shear	φ =	0.9	1		Shear	φ =	0.9	1	
Capacity	φV_n =	20.3	22.5	kips	Capacity	φV_n =	20.3	22.5	kips
DCR:	$V_u/\varphi V_n$ =	0.07	0.09		DCR:	$V_u/\varphi V_n$ =	0.07	0.08	

Demand:

$$V_u = \gamma\left(\frac{\left(\frac{V}{h_{aep}b_w}\right)b_w}{2}\right)$$

Capacity:

$$\Phi V_n = \Phi 0.6 F_y A_g = \Phi 0.6 \mathrm{F_y}(1\mathrm{in})\mathrm{t_{aep}}$$
$$assume\ 1in\ width$$

DCR:

$$DCR = \frac{V_u}{\Phi V_n}$$

Check bending in armored end plate:

		Suite Mean	Suite Max				Suite Mean	Suite Max	
Flexure	γ =	1.3	1		Flexure	γ =	1.3	1	
Demands	M_u =	4.4	6.1	k-in	Demands	M_u =	3.3	4.0	k-in
Flexure	φ =	0.9	1		Flexure	φ =	0.9	1	
Capacity	φM_n =	4.2	4.7	k-in	Capacity	φM_n =	4.2	4.7	k-in
DCR:	$M_u/\varphi M_n$ =	1.04	1.30		DCR:	$M_u/\varphi M_n$ =	0.78	0.86	

Demand:

$$M_u = \gamma\left(\frac{\left(\frac{V}{h_{aep}b_w}\right)b_w^2}{8}\right)$$

Capacity:

$$\Phi M_n = \Phi F_y S_x = \Phi F_y \frac{(1in)t_{aep}^2}{6}$$

DCR:

$$DCR = \frac{M_u}{\Phi M_n}$$

A.5.5 Bearing of armored side plate on shoe end plate

Bearing of the armored side plates on the shoe end plates was then check using the procedure outlined below. The demand for this check is equal to half of the base shear force into the full connection because there are two armored side plates in the assembly.

CLT Wall Calculations

Cheak bearing of armored side plate on shoe end plate:

		Suite Mean	Suite Max	
Bearing Demands	γ =	1.3	1	
	P_u =	43	59	kip
Bearing Capacity	φ =	0.9	1	
	φP_n =	79	88	kip
DCR:	$P_u/\varphi P_n$ =	0.54	0.68	

MPP Wall Calculations

		Suite Mean	Suite Max	
Bearing Demands	γ =	1.3	1	
	P_u =	43	53	kip
Bearing Capacity	φ =	0.9	1	
	φP_n =	79	88	kip
DCR:	$P_u/\varphi P_n$ =	0.54	0.60	

Demand:

$$P_u = \gamma(V/2)$$

Capacity:

$$\Phi P_n = \Phi F_y A_g = \Phi F_y h_{sst} t_{asp}$$

DCR:

$$DCR = \frac{P_u}{\Phi P_n}$$

A.5.6 Armored side plate in shear

The capacity of the side plate in shear was checked using the procedure outlined below. Again, half the demand was used for this check as there are two armored side plates per assembly.

CLT Wall Calculations

Check armored side plate in shear:

		Suite Mean	Suite Max	
shear	γ =	1.3	1	
Demands:	V_u =	43	59	kip
Shear	φ =	0.9	1	
Capacity	φV_n =	422	469	kip
DCR:	$V_u/\varphi V_n$ =	0.10	0.13	

MPP Wall Calculations

		Suite Mean	Suite Max	
shear	γ =	1.3	1	
Demands:	V_u =	43	53	kip
Shear	φ =	0.9	1	
Capacity	φV_n =	422	469	kip
DCR:	$V_u/\varphi V_n$ =	0.10	0.11	

Demand:

$$V_u = \gamma\,(V/2)$$

Capacity:

$$\Phi V_n = \Phi 0.6 F_y A_g = \Phi 0.6 F_y$$

DCR:

$$DCR = \frac{V_u}{\Phi V_n}$$

A.5.7 Shear strength of armor side plate screws

The load transfers between the wood and the side plates through shear in the Simpson Strong-Tie SDS screws. The shear capacity of these screws were checked using the procedure shown below. For this check, the eccentricity of the screw group from the base shear transfer point is accounted for, as shown by the free body diagram at the top of the figure.

CLT Wall Calculations **MPP Wall Calculations**

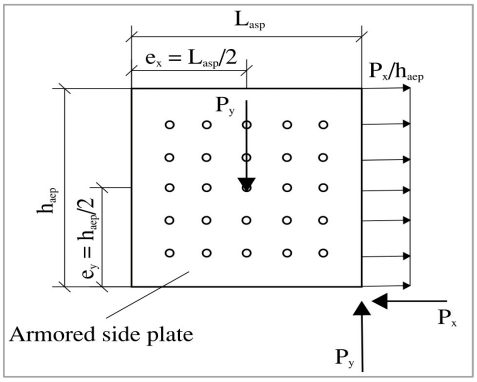

Check shear strength of screws:

		Suite Mean	Suite Max	
Shear Demands	γ =	1.3	1	
	R_u =	43	59	kip
Shear Capacity	φ =	0.65	1	
	φR_n =	45	69	kip
DCR	$R_u/\varphi R_n$ =	0.96	0.86	

		Suite Mean	Suite Max	
Shear Demands	γ =	1.3	1	
	R_u =	43	53	kip
Shear Capacity	φ =	0.65	1	
	φR_n =	45	69	kip
DCR	$R_u/\varphi R_n$ =	0.96	0.77	

Demand:

$$R_u = \gamma\,(V/2)$$

Capacity:

$$\Phi R_n = \Phi K_F V_{screw} n_{screws} \max\left(\left(\frac{e_x}{e_y}\right), \left(\frac{e_y}{e_x}\right)\right)$$

DCR:

$$DCR = \frac{R_u}{\Phi R_n}$$

A.5.8 Shear and moment capacity of shoe end plate

Similar to the armored end plate, the shear and moment capacity of the shoe end plate was checked by modeling the shoe end plate acts as a simply supported beam. The procedure for this check is shown below. As shown, the forces from the armored side plates acts as point loads on the beam and the beam is supported by the shear shoe side plates.

CLT Wall Calculations

Check shear capacity of shoe end plate:

		Suite Mean	Suite Max	
Shear Demands	γ =	1.3	1	
	R_u =	43	59	kip
Shear Capacity	φ =	0.9	1	
	φR_n =	71	79	kip
DCR	$R_u/\varphi R_n$ =	0.60	0.75	

Demand:

$$V_u = \gamma(V/2)$$

Capacity:

$$\Phi V_n = \Phi 0.6 F_y A_g = \Phi 0.6 F_y h_{sst} t_{ss}$$

DCR:

$$DCR = \frac{V_u}{\Phi V_n}$$

Check bending capacity of shoe end plate:

		Suite Mean	Suite Max	
Flexure Demands	γ =	1.3	1	
	M_u =	10.7	14.8	k-in
Flexure Capacity	φ =	0.9	1	
	φM_n =	14.8	16.4	k-in
DCR:	$M_u/\varphi M_n$ =	0.72	0.90	

Demand:

$$M_u = \gamma\left(\frac{V t_{asp}/2}{2}\right)$$

Capacity:

$$\Phi M_n = \Phi F_y S_x = \Phi F_y\left(\frac{t_{ss}^2 h_{sst}}{6}\right)$$

DCR:

$$DCR = \frac{M_u}{\Phi M_n}$$

MPP Wall Calculations

		Suite Mean	Suite Max	
Shear Demands	γ =	1.3	1	
	R_u =	43	53	kip
Shear Capacity	φ =	0.9	1	
	φR_n =	71	79	kip
DCR	$R_u/\varphi R_n$ =	0.60	0.67	

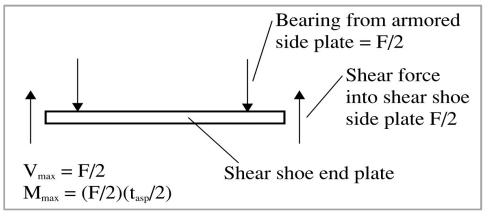

		Suite Mean	Suite Max	
Flexure Demands	γ =	1.3	1	
	M_u =	10.7	13.2	k-in
Flexure Capacity	φ =	0.9	1	
	φM_n =	14.8	16.4	
DCR:	$M_u/\varphi M_n$ =	0.72	0.80	

A.5.9 Shear capacity of shoe side plates

The next capacity check performed for this assembly was to check the shear capacity of the shoe side plates. This was done following the procedure outlined below.

CLT Wall Calculations

Check shear capacity of shoe side plates

		Suite Mean	Suite Max	
Shear Demands	γ =	1.3	1	
	R_u =	43	59	kip
Shear Capacity	φ =	0.9	1	
	φR_n =	115	128	kip
DCR	$R_u/\varphi R_n$ =	0.37	0.46	

MPP Wall Calculations

		Suite Mean	Suite Max	
Shear Demands	γ =	1.3	1	
	R_u =	43	53	kip
Shear Capacity	φ =	0.9	1	
	φR_n =	115	128	kip
DCR	$R_u/\varphi R_n$ =	0.37	0.41	

Demand:

$$V_u = \gamma(V/2)$$

Capacity:

$$\Phi V_n = \Phi 0.6 F_y A_g = \Phi 0.6 F_y t_{sp} L_{sp}$$

DCR:

$$DCR = \frac{V_u}{\Phi V_n}$$

A.5.10 Capacity of the shear shoe weld

The capacity of the weld connecting the shear shoe to the foundation beam was checked using the procedure outlined below. The weld was checked for combined tension bending and shear. A triangular distribution up the height of the shear shoe was assumed, resulting in a moment arm, e, equal to $h_{ss}/3$.

CLT Wall Calculations

Check combined bending and shear of weld (tension)

		Suite Mean	Suite Max	
Weld Demands	γ =	1.3	1	
	R_u =	10.7	14.9	kip
Weld Capacity	φ =	0.75	1	
	φR_n =	11.1	14.8	kip
DCR	$R_u/\varphi R_n$ =	0.96	1.00	

MPP Wall Calculations

		Suite Mean	Suite Max	
Weld Demands	γ =	1.3	1	
	R_u =	10.7	13.2	kip
Weld Capacity	φ =	0.75	1	
	φR_n =	11.1	14.8	kip
DCR	$R_u/\varphi R_n$ =	0.96	0.89	

Demand:

$$R_u = f_r = \sqrt{f_t^2 + f_v^2}$$

$$f_t = \gamma \frac{Mc}{I} = \gamma \frac{(Fe)c}{I} = \gamma \frac{(V/2)(h_{ss}/3)(l_{weld}/2)}{l_{weld}^3/12}$$

$$f_v = \gamma \frac{V/2}{l_{weld}}$$

Capacity:

$$\Phi R_n = \Phi 0.6 F_{EXX} \sqrt{2}/2\, D$$

DCR:

$$DCR = \frac{R_u}{\Phi R_n}$$

A.6 UFP Connections

This section includes the design calculations for the UFP to UFP mount connections for the 10-story test specimen lateral system. See Section 6.6.3 for a conceptual discussion of this assembly and figures. In this section, each capacity check is presented, followed by a figure showing the resulting DCRs and the equations used. These calculations were completed in accordance with AISC [2016].

A.6.1 Demands

In accordance with capacity based design methodologies, the ultimate force of the UFPs were used as the design demand forces. Because there were two types of UFPs in the 10-story building, the ultimate force in both UFPs were calculated and the larger one was used for design. The properties and procedures used to calculate the design demands are shown below (initially from Table 6.5).

UFP Plate - ASTM A572 Gr 50:		**Lower**	**Upper**	
Ultimate stress of UFP:	F_u =	65	65	ksi
Seismic material yield force ratio:	R_t =	1.1	1.1	
Width of UFP:	b_u =	8	8	in
Thickenss of UFP Plate:	t_u =	0.5	0.375	in
Diameter of UFP:	D_u =	6.25	6.375	in

UFP Demand

Ultimate UFP Force:

	Lower UFP	Upper UFP	
F_p =	11.44	6.31	kip
	Controlling UFP		
F_p =	11.44		kip

Demand:
Take larger ulimate UFP force of the lower and upper UFPs to find controlling demand force

$$F_p = R_t \frac{F_u b_u t_u^2}{2D_u}$$

A.6.2 Input Parameters

The input parameters used for the UFP connection calculations in the following sections are shown below.

UFP Bolts - A325:			
Number of bolts:	n_{bolts} =	2	bolts
Diameter of bolts:	d_b =	0.5	in
Nominal hole diameter:	d_h =	0.5625	in
Nominal Shear Strength:	F_{nv} =	54	ksi
Area of bolt:	A_b =	0.196	in
Uniform stress factor:	U_{bs} =	0.5	
Weld Washer:			
Elastic yield stress:	F_y =	50	ksi
Ultimate yield stress:	F_u =	65	ksi
Weld washer thickness:	t_w =	0.25	in
Weld washer width:	w_w =	2	in
Weld washer height:	h_w =	1.5	in
Weld washer bolt hole diameter:	d_h =	0.5625	in
Weld:			
Electrode strength:	F_{EXX} =	70	ksi
size of fillet welds:	D =	0.1875	in
length of weld:	l_{weld} =	1.5	in
number of welds:	n_{weld} =	2	

A.6.3 Shear strength of the bolts

The shear strength of the bolts was calculated as shown below. Note, all requirements for bolt spacing and edge distances were also satisfied in the design.

Check shear strength of bolts (J3-1):

Shear Deamands	γ =	-	
	R_u =	5.72	kip
Shear Capacity	φ =	0.75	
	φR_n =	7.9	kip
DCR	$R_u/\varphi R_n$ =	0.72	

Demand:

$$R_u = F_p/2\ bolts$$

Capacity:

$$\Phi R_n = \Phi F_{nv} A_b$$

DCR:

$$DCR = \frac{R_u}{\Phi R_n}$$

A.6.4 Weld washer design

The size of the weld washer was finalized using the following checks. Note, the same check should also be done for the UFP itself and the plate with the threaded holes for the bolts. However, the weld washer is the thinnest plate and has the smallest edge distances, so it is assumed that checks on the weld washer will control the design. Note that the washers were checked for the controlling horizontal installation orientation.

Bearing and tearout strength at the bolt holes in the weld washer

The bearing and tearout strength of the bolt holes in the weld washer were checked using the following procedure.

Bearing and Tearout Strength at Bolt Holes - Washer (J3-6a & J3-6c):

Shear Deamands	γ =	-	
	R_u =	5.72	kip
Shear Capacity	φ =	0.75	
	φR_n =	6.9	kip
DCR	$R_u/\varphi R_n$ =	0.83	

Demand:

$$R_u = F_p/2\ bolts$$

Capacity:

$$\Phi R_n = \Phi \min\left(1.2\left(\frac{h_w}{2} - \frac{d_b}{2}\right) t_w F_u, 2.4 d_b t_w F_u\right)$$

DCR:

Shear yielding and rupture of the weld washer plates

Shear yielding and shear rupture of the weld washer plates were checked using the following procedures.

Check shear yielding - washer (J4-3):

Shear Deamands	γ =	-	
	R_u =	5.72	kip
Shear Capacity	φ =	1	
	φR_n =	22.5	kip
DCR	$R_u/\varphi R_n$ =	0.25	

Demand:

$$R_u = F_p/2\ bolts$$

Capacity:

$$\Phi R_n = \Phi 0.6 F_y t_w h_w\ (2)$$

DCR:

$$DCR = \frac{R_u}{\Phi R_n}$$

Check shear rupture - washer (J4-4):

Shear Deamands	γ =	-	
	R_u =	5.72	kip
Shear Capacity	φ =	0.75	
	φR_n =	12.8	kip
DCR	$R_u/\varphi R_n$ =	0.45	

Demand:

$$R_u = F_p/2\ bolts$$

Capacity:

$$\Phi R_n = \Phi 0.6 F_u t_w (h_w - (d_h + 1/16\text{"}))2$$

DCR:

$$DCR = \frac{R_u}{\Phi R_n}$$

Block shear strength of the weld washer plates

Block shear in the weld washer plates was checked using the following procedure.

Check Block Shear Strength - Washer (J4-5):

Shear Deamands	γ =	-	
	R_u =	5.72	kip
Shear Capacity	φ =	0.75	
	φR_n =	5.9	kip
DCR	$R_u/\varphi R_n$ =	0.98	

Demand:

$$R_u = F_p/2\ bolts$$

Capacity:

$$\Phi R_n = \min\left(\Phi 0.6F_uA_{nv} + \Phi U_{bs}F_uA_{nt}, \Phi 0.6F_yA_{gv} + \Phi U_{bs}F_uA_{nt}\right)$$

$$\Phi 0.6F_uA_{nv} = \Phi 0.6F_u\left(h_w/2 - 0.5(d_h + 1/16")\right)t_w$$

$$\Phi U_{bs}F_uA_{nt} = \Phi U_{bs}F_u\left(h_w/2 - 0.5(d_h + 1/16")\right)t_w$$

$$\Phi 0.6F_yA_{gv} = \Phi 0.6F_y\ h_w/2\ t_w$$

DCR:

$$DCR = \frac{R_u}{\Phi R_n}$$

UFP to weld washer weld length strength

The length of the welds connection the UFPs and the weld washers were checked using the following procedure.

Weld Length - Washer to UFP:

Shear Deamands	γ =	-	
	R_u =	5.72	kip
Shear Capacity	φ =	0.75	
	φR_n =	12.5	kip
DCR	$R_u/\varphi R_n$ =	0.46	

Demand:

$$R_u = F_p/2\ bolts$$

Capacity:

$$\Phi R_n = \Phi 0.6\ F_{EXX}\left(\sqrt{2}/2\right)D\ l_{weld}n_{welds}$$

DCR:

$$DCR = \frac{R_u}{\Phi R_n}$$

A.7 Diaphragm to Wall Shear Transfer Connection

This section includes the design calculations for the CLT and MPP diaphragm-to-wall shear transfer connections used on the CLT and VLT floors (the two-way, non-sheathed floor systems). See Section 6.6.3 for a conceptional discussion of this assembly and figures. In this section, each capacity check is presented, followed by a figure showing the resulting DCRs and the equations used. The calculations for the shear key, wing plate, and wall insert assembly are presented first, followed by the collector plate designs. These calculations were completed in accordance with AISC [2016]. Refer to Figure 6.36 for a schematic of the connection with dimension labels.

A.7.1 Demands

The demands used to check the capacity of the connections are shown in the procedure below. Peak floor forces from the NLRHA were used (summarized in Table 6.26). The value was taken from the in-plane shear force of the shear key spring. As discussed in Section 6.2.3, the wing plate dimensions used on the CLT and MPP walls were different. However, the same connection was used for all floors for ease of construction. Thus, the peak floor force from the CLT wall and the peak force from the MPP wall was used for design. Note, the force on the roof was the largest of all the floors, making it the design force.

CLT Wall Calculations

Peak MCER diaphragm force demands - per wall
from NLRHA

	Suite Mean	Suite Max	
F =	41	60	kip

MPP Wall Calculations

	Suite Mean	Suite Max	
F =	44	70	kip

A.7.2 Shear Key and wing plate design

Input Parameters

The insert below shows the input parameters used to perform all capacity checks for this assembly and can be referenced for the following sections.

Wall Geometry and Properties:		**CLT**	**MPP**	
Eccentricty from wall to diaphragm:	e =	9.5	9.5	in
Bearing Format Conversion Factor:	K_F =	2.4	2.4	-
Compression design value (trans.):	$F_{c,trans}$ or $F_{c\perp}$ =	1400	750	psi
Adj. compression design value (trans.):	$F_{c,trans}$* =	3360	1800	psi
CLT lam thickness:	t_{lam} =	1.375	-	in
number of vertical lams wall:	n_{vert} =	5	-	lams
number of horizontal lams wall:	n_{horz} =	4	-	lams
Thickness of walls:	b_w =	12.375	9.1875	in
Simpson Strong-Tie 45 Degree screws:				
Mechanical connect. format conversion factor:	K_F =	3.32	3.32	
Allowable steel strength Tension:	T =	2000	2000	lbf
Withdrawal design value:	W =	200	200	lbf/in
Shear key:				
Shear key thickness:	t_{key} =	2	2	in
Shear key width:	w_{key} =	7	7	in
Shear key area:	A_g =	14	14	in^2
Moment of Inertia:	I =	57.2	57.2	in^4
Elastic Section Modulus:	S_x =	16.3	16.3	in^3
Shear key yield stress:	F_y =	50	50	ksi
Edge Plate:				
Edge Plate Thickness:	t_{ep} =	1	1	in
Tonge bearing on inside of wall area:	A_{parall} =	22	36.75	in^2
Wing Plate - weld:				
E70 Electorde welds:	C_1 =	1	1	
length of weld:	l_{weld} =	18.75	18.75	in
spacing of welds:	w =	7	7	in
eccentricity of weld:	e_x =	18.875	18.875	in
k Factor:	k =	0.37	0.37	
a Factor:	a =	1.01	1.01	
C factor from AISC Table 8-5:	C =	1.41	1.41	
size of fillet welds:	D =	0.25	0.25	in
Wing Plate - 45^o screws:				
thickness of wing plate (5/8" max):	t_{wp} =	0.625	0.625	in
45 degree screw length:	L =	8.625	8.625	in
screw length penetration into CLT:	p =	7.27	7.27	in
End grain factor:	C_{eg} =	0.71	0.71	
Screw group eccentricity:	y =	21	24	in
number of screws per screw group:	n_{screws} =	16	14	screws

Shear and flexural yielding of the shear keys

The shear and flexural capacity of the shear key plate was checked as shown in the procedure below. For these calculations, the shear key was assumed to act as a cantilevered section:

fixed to the wing plate with the walls applying a point load force. The elastic modulus was conservatively used for this calculation and a rectangular cross section of the shear key was assumed (i.e., the curved corners of the plate were neglected).

CLT Wall Calculations

Check shear key for yielding in shear:

		Suite Mean	Suite Max	
Shear Demands:	γ =	1.3	1	
	V_u =	54	60	kip
Shear Capacity	φ =	0.9	1	
	φV_n =	378	420	kip
DCR:	$V_u/\varphi V_n$ =	0.14	0.14	

Demand:

$$V_u = \gamma F$$

Capacity:

$$\Phi V_n = \Phi 0.6 F_y A_g = \Phi\ 0.6\ t_{key} w_{key}$$

DCR:

$$DCR = \frac{V_u}{\Phi V_n}$$

Check shear key for yielding in flexure:

		Suite Mean	Suite Max	
Flexure Demands	γ =	1.3	1	
	M_u =	511	574	k-in
Flexure Capacity	φ =	0.9	1	
	φM_n =	735	817	k-in
DCR:	$M_u/\varphi M_n$ =	0.70	0.70	

Demand:

$$M_u = \gamma F e$$

Capacity:

$$\Phi M_n = \Phi F_y S_x = \Phi F_y \left(\frac{t_{key} w_{key}^2}{6}\right)$$

DCR:

$$DCR = \frac{M_u}{\Phi M_n}$$

MPP Wall Calculations

		Suite Mean	Suite Max	
Shear Demands:	γ =	1.3	1	
	V_u =	57	70	kip
Shear Capacity	φ =	0.9	1	
	φV_n =	378	420	kip
DCR:	$V_u/\varphi V_n$ =	0.15	0.17	

		Suite Mean	Suite Max	
Flexure Demands	γ =	1.3	1	
	M_u =	544	662	k-in
Flexure Capacity	φ =	0.9	1	
	φM_n =	735	817	k-in
DCR:	$M_u/\varphi M_n$ =	0.74	0.81	

Shear key wall bearing

The bearing capacity of the inside of the wall from the force of the shear key was checked using the procedure outlined below. A bearing height of the shear key height plus twice the

thickness of the edge plates (shown in the figure below) was assumed. This was conservatively approximated by assuming a 45 degree projection of the load from the inside of the edge plate to the outside of the edge plate (touching the wall edge).

CLT Wall Calculations

Check shear key bearing on CLT wall:

		Suite Mean	Suite Max	
Bearing Demands	γ =	1.3	1	
	R_u =	54	60	kip
Bearing Capacity:	φ =	0.9	1	
	φR_n =	66.5	73.9	kip
DCR	$R_u/\varphi R_n$ =	0.81	0.82	

Demand:

$$R_u = \gamma F$$

Capacity:

$$\Phi R_n = \Phi F_c^* A_{parall} = \Phi K_F F_{c,trans} A_{\parallel}$$

$$A_{\parallel,clt} = \left(\frac{1.375in}{lam}\right)(4lam)(t_{key} + 2t_{ep})$$

$$A_{\parallel,mpp} = b_w(t_{key} + 2t_{ep})$$

DCR:

$$DCR = \frac{R_u}{\Phi R_n}$$

MPP Wall Calculations

		Suite Mean	Suite Max	
Bearing Demands	γ =	1.3	1	
	R_u =	57	70	kip
Bearing Capacity:	φ =	0.9	1	
	φR_n =	59.5	66.2	kip
DCR	$R_u/\varphi R_n$ =	0.96	1.05	

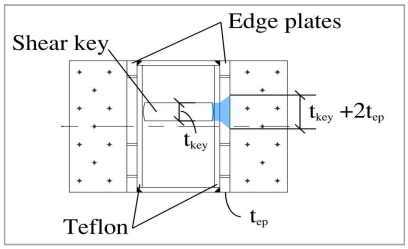

Shear key weld strength

The shear keys were welded to the wing plates. The strength of these welds was checked using AISC [2016] recommendations for eccentrically loaded weld groups as shown in the procedure below.

CLT Wall Calculations

Wing Plate:

Check weld strength:

		Suite Mean	Suite Max	
Weld Demands	γ =	1.3	1	
	R_u =	54	60	kip
Weld Capacity	φ =	0.75	1	
	φR_n =	79	106	kip
DCR	$R_u/\varphi R_n$ =	0.68	0.57	

MPP Wall Calculations

		Suite Mean	Suite Max	
Weld Demands	γ =	1.3	1	
	R_u =	57	70	kip
Weld Capacity	φ =	0.75	1	
	φR_n =	79	106	kip
DCR	$R_u/\varphi R_n$ =	0.72	0.66	

Demand:

$$R_u = \gamma F$$

Capacity:

$$\Phi R_n = \Phi C C_1 D l_{weld}$$

DCR:

$$DCR = \frac{R_u}{\Phi R_n}$$

Wing plate screws in withdrawal and tension

The 45 degree screws in the wing plates were checked for withdrawal and tension as shown in the procedure shown below. These checks were completed considering the entire screw group (see Figure 6.36). The demand was calculated by equating the moment from the force on the shear key and the force in the collectors to the moment created from the two screw groups. The capacity of each screw was calculated using manufacture recommendations from Simpson Strong-Tie. The withdrawal and tension capacities were divided by the square root of two to account for the 45 degree installation angle. In withdrawal, an end grain factor, C_{eg}, of 0.71 was also accounted for per recommendations in the Simpson Strong-Tie design guide. The penetration length of each screw was also based on Simpson Strong-Tie recommendations.

CLT Wall Calculations

Check Screw Group withdrawal:

		Suite Mean	Suite Max	
Withdraw Demands	γ =	1.3	1	
	R_u =	24	27	kip
Withdraw Capacity	φ =	0.65	1	
	φR_n =	25	39	kip
DCR	$R_u/\varphi R_n$ =	0.97	0.71	

MPP Wall Calculations

		Suite Mean	Suite Max	
Withdraw Demands	γ =	1.3	1	
	R_u =	23	28	kip
Withdraw Capacity	φ =	0.65	1	
	φR_n =	22	34	kip
DCR	$R_u/\varphi R_n$ =	1.03	0.81	

Demand:

$$R_u = \gamma \left(\frac{Fe}{y}\right)$$

Capacity:

$$\Phi R_n = \Phi K_F W p/\sqrt{2}\, n_{screws} C_{eg}$$

$$p = L - \left(0.476" - t_{wp}\sqrt{2}\right)$$

DCR:

$$DCR = \frac{R_u}{\Phi R_n}$$

Check Screw Group Tension:

		Suite Mean	Suite Max	
Tension Demands	γ =	1.3	1	
	R_u =	24	27	kip
Tension Capacity	φ =	0.65	1	
	φR_n =	49	75	kip
DCR	$R_u/\varphi R_n$ =	0.50	0.36	

		Suite Mean	Suite Max	
Tension Demands	γ =	1.3	1	
	R_u =	26	28	kip
Tension Capacity	φ =	0.65	1	
	φR_n =	43	66	kip
DCR	$R_u/\varphi R_n$ =	0.61	0.42	

Demand:

$$R_u = \gamma \left(\frac{Fe}{y}\right)$$

Capacity:

$$\Phi R_n = \Phi K_F T/\sqrt{2}\, n_{screws}$$

DCR:

$$DCR = \frac{R_u}{\Phi R_n}$$

A.7.3 Shear key wall insert

Specific capacity calculations were not performed to design most components of the steel insert in the wall panels at the shear key locations (the piece with the Teflon attached). The thickness of the edge plates were controlled by the shear key wall bearing check presented previously. However, no checks were performed for the side plates with the SDS screws. Their dimensions were set to accommodate anchor screws to keep the assembly into place. The SDS screws were installed to prevent movement of the assembly. Bridge plates at the upper

and lower ends of the slotted holes were added to ensure a snug fit of the insert assembly into the wall panel.

A.7.4 Collector plate design

Collector Demands

The design demand forces in the collector plates are equal to the demand forces for the shear keys (shown in Section A.7.1). To perform axial and shear capacity checks on the collector plate assemblies, these shear key point load forces were transformed into axial demand loads and distributed shear force demands as shown in the procedures for the CLT and MPP wall directions below.

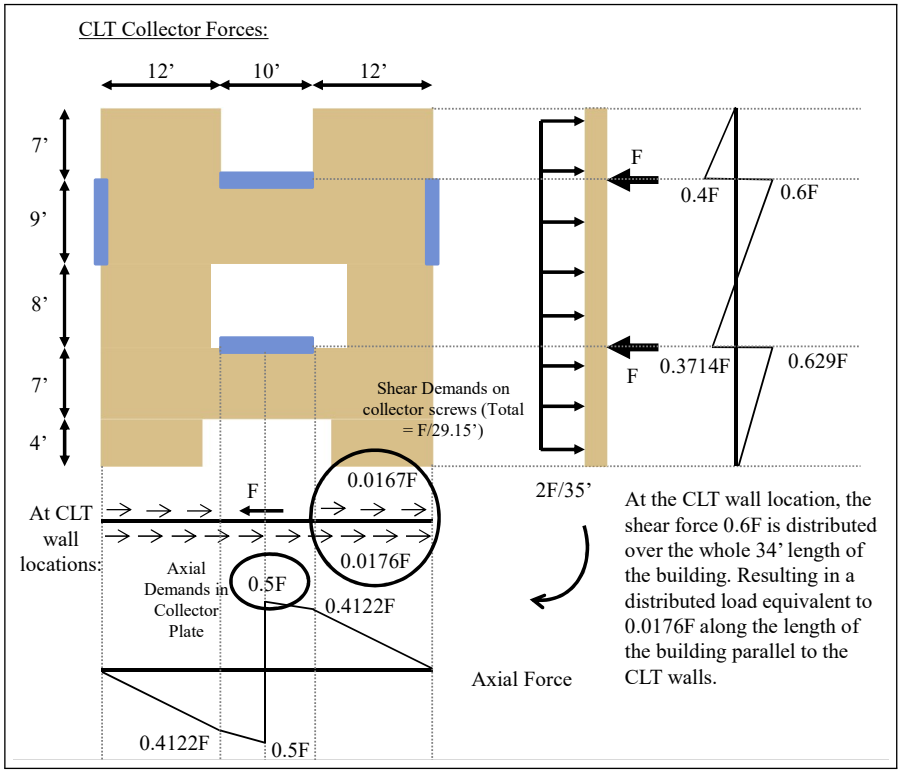

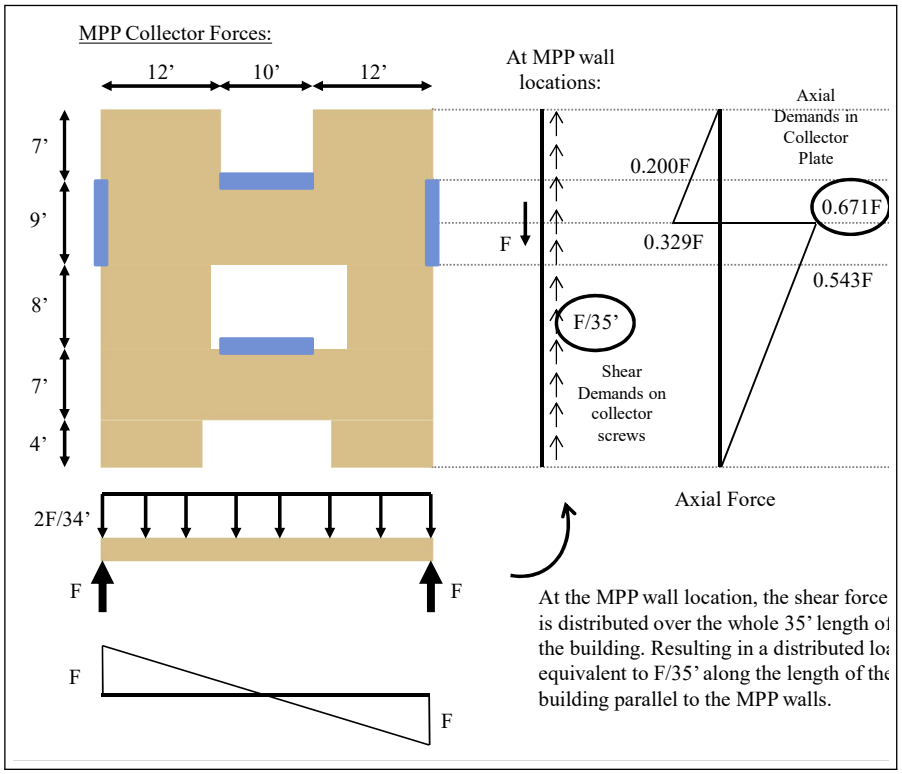

Input Parameters

The insert below shows the input parameters used to perform all capacity checks for the collector assembly and can be referenced for the calculations in the following sections.

Simpson SDS Screws:				
Mechanical connect. format conversion factor:	K_F =	3.32	3.32	
Shear strength of screws:	V_{screw} =	420	420	lb
Collector Geometry and Properties:				
Collector yield stress:	F_y =	50	50	ksi
Modulus of elasticity:	E =	29000	29000	ksi
Effective length factor:	K =	1	1	
MPP collector screw spacing:	spacing =	4.5	4.5	in
Collector plate thickness:	t_c =	0.25	0.25	in
Collector plate width:	w_c =	5	5	in
Collector plate area:	A_g =	1.25	1.25	in^2
Collector plate Radius of gyration:	r =	0.125	0.125	in
Collector plate Slenderness ratio:	KL/r =	36	36	
Collector plate Elastic buckling stress:	F_e =	220.8	220.8	ksi
Collector plate Critical stress:	F_{cr} =	45.5	45.5	ksi
Link plate thickness:	t_{lp} =	0.375	0.375	in
Link plate width:	w_{lp} =	3	3	in
Link plate length (min weld length):	L_{lp} =	5	5	in
Link plate area:	A_g =	1.125	1.125	in^2
Fillet weld size:	D =	0.25	0.25	in
Electrode strength:	F_{EXX} =	70	70	ksi

Shear capacity of collector screws

The shear capacity of the screws connection the collector plates to the diaphragms were calculated using the procedure outlined below. Recommendations from Simpson Strong-Tie were used for the shear capacity of the SDS screws.

CLT Collector Plates:

Check Screw Capacity:

		Suite Mean	Suite Max	
Shear Demands	γ =	1.3	1	
	V_u =	1.85	2.07	k/ft
Shear Capacity	φ =	0.65	1	
	φV_n =	2.42	3.72	k/ft
DCR	$V_u/\varphi V_n$ =	0.76	0.56	

MPP Collector Plates:

		Suite Mean	Suite Max	
Shear Demands	γ =	1.3	1	
	V_u =	1.97	2.39	k/ft
Shear Capacity	φ =	0.65	1	
	φV_n =	2.42	3.72	k/ft
DCR	$V_u/\varphi V_n$ =	0.81	0.64	

Demand:

$$CLT: V_u = \gamma\,(F/29.15ft)$$
$$MPP: V_u = \gamma\,(F/30ft)$$

Capacity:

$$\Phi V_n = \frac{\Phi K_F V_{screw}}{spacing}$$

DCR:

$$DCR = \frac{V_u}{\Phi V_n}$$

Tension and compression capacity of the collector plates

The tension and buckling compression capacity of the collector plates were calculated using the procedures outlined below. In compression, the buckling capacity was calculated using standard practices from AISC [2016] where the unbraced length was taken as the screw spacing.

CLT Collector Plates:

Check Tension Capacity of Collector Plate:

		Suite Mean	Suite Max	
Tension Demands	γ =	1.3	1	
	T_u =	27	30	kip
Tension Capacity	φ =	0.9	1	
	φT_n =	56	63	kip
DCR	$T_u/\varphi T_n$ =	0.48	0.48	

MPP Collector Plates:

		Suite Mean	Suite Max	
Tension Demands	γ =	1.3	1	
	T_u =	38	47	kip
Tension Capacity	φ =	0.9	1	
	φT_n =	56	63	kip
DCR	$T_u/\varphi T_n$ =	0.68	0.75	

Demand:

$$CLT: T_u = \gamma F(0.5)$$
$$MPP: T_u = \gamma F(0.671)$$

Capacity:

$$\Phi T_n = \Phi F_y A_g = \Phi F_y t_c w_c$$

DCR:

$$DCR = \frac{T_u}{\Phi T_n}$$

Check Compression Capacity of Collector Plate:

		Suite Mean	Suite Max	
Compression Demands	γ =	1.3	1	
	P_u =	27	30	kip
Compression Capacity	φ =	0.9	1	
	φP_n =	51	57	kip
DCR	$P_u/\varphi P_n$ =	0.53	0.53	

		Suite Mean	Suite Max	
Compression Demands	γ =	1.3	1	
	P_u =	38	47	kip
Compression Capacity	φ =	0.9	1	
	φP_n =	51	57	kip
DCR	$P_u/\varphi P_n$ =	0.75	0.82	

Demand:

$$CLT: P_u = \gamma F(0.5)$$
$$MPP: P_u = \gamma F(0.671)$$

Capacity:

$$\Phi P_n = \Phi F_{cr} A_g$$

DCR:

$$DCR = \frac{P_u}{\Phi P_n}$$

Tension capacity of the link plate

The tension capacity of the link plate was calculated using the procedure outlined below. The compression capacity of the link plates was not checked because it was welded along its two long sides.

CLT Collector Plates:

Check Tension Capacity of Link Plate:

		Suite Mean	Suite Max	
Tension Demands	γ =	1.3	1	
	T_u =	27	30	kip
Tension Capacity	φ =	0.9	1	
	φT_n =	51	56	kip
DCR	$T_u/\varphi T_n$ =	0.53	0.54	

MPP Collector Plates:

		Suite Mean	Suite Max	
Tension Demands	γ =	1.3	1	
	T_u =	38	47	kip
Tension Capacity	φ =	0.9	1	
	φT_n =	51	56	kip
DCR	$T_u/\varphi T_n$ =	0.76	0.83	

Demand:

$$CLT:\ T_u = \gamma\, F(0.5)$$
$$MPP: T_u = \gamma\, F(0.671)$$

Capacity:

$$\Phi T_n = \Phi F_y A_g = \Phi F_y t_{lp} w_{lp}$$

DCR:

$$DCR = \frac{T_u}{\Phi T_n}$$

Link plate filet weld capacity

The capacity of the filet weld connecting the link plate to the collector plate was calculated using the procedure outlined below.

CLT Collector Plates:

Check Fillet Weld Capacity around Link Plate:

		Suite Mean	Suite Max	
Shear Demands	γ =	1.3	1	
	R_u =	27	30	kip
Shear Capacity	φ =	0.75	1.00	
	φR_n =	56	74	kip
DCR	$R_u/\varphi R_n$ =	0.48	0.41	

MPP Collector Plates:

		Suite Mean	Suite Max	
Shear Demands	γ =	1.3	1	
	R_u =	38	47	kip
Shear Capacity	φ =	0.75	1.00	
	φR_n =	56	74	kip
DCR	$R_u/\varphi R_n$ =	0.69	0.63	

Demand:

$$CLT: R_u = \gamma\, F(0.5)$$
$$MPP: R_u = \gamma\, F(0.671)$$

Capacity:

$$\Phi R_n = \Phi 0.6 F_{EXX}\sqrt{2}/2\ Dl$$

DCR:

$$DCR = \frac{R_u}{\Phi R_n}$$

A.8 PT Bar Connection

This section includes the design calculations for the CLT and MPP top of wall PT saddles used in the 10-story test specimen. See Section 6.6.3 for a conceptional discussion of this assembly and figures. In this section, each capacity check is presented, followed by a figure showing the resulting DCRs and the equations used. The calculations for the PT saddle itself are presented first, followed by the PT jacking hardware piece. These calculations were completed in accordance with AISC [2016]. Refer to Figure A.3 for a schematic of the connection with dimension labels. This schematic also includes the assumed longitudinal and transverse bending directions that will be referenced throughout this section. Note, this connection was designed using capacity based design methodologies.

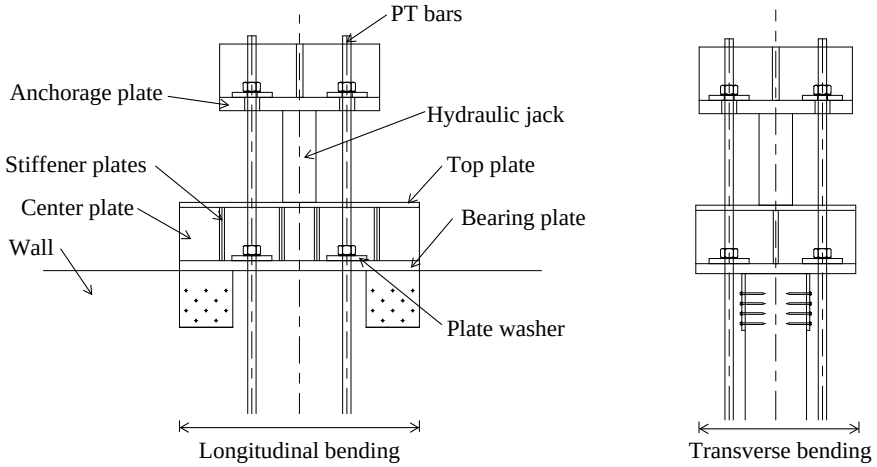

Figure A.3: Schematic of the PT bar saddle and jacking hardware assemblies located at the tops of the mass timber walls

A.8.1 Properties

The insert below shows the input parameters used to perform all capacity checks for this assembly and can be referenced for the following sections.

Wall Geometry and Properties:				
Bearing Format Conversion Factor:	K_F =	2.4	2.4	-
Compression design value (long.):	$F_{c,long}$ or $F_{c\|\|}$ =	1975	2400	psi
Adj. compression design value (long.):	$F_{c,long}$* =	4740	5760	psi
CLT lam thickness:	t_{lam} =	1.375	-	in
number of vertical lams wall:	n_{vert} =	5	-	lams
number of horizontal lams wall:	n_{horz} =	4	-	lams
Thickness of walls:	b_w =	12.375	9.1875	in
PT Bars:				
Ultimate stress:	F_u =	125	125	ksi
Diameter of rods:	d =	1.25	1.25	in
Threads per inch:	n =	7	7	
Net tensile area:	A_{net} =	0.969	0.969	in^2
Number of bars:	n_{bars} =	4	4	bars
PT bar spacing:	s_{pt} =	14.25	14.25	in
PT bar offset:	o_{pt} =	15.75	14	in
PT Saddle Properties:				
Elastic yield stress:	F_y =	50	50	ksi
Longitudinal stiffner spacing:	s_{long} =	9	9	in
Spacing from face of wall to CL of PT:	s =	1.69	2.41	in
Spacing from CL PT to end of anchor PL:	s_2 =	4.13	5.00	in
Length of PT plate washer:	l_{pw} =	8	8	in
Bearing Plate:				
Bearing plate length:	l_{bp} =	36	36	in
Bearing plate width:	w_{bp} =	24	24	in
Bearing plate thickenss:	t_{bp} =	1.5	1.5	in
Center Plate:				
Center plate width:	w_{cp} =	8	8	in
Center plate thickness:	t_{cp} =	0.75	0.75	in
Stiffner plates:				
Stiffner plates width:	w_{sp} =	12	12	in
Stiffner plate thickness:	t_{sp} =	0.75	0.75	in
Top Plate:				
Top plate width:	w_{tp} =	24	24.00	in
Top plate thickness:	t_{tp} =	0.75	0.75	in
Anchorage Plate:				
Anchorage plate length:	l_{ap} =	32	32	in
Anchorage plate width:	w_{ap} =	32	32	in
Anchorage plate thickness:	t_{ap} =	2	2	in
Hydrolic jack:				
Hydrolic jack width:	w_h =	5	5	in

A.8.2 Demands

In accordance with capacity based design methodologies, the ultimate force of the PT bars was used as the design demand force for majority of the connection checks. However, in some instances, the initial PT bar force was used as the demand force to create a more economical design. The demand used for each check is noted in each section. The demand values are summarized below. Reference Table 6.4 for the properties of the PT bars.

PT Bar Demands

Ultimate PT Bar Force		
F_p =	121.14	kip
Initial PT Bar Force		
F_{pti} =	50	kip

Demand:

$$F_p = F_u A_{net}$$

or

$$F_{pti} = 50\ kips$$

A.8.3 Top of Wall PT Saddle

Timber bearing capacity

The bearing capacity of the wall panels at the top of the walls were was checked using the following procedure.

CLT Wall Calculations

Timber Bearing Check:

Bearing Demands	γ =	-	
	P_u =	485	kip
Bearing Capacity	φ =	0.9	
	φP_n =	1056	kip
DCR	$P_u/\varphi P_n$ =	0.46	

MPP Wall Calculations

Bearing Demands	γ =	-	
	P_u =	485	kip
Bearing Capacity	φ =	0.9	
	φP_n =	1715	kip
DCR	$P_u/\varphi P_n$ =	0.28	

Demand:

$$P_u = n_{bars} F_p$$

Capacity:

$$\Phi P_n = \Phi F_c^* A_{\parallel}$$

$$A_{\parallel,clt} = \left(\frac{1.375in}{lam}\right)(5lam) l_{bp}$$

$$A_{\parallel,mpp} = b_w l_{bp}$$

DCR:

$$DCR = \frac{P_u}{\Phi P_n}$$

Transverse shear and moment capacity of the PT saddle bearing plate

The transverse capacity of the saddle connection was checked for shear and bending using the procedure shown below. Additionally, see the calculated transverse bending properties input into the design checks and the figure summarizing the basis of these equations. Note, this check is highly conservative as it just approximates the strength and stiffness of the full connection. An FEM model could have been created to create a more economical design. For this check, the ultimate force in the PT bars was used. This is also conservative because results from NLRHA indicate that the PT bars should only reach 70% of their yield strength. This calculation is also conservative because it does not account for the top plate (see Figure A.3 since the top plate was added after the completion of these calculations.

As shown, for the shear check, only the area of the webs were considered as this will carry majority of the shear force. For the flexure check, the elastic section modulus, S_x, was used to ensure the connection doesn't yield. It was important to ensure elastic behavior so permanent yielding in the connection doesn't inherently result in loss of PT bar force.

CLT Wall Calculations

Check transverse shear capacity of PT saddle:

Shear Deamands	γ =	-	
	V_u =	121	kip
Shear Capacity	φ =	0.9	
	φV_n =	243	kip
DCR	$V_u/\varphi V_n$ =	0.50	

Demand:

$$V_u = F_p$$

Capacity:

$$\Phi V_n = \Phi 0.6 F_y A_w = \Phi 0.6 F_y t_{sp} w_{sp}$$

DCR:

$$DCR = \frac{V_u}{\Phi V_n}$$

Check transverse bending cpacity of PT saddle:

Moment Demands	γ =	-	
	M_u =	1465	k-in
Moment Capacity	φ =	0.9	
	φM_n =	1597	k-in
DCR	$M_u/\varphi M_n$ =	0.92	

Demand:

$$M_u = F_p(s + b_w/4)$$

Capacity:

$$\Phi M_n = \Phi F_y S_x$$

DCR:

$$DCR = \frac{M_u}{\Phi M_n}$$

MPP Wall Calculations

Shear Deamands	γ =	-	
	V_u =	121	kip
Shear Capacity	φ =	0.9	
	φV_n =	243	kip
DCR	$V_u/\varphi V_n$ =	0.50	

Moment Demands	γ =	-	
	M_u =	1368	k-in
Moment Capacity	φ =	0.9	
	φM_n =	1597	k-in
DCR	$M_u/\varphi M_n$ =	0.86	

Transverse bending of PT saddle:

Area:	A =	22.5	22.5 in^2
Centroid:	y_c =	3.5	3.5 in
Moment of inertia:	I_x =	356.6	356.6 in^4
Elastic Section Modulus:	S_x =	35.5	35.5 in^3
Plastic neutral axis:	y_{pna} =	1.25	1.25 in

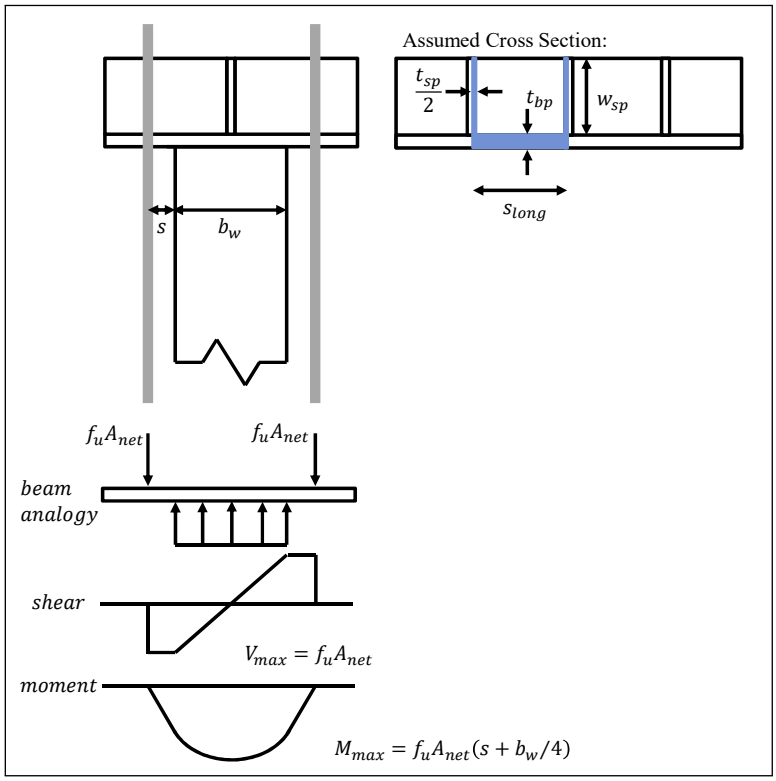

Longitudinal shear and moment capacity of the PT saddle bearing plate

Similar to the previous section, the longitudinal capacity of the saddle connection was checked for shear and bending using the procedure outlined below. Additionally, see the calculated longitudinal bending properties input into the design checks and the figure summarizing the basis of these equations. Note, this check is highly conservative as it just approximates the strength and stiffness of the full connection. An FEM model could have been created to develop a more economical design. For this check, the ultimate force in the PT bars were used. This is also conservative because results from NLRHA indicate that the PT bars should only reach 70% of their yield strength. This calculation is also conservative because it does not account for the top plate (see Figure A.3 since the top plate was added after the completion of these calculations. Note, the DCR values for the moment capacity check exceed 1.0, however, it was determined that this check was conservative enough that the connection would not yield under MCE_R ground motions.

CLT Wall Calculations

Check longitudinal shear capacity of PT saddle:

Shear Deamands	γ =	-	
	V_u =	61	kip
Shear Capacity	φ =	0.9	
	φV_n =	235	kip
DCR	$V_u/\varphi V_n$ =	0.26	

Demand:

$$V_u = F_p/2$$

Capacity:

$$\Phi V_n = \Phi 0.6 F_y A = 0.9(0.6)(50ksi)t_{ap}(s + s_2)$$

DCR:

$$DCR = \frac{V_u}{\Phi V_n}$$

Check longitudinal bending cpacity of PT saddle:

Moment Demands	γ =	-	
	M_u =	151	k-in
Moment Capacity	φ =	0.9	
	φM_n =	98	k-in
DCR	$M_u/\varphi M_n$ =	1.54	

Demand:

$$M_u = \frac{F_p}{8}(2s_{long} - l_{pw})$$

Capacity:

$$\Phi M_n = \Phi F_y S_x$$

DCR:

MPP Wall Calculations

Shear Deamands	γ =	-	
	V_u =	61	kip
Shear Capacity	φ =	0.9	
	φV_n =	300	kip
DCR	$V_u/\varphi V_n$ =	0.20	

Moment Demands	γ =	-		
	M_u =	151	151	k-in
Moment Capacity	φ =	0.9		
	φM_n =	125	125	k-in
DCR	$M_u/\varphi M_n$ =	1.21		

Longitudinal bending of PT Saddle:

Area:	A =	8.72	11.11 in^2
Centroid:	y_c =	0.75	0.75 in
Moment of inertia:	I_x =	1.63	2.08 in^4
Elastic Section Modulus:	S_x =	2.18	2.78 in^3
Plastic neutral axis:	y_{pna} =	0.75	0.75 in

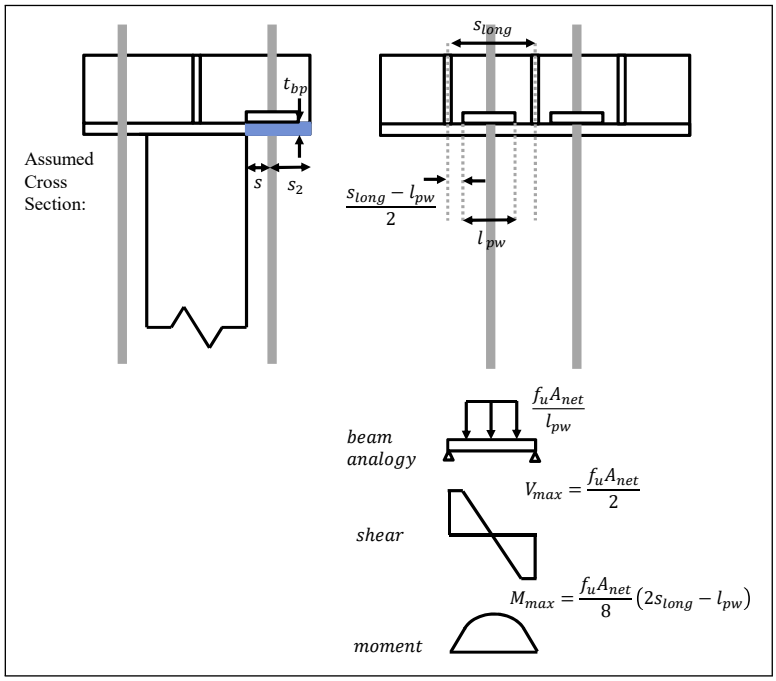

Longitudinal shear and moment capacity of the PT saddle at peak PT force

The longitudinal shear and moment capacity of the full PT saddle (with the top plate) was then checked at the peak PT bar force. The procedure for this check is shown below. The full saddle assembly was modeled as an I beam and the peak shear and moment values were checked. The section properties for this check are also shown along with a figure detailing the check and demand calculations. For this check the peak PT bar forces were used.

CLT Wall Calculations

Check longitudinal shear capacity at peak PT force

Shear Deamands	γ =	-	
	V_u =	136	kip
Shear Capacity	φ =	0.9	
	φV_n =	162	kip
DCR	$V_u/\varphi V_n$ =	0.84	

Demand:

$$V_u = \max\left(\frac{2F_p(l_{bp} - o_{pt})}{l_{bp}}, \frac{2F_p o_{pt}}{l_{bp}}\right)$$

Capacity:

$$\Phi V_n = \Phi 0.6 F_y A_w = \Phi 0.6 F_y w_{cp} t_{cp}$$

DCR:

$$DCR = \frac{V_u}{\Phi V_n}$$

Check longitudinal bending cpacity of PT saddle at peak PT force

Moment Demands	γ =	-	
	M_u =	690	k-in
Moment Capacity	φ =	0.9	
	φM_n =	11976	k-in
DCR	$M_u/\varphi M_n$ =	0.06	

Demand:

$$M_u = \frac{2F_p(l_{bp} - o_{pt})^2}{4l_{bp}}$$

Capacity:

$$\Phi M_n = \Phi F_y S_x$$

DCR:

MPP Wall Calculations

Shear Deamands	γ =	-	
	V_u =	148	kip
Shear Capacity	φ =	0.9	
	φV_n =	162	kip
DCR	$V_u/\varphi V_n$ =	0.91	

Moment Demands	γ =	-	
	M_u =	814	k-in
Moment Capacity	φ =	0.9	
	φM_n =	11976	k-in
DCR	$M_u/\varphi M_n$ =	0.07	

Longitudinal bending of full Saddle:

Area:	A =	60	60 in^2
Centroid:	y_c =	3.96	3.96 in
Moment of inertia:	I_x =	1054.5	1054.5 in^4
Elastic Section Modulus:	S_x =	266.13	266.13 in^3

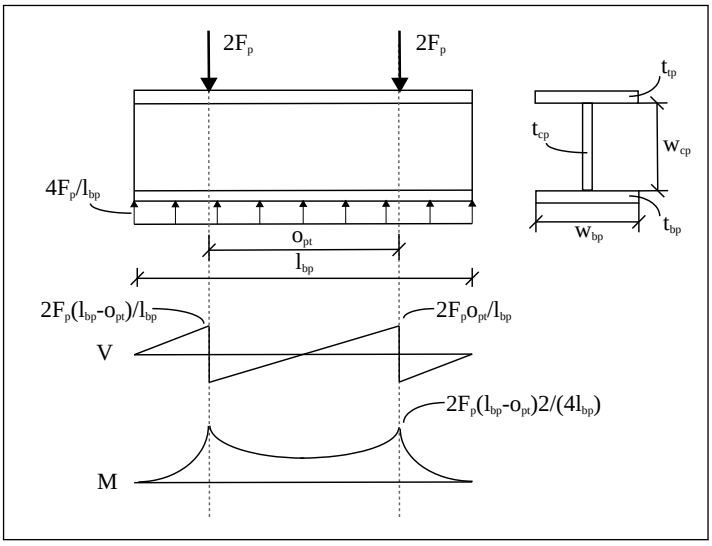

Longitudinal shear and moment capacity of the PT saddle at initial PT force

Similar to the check above, the longitudinal shear and moment capacity of the full PT saddle (with the top plate) was also checked at the initial PT bar force. This is the load case that this assembly would have experienced during pre-stressing of the PT bars. The procedure for this check is shown below. The full saddle assembly was modeled as an I beam and the peak shear and moment values were checked, as shown in the figure detailing the check and the demand calculations. The section properties shown in the previous section were used here. For this check the initial PT bar forces were used for the demand as this is the peak force experienced for this loading case.

CLT Wall Calculations

MPP Wall Calculations

Check longitudinal shear capacity during PT loading

Shear Deamands	γ =	-		Shear Deamands	γ =	-	
	V_u =	86	kip		V_u =	86	kip
Shear Capacity	φ =	0.9		Shear Capacity	φ =	0.9	
	φV_n =	162	kip		φV_n =	162	kip
DCR	$V_u/\varphi V_n$ =	0.53		DCR	$V_u/\varphi V_n$ =	0.53	

Demand:

$$V_u = \frac{4F_{pti}(l_{bp} - w_h)}{2l_{bp}}$$

Capacity:

$$\Phi V_n = \Phi 0.6 F_y A_w = \Phi 0.6 F_y w_{cp} t_{cp}$$

DCR:

$$DCR = \frac{V_u}{\Phi V_n}$$

Check longitudinal bending cpacity of PT loading

Moment Demands	γ =	-		Moment Demands	γ =	-	
	M_u =	667	k-in		M_u =	667	k-in
Moment Capacity	φ =	0.9		Moment Capacity	φ =	0.9	
	φM_n =	11976	k-in		φM_n =	11976	k-in
DCR	$M_u/\varphi M_n$ =	0.06		DCR	$M_u/\varphi M_n$ =	0.06	

Demand:

$$M_u = \frac{4F_{pti}(l_{bp} - w_h)^2}{8l_{bp}}$$

Capacity:

$$\Phi M_n = \Phi F_y S_x$$

DCR:

$$DCR = \frac{M_u}{\Phi M_n}$$

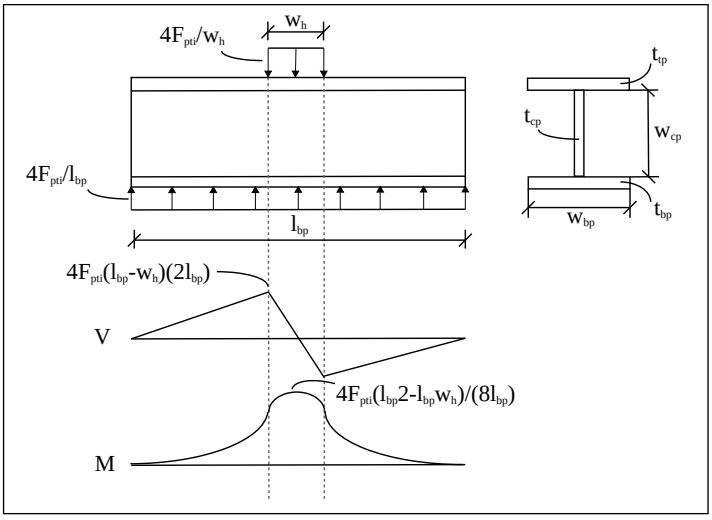

A.8.4 Top of Wall PT Jacking Hardware

Transverse shear and moment capacity of the PT jacking hardware

The transverse shear and moment capacity of the PT jacking hardware piece was checked using the procedure outlined below. Additionally, see the calculated transverse bending properties input into the design checks and the figure summarizing the basis of these equations. Note, this check is highly conservative as it just approximates the strength and stiffness of the full connection. An FEM model could have been created to develop a more economical design. For this check, the initial PT bar force was used to calculate the demand as these pieces were only used for initial post-tensioning purposes.

CLT Wall Calculations **MPP Wall Calculations**

Check transverse shear capacity of PT jacking hardware

Shear Deamands	γ =	-		Shear Deamands	γ =	-	
	V_u =	50	kip		V_u =	50	kip
Shear Capacity	φ =	0.9		Shear Capacity	φ =	0.9	
	φV_n =	729	kip		φV_n =	729	kip
DCR	$V_u/\varphi V_n$ =	0.07		DCR	$V_u/\varphi V_n$ =	0.07	

Demand:

$$V_u = F_{pti}$$

Capacity:

$$\Phi V_n = \Phi 0.6 F_y A_w = \Phi 0.6 F_y \frac{l_{ap} - w_h}{2} t_{ap}$$

DCR:

$$DCR = \frac{V_u}{\Phi V_n}$$

Check transverse moment capacity of PT jacking hardware

Moment Demands	γ =	-		Moment Demands	γ =	-	
	M_u =	331	k-in		M_u =	288	k-in
Moment Capacity	φ =	0.9		Moment Capacity	φ =	0.9	
	φM_n =	405	k-in		φM_n =	405	k-in
DCR	$M_u/\varphi M_n$ =	0.82		DCR	$M_u/\varphi M_n$ =	0.71	

Demand:

$$M_u = \frac{F_{pti}}{4}(2\, o_{pt} - w_h)$$

Capacity:

$$\Phi M_n = \Phi F_y S_x$$

DCR:

Transverse bending capacity of PT jacking hardware:

Area:	A =	27	27 in^2
Centroid:	y_c =	1	1 in
Moment of inertia:	I_x =	9.00	9.00 in^4
Elastic Section Modulus:	S_x =	9.00	9.00 in^3
Plastic neutral axis:	y_{pna} =	1	1 in

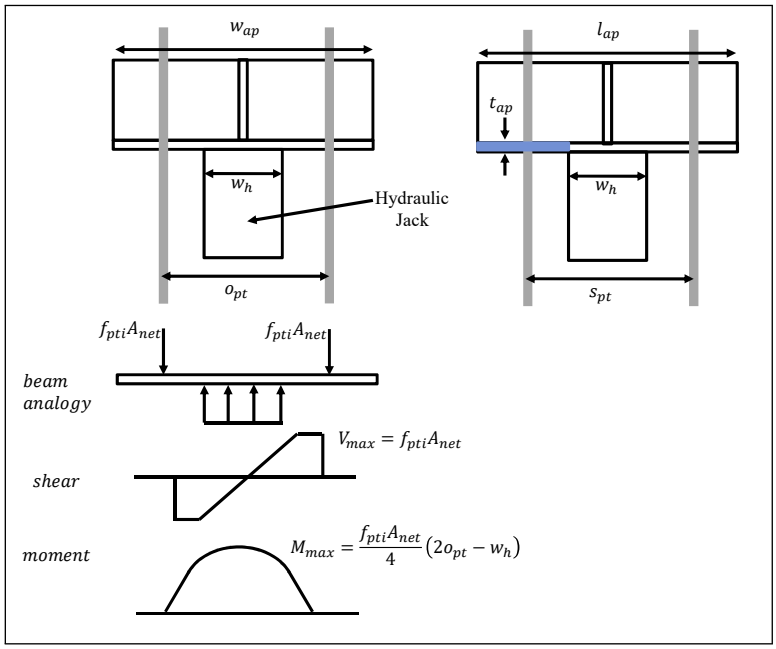

Longitudinal shear and moment capacity of the PT jacking hardware

Similar to the previous check, the longitudinal shear and moment capacity of the PT jacking hardware piece was checked using the procedure outlined below. Additionally, see the calculated longitudinal bending properties input into the design checks and the figure summarizing the basis of these equations. Note, this check is also highly conservative as it just approximates the strength and stiffness of the full connection. An FEM model could have been created to develop a more economical design. For this check, the initial PT bar force was used to calculate the demand as these pieces were only used for initial post-tensioning purposes.

CLT Wall Calculations **MPP Wall Calculations**

Check longitudinal shear capacity of PT jacking hardware

Shear Deamands	γ =	-		Shear Deamands	γ =	-	
	V_u =	50	kip		V_u =	50	kip
Shear Capacity	φ =	0.9		Shear Capacity	φ =	0.9	
	φV_n =	729	kip		φV_n =	729	kip
DCR	$V_u/\varphi V_n$ =	0.07		DCR	$V_u/\varphi V_n$ =	0.07	

Demand:

$$V_u = F_{pti}$$

Capacity:

$$\Phi V_n = \Phi 0.6 F_y A_w = \Phi 0.6 F_y \frac{w_{ap} - w_h}{2} t_{ap}$$

DCR:

$$DCR = \frac{V_u}{\Phi V_n}$$

Check longitudinal moment capacity of PT jacking hardware

Moment Demands	γ =	-		Moment Demands	γ =	-	
	M_u =	294	k-in		M_u =	294	k-in
Moment Capacity	φ =	0.9		Moment Capacity	φ =	0.9	
	φM_n =	405	k-in		φM_n =	405	k-in
DCR	$M_u/\varphi M_n$ =	0.73		DCR	$M_u/\varphi M_n$ =	0.73	

Demand:

$$M_u = \frac{F_{pti}}{4}(2\, s_{pt} - w_h)$$

Capacity:

$$\Phi M_n = \Phi F_y S_x$$

DCR:

$$DCR = \frac{M_u}{\Phi M_n}$$

Top Plate:			
Top plate width:	w_{tp} =	24	24.00 in
Top plate thickness:	t_{tp} =	0.75	0.75 in
Anchorage Plate:			
Anchorage plate length:	l_{ap} =	32	32 in
Anchorage plate width:	w_{ap} =	32	32 in
Anchorage plate thickness:	t_{ap} =	2	2 in

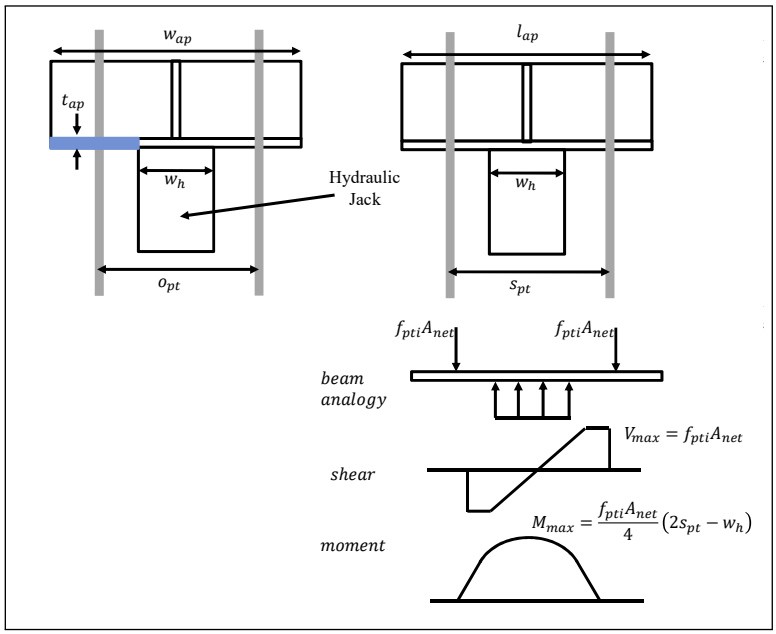
w_{ap}
t_{ap}
w_h
o_{pt}
Hydraulic Jack
l_{ap}
w_h
s_{pt}
$f_{pti}A_{net}$
$f_{pti}A_{net}$
beam analogy
$V_{max} = f_{pti}A_{net}$
shear
$M_{max} = \frac{f_{pti}A_{net}}{4}(2s_{pt} - w_h)$
moment

Appendix B

NHERI TALLWOOD DETAILED STRUCTURAL DRAWINGS

This appendix includes the full set of structural drawings for the NHERI TallWood building specimen. They were developed using a Revit model. All lateral details and connections were design as discussed within this dissertation. These lateral details were incorporated into the full building Revit model by Aleesha Busch at Colorado School of Mines [Busch, 2023].

Note, the gravity connection details included on page S720 of the drawing set were designed by Simpson Strong-Tie. The gravity column base connection are patented and at the time of publication of this document, the beam-to-column connections are patent pending.

SHEET INDEX

Sheet Number	Sheet Name	STEEL FABRICATION SET	Final Revision
S001	Drawing Index and List of Abbreviations	X	X
S002	General Structural Notes	X	X
S003	General Structural Notes	X	X
S101S	Foundation/Level 1 Plan - Structural	X	X
S102S	Level 2 Plan - Structural	X	X
S103S	Level 3 Plan - Structural	X	X
S104S	Level 4 Plan - Structural	X	X
S105S	Level 5 Plan - Structural	X	X
S106S	Level 6 Plan - Structural	X	X
S107S	Level 7 Plan - Structural	X	X
S108S	Level 8 Plan - Structural	X	X
S109S	Level 9 Plan - Structural	X	X
S110S	Level 10 Plan - Structural	X	X
S111S	Roof/Level 11 Plan - Structural	X	X
S201	Building Elevations	X	X
S202	Building Elevations	X	X
S301	Shear Wall Elevations	X	X
S302	Wall Panel Details	X	X
S501	Steel Foundation Details	X	X
S502	Concrete Foundation Details	X	X
S503	Concrete Foundation Details	X	X
S504	Concrete Foundation Steel Detailing	X	X
S505	Foundation Connection Details	X	X
S701	Simpson Gravity Details	X	X
S710	Diaphragm Details	X	X
S711	Sheathing Details		X
S720	Simpson Lateral Details	X	X
S721	Lateral Details	X	X
S722	Lateral Details	X	X
S723	Diaphragm to Wall Lateral Details	X	X
S724	Rocking Wall Wind Details	X	X
S725	Splice Details		X
S801	Stair Details		X
S802	Stair Details		X
S901	CLT Temp. Mounting Angles		X
S902	MPP 1 Temp. Mounting Angle		X
S903	MPP 2 Temp. Mounting Angle		X
S904	MPP 3 Temp. Mounting Angle		X

LIST OF ABBREVIATIONS

A.B.	ANCHOR BOLT
ACI	AMERICAN CONCRETE INSTITUTE
ADD'L.	ADDITIONAL
AESS	ARCHITECTURALLY EXPOSED STRUCTURAL STEEL
AISC	AMERICAN INSTITUTE OF STEEL CONSTRUCTION
ALT.	ALTERNATE
ALUM.	ALUMINUM
ARCH.	ARCHITECT / ARCHITECTURAL
ASCE	AMERICAN SOCIETY OF CIVIL ENGINEERS
ASD	ALLOWABLE STRENGTH DESIGN LOAD LEVEL
ASTM	AMERICAN SOCIETY FOR TESTING AND MATERIALS
AWS	AMERICAN WELDING SOCIETY
BLDG.	BUILDING
BOT.	BOTTOM
BRBF	BUCKLING RESTRAINED BRACED FRAME
C.G.	CENTER OF GRAVITY
C.I.P.	CAST IN PLACE
C.J.	CONTROL JOINT
C.J.P.	COMPLETE JOINT PENETRATION
CL	CENTERLINE
CLR.	CLEAR
CLT	CROSS LAMINATED TIMBER
CMU	CONCRETE MASONRY UNIT
COL.	COLUMN
CONC.	CONCRETE
CONN.	CONNECTION
CONST.	CONSTRUCTION
CONT.	CONTINUOUS
CW	CONNECTED WITH
db	BAR DIAMETER
DBA	DEFORMED BAR ANCHOR
DET.	DETAIL
DIA., Ø	DIAMETER
DIAG.	DIAGONAL
D.L.	DEAD LOAD
DLT	DOWEL LAMINATED TIMBER
DWG.	DRAWING
ELEC.	ELECTRICAL
EL.	ELEVATION
EQ.	EQUAL
EXIST., (E)	EXISTING
EXP.	EXPANSION
EXT.	EXTERIOR
FDN.	FOUNDATION
FIN.	FINISH
FLR.	FLOOR
FRT	FIRE RETARDANT TREATED
FT.	FOOT
FTG.	FOOTING
GA.	GAUGE
GALV.	GALVANIZED
GL	GLULAM
HORIZ.	HORIZONTAL
HSS	HOLLOW STRUCTURAL STEEL
IBC	INTERNATIONAL BUILDING CODE
I.D.	INSIDE DIAMETER
IN.	INCHES
INT.	INTERIOR
K	KIPS
KSF	KIPS PER SQUARE FOOT
KSI	KIPS PER SQUARE INCH
LBS.	POUNDS
L.L.	LIVE LOAD
LLH	LONG LEG HORIZONTAL
LLV	LONG LEG VERTICAL
LOC.	LOCATION
LONG.	LONGITUDINAL
LSL	LAMINATED STRAND LUMBER
LVF	LOW VELOCITY FASTENER
LVL	LAMINATED VENEER LUMBER
MAX.	MAXIMUM
MBMA	METAL BUILDING MANUFACTURERS ASSOCIATION
MECH.	MECHANICAL
MEPF	MECHANICAL, ELECTRICAL, PLUMBING AND FIRE SAFETY
MFR.	MANUFACTURER
MIN.	MINIMUM
MISC.	MISCELLANEOUS
MPH	MILES PER HOUR
MPP	MASS PLYWOOD PANELS
MT	MAGNETIC PARTICLE TESTING
(N)	NEW
N.I.C.	NOT IN CONTRACT
NLT	NAIL LAMINATED TIMBER
NOM.	NOMINAL
NO.	NUMBER
N.T.S.	NOT TO SCALE
o.c.	ON CENTER
O.D.	OUTSIDE DIAMETER
OPP.	OPPOSITE
OSL	ORIENTED STRAND LUMBER
OWJ	OPEN WEB JOIST
PAF	POWDER ACTUATED FASTENER
PART.	PARTITION
P/C	PRECAST
PCF	POUNDS PER CUBIC FOOT
PERIM.	PERIMETER
PL	PLATE
PP	PARTIAL PENETRATION
PSF	POUNDS PER SQUARE FOOT
PSL	PARALLEL STRAND LUMBER
PSI	POUNDS PER SQUARE INCH
P/T	POST-TENSIONED
P.T.	PRESSURE TREATED
PVC	POLYVINYL CHLORIDE
R, RAD.	RADIUS
RCSC	RESEARCH COUNCIL ON STRUCTURAL CONNECTIONS
REF.	REFERENCE
RET.	RETURN
REINF.	REINFORCING
REQ'D.	REQUIRED
REQMTS.	REQUIREMENTS
SCHED.	SCHEDULE
S.C.	SLIP CRITICAL
SCL	STRUCTURAL COMPOSITE LUMBER
SIM.	SIMILAR
SLFS	SEISMIC FORCE RESISTING SYSTEM
S.O.G.	SLAB ON GRADE
SPEC.	SPECIFICATION
SQ.	SQUARE
SS	STAINLESS STEEL
SSMA	STEEL STUD MANUFACTURERS ASSOCIATION
STD.	STANDARD
STRUCT.	STRUCTURAL
SYM.	SYMMETRICAL
THRU	THROUGH
T&G	TONGUE AND GROOVE
TRANS.	TRANSVERSE
TS	LIGHT GAUGE TUBE STEEL
TYP.	TYPICAL
U.N.O.	UNLESS NOTED OTHERWISE
U.T.	ULTRASONIC TESTING
ULT.	ULTIMATE STRENGTH DESIGN LOAD LEVEL
VERT.	VERTICAL
V.I.F.	VERIFY IN FIELD
w/	WITH
WF	WIDE FLANGE
w/o	WITHOUT
W.P.	WORK POINT
WPS	WELDING PROCEDURE SPECIFICATION
WWF	WELDED WIRE FABRIC

NHERI
TallWood
1500 Illinois St.
Golden, CO 80401
303-273-3932

PROJECT:

10-Story Test

10201 Pomerado Road
San Diego, CA 92131

SET ISSUANCE:

Revision 1

DATE ISSUED: 07/30/21

No.	Description	Date
1	Revision 1	07/30/21

SHEET SIZE: 30x42
DRAWN BY: ANB

SHEET:

Drawing Index and List of Abbreviations

S001

F:\10 Story CLT\Revit Files\10 Story Test 03-25-2023.rvt 4/5/2023 9:18:16 AM

GENERAL

STRUCTURAL DRAWINGS ARE A PART OF THE CONTRACT DOCUMENTS AND ARE COMPLEMENTARY TO THE OTHER CONTRACT DOCUMENTS. THE RESEARCH TEAM IS RESPONSIBLE FOR COORDINATING THE REQUIREMENTS FROM THE CONTRACT DOCUMENTS INTO THEIR SHOP DRAWINGS AND WORK. THE RESEARCH TEAM SHALL PROMPTLY REPORT TO THE RESEARCH TEAM ANY ERRORS, INCONSISTENCIES, OR OMISSIONS IN THE CONTRACT DOCUMENTS DISCOVERED BY OR MADE KNOWN TO THE RESEARCH TEAM.

NOTES AND DETAILS ON THE STRUCTURAL DRAWINGS SHALL TAKE PRECEDENCE OVER THE GENERAL STRUCTURAL NOTES AND TYPICAL DETAILS. WHERE NO DETAILS ARE GIVEN, CONSTRUCTION SHALL BE AS SHOWN FOR SIMILAR WORK. WHERE CONFLICT EXISTS, THE MORE STRINGENT OR RESTRICTIVE REQUIREMENT SHALL GOVERN UNTIL CLARIFICATION IS REQUESTED.

CODE REQUIREMENTS:
CONFORM TO THE 2015 INTERNATIONAL BUILDING CODE (IBC).

EXISTING CONDITIONS:
ALL EXISTING CONDITIONS, DIMENSIONS AND ELEVATIONS SHALL BE FIELD VERIFIED. THE CONTRACTOR SHALL NOTIFY THE RESEARCH TEAM OF ANY SIGNIFICANT DISCREPANCIES FROM CONDITIONS SHOWN ON THE DRAWINGS.

DESIGN CRITERIA

DESIGN WAS BASED ON THE STRENGTH AND DEFLECTION CRITERIA OF THE IBC IN ADDITION TO DEAD LOADS, THE FOLLOWING LOADS AND ALLOWABLES WERE USED FOR DESIGN:

GRAVITY SYSTEM CRITERIA		
OCCUPANCY OR USE	**UNIFORM LOAD**	**CONCENTRATED LOAD**
ALL AREAS EXCEPT AS NOTED BELOW	65 PSF L.L.	2,000 LBS
STORS	100 PSF L.L.	300 LBS
*VERTICAL FLOOR DEFLECTION (CLADDING DESIGN)	0.75" UP OR DOWN	
*VERTICAL FLOOR DEFLECTION (INTERIOR)	0.75" UP OR DOWN	
GRAVITY LOADING NOTES:	1. LIVE LOADS REDUCED PER IBC. 2. MEMBERS DESIGNED FOR MORE CRITICAL OF UNIFORM OR CONCENTRATED LOAD.	
WIND CRITERIA		
RISK CATEGORY	II	
MAIN WIND FORCE RESISTING SYSTEM (25 YEAR MRI)	V = 72 MPH BASIC DESIGN WIND SPEED (3-SECOND GUST)	
EXTERIOR COMPONENTS AND CLADDING (700 YEAR MRI)	V = 96 MPH BASIC DESIGN WIND SPEED (3-SECOND GUST)	
INTERIOR COMPONENTS AND CLADDING	V = 64 MPH BASIC DESIGN WIND SPEED (3-SECOND GUST)	
EXPOSURE CATEGORY	C	
SEISMIC CRITERIA		
RISK CATEGORY	II	
SEISMIC DESIGN CATEGORY	D	
SITE CLASS	C	
IMPORTANCE FACTOR	$I_E = 1.0$	
MCE SPECTRAL ACCELERATION	$S_s = 1.378$	$S_1 = 0.48$
SITE COEFFICIENT	$F_a = 1.2$	$F_v = 1.5$
MCER SPECTRAL ACCELERATION	$S_{MS} = 1.654$	$S_{M1} = 0.72$
DESIGN SPECTRAL ACCELERATION	$S_{DS} = 1.102$	$S_{D1} = 0.48$
ANALYSIS PROCEDURE	NONLINEAR RESPONSE HISTORY ANALYSIS	
SEISMIC FORCE RESISTING SYSTEM (SFRS)	X DIRECTION (EAST / WEST) POST-TENSIONED ROCKING MASS TIMBER SHEAR WALLS	Y DIRECTION (NORTH / SOUTH) POST-TENSIONED ROCKING MASS TIMBER SHEAR WALLS
CRITERIA FOR DELEGATED DESIGN ITEMS		
GENERAL CRITERIA	AS INDICATED ABOVE UNDER "GRAVITY SYSTEM CRITERIA", "WIND CRITERIA" AND "SEISMIC CRITERIA"	
MCE STORY DRIFT	XX* FOR EACH STORY BETWEEN LEVEL 2 AND XX XX** FOR EACH STORY BETWEEN LEVEL XX AND ROOF	
SEISMIC FORCES	IN ACCORDANCE WITH ASCE 7-16 SECTION 13.3.1.1 AND REPLACING S_{DS} WITH S_{MS} AND SETTING Rx TO 1.0.	

SUBMITTALS

SUBMIT SHOP DRAWINGS AND OTHER SUBMITTALS TO THE RESEARCH TEAM PRIOR TO FABRICATION AND CONSTRUCTION. ANY CHANGES TO THE CONTRACT DRAWINGS SHALL BE CLEARLY IDENTIFIED AND ARE SUBJECT TO REVIEW AND ACCEPTANCE BY THE RESEARCH TEAM.

FIELD ENGINEERED DETAILS DEVELOPED BY THE CONTRACTOR THAT DIFFER FROM OR ADD TO THE CONTRACT DRAWINGS SHALL BE CLEARLY IDENTIFIED AND ARE SUBJECT TO REVIEW AND ACCEPTANCE BY THE RESEARCH TEAM PRIOR TO CONSTRUCTION.

THE USE OF REPRODUCTIONS OF PHOTOCOPIES OF THE CONTRACT DRAWING S SHALL NOT BE PERMITTED WHEN CAD DURING IT FILES ARE PROVIDED TO THE CONTRACTOR OR SUBCONTRACTORS, IT IS THE RESPONSIBILITY OF THE CONTRACTOR/SUBCONTRACTOR TO REMOVE ALL INFORMATION NOT DIRECTLY RELEVANT TO THE SCOPE OF THE SUBMITTAL AS WELL AS ALL REFERENCES TO OUTSIDE SOURCE FILES.

DELEGATED DESIGN SUBMITTALS SHALL INCLUDE DESIGN DRAWINGS AND CALCULATIONS FOR ITEMS THAT ARE DESIGNED BY OTHERS. DELEGATED DESIGN SUBMITTALS SHALL BE SUBMITTED TO THE RESEARCH TEAM AND ARE SUBJECT TO REVIEW AND ACCEPTANCE PRIOR TO FABRICATION. CALCULATIONS SHALL BE INCLUDED FOR ALL CONNECTIONS TO THE STRUCTURE, CONSIDERING LOCALIZED EFFECTS ON STRUCTURAL ELEMENTS.

SUBMITTALS AND DELEGATED DESIGN SUBMITTALS SHALL INCLUDE THE FOLLOWING:

ITEM	SUBMITTAL	DELEGATED DESIGN SUBMITTAL	COMMENTS
CONCRETE MIX DESIGNS	X		
CONCRETE REINFORCEMENT AND PRETENSIONING STEEL	X		
EMBEDDED STEEL ITEMS	X		
STEEL FOUNDATION ELEMENTS	X		
GLULAM AND LVL BEAM/COLUMN MEMBERS AND ASSOCIATED HARDWARE	X		
CLT, DLT AND GLULAM FLOOR PANELS AND ASSOCIATED HARDWARE	X		
CLT AND MPP WALL PANELS AND ASSOCIATED HARDWARE	X		
EXTERIOR AND INTERIOR COLD FORMED METAL FRAMING		X	REF. TABLE NOTE 1
CURTAIN WALL, WINDOW WALL AND OTHER CLADDING AND GLAZING SYSTEMS		X	REF. TABLE NOTE 1
SEATING		X	REF. TABLE NOTE 1
MEP/FP SYSTEM ANCHORAGE AND BRACING		X	REF. TABLE NOTE 1
PENETRATIONS OF SLABS/DECKS, WALLS, ETC.	X		REF. TABLE NOTE 2

TABLE NOTES:
1. DESIGN SHALL BE BASED ON THE REQUIREMENTS OF THE IBC AND AS NOTED UNDER "CRITERIA FOR DELEGATED DESIGN ITEMS".
2. CONTRACTOR SHALL COORDINATE AND SHOW ALL REQUIRED PENETRATIONS, WITH DIMENSIONS FOR MECHANICAL, ELECTRICAL, PLUMBING, FIRE PROTECTION, TECHNOLOGY AND OTHER SERVICES ON A SINGLE DRAWING FOR REVIEW AT EACH SLAB/DECK, STRUCTURAL WALL AND/OR BEAM.

SPECIAL RESEARCH OBSERVATIONS

THE RESEARCH TEAM WILL PERFORM SPECIAL RESEARCH OBSERVATIONS AT THE STAGES OF CONSTRUCTION LISTED BELOW. CONTRACTOR SHALL PROVIDE SUFFICIENT ADVANCE NOTICE AND ACCESS FOR THE RESEARCH TEAM TO PERFORM THESE OBSERVATIONS.

ITEM	COMMENTS
DURING INITIAL WOOD FRAMING CONSTRUCTION	
DURING MASS TIMBER SHEAR WALL CONSTRUCTION	AFTER FIRST WALL IS ERECTED
DURING DIAPHRAGM PANEL TO PANEL CONNECTION AND CHORD COLLECTOR CONSTRUCTION	AFTER FIRST LEVEL IS INSTALLED
DURING DIAPHRAGM TO WALL CONNECTION CONSTRUCTION	AFTER FIRST CONNECTION IS FULLY INSTALLED
DURING PLACEMENT OF STEEL MASS PLATES	
DURING UPP CONNECTION CONSTRUCTION	AFTER FIRST CONNECTION IS FULLY INSTALLED
DURING SECOND ROCKING JOINT CONSTRUCTION	
DURING POST-TENSIONING OF MASS TIMBER SHEAR WALLS	
AS REQUIRED TO ADDRESS ISSUES	

SPECIAL CONSTRUCTION SEQUENCE CONSIDERATIONS

THE STRUCTURE IS DESIGNED TO FUNCTION AS A UNIT UPON COMPLETION. THE CONTRACTOR IS RESPONSIBLE FOR FURNISHING ALL TEMPORARY BRACING AND/OR SUPPORT THAT MAY BE REQUIRED AS THE RESULT OF THE CONTRACTOR'S CONSTRUCTION METHODS AND/OR SEQUENCES UNTIL COMPLETION.

CONTRACTOR'S CONSTRUCTION AND/OR ERECTION SEQUENCES SHALL RECOGNIZE AND CONSIDER THE EFFECTS OF THERMAL MOVEMENTS OF STRUCTURAL ELEMENTS DURING THE CONSTRUCTION PERIOD.

ADDITIONALLY, THE CONTRACTOR SHALL COMPLY WITH THE FOLLOWING SPECIAL CONSTRUCTION SEQUENCE CONSIDERATIONS:

ITEM	INSTRUCTION
SHEAR WALL BASE TEMPORARY HOLD-DOWNS	TEMPORARY HOLDDOWNS TO RESIST LOADS DURING CONSTRUCTION SHALL BE IN PLACE AT THE BASE OF ALL CLT/MPP SHEAR WALLS UNTIL POST-TENSIONING HAS BEEN COMPLETED
UPP INSTALLATION	UPPS SHALL BE LOOSELY INSTALLED FOR DOWEL ACTION AT CLT/MPP SHEAR WALLS HAS BEEN COMPLETED.
RE-TENSIONING OF POST-TENSIONING BARS	CONTRACTOR SHALL PLAN FOR ONE (1) ADDITIONAL RE-TENSIONING OF POST-TENSIONING BARS AFTER INITIAL POST-TENSIONING

MASS TIMBER

MASS TIMBER CONSTRUCTION INCLUDES CROSS-LAMINATED TIMBER (CLT), NAIL-LAMINATED TIMBER (NLT), DOWEL-LAMINATED TIMBER (DLT), MASS PLYWOOD PANELS (MPP), GLUE-LAMINATED TIMBER (GLT) MEMBERS, MASS TIMBER PANELS (MTP), AND LAMINATED VENEER LUMBER (LVL) MEMBERS.

THE CONTRACTOR IS RESPONSIBLE FOR PROTECTING MASS TIMBER FROM MOISTURE, ENVIRONMENTAL EFFECTS, AND CONSTRUCTION ACTIVITIES DURING CONSTRUCTION. THE CONTRACTOR SHALL REPAIR ANY DAMAGE THAT COMPROMISES THE APPEARANCE OR STRUCTURAL PERFORMANCE OF MASS TIMBER FRAMING AT THE DIRECTION OF THE RESEARCH TEAM.

CONTRACTOR SHALL COORDINATE MASS TIMBER FABRICATION AND ERECTION TOLERANCES WITH OTHER MATERIALS INCLUDING STEEL AND CONCRETE.

CROSS-LAMINATED TIMBER (CLT) AND MASS PLYWOOD PANEL (MPP)

CROSS-LAMINATED TIMBER (CLT) AND MASS PLYWOOD PANEL (MPP) MEMBERS SHALL BE MANUFACTURED IN CONFORMANCE WITH CURRENT ANSI/APA PRG 320 STANDARD FOR PERFORMANCE-RATED CROSS-LAMINATED TIMBER UNLESS NOTED OTHERWISE. DEMONSTRATION OF EQUIVALENCE SHALL BE RESPONSIBILITY OF THE MANUFACTURER. ONE COAT OF END SEALER SHALL BE APPLIED IMMEDIATELY AFTER TRIMMING IN EITHER THE SHOP OR IN THE FIELD.

PANELS SHALL BE WITH LAYUPS AS NOTED ON THE STRUCTURAL PLANS AND OF MINIMUM ALLOWABLE DESIGN PROPERTIES INDICATED BELOW:

CLT/MPP LAYUP, GRADE AND USE	THICKNESS tp (INCHES)	MAJOR STRENGTH PROPERTIES				MINOR STRENGTH PROPERTIES			
		Fb (PSI)	E (10^6 PSI)	Ft (PSI)	Fc (PSI)	Fb (PSI)	E (10^6 PSI)	Ft (PSI)	Fc (PSI)
CLT 5 OR FLOORS	6.875	X	X	X	X	X	X	X	X
FREERS FTB MPP6 FOR SHEAR WALLS	9	X	X	X	X	X	X	X	X
SMARTLAM CLT9 FOR SHEAR WALLS	1.2375	2400	2.0	1925	1975	1000	1.6	650	1400

UNLESS OTHERWISE NOTED ON PLAN, CLT/MPP FLOOR PANELS SHALL BE ORIENTED WITH EXTERIOR LAYERS PERPENDICULAR TO SUPPORTS. REFERENCE PLAN FOR SPLINE AND PANEL EDGE LOCATIONS. CLT/MPP PRODUCTS SHALL CONTAIN AVERAGE MOISTURE CONTENT OF 12% +/- 2% OR LESS AT TIME OF MANUFACTURE.

CONNECTIONS SHALL BE SHOP FABRICATED TO GREATEST EXTENT INCLUDING CUTTING TO LENGTH AND DRILLING HOLES. NOTCHES, DAPS, HOLES, ETC. SHALL BE REPRESENTED ON SHOP DRAWINGS FOR REVIEW BY RESEARCH TEAM. FIELD NOTCHING AND BORING OF CLT/MPP MEMBERS IS NOT ALLOWED UNLESS APPROVED BY RESEARCH TEAM.

NAIL-LAMINATED TIMBER (NLT) AND DOWEL-LAMINATED TIMBER (DLT)

NAIL-LAMINATED TIMBER (NLT) AND DOWEL-LAMINATED TIMBER (DLT) PANELS SHALL BE COMPOSED OF DIMENSIONAL LUMBER SIZE AND GRADE AS NOTED ON THE STRUCTURAL PLANS. INDIVIDUAL BOARDS IN NLT PANELS SHALL BE ARRANGED SUCH THAT END JOINTS IN ADJACENT COURSES ARE STAGGERED AT MIN. END JOINTS THAT ALIGNED ARE FASTENED TOGETHER WITH NAILS. INDIVIDUAL BOARDS IN DLT PANELS SHALL BE ARRANGED SUCH THAT ENDS ARE FASTENED TOGETHER WITH NAILS. INDIVIDUAL BOARDS IN DLT PANELS SHALL BE MANUFACTURED WITH PRE-PLUGGED ENDS AND FASTENED TOGETHER WITH HARDWOOD DOWELS. TWO COATS OF END SEALER SHALL BE APPLIED IMMEDIATELY AFTER TRIMMING IN EITHER THE SHOP OR IN THE FIELD.

PANELS SHALL BE AS NOTED ON THE STRUCTURAL PLANS AND OF MINIMUM ALLOWABLE DESIGN PROPERTIES INDICATED BELOW:

DLT LAYUP, GRADE AND USE	THICKNESS tp (INCHES)	MAJOR STRENGTH PROPERTIES			
		XX	XX	XX	XX
XX FOR FLOORS	XX	X	X	X	X

UNLESS OTHERWISE NOTED ON PLAN, NLT/DLT FLOOR PANELS SHALL BE ORIENTED WITH STRONG AXIS PERPENDICULAR TO SUPPORTS. REFERENCE PLAN FOR SPLINE AND PANEL EDGE LOCATIONS. NLT/DLT PRODUCTS SHALL CONTAIN AVERAGE MOISTURE CONTENT OF 12% +/- 2% OR LESS AT TIME OF MANUFACTURE.

CONNECTIONS SHALL BE SHOP FABRICATED TO GREATEST EXTENT INCLUDING CUTTING TO LENGTH AND DRILLING HOLES. NOTCHES, DAPS, HOLES, ETC. SHALL BE REPRESENTED ON SHOP DRAWINGS FOR REVIEW BY RESEARCH TEAM. FIELD NOTCHING AND BORING OF NLT/DLT MEMBERS IS NOT ALLOWED UNLESS APPROVED BY RESEARCH TEAM.

GLUED-LAMINATED MEMBERS

GLUED-LAMINATED (GLULAM) MEMBERS SHALL BE FABRICATED IN CONFORMANCE WITH CURRENT ANSI STANDARD A190.1 - AMERICAN NATIONAL STANDARD FOR STRUCTURAL GLUED LAMINATED TIMBER OR OTHER CODE- APPROVED DESIGN, MANUFACTURING AND/OR QUALITY ASSURANCE PROCEDURES. EACH MEMBER SHALL BEAR AN ITC OR APA-BWI IDENTIFICATION MARK OR BE ACCOMPANIED BY A CERTIFICATE OF CONFORMANCE. APA-BWI MARKS TO BE PLACED ON SURFACES NOT EXPOSED IN COMPLETED CONSTRUCTION. ONE COAT OF END SEALER SHALL BE APPLIED IMMEDIATELY AFTER TRIMMING IN EITHER THE SHOP OR IN THE FIELD.

GLULAM MEMBERS SHALL BE OF MINIMUM ALLOWABLE DESIGN PROPERTIES AS ESTABLISHED BY ASTM D3737:

GLUED-LAMINATED PANELS				
COMBINATION SYMBOL (SPECIES)	**FLEXURAL STRESS, Fb (PSI)**	**HORIZONTAL SHEAR STRESS Fv (PSI)**	**COMPRESSION STRESS PERP TO GRAIN Fc,perp (PSI)**	**MODULUS OF ELASTICITY (PSI)**
XX	XX	XX	XX	XX

GLULAM PRODUCTS SHALL CONTAIN AVERAGE MOISTURE CONTENT OF 15% OR LESS AT TIME OF MANUFACTURE.

CONNECTIONS SHALL BE SHOP FABRICATED TO GREATEST EXTENT INCLUDING CUTTING TO LENGTH AND DRILLING HOLES. NOTCHES, DAPS, HOLES, ETC. SHALL BE REPRESENTED ON SHOP DRAWINGS FOR REVIEW BY RESEARCH TEAM. FIELD NOTCHING AND BORING OF GLULAM MEMBERS IS NOT ALLOWED UNLESS APPROVED BY RESEARCH TEAM.

WOOD STRUCTURAL PANELS

THE TERM "WOOD STRUCTURAL PANEL" REFERS TO A WOOD-BASED PANEL PRODUCT BONDED WITH A WATERPROOF ADHESIVE AND COVERS BOTH PLYWOOD AND ORIENTED STRAND BOARD (OSB). WOOD STRUCTURAL PANELS SHALL CONFORM TO U.S. DEPARTMENT OF COMMERCE VOLUNTARY PRODUCT STANDARDS PS1 OR PS2 FOR WOOD-BASED STRUCTURAL USE, OR APA PERFORMANCE STANDARD PRP-108 (ICC-ES ESR-2586). PANELS SHALL BE APA RATED SHEATHING, EXTERIOR EXPOSURE 1, OF THE THICKNESS AND SPAN RATING SHOWN ON THE DRAWINGS. PANELS SHALL BE STAMPED WITH THE APA TRADEMARK.

NAIL AND SCREW HEADS SHALL BE DRIVEN FLUSH WITH SHEATHING. DO NOT PENETRATE SURFACE PLY WITH NAIL AND SCREW HEADS. IF NAIL AND SCREW HEADS ARE NOT FLUSH NOTIFY THE RESEARCH TEAM. CONTRACTOR IS RESPONSIBLE FOR ANY REPAIRS NECESSARY DUE TO OVER-PENETRATION OF NAILS OR SCREWS.

LAMINATED VENEER LUMBER

LAMINATED VENEER LUMBER (LVL) MEMBERS SHALL HAVE THE FOLLOWING MINIMUM DESIGN PROPERTIES:

LVL MINIMUM PROPERTIES		
FLEXURAL STRESS, Fb (PSI)	**COMPRESSIVE STRESS, Fc (PSI)**	**MODULUS OF ELASTICITY, E (PSI)**
2,600	3,000	1,700,000

PROPERTIES NOTED ABOVE ARE FOR A 12-INCH MEMBER. DEEPER MEMBERS SHALL BE DESIGNED FOR REDUCED STRESSES PER THE MANUFACTURER'S REQUIREMENTS.

SAWN LUMBER

SAWN LUMBER SHALL CONFORM TO THE REQUIREMENTS AS INDICATED IN THE CURRENTLY ACCEPTED NATIONAL DESIGN SPECIFICATION (NDS) DESIGN VALUES FOR WOOD CONSTRUCTION AND CONFORMING TO THE WEST COAST LUMBER INSPECTION BUREAU OR WESTERN WOOD PRODUCTS ASSOCIATION GRADING RULES. LUMBER SHALL BE THE SPECIES, GRADE, AND MOISTURE CONTENT NOTED BELOW, U.N.O.:

USE	SPECIES AND GRADE	MOISTURE CONTENT
LUMBER 2" TO 3" THICK x 4" TO 6" WIDE	DOUGLAS FIR-LARCH STUD	S-DRY, MC 15, ND

ALL LUMBER IN CONTACT WITH CONCRETE SHALL BE PRESERVATIVE TREATED. UNLESS AN APPROVED MOISTURE BARRIER IS PROVIDED.

WOOD NAILS

ALL FRAMING NAILS SHALL BE THE SIZE AND QUANTITY INDICATED AND CONFORM TO ASTM F 1667, INCLUDING SUPPLEMENT 1, "STANDARD SPECIFICATION OF DRIVEN FASTENERS: NAILS, SPIKES, AND STAPLES" AND ICC-ES REPORT ESR-1539 "POWER-DRIVEN STAPLES AND NAILS". NAILS SHALL BE IDENTIFIED BY LABELS ATTACHED TO THEIR PACKAGING. NAILS NOT IDENTIFIED BY LABELS SHALL BE ACCOMPANIED BY REPORTS INDICATING DIAMETER AND LENGTH AND SHALL BE SUBMITTED TO THE RESEARCH TEAM PRIOR TO FRAMING. THE FOLLOWING NAIL SIZES SHALL BE USED WITH THE NAIL LENGTH DETERMINED BY MINIMUM PENETRATION INTO FRAMING MEMBER:

FRAMING NAILS		
NAIL TYPE	**SHANK DIAMETER (IN.)**	**MINIMUM PENETRATION INTO FRAMING MEMBER (IN.)**
6d	0.113	1.125
8d	0.131	1.375
10d	0.148	1.5
12d	0.148	1.5
16d	0.162	1.5

BOLTS AND LAG SCREWS SHALL CONFORM TO ANSI/ASME STANDARD B18.2.1. ALL BOLTS AND LAG SCREWS SHALL BE INSTALLED WITH STANDARD CUT WASHERS.

WOOD SCREWS

STRUCTURAL SCREWS FOR WOOD-TO-WOOD AND WOOD-TO-STEEL CONNECTIONS SHALL BE AS SHOWN IN THE STRUCTURAL DRAWINGS.

STRUCTURAL SCREWS SHALL BE AS FOLLOWS AS NOTED ON THE STRUCTURAL DRAWINGS:

SCREW NAME	EVALUATION REPORT	SCREW ABBREVIATION
SIMPSON STRONG DRIVE SDS SCREW	ICC ESR-2236	SDS
SIMPSON STRONG DRIVE SDWS SCREW	UES ER-192	SDWS

SCREWS SHALL BE INSTALLED IN STRICT CONFORMANCE WITH THE MANUFACTURER'S RECOMMENDATIONS AND PRODUCT EVALUATION REPORTS.

WHERE COUNTERSUNK SCREWS ARE INSTALLED AT 90 DEGREE IN STEEL-TO-WOOD CONNECTIONS, PREPARE STEEL PLATE TO RECEIVE COUNTERSUNK HEAD. FOR SCREWS INSTALLED AT 45 DEGREES IN STEEL-TO-WOOD CONNECTIONS PROVIDE 45 DEGREE CUP WASHER OR PREPARE STEEL PLATE TO RECEIVE SCREW HEAD AS INDICATED ON DRAWINGS.

REQUESTS FOR SCREW SUBSTITUTIONS SHALL BE SUBMITTED TO THE RESEARCH TEAM IN WRITING ALONG WITH PRODUCT EVALUATION REPORT AND EVIDENCE OF EQUAL OR GREATER CAPACITY TO THE SPECIFIED CONNECTION.

CONTRACTOR IS RESPONSIBLE FOR NOTIFYING RESEARCH TEAM IF SPLITTING OF WOOD OR FASTENER BREAK IS OBSERVED DURING INSTALLATION. FASTENERS ARE TO BE INSTALLED IN SINGLE DRIVE AND SHALL NOT BE BACKED OUT AND RE-DRIVEN.

NHERI
TallWood
1500 Illinois St.
Golden, CO 80401
303-273-3932

PROJECT:

10-Story Test

10201 Pomerado Road
San Diego, CA 92131

SET ISSUANCE:

Revision 1

DATE ISSUED: 07/30/21

No.	Description	Date
1	Revision 1	07/30/21

SHEET SIZE: 30x42
DRAWN BY: ANB

SHEET:

General Structural Notes

S002

4/5/2023 9:18:16 AM

F:\10 Story CLT\Revit Files\10 Story Test.03-25-2023.rvt

STRUCTURAL STEEL

STRUCTURAL STEEL SHALL BE OF THE MATERIAL AND TYPE LISTED BELOW, U.N.O.:

STRUCTURAL STEEL	
SHAPE	MATERIAL GRADE
WIDE FLANGE SHAPES	ASTM A992, GRADE 50
PLATES U.N.O.	ASTM A572, GRADE 50
PLATES, AS NOTED	ASTM A36
CHANNELS AND ANGLES	ASTM A36
HOLLOW STRUCTURAL SECTIONS (RECTANGULAR)	ASTM A500, GRADE C (Fy=50KSI)
HOLLOW STRUCTURAL SECTIONS (ROUND)	ASTM A500, GRADE C (Fy=46KSI)
PIPES	ASTM A53, GRADE B (Fy=35 KSI)

DESIGN, DETAILING, FABRICATION, AND ERECTION SHALL BE IN ACCORDANCE WITH THE "AISC SPECIFICATION FOR THE DESIGN, FABRICATION, AND ERECTION OF STRUCTURAL STEEL FOR BUILDINGS" WITH "COMMENTARY" AND THE "CODE OF STANDARD PRACTICE FOR STEEL BUILDINGS AND BRIDGES", WITH THE FOLLOWING CLARIFICATIONS AND ADDITIONS:

1. CLAUSE 7 SECTIONS 7.5.1 AND 7.5.3 AS FOLLOWS:
   EMBEDMENT LOCATION DRAWINGS SHALL BE SUBMITTED TO THE RESEARCH TEAM FOR INFORMATION ONLY. THE RESEARCH TEAM IS NOT RESPONSIBLE FOR THE APPROVAL OF EMBEDMENT LOCATION DRAWINGS.
2. ADD THE FOLLOWING PARAGRAPH TO SECTION 7.10.3:
   "THE ERECTOR SHALL HAVE THE SOLE RESPONSIBILITY FOR DETERMINING THE MEANS AND METHODS USED TO PROPERLY AND ADEQUATELY BRACE THE FRAMING DURING ERECTION."

BOLTS SHALL CONFORM TO THE ASTM AND RCSC SPECIFICATIONS FOR JOINTS USING HIGH STRENGTH BOLTS. BOLTS SHALL BE ASTM F3125 GRADE A325 AND GRADE A490 WHERE NOTED, AND SNUG-TIGHT UNLESS NOTED OTHERWISE.

WELDING SHALL CONFORM TO THE AWS CODES FOR ARC AND GAS WELDING IN BUILDING CONSTRUCTION. WELDING SHALL BE PERFORMED IN ACCORDANCE WITH A WELDING PROCEDURE SPECIFICATION (WPS) AS REQUIRED IN AWS D1.1. THE WPS VARIABLES SHALL BE WITHIN THE PARAMETERS ESTABLISHED BY THE FILLER-METAL MANUFACTURER. FOR MEMBERS INCLUDED IN THE SEISMIC FORCE RESISTING SYSTEM, REQUIREMENTS OF AWS D1.8 SHALL APPLY.

FOR MEMBERS AND CONNECTIONS THAT ARE PART OF THE SEISMIC FORCE RESISTING SYSTEM, DISCONTINUITIES CREATED BY ERRORS OR BY FABRICATION OR ERECTION PERATIONS, SUCH AS TACK WELDS, ERECTION AIDS, AIR-ARC GOUGING, AND FLAME CUTTING, SHALL BE REPAIRED AS REQUIRED BY THE RESEARCH TEAM.

WELDS SHALL BE MADE USING E70XX ELECTRODES AND SHALL BE 3/16" MINIMUM, UNLESS OTHERWISE NOTED. WELDING SHALL BE BY AWS CERTIFIED WELDERS.

NON-SHRINK GROUT USED UNDER BEARING AND BASE PLATES SHALL BE ASTM C 1107, FACTORY-PACKAGED, NONMETALLIC AGGREGATE GROUT, NONCORROSIVE, NONSTAINING, MIXED WITH WATER TO CONSISTENCY SUITABLE FOR APPLICATION AND A 30-MINUTE WORKING TIME. GROUT STRENGTH SHALL BE 8,000 PSI MINIMUM AT 28 DAYS.

ALL STEEL ASSEMBLIES IN CONTACT WITH WOOD SHALL BE SHOP PRIMED AT A MINIMUM. CONTRACTOR IS RESPONSIBLE FOR CLEANING STEEL RESIDUE AFTER FIELD CUTTING AND FIELD WELDING PRIOR TO THE ERECTION OF EXPOSED WOOD MEMBERS.

COLD-FORMED METAL FRAMING

STEEL STUDS SHALL BE C-STUDS WITH A MINIMUM YIELD STRENGTH OF 33,000 PSI FOR 33 AND 43 MIL AND 50,000 PSI FOR 54, 68 AND 97 MIL THICKNESSES. GAUGE PLATE AND STRAPS SHALL HAVE A MINIMUM YIELD STRENGTH OF 33,000 PSI FOR 33 AND 43 MIL AND 50,000 PSI FOR 54, 68 AND 97 MIL THICKNESSES.

THE AMERICAN IRON AND STEEL INSTITUTE AND STEEL STUD MANUFACTURERS ASSOCIATION (SSMA) STANDARDS ARE USED IN THIS PACKAGE. PRODUCTS USED SHALL MEET OR EXCEED AISI STANDARDS AND ARE DESIGNATED BY THE FOLLOWING FOUR-PART IDENTIFICATION CODE, WITH ALL DIMENSIONS IN 1/100 INCHES:

EXAMPLE: 362 S 162 - 33

- 362 — INDICATES WEB DEPTH (IN 1/100 OF AN INCH)
- S — INDICATES SHAPE STYLE (S, T, U OR F)
- 162 — INDICATES FLANGE WIDTH (IN 1/100 OF AN INCH)
- 33 — INDICATES MATERIAL MIL THICKNESS (1 MIL = 1/1,000 INCH)

PROVIDE BRIDGING ADEQUATE TO DEVELOP THE FULL MOMENT CAPACITY OF STUDS IN CONFORMANCE WITH THE STEEL STUD MANUFACTURERS ASSOCIATION'S (SSMA) RECOMMENDATIONS.

ALL FIELD CUTTING OF STUDS MUST BE BY SAWING, SHEARING, OR PLASMA CUTTING. OTHER CUTTING METHODS OF COLD-FORMED MEMBERS ARE NOT ALLOWED, UNLESS NOTED OTHERWISE. NO NOTCHING OR DOPING OF STUDS AND NO SPLICING OF WALL STUDS OR HEADERS IS ALLOWED. CONTRACTOR TO ENSURE PUNCH OUT ALIGNMENT WHEN ASSEMBLING LATERAL BRACING AND FIELD CUTTING STUDS TO LENGTH. ALL HEADERS BUILT-UP BEAMS ARE TO BE CONSTRUCTED WITH UNPUNCHED MATERIAL ONLY.

COLD-FORMED FRAMING CONNECTIONS SHALL BE AS FOLLOWS:

COLD-FORMED METAL FRAMING CONNECTIONS	
FASTENER	PRODUCT
SCREWS	ELCO DRIL-FLEX OR HILTI KWIK-FLEX (ESR-3332)
NUTS	HILTI X-U (ESR-2269)

FOR SCREWS, PROVIDE 3/4" MINIMUM CLEARANCE FROM ALL EDGES AND 3/4" MINIMUM CENTER TO CENTER SPACING. FASTENERS OF COMPARABLE SPECIFICATIONS AND LOAD CAPACITIES MAY BE SUBMITTED FOR APPROVAL.

WELDING SHALL CONFORM WITH AWS D1.3.

CONCRETE MIX DESIGNS

CONCRETE WORK SHALL CONFORM TO CHAPTER 19 OF THE IBC. CONCRETE STRENGTHS SHALL BE VERIFIED BY STANDARD CYLINDER TESTS PER ASTM C39. CONCRETE MIX TO BE DESIGNED AND PROPORTIONED BY THE CONTRACTOR IN ACCORDANCE WITH ACI 318-14 CHAPTER 26. ACI 301-16 CHAPTER 4 AND THE FOLLOWING INFORMATION:

MIX ID	USE	f'c (PSI)	TEST AGE (DAYS)	MAX. W/CM RATIO (NOTE 1)	MAX. AGG. SIZE	EXPOSURE CLASS			
A	MILD FOUNDATION SLABS	5,000	28	N/A	3/4"	F1	S0	W0	C1

TABLE NOTES:
1. ESTABLISH W/CM RATIO BASED ON STRENGTH, NOT MAXIMUM. CONTRACTOR TO SUBMIT MIX DESIGN FOR REVIEW.
2. REF. ACI 318-14 TABLE 19.3.2.1 FOR ADDITIONAL MIX REQUIREMENTS SPECIFIC TO EXPOSURE CLASS.
3. ORDERING 8,000 PSI READY MIX SUCH THAT THE SLABS CAN BE MOVED EARLY.

A WATER-REDUCING ADMIXTURE CONFORMING TO ASTM C494 USED IN STRICT ACCORDANCE WITH THE MANUFACTURER'S RECOMMENDATIONS SHALL BE INCORPORATED IN CONCRETE MIX DESIGNS. A HIGH-RANGE WATER-REDUCING (HRWR) ADMIXTURE CONFORMING TO ASTM C494 TYPE F OR G MAY BE USED IN CONCRETE MIXES PROVIDING THAT THE SLUMP DOES NOT EXCEED 10".

THE CONTRACTOR SHALL SUBMIT CONCRETE MIX DESIGNS ALONG WITH TEST DATA COMPLIANT WITH ACI 301-16 AND ACI 318-14 A MINIMUM OF TWO WEEKS PRIOR TO PLACING CONCRETE. NO WATER MAY BE ADDED TO CONCRETE IN THE FIELD UNLESS SPECIFICALLY APPROVED IN WRITING BY THE CONCRETE SUPPLIER AND RESEARCH TEAM IN CONJUNCTION WITH THE CONCRETE MIX DESIGN.

CONCRETE REINFORCING STEEL

CONCRETE REINFORCEMENT SHALL BE AS LISTED BELOW. ASTM A706 REINFORCEMENT MAY BE SUBSTITUTED FOR ASTM A615 REINFORCEMENT.

REINFORCING LOCATION	MATERIAL GRADE
REINFORCING TO BE WELDED	ASTM A706 GRADE 60
ALL OTHER USES U.N.O.	ASTM A615 GRADE 60

ALL REINFORCING STEEL SHALL BE SECURELY TIED IN PLACE WITH #16 ANNEALED IRON WIRE. BARS SHALL BE SUPPORTED ON WELL-CURED CONCRETE BLOCKS OR APPROVED METAL OR PLASTIC CHAIRS, AS SPECIFIED BY THE CRSI MANUAL OF STANDARD PRACTICE, MSP-1, REINFORCING STEEL SHALL BE DETAILED IN ACCORDANCE WITH ACI 315, "ACI MANUAL OF STANDARD PRACTICE FOR DETAILING REINFORCED CONCRETE STRUCTURES".

REINFORCING BARS SHALL NOT BE BENT OR STRAIGHTENED IN THE FIELD WITHOUT APPROVAL OF THE RESEARCH TEAM.

LAP ALL REINFORCING BARS PER THE TYPICAL LAP SPLICE LENGTH SCHEDULES, EXCEPT AS NOTED ON DRAWINGS. USE LAP LENGTH FOR SMALLER BAR WHEN SPLICING DIFFERENT BAR SIZES.

TYP. WALL AND SLAB LAP SPLICE LENGTH SCHEDULE (IN.)		
BAR SIZE	SLAB BOTTOM BARS	SLAB TOP BARS
	f'c = 5,000 PSI	f'c = 5,000 PSI
#3	16	16
#4	24	30
#5	28	36

TABLE NOTES:
1. SPLICE LENGTHS APPLY TO ASTM A615 OR ASTM A706 GRADE 60 DEFORMED REINFORCING BARS ONLY.
2. SPLICE LENGTHS ARE BASED ON THE CLEAR COVER AND MINIMUM BAR CLEAR SPACING INDICATED BELOW.

REINFORCING STEEL SHALL HAVE PROTECTION AND SPACING AS FOLLOWS:

CONCRETE COVER		
USE	CLEAR COVER	MIN. CLEAR SPACING
MILD FOUNDATION SLABS	1" (INCLUDING COVER TO TIES)	2db OR 1"

CONCRETE EMBEDMENTS

HEADED SHEAR STUDS SHALL BE NELSON HEADED ANCHORS WITH FLUXED ENDS (ICC ESR-2856) OR APPROVED ALTERNATE. CAST-IN-PLACE ANCHOR BOLTS SHALL BE HEADED BOLTS CONFORMING TO ASTM F1554 GRADE 55, MEETING SUPPLEMENTAL REQUIREMENT S1 (WELDABLE) U.N.O. NO LOADS OR WELDS SHALL BE PLACED ON EMBEDDED PLATES OR ANGLES FOR MINIMUM OF 7 DAYS AFTER CASTING.

POST-INSTALLED CONCRETE ANCHORS

POST-INSTALLED CONCRETE ANCHORS SHALL BE THE FOLLOWING PRODUCTS, U.N.O.:

TYPE	APPROVED ANCHORS
EXPANSION	SIMPSON STRONG-BOLT 2 (ICC ESR-3037)
CONCRETE SCREW	SIMPSON TITEN HD (ICC ESR-2713)
ADHESIVE ANCHORS	SIMPSON SET-XP (ICC ESR-2508)

ANCHORS SHALL BE INSTALLED IN STRICT CONFORMANCE WITH THE MANUFACTURER'S RECOMMENDATIONS AND PRODUCT EVALUATION REPORTS. EMBEDMENTS SPECIFIED ON DRAWINGS ARE "EFFECTIVE" EMBEDMENTS. REFERENCE MANUFACTURER LITERATURE FOR CORRESPONDING ACTUAL EMBEDMENT DEPTHS. DO NOT CUT REINFORCING IN CONCRETE DURING INSTALLATION.

NO LOADS OR WELDS SHALL BE PLACED ON EMBEDDED PLATES OR ANGLES FOR A MINIMUM OF 7 DAYS AFTER CASTING. ADHESIVE ANCHORS SHALL NOT BE INSTALLED FOR A MINIMUM OF 21 DAYS AFTER CASTING CONCRETE.

NHERI
TallWood

1500 Illinois St.
Golden, CO 80401
303-273-3932

PROJECT:

10-Story Test

10201 Pomerado Road
San Diego, CA 92131

SET ISSUANCE:

Revision 1

DATE ISSUED: 07/30/21

No.	Description	Date
1	Revision 1	07/30/21

SHEET SIZE: 30x42
DRAWN BY: ANB

SHEET:

General Structural Notes

S003

4/5/2023 9:18:17 AM

F:\10 Story CLT\Revit Files\10 Story Test 03-25-2023.rvt

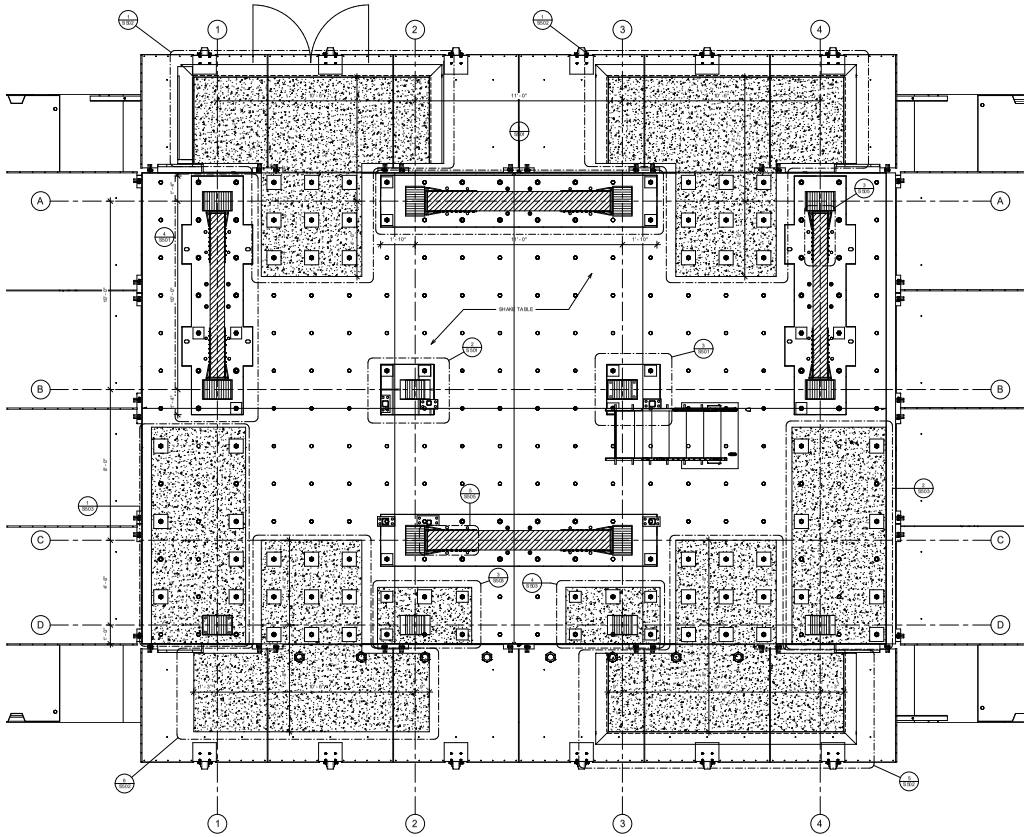

1 Level 1.1
1/2" = 1'-0"

NOTES
1. SEE INDIVIDUAL FOUNDATION PIECE DETAIL DRAWINGS FOR PRE-TENSION INFORMATION

F:\10 Story CLT\Revit Files\10 Story Test 03-25-2023.rvt 4/5/2023 9:18:18 AM

NHERI
TallWood

1500 Illinois St.
Golden, CO 80401
303-273-3932

PROJECT:

10-Story Test

10201 Pomerado Road
San Diego, CA 92131

SET ISSUANCE:

Revision 1

DATE ISSUED: 07/30/21

No.	Description	Date
1	Revision 1	07/30/21

SHEET SIZE: 30x42
DRAWN BY: ANB

SHEET:

Foundation/Level 1 Plan - Structural

S101S

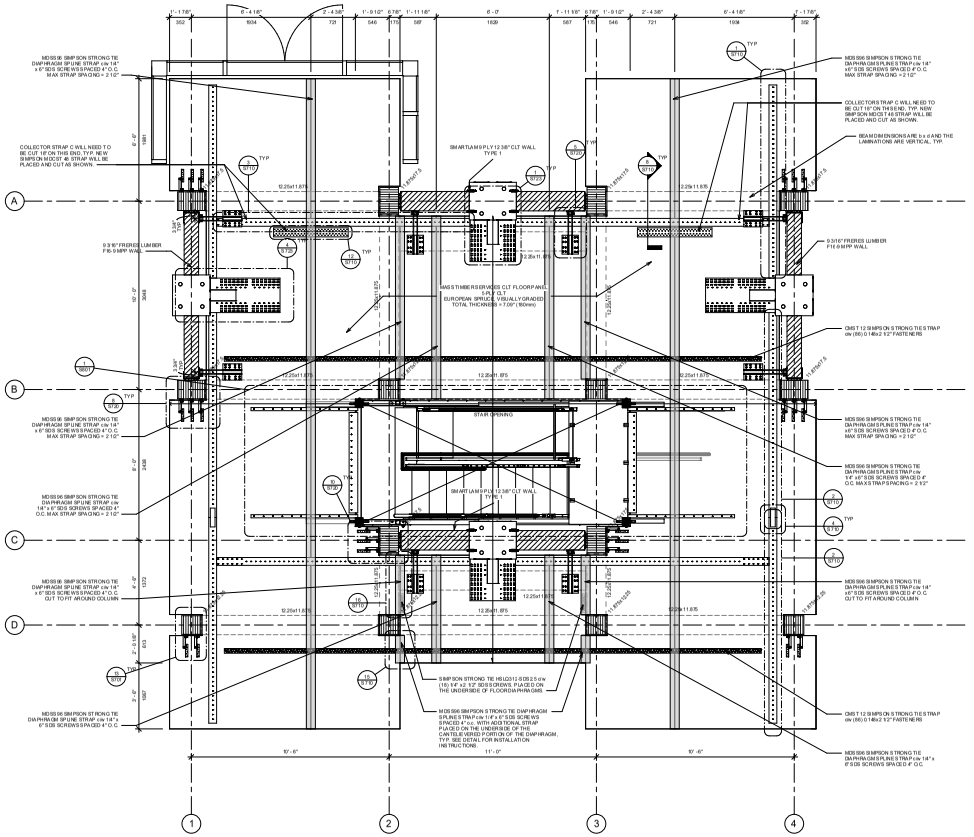

1 Level 2
1/2" = 1'-0"

NOTES:
1. MASS TIMBER SERVICES CLT FLOOR PLAN
2. CLT WILL NOT HAVE ANY SHEATHING
3. THERE IS A 3/4" GAP BETWEEN COLUMN AND DIAPHRAGM EDGES

F:\10 Story CLT\Revit Files\10 Story Test.03-25-2023.rvt 4/5/2023 9:18:19 AM

NHERI TallWood

1500 Illinois St.
Golden, CO 80401
303-273-3932

PROJECT:

10-Story Test

10201 Pomerado Road
San Diego, CA 92131

SET ISSUANCE:

Revision 1

DATE ISSUED: 07/30/21

No.	Description	Date
1	Revision 1	07/30/21

SHEET SIZE: 30x42
DRAWN BY: ANB

SHEET:

Level 2 Plan - Structural

S102S

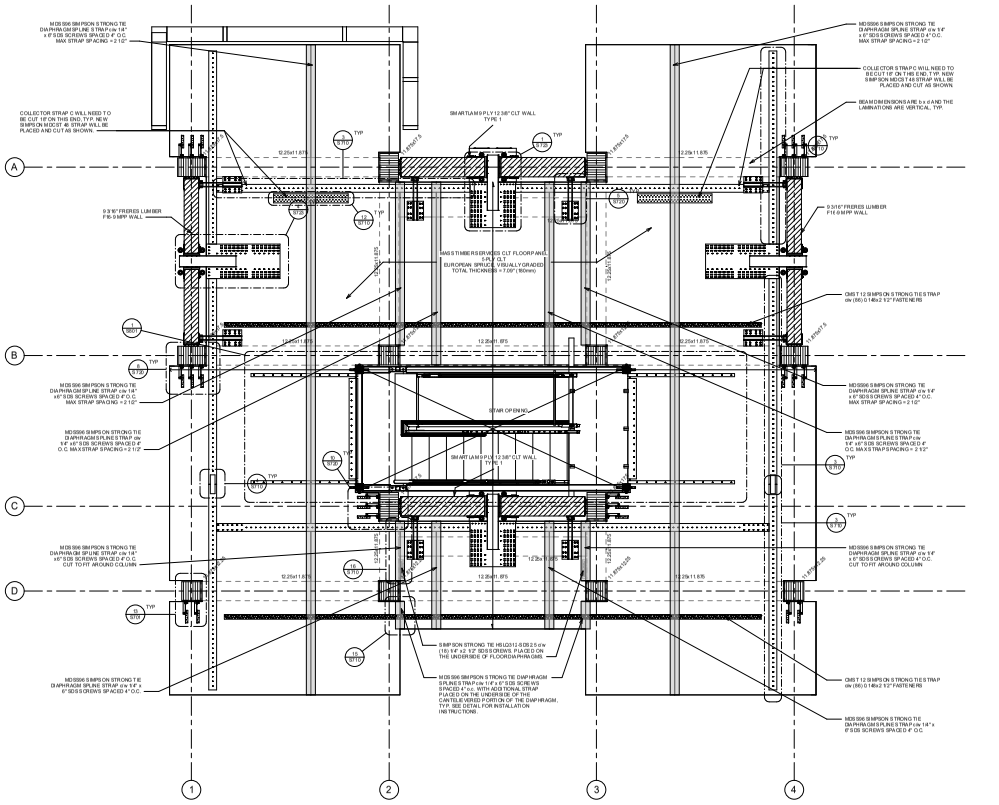

1 Level 3
1/2" = 1'-0"

NOTES:
1. MASS TIMBER SERVICES CLT FLOOR PLAN
2. CLT WILL NOT HAVE ANY SHEATHING
3. THERE IS A 3/4" GAP BETWEEN COLUMN AND DIAPHRAGM EDGES
4. REFERENCE SHEET 102S FOR DIMENSIONS

F:\10 Story CLT\Revit Files\10 Story Test.03-25-2023.rvt
4/5/2023 9:18:20 AM

NHERI
TallWood
1500 Illinios St.
Golden, CO 80401
303-273-3932

PROJECT:

10-Story Test

10201 Pomerado Road
San Diego, CA 92131

SET ISSUANCE:

Revision 1

DATE ISSUED: 07/30/21

No.	Description	Date
1	Revision 1	07/30/21

SHEET SIZE: 30x42
DRAWN BY: ANB

SHEET:

Level 3 Plan - Structural

S103S

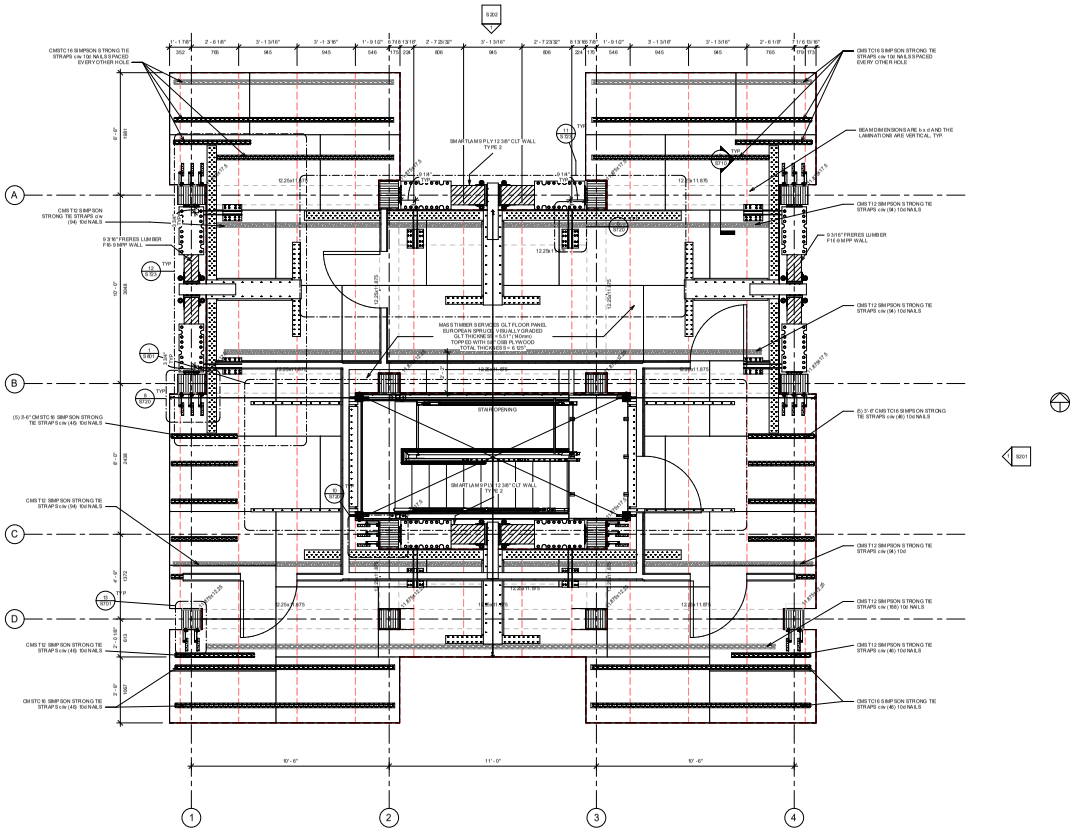

Level 4
1/2" = 1'-0"

NOTES:
1. MASS TIMBER SERVICES GLT FLOOR PLAN
2. TOTAL FLOOR THICKNESS INCLUDES 5/8" SHEATHING
3. THERE IS A 1/4" GAP BETWEEN COLUMN AND DIAPHRAGM EDGES
4. GROOVE AND TONGUE CONNECTIONS ARE USED BETWEEN PANELS
5. FOR SHEATHING DETAILS SEE SHEET T11

F:\10 Story CLT\Revit Files\10 Story Test.03-25-2023.rvt
4/5/2023 9:18:21 AM

NHERI
TallWood

1500 Illinois St.
Golden, CO 80401
303-273-3932

PROJECT:

10-Story Test

10201 Pomerado Road
San Diego, CA 92131

SET ISSUANCE:

DATE ISSUED:

No.	Description	Date

SHEET SIZE: 30x42
DRAWN BY: ANB

SHEET:

Level 4 Plan - Structural

S104S

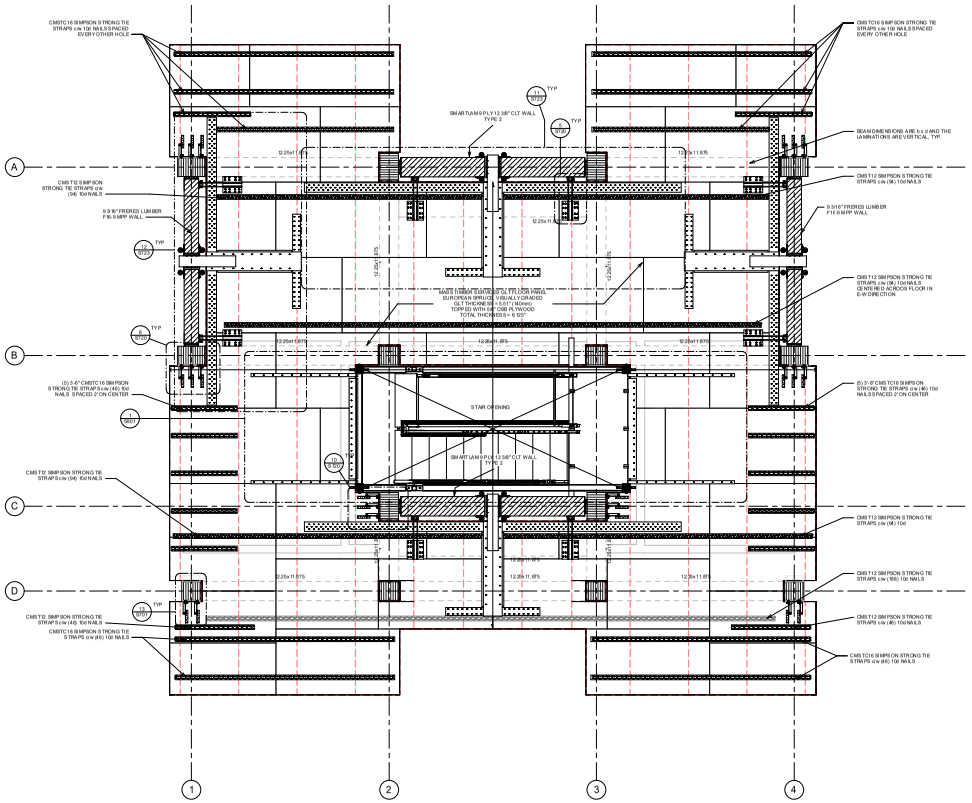

1 Level 5
1/8" = 1'-0"

NOTES:
1. MASS TIMBER SERVICES GLT FLOOR PLAN
2. TOTAL FLOOR THICKNESS INCLUDES 5/8" SHEATHING
3. THERE IS A 3/4" GAP BETWEEN COLUMN AND DIAPHRAGM EDGES
4. GROOVE AND TONGUE CONNECTIONS ARE USED BETWEEN PANELS
5. FOR SHEATHING DETAILS SEE SHEET 7.11
6. FOR PANEL DIMENSIONS REFERENCE S104S

F:\10 Story CLT\Revit Files\10 Story Test.03-25-2023.rvt
4/5/2023 9:18:23 AM

NHERI
TallWood

1500 Illinois St.
Golden, CO 80401
303-273-3932

PROJECT:

10-Story Test

10201 Pomerado Road
San Diego, CA 92131

SET ISSUANCE:

DATE ISSUED:

No.	Description	Date

SHEET SIZE: 30x42
DRAWN BY: ANB

SHEET:

Level 5 Plan - Structural

S105S

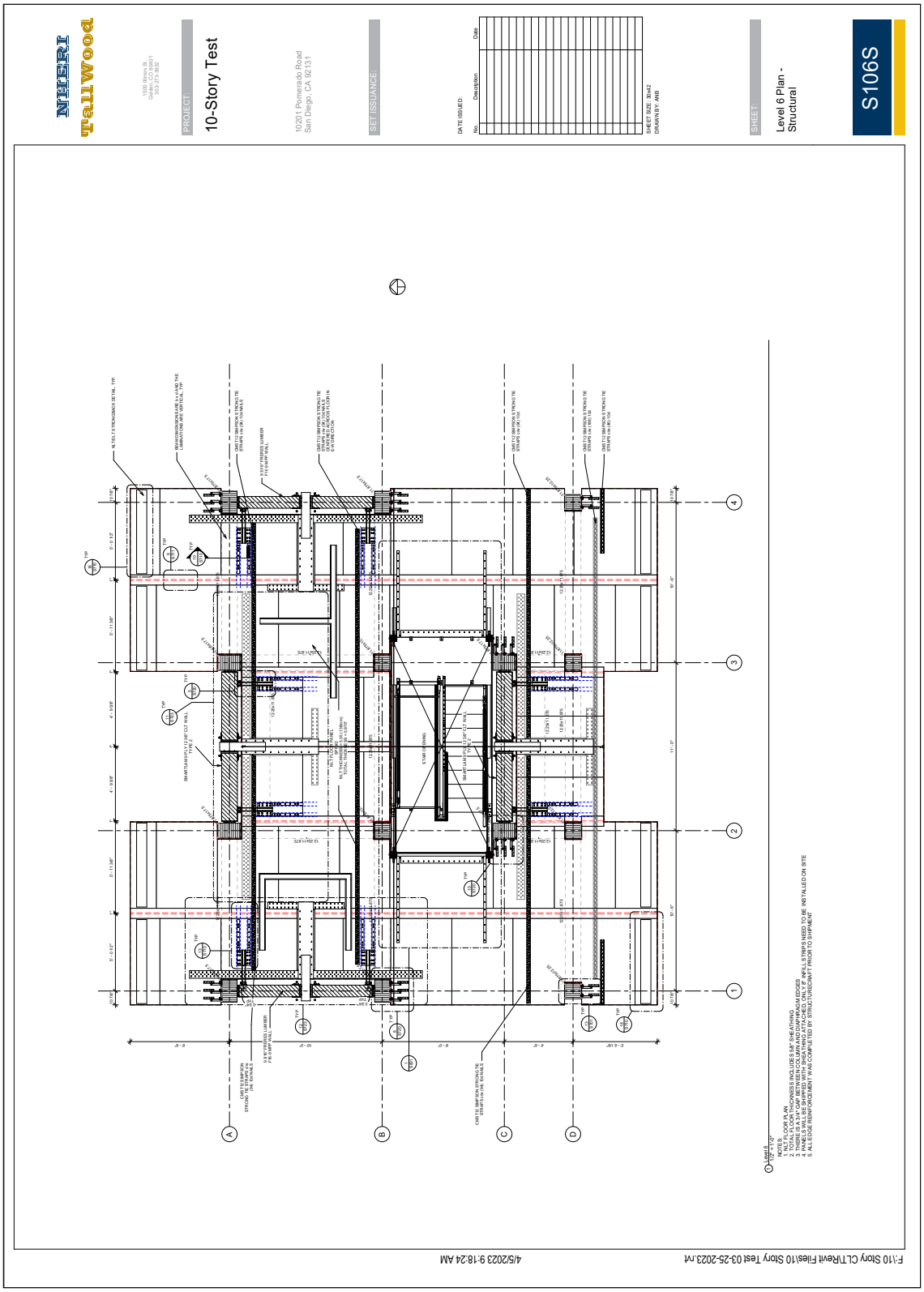
MERRI TallWood
1560 Wynkoop St
Denver, CO 80201
303.273.3632
PROJECT:
10-Story Test
10201 Pomerado Road
San Diego, CA 92131
SET ISSUANCE:
DATE ISSUED:
No. Description Date
SHEET SIZE: 30x42
DRAWN BY: ANB
SHEET:
Level 6 Plan - Structural
S106S
F:\10 Story CLT\Revit Files\10 Story Test 03-25-2023.rvt
4/5/2023 9:18:24 AM

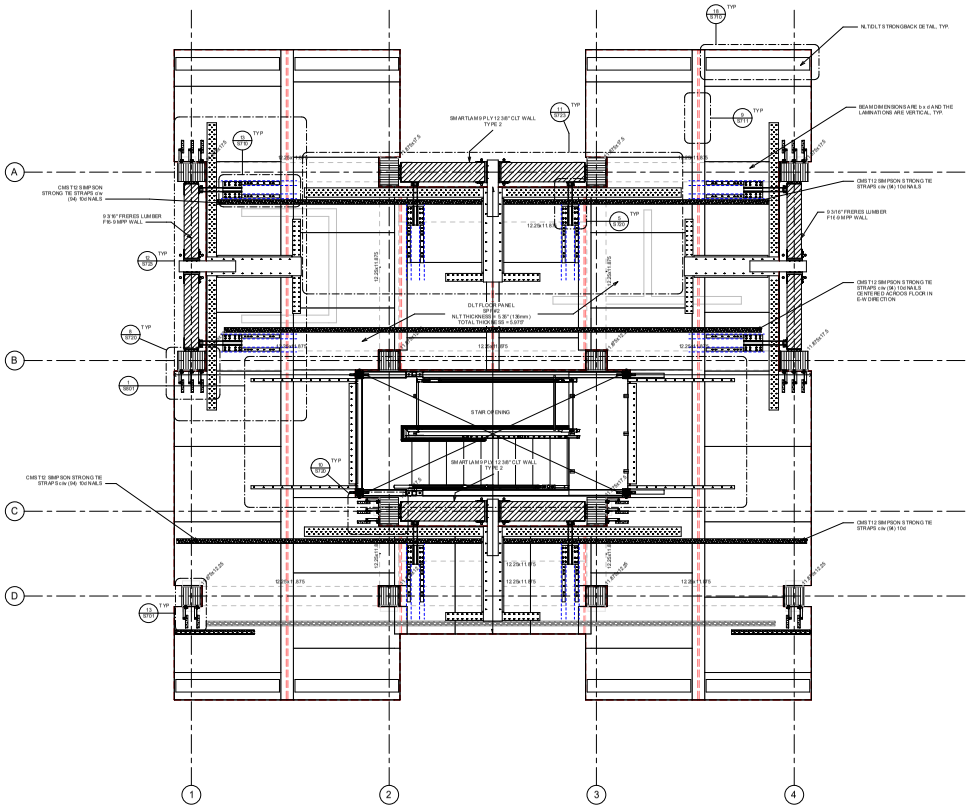

Level 7
1/2" = 1'-0"

NOTES:
1. DLT FLOOR PLAN
2. TOTAL FLOOR THICKNESS INCLUDES 5/8" SHEATHING
3. THERE IS A 3/4" GAP BETWEEN COLUMN AND DIAPHRAGM EDGES
4. PANELS WILL BE SHIPPED WITH SHEATHING ATTACHED, ONLY 8" INFILL STRIPS NEED TO BE INSTALLED ON SITE
5. ALL EDGE REINFORCEMENT WAS COMPLETED BY STRUCTURECRAFT PRIOR TO SHIPMENT
6. FOR PANEL DIMENSIONS REFERENCE S106S

F:\10 Story CLT\Revit Files\10 Story Test.03-25-2023.rvt
4/5/2023 9:18:25 AM

NHERI
TallWood

1500 Illinois St.
Golden, CO 80401
303-273-3932

PROJECT:

10-Story Test

10201 Pomerado Road
San Diego, CA 92131

SET ISSUANCE:

DATE ISSUED:

No.	Description	Date

SHEET SIZE: 30x42
DRAWN BY: ANB

SHEET:

Level 7 Plan - Structural

S107S

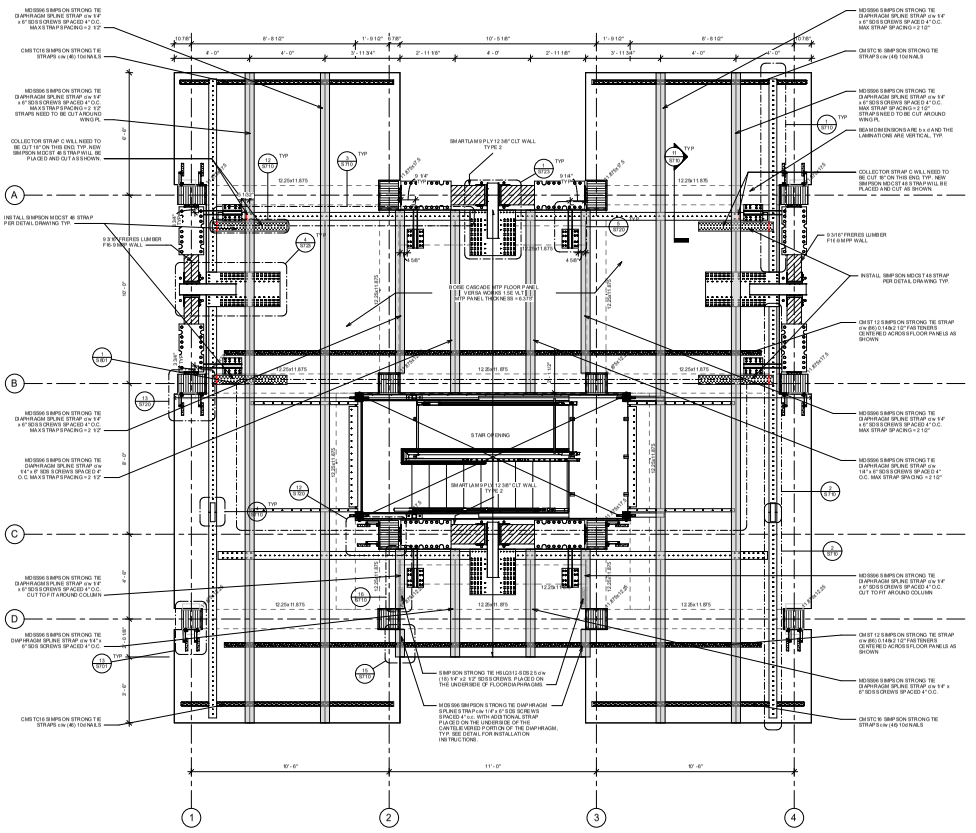

1 Level 8
1/2" = 1'-0"

NOTES:
1. BOISE CASCADE MTP FLOOR PLAN
2. NO SEATHING ON MTP FLOOR PANELS
3. THERE IS A 3/4" GAP BETWEEN COLUMN AND DIAPHRAGM EDGES

4/5/2023 9:18:26 AM

F:\10 Story CLT\Revit Files\10 Story Test.03-25-2023.rvt

NHERI
TallWood

1500 Illinois St.
Golden, CO 80401
303-273-3932

PROJECT:

10-Story Test

10201 Pomerado Road
San Diego, CA 92131

SET ISSUANCE:

DATE ISSUED:

No.	Description	Date

SHEET SIZE: 30x42
DRAWN BY: ANB

SHEET:

Level 8 Plan - Structural

S108S

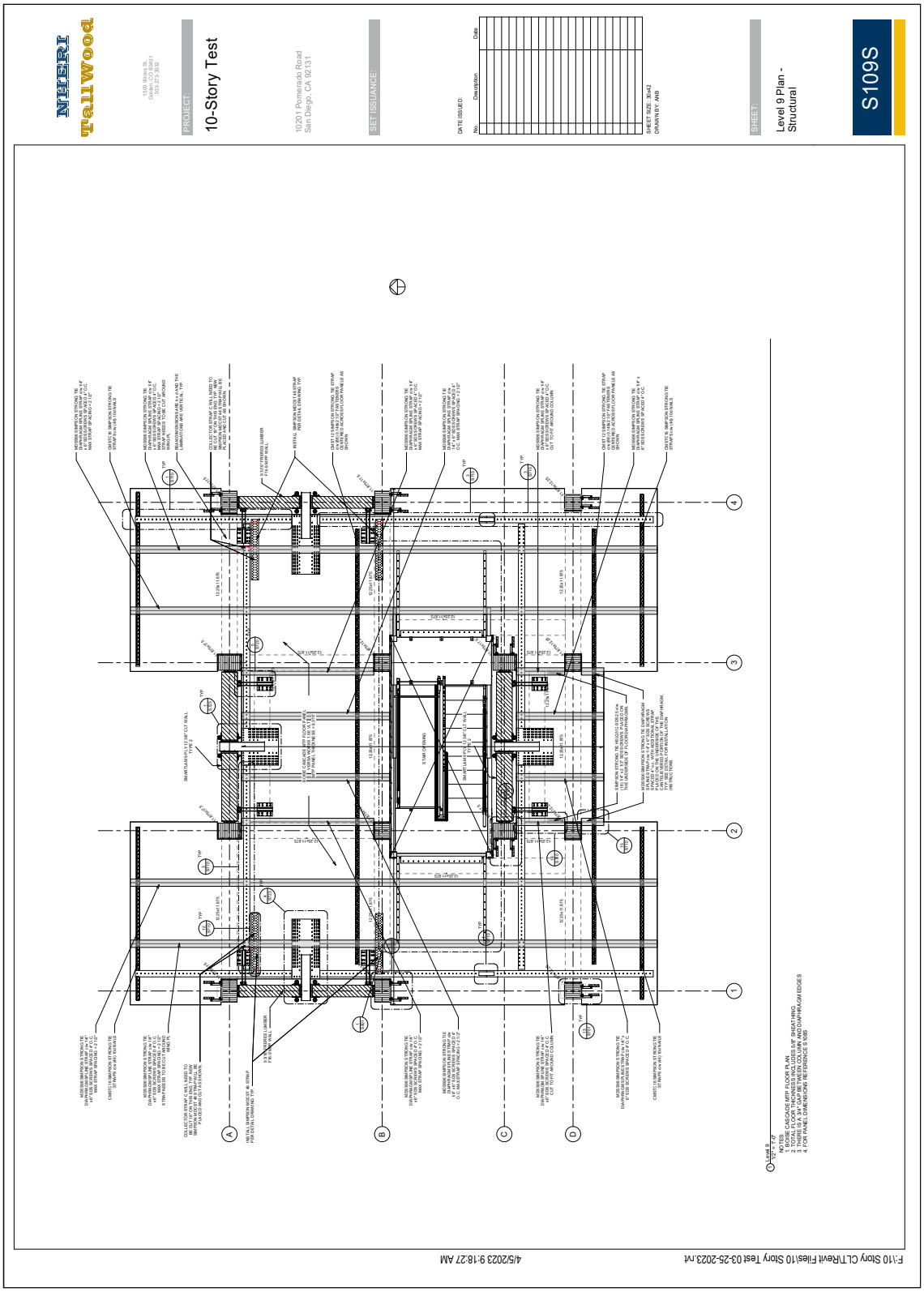
NEBRI
TallWood
PROJECT:
10-Story Test
10201 Pomerado Road
San Diego, CA 92131
SET ISSUANCE:
DATE ISSUED:
No. Description Date
SHEET SIZE: 30x42
DRAWN BY: ANB
SHEET:
Level 9 Plan - Structural
S109S
F:\10 Story CLT\Revit Files\10 Story Test 03-25-2023.rvt
4/5/2023 9:18:27 AM

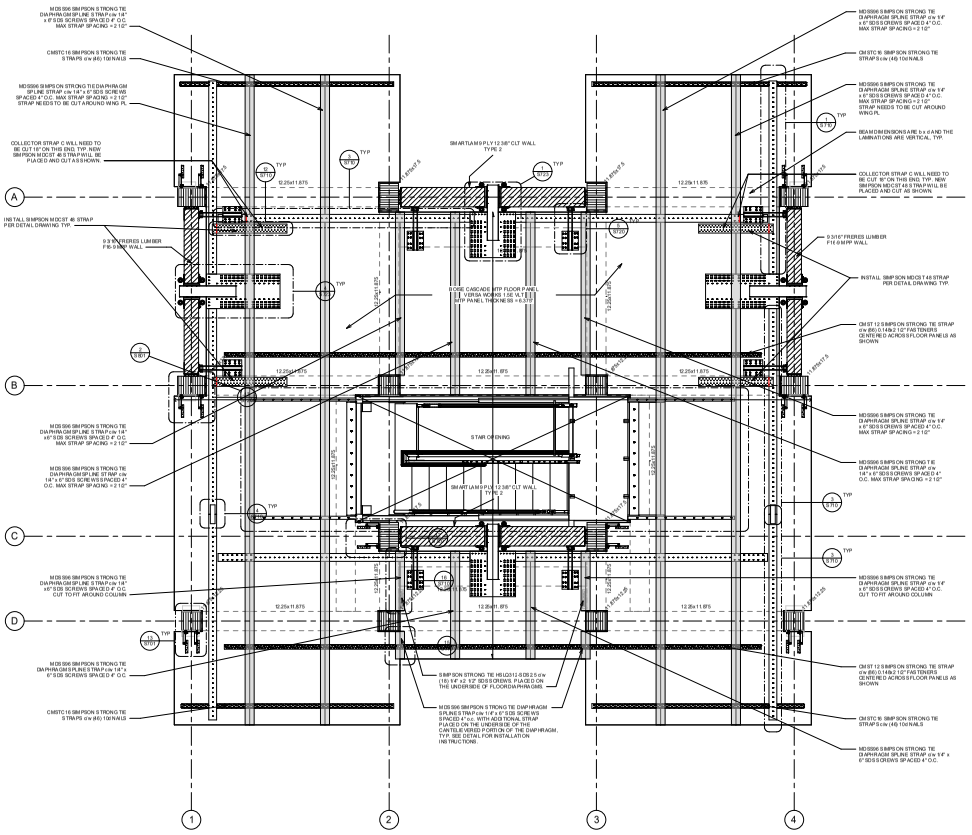

1 Level 10
1/2" = 1'-0"

NOTES:
1. BOISE CASCADE MTP FLOOR PLAN
2. TOTAL FLOOR THICKNESS INCLUDES 5/8" SHEATHING
3. THERE IS A 3/4" GAP BETWEEN COLUMN AND DIAPHRAGM EDGES
4. FOR PANEL DIMENSIONS REFERENCE S108

NHERI TallWood

1500 Illinois St.
Golden, CO 80401
303-273-3932

PROJECT:

10-Story Test

10201 Pomerado Road
San Diego, CA 92131

SET ISSUANCE:

DATE ISSUED:

No.	Description	Date

SHEET SIZE: 30x42
DRAWN BY: ANB

SHEET:

Level 10 Plan - Structural

S110S

4/5/2023 9:18:28 AM

F:\10 Story CLT\Revit Files\10 Story Test 03-25-2023.rvt

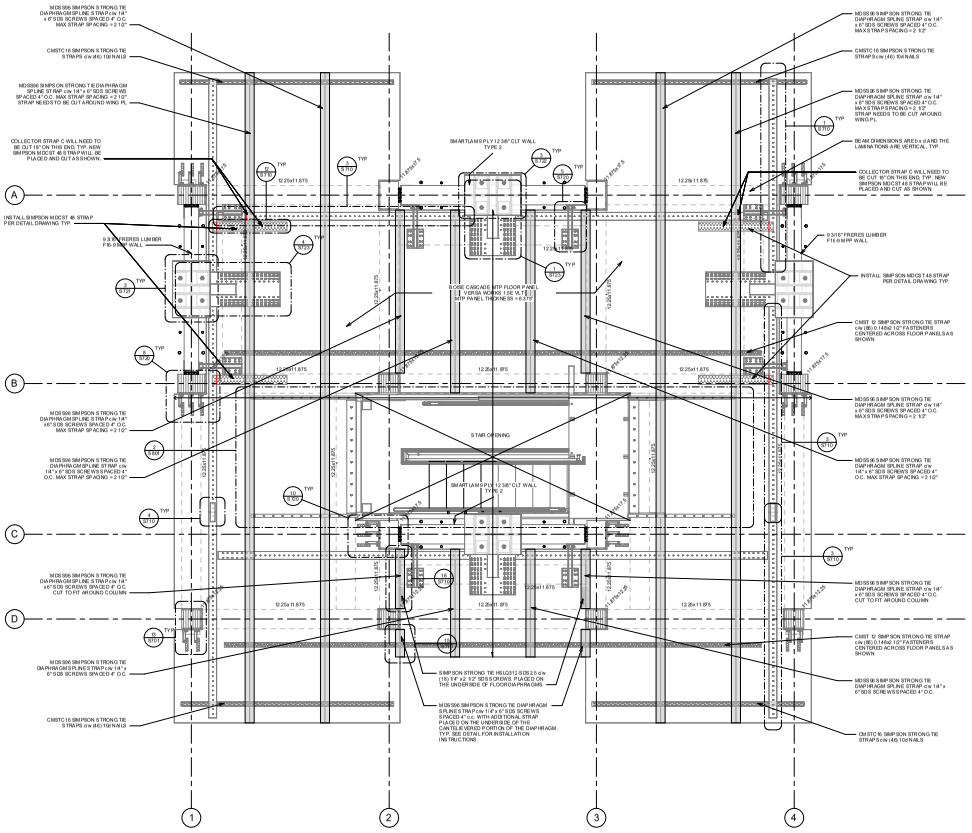

1 Roof Framing Plan
1/2" = 1'-0"

NOTES:
1. BOISE CASCADE MTP FLOOR PLAN
2. TOTAL FLOOR THICKNESS INCLUDES 5/8" SHEATHING
3. THERE IS A 3/4" GAP BETWEEN COLUMN AND DIAPHRAGM EDGES
4. FOR PANEL DIMENSIONS REFERENCE S 108.5
5. REFERENCE S7 10 FOR COLLECTOR LAYOUT

F:\10 Story CLT\Revit Files\10 Story Test.03-25-2023.rvt
4/5/2023 9:18:29 AM

NHERI TallWood

1500 Illinois St.
Golden, CO 80401
303-273-3932

PROJECT:

10-Story Test

10201 Pomerado Road
San Diego, CA 92131

SET ISSUANCE:

DATE ISSUED:

No.	Description	Date

SHEET SIZE: 30x42
DRAWN BY: ANB

SHEET:

Roof/Level 11 Plan - Structural

S111S

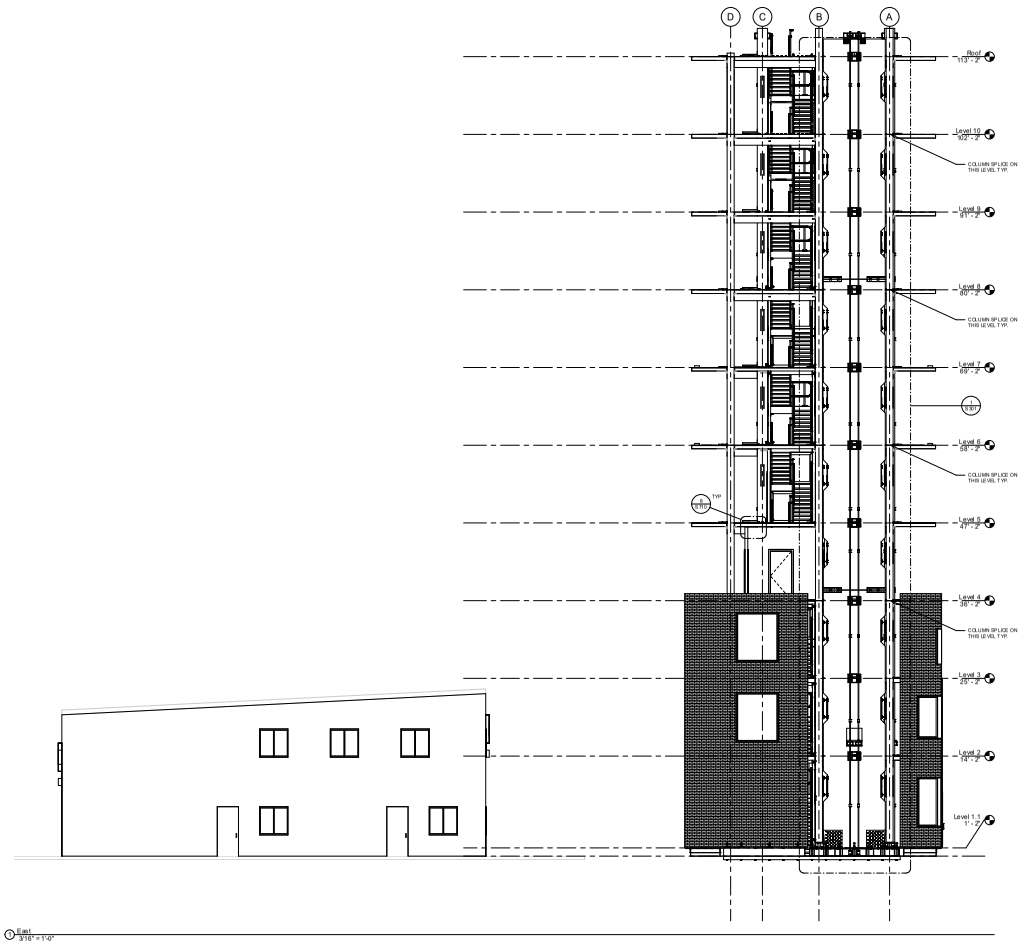

F:\10 Story CLT\Revit Files\10 Story Test 03-25-2023.rvt 4/5/2023 9:18:31 AM

NHERI
TallWood

1500 Illinois St.
Golden, CO 80401
303-273-3932

PROJECT:

10-Story Test

10201 Pomerado Road
San Diego, CA 92131

SET ISSUANCE:

DATE ISSUED:

No.	Description	Date

SHEET SIZE: 30x42
DRAWN BY: ANB

SHEET:

Building Elevations

S201

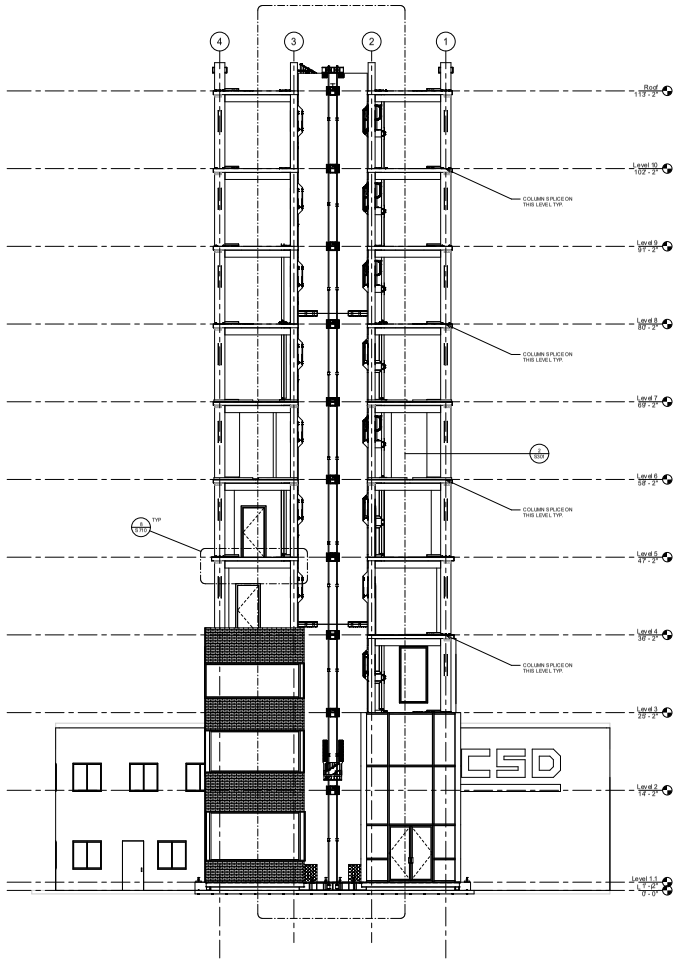

F:\10 Story CLT\Revit Files\10 Story Test 03-25-2023.rvt 4/5/2023 9:18:33 AM

NHERI
TallWood

1500 Illinois St.
Golden, CO 80401
303-273-3932

PROJECT:

10-Story Test

10201 Pomerado Road
San Diego, CA 92131

SET ISSUANCE:

DATE ISSUED:

No.	Description	Date

SHEET SIZE: 30x42
DRAWN BY: Author

SHEET:

Building Elevations

S202

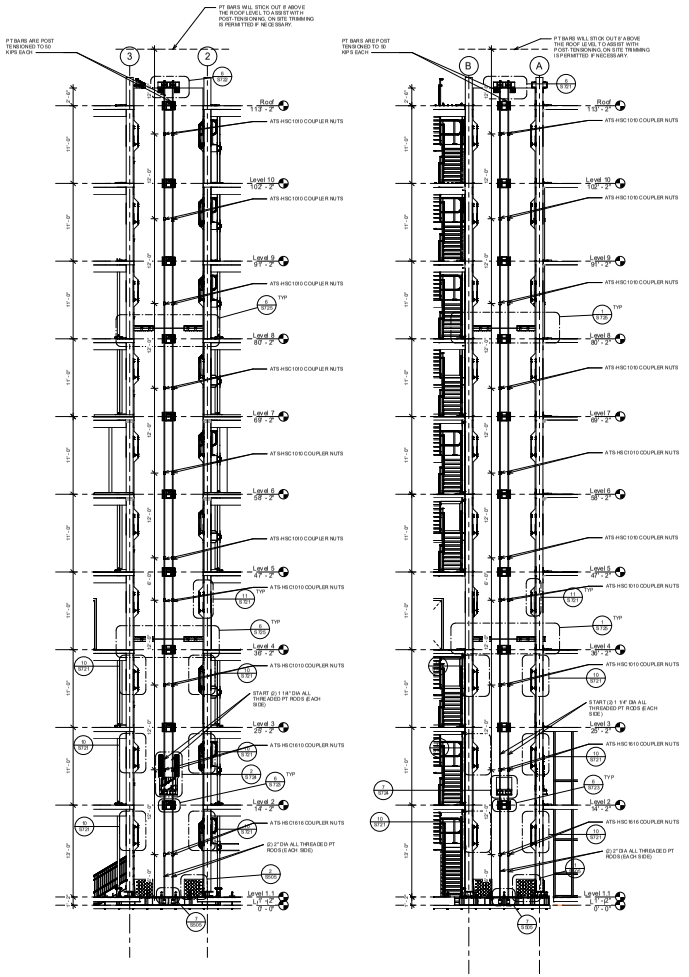

F:\10 Story CLT\Revit Files\10 Story Test.03-25-2023.rvt 4/5/2023 9:18:37 AM

NHERI
TallWood
1500 Illinois St.
Golden, CO 80401
303-273-3932

PROJECT:

10-Story Test

10201 Pomerado Road
San Diego, CA 92131

SET ISSUANCE:

DATE ISSUED:

No.	Description	Date

SHEET SIZE: 30x42
DRAWN BY: ANB

SHEET:

Shear Wall Elevations

S301

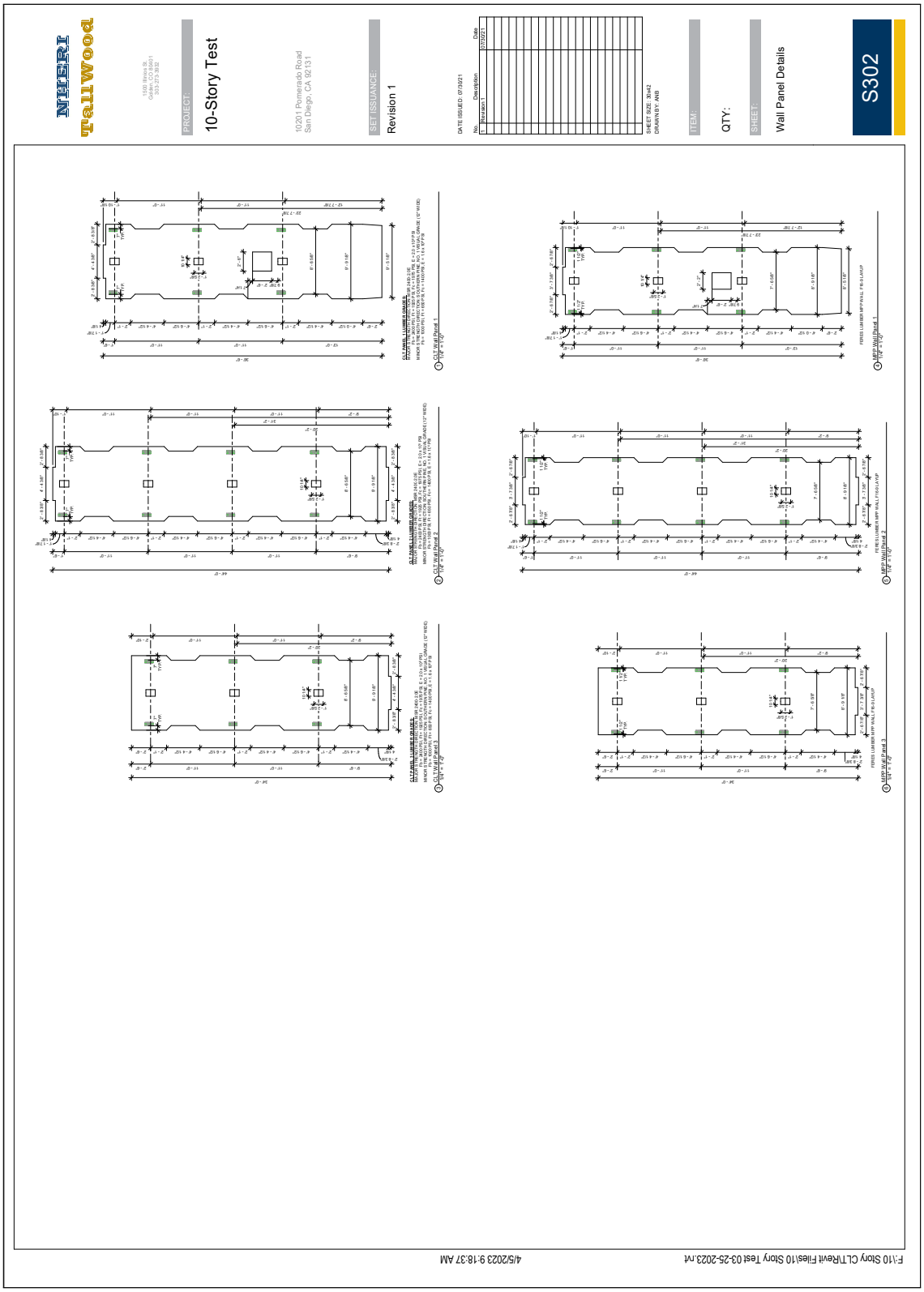
MiTek
TallWood
1900 Illinois St
Golden, CO 80401
303.273.3932
PROJECT:
10-Story Test
10201 Pomerado Road
San Diego, CA 92131
SET ISSUANCE:
Revision 1
DATE ISSUED: 07/30/21
No. Description Date
1 Revision 1 07/30/21
SHEET SIZE: 30x42
DRAWN BY: ANB
ITEM:
QTY:
SHEET:
Wall Panel Details
S302
F:\10 Story CLT\Revit Files\10 Story Test 03-25-2023.rvt
4/5/2023 9:18:37 AM

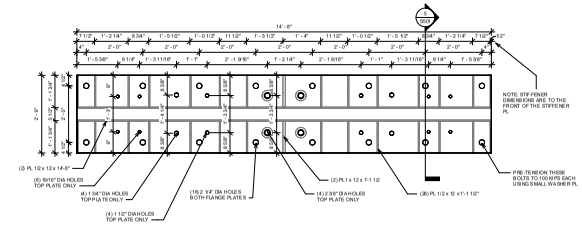

1 CLT Foundation Beam
3/4" = 1'-0"

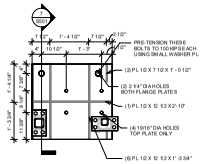

2 B2 Steel Column Foundation Plan
3/4" = 1'-0"

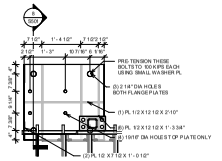

3 B3 Steel Column Foundation
3/4" = 1'-0"

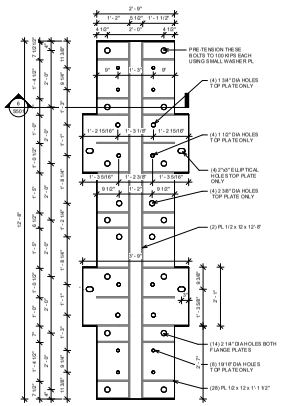

4 MPP Wall Foundation
3/4" = 1'-0"

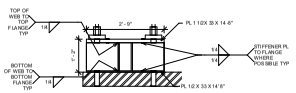

5 CLT Section View
3/4" = 1'-0"

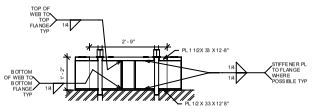

6 MPP Section View
3/4" = 1'-0"

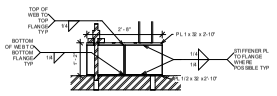

7 B2 Column Section View
3/4" = 1'-0"

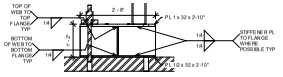

8 B3 Column Section View
3/4" = 1'-0"

F:\10 Story CLT\Revit Files\10 Story Test.03-25-2023.rvt

4/5/2023 9:18:38 AM

NHERI TallWood

1500 Illinios St.
Golden, CO 80401
303-273-3932

PROJECT:

10-Story Test

10201 Pomerado Road
San Diego, CA 92131

SET ISSUANCE:

DATE ISSUED:

No.	Description	Date

SHEET SIZE: 30x42
DRAWN BY: ANB

SHEET:

Steel Foundation Details

S501

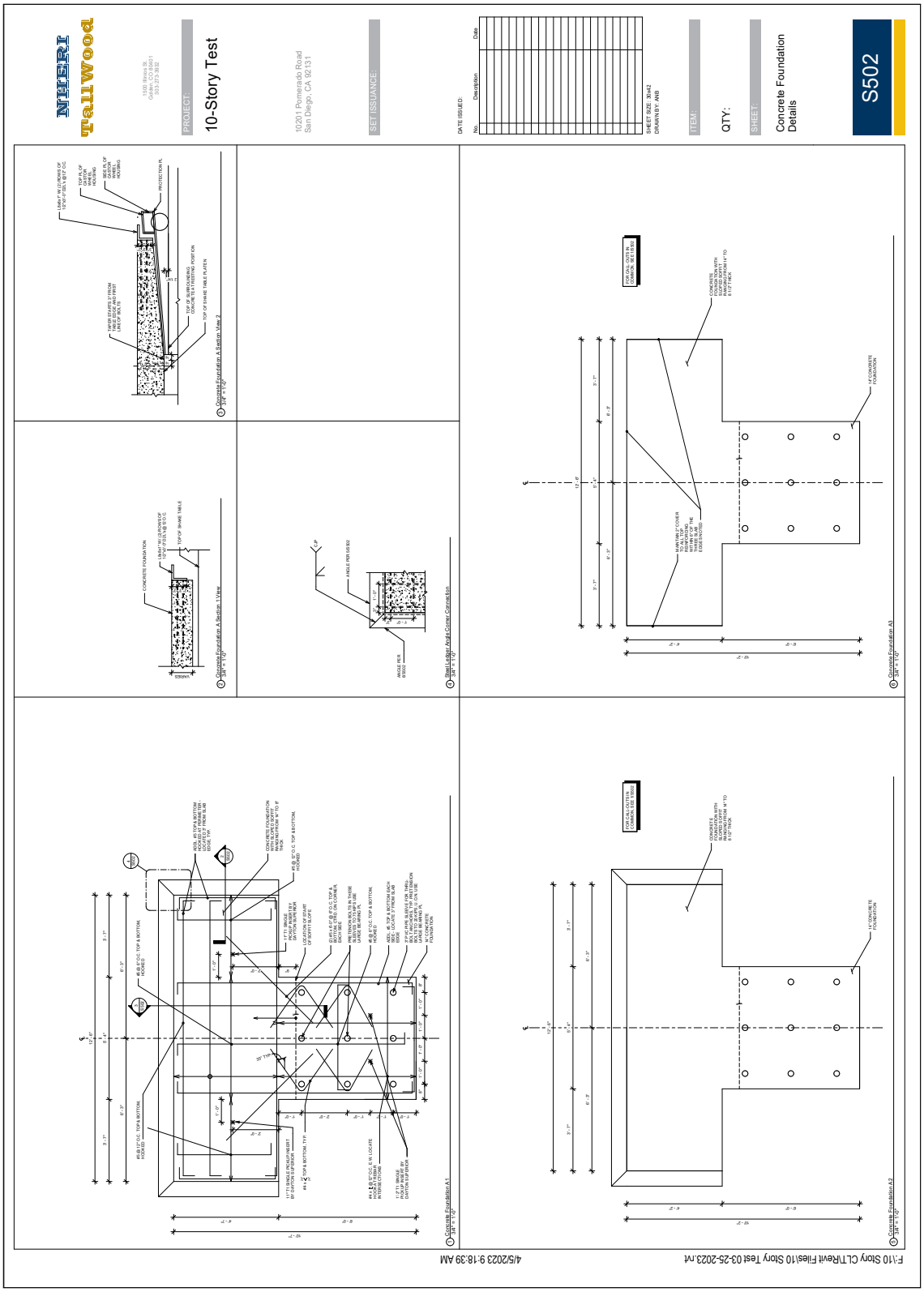
NHERI
TallWood
1160 Illinois St
Golden, CO 80401
303.273.3632
PROJECT:
10-Story Test
10201 Pomerado Road
San Diego, CA 92131
SET ISSUANCE:
DATE ISSUED:
No. Description Date
SHEET SIZE: 30x42
DRAWN BY: ANB
ITEM:
QTY:
SHEET:
Concrete Foundation Details
S502
Concrete Foundation A Section 1 View
Concrete Foundation A Section View 2
Steel Ledger Angle Corner Connection
Concrete Foundation A1
Concrete Foundation A2
Concrete Foundation A3
F:\10 Story CLT\Revit Files\10 Story Test 03-25-2023.rvt
4/5/2023 9:18:39 AM

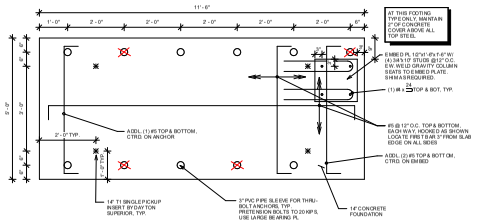

1 Concrete Foundation B1
3/4" = 1'-0"

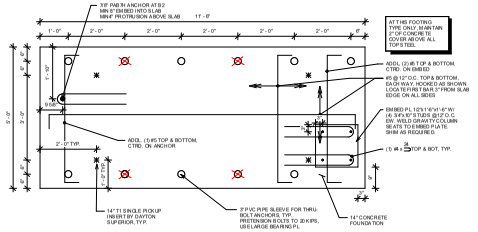

2 Concrete Foundation B2
3/4" = 1'-0"

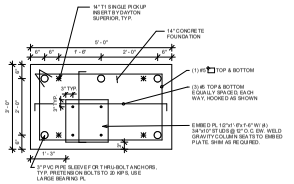

3 Concrete Foundation C1
3/4" = 1'-0"

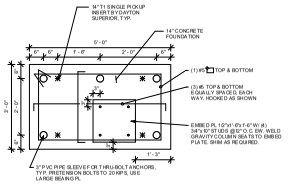

4 Concrete Foundation C2
3/4" = 1'-0"

4/5/2023 9:18:39 AM

F:\10 Story CLT\Revit Files\10 Story Test 03-25-2023.rvt

NHERI TallWood

1500 Illinois St.
Golden, CO 80401
303-273-3932

PROJECT:

10-Story Test

10201 Pomerado Road
San Diego, CA 92131

SET ISSUANCE:

DATE ISSUED:

No.	Description	Date

SHEET SIZE: 30x42
DRAWN BY: ANB

ITEM:

QTY:

SHEET:

Concrete Foundation Details

S503

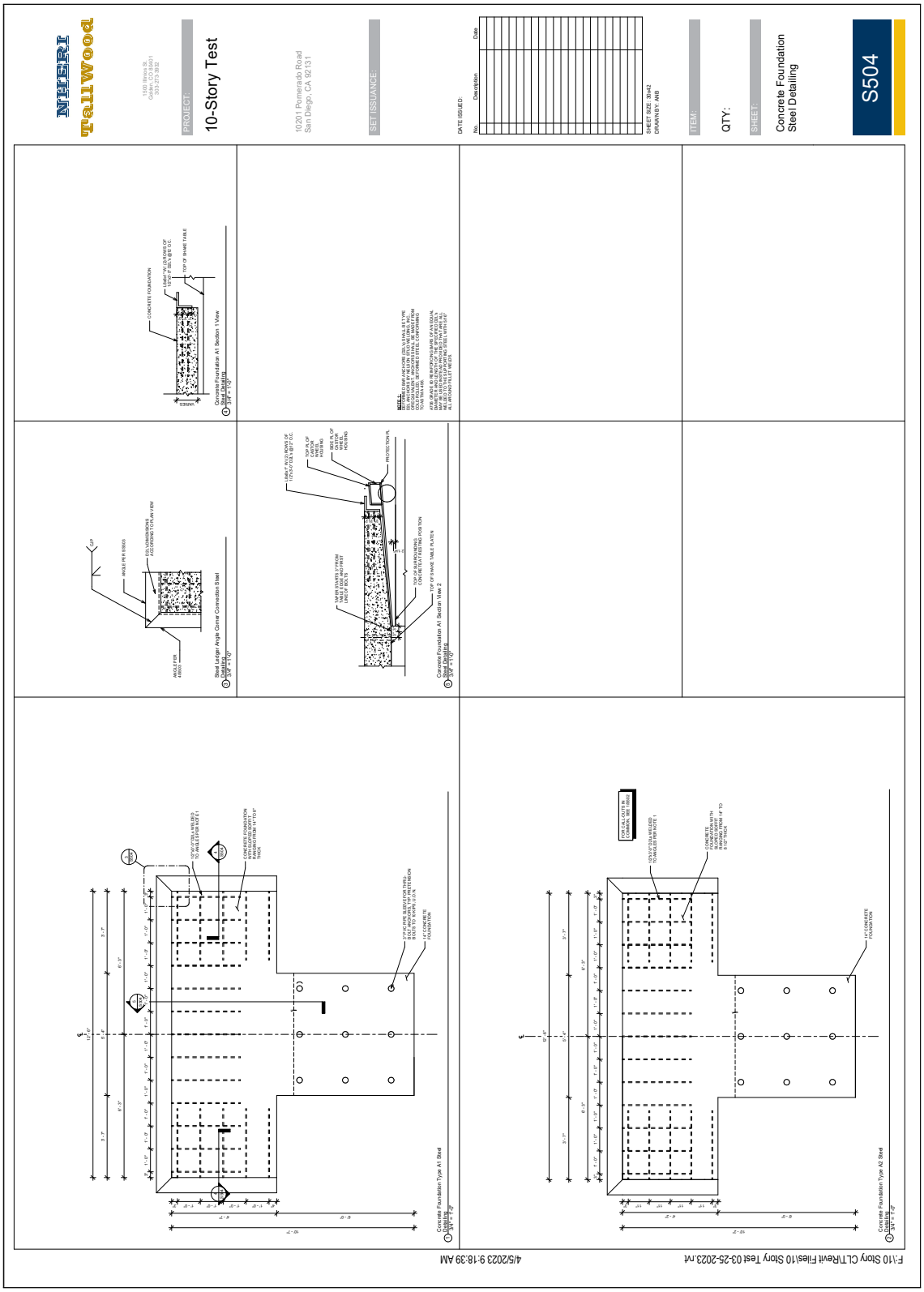
NHERI
TallWood
PROJECT:
10-Story Test
10201 Pomerado Road
San Diego, CA 92131
SET ISSUANCE:
DATE ISSUED:
No. Description Date
SHEET SIZE: 30x42
DRAWN BY: ANB
ITEM:
QTY:
SHEET:
Concrete Foundation
Steel Detailing
S504
Steel Ledger Angle Corner Connection Steel
Detailing
3/4" = 1'-0"
Concrete Foundation A1 Section 1 View
Steel Detailing
3/4" = 1'-0"
Concrete Foundation A1 Section View 2
Steel Detailing
3/4" = 1'-0"
Concrete Foundation Type A1 Steel
Detailing
3/4" = 1'-0"
Concrete Foundation Type A2 Steel
Detailing
3/4" = 1'-0"
4/5/2023 9:18:39 AM
F:\10 Story CLT\Revit Files\10 Story Test 03-25-2023.rvt

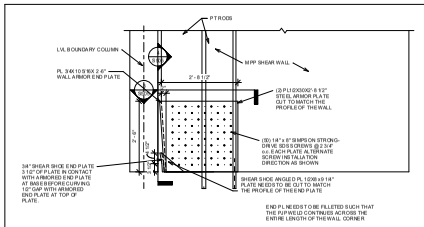

1 MPP Rocking Wall Toe Detail Elevation
3/4" = 1'-0"

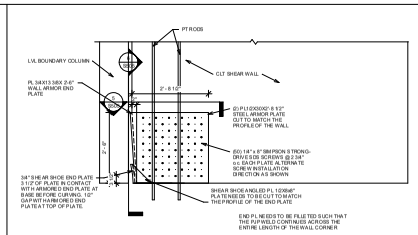

2 CLT Rocking Wall Toe Detail Elevation
3/4" = 1'-0"

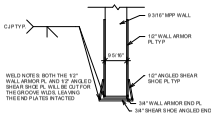

3 MPP Rocking Wall Toe Plan View
3/4" = 1'-0"

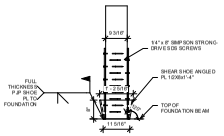

4 MPP Rocking Wall Toe Detail Section
3/4" = 1'-0"

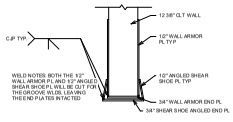

5 CLT Rocking Wall Toe Plan View
3/4" = 1'-0"

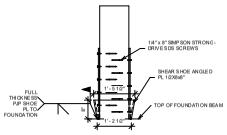

6 CLT Rocking Wall Toe Detail Section
3/4" = 1'-0"

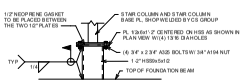

7 Stair Base Attachment Column 1 Elevation
3/4" = 1'-0"

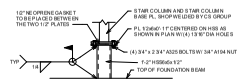

8 Stair Base Attachment Column 2 Elevation
3/4" = 1'-0"

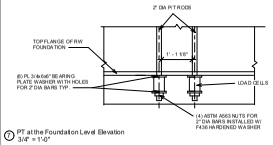

9 PT at the Foundation Level Elevation
3/4" = 1'-0"

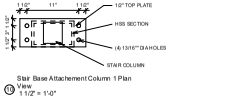

10 Stair Base Attachment Column 1 Plan View
1 1/2" = 1'-0"

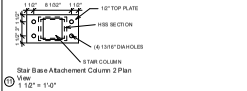

11 Stair Base Attachment Column 2 Plan View
1 1/2" = 1'-0"

NHERI
TallWood
1500 Illinois St.
Golden, CO 80401
303-273-3932

PROJECT:

10-Story Test

10201 Pomerado Road
San Diego, CA 92131

SET ISSUANCE:

DATE ISSUED:

No.	Description	Date

SHEET SIZE: 30x42
DRAWN BY: ANB

SHEET:

Foundation Connection Details

S505

4/5/2023 9:18:40 AM

F:\10 Story CLT\Revit Files\10 Story Test.03-25-2023.rvt

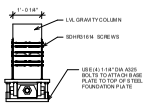

Simpson Gravity Column Base Connection
Elevation View 1
3/4" = 1'-0"

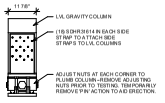

Simpson Gravity Column Base Connection
Elevation View 2
3/4" = 1'-0"

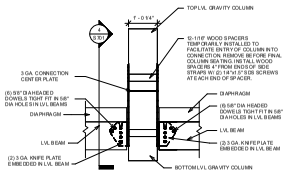

Simpson Gravity Column Double Sided
Splice Connection Elevation View
3/4" = 1'-0"

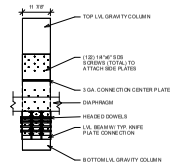

Simpson Gravity Column Double Sided
Splice Connection Section View
3/4" = 1'-0"

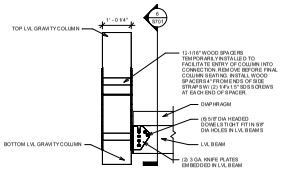

Simpson Gravity Column Single Sided
Splice Connection Elevation View
3/4" = 1'-0"

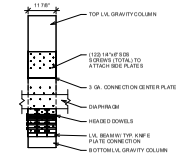

Simpson Gravity Column Single Sided
Splice Connection Section View
3/4" = 1'-0"

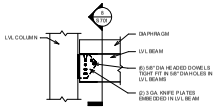

Simpson Stand Alone Beam to Column
Connection Elevation View
3/4" = 1'-0"

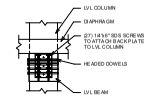

Simpson Stand Alone Beam to Column
Connection Section View
3/4" = 1'-0"

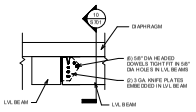

Simpson Stand Alone Beam to Beam
Connection Elevation View
3/4" = 1'-0"

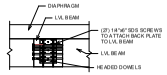

Simpson Stand Alone Beam to Beam
Connection Section View
3/4" = 1'-0"

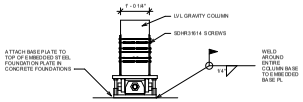

Simpson Bounding Column Concrete
Foundation Base Connection Elevation View
1
3/4" = 1'-0"

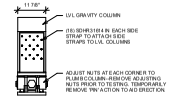

Simpson Bounding Column Concrete
Foundation Base Connection Elevation View
3/4" = 1'-0"

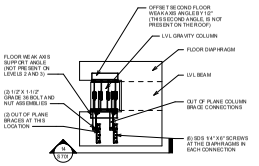

Gravity Column Out of Plane Bracing Plan
View
3/4" = 1'-0"

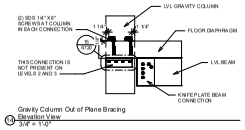

Gravity Column Out of Plane Bracing
Elevation View
3/4" = 1'-0"

4/5/2023 9:18:41 AM

F:\10 Story CLT\Revit Files\10 Story Test 03-25-2023.rvt

NHERI
TallWood

1500 Illinois St.
Golden, CO 80401
303-273-3932

PROJECT:

10-Story Test

10201 Pomerado Road
San Diego, CA 92131

SET ISSUANCE:

DATE ISSUED:

No.	Description	Date

SHEET SIZE: 30x42
DRAWN BY: ANB

SHEET:

Simpson Gravity Details

S701

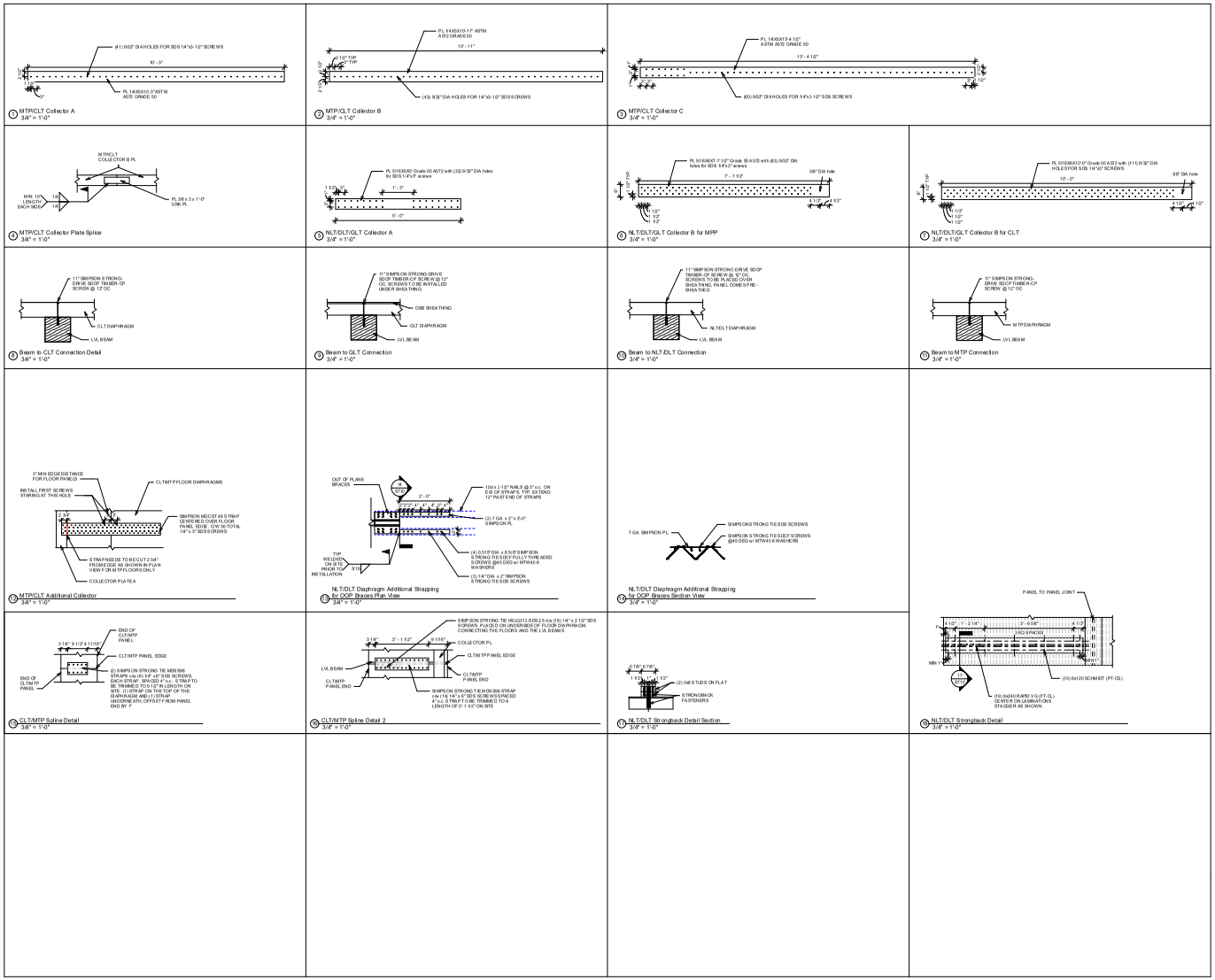

NHERI TallWood

1500 Illinois St.
Golden, CO 80401
303-273-3932

PROJECT:

10-Story Test

10201 Pomerado Road
San Diego, CA 92131

SET ISSUANCE:

DATE ISSUED:

No.	Description	Date

SHEET SIZE - 30x42
DRAWN BY: ANB

SHEET:

Diaphragm Details

S710

4/5/2023 9:18:42 AM

F:\10 Story CLT\Revit Files\10 Story Test 03-25-2023.rvt

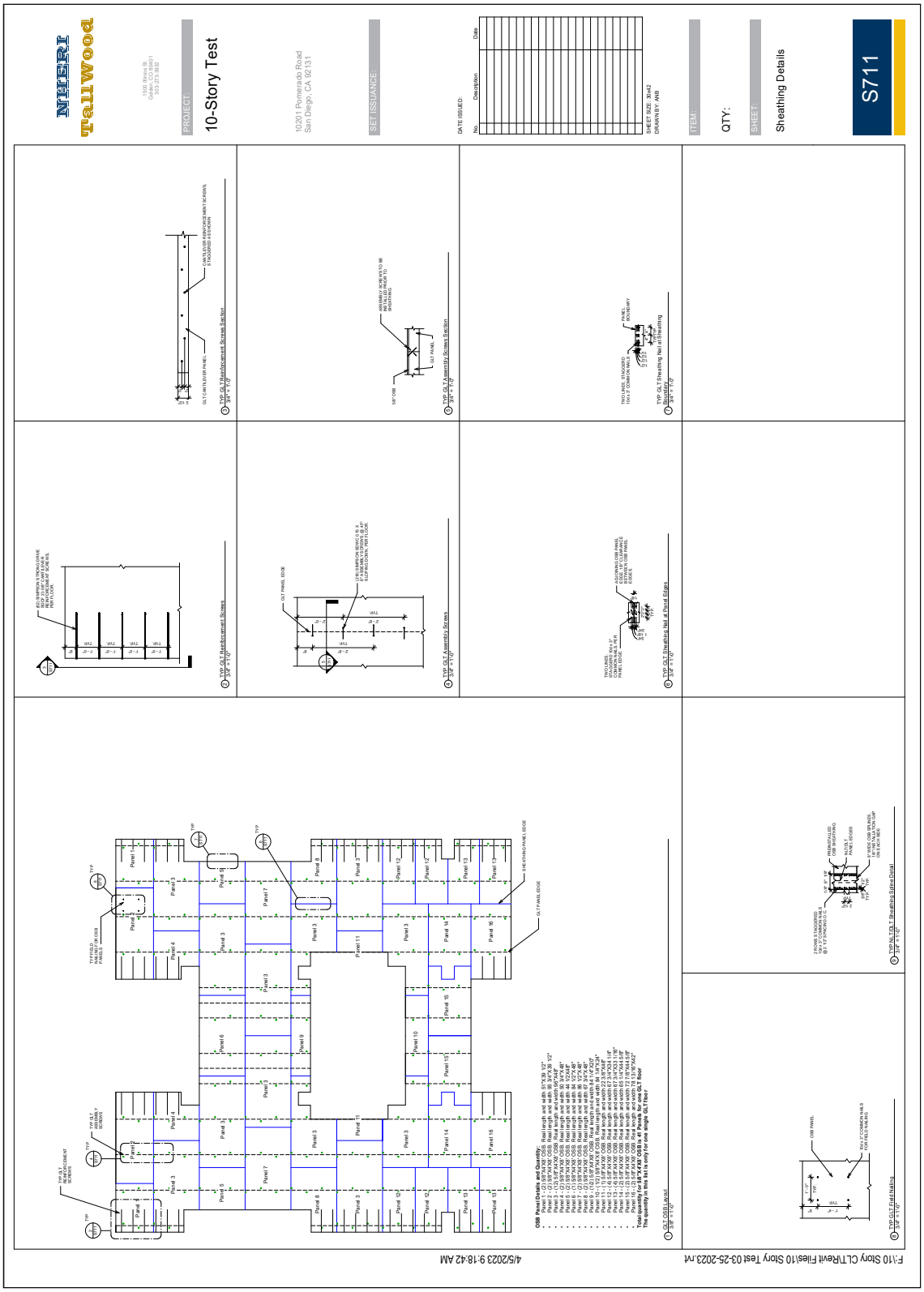
MIBRI
Tallwood
PROJECT:
10-Story Test
10201 Pomerado Road
San Diego, CA 92131
SET ISSUANCE:
DATE ISSUED:
No. Description Date
SHEET SIZE: 30x42
DRAWN BY: ANB
ITEM:
QTY:
SHEET:
Sheathing Details
S711
OSB Panel Details and Quantity:
Panel 1 - (2) 3/8"X4'X8' OSB; Real length and width: 51"X39 1/2"
Panel 2 - (1) 3/8"X4'X8' OSB; Real length and width: 39"X39 1/2"
Panel 3 - (13) 6'4"X4'X8' OSB; Real length and width: 80"X48"
Panel 4 - (2) 3/8"X4'X8' OSB; Real length and width: 80"X22 1/2"
Panel 5 - (2) 3/8"X4'X8' OSB; Real length and width: 44 1/2"X48"
Panel 6 - (1) 3/8"X4'X8' OSB; Real length and width: 80 1/2"X48"
Panel 7 - (1) 3/8"X4'X8' OSB; Real length and width: 80 1/2"X 48"
Panel 8 - (2) 3/8"X4'X8' OSB; Real length and width: 80"X 44 1/2"
Panel 9 - (2) 3/8"X4'X8' OSB; Real length and width: 80"X 34"X 48"
Panel 10 - (2) 3/8"X4'X8' OSB; Real length and width: 80"X 24"X 48"
Panel 11 - (10) 3/8"X4'X8' OSB; Real length and width: 94 1/4"X 48"
Panel 12 - (4) 5/8"X4'X8' OSB; Real length and width: 81 3/4"X94 1/4"
Panel 13 - (4) 5/8"X4'X8' OSB; Real length and width: 81 3/4"X44 5/8"
Panel 14 - (2) 5/8"X4'X8' OSB; Real length and width: 81 1/4"X44 5/8"
Panel 15 - (2) 5/8"X4'X8' OSB; Real length and width: 81 1/4"X24 5/8"
Panel 16 - (2) 5/8"X4'X8' OSB; Real length and width: 73 3/8"X42"
Total quantity in this list is only for one single GLT floor
The quantity in this list is only for one single GLT floor
SET OSB Layout
TYP GLT Sheathing Nail at Panel Edges
TYP GLT Sheathing Nail at Boundary
TYP GLT Assembly Screws Section
TYP GLT Reinforcement Screws Section
TYP GLT Reinforcement Screws
TYP GLT Assembly Screws
TYP GLT Sheathing Nailing Section
TYP OSB Panelizing
F:\10 Story CLT\Revit Files\10 Story Test 03-25-2023.rvt
4/5/2023 9:18:42 AM

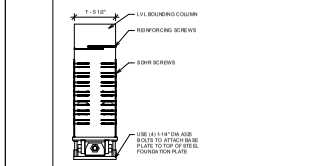

Simpson Bounding Column Steel Foundation Base Connection Elevation View
1 3/4" = 1'-0"

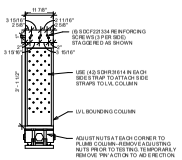

Simpson Bounding Column Steel Foundation Base Connection Elevation View
2 3/4" = 1'-0"

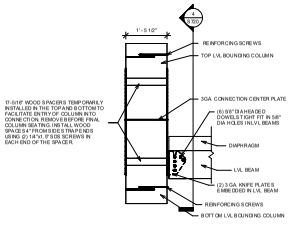

Simpson Bounding Column Splice Connection Elevation View
3 3/4" = 1'-0"

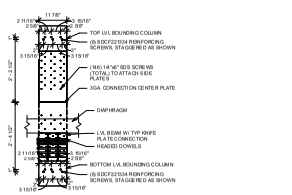

Simpson Bounding Column Splice Connection Section View
4 3/4" = 1'-0"

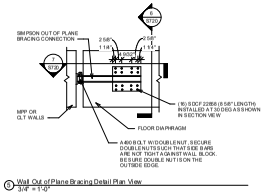

Wall Out of Plane Bracing Detail Plan View
5 3/4" = 1'-0"

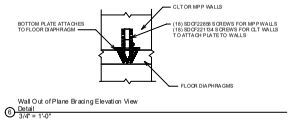

Wall Out of Plane Bracing Elevation View Detail
6 3/4" = 1'-0"

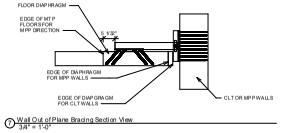

Wall Out of Plane Bracing Section View
7 3/4" = 1'-0"

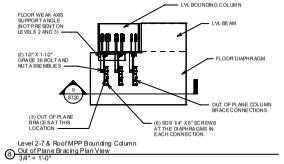

Level 2-7 & Roof MPP Bounding Column Out of Plane Bracing Plan View
8 3/4" = 1'-0"

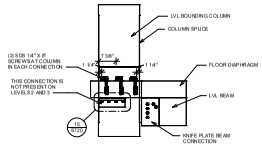

Level 2-7 & Roof MPP Bounding Column Out of Plane Bracing Elevation View
9 3/4" = 1'-0"

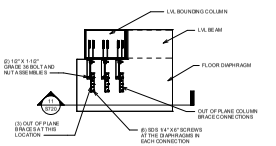

Level 2-7 & Roof CLT Bounding Column Out of Plane Bracing Plan View
10 3/4" = 1'-0"

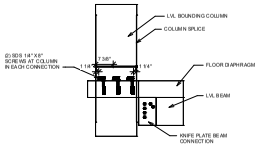

Level 2-7 & Roof CLT Bounding Column Out of Plane Bracing Elevation View
11 3/4" = 1'-0"

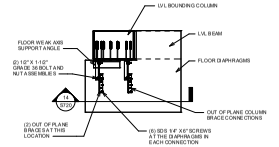

Level 8-10 MPP Bounding Column Out of Plane Bracing Plan View
12 3/4" = 1'-0"

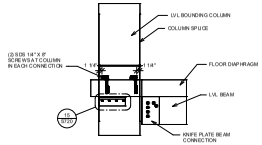

Level 8-10 MPP Bounding Column Out of Plane Bracing Elevation View
13 3/4" = 1'-0"

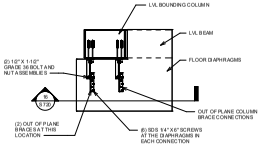

Level 8-10 CLT Bounding Column Out of Plane Bracing Plan View
14 3/4" = 1'-0"

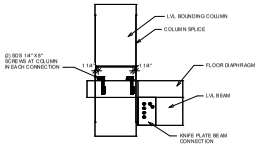

Level 8-10 CLT Bounding Column Out of Plane Bracing Elevation View
15 3/4" = 1'-0"

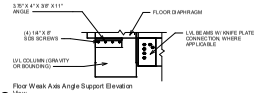

Floor Weak Axis Angle Support Elevation View
16 3/4" = 1'-0"

4/5/2023 9:18:44 AM

F:\10 Story CLT\Revit Files\10 Story Test 03-25-2023.rvt

NHERI TallWood

1500 Illinois St.
Golden, CO 80401
303-273-3932

PROJECT:

10-Story Test

10201 Pomerado Road
San Diego, CA 92131

SET ISSUANCE:

DATE ISSUED:

No.	Description	Date

SHEET SIZE: 30x42
DRAWN BY: ANB

SHEET:

Simpson Lateral Details

S720

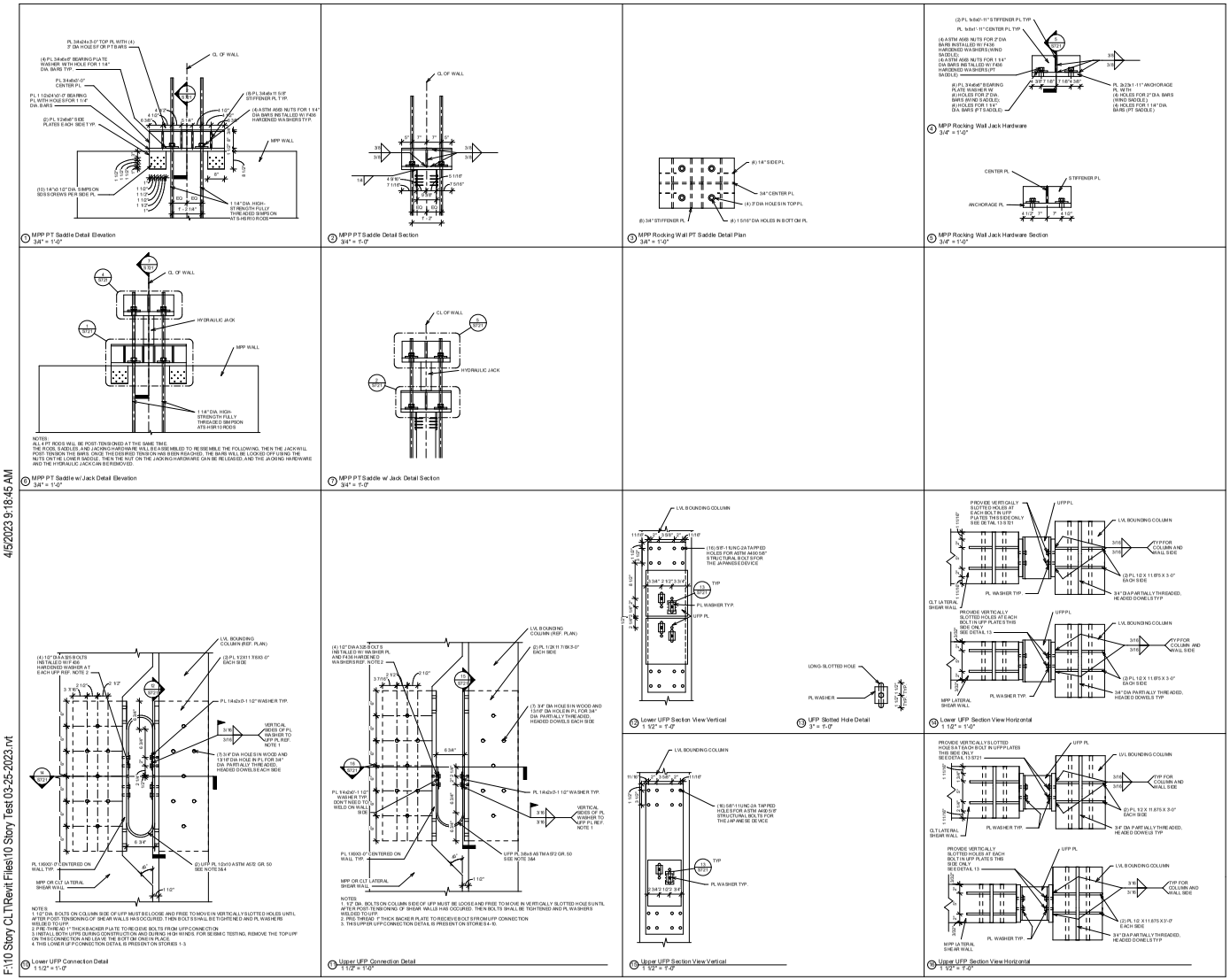

4/5/2023 9:18:45 AM

F:\10 Story CLT\Revit Files\10 Story Test 03-25-2023.rvt

NHERI TallWood

1500 Illinois St.
Golden, CO 80401
303-273-3932

PROJECT:

10-Story Test

10201 Pomerado Road
San Diego, CA 92131

SET ISSUANCE:

DATE ISSUED:

No.	Description	Date

SHEET SIZE: 30x42
DRAWN BY: ANB & SJW

ITEM:

QTY:

SHEET:

Lateral Details

S721

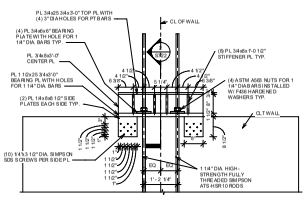

1 CLT PT Saddle Detail Elevation
3/4" = 1'-0"

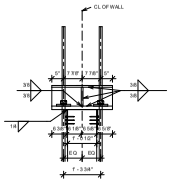

2 CLT PT Saddle Detail Section
3/4" = 1'-0"

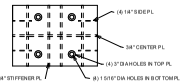

3 CLT Rocking Wall PT Saddle Detail Plan
3/4" = 1'-0"

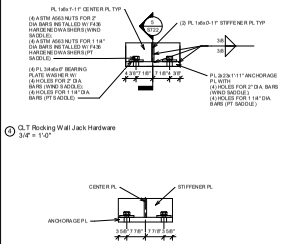

4 CLT Rocking Wall Jack Hardware
3/4" = 1'-0"

5 CLT Rocking Wall Jack Hardware Section
3/4" = 1'-0"

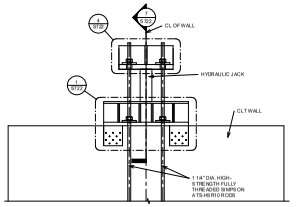

NOTES
ALL 4 PT RODS WILL BE POST-TENSIONED AT THE SAME TIME.
THE RODS, SHOES, AND JACKING HARDWARE WILL BE ASSEMBLED TO RESEMBLE THE FOLLOWING, THEN THE JACKING IS POST-TENSION THE BARS. ONCE THE DESIRED TENSION HAS BEEN REACHED, THE BARS WILL BE LOCKED OFF AT THE TOP OF THE WALL AND THE JACKING HARDWARE CAN BE RELEASED. AND THE JACKING HARDWARE AND THE HYDRAULIC JACK CAN BE REMOVED.

6 CLT PT Saddle w/ Jack Detail Elevation
3/4" = 1'-0"

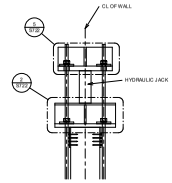

7 CLT PT Saddle w/ Jack Detail Section
3/4" = 1'-0"

NHERI
TallWood
1500 Illinois St.
Golden, CO 80401
303-273-3932

PROJECT:

10-Story Test

10201 Pomerado Road
San Diego, CA 92131

SET ISSUANCE:

DATE ISSUED:

No.	Description	Date

SHEET SIZE: 30x42
DRAWN BY: ANB & SJW

ITEM:

QTY:

SHEET:

Lateral Details

S722

4/5/2023 9:18:45 AM

F:\10 Story CLT\Revit Files\10 Story Test 03-25-2023.rvt

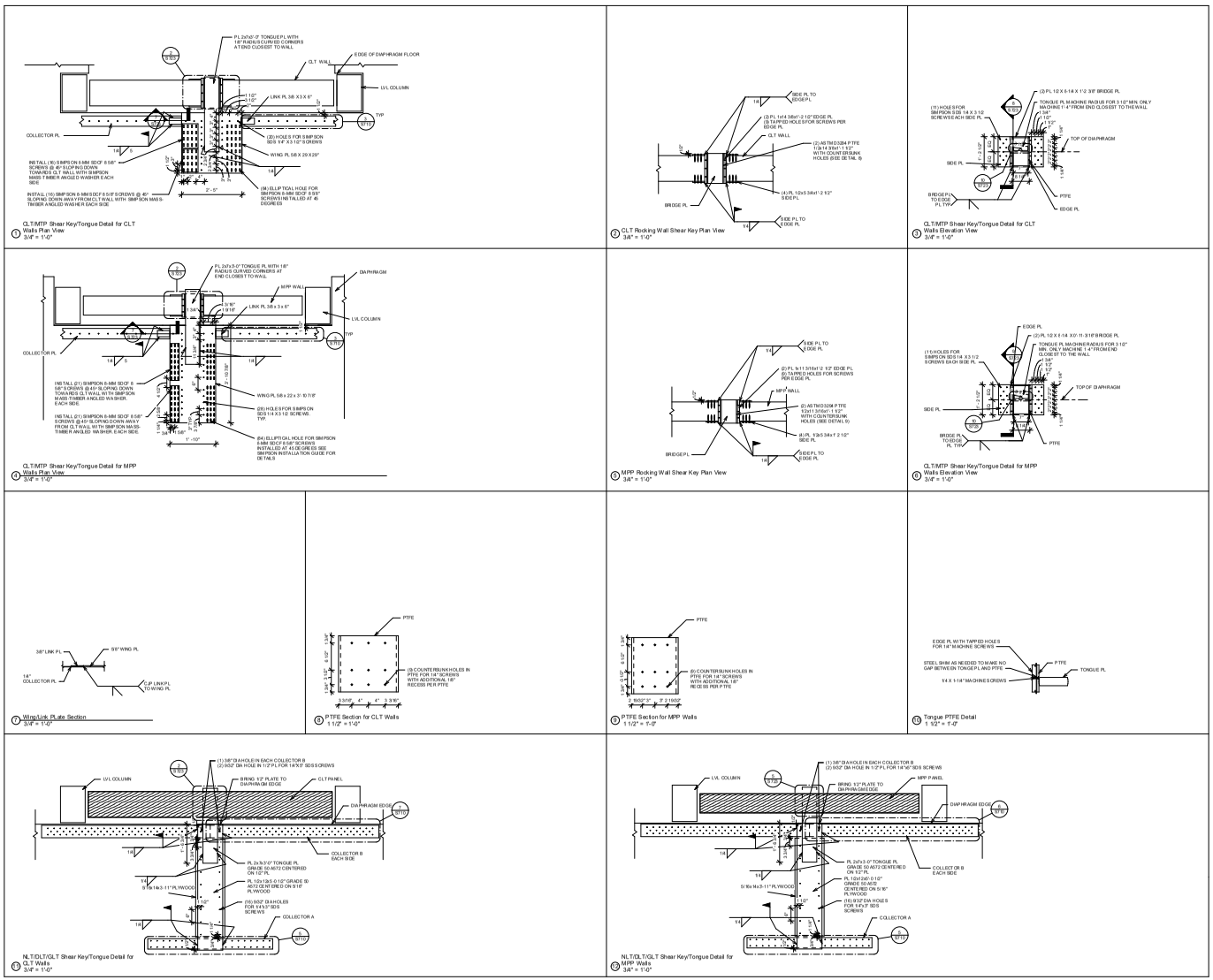

4/5/2023 9:18:46 AM

F:\10 Story CLT\Revit Files\10 Story Test 03-25-2023.rvt

NHERI TallWood

1500 Illinois St.
Golden, CO 80401
303-273-3932

PROJECT:

10-Story Test

10201 Pomerado Road
San Diego, CA 92131

SET ISSUANCE:

DATE ISSUED:

No.	Description	Date

SHEET SIZE: 30x42
DRAWN BY: ANB & SJW

ITEM:

QTY:

SHEET:

Diaphragm to Wall Lateral Details

S723

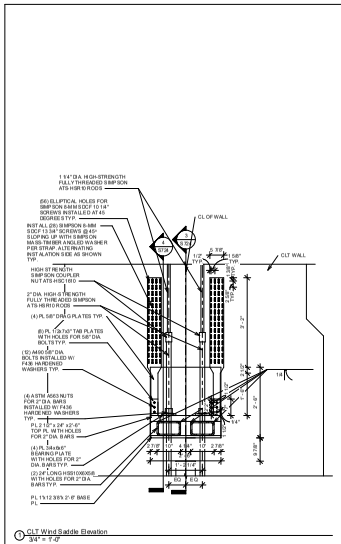

1 CLT Wind Saddle Elevation
3/4" = 1'-0"

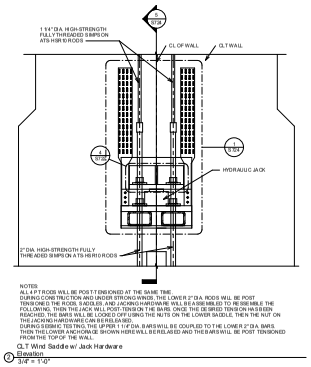

NOTES
ALL PT RODS WILL BE POST-TENSIONED AT THE SAME TIME DURING CORE ERECTION AND UNDER STRONG WINDS. THE LOWER 2" DIA. RODS WILL BE POST-TENSIONED TO THE ROOF. SADDLES AND JACKING HARDWARE WILL BE ASSEMBLED TO RESEMBLE THE FOLLOWING. THEN THE JACK WILL POST-TENSION THE BARS. ONCE THE DESIRED TENSION HAS BEEN REACHED, THE BARS WILL BE LOCKED OFF USING THE NUTS ON THE LOWER SADDLE. THEN THE NUT ON THE JACKING HARDWARE CAN BE RELEASED.
DURING SEISMIC TESTING, THE UPPER 1 1/4" DIA. BARS WILL BE COUPLED TO THE LOWER 2" DIA. BARS. THEN THE LOWER ANCHORAGE SHOWN HERE WILL BE RELEASED AND THE BARS WILL BE POST-TENSIONED FROM THE TOP OF THE WALL.

2 CLT Wind Saddle w/ Jack Hardware Elevation
3/4" = 1'-0"

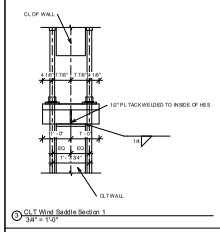

3 CLT Wind Saddle Section 1
3/4" = 1'-0"

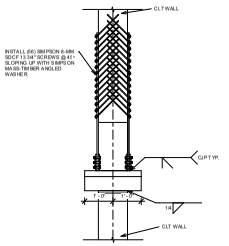

4 CLT Wind Saddle Section 2
3/4" = 1'-0"

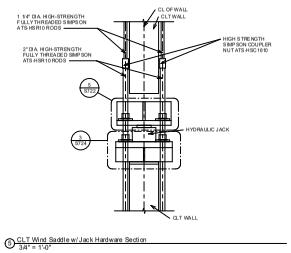

5 CLT Wind Saddle w/ Jack Hardware Section
3/4" = 1'-0"

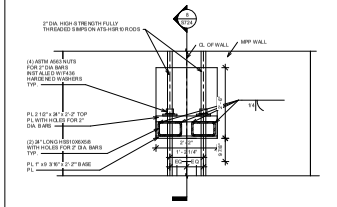

6 MPP Wind Saddle Elevation
3/4" = 1'-0"

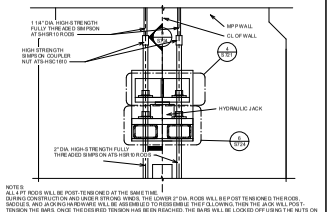

NOTES
ALL PT RODS WILL BE POST-TENSIONED AT THE SAME TIME DURING CONSTRUCTION AND UNDER STRONG WINDS. THE LOWER 2" DIA. RODS WILL BE POST-TENSIONED TO THE RODS. SADDLES AND JACKING HARDWARE WILL BE ASSEMBLED TO RESEMBLE THE FOLLOWING. THEN THE JACK WILL POST-TENSION THE BARS. ONCE THE DESIRED TENSION HAS BEEN REACHED, THE BARS WILL BE LOCKED OFF USING THE NUTS ON THE LOWER SADDLE. THEN THE NUT ON THE JACKING HARDWARE CAN BE RELEASED.
DURING SEISMIC TESTING, THE UPPER 1 1/4" DIA. BARS WILL BE COUPLED TO THE LOWER 2" DIA. BARS. THEN THE LOWER ANCHORAGE SHOWN HERE WILL BE RELEASED AND THE BARS WILL BE POST-TENSIONED FROM THE TOP OF THE WALL.

7 MPP Wind Saddle w/ Jack Hardware Elevation
3/4" = 1'-0"

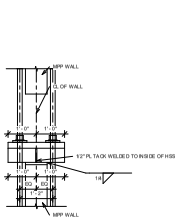

8 MPP Wind Saddle Section
3/4" = 1'-0"

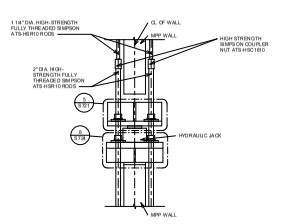

9 MPP Wind Saddle w/ Jack Hardware Section
3/4" = 1'-0"

F:\10 Story CLT\Revit Files\10 Story Test.03-25-2023.rvt
4/5/2023 9:18:47 AM

NHERI TallWood

1500 Illinois St.
Golden, CO 80401
303-273-3932

PROJECT:

10-Story Test

10201 Pomerado Road
San Diego, CA 92131

SET ISSUANCE:

DATE ISSUED:

No.	Description	Date

SHEET SIZE: 30x42
DRAWN BY: ANB & SJW

ITEM:

QTY:

SHEET:

Rocking Wall Wind Details

S724

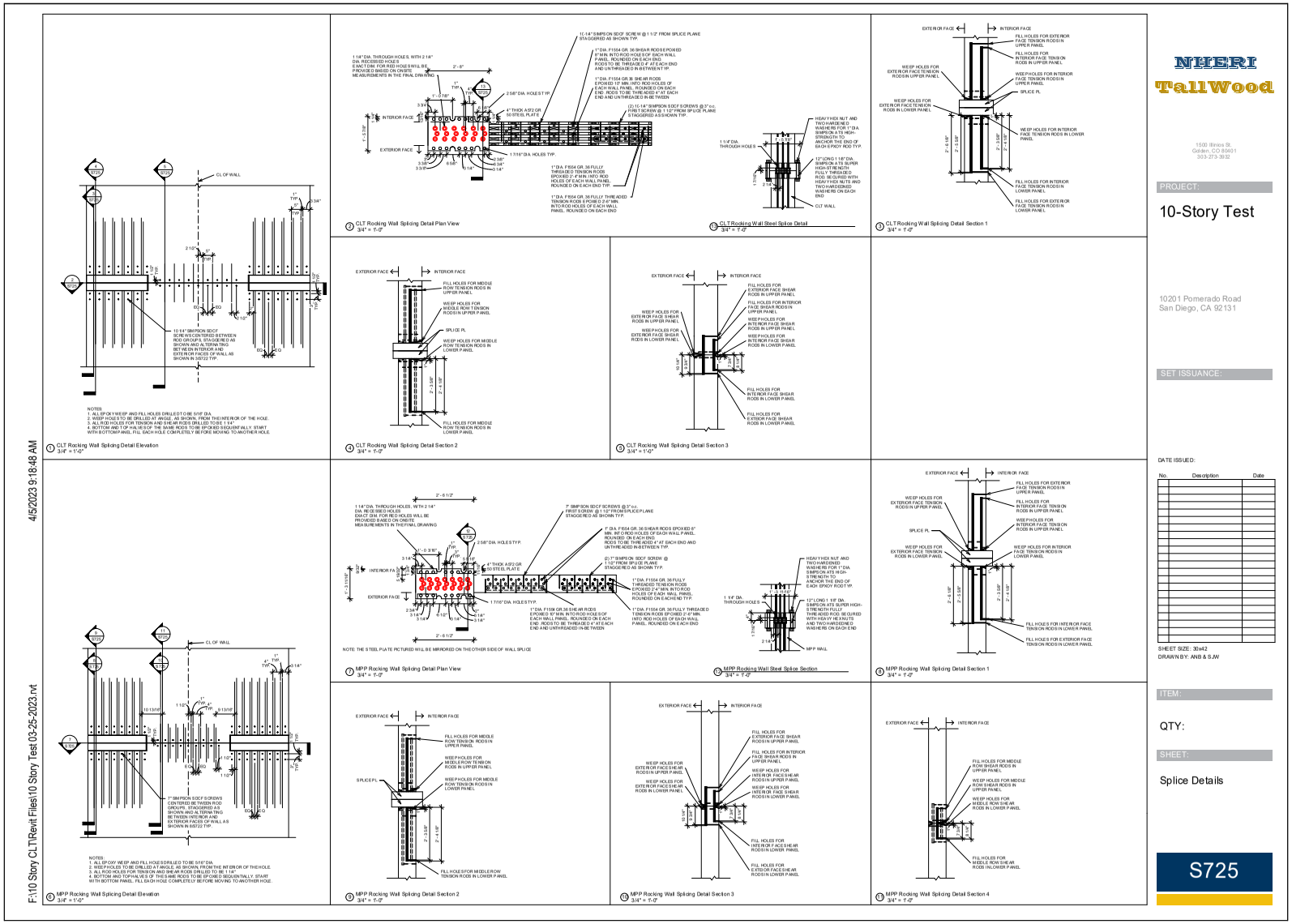

F:\10 Story CLT\Revit Files\10 Story Test 03-25-2023.rvt 4/5/2023 9:18:48 AM

NHERI TallWood
1500 Illinois St.
Golden, CO 80401
303-273-3932

PROJECT:

10-Story Test

10201 Pomerado Road
San Diego, CA 92131

SET ISSUANCE:

DATE ISSUED:

No.	Description	Date

SHEET SIZE: 30x42
DRAWN BY: ANB & SJW

ITEM:

QTY:

SHEET:

Splice Details

S725

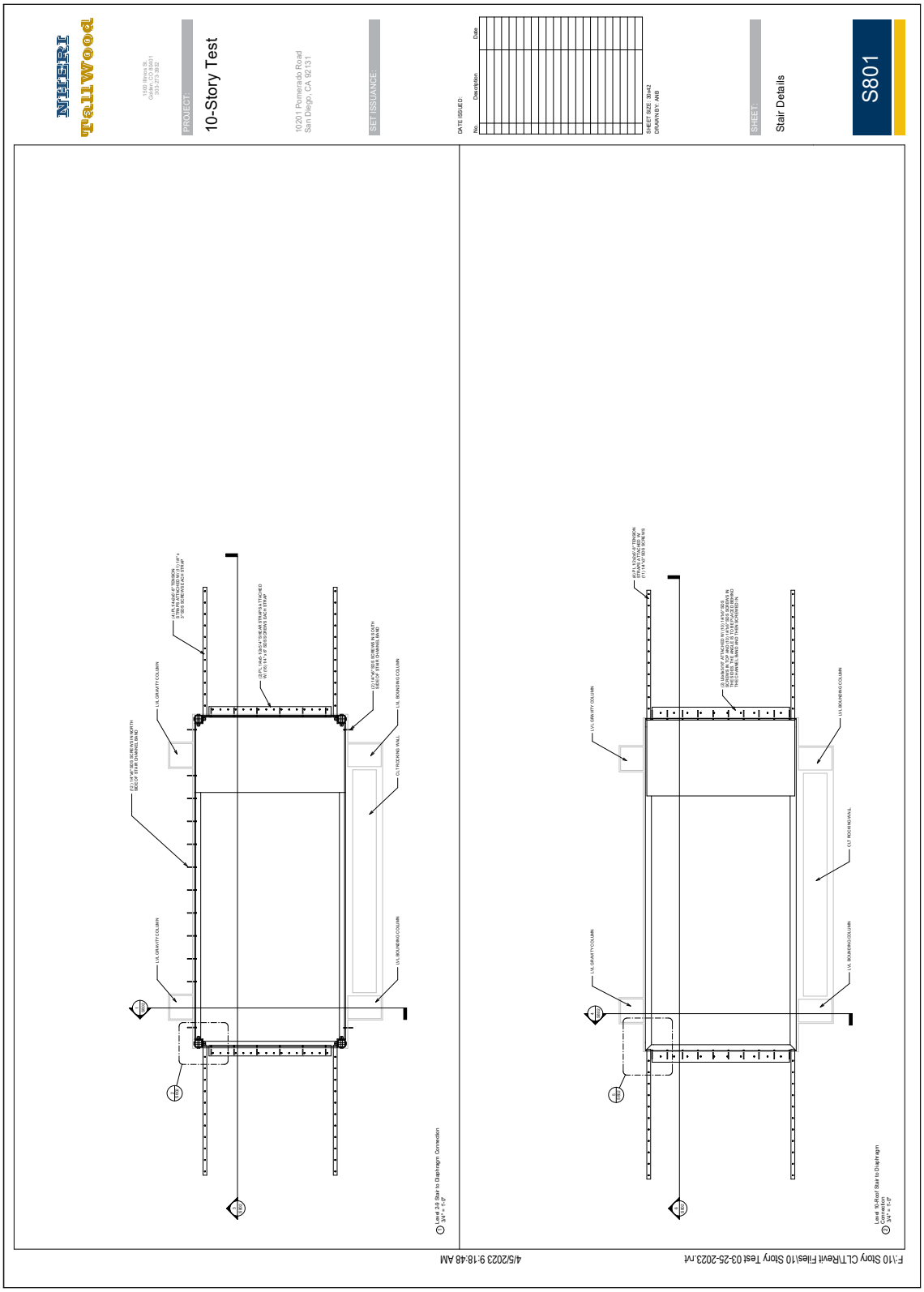
MIBRI
TallWood
1960 Illinois St
Golden, CO 80401
303-273-3602
PROJECT:
10-Story Test
10201 Pomerado Road
San Diego, CA 92131
SET ISSUANCE:
DATE ISSUED:
No. Description Date
SHEET SIZE: 30x42
DRAWN BY: ANB
SHEET:
Stair Details
S801
Level 10 Stair to Diaphragm Connection
3/4" = 1'-0"
Level 10-Roof Stair to Diaphragm Connection
3/4" = 1'-0"
4/5/2023 9:18:48 AM
F:\10 Story CLT\Revit Files\10 Story Test 03-25-2023.rvt

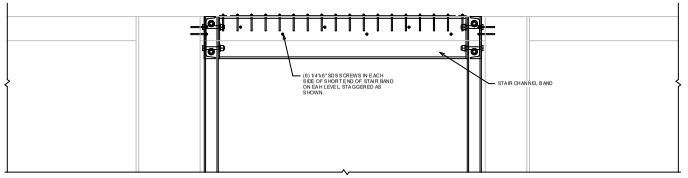

Level 2-9 Stair to Diaphragm Connection
Section 1
3/4" = 1'-0"

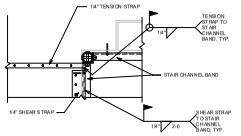

Level 3-9 Stair to Diaphragm Connection
Detail
3/4" = 1'-0"

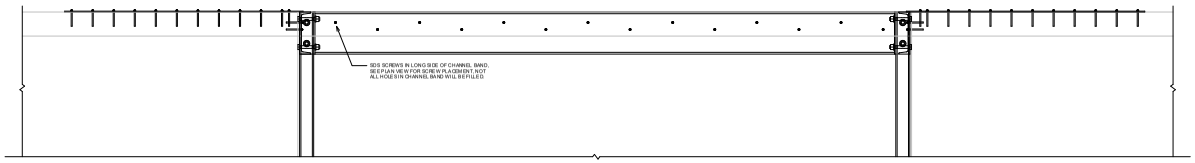

Level 2-9 Stair to Diaphragm Connection
Section 2
3/4" = 1'-0"

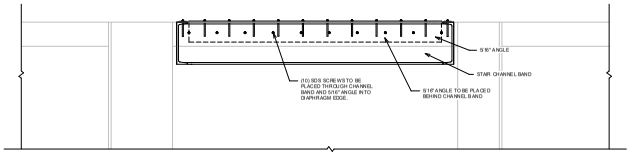

Level 10-Roof Stair to Diaphragm
Connection Section 1
3/4" = 1'-0"

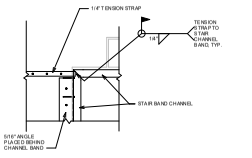

Level 10-Roof Stair to Diaphragm
Connection Detail 1
3/4" = 1'-0"

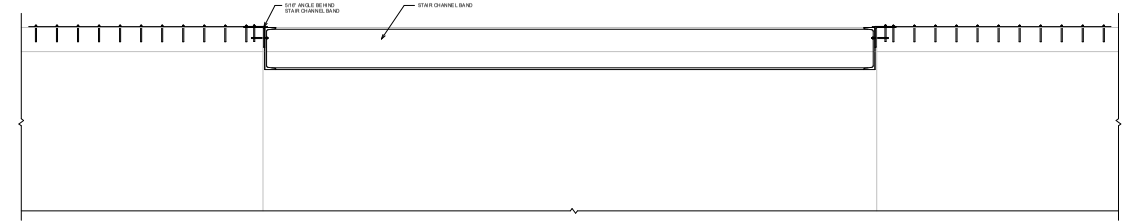

Level 10-Roof Stair to Diaphragm
Connection Section 2
3/4" = 1'-0"

F:\10 Story CLT\Revit Files\10 Story Test.03-25-2023.rvt

4/5/2023 9:18:48 AM

NHERI
TallWood

1500 Illinois St.
Golden, CO 80401
303-273-3932

PROJECT:

10-Story Test

10201 Pomerado Road
San Diego, CA 92131

SET ISSUANCE:

DATE ISSUED:

No.	Description	Date

SHEET SIZE: 30x42
DRAWN BY: ANB

ITEM:

QTY:

SHEET:

Stair Details

S802

Appendix C

PHASE 1 TESTING PLAN FOR THE NHERI TALLWOOD 10-STORY TEST SPECIMEN

This appendix lists the full testing plan executed on Phase 1 of the NHERI TallWood tests. Table C.1 summarizes all the tests completed for Phase 1 (including both the official and unofficial tests). As shown in the table, the first three days of testing (April 20th, 27th, and 28th of 2023) were all apart of table tuning and pre-testing. During this period, the shake table facility and the shake table manufactures ran multiple ground motion tests and white noise tests to test the operation of the shake table and explore different correction and tuning methods to get the best possible performance from the shake table considering the response of the building on the table. These were all small shaking ground motions that did not result in any damage. The following four days of testing (May 1st, 2nd, 3rd, and 4th of 2023) were intended to be the official start of the Phase 1 testing sequence; however, it was later discovered that the DAQs were not properly synced. Data is available for and days preceding May 5th, 2023, however, the instrument recordings are out of phase. Any tests completed prior to May 5th, 2023 were considered unofficial tests. During these days of testing no major structural damage was observed. Once the DAQ syncing issue was identified and resolved, the Phase 1 testing sequence was re-started on May 5th, 2023. For the context of this document, official testing began on May 5th, 2023 as this is when reliable instrumentation data is available.

In Table C.1 the columns outline the following information:

- Date: Date in which the tests were complete.
- Test ID: Identification number. The white noise tests were not given a unique identification number as they were not studied in detail within this document.

Additionally, ground motion tests prior to May 5th, 2023 were also not given unique identification numbers as data was not properly collected for these tests and were thus not studied in detail within this document. Ground motion tests within the official testing sequence are numbered by their hazard level, followed by a sequential number for that hazard level.

- Hazard Level: Hazard level for which the ground motion test falls under. White noise tests are not included within a hazard level.
- Dir.: Direction the ground motion test or white noise test were executed. X direction is East-West. Y direction is North-South. Z direction is vertical.
- EQ Source: Earthquake source the ground motion test motion corresponds to.
- Suite #: Number corresponding the the design ground motion suite number for referencing more detailed information about the executed ground motion. See Tables 6.11 and 6.12.
- Earthquake Name: Name of the earthquake ground motion.
- Scale Factor: Target ground motion scale factor in the horizontal and vertical directions. If both X and Y components were run, the scale factors in the X and Y directions were always equal.
- UCSD MID: Motion identification number used by the UCSD shake table facility to number the ground motion records for data saving purposes.
- Run Time: Approximate start and end times of each ground motion recording on the date specified. For motions with no times listed, the time was not recorded.

In general, ground motions increase in hazard level throughout the testing sequence. For most motions, the ground motion was run first in the X direction, then the Y direction, then the X and Y directions, followed by all three components. This was done to study the performance of the building in each direction individually. Each MCE_R was only run once with all components to reduce the amount of stress put on the lateral system and preserve the integrity of the building for the tests after Phase 1.

As shown in Table C.1, all horizontal scale factors for the ground motion tests in the test sequence are equal to the target scale factors listed in Table 7.1. However, vertical target scale factors in the test sequence did not always equal the target scale factors listed in Table 7.1. Because the performance of the nonstructural elements under vertical excitation were unknown, some of the vertical ground motions were first run at 50% of the scale factor listed in Table 7.1 to minimize the possibility of unexpected damage from the vertical motions.

May 9th, 2023 was a designated day for media viewing. For this day 475-year return period motions were run to reduce the possibly of damage occurring and at least one United States ground motion recording was desired. The 475-year return period design suite does not contain any well known earthquake recordings from the United States, thus ground motion #4 from the 975-year return period design suite motions, scaled down to match the 475-year return period hazard level. This ground motion is from the well known 1994 Northridge Earthquake in California. In total, this 475-year return period motion that is not from the original suite of design motions was run 6 times (noted by the single asterisk in the Suite # column in Table C.1).

With the exception of two ground motion tests, all tests corresponded to a defined hazard level and ground motion listed in Table 7.1 (noted with double asterisks in the hazard level column). The first exception is the second ground motion test on April 4th, 2023. This ground motion was run at a scale factor of twice the 43-year RP hazard scale factor. The second exception is the first ground motion test on May 18th, 2023. During this test, the shake table was not under full pressure and thus ran at an unknown scale factor.

Table C.1: 10-Story ground motion testing sequence

Date	Test ID	Hazard Level	Dir.	EQ Source	Suite #	Earthquake Name	Scale Factor Horiz.	Scale Factor Vert.	UCSD MID	Run Time Start	Run Time End
Table Tuning and Pre-Testing											
4/20/2023	WN	-	X	-	-	-	-	-	-	-	-
	WN	-	Y	-	-	-	-	-	-	-	-
	-	43	X	Intraslab	11	Ferndale	0.525	0	1	-	-
	WN	-	X	-	-	-	-	-	-	-	-
	WN	-	Y	-	-	-	-	-	-	-	-
	-	NA**	X	Intraslab	11	Ferndale	1.05	0	2	-	-
	WN	-	X	-	-	-	-	-	-	-	-
	WN	-	Y	-	-	-	-	-	-	-	-
	-	43	XY	Intraslab	11	Ferndale	0.525	0	3	-	-
	WN	-	X	-	-	-	-	-	-	-	-
	WN	-	Y	-	-	-	-	-	-	-	-
	-	43	XY	Intraslab	11	Ferndale	0.525	0	4	-	-
	WN	-	X	-	-	-	-	-	-	-	-
	WN	-	Y	-	-	-	-	-	-	-	-
	-	43	XY	Intraslab	11	Ferndale	0.525	0	7	-	-
	-	43	XY	Intraslab	11	Ferndale	0.525	0	7	-	-
	-	43	XY	Intraslab	11	Ferndale	0.525	0	8	-	-
	-	43	XY	Intraslab	11	Ferndale	0.525	0	9	-	-
	-	43	XY	Intraslab	11	Ferndale	0.525	0	10	-	-
	-	43	XY	Intraslab	11	Ferndale	0.525	0	11	-	-
	WN	-	X	-	-	-	-	-	-	-	-
	WN	-	Y	-	-	-	-	-	-	-	-
4/27/2023	WN	-	X	-	-	-	-	-	-	-	-
	WN	-	X	-	-	-	-	-	-	-	-
	WN	-	Y	-	-	-	-	-	-	-	-

continued . . .

. . . continued

Date	Test ID	Hazard Level	Dir.	EQ Source	Suite #	Earthquake Name	Scale Factor Horiz.	Scale Factor Vert.	UCSD MID	Run Time Start	Run Time End
	WN	-	X	-	-	-	-	-	-	-	-
	WN	-	Y	-	-	-	-	-	-	-	-
4/28/2023	-	225	XY	Intraslab	11	Ferndale	1.684	0	12	-	-
	WN	-	X	-	-	-	-	-	-	-	-
	WN	-	Y	-	-	-	-	-	-	-	-
Start of Phase 1 Testing Sequence: DAQ not Working											
	WN	-	X	-	-	-	-	-	-	14:08:25	14:09:55
	WN	-	Y	-	-	-	-	-	-	14:12:10	14:13:50
	-	43	X	Intraslab	11	Ferndale	0.525	0	13	14:17:55	14:19:20
	-	43	Y	Intraslab	11	Ferndale	0.525	0	14	14:21:35	14:23:15
	-	43	XY	Intraslab	11	Ferndale	0.525	0	15	14:26:00	14:27:45
	-	43	X	Interface	6	Tohoku	0.253	0	16	15:33:45	14:36:10
	-	43	Y	Interface	6	Tohoku	0.253	0	17	15:05:00	15:07:25
	-	43	XY	Interface	6	Tohoku	0.253	0	18	15:10:10	15:12:35
	-	43	X	Crustal	3	Niigata, Japan	0.246	0	19	15:15:25	15:16:55
	-	43	Y	Crustal	3	Niigata, Japan	0.246	0	20	15:19:10	15:20:45
5/1/2023	-	43	XY	Crustal	3	Niigata, Japan	0.246	0	21	15:25:05	15:27:00
	WN	-	X	-	-	-	-	-	-	15:29:25	15:30:55
	WN	-	Y	-	-	-	-	-	-	15:32:30	15:34:00
	-	43	XYZ	Intraslab	11	Ferndale	0.525	0.525	22	15:50:45	15:52:20
	WN	-	X	-	-	-	-	-	-	15:54:25	15:56:00
	WN	-	Y	-	-	-	-	-	-	15:58:20	15:59:50
	-	225	X	Intraslab	11	Ferndale	1.684	0	23	16:02:50	16:04:15
	-	225	Y	Intraslab	11	Ferndale	1.684	0	24	16:06:30	16:08:00
	WN	-	X	-	-	-	-	-	-	-	-
	WN	-	Y	-	-	-	-	-	-	-	-

continued . . .

. . . continued

Date	Test ID	Hazard Level	Dir.	EQ Source	Suite #	Earthquake Name	Scale Factor Horiz.	Scale Factor Vert.	UCSD MID	Run Time Start	Run Time End
5/2/2023	WN	-	X	-	-	-	-	-	-	10:39:15	10:40:55
	WN	-	Y	-	-	-	-	-	-	10:42:40	10:44:15
	-	225	XY	Intraslab	11	Ferndale	1.684	0	35	10:47:45	10:49:25
	-	225	X	Interface	6	Tohoku	0.812	0	26	11:18:15	11:20:30
	-	225	Y	Interface	6	Tohoku	0.812	0	27	11:23:15	11:25:35
	-	225	XY	Interface	6	Tohoku	0.812	0	28	11:28:20	11:30:40
	WN	-	X	-	-	-	-	-	-	11:36:05	11:38:20
	WN	-	Y	-	-	-	-	-	-	11:40:05	11:41:40
	-	225	X	Crustal	3	Niigata, Japan	0.79	0	29	13:43:35	13:45:00
	-	225	Y	Crustal	3	Niigata, Japan	0.79	0	30	13:47:05	13:48:30
	-	225	XY	Crustal	3	Niigata, Japan	0.79	0	31	13:51:15	13:52:50
	WN	-	X	-	-	-	-	-	-	13:56:00	13:57:35
	WN	-	Y	-	-	-	-	-	-	14:00:00	14:01:40
	-	475	X	Intraslab	11	Ferndale	2.524	0	32	14:56:30	14:58:40
	-	475	Y	Intraslab	11	Ferndale	2.524	0	33	15:01:35	15:03:15
	-	475	XY	Intraslab	11	Ferndale	2.524	0	34	15:06:15	15:07:50
	WN	-	X	-	-	-	-	-	-	15:10:50	15:12:35
	WN	-	Y	-	-	-	-	-	-	15:14:25	15:15:55
5/3/2023	WN	-	X	-	-	-	-	-	-	10:23:25	10:25:00
	WN	-	Y	-	-	-	-	-	-	10:27:30	10:29:00
	-	475	X	Crustal	3	Chi-Chi	4.323	0	35	10:31:40	10:33:05
	-	475	Y	Crustal	3	Chi-Chi	4.323	0	36	10:35:50	10:37:15
	-	475	XY	Crustal	3	Chi-Chi	4.323	0	37	10:39:45	10:41:40
	WN	-	X	-	-	-	-	-	-	10:46:00	10:50
	WN	-	Y	-	-	-	-	-	-	10:51:05	10:52:30
	-	225	XYZ	Crustal	3	Niigata, Japan	0.79	0.79	38	15:36:50	15:39:00
	WN	-	X	-	-	-	-	-	-	-	-
	WN	-	Y	-	-	-	-	-	-	-	-

continued . . .

. . . continued

Date	Test ID	Hazard Level	Dir.	EQ Source	Suite #	Earthquake Name	Scale Factor Horiz.	Scale Factor Vert.	UCSD MID	Run Time Start	Run Time End
5/4/2023	WN	-	X	-	-	-	-	-	-	15:17:50	15:19:10
	WN	-	Y	-	-	-	-	-	-	15:21:35	15:23:30
	-	475	X	Crustal	4*	Northridge-01	2.816	0	39	15:26:00	15:27:25
	-	475	Y	Crustal	4*	Northridge-01	2.816	0	40	15:29:20	15:31
	-	475	XY	Crustal	4*	Northridge-01	2.816	0	41	15:33:20	15:34:30
	WN	-	X	-	-	-	-	-	-	15:37:55	15:39:30
	WN	-	Y	-	-	-	-	-	-	15:41:35	15:43:05
Start of Phase 1 Testing Sequence: DAQ Working											
5/5/2023	225-01	225	XY	Intraslab	11	Ferndale	1.684	0	42	-	-
	WN	-	X	-	-	-	-	-	-	-	-
	WN	-	Y	-	-	-	-	-	-	-	-
5/8/2023	WN	-	X	-	-	-	-	-	-	09:54:30	-
	WN	-	Y	-	-	-	-	-	-	09:58:25	09:59:55
	475-01	475	XYZ	Crustal	4*	Northridge-01	2.816	1.408	43	10:05:05	10:06:35
	475-02	475	XYZ	Crustal	4*	Northridge-01	2.816	2.816	44	10:13:35	10:14:50
	WN	-	X	-	-	-	-	-	-	10:18:50	-
	WN	-	Y	-	-	-	-	-	-	10:22:10	10:23:35
5/9/2023	475-03	475	XYZ	Crustal	4*	Northridge-01	2.816	2.816	45	10:31:25	10:32:30
	475-04	475	XY	Crustal	3	Chi-Chi	4.323	0	46	10:36:50	10:38:15
5/10/2023	WN	-	X	-	-	-	-	-	-	09:08:50	09:10:10
	WN	-	Y	-	-	-	-	-	-	09:11:55	09:13:15
	43-01	43	X	Intraslab	11	Ferndale	0.525	0	47	09:16:25	09:17:50
	43-02	43	Y	Intraslab	11	Ferndale	0.525	0	48	09:20:30	09:21:50
	43-03	43	XY	Intraslab	11	Ferndale	0.525	0	49	09:23:50	09:25:15
	43-04	43	X	Interface	6	Tohoku	0.253	0	50	09:29:15	09:31:30
	43-05	43	Y	Interface	6	Tohoku	0.253	0	51	09:33:25	09:35:45
	43-06	43	XY	Interface	6	Tohoku	0.253	0	52	09:37:30	09:39:45
	43-07	43	X	Crustal	3	Niigata, Japan	0.246	0	53	09:42:20	09:43:45
	43-08	43	Y	Crustal	3	Niigata, Japan	0.246	0	54	09:45:40	09:47:10

continued . . .

. . . continued

Date	Test ID	Hazard Level	Dir.	EQ Source	Suite #	Earthquake Name	Scale Factor Horiz.	Scale Factor Vert.	UCSD MID	Run Time Start	Run Time End
	43-09	43	XY	Crustal	3	Niigata, Japan	0.246	0	55	09:49:05	09:50:40
	43-10	43	XYZ	Intraslab	11	Ferndale	0.525	0.525	56	09:53:55	09:55:20
	WN	-	X	-	-	-	-	-	-	09:58:10	09:59:35
	WN	-	Y	-	-	-	-	-	-	10:01:55	10:03:25
	225-02	225	X	Intraslab	11	Ferndale	1.684	0	57	10:23:10	10:24:40
	225-03	225	Y	Intraslab	11	Ferndale	1.684	0	58	10:26:25	10:27:45
	225-04	225	XY	Intraslab	11	Ferndale	1.684	0	59	10:29:45	10:31:10
	225-05	225	X	Interface	6	Tohoku	0.812	0	60	10:34:30	10:36:40
	225-06	225	Y	Interface	6	Tohoku	0.812	0	61	10:39:40	10:41:55
	225-07	225	XY	Interface	6	Tohoku	0.812	0	62	10:44:35	00:00:00
	WN	-	X	-	-	-	-	-	-	10:50:35	10:52:05
	WN	-	Y	-	-	-	-	-	-	10:54:15	10:55:50
5/10/2023	475-05	475	X	Crustal	4*	Northridge-01	2.816	0	63	10:59:35	11:00:45
. . . continued	475-06	475	Y	Crustal	4*	Northridge-01	2.816	0	64	11:03:05	11:04:20
	475-07	475	XY	Crustal	4*	Northridge-01	2.816	0	65	11:06:35	11:07:50
	WN	-	X	-	-	-	-	-	-	11:10:55	11:12:20
	WN	-	Y	-	-	-	-	-	-	11:14:05	11:15:30
	225-08	225	X	Crustal	3	Niigata, Japan	0.79	0	66	14:11:25	14:12:45
	225-09	225	Y	Crustal	3	Niigata, Japan	0.79	0	67	14:15:20	14:16:50
	225-10	225	XY	Crustal	3	Niigata, Japan	0.79	0	68	14:18:35	14:20:00
	225-11	225	XYZ	Crustal	3	Niigata, Japan	0.79	0.79	69	14:21:55	14:23:20
	WN	-	X	-	-	-	-	-	-	14:26:15	14:27:45
	WN	-	Y	-	-	-	-	-	-	14:29:35	14:31:00
	475-08	475	X	Crustal	3	Chi-Chi	4.323	0	70	14:33:40	14:35:05
	475-09	475	Y	Crustal	3	Chi-Chi	4.323	0	71	14:38:05	14:39:30
	WN	-	X	-	-	-	-	-	-	14:42:15	14:43:40
	WN	-	Y	-	-	-	-	-	-	14:46:10	14:47:35

continued . . .

. . . continued

Date	Test ID	Hazard Level	Dir.	EQ Source	Suite #	Earthquake Name	Scale Factor Horiz.	Scale Factor Vert.	UCSD MID	Run Time Start	Run Time End
5/11/2023	WN	-	X	-	-	-	-	-	-	10:10:35	10:12:10
	WN	-	Y	-	-	-	-	-	-	10:13:40	00:00:00
	475-10	475	X	Intraslab	11	Ferndale	2.524	0	72	10:17:45	10:19:15
	475-11	475	Y	Intraslab	11	Ferndale	2.524	0	73	10:21:45	10:23:05
	475-12	475	XY	Intraslab	11	Ferndale	2.524	0	74	10:25:45	10:27:35
	475-13	475	XYZ	Intraslab	11	Ferndale	2.524	2.524	75	10:32:50	10:34:15
	WN	-	X	-	-	-	-	-	-	10:40:15	10:41:45
	WN	-	Y	-	-	-	-	-	-	10:43:25	10:45:00
	475-14	475	X	Interface	6	Tohoku	1.215	-	76	11:02:10	11:05:50
	WN	-	X	-	-	-	-	-	-	11:12:55	11:14:15
	WN	-	Y	-	-	-	-	-	-	11:17:20	11:18:40
	975-01	975	X	Crustal	4	Northridge-01	3.931	0	77	14:01:10	14:02:30
	975-02	975	Y	Crustal	4	Northridge-01	3.931	0	78	14:16:40	14:18:00
	WN	-	X	-	-	-	-	-	-	14:20:35	14:20:05
	WN	-	Y	-	-	-	-	-	-	14:23:55	14:23:20
	975-03	975	XY	Crustal	4	Northridge-01	3.931	0	79	14:38:25	14:39:25
	WN	-	X	-	-	-	-	-	-	14:42:45	14:44:10
	WN	-	Y	-	-	-	-	-	-	14:46:05	14:47:40
5/12/2023	WN	-	X	-	-	-	-	-	-	31:40:00	10:17:25
	WN	-	Y	-	-	-	-	-	-	10:19:10	10:20:30
	475-15	475	XYZ	Crustal	3	Chi-Chi	4.323	0.7	80	10:26:05	10:27:30
	475-16	475	XYZ	Crustal	3	Chi-Chi	4.323	1.4	81	10:43:00	10:44:25
	WN	-	X	-	-	-	-	-	-	10:55:10	10:56:35
	WN	-	Y	-	-	-	-	-	-	10:58:20	10:59:50
	975-04	975	X	Interface	5	Tohoku	1.696	-	82	11:29:10	11:32:55
	WN	-	X	-	-	-	-	-	-	13:51:25	13:52:50
	WN	-	Y	-	-	-	-	-	-	10:54:40	-

continued . . .

. . . continued

Date	Test ID	Hazard Level	Dir.	EQ Source	Suite #	Earthquake Name	Scale Factor Horiz.	Scale Factor Vert.	UCSD MID	Run Time Start	Run Time End
5/15/2023	WN	-	X	-	-	-	-	-	-	09:12:45	09:14:05
	WN	-	Y	-	-	-	-	-	-	09:15:45	09:17:10
	975-05	975	X	Intraslab	11	Ferndale2	3.356	0	83	09:19:10	09:20:05
	975-06	975	Y	Intraslab	11	Ferndale2	3.356	0	84	09:58:45	09:59:55
	975-07	975	XY	Intraslab	11	Ferndale2	3.356	0	85	10:11:35	10:12:55
	WN	-	X	-	-	-	-	-	-	10:15:45	10:17:10
	WN	-	Y	-	-	-	-	-	-	10:18:55	10:20:20
	975-08	975	XYZ	Crustal	4	Northridge-01	3.931	3.931	86	13:38:05	13:39:20
	WN	-	X	-	-	-	-	-	-	13:44:50	13:46:20
	WN	-	Y	-	-	-	-	-	-	13:48:15	13:50:00
5/16/2023	WN	-	X	-	-	-	-	-	-	11:03:00	11:04:45
	WN	-	Y	-	-	-	-	-	-	11:06:10	11:07:40
	975-09	975	XYZ	Intraslab	11	Ferndale2	3.356	1.257	87	11:11:05	11:12:35
	WN	-	X	-	-	-	-	-	-	11:15:20	11:17
	WN	-	Y	-	-	-	-	-	-	11:19:30	11:21:00
5/17/2023	WN	-	X	-	-	-	-	-	-	11:16:50	11:18:20
	WN	-	Y	-	-	-	-	-	-	11:20:05	11:21:40
	MCER-01	MCE_R	XYZ	Crustal	5	Loma Prieta	3.957	1.72	88	11:25:40	11:26:50
	WN	-	X	-	-	-	-	-	-	11:34:45	11:36:20
	WN	-	Y	-	-	-	-	-	-	11:38:00	11:39:20
5/18/2023	WN	-	X	-	-	-	-	-	-	11:14:25	11:15:50
	WN	-	Y	-	-	-	-	-	-	11:17:50	11:19:15
	-	NA**	XYZ	Intraslab	11	Ferndale2	-	-	89	11:21:40	11:23:10
	WN	-	X	-	-	-	-	-	-	11:25:00	11:26:40
	WN	-	Y	-	-	-	-	-	-	11:27:45	11:29:05
	WN	-	X	-	-	-	-	-	-	14:36:50	14:38:10
	WN	-	Y	-	-	-	-	-	-	14:40:00	14:41:20
	MCER-02	MCE_R	XYZ	Intraslab	11	Ferndale2	4.538	2.25	90	14:43:25	14:44:35
	WN	-	X	-	-	-	-	-	-	14:48:45	14:50:10

continued . . .

. . . continued

Date	Test ID	Hazard Level	Dir.	EQ Source	Suite #	Earthquake Name	Scale Factor Horiz.	Scale Factor Vert.	UCSD MID	Run Time Start	Run Time End
	WN	-	Y	-	-	-	-	-	-	14:52:15	14:54:05
5/18/2023	975-10	975	X	Interface	6	Tokachi	3.462	-	91	15:26:00	15:28:10
. . . continued	WN	-	X	-	-	-	-	-	-	15:36:15	15:37:35
	WN	-	Y	-	-	-	-	-	-	15:40:45	15:42:10
	WN	-	X	-	-	-	-	-	-	14:11:35	14:12:55
	WN	-	Y	-	-	-	-	-	-	14:14:40	14:16:05
	975-11	975	XYZ	Crustal	2	Victoria, Mexico	4.999	4	92	14:18:50	14:19:50
	WN	-	X	-	-	-	-	-	-	14:23:00	14:24:25
	WN	-	Y	-	-	-	-	-	-	14:25:50	14:27:20
5/19/2023	MCER-03	MCE_R	X	Interface	7	Tohoku	2.298	-	93	14:34:20	14:38:15
	WN	-	X	-	-	-	-	-	-	14:52:20	14:53:35
	WN	-	Y	-	-	-	-	-	-	14:55	-
	975-12	975	XYZ	Crustal	4	Northridge-01	3.931	3.931	94	16:29:40	16:30:50
	WN	-	X	-	-	-	-	-	-	16:36:20	16:37:40
	WN	-	Y	-	-	-	-	-	-	16:39:10	16:40:30
	WN	-	X	-	-	-	-	-	-	9:38	-
	WN	-	Y	-	-	-	-	-	-	9:41	-
	43-11	43	XYZ	Intraslab	11	Ferndale	0.525	0.525	95	9:45	-
	43-12	43	XY	Crustal	3	Niigata, Japan	0.246	0	96	9:48	-
	225-12	225	XY	Intraslab	11	Ferndale	1.684	0	97	9:52	-
5/22/2023	225-13	225	XYZ	Crustal	3	Niigata, Japan	0.79	0.79	98	9:56	-
	225-14	225	XY	Interface	6	Tohoku	0.812	0	99	10:00	-
	475-17	475	XYZ	Crustal	3	Chi-Chi	4.323	1.4	100	10:11	-
	WN	-	X	-	-	-	-	-	-	10:16	-
	WN	-	Y	-	-	-	-	-	-	10:19	-

* Motion not in 475-year return period design suite. Scaled from 975-year return period design suite.
** Motion not scaled to defined hazard level.